②

**CHEMICAL
RESEARCH,
DEVELOPMENT &
ENGINEERING
CENTER**

CRDEC-SP-010

AD-A213 370

PROCEEDINGS OF THE 1988 SCIENTIFIC CONFERENCE CONFERENCE ON OBSCURATION AND ON OBSCURATION AND AEROSOL RESEARCH

**DTIC
S ELECTE
OCT 10 1989
D D**

Elmer H. Enquist
Deborah A. Clark

BATTELLE-EDGEWOOD OPERATIONS
Edgewood, MD 21040

June 1989

**U.S. ARMY
ARMAMENT
MUNITIONS
CHEMICAL COMMAND**

89 10 10095

Disclaimer

The findings in this report are not to be construed as an official
Department of the Army position unless so designated by other authorizing
documents.

REPORT DOCUMENTATION PAGE		Form Approved OMB No. 0704-0188

1a. REPORT SECURITY CLASSIFICATION	1b RESTRICTIVE MARKINGS
UNCLASSIFIED	

2a. SECURITY CLASSIFICATION AUTHORITY	3. DISTRIBUTION/AVAILABILITY OF REPORT
	Approved for public release; distribution
2b. DECLASSIFICATION/DOWNGRADING SCHEDULE	is unlimited.

4. PERFORMING ORGANIZATION REPORT NUMBER(S)	5. MONITORING ORGANIZATION REPORT NUMBER(S)
CRDEC-SP-010	

6a. NAME OF PERFORMING ORGANIZATION	6b. OFFICE SYMBOL (If applicable)	7a. NAME OF MONITORING ORGANIZATION
Battelle-Edgewood Operations		

6c. ADDRESS (City, State, and ZIP Code)	7b. ADDRESS (City, State, and ZIP Code)
2113 Emmorton Park Road - Suite 200 Edgewood, MD 21040	

8a. NAME OF FUNDING/SPONSORING ORGANIZATION	8b. OFFICE SYMBOL (If applicable)	9 PROCUREMENT INSTRUMENT IDENTIFICATION NUMBER
CRDEC	SMCCR-RSP-B	

8c. ADDRESS (City, State, and ZIP Code)	10. SOURCE OF FUNDING NUMBERS			
	PROGRAM ELEMENT NO.	PROJECT NO.	TASK NO.	WORK UNIT ACCESSION NO
Aberdeen Proving Ground, MD 21010-5423		1C161102	A71A	

11. TITLE (Include Security Classification)

Proceedings of the 1988 Scientific Conference on Obscuration and Aerosol Research

12. PERSONAL AUTHOR(S)
Engquist, Elmer H., and Clark, Deborah A.

13a. TYPE OF REPORT	13b. TIME COVERED	14 DATE OF REPORT (Year, Month, Day)	15 PAGE COUNT
Special Publication	FROM 88 Jan TO 88 Dec	1989 June	388

16. SUPPLEMENTARY NOTATION

POC: Dr. Edward Stuebing, SMCCR-RSP-B, (301) 671-3089

17. COSATI CODES			18. SUBJECT TERMS (Continue on reverse if necessary and identify by block number)			
FIELD	GROUP	SUB-GROUP	Obscurants	Aerosols	Extinction,	Transmission
15	06		Obscuration	Aerosol	Absorption,	Infrared
			Scattering	Sizing	Smoke,	(Continued on Reverse)

19. ABSTRACT (Continue on reverse if necessary and identify by block number)

In this report, 30 papers presented at the 1988 Scientific Conference on Obscuration and Aerosol Research are included under the headings of Physical and Chemical Properties of Aerosols, Aerosol Characterization Methods, and Optical Properties of Aerosols.

20. DISTRIBUTION/AVAILABILITY OF ABSTRACT	21. ABSTRACT SECURITY CLASSIFICATION
☒ UNCLASSIFIED/UNLIMITED ☐ SAME AS RPT ☐ DTIC USERS	UNCLASSIFIED

22a. NAME OF RESPONSIBLE INDIVIDUAL	22b TELEPHONE (Include Area Code)	22c OFFICE SYMBOL
SANDRA J. JOHNSON	(301) 671-2914	SMCCR-SPS-T

DD Form 1473, JUN 86 — Previous editions are obsolete.

18. SUBJECT TERMS (continued)

Electromagnetic scattering
Millimeter wave radiation
Submillimeter wave radiation
Visible radiation
Electromagnetic waves
Spherical particles
Mie scattering
Rayleigh scattering
Raman scattering
Concentration sampling
Particle dynamics
Diffusive mixing
Aerosol growth
Nucleation,
Smoke generation
Aerosol generation
Photoionization
Conductivity
Chemical characterization
Phosphorus smoke
Fluorescence
Aerosol clusters
Spheres
Cylinders
Rough particles
Irregular particles
Nonspherical particles
Particle aggregates
Particle chains
Infrared emission
Cooperative scattering
Dependent scattering
Multiple scattering
Radiative transfer
Coagulation
Condensation
Liquid drop
Drop growth
Fog oil smoke
Diesel oil smoke
Particle mechanics
Atmospheric optics
Atmospheric dispersion
cloud dynamics
Scavenging
Aerosol collectors
Aerosol elimination
Aerosol characterization
Particle Sizing
Hygroscopic smokes
Particle size distribution
Particle orientation distribution

Optical constants
Optical properties
Anomalous diffraction
Attenuated total reflectior
Reflection spectroscopy
ATR
Far-infrared
Refractive index
Index of refraction
Inversion
Inversion techniques
Gypsum
Natural minerals
Minerals
Metal
Metallic particles
Powdered minerals
Complex refractive index
Effective media
High energy laser
Particles
Aersol particles
SERS
Surface Enhanced Raman Scattering
Dielectric particles
Conducting particles
Cylindrical particles
Fibers
Conducting fibers
Gas-aerosol reactions,
Transport phenomena
Aerosol measurement
Spheroids
Laser pulses
Optical pulses
Pulse propagation
Clouds
Laser
Radiation transport
Fourier analysis
Plume mechanics
Light
Plumes
Properties

PREFACE

The 1988 U.S. Army Chemical Research, Development and Engineering Center Scientific Conference on Obscuration and Aerosol Research was held 21-24 June 1988 at the Edgewood Area Conference Center of Aberdeen Proving Ground, Maryland. The Conference is held annually, the last full week in June, under the direction of Dr. Edward Steubing, Research Area Coordinator, Aerosol Science.

The Conference is an informal forum for scientific exchange and stimulation among investigators in the side variety of disciplines required for aerosol research including a description of an obscuring aerosol and its effects. The participants develop some familiarity with the U.S. Army aerosol and obscuration science research programs and also become personally acquainted with the other investigators and their research interests and capabilities. Each attendee is invited to present any aspect of a topic of interest and may make last minute changes or alterations in his presentation as the flow of ideas in the Conference develops.

While all participants in the Conference are invited to submit papers for the proceedings of the Conference, each investigator, who is funded by the U.S. Army Research Program, is requested to provide one or more witten papers that document specifically the progress made in his funded effort in the previous year and indicating future directions. Also, the papers for the proceedings are collected in the Fall to allow time for the fresh ideas that arise at the Conference to be incorporated. Therefore, while the papers in these proceedings tend to closely correspond to what was presented at the Conference, there is not an exact correspondence.

The reader will find the items relating to the Conference itself, photographs, the list of attendees, and the agenda in the appendixes following the papers and in the indexes pertaining to them.

The use of trade names or manufactures' names in this report does not constitute an official endorsement of any commercial products. This report may not be cited for purposes of advertisement.

Reproduction of this document in whole or in part is prohibited except with permission of the Commander, U.S. Army Chemical Research, Development and Engineering Center, ATTN: SMCCR-SPS-T, Aberdeen Proving Ground, Maryland 21010-5423. However, the Defense Technical Information Center and the National Technical Information Service are authorized to reproduce this document for U.S. Government purposes.

This document has been approved for release to the public.

Blank

CONTENTS

Blank

I. AEROSOL DYNAMICS

Blank

AIRBORNE STUDIES OF THE INFLUENCE OF ENTRAINMENT ON THE
VERTICAL AND HORIZONTAL MICROPHYSICAL STRUCTURE
OF SMALL CUMULUS CLOUDS

J. Latham
Physics Dept., University of Manchester Institute of Science and Technology
PO Box 88, Manchester M60 1QD, UK

This paper outlines research performed by my colleague Dr Alan Blyth and myself, which will be published in more extensive form in the meteorological literature.

Although recent major field experiments have yielded significant quantities of information on the fine-scale microphysical structure at essentially constant altitude within clouds, little data is available on the associated vertical structure. In an attempt to redress this deficiency we present and discuss measurements made using the University of Wyoming King Air research aeroplane, during the CCOPE experiment conducted in Montana, USA, in the summer of 1981. We restrict our attention to non-precipitating, essentially ice-free cumulus clouds which were studied either by making a series of horizontal penetrations at different altitudes encompassing almost all of the depth of the cloud (typically 2 to 3 km) over as short a period as possible. The principal microphysical measurements (obtained using a PMS Forward Scattering Spectrometer Probe, FSSP) were of liquid-water content (L, also measured with a Johnson-Williams device); cloud droplet size distribution ($n(d)$), where d is the droplet diameter within the range 2 to 32 μm; and the droplet number concentration (N). These parameters were recorded at 10 Hz, corresponding to a spatial discrimination of about 10 m; information on N was also available at 50 Hz (~ 2 m). Standard meteorological parameters and size distributions of larger hydrometeors were also measured, but it was necessary to sacrifice the quantity of the dynamical data in order to minimise the time over which the vertical structure was determined.

We concentrate attention herein on describing the microphysical structure (especially in the vertical), examining the role of entrainment of environmental air in producing it, and discussing the embryonic raindrops which the PMS 1-D probe revealed were often present in particular regions of the clouds studied.

Information was gathered in flights through 7 clouds. On some occasions we present diagrams which superimpose data from all 7 clouds. On other occasions - where we

are particularly concerned to examine fine structure - we present comprehensive data from one particular case study (Cloud A, 23 June), in which the observed relationships were characteristic of those found in all cases. Over the 7 case studies the cloud base temperature (TB), the cloud top temperature (TT) and the cloud depth (CD) ranged roughly from 13°C to -3°C, -6°C to -15°C and 1.5 km to 3.5 km respectively; the corresponding values of these parameters for Cloud A were 5.5°C, -15°C and 2.5 km. Microphysical structure, generally speaking, was found almost everywhere within the clouds studied, independent of the distances from their horizontal and vertical boundaries at all scales down to the lowest limit of measurement ($^\sim$ 2 m). Characteristic examples of significant fluctuations in L, N and mean droplet diameter d measured at 10 Hz during horizontal penetrations through the upper and lower regions of Cloud A are shown in Figures 1 and 2 respectively. Consecutive droplet spectra, illustrating structure in n(d) on spatial scales down to 10 m in this cloud, are presented in Figure 3. Values of the coefficient of variability, K, are seen (Figure 4) to be usually in excess of unity at all 6 levels of penetration of Cloud A, indicating considerable structure in N, which is not simply due to random distributions of the droplets. On the other hand, on many occasions, K $^\sim$ 1 in adiabatic regions.

Figures 5, 6 and 7 present 10 Hz scatterplots of L/LA (LA is the adiabatic liquid-water content), N and d respectively for all altitudes, Z, above cloud base at which penetrations were made through Cloud A. The cloud is seen to be substantially sub-adiabatic at every level, with wide ranges in individual values of L/LA, and average values ranging from about 0.2 to 0.4. Individual values of N are seen to vary enormously at each level; the average values increasing slowly with Z. Less scatter is observed in the 10 Hz values of d, the average values being substantially less than the calculated adiabatic ones, which always exceed the peak values of d. Examination of Figures 5, 6 and 7 reveal that reductions in N and d below the maximum (adiabatic) values at each level contribute about equally to the sub-adiabaticity in L.

There can be little doubt that the microphysi al structure found in the clouds is a consequence of entrainment. Paluch analyses, which were performed where possible indicate that entrainment occurs at all levels, the source of the entrained air at any level lying between that level and no more than about 1 km above it. The substantial levels of sub-adiabaticity resulting from entrainment will shorten droplet lifetimes significantly, which may have important chemical implications - as might also, the role

12

of entrainment in replenishing depleted supplies of oxidants.

Figures 8 and 9 show the distribution with Z of L/LA and N respectively for all clouds studied. The scatter in L/LA is appreciable, but the tendency reported by Warner (1970) - curve displayed - for it to diminish rapidly with Z is not confirmed in our studies. In each, L/LA is roughly independent of Z. Substantial variability is found in N, with a tendency for the average droplet concentration to increase with altitude above cloud base, possibly as a consequence of activation of condensation nuclei at higher levels where the updraught is stronger and/or L has been diminished by entrainment.

Analysis of 1-D probe data for three particular detailed multipenetration studies of ice-free clouds on 27 July, revealed the presence of substantial concentrations ($\tilde{} 10$ /1 of water drops in the approximate size range 60 to 120 μm in the central and upper regions, but not near cloud base. Adiabatic spectra - determined from calculations based on measurements made in the lowest regions penetrated - indicate that the largest droplets grown by condensation are too small to produce the observed embryonic raindrops. The fact that they were not found in the lowest penetration through each cloud, and the observation (Figure 10) that their number concentrations at any level do not systematically increase with increasing L, militate against the idea that they were formed on giant nuclei. Whether or not their presence is attributable to the ingestion of the residue of a decaying thermal by a newer one, enhanced growth associated with entrainment or some other mechanism remains to be established.

REFERENCE

Warner, J.: 1970 On steady-state one-dimensional models of cumulus convection. J Atmos Sci, 27 (1970) 1035-1040.

13
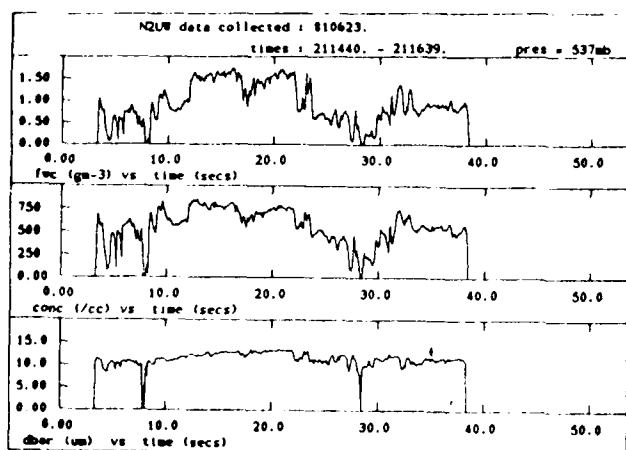
Figure 1. Cloud A. Variation of L, N and $\bar{d}$ with time t for one penetration.
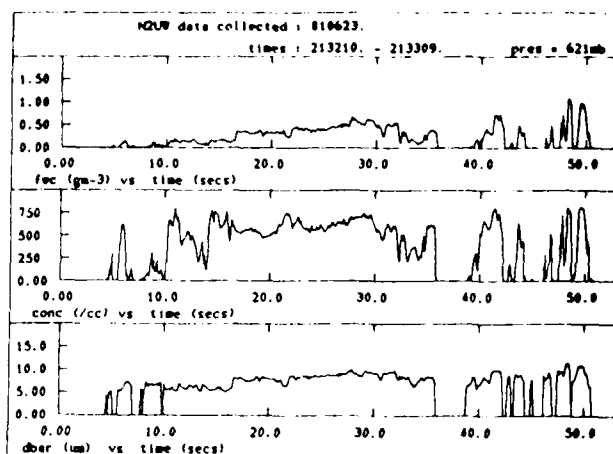
Figure 2. Cloud A. As Figure 1.
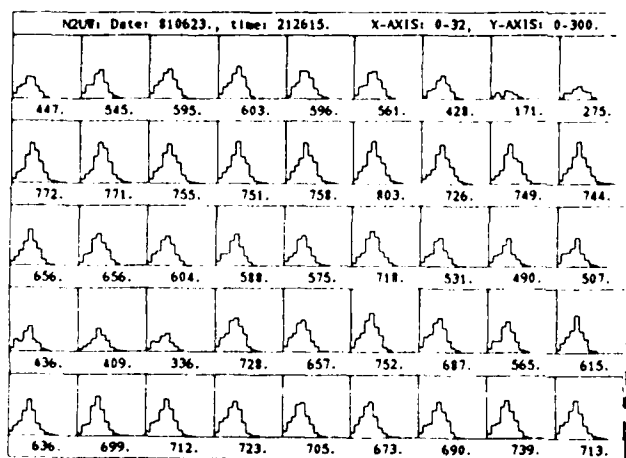
Figure 3. Cloud A. Consecutive 10 Hz droplet spectra. The number under each spectrum is N (cm^{-3}).
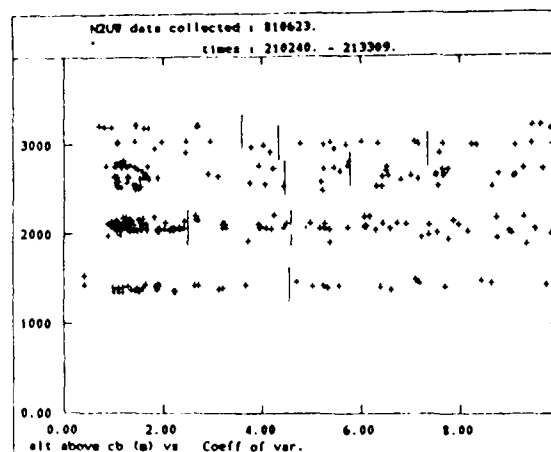
Figure 4. Cloud A. Values of K for each penetration.
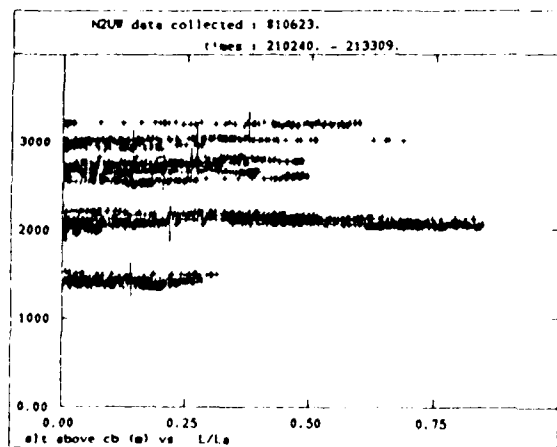
Figure 5. Cloud A. L/LA values for each penetration (10 Hz).
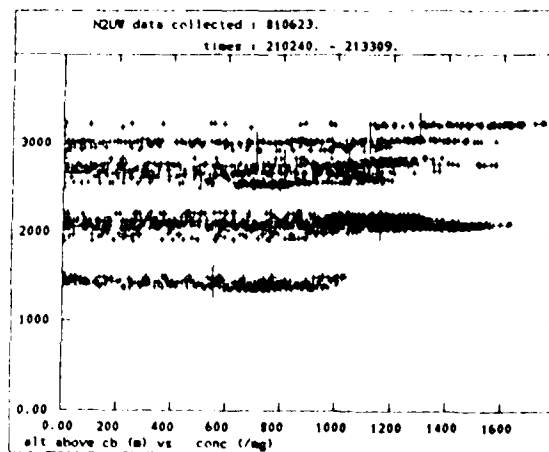
Figure 6. Cloud A. N values (/mg) for each penetration (10 Hz).
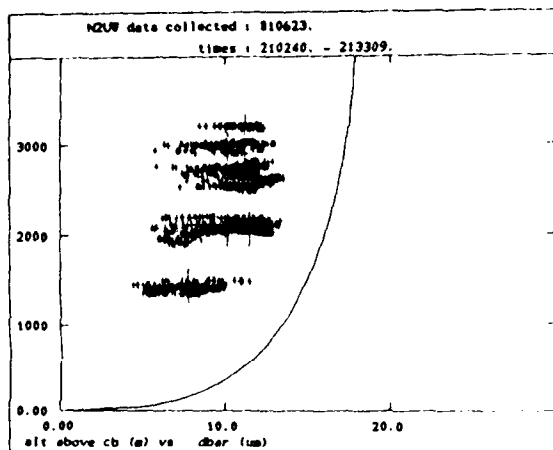
Figure 7. Cloud A. d values (µm) for each penetration (10 Hz). The solid line is for adiabatic growth.
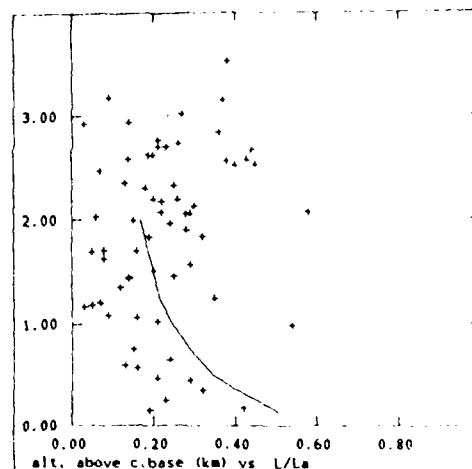
Figure 8. All 7 clouds. Variation of L/LA with height above cloud base. The solid line is from Warner (1970). Points are averages for each penetration.
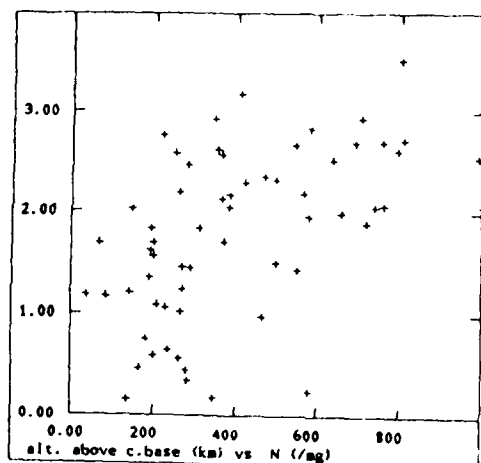
Figure 9. All 7 clouds. Variation of N (/mg) with height above cloud base. Points are averages for each penetration.
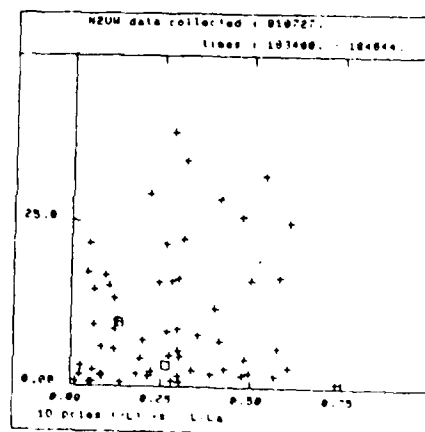
Figure 10. Variation of concentration of embryonic raindrops (/l) with L/LA. Cloud E (27 July)

Blank

PARTICLE FORMATION IN SHOCKED FLOWS

B. J. Jurcik, Jr. and J. R. Brock

Chemical Engineering Department

University of Texas

Austin, Texas 78712

RECENT PUBLICATIONS, SUBMITTALS FOR PUBLICATION AND PRESENTATIONS:

J. C. Carls AND J. R Brock, "Explosion of a water droplet by pulsed laser heating", Aerosol Sci. Tech.7, 79-90 (1987)

S. G. Kim and J. R. Brock, "Aerosol growth and dynamics" in R. Kohl, Ed., *Proceedings of the 1986 CRDEC Conference on Obscuration and Aerosol Research*, R. H. Kohl and Assoc., 1987.

J. C. Carls and J. R. Brock, "Laser induced explosion of particles" in R. Kohl, Ed., *Proceedings of the 1986 CRDEC Conference on Obscuration and Aerosol Research*, R. H. Kohl and Assoc., 1987.

S. Davies and J. R. Brock, "Laser evaporation of droplets" in R. Kohl, Ed., *Proceedings of the 1986 CRDEC Conference on Obscuration and Aerosol Research*, R. H. Kohl and Assoc., 1987.

Y. L Chen, I. Trachtenberg and J. R. Brock, "Aerosol jet etching of fine patterns", Appl. Physics Lett. 51, 2203 (1987).

J. C. Carls and J. R. Brock, "Explosive vaporization of a single water droplet by pulsed laser radiation", *Proceedings of the 1987 CRDEC Conference on Obscuration and Aerosol Research*, CRDEC, U. S. Army, 1988

H. Kosuge and J. R. Brock, "Studies in aerosol formation and growth", *Proceedings of the 1987 CRDEC Conference on Obscuration and Aerosol Research*, CRDEC, U. S. Army, 1988.

G. Moncivais, J. C. Carls and J. R. Brock, "Rapid acquisition of raman spectra from optically levitated particles" *Proceedings of the 1987 CRDEC Conference on Obscuration and Aerosol Research*, CRDEC, U. S. Army, 1988

J. C. Carls and J. R. Brock, "Propagation of laser breakdown and detonation waves in transparent droplets", Optics. Letters 13 273 (1988).

D. Zehavi, P. Kuhn and J. R. Brock, "Binary aerosol formation in a laminar coaxial jet", J. Aerosol Sci. 4 462 (1988).

J. C. Carls and J. R. Brock, "Explosive vaporization of single droplets by lasers: comparison of models with experiments" Optics Letters 13 (1988)

J. C. Carls and J. R. Brock, "On laser droplet vaporization models", Applied Optics, In Press

B. Jurcik, H. Kosuge and J. R. Brock, "Particle nucleation and growth in supersonic jets", submitted for publication, 1988.

B. Jurcik and J. R. Brock, "A study of low pressure particle impaction processes", submitted for publication., 1988.

G. Moncivais, J. C. Carls and J. R. Brock, "Time resolved Raman spectroscopy from optically levitated reacting particles", submitted for publication, 1988.

H. Kosuge and J. R. Brock, "Particle formation in jets", American Association for Aerosol Research Conference, Seattle, Washington, September 1988.

J. C. Carls and J. R. Brock, "Interaction of high energy laser radiation with particles", American Association for Aerosol Research Conference, Seattle, Washington, September 1988.

ABSTRACT

Development of a two dimensional model for simulation of particle nucleation and growth in shocked flows is described. Specifically, simulations have been carried out for axisymmetric, supersonic free jets. Some comparisons between simulation results and experimental results are pressented. Particle formation and growth are found to occur behind the Mach disks, or normal shocks, found in such flows. Future work is described briefly.

INTRODUCTION

An important mechanism for production of aerosol involves the sudden adiabatic cooling and subsequent particle nucleation which occurs in supersonic jets, explosions, laser detonations, etc. In these situations, aerosol is formed in the presence of shocks, in some cases with very complex structures. At present, this is a poorly understood area in aerosol science. Particle formation in expanding jets has been used extensively in the experimental study of condensed phase structure (e.g. Valente and Bartell, 1983, Castleman and Keesee, 1983, Cohen et al., 1987), the deposition of high quality metal and semiconductor films via the ionized cluster beam technique (Takagi, 1986, 1983, Yang and Lu,1984), fusion technology (Hagena, 1980), and for the experimental study of homogeneous nucleation (Wegener and Wu, 1977). The formation of a condensed phase in wind tunnels (Hill, 1966), rocket nozzle exhausts (Crowe and Willoughby, 1967), and in the sampling of gas from high pressure cylinders (Wen and Kasper, 1987) occurs by similar mechanisms but is an undesired effect.

In order to develop simulation methods for these processes we have studied the nucleation and growth of particles formed in supersonic jets and expansions. Most of the numerical studies on particle formation in supersonic jets have used the severe restriction of one dimensional flows. Our approach has been to develop the most rigorous simulation possible so that the vast experimental literature on this subject which has developed over the past few years will be available for this model development work. This paper describes our approach. First, details are given of our model for particle nucleation and growth occurring in a two dimensional axisymmetric expanding jet. Then, some of our model verification work is described. Finally, some of our results are presented on particle formation occurring in the complex shock structures found in supersonic jets.

THEORY

The mechanism for particle formation in expanding jets is depicted graphically in Fig. 1, which is a P-T diagram for nitrogen. Since molecular transport processes are negligible within a supersonic jet, the expansion is isentropic up to the point where the gas becomes so supersaturated that particle nucleation occurs. At this point, the heat of condensation released by the phase change causes the expansion to deviate from the isentrope. This point, where the gas flow deviates from the isentrope, is called the "onset point".

Our model for particle formation in supersonic jets involves solution of the Euler equations along with the a closed set of "exact" moment equations for the nucleation and particle growth. Particle nucleation and growth are handled "exactly" within the restrictions that particles only grow by condensation and that evaporation is negligible (Mcgraw and Saunders, 1984). Also, the Becker-Doring-Zeldovich classical formulation of nucleation is employed with its well recognized deficiencies. These resultant set of equations describing particle formation in axisymmetric flows have the form:

$$\frac{\partial U}{\partial t} + \frac{1}{r}\frac{\partial}{\partial r}(rF) + \frac{\partial}{\partial z}(G) = S$$

$$U = \left\{ \begin{array}{c} \rho \\ \rho v_r \\ \rho v_z \\ \rho e \\ \mu_0 \\ \mu_1 \\ \mu_2 \end{array} \right\} \quad F = \left\{ \begin{array}{c} \rho u \\ \rho u^2 + P \\ \rho uv \\ u(\rho e + P) \\ u\mu_0 \\ u\mu_1 \\ u\mu_2 \end{array} \right\} \quad G = \left\{ \begin{array}{c} \rho v \\ \rho uv \\ \rho v^2 + P \\ v(\rho e + P) \\ v\mu_0 \\ v\mu_1 \\ v\mu_2 \end{array} \right\} \quad S = \left\{ \begin{array}{c} -\beta\mu_2 m_1 \\ \frac{P}{r} \\ 0 \\ -\Delta H_{vap}\beta\mu_2 m_1 \\ J \\ r^* J + v_1\beta\mu_0 \\ 4\pi r^{*2}J + 8\pi v_1\beta\mu_1 \end{array} \right\}$$

where ρ is the mass density, u and v are the fluid velocity components, e is the internal plus kinetic energy , P the pressure, and the μ_i are the first three moments of the particle size distribution. J is the nucleation source strength, m_1 is the monomer mass, v_1 is the monomer volume, β is the number flux and r^* is the critical nucleus size. ΔH_{vap} is the heat of vaporization. This set of equations is solved to obtain the spatial distribution of particles and their relative sizes.

We believe that our simulation studies are important. For example, up to now the vast amount of experimental work on cluster formation in supersonic jets has only been interpreted and guided by models that are steady state and one dimensional.

The numerical simulation of high speed compressible flows is a difficult if not impossible job for most numerical methods. The primary reason for the difficulty is that regions of both subsonic and supersonic flow can exist. Separating the subsonic and supersonic regions are narrow regions (shocks) where large gradients in the flow variables occur. With the usual assumption of inviscid flow the shocks appear as discontinuities in the compressible flow equations.

The discontinuities wreak havoc with most numerical methods since the solution attempts to satisfy the equations in an "average" sense leading to oscillations in the computed solution. For linear equations these oscillations may be acceptable, but for nonlinear equations the oscillations can quickly grow to nonsensical solutions. The way to get around this problem is to smooth the discontinuity over several space points and use finer grids.

Over the years several numerical methods have been developed for solving the compressible flow equations. The predominate methods have been finite difference based-- e.g. Macormick's, Lax-Wendroff, Godunov, and the Flux Corrected Transport methods. In recent years however, finite element methods have been developed for the compressible flow equations. The motivating force behind the development of finite element methods has been its ability to use unstructured grids and retain a high order of accuracy in regions where the solution is smooth.

19

Three different general classes of finite element methods have been developed for the compressible flow equations, Taylor-Galerkin (Baker and Kim, 1986), Characteristic Galerkin (Morton and Sweby, 1987), and Petrov-Galerkin (Hughes and Tezduyar, 1984) methods. Characteristic Galerkin methods use moving coordinates and reinterpolation onto the original mesh. Petrov-Galerkin methods use discontinuous test functions. Taylor-Galerkin methods differ from most finite element methods in that the time discretization is performed prior to the spatial discretization. It has been shown (Lohner et al., 1984) that the three methods are quite similar. After some testing we have adopted a Flux Corrected Transport-Finite Element Method (FCT-FEM) that uses the Taylor-Galerkin algorithm as the high order method (Morgan et al., 1986).

RESULTS

In numerical simulation, it is of first importance to confirm the validity of the procedures by comparison with either analytical solutions or with experimental data. For axisymmetric supersonic flows, there are no analytical solutions available. Fortunately, there is a wealth of experimental data. Because of space limitations, only a few comparisons of the model with experiment will be presented here. We restrict this to underexpanded sonic jets issuing from circular nozzles with no condensation.

For highly underexpanded, steady state jets, Ashkenas and Sherman (1966) provide well verified empirical formulas for the centerline Mach number distribution and Mach disk location. Fig. 2a and 2b show the model computation results compared to Ashkenas-Sherman's formulas for two jets for centerline Mach numbers as a function of dimensionless downstream distance, Z/D , where Z is the downstream distance and D is the nozzle diameter. The jets are different because the pressure and density ratios are different (defined as property at the nozzle exit divided by the property in the ambient gas). The model calculation agree well with these experimental results and have captured the shock position accurately.

Fig. 3a shows the steady state density contours obtained experimentally by Ladenburg (1949) by a shadowgraph method at a pressure ratio of 2.75 and density ratio of 3.36 Simulation at these same conditions was carried out. Fig. 3b shows the corresponding density contours to Fig. 3a. Detailed comparison of the data of Figs. 3a and 3b have been carried out and the model calculations agree very well with Ladenburg's experimental results.

The model has been used for a number of simulations of particle formation and growth and a result from this work will be presented here. The pressure ratio was set at 4.1206 to correspond to the experimental investigations of Goglia (1961) who studied particle formation occurring *inside* supersonic nozzles. Goglia's work was chosen for comparison since the fluid states were well defined in his experiments. Since the model used here is for a free jet, the comparison is not exact and it was necessary to adjust the density ratio to a value of 12 to obtain particle formation; Goglia obtained particle formation *inside* the nozzle at a density ratio of 10 . The simulation is for an unsteady state at a time of 0.5 msec. after release of the jet. Fig. 4 shows the pressure field in the jet and

clearly depicts the complex shock structures associated with axisymmetric jets. The jet boundary, barrel shock, Mach disk, and other features are quite evident. Fig. 5 shows the axial velocity profile as a function of downwind distance. Figs. 4 and 5 are useful in understanding the regions where particle formation occurs in this jet. Figs. 6a, 6b and 6c are respectively the particle number concentration (#/cc), and the first and second moment of the particle distribution (mu1 and mu2) for the particles formed by nucleation in this jet. As is evident, particles are formed in the regions just behind the Mach disks. In these particular simulations, the particles are very small and perhaps should be more accurately referred to as clusters.

We plan to continue this work and refine the model for particle formation and growth using the wealth of experimental information available in the literature on cluster formation in free jets. It is also anticipated that the model development can be refined to the point where situations of direct interest to the Army's programs can be simulated, such as smoke produced by ordinance explosions.

ACKNOWLEDGMENT

REFERENCES

Ashkenas, H., and F. S. Sherman, 1966. *Rarefied Gas Dynamics*, Vol. 2, Academic Press NY, 84-105.

Baker, A. J., and J. W. Kim, 1986. *Finite Element Methods for Nonlinear Problems*. Springer, Berlin, 775-789.

Castleman, A. W., Jr., and R. G. Keesee, 1983. *Aerosol Science and Technology*, 2, 145-152.

Cohen, M. L., M. Y. Chou, W. D. Knight, and W. A. de Heer, 1987. *J. Phys. Chem.*, 91, 3141 - 3149.

Crowe, C. T., and P. G. Willoughby, 1967. *AIAA J.*, 5, 1300-1304.

Duker, M. and G. Koppenwallner, 1980. *Rarefied Gas Dynamics, Pt. 2*, Academic Press, N.Y., 1190-1210.

Goglia, G. L., and G. J. Van Wylen, 1961. *J. Heat Transfer*, 83, 27-32.

Hill, P. G., 1966. *Fluid Mech.*, 25, 593-620.

Hughes, T. J. R., and T. E. Tezduyar, 1984. *Comp. Meth. Appl. Mech. and Eng.*, 45, 217-284.

Ladenburg, R., C. C. Van Voorhis, and J. Winkler, 1949. *Physical Review*, 76, 662-677.

Lohner,R., K. Morgan, and O. C. Zienkiewicz,1984. *International Journal for Numerical Methods in Fluids*, 4, 1043-1063.

Morgan K.,R. Lohner,J. R. Jones, J. Peraire,and M. Vahdati, Proc. 6th int. Symp Finite Element Methods in Flow Problems, INRIA (1986).

Mcgraw, R., and J. H. Saunders, 1984. *Aerosol Sci. and Tech.*, 3, 367-380.

Morton, K. W., and D. K. Sweby, 1987. *J. Comp. Phy.*, 73, 2-3-230.

Takagi, T., 1984. *J. Vac. Sci. Tech.A*, 2, 382-388.

Takagi, T., 1986. *Z. Phys. D.*, 3, 270-278.

Valente, E. J., and L. S. Bartell, 1983. *J. Chem. Phys.*, 80, 1451-1457.

Wegener, P. P., and B. J. C. Wu, 1977. *Advances in Colloid and Interace Sci.*, 7, 325-417.

Wen, H. Y., and G. Kasper, 1988. *J. Aerosol Sci.*, 19, 153-156.

Yang, S. N., and T. M. Lu, 1984. *J. Appl. Phys.*, 58, 541-544.
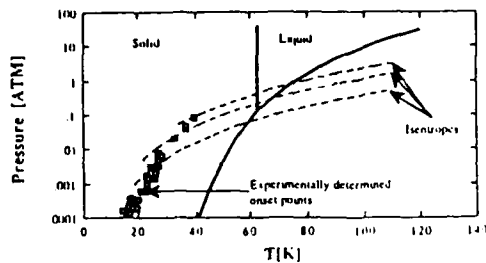
Figure 1 P - T diagram for N_2 Flow upstream of the Mach disk follows the isentrope crossing the equilibrium line, causing measurable particle formation at the onset point Onset data from Duker and Koppenwallner, 1980
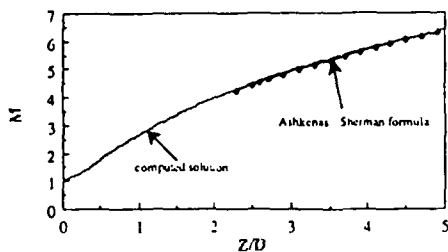
Figure 2a Comparision of calculated solution and Ashkenas-Sherman formulas. $P_e/P_\infty = 80$, $\rho_e/\rho_\infty = 100$.
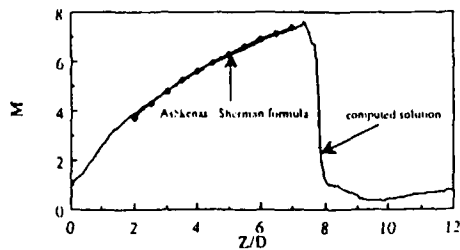
Figure 2b Comparision of calculated solution and Ashkenas-Sherman formulas. $P_e/P_\infty = 76$, $\rho_e/\rho_\infty = 114$.
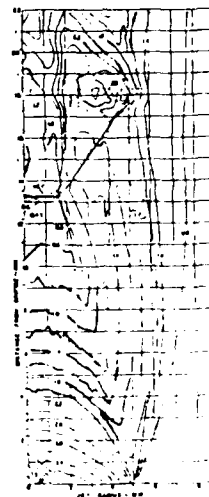
Figure 3a Measured density contours for $P_e/P_\infty = 3.36$, $\rho_e/\rho_\infty = 2.75$ from Ladenburg et al. 1949.
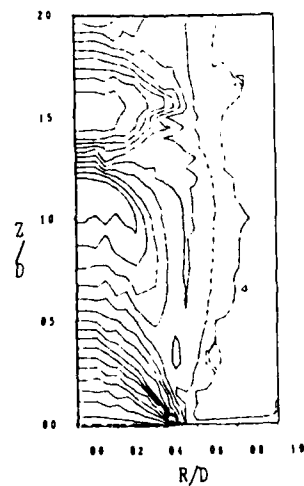
Figure 3b Calculated density countours for $P_e/P_\infty = 3.36$, $\rho_e/\rho_\infty = 2.75$.

22

Figure 5 Axial velocity profile on centerline for particle formation simulation $Pe_tT_\infty = 412$, $Pe/\delta_\infty = 12$

VZ (m/s)

Z/D

Figure 4 Calculated pressure field for particle formation simulation $Pe_tT_\infty = 412$, $Pe/\delta_\infty = 12$
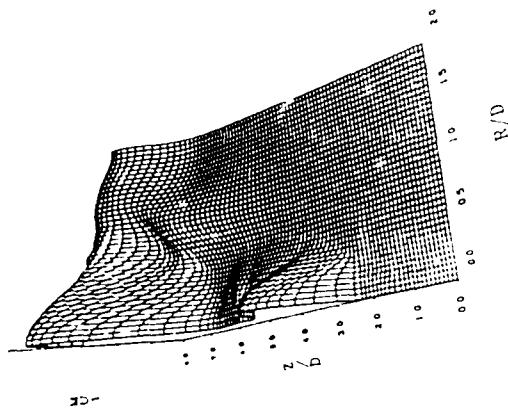
Figure 6b First moment of N_2 particle size distribution
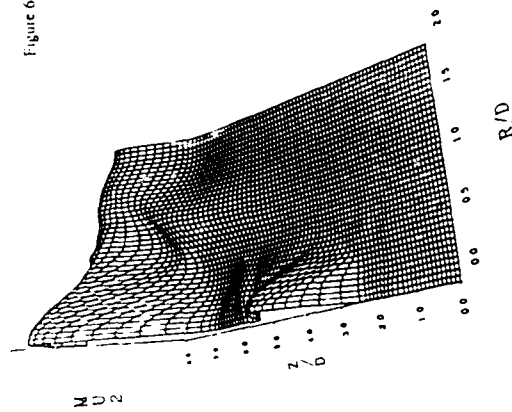
Figure 6c Second moment of N_2 particle size distribution

Figure 6a Number concentration (#/cc) of N_2 particles formed

24

Wind Tunnel Simulation of Obscuration
Fluctuations by Aerosol Plumes

M. Poreh and J. E. Cermak
Colorado State University
Fort Collins, Colorado 80523

ABSTRACT

A novel IR/CO_2 system is being developed for study of obscuration fluctuations in small-scale, wind-tunnel models. Preliminary measurements depict the intermittent nature of obscuration by a single ground-level neutrally buoyant plume.

INTRODUCTION

Obscuration by aerosol plumes is related to the integral of their concentrations along the line of vision. The value of this integral can fluctuate considerably with time due to the unsteady, turbulent nature of atmospheric diffusion.

A novel system for measuring the instantaneous fluctuating value of such integrals in small-scale wind-tunnel models has been proposed [1]. The system, shown schematically in Fig. 1, measures the absorption of a narrow band IR radiation across a plume of carbon dioxide mixed with helium, to produce the desired buoyancy. The averaged value of the concentration along the path is calculated from the measurements of radiation intensity.

A preliminary test system has been assembled and used to measure the mean and fluctuating values of the Vertical Integrated Concentration (VIC), defined as:

$$VIC\ (x,y,t) = \int_0^\infty c(x,y,z,t)\ dz \ \ ,$$

downstream from a ground-level point source of a neutrally buoyant plume in a simulated atmospheric boundary layer with neutral stratification. The geometric scale factor of the model was approximately 1:600.

SUMMARY OF THE RESULTS

Measurements were made of the fluctuating value of VIC^*,

$$VIC^* = VIC \cdot U \cdot \delta^2 / Q \quad ,$$

where U and δ are the characteristic velocity and thickness of the atmospheric boundary layer and Q is the source strength.

The mean values of VIC^*, denoted by $VICA^*$, were calculated from the measurements. An approximate model for calculating the average value of $VICA^*$ was developed and was found to be in good agreement with the measurements, as shown in Fig. 2. Measurements of $VIC^*(T^*)$, where T^* is the dimensionless time tU/δ, at different stations along the axis of the plume ($y = 0$) are shown in Fig. 3. The data depict the decay of VIC with x. The measurements of VIC^* at off-center locations, shown in Fig. 4, depict the intermittent nature of obscuration by a single plume, which is controlled by the meandering of the plume in the turbulent atmospheric surface layer.

It was also found that within the range 300 - 1200 m from the source, the probability P that the relative value $VIC(t)/VICA$ at any location exceeds a given ratio is a function of y/σ only, where $\sigma(x)$ is the characteristic lateral size of the mean plume, which can be predicted by numerous diffusion models [2]. The measured distributions of P along the centerline of the plume ($y/\sigma = 0$) and at $y/\sigma = 2.3$ depict a clear similarity of the probability distributions at different distances, as shown in Figs. 5 and 6.

Planned Future Studies

It is planned to build an improved IR/CO_2 system in the Meteorological Wind Tunnel at Colorado State University, for studying the dynamic characteristics of obscuration by aerosol plumes in small-scale models for different surface roughnesses, source elevations, plume buoyancies, atmospheric stabilities and multiple-source configurations.

REFERENCES

1. M. Poreh and J. E. Cermak, "Experimental Study of Aerosol Plume Dynamics; Part III: Wind-tunnel Simulation of Vertical Integrated Concentration Fluctuations," Annual Progress Report to CRDC, CER87-88MP-JEC4, December 1987.

2. M. Poreh and J. E. Cermak, "Experimental Study of Aerosol Plume Dynamics; Part I: Wind-tunnel Study of Diffusion and Deposition of Particles with Appreciable Settling Velocities," Annual Progress Report to CRDC, CER86-87MP-JEC1, September 1986.
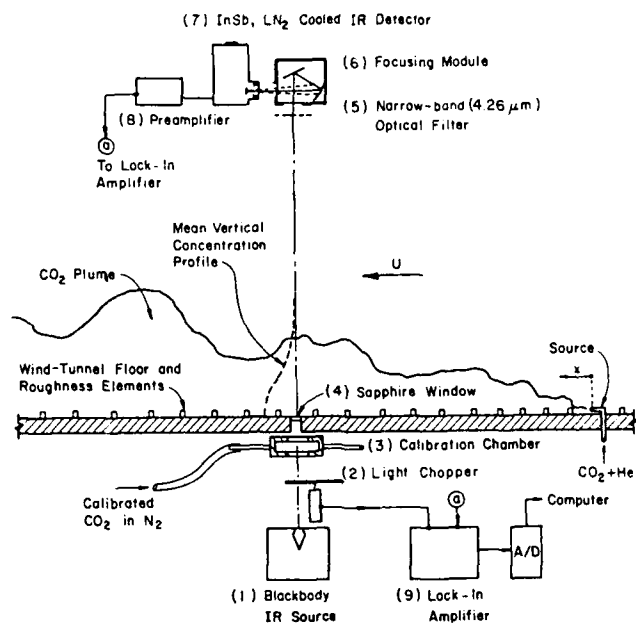
FIGURE 1. SCHEMATIC DESCRIPTION OF THE EXPERIMENTAL
CONFIGURATION.
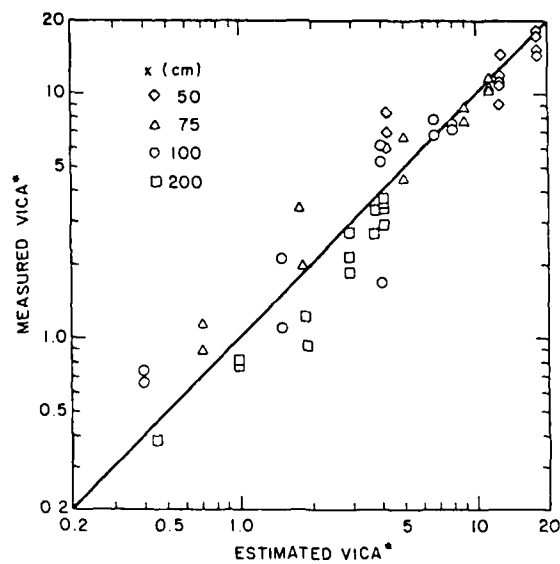
FIGURE 2. COMPARISON OF THE MEASURED AND ESTIMATED
VALUES OF VICA*.

27

FIGURE 4. TYPICAL FLUCTUATION OF VIC* OFF THE CENTERLINE OF THE PLUME.

FIGURE 3. TYPICAL FLUCTUATION OF VIC* ALONG THE CENTERLINE OF THE PLUME.

28
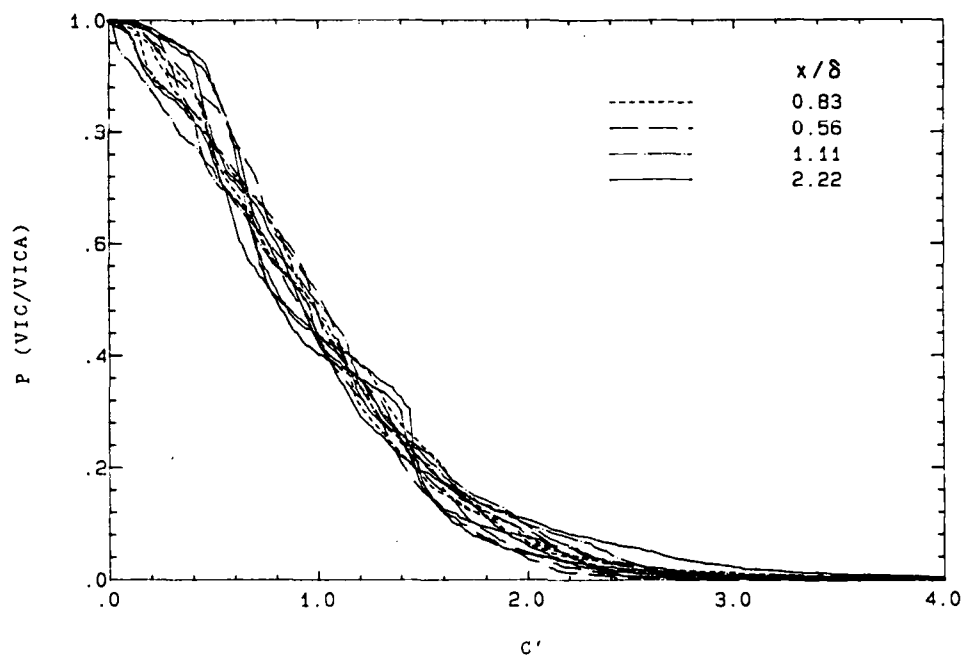
FIGURE 5. THE PROBABILITY THAT VIC/VICA EXCEEDS C' ALONG THE CENTERLINE OF THE PLUME (y = 0).
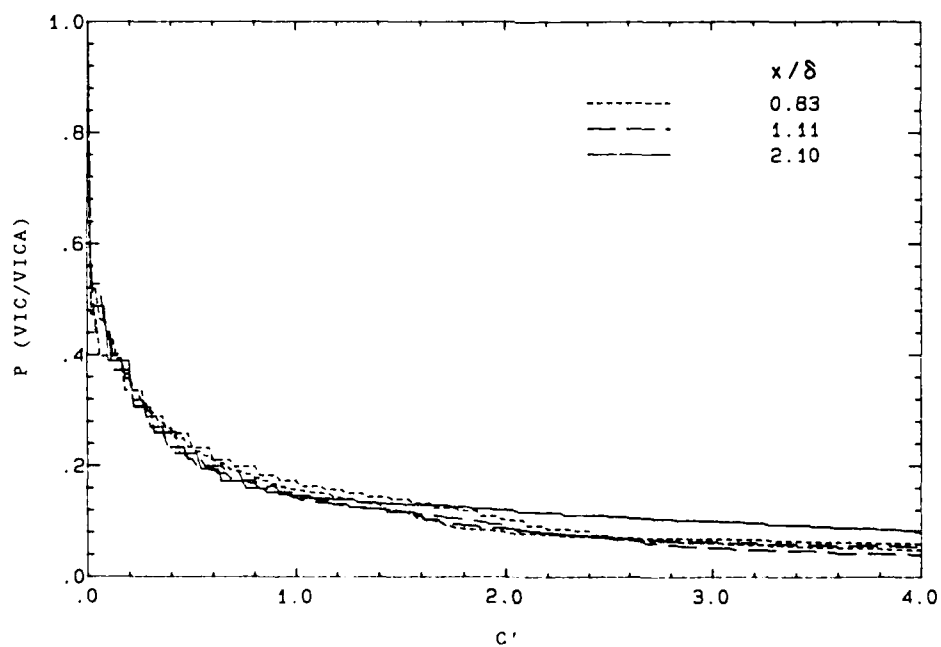
Blank

II. AEROSOL CHARACTERIZATION METHODS

Blank

AN INSTRUMENT TO MEASURE THE SIZE, VELOCITY

AND CONCENTRATION OF PARTICLES IN A FLOW

Cecil F. Hess

MetroLaser
18004 Skypark Blvd, #254
Irvine, CA   92714-6428

ABSTRACT

A technique to measure the size, velocity and concentration of particles in a flow is discussed. An instrument to measure particles as small 0.5 μm moving at 1000 m/s was developed based on this technique. Two small beams of one color cross in the middle of two crossing larger beams of different color. The small beams, thus, define the middle of the larger beams, a region in which the intensity is almost constant. The particle size is obtained from the absolute intensity of the light scattered by particles crossing this uniform intensity region. Two velocity components are measured from the two independent fringe patterns.

The concentration is obtained from the probe volume size, and the size and velocity distributions of the particles. Results are presented for sprays of predictable characteristics and for polystyrene particles between 1.1 μm and 3.3 μm. It is shown that the method has an excellent size resolution and its accuracy is better than 10% of the particle size studied.

INTRODUCTION

A nonintrusive single-particle counter to measure the size, velocity and concentration of particles in a particle laden flow is described here. The method bases the size information on the absolute scattered light of individual particles crossing the middle of a Gaussian laser beam, as described in Reference (1). The velocity is obtained from the Doppler frequency arising when the particles cross an interference pattern of fringes. This method is referred to as the IMAX. Obtaining the particle size from the absolute scattered light has always been an attractive straightforward method due to its high dynamic range, and because it can be used with both liquid and solid particles, even in those cases where the particles are nonspherical and of an unknown index of refraction. Its use with lasers has been limited until recently due to their nonuniform intensity profile, typically Gaussian. The limitation stems from the fact that particles crossing through the center of the Gaussian beam scatter more light than those crossing through the edge, thus, appearing as larger particles. This ambiguity
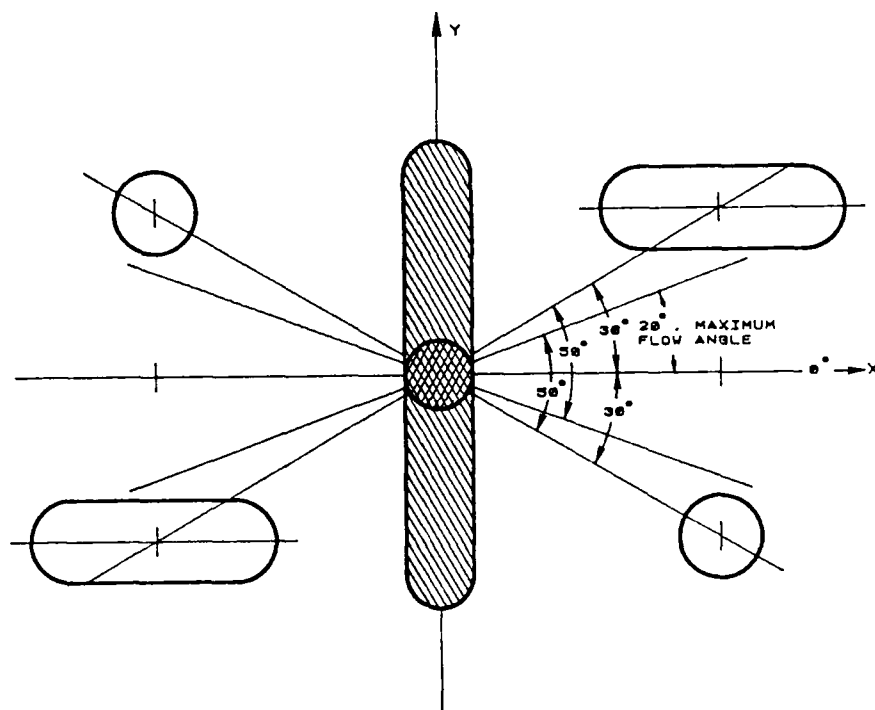
FIGURE 1. ELONGATED IMAX PROBE VOLUME.

has been overcome by identifying the middle of laser beams with the crossing of two smaller beams of different wavelength or polarization. Only particles traveling through the small beams and therefore, the middle of the large beams, are processed. The typical configuration of this method uses two blue (0.488 μm) beams crossing in the middle of two green (0.5145 μm) beams to produce two independent fringe patterns. Thus, the particle size and two components of the velocity are simultaneously obtained for each and every particle crossing the probe volume.

Very high speed electronics have been developed to measure particles as small as 0.5 μm traveling at 1000 m/s. The technique finds application in a variety of two-phase flows in which the spatial resolution of the size and velocity are required. Examples are sprays and aerosols, dust clouds and particle laden flows in which the velocity of the particles and gas are independently needed, and high speed wind tunnels in which the particle size is needed to verify if the particle followed the flow. Similar methods have independently been proposed and demonstrated by other researchers[2,3] as well as methods generically referred to as "top hat".[4]

In this work we describe the theoretical basis of the technique, an instrument developed based on it, and present results which validate the instrument performance.

DESCRIPTION OF OPTICAL TECHNIQUE

Figure 1 illustrates one of the possible probe volumes of this method. It is obtained by crossing two laser beams of wavelength λ_1 in

34

the middle of two laser sheets of wavelength λ_2. Two independent fringe patterns are formed and only particles exhibiting an ac modulation from both fringe patterns, and meeting a coincidence criterium, are accepted as valid. The fringe patterns are chosen such that the particles cross $\pm$ 20° from the X axis and therefore, through the middle of the laser sheet. For totally random particle directions, the large probe volume must be circular as described in Reference (1). The receiver collecting the scattered light will normally have a spatial aperture (pinhole) which is schematically shown by the broken vertical lines. Thus, the effective blue and green probe volumes are almost identical. This is not a requirement, but it helps in the presence of high particle concentrations.

If we refer to the small beam as 1 and the large beam as 2, the intensity profiles in the probe volume can be spectrally separated and given by

$$I_1 = 2 I_{o_1} \exp \left[\left(\frac{-2}{b_{o_1}^2} \right) \right] (x^2 + y^2 + z^2 \gamma^2/4) \right] \left[1 + \cos \frac{4\pi x \sin (\gamma_1/2)}{\lambda_1} \right], \quad (1)$$

and

$$I_2 = 2 I_{o_2} \exp \left(\frac{-2 x^2}{b_{o_2}^2} \right) \left[1 + \cos \frac{4\pi x \sin (\gamma_2/2)}{\lambda_2} \right]. \quad (2)$$

Where it has been assumed that $z\gamma/2 \approx o$ (which is an excellent assumption since a pinhole in the receiver will limit z), and that the intensity of the large beams is only measured over the region defined by the small beams. I_o is the center intensity, γ the intersection angle, b_o the waist radius, λ the laser wavelength, and x, y, z are the coordinates. The intensity scattered by a particle is given by:

$$I_{s_1} = 2 I_{o_1} K_1 (d,n,\theta,\Omega,\lambda_1) \ G_1 \ \exp \left[\left(-\frac{2}{b_{o_1}^2} \right) \left(x^2 + y^2 \right) \right]$$

$$\cdot \left[1 + \cos 2 \frac{\pi \gamma x}{\lambda_1} \cdot V \right], \quad (3)$$

and

$$I_{s_2} = 2 I_{o_2} K_2 (d,n,\theta,\Omega,\lambda_2) \ G_2 \ \exp \left(\frac{-2x^2}{b_{o_2}^2} \right)$$

$$\cdot \left[1 + \cos 2 \frac{\pi \gamma x}{\lambda_2} \cdot V \right], \quad (4)$$

where K is the scattering cross section which can be obtained by the Lorentz-Mie[5] theory, or for very large spherical particles using the geometric approximations described in Reference (6). K is, in general, a complex function of size d, the index of refraction n, the collection angle θ, the solid angle of collection Ω, the wavelength λ, and the polarization. G is the gain function of the instrument, and V is the visibility of the measured signal.

It should be pointed out that although the visibility is, in general, not an adequate sizing parameter[7], it represents an important

aspect of the Doppler signal. That is, it establishes the modulation of the ac component. The size of the particle is obtained after low-pass filtering the signal given by Equation (4). Thus, the cosine term is cancelled out. The scattered intensity is then measured as a function of x, and its peak value is registered (x = o). It is then obtained:

$$I_{s_2} = 2 I_{o_2} K_2 G_2 .$$ (5)

where I_{o_2} and G_2 are calibrated parameters of the instrument, and K_2 is solved for the diameter d. The two velocity components are obtained from the cosine terms of Equations (3) and (4) in the classical Doppler way.

Notice that for particles larger than the wavelength, the scattered light collected near on-axis (θ = o) can be described using Fraunhofer diffraction theory. There, the scattering coefficient is given by:

$$K = \frac{d^2}{4r^2} \int_{A_{lens}} \frac{J_1^2 (\alpha \sin \theta)}{\sin^2 \theta} dA,$$ (6)

where $\alpha = \pi d/\lambda$ is the size parameter, J_1 is the Bessel function of the first kind, and r the distance from the probe volume to the lens. Equation (6) shows that the scattered light is independent of index of refraction and, furthermore, since diffraction is a function of the particle cross section, some irregularities in the particle shape can be tolerated.

For particles with diameters near the wavelength, the scattering cross section must be obtained solving the Mie scattering equations numerically. The functional relationship between the diameter and K_2 can be quite complex. It is necessary to find the conditions under which the ambiguities, if any, are within tolerable error margins. The computations were made on an IBM AT computer. Parametric studies were conducted to establish optimum experimental conditions. These parameters include the angle of collection (θ), the solid angle of collection (Ω) and index of refraction ($n_1 - in_2$).

Since the index of refraction of the particles in many applications may be quite different, it is important to establish conditions which are less sensitive to these variations. Both real (n_1) and imaginary (n_2) parts of the refractive indices were varied to check the sensitivity of these parameters. Figures 2 and 3 show the scattered intensity as a function of the particle size parameter α for different values of n_1 and n_2 at different scattered angles.

It was concluded from the above calculations that shallow angles of collection ($\theta < 7°$) offer the most favorable conditions.

THE PROBE VOLUME

The probe volume is the product of the cross sectional area of sensitivity A(d) times the sampling length. Its theoretical foundation is described in Reference (1). A(d), as shown, is a function of diameter since particles that scatter light with large modulation (large amplitude and visibility) are detectable over a larger region than those

36
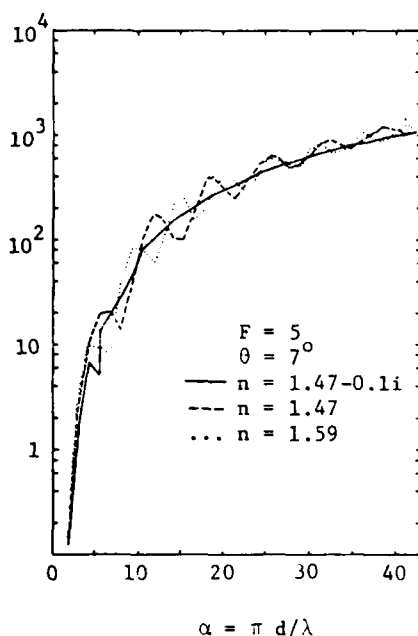
FIGURE 2. SCATTERED INTENSITY
INTEGRATED OVER AN F #5 LENS
CENTERED AT 7°.
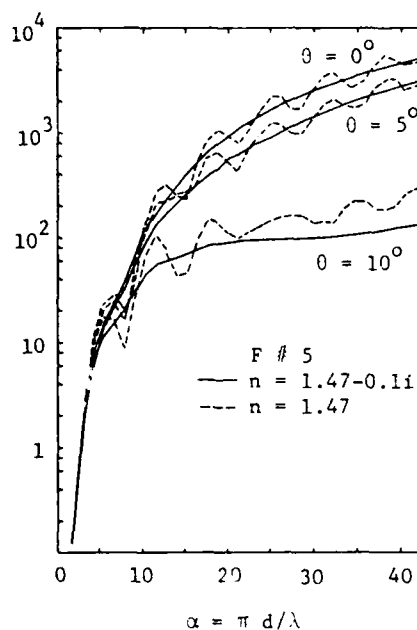
FIGURE 3. SCATTERED INTENSITY
INTEGRATED OVER AN F #5 LENS
CENTERED AT 0, 5° AND 10°.

with less modulation. As a result, the probability of detecting a particle is a function of its size. This probe volume is required to correct the cou,ts of the size histograms and to obtain the concentration or number density of particles. In the IMAX technique, it is the probe volume of the small beams which is of interest since the intensity of the large probe volume remains constant throughout the measurement region. The cross sectional area of sensitivity, A(d), was verified experimentally using monodisperse droplets of known size. Since A(d) varies only with the coordinate y, it was only necessary to measure y experimentally. The z dimension was, however, checked for completeness. A Berglund-Liu droplet generator was mounted on a precision x-y micrometric traverse so that the droplets could be positioned anywhere in the probe volume. The orifice of the Berglund-Liu was kept very close to the probe volume to minimize errors due to the wander of the string of droplets. Data were also collected several times to further reduce the errors.

A very difficult part of this experiment was determining the edge of the probe volume for any particular size droplet. Theoretically, the edge of the probe volume is calculated by the expression given for y. Experimentally, there is a region near the edge of the PV where the rate of acquisition drops off. That is, some of the signals (droplets) are processed by the electronics and some are not. The electronics used here imposed an upper limit on the data rate of about 6 kHz, while the drops can be generated at a frequency of up to 60 kHz.

In defining the edge of the probe volume the data rate of signal acceptance was observed. One criterion corresponded to the location where the data rate dropped to about 90% of the maximum rate. Another criterion corresponded to a data rate very close to zero. Notice that, in principle, all the measured droplets are identical and are traveling exactly through the same trajectory. Therefore, the data rate should be

37

either zero or have a fixed constant value. In actuality, the droplet
trajectory can change by a few microns, therefore, causing some droplets
to cross inside the probe volume while others cross outside. In addi-
tion, the droplets could vary in size, although we had no evidence of
this.

The droplet generator was traversed from the position of peak
intensity to the position of 90% data rate, and then zero data rate.
The respective relative movements were recorded in each case. The 90%
data rate corresponds to a conservatively small probe volume referred to
in Figure 4 as y_{small}, while the zero data rate corresponds to a conser-
vatively large probe volume and is indicated as y_{large}. Also, shown in
Figure 4 are the average of y_{small} and y_{large}, and the theoretically
predicted value.

Since the size range of droplets produced by the monodisperse
droplet generator is rather limited, we extended the measurements by
simulating the amplitude and visibility corresponding to different size
particles. This was easily accomplished by masking the receiver. To
further validate the probe volume algorithm some spray measurements were
performed.

The following results correspond to a spray produced by a pres-
sure nozzle (Spray Systems TG0.3 at 50 psi and 50 mm from the tip).
These results are adequate to show trends and gross changes in the dis-
tributions. However, considerable transient variations were observed in
both the size and velocity distributions. These variations were the
result of changes in the spray pattern produced by the above-mentioned
nozzle. Simple visual observations of the spray pattern indicated
changes from conical to flattened sprays. Nevertheless, recognizing
that a standard invariable spray is not available, we proceeded to make
measurements that would allow us to test the probe volume algorithm.
These measurements are shown in Figures 5a and 5b.

Figure 5a shows the raw data, while Figure 5b shows the probe
volume corrected data. Comparing the raw and the probe volume corrected
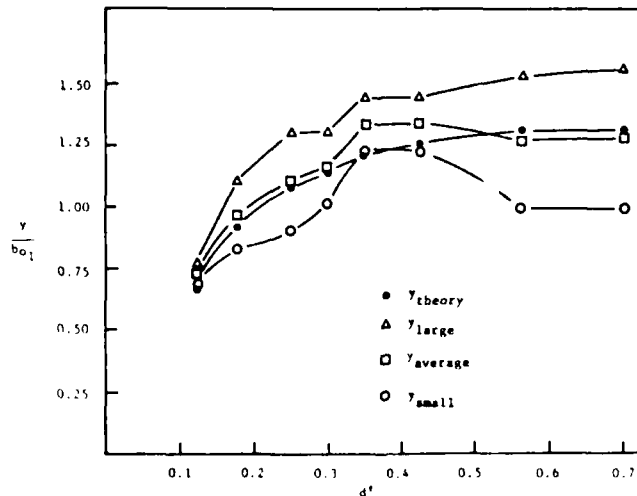
FIGURE 4. PROBE VOLUME AS A FUNCTION OF PARTICLE SIZE.

(a)　　　　　　　　　　　　　　(b)
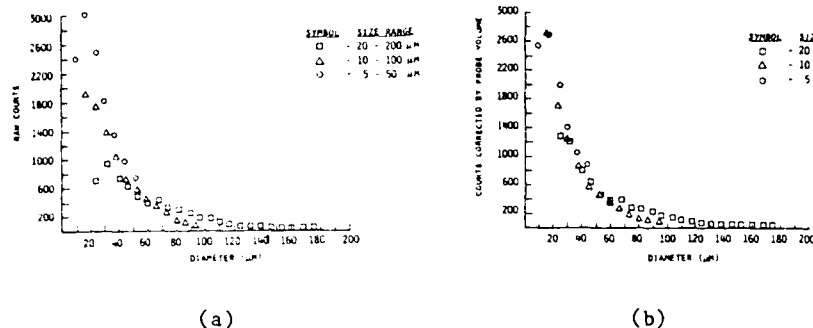
FIGURE 5.　IMAX MEASUREMENTS OF A SPRAY AT A RADIAL POSITION OF 0 mm.
　　　　　a) RAW DATA;　b) PROBE VOLUME CORRECTED SIZE DISTRIBUTION.

data, it is quite apparent how signal detectability influences the
number of counts in the histograms.　For instance, it is more difficult
to detect a 25 μm droplet in the size range of 20 to 200 μm than in the
size range of 5 to 50 μm.　This change in sensitivity is what the probe
volume is all about, and it is characteristic of any optical technique
(for instance, in photography the data rate must be corrected by the
depth of field).

In order to test the resolution of the system, data were obtained
using three different size ranges:　5 to 50 μm, 10 to 100 μm and
20 to 200 μm.　This is one of the most difficult self-consistency tests
imposed on any technique and most available techniques will show a shift
in the predicted data.　IMAX shows excellent matching of the data in the
overlapping region, as illustrated in Figure 5b.

DESCRIPTION OF APPARATUS

An instrument has been developed to measure two velocity compo-
nents and the size of particles as small as 0.5 μm traveling at 1000 m/s.
The peak amplitude dynamic range of this instrument is 1000 to 1.　The
corresponding size range depends on the functional relationship between
the particle diameter and the scattered intensity.　For particles larger
than 5 μm, the size dynamic range is about 30:1.

The transmitter is shown on Figure 6.　Four beams from an argon-
ion laser are crossed to form a probe volume consisting of two crossing
blue beams in the middle of two crossing green sheets.　The transmitter
is made of individual disks containing prealigned optical elements.　All
the disks are compressed together by three rods to form a very rugged
unit which can be rotated as a whole to change the orientation of the
fringes when required.　Fine lockable adjustments are provided to ensure
that the four beams cross at their waists and to correct for beam
steering resulting when the beams travel through thick glass windows.

The receiver is essentially a telescope with two photomultipliers
to collect the light scattered by particles crossing the sample volume.
This beam is split in two via a beam splitter and a mirror system; each
beam is focused on the pinhole of the corresponding PMT housing.　The

39
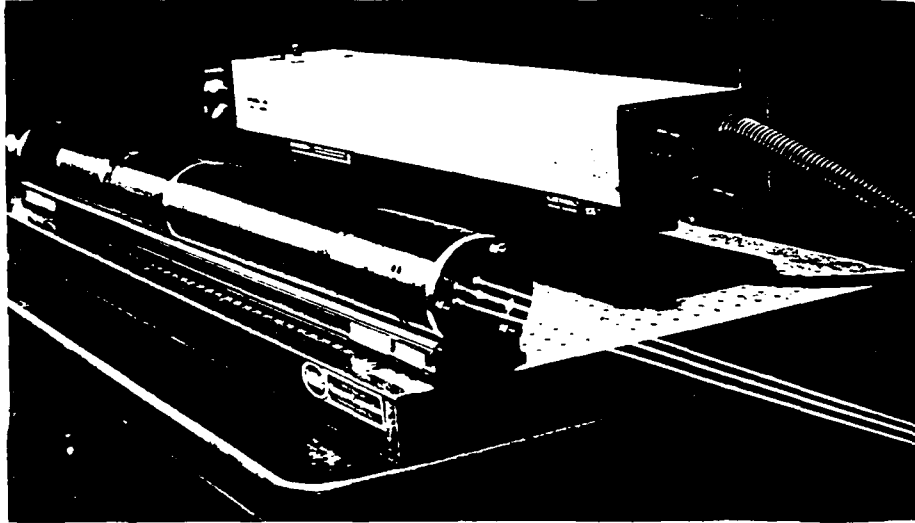
FIGURE 6. TRANSMITTER WITH FOUR LASER BEAMS TO MEASURE
THE SIZE AND TWO VELOCITY COMPONENTS.

colors are separated by means of narrow-band filters internal to the PMT housings. The outputs of the two PMTs are then electronically processed, and information about the size and velocity of individual spheres crossing the probe volume is thus obtained. An electronic processor was developed for this purpose, and a dedicated microprocessor was interfaced to store, display, and analyze the acquired data.

The sizing processor is built in a computer card and resides in an IBM PC or AT. It can be interfaced to a variety of Doppler processors. The settings are addressed from the keyboard of the computer. Thus, parameters such as PMT high voltage, velocity range, and threshold, are selected from the keyboard. The data rate depends on whether the system is set to collect two velocity components with the proper coincidence, or only one. In the first case, the data rate is about 20 kHz. Figure 7 shows the monitor output with the U and V velocity components and the particle diameter. These three parameters, as well as the time of arrival of each particle, are stored correlated in the computer memory. Thus, relationships between size and velocity, as well as turbulent characteristics, are readily obtainable.

RESULTS

The experiments reported here were conducted to validate the performance characteristics of the instrument. This is a very difficult task given the absence of a standard spray. It has been shown[7] that the ability of an instrument to respond to a vertical string of monodisperse drops is no guarantee of its performance. Furthermore, proving repeatability in the measurement of an unknown spray, at best, may show that the instrument remained aligned. Using the SMD as a sizing parameter can be deceiving since it is highly influenced by the large drops and does not show the ability of the instrument to respond to the full size distribution.

U velocity(m/s)   0.5 Size(microns) 7.1

Samples
Total   :3263
Valid   :3242

ElapsedTime:0.6

ENTER to continue
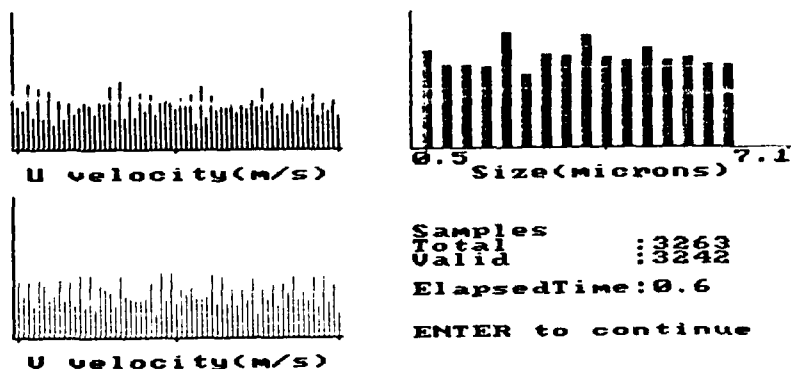
U velocity(m/s)

FIGURE 7.   MONITOR DISPLAY OF THE SIZE AND
             TWO VELOCITY COMPONENT HISTOGRAMS.

We conducted two kinds of validation experiments. In the first we sprayed dry polystyrene particles of known size and combined different size particles to produce sprays of prescribed characteristics. In the second, we used the Berglund-Liu droplet generator and introduced dispersion air to form a spray of monodisperse, bimodal and trimodal droplets. We basically repeated the experiments reported in Reference (8).

Polystyrene Particle Generator

We used polystyrene particles of 1.1 μm, 1.74 μm, 2.7 μm and 3.3 μm in diameter. These are latex particles made by Dow Chemicals of good size uniformity and of spherical shape. The particles come suspended in water with a concentration of 10% by weight. A few droplets of the particle suspension were introduced and diluted in a nebulizer. An air compressor provided the air flow to produce a mist carrying the polystyrene particles out of the nebulizer and into a heated chamber. There the water was evaporated and the particles were sprayed over the probe volume.

Different size particles could be introduced into the nebulizer, thus producing monodisperse, bimodal, trimodal and quadrumodal distributions. The compressor was also used to trap the particles after they passed through the probe volume to avoid contaminating the surrounding environment.

Results of the Polystyrene Sprays

The measurements reported here were obtained with a small breadboard using a 5 mW HeNe laser. The probe volume was formed using two orthogonal polarizations.[9]

The system was calibrated and tested with polystyrene latex particles of uniform and known size. The size and uniformity of the particles were checked with a microscope and agreed with the manufacturer's specifications.

Size and velocity distributions of the polystyrene particles flowing out of the heating chamber were obtained. First, we obtained the size corresponding to monodisperse particles, and we used it as calibration. We then proceeded to obtain bimodal size distributions. Figure 8a shows the distribution corresponding to 1.74 μm and 3.3 μm. The calibation was based on the 1.74 μm particles. The arrow with the 3.3 μm mark indicates the value predicted by the Mie calculations. In

41

Figure 8b an intermediate size of 2.7 µm was added and the calibration high voltage was increased to decrease the size range. As before, the calibration was based on the 1.74 µm, and the arrows point at the numerically predicted values. The 3.3 µm was measured very accurately, but the measurement of the 2.7 µm particles was off by two bins. This error was consistent and very repeatable. We attribute it to the oscillations found in the scattering function. Figure 8c shows the distributions corresponding to four different latex particles. As before, the calibration was obtained with the 1.74 µm particles. The results clearly indicate that the instrument is very accurate and sensitive to changes of a fraction of a micron.

Results of the Water Sprays

These measurements were obtained with the apparatus described in Reference 1.

A vibrating orifice droplet generator was used to produce strings and sprays of known size droplets. This generator produces a string of droplets of equal size and spacing. These droplets can be dispersed with external air to produce a spray of monodisperse droplets, or under some dispersion conditions the primary droplets will collide and form doublets and triplets.[8] The procedure used in these experiments was to produce a string of large monodisperse droplets to calibrate the instrument. Smaller droplets were then produced by increasing the frequency of vibration of the orifice, and with the dispersion air a spray of these droplets was formed. The spray angle was ~10°, and the number density was typically 500/cm³. The calibration point was provided by a string of 110 µm droplets produced with a flow rate of 0.21 cm³/min and a frequency of 5 kHz. Note that the droplet size can be precisely estimated given the flow rate and number of equal droplets produced. A spray of primary droplets of 49 µm (produced with a flow rate of 0.21 cm³/min and frequency of 56.9 kHz) was then produced with the dispersion air. Figure 9(a) shows the measurements of the spray of primary droplets. Figure 9(b) shows the measurements of a spray formed of primary droplets and doublets. The sizes predicted, given the flow rate and frequency of droplet generation, are 49 and 62 µm. The sizes measured with the instrument were 46 and 57 µm, respectively. Figure 9(c) extends the measurements of Figure 9(b) to the presence of triplets. The predicted sizes in this case are 49, 62, and 70 µm. Note that the measured diameters of the doublets and triplets are related to the primary droplets by $2^{1/3}$ and $3^{1/3}$, respectively.

CONCLUSIONS

A method has been presented to measure the size and velocity of particles in a flow. The particle size can range from about 0.5 µm to 5000 µm with a possible 30:1 dynamic range for any one configuration. The method extends the well-established laser Doppler velocimetry to simultaneously measure the size and velocity of individual particles crossing the probe volume.

Results obtained with monodisperse, bimodal and trimodal sprays, and with different size polystyrene particles demonstrate the high resolution and accuracy of the technique. The big advantages offered by this system are: 1) It uncouples the size and velocity measurements which permits choosing a fringe spacing to match the velocity without interfering with the size measurement; 2) It uses absolute intensity to measure the size, which leads to the measurement of irregularly shaped particles by collecting and analyzing the diffracted component of the scatterd light; 3) It measures simultaneously the size and velocity of particles with high resolution over a broad dynamic range.
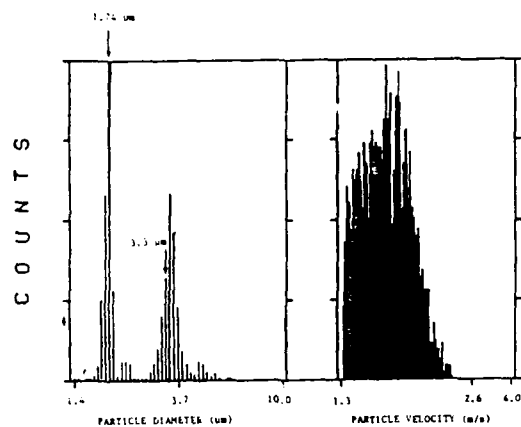
FIGURE 8a. SIZE AND VELOCITY HISTOGRAMS OF 1.74 μm AND 3.3 μm POLYSTY-
RENE SPHERES IN AIR. PHOTOMULTIPLIER TUBE HIGH VOLTAGE = 500 VOLTS.
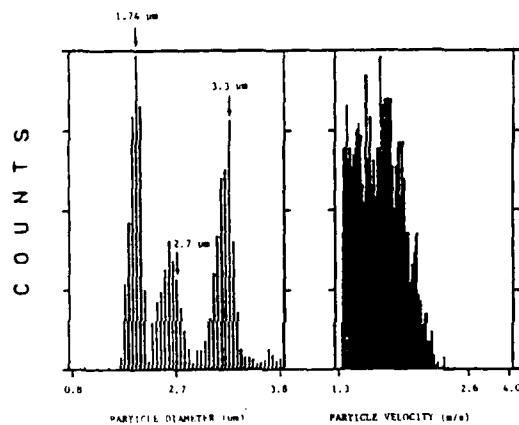
FIGURE 8b. SIZE AND VELOCITY HISTOGRAMS OF 1.74 μm, 2.7 μm, AND 3.3 μm
POLYSTYRENE SPHERES IN AIR. PHOTOMULTIPLIER HIGH VOLTAGE = 550 VOLTS.
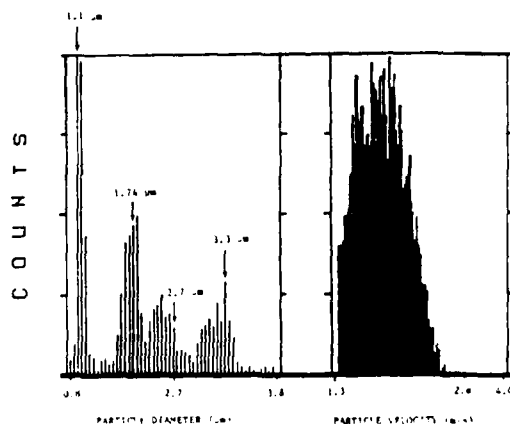
FIGURE 8c. SIZE AND VELOCITY HISTOGRAMS OF 1.1 μm, 1.74 μm, 2.7 μm,
and 3.3 μm POLYSTYRENE SPHERES IN AIR. PHOTOMULTIPLIER HIGH VOLTAGE
= 550 VOLTS.

43
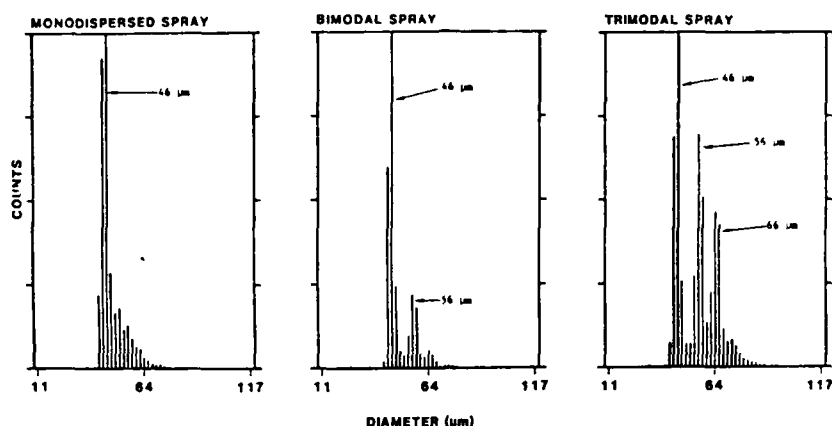
FIGURE 9. IMAX DROPLET SIZE MEASUREMENTS.

REFERENCES

1. C. F. Hess, "Nonintrusive Optical Single-Particle Counter for
    Measuring the Size and Velocity of Droplets in a Spray," Applied
    Optics, Vol. 23, No. 23 (1984).
2. M. L. Yeoman, B. J. Azzopardi, H. J. White, C. J. Bates, and
    P. J. Roberts, "Optical Development and Application of a Two
    Color LDA System for the Simultaneous Measurement of Particle
    Size and Particle Velocity," in Engineering Applications of Laser
    Velocimetry, Winter Annual Meeting ASME, Phoenix, Arizona, 14-19
    Nov. 1982.
3. G. Gousbet, P. Gougeon, G. Gréhan, J. N. Le Toulouzan, N. Lhuissier,
    "Laser Optical Sizing, from 100 Å to 1 mm − Diameter and from
    0 to 1 Kg/m³ Concentration," in AIAA 20th Thermophysics Confer-
    ence, 85-1083, Williamsburg, Virginia, 19-21 June 1985.
4. P. R. Ereaut, A. Ungut, A. J. Yule, and N. Chigier, "Measurement of
    Drop Size and Velocity in Vaporizing Sprays," in Proceedings
    Second International Conference of Liquid Atomization and Spray
    Systems, Madison, Wisconsin. (20-24 June 1982), p. 261.
5. H. C. van de Hulst, "Light Scattering by Small Particles" Wiley, New
    York, 1962, Chapter 9.
6. H. C. van de Hulst, "Light Scattering by Small Particles" Wiley, New
    York 1962, Chapter 12.
7. C. F. Hess, "A Technique Combining the Visibility of a Doppler Signal
    with the Peak Intensity of the Pedestal to Measure the Size and
    Velocity of Droplets in a Spray," in AIAA Twenty-Second Aerospace
    Sciences Meeting, 84-0203, Reno, Nevada, 9-12 January 1984.
8. B. Y. H. Liu, R. N. Berglund, and T. K. Argawal, "Experimental
    Studies of Optical Particle Counters," Atmos. Environ. 18, 717
    (1974).
9. C. F. Hess, "A Technique to Measure the Size of Particles in Laser
    Doppler Velocimetry Applications", Proceedings of the Interna-
    tional Symposium on Laser Anemometry, FED − Vol. 33, pp. 119-125.
    American Society of Mechanical Engineers, Winter Annual Meeting
    (1985).

OPTICAL PROPERTIES OF SELECTED MATERIALS

David M. Wieliczka and Marvin R. Querry
Department of Physics
University of Missouri-Kansas City, Missouri 64110

RECENT PUBLICATIONS, SUBMITTALS FOR PUBLICATIONS, AND PRESENTATIONS:

A) M.R. Querry and D.M. Wieliczka, "Optical Properties of Selected Minerals, Metals, Optical Materials, Soot and Liquids," p.   ,Proceedings of the 1987 CRDEC Scientific Conference on Obscuration and Aerosol Research, R.H. Kohl, Ed., submitted September 1987.

B) D.M. Wieliczka, M.R. Querry and Shengshan Weng, "Thin Wedge-Shaped Cell for Highly Absorbent Liquids," p. 595, Proceedings of the 1987 CRDEC Scientific Conference on Chemical Defense Research.

C) D.M. Wieliczka, Shengshan Weng, and M.R. Querry, "Optical Constants of SF-96, DMMP, DIMP, DEP, and DES," p. 1291, Proceedings of the 1987 CRDEC Scientific Conference on Chemical Defense Research.

D) Shengshan Weng, "Complex Refractive Indices of Selected Liquids," M.S. Thesis, University of Missouri - Kansas City (1987).

E) Zhiqin Huang, "Attenuated Total Reflection Applied to Liquids," M.S. Thesis, University of Missouri - Kansas City (1988).

F) M.R. Querry, D.M. Wieliczka, and Shengshan Weng, "Optical Constants of SF-96, DMMP, DIMP, DEP, and DES," Presented at the 1988 March meeting of the American Physical Society.

G) D.M. Wieliczka and M.R. Querry, "Four Methods to Measure the Complex Refractive Indices of Liquids and Solids at Carbon Dioxide Laser Wavelengths in the Infrared Spectral Region," Final Technical Report for CRDEC contract DAAA-15-85-K-0013, Approx. 435 pp., submitted September 1988.

H) D.M. Wieliczka, Shengshan Weng, M.R. Querry, "Wedge-Shaped Cell for Highly Absorbent Liquids: Infrared Optical Constants of Water," Applied Optics, submitted 1988.

CONTRIBUTIONS TO THE U.S. ARMY CRDEC COMPUTER DATABASE FOR OPTICAL CONSTANTS:

A) D.M. Wieliczka, M.R. Querry, and Shengshan Weng, "Optical Constants of Ethyl Alcohol: 400-8000 cm^{-1},"(1988).

B) M.R. Querry, Shengshan Weng, and D.M. Wieliczka, "Optical Constants of Methyl Alcohol: 400-8000 cm^{-1},(1988).

C) Shengshan Weng, D.M. Wieliczka, and M.R. Querry, "Optical Constants of Glycerin: 400-8000 cm^{-1},(1988).

ABSTRACT

We have developed a thin wedge-shaped cell used in measuring the absorption spectra of liquids. The design allows for accurate determination of the wedge angle and injection of the sample fluid without disturbing the cell. We have employed teflon seals to provide greater assurance of sample retention. Additionally, the cell provides for a variation of windows to allow optimum measurements in the desired spectral range. We have used the cell with both UV grade fused silica and zinc selenide windows to obtain Lambert absorption coefficients of eleven liquids, water, methyl alcohol, ethyl alcohol, SF96, fogoil, diesel fuel, DES, DEP, DMMP, DIMP, and glycerin.

The complex refractive index $N(\nu)$ as a function of wave number is defined as:

$$N(\nu) = n(\nu) + i \, k(\nu) \qquad\qquad (1)$$

where the wave number, ν , is the inverse of the wavelength, and has units of cm^{-1}; $n(\nu$ is called the reflection coefficient; and $k(\nu)$ is the extinction coefficient. The extinction coefficient, $k(\nu)$, can be determined provided the Lambert absorption coefficient is known using the following equation:

$$k(\nu) = \alpha(\nu) \, (4\pi\nu)^{-1} \qquad\qquad (2)$$

where $\alpha(\nu)$ is the Lambert absorption coefficient. The simplicity of equation (2) relating the Lambert absorption coefficient to the extinction coefficient is contrasted to the difficulty in performing the experimental measurements on liquids.

One very common experiment in determining $\alpha(\nu)$ for liquids is using a wedge-shaped cell. Two measurements of spectral absorbance $A(\nu,z)$ with the same wave number, ν , of electromagnetic radiation and with the same cell windows but with different thickness z_1 and z_2 of the absorbing liquid are needed, the absorbance measurements then provide:

$$k(\nu) = - [A(\nu,z_2) - A(\nu,z_1)]/[4\pi\nu(\log_{10}e)(z_2 - z_1)] \qquad\qquad (3)$$

The real part of the complex refractive index $n(\nu)$ can be calculated by Kramers-Kronig analysis of $k(\nu)$.

For the purpose of determining accurate k values of highly absorbent liquids, the wedge-shaped cell technique is the most direct. In 1962, Bauman[1] presented a variable-space and fixed liquid cell. The variable-space cell was designed using a frame spacer held by two windows, with the liquid sample introduced into the cell by capillary action. A 1971 paper by Robertson and Williams[2] described the use of a unique absorption cell to measure the Lambert absorption coefficient for water, in the spectral region between 4000 and 288 cm^{-1} wave number, employing two optically flat infrared transmitting windows of CaF_2 or KRS-5. Neoprene strips were used to seal the edges of the cell. The sample thickness could be varied uniformly from zero thickness at its vertex to 20 m thickness at its base. Tyler, Taylor, and Querry[3] published a paper in 1978, describing a thin-wedge-shaped cell for highly absorbent liquids. Liquids were held in the cell by surface tension. The maximum thickness of the wedge could be varied using feeler stock according to the application and surface tension of the liquid sample.

The cell we have designed, constructed, and used is based on the design of Tyler, et al..[3] It is designed for the purpose of avoiding serious errors during the measurement of the Lambert absorption coefficient of liquids; to be able to study materials with high vapor pressure, and to also allow for variable maximum thickness to compensate for variations in the Lambert absorption coefficient. In addition the cell was constructed in a manner to allow for uniform filling by the liquid without the need to dissamble the cell after the apex angle is determined.

An exploded view of the wedge-shaped absorption cell, cell holder, and translation unit is shown in Fig. 1. The windows are positioned in the aluminum holder, 1, and are squared with respect to each other through to also allow for variable maximum thickness to compensate for variations in the Lambert absorption coefficient. In addition the cell was constructed in a manner to allow for uniform filling by the liquid without the need to dissamble the cell after the apex angle is determined.

An exploded view of the wedge-shaped absorption cell, cell holder, and translation unit is shown in Fig. 1. The windows are positioned in the aluminum holder, 1, and are squared with respect to each other through the use of the threaded ball plungers, 7', 7", 8', 8", 9', 9", 10', 10". Two stainless steel posts, 5' and 5", are used as backstops and alignment posts for the teflon seal on the right side of the cell. Pressure is applied to the teflon seal on the right side of the cell through a U shaped aluminum holder, 13", and the set screws, 20' and 20". The stainless steel shim-stock is held in position by the aluminum blocks, 4' and 4". The windows are finally held rigid against the aluminum holder by the toggle clamps, 2' and 2". The entire cell can be translated vertically by the Unislide mechanism, 17, through a distance of 50 mm. The vertical position is measured through the use of the dial indicator to an accuracy of 0.01 mm. The components which make this cell unique

are the manifolds, 12' and 12". The other components are common to most applications
of the wedge-shaped cell technique, a complete list of components can be obtained from
either of the authors.

The use of the manifolds and teflon seals allow the cell to be constructed and
the apex angle to be measured with an air gap between the windows. The liquid can
then be injected between the windows without dissassembling the unit providing an
accurate value for the apex angle, and therefore the sample thickness. In additiou,
the use of teflon seals provides for a tight seal of the unit to prevent loss of the
sample during the absorbance measurements and also allows the study of liquids with a
high vapor pressure.

Before the experiment, the wedge-shaped-cell unit is cleaned with methyl alcohol
and ethyl alcohol in an ultrasonic cleaner. The cell is assembled according to Fig. 1
using the feeler stock for the appropriate absorption coefficient to be measured.
Several runs must be performed to obtain the maximum sensitivity in each spectral
range. The thickness of the feeler stock used in this experiment ranged from 0.1 m
to 25 m.

After the cell is assembled the wedge angle is determined through the use of a
He-Ne laser interferometer. The cell is translated via a stepper motor and the
pattern of interference fringes is acquired in digital form using an entrance slit
assembly preceeding a photomultiplier tube. The output of the photomultiplier tube is
appropriately connected to an A/D channel of a Data Acquisition and Control Adapter
installed in an IBM PS/2 - 30 computer. The intensity as a function of cell position,
z, is given by

$$I(z) = A + B \cos(4\pi z \nu_0 \tan \beta + \phi) \qquad (4)$$

where A and B are constants, ν_0 = 15,802.8 cm^{-1} is the frequency of the HeNe laser
light,   is the apex angle of the wedge-shaped volume, and   is an arbitrary phase
factor. The Fourier transform of Eqn. (4) gives

$$I(\nu) = (2\pi)^{1/2}(A \delta(\gamma) + B \{ \delta(\gamma - \zeta)e^{i\phi} + \delta(\gamma + \zeta)e^{-i\phi} \}) \qquad (5)$$

where $\gamma = 2\pi\nu$, and $\zeta = 4\pi\nu_0 \tan\beta$. Thus,

$$\tan\beta = \nu/(2\nu_0) = m/(2\nu_0 N \Delta z) \qquad (6),$$

where m is the integer position of $\delta(\gamma - \zeta)$ in the interval $0 \leq m \leq (N/2)-1$ of the
Digital Fast Fourier Transform (DFFT) used in this work, N is the number of data
points in the digitized interference pattern, and Δz is the incremental Z direction
displacement of the cell between data points in the digitized interference pattern.
In Eqn. (6) we used the relations $\nu = m\Delta\nu$ and $N = (\Delta z \Delta\nu)^{-1}$. Consideration of
minima and maxima, where the argument of the cosine function in Eqn. (4) was
respectively $2m\pi$ and $(2m+1)\pi$, also provided Eqn. (6) and demonstrated that m in
Eqn. (6) is the number of minima or maxima in the digitized interference pattern.
Once the apex angle was known the wedge was slowly filled with the sample by
injection through a syringe into either of the side manifolds. The injection is
stopped when the fluid level appears in the tygon tube attached to the opposite side
manifold.

The data presented here spans the spectral region of 500 cm^{-1} to 8000 cm^{-1}. Two
window materials were employed to span this region, fused silica, 3623-8000 cm^{-1}, and
zinc selenide, 500-4000 cm^{-1}. The spectral intensity measurements were performed by
two instruments, Varian-Cary-2300 UV-VIS-near IR and a Perkin-Elmer 580B IR
spectrophotometer. Both instruments are double beam spectrophotometers capable of
absorbance measurements. Spectral intensity was measured at four heights of the cell
from which six combination subtractions were used to compute the imaginary part of the
complex refractive index.

The extinction coefficient and index of refraction for ethyl alcohol is presented
in Figs. 2 and 3, respectively.[4] The data presented in these figures are compilations
of many spectral scans. The wedge angle was optimized for each spectral range due to
the varying absorption coefficient. The data was then superimposed to provide a
spectral scan over the entire wave number range.

The corresponding data for methyl alcohol and glycerin is presented in Figs. 4

and 5 and in Figs. 6 and 7, respectively.

REFERENCES

1. R.P. Bauman, Absorption Spectroscopy (John Wiley & Sons Inc., 1962), pp. 186-188.

2. C.W. Robertson and D. Williams, J. Opt. Soc. Am. 61, 1316 (1971).

3. I.L. Tyler, G. Taylor, and M.R. Querry, Applied Optics, 17, 960 (1978).

4. Results for all of the liquids may be obtained from the authors.

5. G.M. Hale and M.R. Querry, Applied Optics, 12, 555 (1973).

6 A.N. Rusk, D. Williams, and M.R. Querry, J. Opt. Soc. 61, 895 (1971).
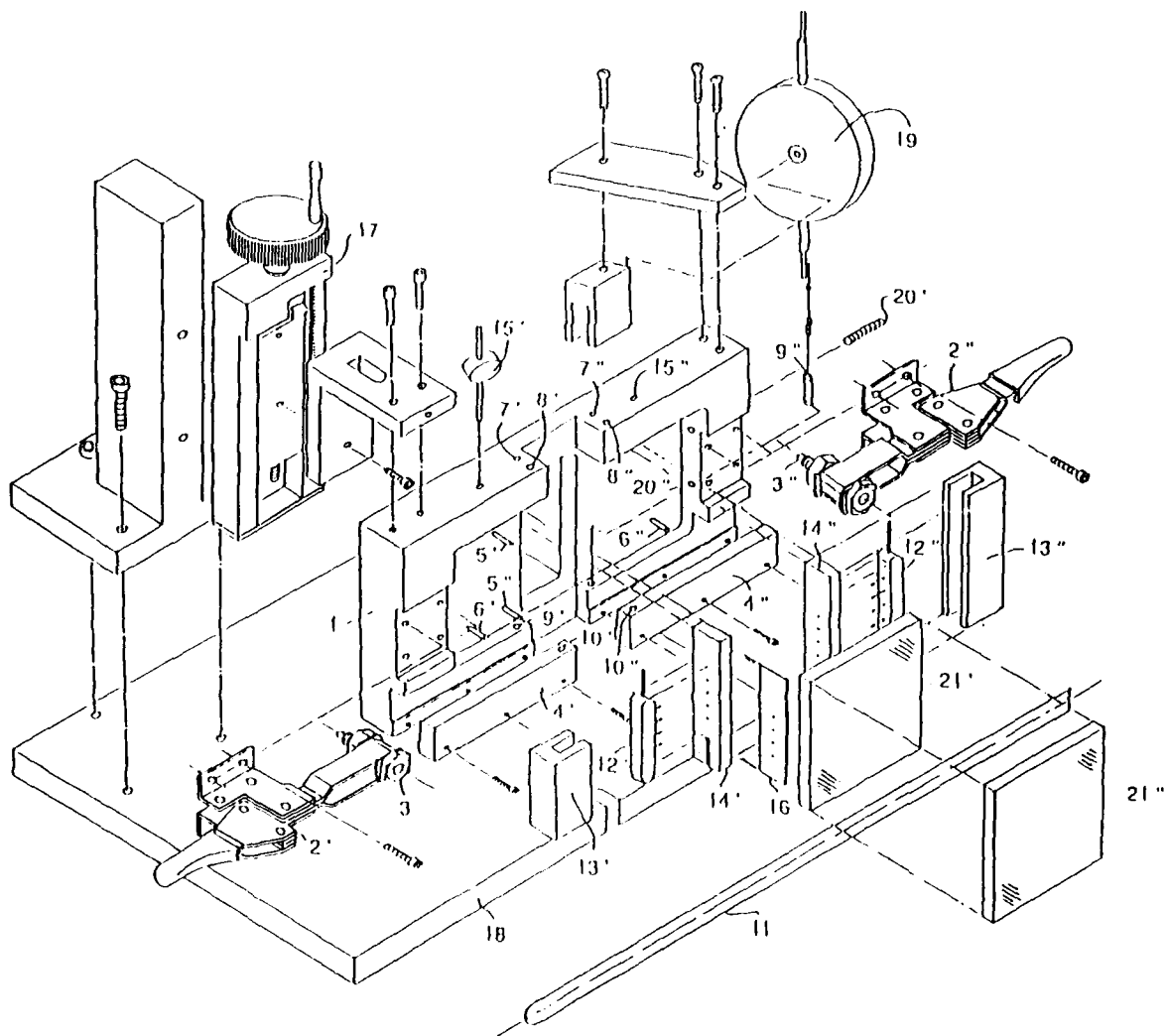
FIGURE 1. Exploded view of the thin-wedge-shaped cell, cell holder and translationo stage.

Ethyl Alcohol
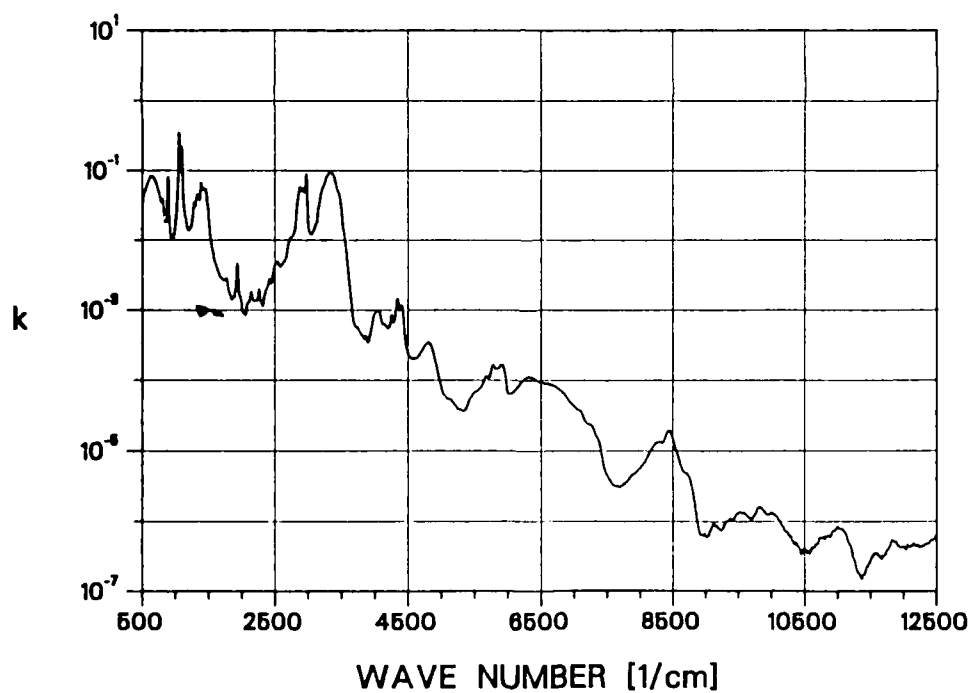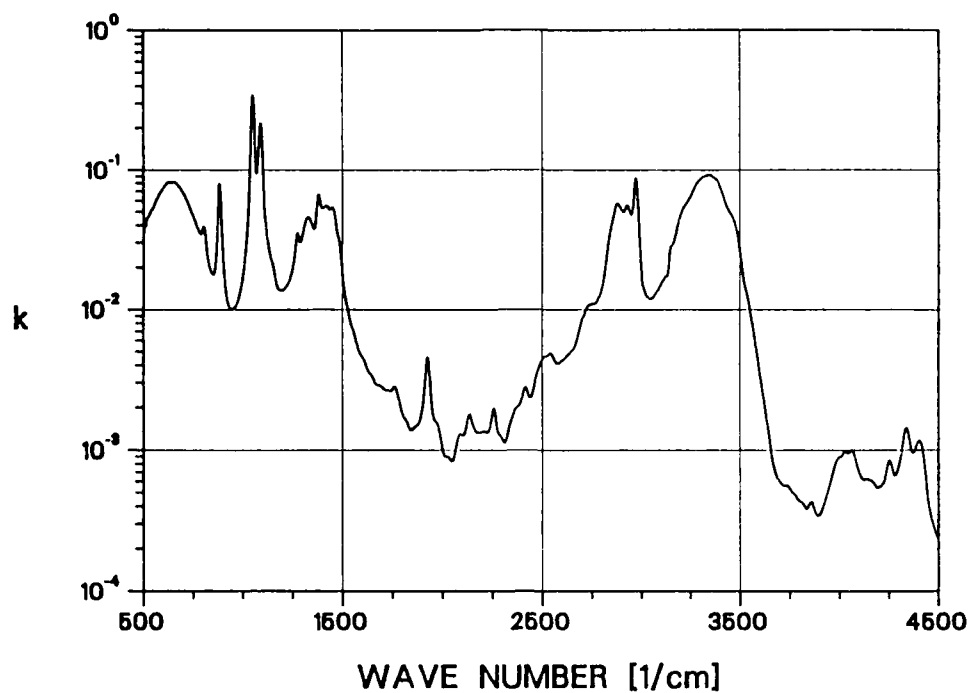
FIGURE 2. Extinction coefficient for ethyl alcohol in the spectral range 500 cm^{-1} to 12500 cm^{-1}.

Ethyl Alcohol
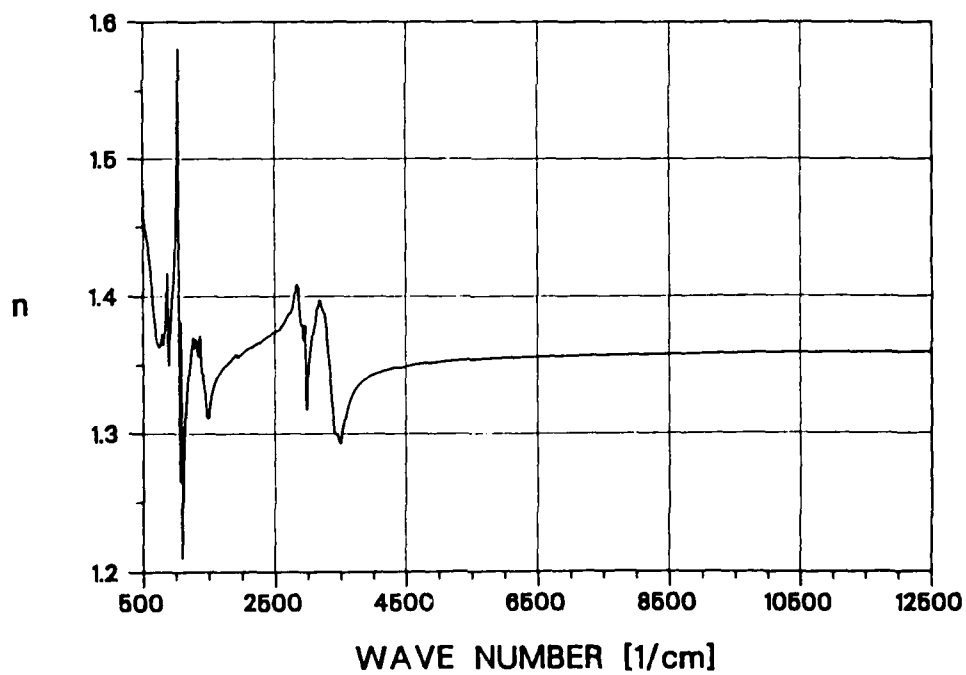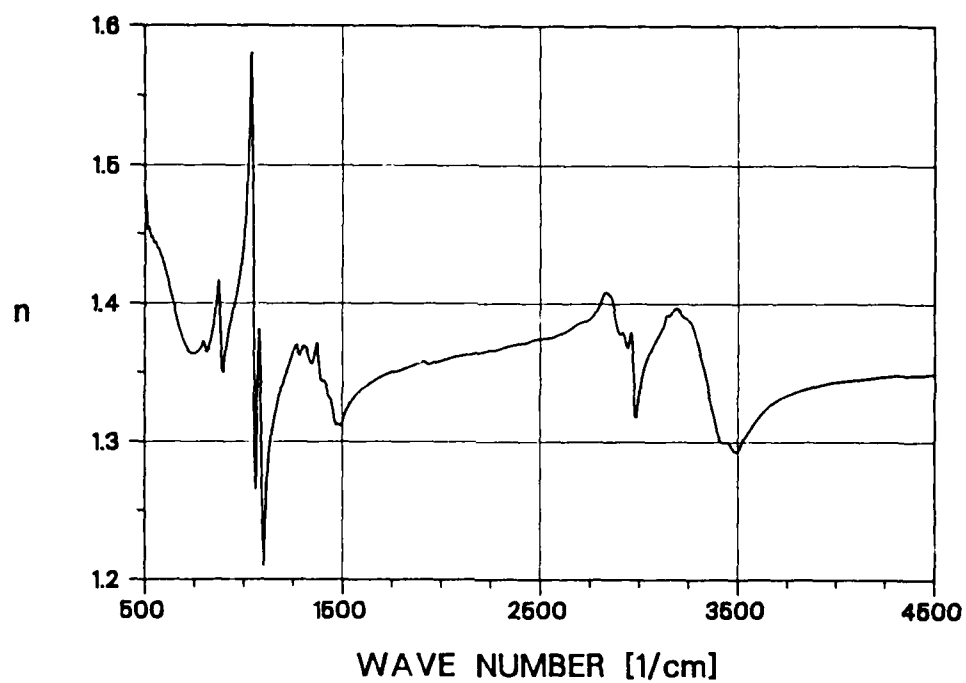
FIGURE 3. Index of refraction for ethyl alcohol in the spectral range 500 cm^{-1} to 12500 cm^{-1}.
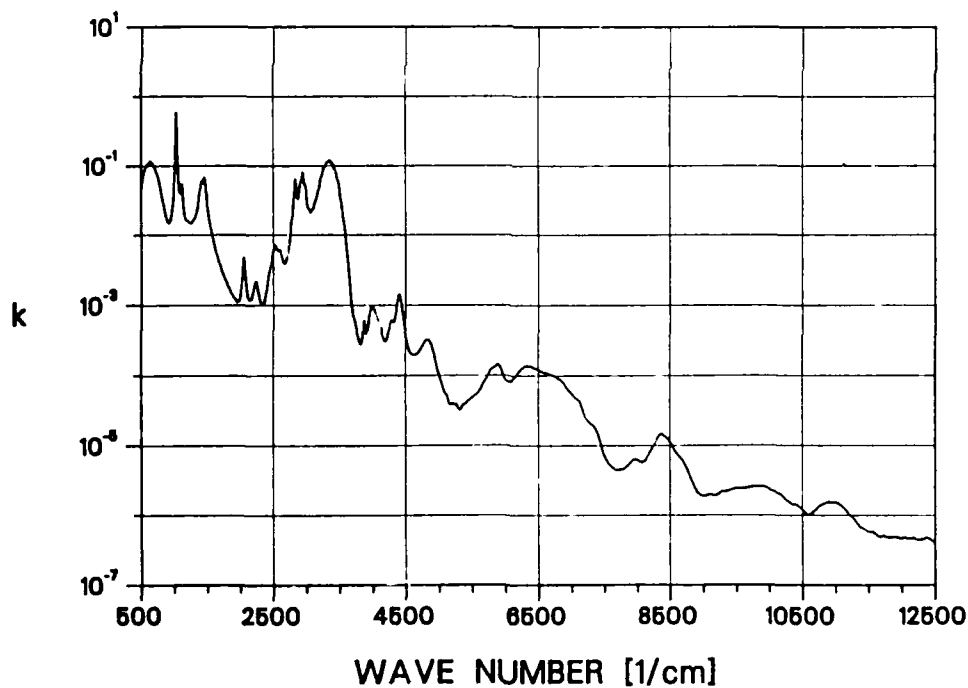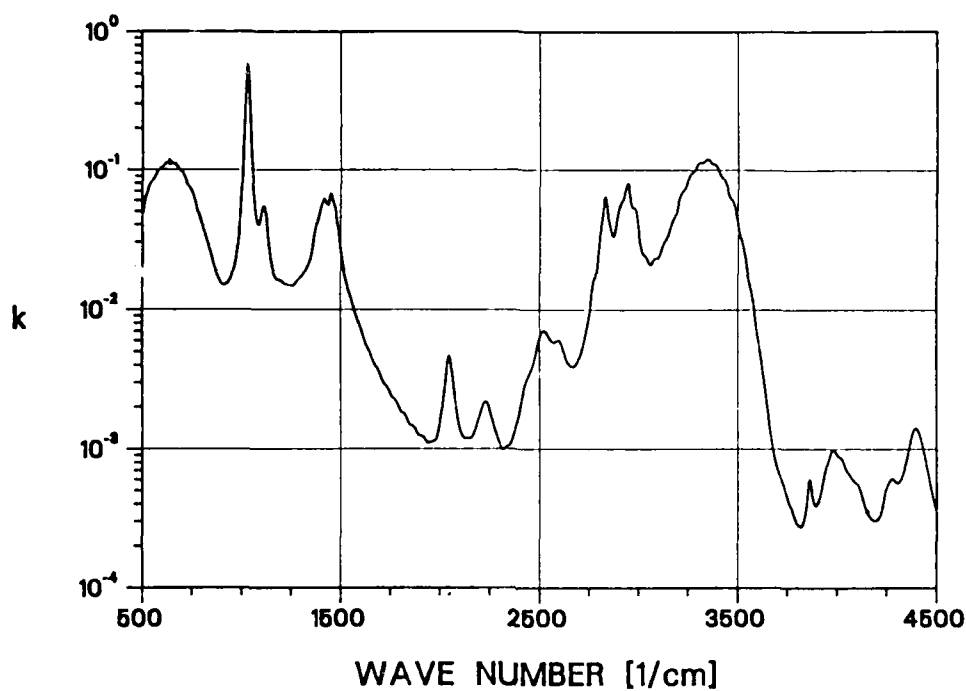
Methyl Alcohol

FIGURE 4. Extinction coefficient for methyl alcohol in the spectral range 500 cm^{-1} to 12500 cm^{-1}.
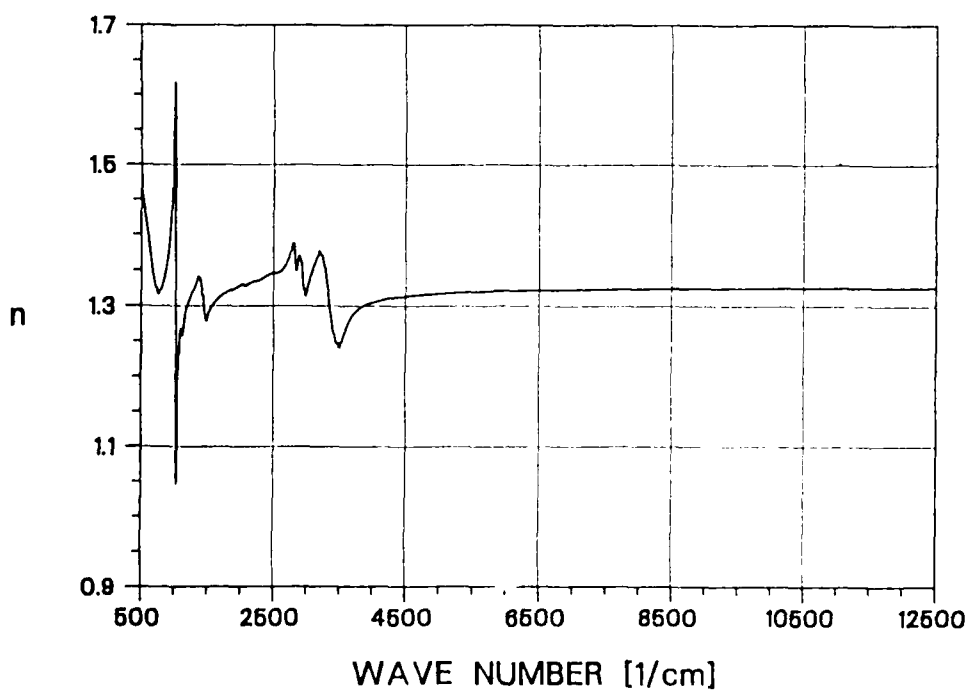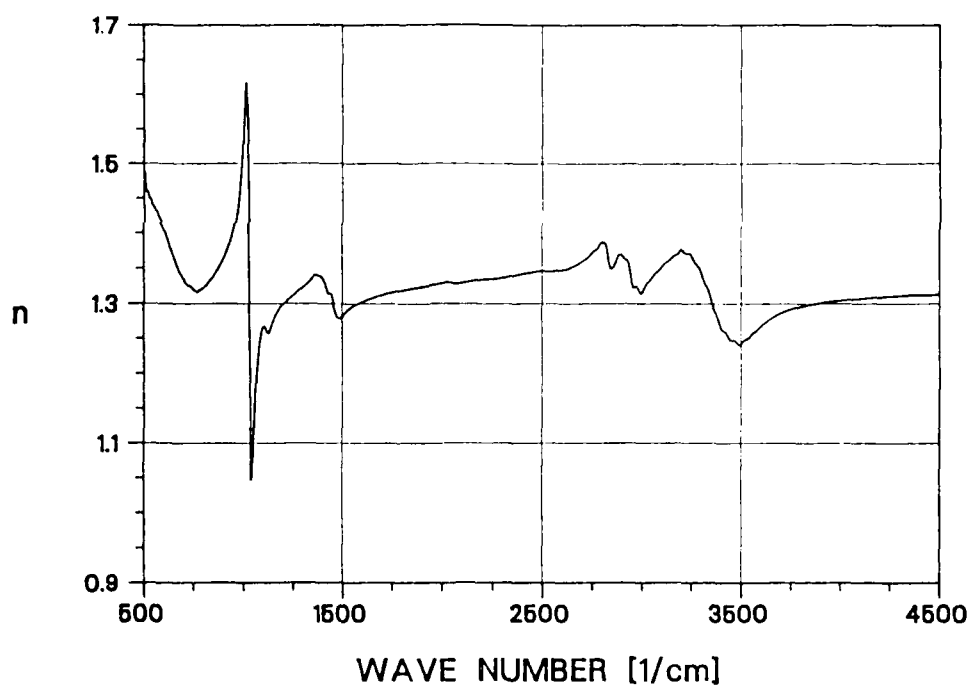
Methyl Alcohol

FIGURE 5. Index of refraction for methyl alcohol in the spectral range 500 cm^{-1} to 12500 cm^{-1}.
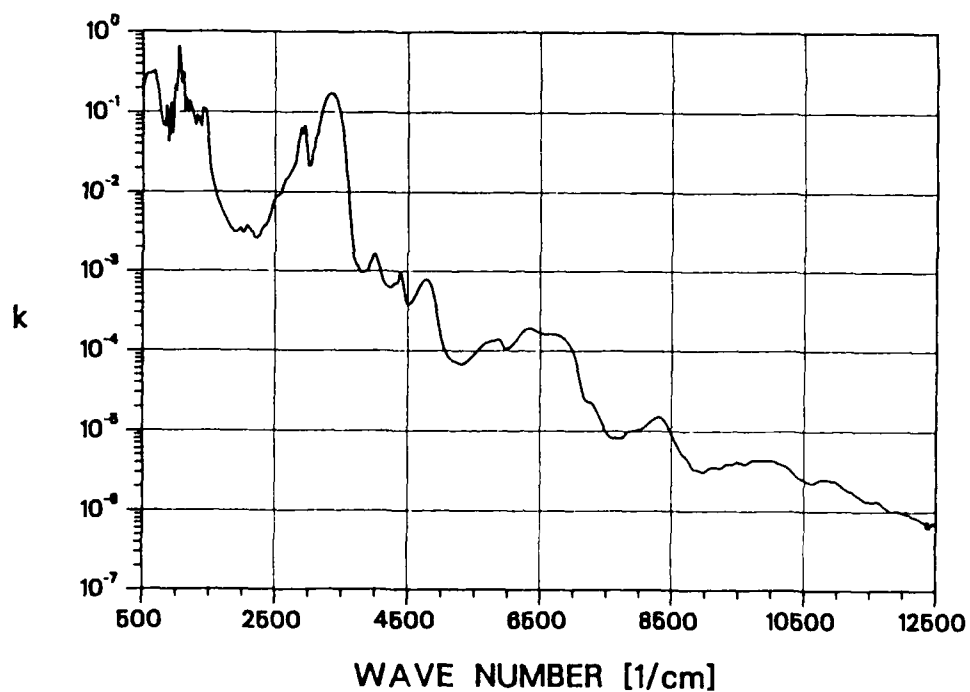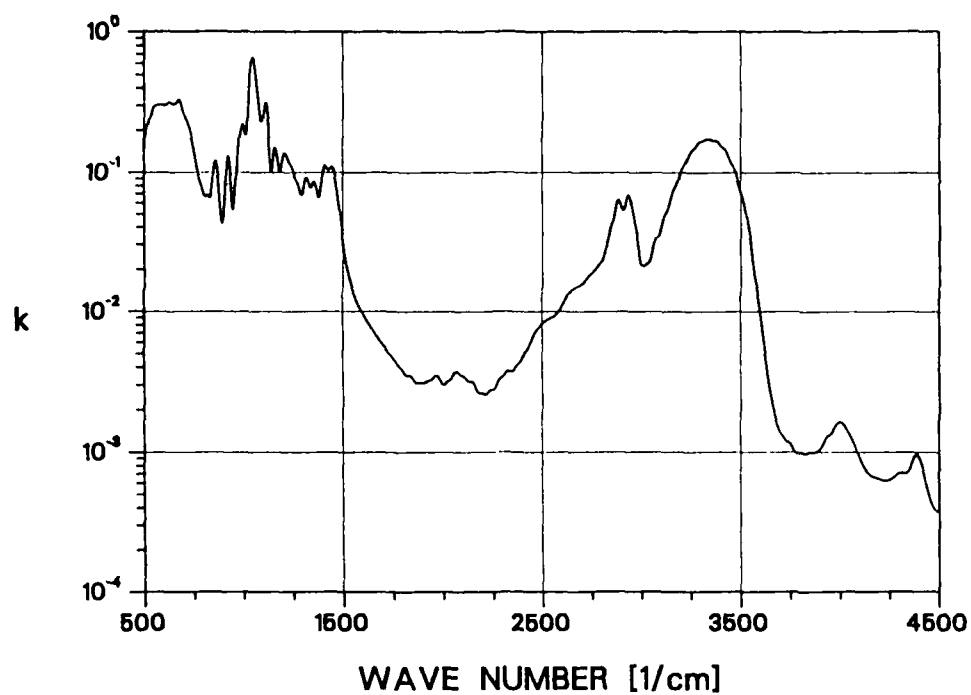
Glycerin

FIGURE 6. Extinction coefficient for glycerin in the spectral range 500 cm^{-1} to 12500 cm^{-1}.
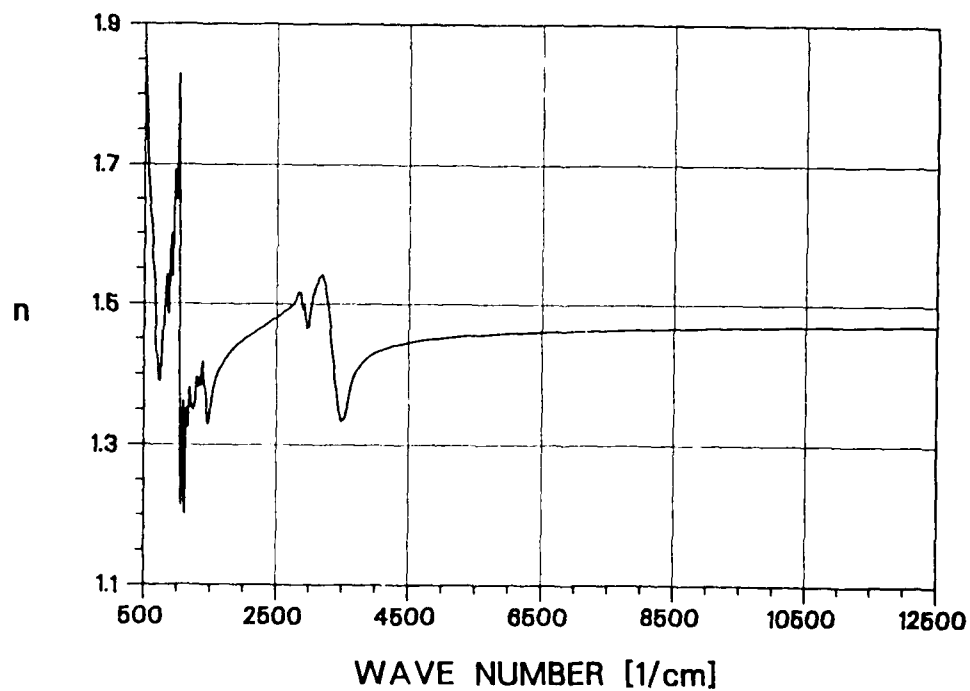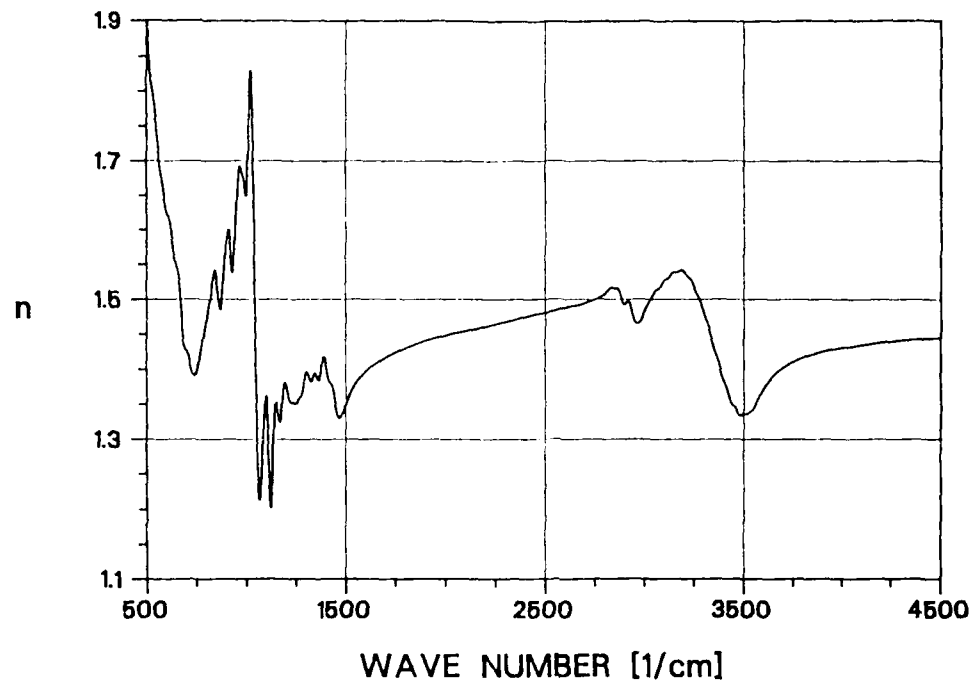
Glycerin

FIGURE 7. Index of refraction for glycerin in the spectral range 500 cm^{-1} to 12500 cm^{-1}.

Blank

PHASE DIFFERENTIAL SCATTERING AND POLYDISPERSITY

R.G. Johnston and G.C. Salzman
Los Alamos National Laboratory
Los Alamos, NM 87545

ABSTRACT

We have developed a new light scattering technique called Phase Differential Scattering (PDS), which utilizes a two-frequency, Zeeman effect laser. Some of our theoretical PDS results are presented here and compared with experimental measurements on aqueous suspensions of microspheres. According to theory, PDS should be very sensitive to average sphere size. We find experimentally, however, that the effects of polydispersity appear to be less than expected. The Zeeman laser has other potential applications for aerosol research.

There is more information contained in elastically scattered light than available from simple measurements of the scattered irradiance.[1] The phase and polarization of the scattered light are highly dependent on the size, morphology, and internal structure of the scattering particles.[1,2] We have developed a new light scattering technique, called Phase Differential Scattering (PDS),

57

that provides certain kinds of phase and polarization information. Details of the technique, its relation to other scattering methods, and its advantages/ disadvantages are discussed in references 2 and 3.

Briefly, PDS involves scattering the light of a two-frequency, Zeeman effect laser from a collection of particles. The 1 mW Zeeman laser emits two collinear, orthogonally polarized laser lines near 632.8 nm.[4] They differ by only 250 kHz in frequency (3.3×10^{-7} nm in wavelength). When the beam from this laser is scattered from a sample and the scattered light passes through an analyzing polarizer, the two laser lines interfere on the photodetector, producing a 250 kHz beat frequency. PDS involves measuring the amplitude (Γ) and the phase (γ) of this 250 kHz sine wave signal.

The transmission axis of the analyzing polarizer can be oriented at $0°$, $45°$, or $90°$ with respect to the scattering plane. Any other orientation gives redundant information.[2,3] Only the $45°$ orientation will be discussed here, although the $0°$ and $90°$ orientations are potentially the most interesting.[2]

A theory for PDS can best be developed using the amplitude scattering matrix.[2,3] The theoretical results presented here, however, are expressed in terms of the more familiar Mueller scattering matrix. When a sample scatters light, the Stokes parameters for the scattered light are related to the Stokes parameters for the incident light by:[1]

$$
\begin{pmatrix} I_s \\ Q_s \\ U_s \\ V_s \end{pmatrix} = \frac{1}{k^2 r^2} \begin{pmatrix} S11 & S12 & S13 & S14 \\ S21 & S22 & S23 & S24 \\ S31 & S32 & S33 & S34 \\ S41 & S42 & S43 & S44 \end{pmatrix} \begin{pmatrix} I_i \\ Q_i \\ U_i \\ V_i \end{pmatrix} \tag{1}
$$

where Sij is the i,j element of the Mueller scattering matrix, the subscript i or s refers to the incident or scattered light, $k = 2\pi/\lambda$, λ is the wavelength, and r is the distance from the scatterers to the photodetector.

We have previously presented a PDS theory for scattering from a single arbitrary particle, or from a collection of identical (monodisperse) spheres.[2,3] The PDS phase, γ, for such scatterer(s), with the analyzing polarizer oriented at 45°, is:

$$\gamma = \arctan \frac{S34 + S14}{S33 + S13} \tag{2}$$

Here, we give the theoretical prediction for a collection of arbitrary particles. The PDS phase, γ, for such a collection is (analyzing polarizer at 45°):

$$\gamma = \arctan \frac{\Sigma (S34) + \Sigma (S14)}{\Sigma (S33) + \Sigma (S13)} \tag{3}$$

where Σ (Sij) is a sum over particles, i.e., it is the sum of the Sij matrix elements for each separate particle in the collection.

Note that Eq (3) does not follow trivially from Eq (2). The Mueller scattering matrix for a collection of particles is the sum of the individual particle scattering matrices.[1] This additive property, however, is not automatically guaranteed for an arbitrary function of matrix elements.

For optically inactive spheres, S13 = S14 = 0 and Eq (3) becomes

$$\gamma = \arctan \frac{\Sigma (S34)}{\Sigma (S33)} \tag{4}$$

Figures 1 and 2 show experimental and theoretical results for PDS scattering from an aqueous suspension of polystyrene latex microspheres (n = 1.59). According to the manufacturer, the mean sphere diameter was 2.95 μm, with a standard deviation of 0.13 μm. Figure 1 shows the PDS phase, γ, plotted as a function of scattering angle. The solid line represents the experimental results for an aqueous suspension with 5.3 x 10^5 microspheres per mliter. Multiple scattering significantly reduces the amplitude of the ripples seen in the curve, but not the locations of the peaks and valleys.[3] The dashed and dotted curves show theoretical predictions for scattering from monodisperse spheres of 2.85 μm and 2.95 μm diameter, respectively. The agreement between

the experimental curve and the theoretical 2.85 μm curve would be even better if multiple scattering effects were considered.[3]

Figure 2 shows the theoretical effects of polydispersity. For comparison, the solid curve shows the same experimental data as seen in Figure 1. The dashed curve represents a theoretical prediction using Eq (4) and the (non-Gaussian) microsphere size distribution measured with an electron scanning microscope. The dotted curve gives the predicted PDS curve for a Gaussian size distribution with standard deviation 0.13 μm. Neither the dashed nor dotted curve show much ripple structure for scattering angles between 80° and 130°. The experimental PDS curve shows much more structure. It agrees with the 2.85 μm monodisperse prediction better than with predictions for polydisperse spheres. We've found similar results for other sizes of microspheres.

This result is interesting, because it suggests that, while PDS should be very sensitive to average sphere size (as seen in Figure 1), it is affected less by polydispersity than expected (as seen in Figure 2). We are exploring the reasons for this result and attempting to improve our methods of determining particle size distributions. The relevance of this issue is that many aerosols or hydrosols of practical interest are highly polydisperse.

Now the PDS phase, γ in Eq (4), equals the arctan of the ratio of Σ S34 and Σ S33. Our PDS instrument can also measure Σ S34 and Σ S33 separately for a collection of microspheres. Measurements of γ, however, have several advantages. The ratio of Σ (S34) to Σ (S33) is relatively insensitive to fluctuations in laser intensity and sphere concentration, it requires no experimental calibration factor, and corrections for residual stress birefringence in the optics are simple and accurate.[2,3]

Finally, we are modifying the Zeeman laser in hopes of making practical chiral scattering measurements, that is, measurements with the analyzing polarizer oriented at 0° or 90° with respect to the scattering plane. A higher power Zeeman laser would be helpful for such measurements. We are exploring

other interferometric applications of the Zeeman effect laser that may be of interest for studying aerosols. These include ultrasensitive measurements of bulk aerosol density and "weighing" of individual aerosol particles.

REFERENCES

1. C.F. Bohren and D.R. Huffman, Absorption and Scattering of Light by Small Particles (Wiley, New York, 1983).
2. R.G. Johnston, S.B. Singham, and G.C. Salzman, "Polarized Light Scattering," Comments on Molecular and Cellular Biophysics 5, 171 (1988), and references therein.
3. R.G. Johnston, S.B. Singham, and G.C. Salzman, "Phase Differential Scattering from Microspheres," Applied Optics 25, 3566 (1986).
4. Optra, Inc., Peabody, MA.

ACKNOWLEDGEMENTS
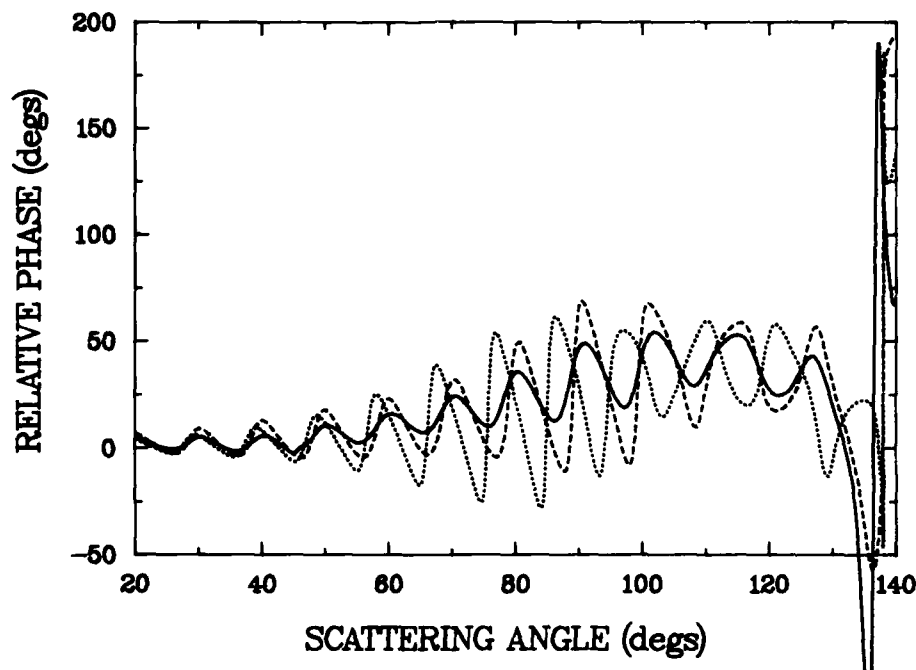
FIGURE 1 - PDS is sensitive to average sphere size. The solid curve shows
experimental measurements of the PDS phase, γ, plotted as a function of
scattering angle for scattering from an aqueous suspension of microspheres.
According to the manufacturer, the average sphere diameter was 2.95 μm, with a
standard deviation of 0.13 μm. The dashed and dotted curve show theoretical
predictions, using Eq (4) for scattering from monodisperse spheres of diameter
2.85 μm and 2.95 μm, respectively. Note the agreement between the solid
experimental curve and the dashed, 2.85 μm, theoretical curve. The divergence
in γ near a scattering angle of 135 degrees is discussed in reference 3.
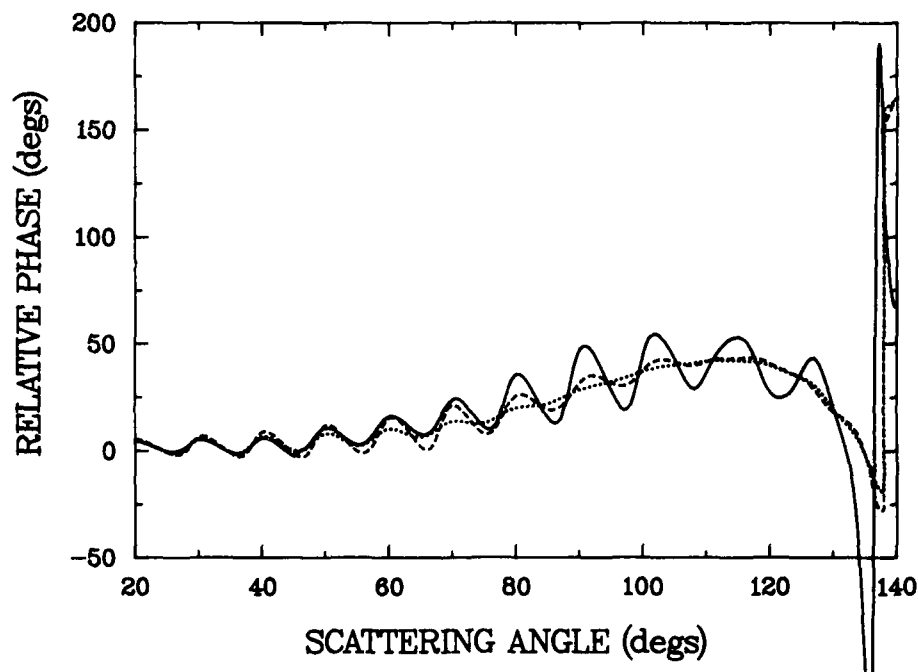
FIGURE 2 - Experimental PDS curves for microspheres show more structure (i.e. "ripples") than would be expected, given the scatterers' measured polydispersity. The solid curve is the same experimental data seen in Figure 1. The dotted curve is the theoretical prediction for a Gaussian size distribution given the manufacturer's reported standard deviation of 0.13 μm. The dashed curve shows the PDS prediction for the actual size distribution that we measured. Neither theoretical curve shows much structure between scattering angles of 80 degreees and 130 degrees. The experimental PDS curve showed closer agreement with the monodisperse 2.85 μm theoretical curve in Figure 1.

Blank

III. NONLINEAR EFFECTS AT HIGH ENERGY

Blank

EXPERIMENTAL AND THEORETICAL ANALYSIS OF LIQUID DROPLETS MOVING THROUGH A FOCUSED CO_2 LASER BEAM

J.P. Barton, D.R. Alexander, and S.A. Schaub
Center for Electro-Optics
College of Engineering
University of Nebraska-Lincoln
Lincoln, NE 68588-0525

RECENT PUBLICATIONS, SUBMITTALS FOR PUBLICATION, AND PRESENTATIONS:

A). D.R. Alexander and J.G. Armstrong, "Explosive vaporization of aerosol drops under irradiation by a CO_2 laser beam," Appl. Opt., **26**, 533 (1987).

B). D.R. Alexander, J.P. Barton, S.A. Schaub, and M.A. Fitzwater, "Beam propagation effects resulting from the electric field strengths for spheres and cylinders: internal and near field," presentation at the Workshop on the Physics of Directed Energy Propagation in the Atmosphere," U.S. Army Atmospheric Sciences Laboratory (ASL) at New Mexico State University, Las Cruces. New Mexico, January 27-28, 1987.

C). D.R. Alexander, J.P. Barton, S.A. Schaub, and M.A. Emanuel, "Experimental and theoretical analysis of the interaction of CO_2 laser radiation with fluid cylinders and adjacent spheres," presentation at the 1987 CRDEC Conference on Obscuration and Aerosol Research, June, 1987.

D). D.R. Alexander, J.P. Barton, S.A. Schaub, M.A. Emanuel, and J. Zhang, "Experimental and theoretical analysis of the interaction of laser radiation with fluid cylinders and spheres," Proceedings of the 1987 CRDEC Conference on Obscuration and Aerosol Research.

E). M.A. Emanuel, "Explosive vaporization of spherical and cylindrical aerosols: comparison between experimental results using a CO_2 laser and internal and scattered optical fields," Masters Thesis, Mechanical Engineering Department, Center for Electro-Optics, University of Nebraska-Lincoln, Lincoln, Nebraska, 68588-0525, October, 1987.

F). S.A. Schaub, D.R. Alexander, J.P. Barton, and M.A. Emanuel, "Focused laser beam interactions with methanol droplets: effects of relative beam diameter," submitted to Applied Optics. May, 1988.

G). J.P. Barton, D.R. Alexander, and S.A. Schaub, "Experimental and theoretical analysis of liquid droplets moving through a focused CO_2 laser beam," presentation at the 1988 CRDEC Conference on Obscuration and Aerosol Research, June, 1988.

H). J.P. Barton, D R. Alexander, and S.A. Schaub, "Internal and near-surface electromagnetic fields for a spherical particle in a focused laser beam," poster presentation at the 1988 CRDEC Conference on Obscuration and Aerosol Research, June, 1988.

I). D.R. Alexander, D.E. Poulain, J.P. Barton, S.A. Schaub, and J. Zhang, "Nonlinear effects of excimer laser radiation with solid particles in a vacuum," presentation at the 1988 CRDEC Conference on Obscuration and Aerosol Research, June, 1988.

J). S.A. Schaub, D.R. Alexander, and J.P. Barton, "Theoretical model for the image formed by a spherical particle in a coherent imaging system: comparison to experiment," submitted to Optical Engineering, July, 1988.

K). J.P. Barton, D.R. Alexander, and S.A. Schaub, "Internal and near-surface electromagnetic fields for a spherical particle irradiated by a focused laser beam," J. Appl. Phys., **64**, 1632 (1988).

L). J.P. Barton, D.R. Alexander, and S.A. Schaub, "Spherical particle irradiated by a tightly-focused laser beam: focal point positioning effects at resonance conditions," submitted to the Journal of Applied Physics, September, 1988.

Abstract

A simplified theoretical model for predicting the threshold power for explosive fragmentation of liquid droplets falling thro igh the focal point of a tightly-focused, continuous, Gaussian-profiled laser beam has been developed. Theoretically-predicted and corresponding experimentally-measured explosive fragmentation threshold power/droplet velocity ratios are compared for CO_2 laser irradiated water droplets within a size parameter range of 5 to 25. The theoretical and experimental data were in agreement within a factor of about two. Future refinements of the theoretical modeling and the experimental procedure are discussed.

I. Introduction

An experimental and theoretical analysis of the transient heating of 20 μm to 80 μm diameter (5 to 25 size parameter) liquid droplets falling through the focal point of a **tightly-focused**, fundamental (TEM$_{00}$ mode), linearly-polarized, Gaussian-profiled, 10.6 μm dominant wavelength, **continuous** CO_2 laser beam is considered. A theoretical analysis of this problem is now possible due to our recent development of a spherical particle/arbitrarily-defined beam interaction theory[1] that permits a computationally-efficient means for determining the internal electromagnetic fields within a spherical droplet offset from the focal point of a tightly-focused Gaussian beam. Of particular interest is the development of a theoretical model to predict laser threshold power for the explosive fragmentation of the droplets, for these conditions, as a function of such parameters as beam waist diameter, droplet diameter, and droplet thermo/optical properties. An agreement between theoretically-predicted explosive fragmentation threshold power with the corresponding experimentally-measured values would support the physical mechanism assumptions of the theoretical model. Presented here is our preliminary effort at theoretically modeling falling droplet/tightly-focused laser beam heating and an initial comparison (including discussion) between theoretically-predicted and experimentally-measured explosive fragmentation threshold powers for water droplets in a size parameter range of 5 to 25.

A theoretical analysis of the transient heating of a liquid droplet irradiated by a laser pulse has been previously investigated by Prishivalko and Leiko[2] and by Pendleton.[3] In both of these analyses, monochromatic **plane wave** illumination upon a spherical particle was assumed, so Lorenz-Mie theory was appropriately applied to determine the internal electromagnetic field distributions necessary for the calculation of the spatially-distributed heating within the droplet. Such an incident plane wave assumption would be valid for conditions where the incident laser beam intensity is uniform over the projected area of the droplet, as might be the case if the local beam diameter

is much greater than the diameter of the droplet. Lorenz-Mie theory, and thus the analyses of Prishivalko and Leiko[2] and of Pendleton,[3] is not applicable for a spherical droplet moving through the focal point of a tightly-focused beam, as is of interest here.

Prishivalko,[4] utilizing an empirical criterion, claimed good agreement (5-10%) with experimental intensity threshold measurements for the explosive fragmentation of 20 μm to 60 μm diameter water droplets irradiated by a 10.6 μm wavelength CO_2 laser pulse. Calculations by Pendleton[3] were consistent with the pulsed CO_2 laser fragmentation patterns observed by Kafalas and Ferdinand.[5] Otherwise, there appears to be little detailed theoretical/experimental comparisons for CO_2 laser heating of liquid droplets in the explosive fragmentation regime. To our knowledge there has been no previous detailed theoretical/experimental comparisons for liquid droplets falling through the focal point of a tightly-focused, continuous, CO_2 laser beam.

II. Experimental Arrangement

The experimental arrangement and procedure are described in detail in Ref. 6; only a general description will be provided here. A schematic of the experimental arrangement is shown in Fig. 1. The fundamental (TEM$_{00}$ mode), linearly polarized, Gaussian-profiled beam from a 100 W maximum power, 10.6 μm dominant wavelength, continuous CO_2 laser is focused to an estimated 100 μm beam waist diameter. A ordered stream of monodispersed liquid droplets, produced by a vibrating orifice droplet generator, is directed through the focal point of the CO_2 laser beam. The droplets fall vertically downward, parallel to the electric field polarization direction of the linearly-polarized CO_2 laser beam. A phase/Doppler particle analyzer (not shown in Fig. 1) is used to monitor the size and velocity of the liquid droplets. Droplets enter the 100 μm diameter CO_2 laser focal point with a velocity of the order 10 m/s, resulting in a beam exposure time of approximately 10 μs. The dynamics of the CO_2 laser/liquid droplet interaction are imaged using a back illumination, pulsed N_2 laser (337 nm wavelength, $\approx$ 10 ns pulse width)/vidicon camera-based imaging system.

For a particular droplet stream, it was observed that there existed a rather distinct CO_2 laser threshold power for explosive fragmentation of the droplets. Below the threshold power, the droplets would fall through the CO_2 laser beam focal point with no detectable shape distortion. Above the CO_2 laser threshold power the droplets would violently shatter. The threshold power for explosive fragmentation of water (distilled) droplets was experimentally measured as a function

69

of droplet diameter. The experimental procedure is as follows. For a particular droplet stream, the droplet diameter and velocity are measured using the phase/Doppler particle analyzer. The power of the CO_2 laser is then gradually increased until explosive fragmentation is observed on the pulsed N_2 laser imaging system. The droplet stream is then removed from the CO_2 laser focal point and the threshold power measured using a power meter.

Threshold power measurements were obtained for droplet diameters from 20 μm to 80 μm. Defining the droplet size parameter, α, as the ratio of the droplet circumference to the incident beam wavelength,

$$\alpha = \frac{2\pi a}{\lambda},$$

where a is the droplet radius, this range of droplet diameters corresponds to a size parameter range of about 5 to 25.

Typically, threshold powers for explosive fragmentation were of the order of 10 W for water droplets within the range of size parameters considered. Calculated focal point threshold intensities for these experiments are thus of the order of 10^5 W/cm^2. A summary of nominal operating parameters is given in Table 1.

III. Theoretical Modeling

Only theoretical modeling of the state of the droplet up to the time at which explosive fragmentation initiates is considered. A simplified theoretical model, appropriate for our experimental conditions, was developed as a first attempt at predicting required threshold powers for droplet explosive fragmentation as a function of such parameters as beam waist diameter, droplet diameter, and droplet thermo/optical properties. The simplified theoretical model will serve as the basis for developing more sophi..ticated and complete theoretical models as might be warranted by experimental comparisons and observations. Major assumptions of the simplified theoretical model are listed and discussed in the following.

Criteria for explosive fragmentation: 0.9 T_{cr} superheat temperature limit. Similar to the approach of Prishivalko[2,4] and Pendleton,[3] it was assumed that the explosive fragmentation of the liquid droplets results from the superheating of the droplet liquid to the superheat limit, at which time spontaneous vapor nucleation occurs and the droplet is shattered by rapidly expanding vapor

70

bubbles. The threshold nature of the laser power necessary to explosively fragment the droplets and the observation of vapor bubbles within the liquid droplets during the initial stages of droplet fragmentation provide experimental justification for this assumption. Zemlyanov and Kuzikovskii[7] also indicate that such "shock boiling" is the correct mechanism for CO_2 laser irradiated water droplet explosive fragmentation for an intensity range similar to that of our experiments ($\approx 10^4$ to 10^5 W/cm^2). Skripov[8] deduced that a freely suspended, pure liquid may obtain a superheated temperature of nine-tenths its critical temperature before spontaneous vapor nucleation initiates. Using this $0.9T_{cr}$ criterion, the superheat limit is then 583 K (310 °C) for water. Superheat temperatures for liquid water approximately equal to this value have been obtained during carefully controlled experiments.[9] The theoretically calculated minimum laser power required to raise the temperature of any point within the liquid droplet to 0.9 T_{cr}, after the droplet has fallen entirely through the focal point of the laser beam, was chosen as the criteria for predicting the explosive fragmentation threshold power.

Neglect hydrodynamic effects. For laser powers just below threshold for explosive fragmentation, the droplets were experimentally observed to fall through the focal point of the beam with no noticeable shape distortion. It is assumed that the heating for our conditions is sufficiently slow so that possible thermally-induced hydrodynamic effects such as thermal shock do not occur and the droplet remains spherical during heating. Thermal expansion of the droplet is also neglected, so the droplet is assumed to have a constant diameter during heating.

Temperature independent optical properties. The assumption of a single, uniform complex index of refraction, $\bar{n}$, for the droplet is necessary for the electromagnetic field calculations. It is recognized that the complex index of refraction of a liquid can be temperature dependent, and spatially-distributed heating within the droplet can create a spatially-distributed complex index of refraction. However, electromagnetic field calculations for such an inhomogeneous sphere are exceedingly difficult and the temperature dependence of the complex index of refraction for liquids, from room temperature to $0.9T_{cr}$, at the CO_2 wavelength is not well known.

Neglect internal heat conduction and droplet surface heat convection/evaporation losses. A characteristic time for heat conduction within the droplet can be determined in terms of the thermal diffusivity of the liquid, α_{th}, and the droplet radius, a,

$$\Delta t = a^2 / \alpha_{th}.$$

Using the room temperature thermal diffusivity of water, 1.44×10^{-7} m^2/s, and a droplet radius of 10 μm this expression gives a characteristic time for heat conduction of 694 μs, which is much greater than the approximately 10 μs heating time of droplet beam exposure. Thus, in order to simplify the calculations, internal heat conduction is neglected during the laser heating time of the droplet. If heat conduction is neglected then droplet surface losses would not affect the interior temperatures of the droplet, and thus possible surface heat losses by either heat convection or evaporation are also neglected.

The geometrical arrangement for the theoretical calculations is shown in Fig. 2. As shown, the origin of the (x_o, y_o, z_o) coordinate system is located at the focal point of the assumed focused, fundamental (TEM$_{00}$ mode), linearly-polarized, Gaussian-profiled, monochromatic beam. The focused Gaussian beam propagates in the $+z_o$ axis direction with electric field polarization in the perpendicular x_o axis direction. The (x,y,z) coordinate system is attached to the center of the spherical droplet. The droplet is assumed to fall at constant velocity, v_o, along the beam x_o axis through the focal point of the beam, as shown in Fig. 2.

The electromagnetic field components of the focused Gaussian beam were determined using the first order corrected paraxial Gaussian beam description of Davis.[1,10] The electromagnetic field distribution within the droplet, which depends upon the position of the droplet relative to the focal point of the beam, was computed using the spherical particle/arbitrarily-defined beam interaction theory of our earlier paper.[1] The spatially-distributed volumetric heat rate within the droplet, $\dot{Q}'''(\vec{r}, t)$, which varies in time as the droplet falls through the profile of the beam, can be related to the electric field magnitude by

$$\dot{Q}'''(\vec{r}, t) = \frac{1}{2}\sigma |\vec{E}(\vec{r}, t)|^2, \tag{1}$$

where σ is the electrical conductivity of the droplet liquid at the incident beam frequency. The electrical conductivity can be related to the real and imaginary parts of the liquid complex index of refraction by

$$\sigma = \frac{n_R n_I c}{\lambda} \tag{2}$$

The square of the electric field magnitude can be eliminated in terms of the normalized source function, $\bar{S}(\vec{r}, t)$, which is defined as

$$\tilde{S}(\vec{r},t) = \frac{|\vec{E}(\vec{r},t)|^2}{|E_o|^2}, \tag{3}$$

where $|E_o|^2$, for these calculations, is the electric field magnitude squared at the focal point of the incident beam which, for a focused Gaussian beam, can be expressed in terms of the beam power, P, and the beam waist radius, w_o:

$$|E_o|^2 = \frac{16}{c} \frac{P}{w_o^2}. \tag{4}$$

Substituting from Eqs. (2), (3), and (4) into Eq. (1) provides an expression for $\dot{Q}'''$ in terms of more fundamental parameters,

$$\dot{Q}'''(\vec{r},t) = \frac{8 n_R n_I P}{\lambda w_o^2} \tilde{S}(\vec{r},t) \tag{5}$$

where $\tilde{S}(\vec{r},t)$ is determined using a computer program based on the spherical particle/arbitrary incident beam interaction theory discussed in Ref. 1. For our CO_2 laser/water droplet explosive fragmentation experiments, typical laser powers were of the order of 10 W and normalized source function values were, at the maximum, of the order of 1, which would correspond to a calculated maximum volumetric heat rate, using Eq. (5), of $\approx 3 \times 10^8$ W/cm^3.

As expressed in Eq. (5), the volumetric heat rate is directly proportional to the normalized source function, thus plots of the normalized source function provide an indication of the spatially-distributed heating within the droplet. Normalized source function calculations were performed for water droplets for conditions corresponding to our experimental arrangement ($\lambda = 10.6\ \mu m$, $w_o = 50\ \mu m$, and, for water, $\bar{n} = 1.179 + i0.072$). As an example, shown in Figs. 3, 4, and 5 are normalized source function distributions in the x-z plane for a 40 μm diameter water droplet with the center of the droplet located one beam waist radius above the beam focal point (Fig. 3), one-half beam waist radius above the beam focal point (Fig. 4), and at the beam focal point (Fig. 5). In Figs. 3, 4, and 5, and all subsequent Figs., the spatial coordinates are normalized relative to the droplet radius and external normalized source function values have been artificially suppressed to zero. As can be seen in Figs. 3, 4, and 5, the normalized source function, and thus the volumetric heat rate, increases as the droplet approaches the beam axis, as would be expected for such a Gaussian-profiled beam. For droplet positioning at the beam focal point, Fig. 5, the

73

normalized source function distribution is similar to that for the corresponding case with plane wave illumination, shown in Fig. 6. However, for droplet positioning away from the beam focal point, there is preferential heating within the part of the droplet nearest the beam focal point as can be seen in Figs. 3 and 4.

The temperature distribution within the droplet, and the theoretically-predicted explosive fragmentation threshold power, can be determined by integrating the volumetric heating rate over time for each spatial position within the droplet. Since in the simplified theoretical model internal heat conduction and surface losses are being neglected, the general heat equation for any point within the droplet takes the form of

$$\rho \frac{\partial u(\vec{r}, t)}{\partial t} = \dot{Q}'''(\vec{r}, t)$$

or, after integration,

$$u(\vec{r}, t) - u(\vec{r}, 0) = \frac{1}{\rho} \int_0^t \dot{Q}'''(\vec{r}, t') dt' \tag{6}$$

where u is the internal energy per unit mass and ρ is the liquid mass density (assumed constant). Substituting from Eq. (5) gives

$$u(\vec{r}, t) - u(\vec{r}, 0) = \frac{8 n_R n_I P}{\rho \lambda w_o^2} \int_0^t \tilde{S}(\vec{r}, t') dt'. \tag{7}$$

Since the droplet is assumed to fall at a constant velocity, v_o, the position of the center of the droplet on the x_o axis can be related to time by

$$x_o(t) = x_o(0) - v_o t \tag{8}$$

where $x_o(0)$, the initial position of the droplet, is assumed to be well above the intensity profile of the beam. Using Eq. (8), the variable of integration of Eq. (7) can be changed so that

$$\frac{u(\vec{r}, t) - u(\vec{r}, 0)}{\frac{8 n_R n_I}{2 \pi \rho w_o^2} \frac{P}{v_o}} = \alpha \int_{\tilde{x}_o(t)}^{\tilde{x}_o(0)} \tilde{S}(\vec{r}, \tilde{x}_o') d\tilde{x}_o' = \widetilde{\Delta T}(\vec{r}, \tilde{x}_o) \tag{9}$$

where $\tilde{x}_o = x/a$ is the position of the center of the droplet normalized relative to the droplet radius and the integral of Eq. (9), which is determined numerically, is defined as $\widetilde{\Delta T}(\vec{r}, t)$ since,

if a constant specific heat is assumed, this integral provides a normalized temperature distribution within the droplet as a function of droplet position along the x_o axis of the beam.

As an example, Figs. 7 - 12 show the x-z plane distribution of $\widetilde{\Delta T}$ for a 40 μm diameter water droplet falling through the focal point of a laser beam for conditions corresponding to those of our experiments ($\lambda = 10.6 \ \mu m$, $w_o = 50 \ \mu m$, and, for water, $\bar{n} = 1.179 + i0.072$). Figures 7 - 12 are for the droplet center located one beam waist radius above the focal point (Fig. 7), one-half beam waist radius above the focal point (Fig. 8), at the focal point (Fig. 9), one-half beam radius below the focal point (Fig. 10), one beam radius below the focal point (Fig. 11), and two beam radii below the focal point (Fig. 12). After two beam radii below the focal point there is insignificant additional heating for the 40 μm diameter water droplet for these conditions.

The sequence of Figs. 7 - 12 demonstrates the heating pattern of the droplet as it falls through the focal point of the beam. The $\widetilde{\Delta T}$ distribution increases in amplitude as the droplet falls through the Gaussian intensity profile of the beam. At the beam focal point, Fig. 9, the droplet is preferentially heated on the bottom half because this part of the droplet has been exposed to a greater fraction of the beam profile than the top half of the droplet. After falling entirely through the beam, Fig. 12, the distribution of $\widetilde{\Delta T}$ is symmetrical with regard to bottom and top halves of the droplet. (If internal heat conduction were included in the theoretical model, this would not necessarily be the case.)

The threshold power for explosive fragmentation is calculated by first determining the maximum value of $\widetilde{\Delta T}$ after the droplet has fallen entirely through the beam profile, and then evaluating, using Eq. (9), the laser power necessary to bring the temperature of this point up to $0.9T_{cr}$. Since laser power, P, and droplet velocity, v_o, occur as a ratio in our simplified model, the threshold criteria is expressed as the ratio of these two quantities:

$$\left. \frac{P}{v_o} \right)_{0.9T_{cr}} = \frac{\Delta u \big)_{0.9T_{cr}}}{\frac{8 n_g n_i}{2 \pi \rho w_o^2} \widetilde{\Delta T}_{max}}, \tag{10}$$

where $\Delta u\big)_{0.9T_{cr}} = u(0.9T_{cr}) - u(T_{initial})$, $T_{initial}$ is the droplet temperature before entering the beam (taken as 20 °C for our calculations), and $\widetilde{\Delta T}_{max}$ is the maximum value of $\widetilde{\Delta T}$ within the droplet after falling entirely through the beam.

Substituting values for our experimental conditions gives an explosive fragmentation threshold criteria for water of

$$\left.\frac{P}{v_o}\right)_{0.9T_{cr}} = \frac{30.0}{\widetilde{\Delta T}_{max}}[W/(m/s)].\qquad(11)$$

For comparison, laser power/droplet velocity ratios for normal atmospheric pressure boiling were also calculated using $\Delta u_{boiling} = u(100\ {}^\circ C) - u(T_{initial})$ instead of $\Delta u_{0.9T_{cr}}$ in Eq. (10) with a resulting value for water of

$$\left.\frac{P}{v_r}\right)_{boiling} = \frac{7.73}{\widetilde{\Delta T}_{max}}[W/(m/s)].\qquad(12)$$

Continuing the example of the 10 μm diameter water droplet for our experimental conditions, it was determined the maximum value of $\widetilde{\Delta T}$ after the droplet has fallen completely through the beam focal point, (see Fig. 12) was 28.6 . Substituting into Eq. (11), an explosive fragmentation threshold power/droplet velocity ratio of 0.95 [W/(m/s)] is theoretically-predicted for the 40 μm diameter water droplet

IV. Theoretical/Experimental Comparison

A comparison between theoretically-predicted explosive fragmentation threshold power/droplet velocity ratio and the corresponding experimentally-measured values is shown in Fig. 13 for water droplets in the sized parameter range from 5 to 25. The solid line labeled "superheat" in Fig. 13 is the theoretically-predicted explosive fragmentation threshold power/droplet velocity ratio using the $0.9T_{cr}$ (310 $^\circ C$) maximum temperature criteria. The solid line labeled "boiling" is the theoretically-predicted threshold power/droplet velocity ratio necessary to raise the maximum temperature to the atmospheric pressure boiling point (100 °C). For size parameters less than about 9 ($\approx$ 30 μm diameter), the theoretically-predicted maximum temperature point within the water droplet occurs on the shadow (unilluminated) side of the droplet and, indeed, for water droplets of size parameter less than about 9, it was experimentally observed on the pulsed N_2 laser imaging system that explosive fragmentation would initiate on the shadow side. For size parameters greater than about 9, the theoretically-predicted maximum temperature point occurs on the illuminated side of the water droplet and, consistent with the theoretical model, for size parameters greater than about 9 it was experimentally observed that explosive fragmentation would initiate on the illuminated side of the droplet.

The corresponding experimentally-measured values of explosive fragmentation threshold power /droplet velocity ratio (represented in Fig. 13 by the hollow circles) demonstrated a degree of

nonrepeatability from one test day to the next beyond that expected due to normal variations in experimental conditions and procedures. Because of this, no statistical averaging of the experimental data was performed, and all individual raw data points are presented in Fig. 13. The experimental data cluster about the theoretically-predicted "superheat" line, which suggests that the liquid droplets are being significantly superheated before explosive fragmentation. The theoretically-predicted explosive fragmentation threshold power/droplet velocity ratio agrees with the experimental measurements over the 5 to 25 size parameter range within a factor of about two. The theoretically-predicted decrease in required explosive fragmentation threshold power/droplet velocity ratio for size parameter less than about 9 (when explosive fragmentation initiation goes from illuminated side to shadow side) is not seen in the experimental data.

The degree of nonrepeatability of experimental data may be a result of the influence of additional physical mechanisms not included in the simplified theoretical model which are variable from one experimental setup to the next. One concern is the quality of the droplet stream. The consistency and spherical nature of the droplet stream is monitored using the pulsed N_2 laser imaging system and experimental measurements are taken only when the droplet stream is of apparent high quality. Small internal oscillations of droplet shape (≈ 1 μm and less) would be undetectable on the imaging system and may influence the required threshold power. The individual droplets may be rotating or possess internal circulation, both of which would explain the occasional higher than expected explosive fragmentation threshold power. It is also known that the droplets leaving the vibrating orifice droplet generator may be electrically-charged, which may or may not affect the path of the droplet through the laser beam focal point and the required explosive fragmentation threshold power. These and several other physical mechanisms are being considered and analyzed for their contribution to the required explosive fragmentation threshold power measurements.

V. Summary and Future Work

A simplified theoretical model, utilizing the spherical particle/arbitrarily-defined beam interaction theory of our Ref. 1, has permitted, for the first time, a direct comparison between theoretically-predicted and experimentally-measured explosive fragmentation threshold powers for a droplet falling through a tightly-focused, continuous, laser beam. Agreement between theory and experiments would imply a good understanding of the underlying physical mechanisms of the process. For our experimental conditions, theoretically-predicted and experimentally-measured threshold

power/droplet velocity ratios were in agreement within a factor of about two for the explosive fragmentation of CO_2 laser irradiated water droplets in the size parameter range of 5 to 25.

Future work includes analyzing and improving the repeatability of the experimental measurements, and refining the theoretical model by including internal heat conduction and surface convection and evaporation losses. Comparisons between theory and experiment for liquids other than water (such as methanol) are also underway and being analyzed.

Acknowledgements

References

1. J.P. Barton, D.R. Alexander, and S.A. Schaub, "Internal and near-surface electromagnetic fields for a spherical particle irradiated by a focused laser beam," J. Appl. Phys., 64, 1632 (1988).
2. A.P. Prishivalko and S.T. Leiko, "Radiative heating and evaporation of droplets," Sov. J. App. Spectroscopy, 33, 1137 (1980).
3. J.D Pendleton, "Water droplets irradiated by a pulsed CO_2 laser: comparison of computed temperature contours with explosive vaporization patterns," Appl. Opt., 24, 1631 (1985).
4. A.P. Prishivalko, "Vaporization and explosion of water droplets on exposure to radiation with inhomogeneous internal heat evolution," Sov. J. Quantum Electron., 9, 851 (1979).
5. P. Kafalas and A.P. Ferdinand, Jr., "Fog droplet vaporization and fragmentation by a 10.6 μm laser pulse," Appl. Opt., 12, 29 (1973).
6. D.R. Alexander and J.G. Armstrong, "Explosive vaporization of aerosol drops under irradiation by a CO_2 laser beam," Appl. Opt., 26, 533 (1987).
7. A.A. Zemlyanov and A.V. Kuzikovskii, "Modeling of the gasdynamic regime of an exploding water droplet in a high-power pulsed light field," Sov. J. Quantum Electron., 10, 876 (1980).
8. V.P. Skripov, Metastable Liquids, (Wiley, New York, 1974), p. 177.
9. J.P. Hartnett and T.F. Irvine, Jr., eds., Advances in Heat Transfer, Vol. 10, (Academic Press, New York, 1974), pp. 92-110.
10. L.W. Davis, "Theory of electromagnetic beams," Phys. Rev. A, 19, 1177 (1979).

CO₂ Laser Experiment Arrangement

TOP VIEW
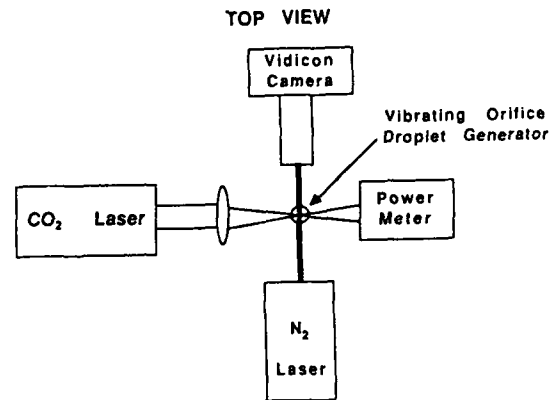
Fig. 1. Experimental arrangement for CO_2 laser/liquid droplet explosive fragmentation threshold power measurements.

Geometrical Arrangement
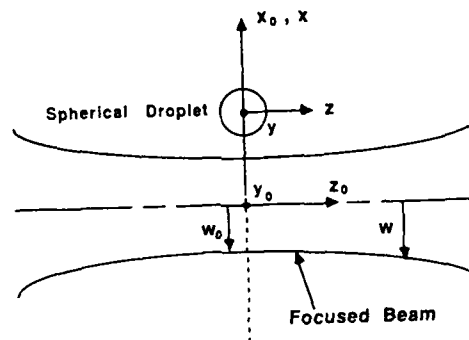
Fig. 2. Geometrical arrangement for theoretical modeling of liquid droplet falling through the focal point of a focused Gaussian laser beam.

Nominal Operating Parameters

CO$_2$ Laser:
continuous
10.6 μm wavelength
TEM$_{00}$ mode
Gaussian profile
linear polarization
$P \approx 10W$
$2w_0 = 100\mu$m
$I_0 \approx 10^5$ W/cm^2

Droplets:
water, $\overline{n} = (1.179, 0.072)$
$2a = 20\mu$m to 100 μm
$\alpha = 2\pi a / \lambda_0 = 6$ to 30
velocity, $v \approx 10$ m/s
beam exposure time ≈ 10 μs

N$_2$ Laser Imaging:
337 nm wavelength
≈ 10 ns pulse

Table 1. Nominal operating parameters for CO$_2$ laser/water droplet explosive fragmentation threshold power experiments.
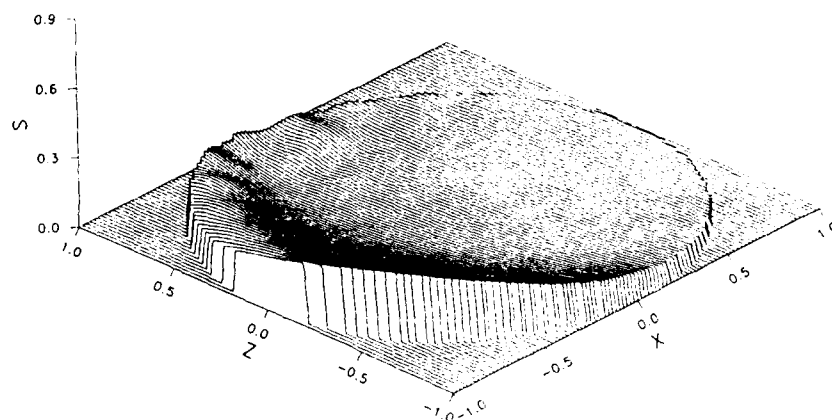
Fig. 3. Normalized source function distribution in the transverse (x-z) plane for a 40 μm diameter water droplet located 50 μm above the focal point of a 50 μm beam waist radius, 10.6 μm wavelength, focused Gaussian laser beam propagating in the + z axis direction and linearly polarized in the x axis direction.
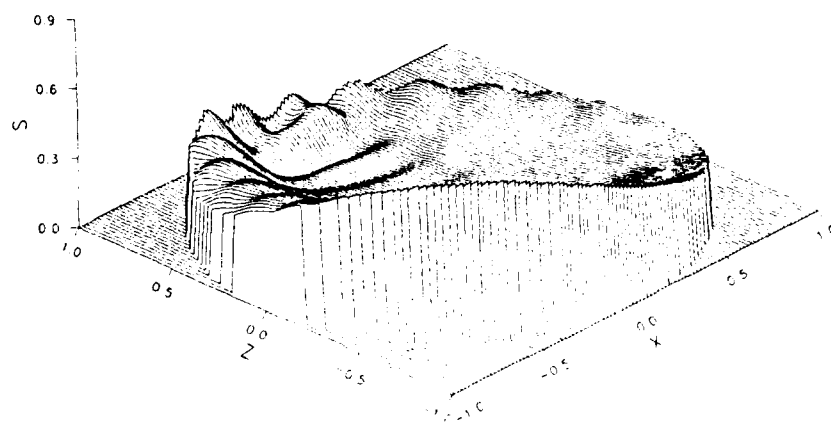
Fig. 4. Normalized source function distribution in the transverse (x-z) plane for a 40 μm diameter water droplet located 25 μm above the focal point of a 50 μm beam waist radius, 10.6 μm wavelength, focused Gaussian laser beam propagating in the + z axis direction and linearly polarized in the x axis direction.

81
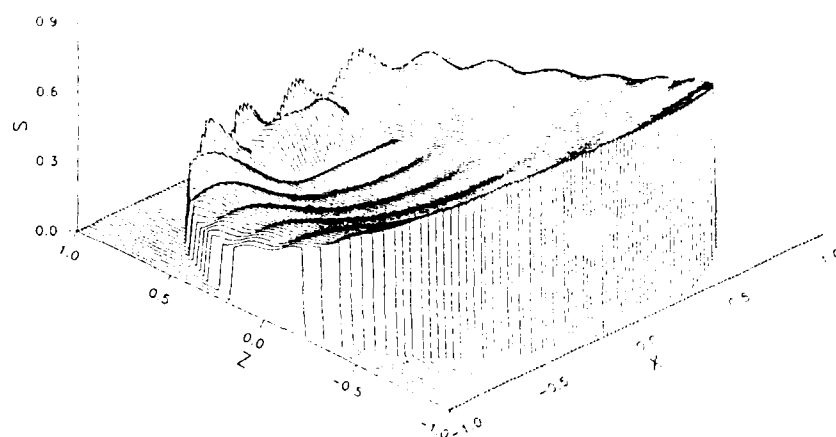
Fig. 5. Normalized source function distribution in the transverse (x-z) plane for a 40 μm diameter water droplet located at the focal point of a 50 μm beam waist radius, 10.6 μm wavelength, focused Gaussian laser beam propagating in the + z axis direction and linearly polarized in the x axis direction.

Fig. 6. Normalized source function distribution in the transverse (x-z) plane for a 40 μm diameter water droplet irradiated by a 10.6 μm wavelength plane electromagnetic wave propagating in the + z axis direction and linearly polarized in the x axis direction.
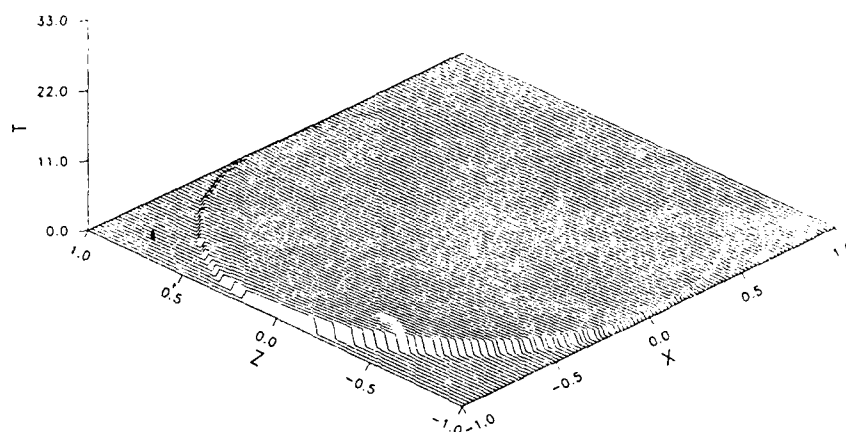
Fig. 7. $\widetilde{\Delta T}$ distribution in the transverse (x-z) plane for a 40 μm diameter water droplet located 50 μm above the focal point of a 50 μm beam waist radius, 10.6 μm wavelength, focused Gaussian laser beam propagating in the + z axis direction and linearly polarized in the x axis direction.
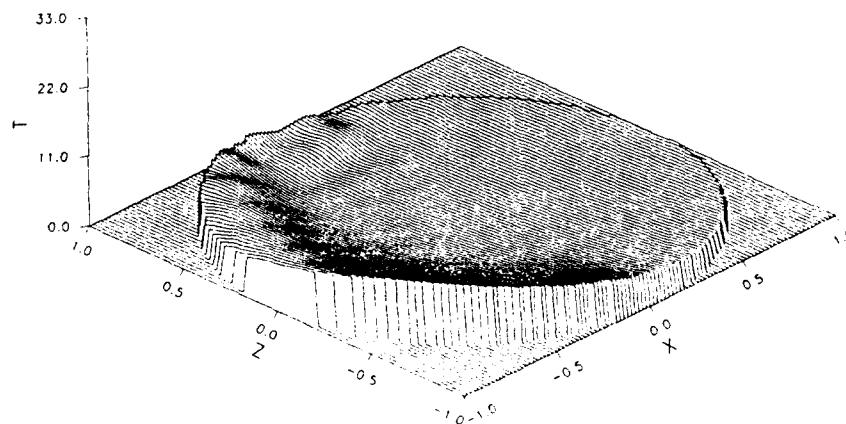
Fig. 8. $\widetilde{\Delta T}$ distribution in the transverse (x-z) plane for a 40 μm diameter water droplet located 25 μm above the focal point of a 50 μm beam waist radius, 10.6 μm wavelength, focused Gaussian laser beam propagating in the + z axis direction and linearly polarized in the x axis direction.
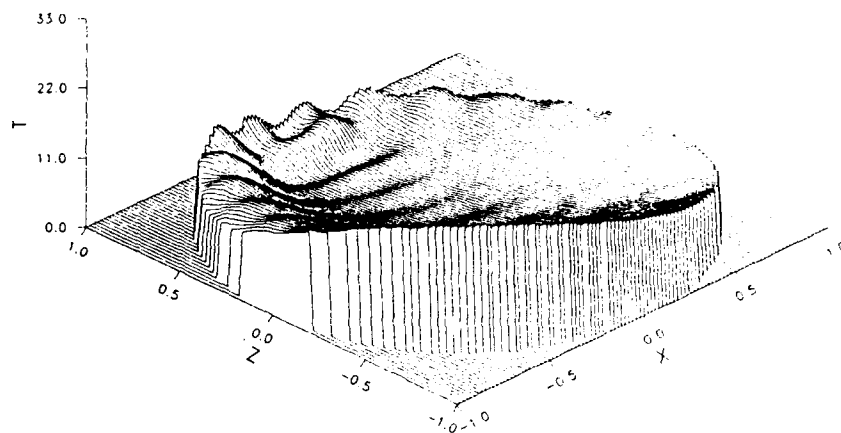
Fig. 9. $\widehat{\Delta T}$ distribution in the transverse (x-z) plane for a 40 μm diameter water droplet located at the focal point of a 50 μm beam waist radius, 10.6 μm wavelength, focused Gaussian laser beam propagating in the + z axis direction and linearly polarized in the x axis direction.
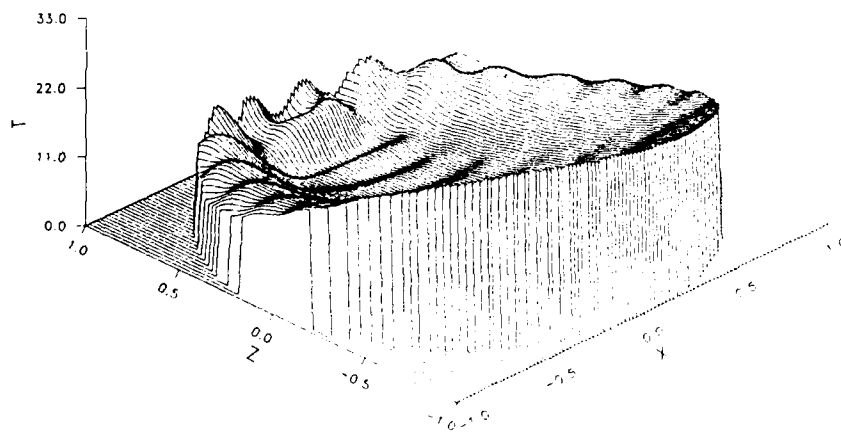
Fig. 10. $\widehat{\Delta T}$ distribution in the transverse (x-z) plane for a 40 μm diameter water droplet located 25 μm below the focal point of a 50 μm beam waist radius, 10.6 μm wavelength, focused Gaussian laser beam propagating in the + z axis direction and linearly polarized in the x axis direction.

84
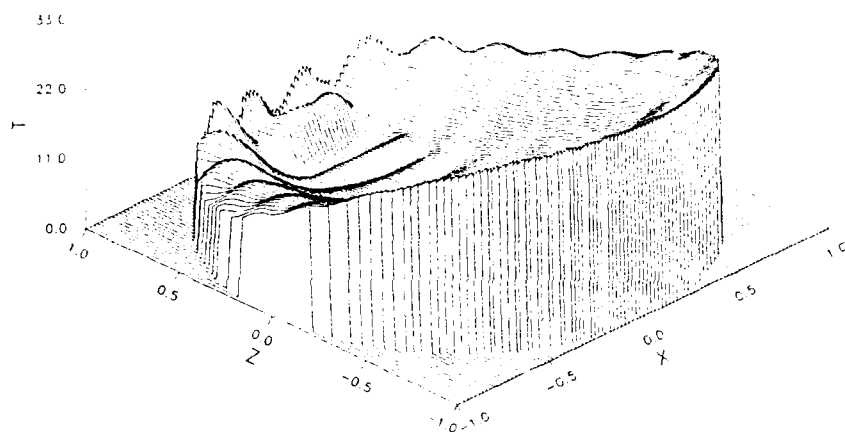
Fig. 11. $\widetilde{\Delta T}$ distribution in the transverse (x-z) plane for a 40 μm diameter water droplet located 50 μm below the focal point of a 50 μm beam waist radius, 10.6 μm wavelength, focused Gaussian laser beam propagating in the + z axis direction and linearly polarized in the x axis direction.

Fig. 12. $\widetilde{\Delta T}$ distribution in the transverse (x-z) plane for a 40 μm diameter water droplet located 100 μm below the focal point of a 50 μm beam waist radius, 10.6 μm wavelength, focused Gaussian laser beam propagating in the + z axis direction and linearly polarized in the x axis direction.
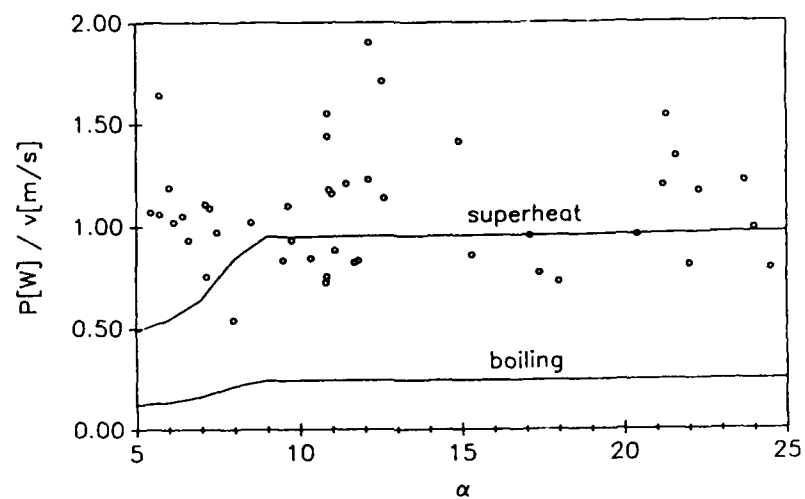
Fig. 13. Comparison between experimental and theoretical explosive fragmentation threshold power/droplet velocity ratio values for water droplets falling through the focal point of a 100 μm beam waist diameter, 10.6 μu dominant wavelength, linearly polarized, continuous CO_2 laser beam.

Numerical Solution of the Riemann Problem in the Presence of an External Energy Source.

B. Yudanin and P. Hu

Physics Dept., City College of the City University of New York, N. Y. 10031

M. Lax

Physics Dept., City College of the City University of New York, N. Y. 10031
and AT & T Bell Laboratories, Murray Hill, New Jersey 07974

Recent Publications, Submittals for Publications and Presentations.

[1] B. Yudanin, M. Lax, "POST Adaptation for a Numerical Solution of the Spherically-Symmetric Riemann Problem," J. of Computational Physics, (submitted).

[2] B. Yudanin, M. Lax, "Hydrodynamical Response to Uniform Laser Absorbtion in a Droplet," in *Proceedings of the CRDC* 1985 Scientific Conference on Obscuration and Aerosol Research, edited by R. H. Kohl and D. Stroud (1985).

[3] M. Lax, B. Yudanin, "Early-Time Hydrodynamic Response to Pulsed Laser Radiation," Digest - Intl. Conf. on Optical and Millimeter Wave Propagation and Scattering in the Atmosphere, Florence, Italy, 1986.

Abstract

We obtain a numerical solution for the problem of hydrodynamical motion of a gas in the shock-tube in the presence of a heat source. Two numerical procedures were discussed. One is based on the Godunov scheme. The other procedure uses the method of "folding", described by the authors in a previous paper. This method utilizes the standard package POST, designed to solve a set of partial differential equations in one space and time variables. POST was successfully used for the problem of propagation of a spherical shock. A comparison of the results from the two methods mentioned above is provided. This comparison is needed because the Godunov scheme as used by CAVEAT neglects the heat source during one phase of the calculation. This paper provides a preliminary test of validity of such a use of the Godunov algorithm.

October 23, 1988

I. Introduction.

Recent experiments of a droplet under strong laser radiation have attracted much interest[4]. The dynamical coupling between the electromagnetic energy absorbed by the matter inside and outside the droplet and the hydrodynamic motion of the droplet and the surrounding air makes the problem complex. Theoretical investigation of this problem is still much behind experiment. It seems impossible to find an analytical solution for this problem, and numerical calculations are required.

The problem of interaction of an electromagnetic wave and matter involves the solution of a coupled system of the Maxwell equations together with the hydro equations. As a first approximation in the attacking the problem, the coupling can be replaced by an external energy source, proportional to the intensity of the irradiation, for the hydrodynamical system and by a change in the index of refraction due to the change in the matter density for the electromagnetic part of the problem.

In this paper we are concerned with the hydrodynamical part of the problem. More specifically, we are interested with the development of the droplet under the influence of an external energy source. In order to study the motion of a droplet in the presence of an energy source, a good hydro-code is needed. CAVEAT[5], (a code developed with many man-years of effort at Los Alamos) seems to be a good candidate for this purpose. This code is based on the Godunov algorithm[6] and it handles a set of hydrodynamical equations in two spatial dimensions and time.

The original Godunov scheme was designed for solving the one dimensional gas-dynamical equations in the absence of external heat sources. According to Godunov's procedure, the space is divided into a number of cells. For each cell two kinds of values of the hydrodynamical variables are defined. They are the interfacial (cell boundary) values and the average over cell values. The initial cell averaged values are given first. Then each cell boundary can be treated as an infinite surface with uniform media in each side given by properties at the center of the adjacent cells. One can use the analytic solution of this one dimensional "Riemann" problem of shock creation and propagation into a perfect gas due to the initial difference in pressure in two adjacent regions of the gas. This solution provides the time development of interfacial values at the boundaries of the cells. This is the Riemann part of the solution. Next one can calculate the average values at the cells (mid-points) for the next time step by solving the discretized hydro-equations using

the Riemann information at the previous time. This is the Lagrangian[*] part of the solution. For the case when an energy source is present, modifications should be made to Godunov's procedure, which could affect both the Lagrangian part of the scheme and the Riemann solver. It seems to us that the numerical codes used for the hydro equations based on Godunov's idea tend to incorporate the influence of the energy source only in the Lagrangian part of the calculations. They retain the original one-dimensional solution of the Riemann problem without the heat source for those equations which relate the interfacial values to the cell ones. This will produce an error.

Another approximation was made by Dukovitz[7] for the solution of the Riemann problem without source. The original one dimensional solution is constructed by using the shock conditions (Hugoniot) and the rarefaction wave conditions[8] for the perfect gas. The rarefaction wave conditions are difficult to employ when a realistic equation of state is used. For the CAVEAT code, Dukovitz proposed to use a "double shock" approximation (rarefaction wave conditions are replaced by shock conditions). It shortens the calculations considerably for a general equation of state for the liquid involved.

If a heat source is present the Hugoniot (shock) conditions are not changed unless the heat is supplied at the shock surface. On the other hand, the rarefaction wave conditions rely upon adiabaticity along the stream line. The adiabatic invariant, $p \, \rho^{-\gamma}$, will be changed by a factor of $\exp(\int_{t}^{t+\delta t} \frac{Q}{e} dt)$ (see Eq.3,4 and also see Ref.2) in the presence of the external energy source. Here Q is the energy source per unit mass and e is the specific energy of the gas. It suggests that we must choose $\delta t < e/Q$ in order to maintain the desired accuracy in the   culations. As a result for a sufficiently large energy source the execution time for the code will increase tremendously.

There is another way of dealing with this problem. Instead of the no source Riemann solution one can use a solution, which incorporates the source. But such a solution is unknown as of now. Or we can use the method of characteristics near those points where the solution exhibits a nonanalytic behavior and use a small number of mesh points and standard schemes in the other regions. The second proposal is implemented in Sec. III.

---

[*] This hydrodynamical iteration step can be Eulerian as well as Lagrangian.

II. Description of the test problem.

In order to check the accuracy of CAVEAT and other codes, derived from the original Godunov's method, when a heat source is present, we have designed the following test problem.

A piston, located initially at the origin, moves with constant speed in a one dimensional tube, filled with a perfect gas. An external energy source pumps energy into the gas. The rate of energy absorption is proportional to the density of the gas. Mathematically this problem can be described by the following system of equations:

$$\frac{\partial \rho}{\partial t} + \frac{\partial \rho \upsilon}{\partial x} = 0$$

$$\frac{\partial (\rho \upsilon)}{\partial t} + \frac{\partial (p + \rho \upsilon^2)}{\partial x} = 0 \tag{2}$$

$$\frac{\partial E}{\partial t} + \frac{\partial \upsilon (E + p)}{\partial x} = W \tag{3}$$

where ρ, p and υ are density, pressure and velocity respectively. Here $E = \rho(e + \frac{1}{2}\upsilon^2)$, $e = p/\rho(\gamma - 1)$ is the specific energy and W is the energy source. If we set $\tilde{x} = x/x_o$, $\tilde{t} = t_o$, $\tilde{p} = p/p_o$, $\tilde{\rho} = \rho/\rho_o$, $\tilde{\upsilon} = \upsilon/c_o$ the equations retain their form (except that in Eq.2 above p is replaced by $\tilde{p}/\gamma$) and apply to the dimensionless variables $\tilde{p}$, $\tilde{\rho}$, $\tilde{\upsilon}$ and $\tilde{e}$. In the remaining part of the paper the "~" will be omitted. We have chosen as units for the transformation to dimensionless form the following: for the distance - $x_o = 10\mu m$, for the density and pressure the initial ρ_o and p_o. For the velocity we use $c_o = \sqrt{\gamma p_o/\rho_o}$ the sound velocity of the undisturbed gas. In this case, for the time we can use $t_o = x_o/c_o$ and for the energy source - $Q_o = p_o/\rho_o t_o$.

Two cases were considered: source constant in space

$$W = Q\rho \tag{4}$$

and a source with Gaussian distribution located on the piston

$$W = Q\rho \exp\left[-\frac{(x - U_{\text{piston}}t)^2}{2\sigma^2}\right] \tag{5}$$

For our calculations, we chose the dimensionless width of the Gaussian to be $\sigma = 0.2$ and the source strength Q to be $10^{14}/1.29$ Watts/kg, which corresponds to a dimensionless $Q = 30.2$. The dimensionless piston velocity U_{piston} is 0.589.

We solve this problem for the piston which ...oves to the right into the gas, producing a compression shock and for the piston, which moves to the left out of the gas. In the latter case a rarefaction wave is developed and it moves away from the piston into the gas.

III. POST adaptation.

In this section we apply a general purpose package (POST[9,10]) for solving a set of {partial d}ifferential equations in one space and time together with a set of ordinary differential equations in time to the one dimensional hydrodynamical equations with external heat source present. The ability of POST to handle an additional set of ordinary differential equations lets us (by transformating the singular points to rest) track the shock and rarefaction waves should they arise. In the regions free of discontinuities, POST is used as a numerical code for the solution of a system of {partial d}ifferential equations (hydro equations).

As we have stated above, our test problem considers both compressing and receding pistons. For both cases, the region of interest will be between the piston and the head of the wave - either shock or rarefaction. In front of those waves the gas would have been undisturbed, if the source had not been added. For the source which is independent of the spatial coordinate, it is obvious that the velocity and the density in front of the specified waves retain their original values ($\upsilon = 0$; $\rho = \rho_o$) and only the pressure is changed. This change in the pressure can be simply calculated by integrating the equation:

$$\frac{\partial p}{\partial t} + \upsilon \frac{\partial p}{\partial x} = Q\rho(\gamma - 1) \tag{3'}$$

(which follows from Eq.2 and Eq.3). With $\upsilon = 0$ and constant ρ Eq.3' yields

$$p = (\gamma - 1)Q\rho t . \tag{6}$$

The knowledge of the analytical solution [Eq.(6) together with constant velocity and density] allows us to omit the region in front of the waves from our numerical calculations.

For the Gaussian source, the problem is a little more complicated because the region

in front of the wave should also be taken into account. We have designed a method which permits POST to be applied to such problems. This ethod is based on "folding" the region in front of the wave onto the region behind it. For a complete discussion we refer the reader to Ref. 8.

In order to track the singularities in the wave solution of the specified problems we will locate them and write a set of ordinary differential equations which describes the motion of the points at which singularities occur. The first point, for both cases, is the position of a moving piston. At this point the velocity of the gas must be equal to the piston velocity. No other conditions on the variables (such as pressure and density) can be specified at this point.

For the compressing piston the second point of singularity is at the position of the shock. The hydrodynamical variables on the shock satisfy the Hugoniot jump conditions for a perfect gas:

$$U_{shock} = \frac{p_- - p_+}{\upsilon_-} \tag{7}$$

$$\rho = \frac{\gamma + 1}{\gamma - 1} - \frac{4\gamma}{\gamma - 1} \frac{1}{p_-(\gamma - 1) + p_+(\gamma + 1)} \tag{8}$$

$$U_{shock}^2 = \frac{1}{2\gamma}(p_-(\gamma + 1) + p_+(\gamma - 1)) \tag{9}$$

The above equations are the familiar Hugoniot conditions in dimensionless form without specifying that the velocity ahead of the shock must vanish and the pressure ahead of the shock must be constant. On the contrary, the pressure ahead of the shock depends on the heat source.

For the receding piston, the equations for the velocities of the head and tail of the rarefaction wave (see Fig.1) can be obtained by using the fact that each point in the wave (the head and the tail as well) propagates with the local sound velocity relative to the gas, e.g.:

$$U_{head} = \upsilon - (\frac{p}{\rho})^{1/2} \quad \text{at} \quad x = X_{head} \tag{10}$$

$$U_{\text{tail}} = \upsilon - \left(\frac{p}{\rho}\right)^{1/2} \quad \text{at} \quad x = X_{\text{tail}} \tag{11}$$

The rest of the procedure follows closely that of Ref. 1.

IV. Godunov algorithm

We use the first order Godunov method to solve the one-dimensional hydrodynamic equations in the Lagrangian coordinates,

$$\frac{\partial \rho^{-1}}{\partial t} - \frac{\partial \upsilon}{\partial \xi} = 0 \tag{12}$$

$$\frac{\partial \upsilon}{\partial t} + \frac{\partial p}{\partial \xi} = 0 \tag{13}$$

$$\frac{\partial E}{\partial t} + \frac{\partial \upsilon p}{\partial \xi} = \frac{W}{\rho} \tag{14}$$

with the "mass" coordinate, ξ, defined by:

$$d\xi = \rho dx , \tag{15}$$

the Eulerian velocity $\upsilon = \partial x / \partial t$, and W is defined in Eqs.(4,5).

In our numerical calculation, the energy term affects only the time step iteration process (as in CAVEAT). On the other hand the energy source may demand a modified Riemann solver. But even at this point the CAVEAT code (and we follow it) still uses the same algorithm as that of Godunov to calculate the interfacial values as if there were no source. This approximation could lead to inaccuracy. The source of this discrepancy lies in the adiabatic condition:

$$p(t)\rho^{-\gamma}(t) = p(t_o)\rho^{-\gamma}(t_o) \tag{16}$$

which is no longer valid if energy is supplied to the system. The above condition is used in the Riemann solver of the original Godunov algorithm. The accuracy of this approximation will be tested by the following numerical comparison with POST.

V. Results and discussion

We have calculated the hydrodynamic motion of the one dimensional shock-tube problem with an energy source by using both POST and the first order Godunov method. The results at t=10ns for these two different approaches are given in Figs. 1-6.

Figs. 1-3 describe results, for the receding piston problem, which creates a rarefacation wave. A uniform (in space) energy source is distributed *everywhere* in the system. As can be seen from these figures, the results obtained by POST and by the Godunov method are in good agreement except for the pressure (Fig. 2). The results due to Dukowicz's double shock wave approximation are very close to those of the original Godunov method.

In Figs. 4-6 we present the results for the problem where the piston pushes the air out of the tube to the right. Consequently a compressive shock wave is created. In this case a Gaussian source, localized relative to the piston, is considered. Spikes occur around the shock wave with the Godunov method because we have used only the first order Godunov algorithm. These spikes can be reduced by using the second order Godunov approach as was pointed by Van Leer [11].

In conclusion we can say that the Godunov method gives quite good results for a source strength of the order of 10^{14} [W/kg]. Comparison with the POST method shows a discrepancy of about 2%. We are not yet prepared to claim that this discrepancy is real. The principal conclusion is that the Godunov algorithm seems to work even better than expected.

References

[1]B. Yudanin, M. Lax, J. of Computational Physics, (submitted).

[2]B. Yudanin, M. Lax, "Hydrodynamical Response to Uniform Laser Absorbtion in a Droplet," in 1985 Scientific Conference on Obscuration and Aerosol Research, edited by R. H. Kohl and D. Stroud (1985).

[3]M. Lax, B. Yudanin, "Early-Time Hydrodynamic Response to Pulsed Laser Radiation," Digest - Intl. Conf. on Optical and Millimeter Wave Propagation and Scattering in the Atmosphere, Florence, Italy, 1986.

[4]W. F. Hsieh, J. B. Zheng, C. F. Wood, B. T. Chu and R. K. Chang, Opt. Lett. 12, 576 (1987).

[5]F.L. Addessio, D.E. Carroll, J.K. Dukowicz, F.H. Harlow, J. N. Johnson, B.A. Kashiwa, M.E. Maltrud, and H. M. Ruppel CAVEAT: A Computer Code for Fluid Dynamics Problems with Large Distortion and Internal Slip. (1985)

[6]S. K. Godunov, Matematicheskii Sbornik. 47, 271, (1959).

[7]J. K. Dukowicz, J. of Computational Physics, 61, 119, (1985).

[8]G. B. Whitham, Linear and Nonlinear Waves (Wiley, New York, 1974).

[9]N. L. Schryer, Parial Differential Equations in One Space Variable (A.T.&T. Bell laboratories Computing Science technical Report No. 115).

[10]N. L. Schryer, Numerical Solution of Coupled Systems of Partial Differential Equations in One Spatial Variable and Time (Elliptic Problem Solvers, Ed. M. H. Schultz, Academic Press, 1981, pp 413-417).

[11]B. Van Leer, J. of Computational Physics, 32, 137, (1979).
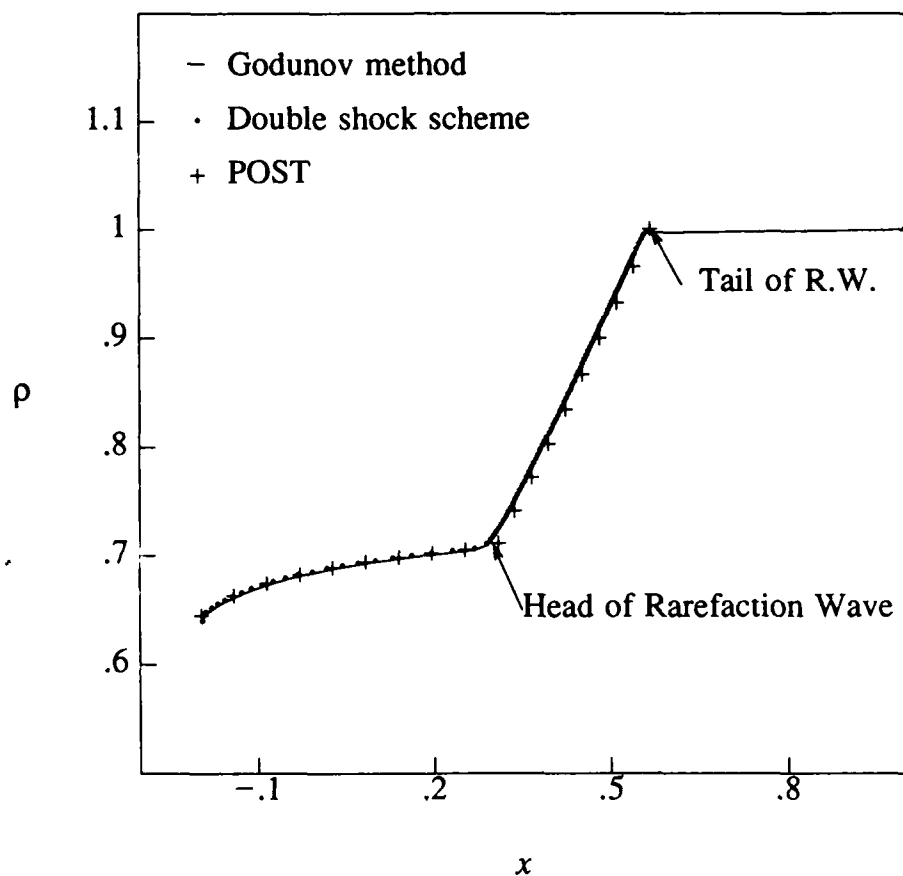
FIG. 1. A numerical solution for the density in the one-dimensional shock-tube problem at time t=10nsec. The units for the dimensionless density are initial density of the undisturbed gas. The dimensionless coordinate is in units of $10\mu m$. In this case we have used an energy source constant in the space and proportional to the density of the gas. The piston, which was initially at point $x=0$, moves to the left with constant velocity $0.589c_o$. The piston recedes from the gas, creating a rarefection wave, which propagates into the undisturbed gas to the right.
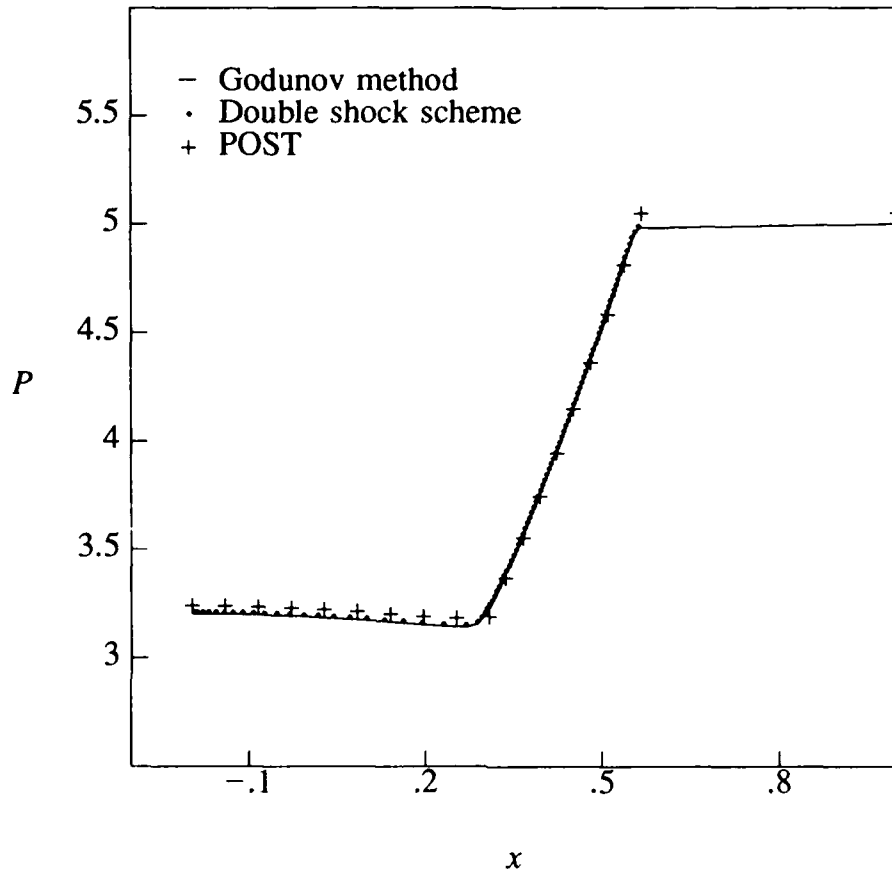
FIG. 2. The numerical solution for the pressure in the same problem as in Fig. 1. The results from the Godunov schemes and from the POST are slightly different. The difference is more apparent than in the density, because the pressure is a "fast" responding hydrodynamical variable to the energy deposition. The inaccuracy in the rarefaction wave conditions used in the Godunov's algorithm affects the position of the head and tail of the rarefaction wave.

97
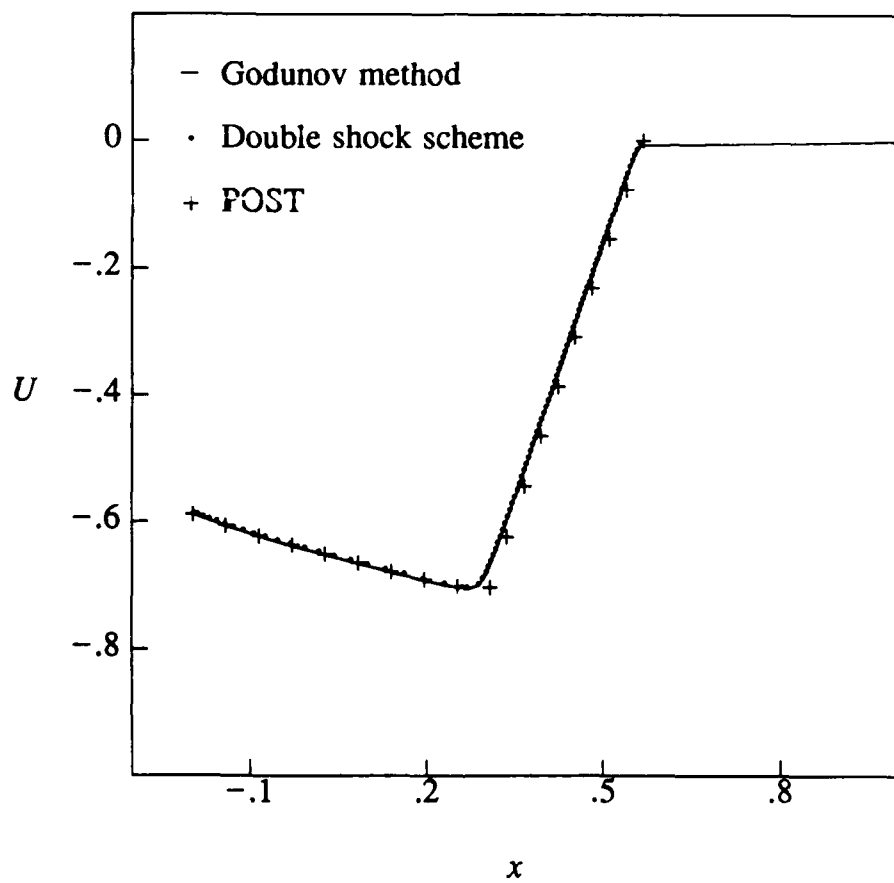
FIG. 3. The numerical solution for the velocity in the same problem as in Fig. 1.
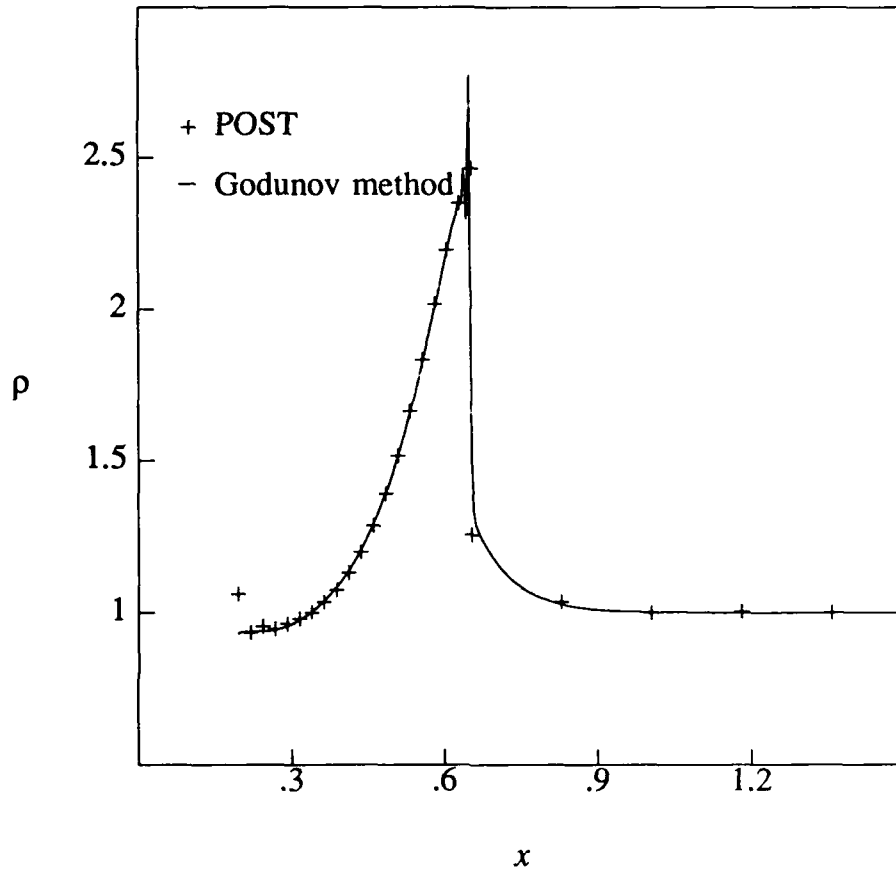
FIG. 4. A numerical solution for the density in the one-dimensional shock-tube prob-
lem at time t=10nsec. The units for the dimensionless density are initial density of the
undisturbed gas. The dimensionless coordinate is in the units of $10\mu m$. In this case we
have used an energy source with Gaussian distribution located on the piston and propor-
tional to the density of the gas. The piston, which was initially at point x=0, moves into
the gas to the right with constant velocity $0.589c_o$. The piston compresses the gas on the
right of it and creates a strong shock wave propagating into undisturbed gas. The energy
source raises the pressure of the gas behind the shock much more, than in front of it, there-
fore the shock accelerates.
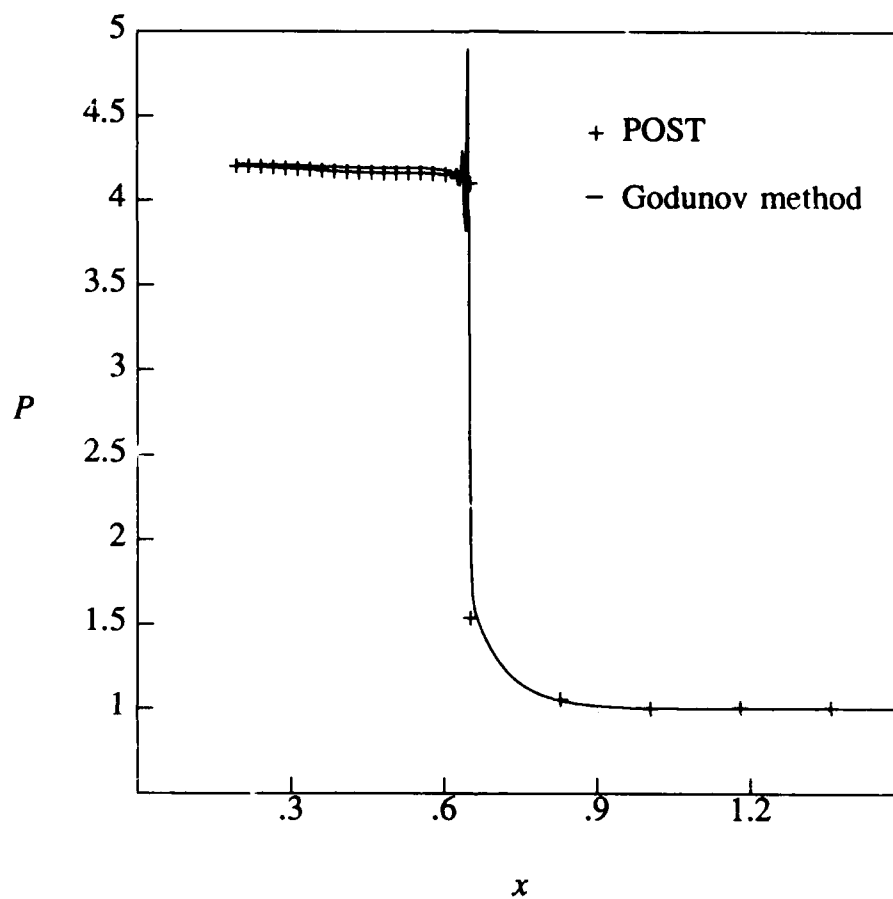
FIG. 5. The numerical solution for the pressure in the same problem as in Fig. 4. The spikes in the solution via Godunov's scheme are due to the first order algorithm and a relatively small number of mesh points (1000).

FIG. 6. The numerical solution for the velocity in the same problem as in Fig. 4.

Blank

EXPLOSIVE VAPORIZATION OF SINGLE PARTICLES BY LASERS:

COMPARISON OF MODELS WITH EXPERIMENTS

J. C. Carls and J. R. Brock
Department of Chemical Engineering
The University of Texas at Austin
Austin, Texas 78712

RECENT PUBLICATIONS, SUBMITTALS FOR PUBLICATION AND PRESENTATIONS:

J. C. Carls AND J. R. Brock, "Explosion of a water droplet by pulsed laser heating", Aerosol Sci. Tech.7, 79-90 (1987)

S. G. Kim and J. R. Brock, "Aerosol growth and dynamics" in R. Kohl, Ed., Proceedings of the 1986 CRDEC Conference on Obscuration and Aerosol Research, R. H. Kohl and Assoc., 1987.

J. C. Carls and J. R. Brock, "Laser induced explosion of particles" in R. Kohl, Ed., Proceedings of the 1986 CRDEC Conference on Obscuration and Aerosol Research, R. H. Kohl and Assoc., 1987.
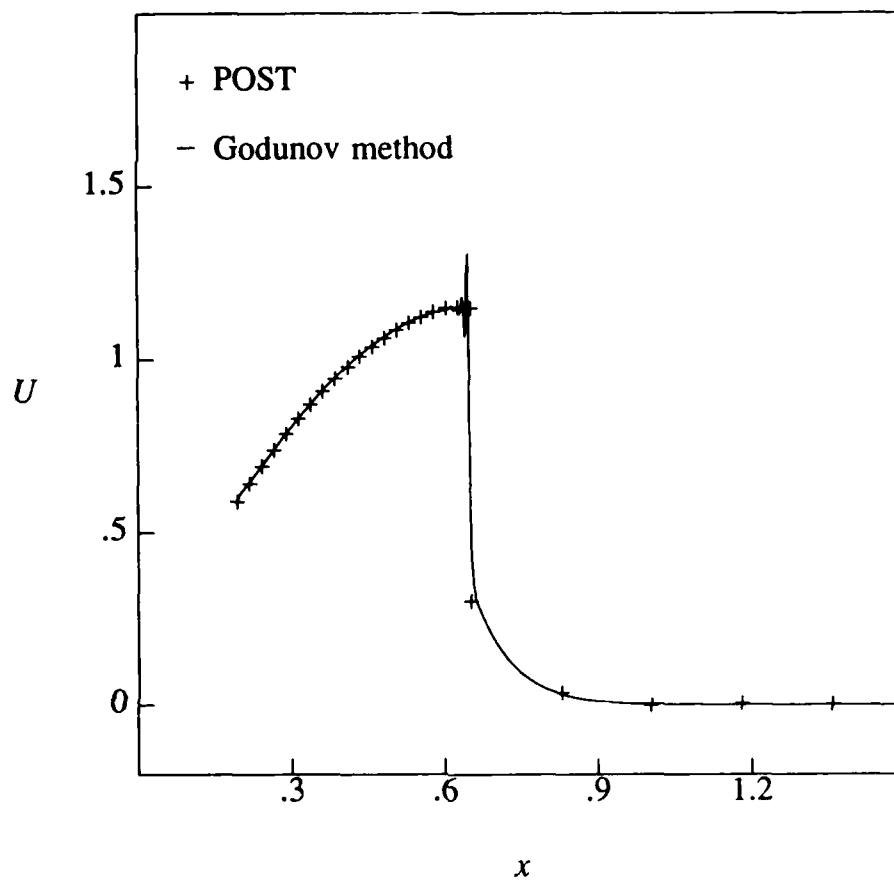
S. Davies and J. R. Brock, "Laser evaporation of droplets" in R. Kohl, Ed., Proceedings of the 1986 CRDEC Conference on Obscuration and Aerosol Research, R. H. Kohl and Assoc., 1987.

Y. L Chen, I. Trachtenberg and J. R. Brock, "Aerosol jet etching of fine patterns", Appl. Physics Lett. 51, 2203 (1987).

J. C. Carls and J. R. Brock, "Explosive vaporization of a single water droplet by pulsed laser radiation", Proceedings of the 1987 CRDEC Conference on Obscuration and Aerosol Research, CRDEC, U. S. Army, 1988

H. Kosuge and J. R. Brock, "Studies in aerosol formation and growth", Proceedings of the 1987 CRDEC Conference on Obscuration and Aerosol Research, CRDEC, U. S. Army, 1988.

G. Moncivais, J. C. Carls and J. R. Brock, "Rapid acquisition of raman spectra from optically levitated particles" Proceedings of the 1987 CRDEC Conference on Obscuration and Aerosol Research, CRDEC, U. S. Army, 1988

J. C. Carls and J. R. Brock, "Propagation of laser breakdown and detonation waves in transparent droplets", Optics. Letters 13 273 (1988).

D. Zehavi, P. Kuhn and J. R. Brock, "Binary aerosol formation in a laminar coaxial jet", J. Aerosol Sci. 4 462 (1988).

J. C. Carls and J. R. Brock, "Explosive vaporization of single droplets by lasers: comparison of models with experiments" Optics Letters 13 (1988)

J. C. Carls and J. R. Brock, "On laser droplet vaporization models", Applied Optics, In Press

B. Jurcik, H. Kosuge and J. R. Brock, "Particle nucleation and growth in supersonic jets", submitted for publication, 1988.

B. Jurcik and J. R. Brock, "A study of low pressure particle impaction processes", submitted for publication., 1988.

G. Moncivais, J. C. Carls and J. R. Brock, "Time resolved Raman spectroscopy from optically levitated reacting particles", submitted for publication, 1988.

H. Kosuge and J. R. Brock, "Particle formation in jets", American Association for Aerosol Research Conference, Seattle, Washington, September 1988.

J. C. Carls and J. R. Brock, "Interaction of high energy laser radiation with particles", American Association for Aerosol Research Conference, Seattle, Washington, September 1988.

ABSTRACT

A computer model of the explosive vaporization of single water droplets by pulsed CO_2 laser radiation is compared with the relevant experiments. The model shows excellent quantitative agreement with the experiments, apparently the first time such agreement has been observed. The importance of fluid mechanics during the pulse is demonstrated, and a second computer model illustrates how a spherically symmetric explosion can evolve even under conditions of nonuniform heating. The two models reconcile the differences between predictions made by Mie theory and observations of droplet heating.

INTRODUCTION

Several models have been presented recently that model the explosive vaporization of single droplets[1,2,3]. All of these models agree qualitatively with the relevant experiments, but to our knowledge no one has shown quantitative agreement between the models and the experiments. Here, we compare results from our model with the explosive vaporization data of Kafalas and Herrmann (K & H)[4]. This data set, though fairly old, still represents the most comprehensive data available on the explosive vaporization of water droplets by CO_2 (10.6 mm) radiation.

COMPARISON OF THEORY AND EXPERIMENT

The fluid conservation equations describe explosive vaporization. These were solved subject to absorption of energy from a laser pulse. The hydrodynamic model is described in detail in Carls and Brock[3]. Unlike that model, here the laser pulse is allowed to be of finite length, and was chosen to match the experiment. The absorption coefficient was allowed to vary quadratically with density, after Feiock and Goodwin[5]. A square wave pulse having the same total energy and approximately the same pulse length as in the experiments was used in the model. Table 1 compares the range of pulses from the experiments with that used in the model. The droplet diameter was chosen to be 50 mm because K & H based many of their conclusions on this size. The data presented by K & H is for the late stages of the explosion, when the air shock has expanded to up to 300 times the initial droplet radius. This disparity in sizes poses difficulty for a numerical calculation, and so an expanding mesh was employed to keep the calculation time acceptable without loss of resolution in the early stages of the expansion.

Table 1. Range of Experimental parameters, and those used in the model.

	Experiment	Model
Droplet Diameter (mm)	44 - 62	50
Laser Pulse Length (nsec)	175 ± 25 FWHM[a]	225 square wave
Laser Fluence (J / cm^2)	5 - 15	5 - 15
Laser Intensity (MW/cm^2)	10 - 30	22.2 - 66.6

[a]Full Width at Half Maximum

K & H state that the explosion was spherically symmetric for droplets of diameter less than about 70 mm unless the laser pulse energy was not enough to completely vaporize the droplet. This implies that absorption in the droplet was uniform in some sense, leading to spherically symmetric flow. As a result, the electromagnetic (EM) field in the model was assumed to be uniform over the droplet throughout the pulse, and the motion was assumed to be spherically symmetric.

Figure 1 shows the results of the calculation compared with the (replotted) data of K & H. The position of the air shock wave is shown as a function of time. As can be seen, agreement between the computed curve and the data is

?

exceptional. Bear in mind that the model uses no adjustable parameters, the governing equations are solved subject to a realistic absorption coefficient and equation of state for water[6]. In addition, the model is sensitive to the relevant experimental parameters. For example, the computed trajectory of the air shock diverges from the data set when the pulse energy is varied, as well as when the pulse length is varied at constant pulse energy. The case to case variation for different pulses occurs during the transient period of the flow. In the later stages of the expansion, the air shock degrades into a sound wave, and the slope of each trajectory reaches the same final value, corresponding to the sound speed in air. The excellent agreement between model and experiment also verifies the quadratic dependence of the absorption coefficient on density. A more complete description of the model and the cases that were run will be published later.

DISCUSSION

The very good agreement between model and experiment indicates that the assumption of a uniform field and spherical symmetry was correct. An analysis based solely on Mie theory, however, would never lead to this assumption. Figure 2 shows the "source function"[7,8] for a 50 mm diameter water droplet and 10.6 mm radiation. As can be seen, the EM energy distribution is quite non-uniform. How, then, does seemingly uniform heating and spherically symmetric motion arise? The answer is bound up in the fact that the pulse length in the experiment is much longer than (~ ten times) the droplet's acoustic transit time (ATT)[3]. The ATT is the time a sound wave needs to traverse the droplet, and measures how fast the droplet responds through fluid flow. Pulses long compared to the ATT allow the droplet to flow in response to localized heating. This ability to flow can lead to uniform heating during the pulse.

To illustrate how symmetric motion can arise from nonuniform heating, a second, one dimensional model was devised. In this model, a water slab, infinite in two directions but of finite thickness in the direction of the laser, was heated by a laser pulse impinging on one surface. A transparent gas surrounds the slab on either side. The thickness of the slab was comparable to the diameter of the droplets in the preceeding model. A similar model is described in Reference 9. By irradiating the slab on one side, it heats in a very asymmetric manner. Beer's law is assumed to describe the absorption. Figure 3 is a schematic diagram of the model.

Since water absorbs strongly at 10.6 mm (a ~ 10^5 m^{-1}), the penetration depth of the radiation is in the tens of micrometers, and so it is strongly attenuated when it reaches the shadowed face. As the water at the irradiated face absorbs and heats, its pressure rises and it expands into the surrounding gas, vaporizing. As the water expands, it becomes more transparent since its absorption coefficient depends on density[5]. As a result, the radiation penetrates more deeply into the water slab, heating liquid regions that were previously undisturbed.

Figure 4(a) shows the fluid evolution of a 50 mm slab irradiated by the pulse from Table 1. The irradiated portion of the slab expands rapidly as it heats, allowing the radiation to heat more deeply into the slab. In this case, the radiation cannot "burn" all the way through the slab before the end of the pulse. Thus, the shadowed part of the slab does not vaporize completely, and a region of high density remains, expanding more slowly than the completely vaporized material from the irradiated part. The density profile retains substantial asymmetry, even to the last profile, at a time that is five times the original pulse length, and 50 times the original ATT of the slab.

If the slab thickness is decreased, and the slab is subjected to an identical pulse, the results change. For a thickness

105

of 37.5 mm, the initial heating distribution is still very non-uniform, but the fluid evolution changes as shown in Figure 4(b). At early times, the density profiles show a large degree of asymmetry, but as time goes on, the profiles become more symmetric about the initial slab centerline. In this case, the pulse is able to burn completely through the slab. This allows material in the shadowed part of the slab to absorb essentially the same amount of energy per unit of mass, even though the energy is absorbed in the late stages of the pulse lifetime. As a result, the asymptotic fluid flow is roughly the same as would evolve if the EM field were uniform throughout the pulse.

These results show that, even when the instantaneous EM fields are never spatially uniform, the time averaged absorption can be for certain cases. If one looks at the late stages of flow in these systems (as did K & H) one finds symmetric fluid flow because the non-uniformity of heating is averaged out over the life of the pulse. Recall that this can only occur when the fluid can respond to the applied stress, that is, when the pulse is much longer than the ATT. These results are strengthened by, and explain the fact that, when the droplet size was the same in each case, K & H saw asymmetric flow for a pulse having less energy than needed to completely vaporize the droplet [see Figure 4(a)], and symmetric flow for a pulse having more energy [see Figure 4(b)]. Finally, recalling the excellent agreement between the model and the data of K & H, explosive vaporization can be modeled successfully by assuming uniform EM fields and spherical symmetry for droplets up to about 70 mm in diameter for 10.6 mm radiation if: (1) the pulse length is much longer than the ATT, (2) the pulse energy is sufficient to completely vaporize but not to ionize the droplet, and (3) the late stages of flow are of greatest interest. These conditions apply to a wide range of practical pulses, and to most atmospheric fog and cloud droplet size classes. Experiments that examine the early stages of these pulses and the induced flow, however, should reveal the asymmetry of the heating process.

ACKNOWLEDGMENTS

REFERENCES

1. Armstrong, R. L., and Zardecki, A., *J. Appl. Phys.*, to be published.
2. Chitanvis, S. M., *J. Appl. Phys.*, **62**, 4387 (1987).
3. Carls, J. C., and Brock, J. R., *Aerosol Sci. Tech.*, **7**, 79 (1987).
4. Kafalas, P., and Herrmann, J., *Appl. Opt.*, **12**, 772 (1973).
5. Feiock, F. D., and Goodwin, L. K., *J. Appl. Phys.*, **43**, 5061 (1972).
6. Kestin, J., Sengers, J. V., Kamgar-Parsi, B., and Levelt-Sengers, J. M. H., *J. Phys. Chem. Ref. Data*, **13**, 175 (1984).
7. Pendleton, J. D., *Appl. Opt.*, **24**, 1631 (1985).
8. Prishivalko, A. P., *Sov. Phys. J.*, **26**, 149 (1983).
9. Carls, J. C., and Brock, J. R., *Opt. Lett.*, **13**, 273 (1988).

Figure 2.
"Source Function" showing nonuniform energy EM distribution for a 50 μm diameter water droplet irradiated by unpolarized 10.6 μm laser radiation. See References 7 and 8.

Figure 1.
Comparison of experimental and computed shock position as a function of time for water droplets exploding under laser irradiation. Each triangle represents the measurement of one shock position from a single droplet (see Ref. 1.) The curve was computed using no adjustable parameters. The pulse and droplet characteristics for model and experiment are listed in Table 1. The irradiance in the model was 44.4 MW/cm².

Figure 3.
Schematic of model used to investigate symmetric explosions arising from asymmetric heating. A high density slab is irradiated from one side by a laser. Beer's law describes the absorption, and the radiation attenuates as it traverses the slab.
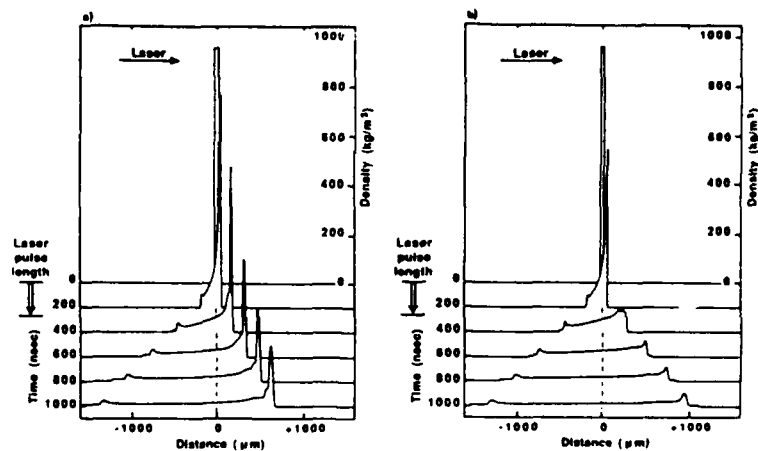
Figure 4. Comparison of laser induced explosion of water slabs of two different thicknesses, a) 50 μm, and b) 37.5 μm. The pulse is identical to that used in Figure 1. Each figure shows the time evolution of the density. The initial motion is asymmetric in each case because of nonuniform heating. In a), asymmetry persists throughout the flow history. In b), however, the smaller thickness allows symmetric motion to develop because of the influence of fluid flow on the absorption. See text.

108

STIMULATED BRILLOUIN SCATTERING IN SOLID AEROSOLS

Shirish M. Chitanvis

Theoretical Division, Los Alamos National Laboratory, Los Alamos, NM 87545

ABSTRACT.

We estimate the differential scattering cross-section due to SBS in a glass bead which is much larger than the wavelength of a high energy laser beam which irradiates it. We consider three possible scenarios:(a) neither the incident nor the Stokes wavelength is on a Mie resonance; (b) only the stokes wavelength is on resonance; (c) the incident wavelength and the stokes wavelength are on a Mie resonance. For the first two cases, we find that the SBS scattering cross-section is extremely small compared to the geometric/Mie cross-section. It follows as a corollary that SBS in a glass bead will be insufficient to shatter it in these two cases. In the last case, it is quite possible that due to the build up of high fields on-resonance within the spherical bead, the bead might be shattered. The chance of such an event occurring in a polydisperse distribution of spherical beads is generally not expected to be very high.

I. Introduction.

The following is a summary of the manner in which SBS may be included in a hydrodynamic description.

We also point out how this approach (coupled with some assumptions) finally leads to a scattering cross-section for aerosols in two limits: (a)radius smaller than the incident wavelength; (b) radius much larger than the incident wavelrngth.

II. General Formulation:

The hydrodynamic equations are:[1]

$$\partial \rho / \partial t = - \nabla \cdot \rho v \qquad (1)$$

$$\rho \, Dv/Dt = - \nabla P - \nabla \phi + \eta \, \nabla^2 v \qquad (2)$$

$$\rho \, C_v \, DT/Dt = - P \, \nabla \cdot v + \alpha I \; ; \, \text{but} \; \alpha = 0 \; \text{(transparent)} \Rightarrow P\rho^{-\gamma} = \text{constant}. \qquad (3)$$

where.

$$\phi = - P_S \cdot E_L \qquad (4)$$

with

$$P_S = \chi_c \, E_S^* \qquad (5)$$

P_S , the poolarization should not be confused with P the hydrodynamic pressure.

Note that foor the moment we have chosen α the absorption per unit length to be zero, since we warish to see how glass in particular may shatter via SBS, and the imaginary part of the reefractive index (best estimate so far) is $\sim 10^{-5} << 1$ (at $\lambda = 1.06 \mu m$).

E_L and E_s refer to the laser field and the stokes field respectively. The "peculiar" form of the $P \cdot E$ term was chosen to yield phase matching for the Brillouin effect. We shall use scalar eequations to describe the laser and the stokes fields.

$$(\epsilon_0/c^2)\partial^2 E_L / \partial t^2 - \nabla^2 E_L = -(1/c^2)\partial^2 P'_S/\partial t^2 \qquad (6)$$

$$(\epsilon_0/c^2)\partial^2 E_S / \partial t^2 - \nabla^2 E_S = -(1/c^2)\partial^2 P'_L/\partial t^2 \qquad (7)$$

with

---

[1] W. Kaiser and M. Maier, Laser Handbook Vol II., page 1114

$$P'_S = (\partial \chi / \partial \rho_0)(\rho - \rho_0) E_S \qquad (8)$$

$$P'_L = (\partial \chi / \partial \rho_0)(\rho - \rho_0)^* E_L \qquad (9)$$

Linearizing Eqns. (1)-(2), with $\rho = \rho_0 + \rho'$, $v = 0 + v'$, $\rho' << \rho_0$, $v << c_{sound}$:

$$\partial \rho' / \partial t = -\rho_0 \nabla \cdot v' \qquad (10)$$

$$\rho_0 \partial v' / \partial t = -(\gamma R / \mu) \nabla \rho' - \nabla \phi + \eta \nabla^2 v' \qquad (11)$$

Eqns. (6)-(7) and Eqns.(10)-(11) are coupled and need to be solved selfconsistently. We shall attempt to solve these equations approximately.

We first differentiate (10) with respect to time, take the divergence of (11), and obtain an equation for ρ' alone:

$$\partial^2 \rho' / \partial t^2 = (\gamma R / \mu) \nabla^2 \rho' + \chi_0 \nabla^2 (E_L E^*_S) + (\eta / \rho_0) \nabla^2 (\partial \rho' / \partial t) \qquad (12)$$

As an approximation we use:

$$E_L = \xi_L(r) \exp i[\sqrt{\epsilon_0} k_L \cdot r - \omega_L t] \qquad (13)$$

$$E_S = \xi_S(r) \exp i[\sqrt{\epsilon_0} k_S \cdot r - \omega_S t] \qquad (14)$$

$$\rho' = \rho^0 \exp i[k \cdot r - \omega t] ; k = \sqrt{\epsilon_0}(k_L - k_S) ; \omega = \omega_L - \omega_S \qquad (15)$$

ξ_L, ξ_S vary slowly in space ($|\partial \xi_{S,L}(r) / \partial r| << |k_{S,L} \xi_{S,L}(r)|$ and ρ^0 is a constant amplitude. (Note that $\rho^0 \neq \rho_0$)

Substituting (13)-(15) into (12), we get:

$$\rho^0 = \chi_0 \xi_L \xi^*_S k^2 / [k^2 c_0^2 - \omega^2 - i \eta \omega k^2 / \rho_0] ; c_0^2 = \gamma R / \mu \qquad (16)$$

We do not impose any boundary conditions since, as a first approximation we are treating the aerosol as an infinite medium.

Inserting (16) into (6) and (7), we get the following coupled equations for the electromagnetic fields:

$$[\, \nabla^2 + k_L^2 \,]\, \xi_L(r) = -(\epsilon_0-1)k_L^2\xi_L(r) - 4\pi k_L^2\, \partial\chi/\partial\rho_0\, \rho^0\, \xi_S(r) \qquad (17)$$

$$[\, \nabla^2 + k_S^2 \,]\, \xi_S(r) = -(\epsilon_0-1)k_S^2\xi_S(r) - 4\pi k_S^2\, \partial\chi^*/\partial\rho_0\, \rho^{0*}\, \xi_L(r) \qquad (18)$$

Note that we have chosen to work in the steady state regime.

Although (17) and (18) have been obtained for a bulk medium, we shall insist, for conveneince, that they hold when we are considering SBS in small aerosols as well. With this caveat in mind, we note that the right hand sides of (17) and (18) are non zero only within the confines of the aerosols. These coupled equations then describe a scattering problem.

III. Aerosols smaller than the incident wavelength.

The scattering problem described by (17)-(18) is solved using Green's function techniques.

$$\xi_L(r) = \xi^0_L(r) + \int d^3r'\, G_0(k_L,r-r')[-(\epsilon_0-1)k_L^2\xi_L(r)-4\pi k_L^2\, \partial\chi/\partial\rho_0\, \rho^0\,]\xi_S(r') \qquad (19)$$

$$\xi_S(r) = \xi_{noise} + \int d^3r'\, G_0(k_S,r-r')[-(\epsilon_0-1)k_S^2\xi_S(r)-4\pi k_S^2\, \partial\chi^*/\partial\rho_0\, \rho^{0*}]\, \xi_L(r')$$

$$(20)$$

$$G_0(k,r-r') = (1/4\pi)\, \exp\, ik|r-r'|\,/\,|r-r'| \qquad (21)$$

There is no inhomogeneous term on the right hand side of (20) since the stokes field is generated by the laser field.

Assuming that the aerosol is situated around the origin and has a radius a which is small compared to the wavelength, we approximate the integrands in (19)-(20) by their values at the origin , so that:

$$\xi_L(r) \approx \xi^0{}_L(r) + (a^3/3)(\exp(ik_L r)/|r-a|)[-(\epsilon_0-1)k_S{}^2\xi_S(r) - 4\pi k_L{}^2 \partial\chi/\partial\rho_0\rho^0]\xi_S(0)$$

$$(22)$$

$$\xi_S(r) \approx (a^3/3)(\exp(ik_S r)/|r-a|)[-(\epsilon_0-1)k_S{}^2\xi_S(r) - 4\pi k_S{}^2\, \partial\chi^*/\partial\rho_0\, \rho^{0*}]\xi_L(0)$$

$$(23)$$

These algebraic, coupled equations are solved trivially. Secondly, letting $r \gg a$, we may identify the SBS scattering cross-section as the square of the coefficient of $\exp(ikr)/r$ in the third term on the right hand side of (22):

$$d\sigma_L{}^{\rightarrow S}/d\Omega = \pi a^2\,(16\pi/9)\,(x_L{}^4\,x_S{}^4)\,|\partial\chi/\partial\rho_0|^2\,|\rho^0|^2\,\cdot$$

$$1\,/\,[\,(1 - x_L{}^2 x_S{}^2\,|\partial\chi/\partial\rho_0|^2\,Re\rho^0/3)^2 + (x_L{}^2 x_S{}^2\,|\partial\chi/\partial\rho_0|^2\,Im\rho^0/3)^2\,]$$

$$(24)$$

where $x_L = k_L a$, $x_S = k_S a$. Note that the cross-section goes as $k_L{}^4 \geq k_S{}^4$ as compared to the Rayleigh cross-section which goes as $k_L{}^4$.

IV. Aerosols larger than the wavelength.

In this section, we shall estimate the SBS cross-section from a sphere large compared to the wavelength. This limit is opposite to the one we had considered in the previous section. The reason for investigating this limit is that our glass beads are of radius a = 15 μm, at a wavelength λ_L = 0.351 μm and λ_L = 1.06 μm. This gives a size parameter $x_L = 2\pi a/\lambda_L \sim 300$ and 90 respectively.

Three cases are possible:(a) Neither the incident nor the SBS fields are on a Mie resonance. (b) Only the SBS field is on a Mie resonance. (c) Both the incident and the SBS fields are on a Mie resonance.

It will turn out that the first two cases contribute negligibly to the scattering cross-section. The third case however can indeed lead to the shattering of the droplet. But this case does imply that the the size parameter has to be chosen rather carefully.

Case (a):
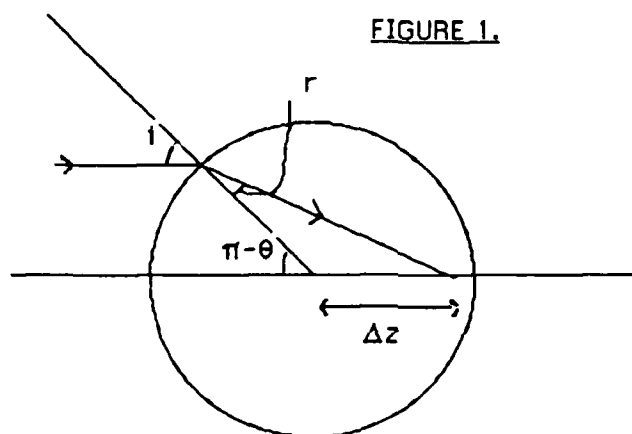
FIGURE 1.

Since the size parameter is so large. we shall use ray tracing to deduce the geometric focusing effects within the bead. Figure 1 shows the focusing effect due to the curvature of the bead. Using plane geometry, the distance Δz shown in the figure is given by:

$$\Delta z = a / [\cos\theta + (n^2(\lambda) - \sin^2\theta)^{1/2}] \tag{25}$$

where $n(\lambda)$ is the refractive index of the bead. This expression leads to a focusing of sorts (see Fig. 2), over a distance ω :

$$\omega = \Delta z(\theta=\pi) - \Delta z(\theta=\pi/2) \qquad (26)$$

The "mean" focal length is z_f :

$$z_f = 1/2 \ (\ \Delta z(\theta=\pi) + \Delta z(\theta=\pi/2)\ ) \qquad (27)$$

FIGURE 2.
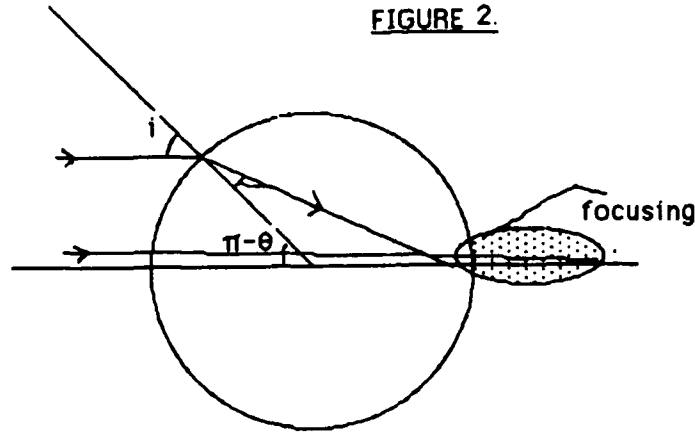
The effect of the curved surface of the bead is then to produce a focused beam out of the incident plane wave. The refracted electric field just inside the surface of the bead (before SBS sets in) is:

$$E(r,t) = \{\ E_0/\sqrt{s(z)}\ \}\ \exp(i\sqrt{\epsilon_0}k_L z) \cdot$$

$$\exp\{-\rho^2/\rho_0^2 s(z)\}\ \exp\{i\sqrt{\epsilon_0}k_L \rho^2\ ds(z)/dz\ /s(z)\} \qquad (28)$$

where

$$\rho_0^2\ s(z) = (z-z_f)^2 + \omega^2 \qquad (29)$$

The final crucial simplification is described in Fig. 3, which shows the equivalent problem we shall consider, so that we shall not have too many problems in doing

integrations. As indicated in Fig. 3, the equivalent straight surfaces are such that they give the focusing effect discussed in (28) and (29).[+]

[+] If a better approach exists for treating the focusing effect, the results may be substituted in (4) and (5).

FIGURE 3.

THE REAL PROBLEM

THE EQUIVALENT PROBLEM
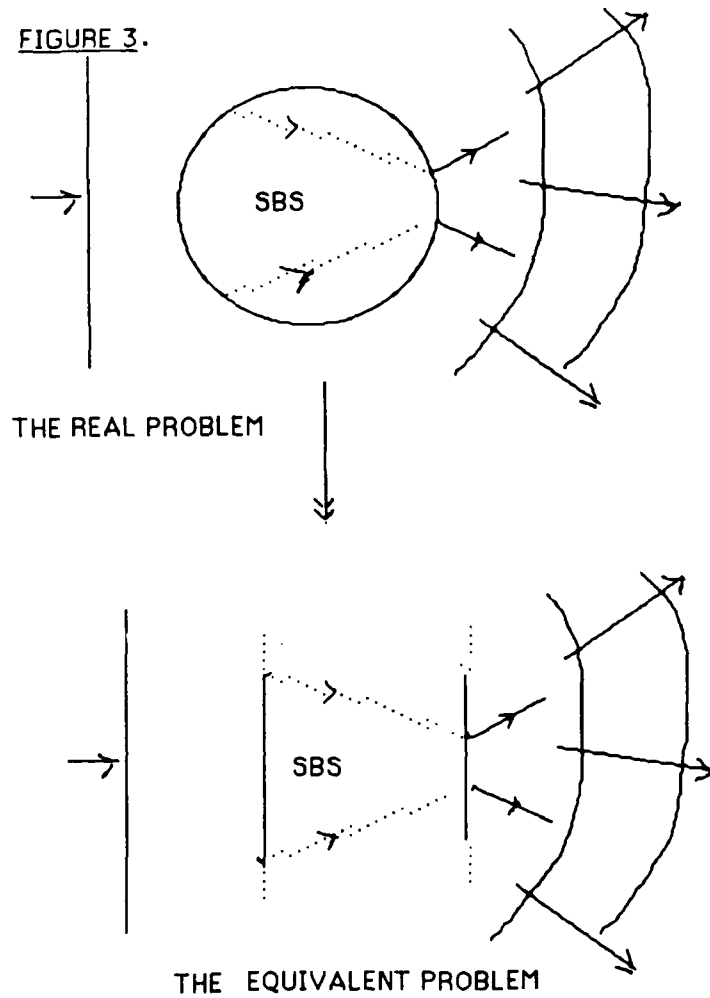
The approach now will be to estimate the field inside the bead due to SBS, so that the differential scattering cross-section may be obtained from the asymtotic form of the Lippmann-Schwinger equation (we are using the scalar approximation to the vector

wave equation for the electric field). The Lippmann-Schwinger equations for the pump and the laser fields are given by (17)-(18):

The integral equation for the pump field then follows:

$E_L(r) = E_L{}^{inc}(r) +$

$(1/4\pi) \int_{aer} d^3r' \exp(ik_L |r-r'|)/|r-r'| [-(\epsilon_0-1)k_L{}^2+\nu_L \, I_s(r')] E_L(r')$

$$(30)$$

where

$$\nu_L = -4\pi\epsilon_0 k_L{}^2 \, \partial\chi/\partial\rho_0 \, \chi_0 \, k^2 / [c_0{}^2 k^2 - \omega^2 - i\eta k^2 \omega/\rho_0] \qquad (31)$$

we have used Eqn(16) for ρ^0 from the section I. Remember, k is the difference in the pump and stokes wave vectors, and ω is the line shift.

We shall approximate the internal field by propagating in a 1-D mode within the droplet, the argument being that the propagation distance within the droplet is not sufficient for diffraction effects to set in.

$$E_L(r) = \exp(i\sqrt{\epsilon_0}k_L z) \, \xi_L(r) \qquad (32)$$

$$E_s(r) = \exp(-i\sqrt{\epsilon_0}k_s z) \, \xi_s(r) \qquad (33)$$

we get

$$2i\sqrt{\epsilon_0}k_L \, \partial\xi_L(r)/\partial z = \nu_L [\xi_s(r) \, \xi_s{}^*(r)] \, \xi_L(r) \qquad (34)$$

and

$$-2i\sqrt{\epsilon_0}k_s \, \partial\xi_s(r)/\partial z = (-1) \cdot \nu^*{}_s [\xi_L(r) \, \xi_L{}^*(r)] \, \xi_s(r) \qquad (35)$$

where ν_L has been defined above, and ν_S^* is given by

$$\nu_S^* = -4\pi \epsilon_0 k_S^2 \int d\rho_c \, \chi_c \, k^2 / [\omega_c^2 k^2 - \omega^2 + i\Gamma_k^2 \omega/\rho_c] \tag{36}$$

The extra minus sign on the right hand side of (35) comes from the fact that the stokes field is taken to propagate in the anti-parallel direction, so that the change in ξ_S should be measured in the anti-parallel direction also.

It is extremely interesting to note that besides the anti-parallel stokes component, the equations also permit a solution that propagates in the same direction as the laser field itself. This component is seen to be weaker than the anti-parallel component, and is presumably difficult to distinguish from the laser beam itself, since the SBS shift is extremely small. This point appears to have been missed by most pedagogical presentations of SBS in the literature.

An equation similar to (35) may be written down for $I_S = \xi_S(r) \cdot \xi_S^*(r)(c/4\pi)$, where c is the speed of light.

$$\xi_L(z) = E_L^0 \exp(-i \nu_L' i_S z / 2\sqrt{\epsilon_0} k_L) \tag{37}$$

$$\approx E_L^0 \quad \text{(within the glass bead)} \tag{40a}$$

$$I_S(z) = I_{noise} \{ \exp(|Im \, \nu_S^*| i_L z / \sqrt{\epsilon_0} k_S) - 1 \} \tag{38}$$

$$\approx I_{noise} |Im \, \nu_S^*| i_L z / \sqrt{\epsilon_0} k_S \quad \text{(within the glass bead)} \tag{41a}$$

where $\nu_L' = (4\pi/c)\nu_L$ and $\nu_S = (4\pi/c)\nu_S$. We shall take $I_{noise} \sim e^{-25}$. Note that (37) yields a laser field whose intensity ($I_L = (c/4\pi)\xi_L^*\xi_L$) depletes exponentially (ν_L is complex) as it propagates up the z-axis, while (38) yields the stokes intensity building up down the z-axis. Equations (40a) and (41a) are substituted in (30).

119

We shall now take the asymptotic limit of (30), as $r \rightarrow \infty$. The coefficient of $\exp(ik_L z)/r$ which is proportional to $\partial \chi / \partial \rho_c$ yields the SBS scattering amplitude:

$$f_{SBS}(\Omega) = V \int dz' \exp ik_L z'(1-\sqrt{\epsilon_0}\cos\theta) \ (z'/s^{3/2}(z')) \cdot$$

$$\exp [i\sqrt{\epsilon_0}k_L \ ds(z')/dz' \ / \ s(z')] \cdot$$

$$\int d^2\rho' \ (2\pi) \ J_0(\sqrt{\epsilon_0}k_L\rho'\sin\theta) \ \exp -3\rho'^2/2\rho_0^2 s(z')$$

$$(39)$$

The Bessel function in (39) was obtained by integrating over the azimuthal angle, and

$$V = -\nu_L \ |Im\nu'_s{}^* /2\sqrt{\epsilon_0}k_s| \ E_0^4 \qquad (40)$$

In evaluating the scattering amplitude, the ρ' integration is carried out first, setting the limits of integration from 0 to ∞. We do not believe this causes much of a problem especially in view of the gaussian decay in (28). The Hankel transform of a Gaussian can be found in the Bateman Manuscript Project (Integral Transforms Vol. II), and the result is a Gaussian times a modified Bessel function of the third kind, of order 1/2 which is simply a Gaussian, and the result is:

$$f_{SBS}(\Omega) = 2\pi V \int dz' \exp ik_L z'(1-\sqrt{\epsilon_0}\cos\theta) \ (z'/s^{3/2}(z')) \cdot$$

$$\sqrt{(\pi/8)} \ \alpha^{-1}(z') \ \exp -\epsilon_0 k_L^2 \ \sin^2\theta/4\alpha(z') \qquad (41)$$

where

$$\alpha(z) = 3 \ /(2\rho_0^2 \ s(z')) + i\sqrt{\epsilon_0}k_L \ ds(z)/dz \ /s(z) \qquad (42)$$

We estimate the mean value of the z' integral by setting z'=zf in the z' integration, with the understanding that it is in the neighborhood of zf that the integrand will achieve its maximum value. In what follows, we shall choose the refractive index $n(\lambda) = 1.5$ (for

120

glass). Taking the absolute square of the scattering amplitude, we obtain the differential scattering cross-section:

$$d\sigma_{L \to S}/d\Omega = \pi a^2 \exp(-\theta^2/\theta_c^2) [\tau^2 N/2^5] \, c^2 \text{ noise}^2 \, x_L^4 \, x_S^2 \, (c g_B/4\pi \sqrt{\epsilon_c} k_S)^4$$

$$(2\pi\nu_B)^4 [1 + (2\pi\nu_B/\Gamma_B)^2] \tag{43}$$

where

$$\theta_c^2 = 6/(\sqrt{\epsilon_0} k_L a \phi)^2 \tag{44}$$

(for $n = 1.5$, $\phi \approx 1.1$). Similarly, for $n = 1.5$, $N \approx 17.75$.

$$x_L = \sqrt{\epsilon_c} 2\pi a/\lambda_L \tag{45}$$

$$x_S = \sqrt{\epsilon_c} 2\pi a/\lambda_S \tag{46}$$

$$k_S = \sqrt{\epsilon_c} 2\pi/\lambda_S \tag{47}$$

ν_B is the SBS line shift, g_B is the SBS gain, Γ_B is the SBS line width. These three numbers are available in tables. Some effort was expended in reducing the formula to contain these three "measurable" mumbers.

Note the dependence of the differential scattering cross-section on the various parameters. Note also the Gaussian dependence on the scattering angle. The width of this function is aproximately that expected from Mie scattering.

Using the following number for glass:

$k_L = 2\pi/1.06\mu m \sim 10^7 \text{ m}^{-1}$ (wavenumber)

$g_B = 2 \times 10^{-10}$ (m/W) (gain)

$2\pi\nu_B \approx 3 \times 10^{10}$ Hz (stokes frequency)

$\Gamma_B = 10^9$ Hz $\qquad\qquad$ (line shift)

$a = 1.5 \times 10^{-5}$ m $\qquad\qquad$ (radius)

$E_c^2 = (4\pi/c)\, I_0$ $\qquad\qquad$ (energy density: I_c is the flux W/cm²)

We then get:

$$d\sigma_{L\to s}/d\Omega \approx 10^{-91}\, I_{noise}^2\, I_c^2 \qquad\qquad (48)$$

where $I_{noise} \sim e^{-25} \sim 10^{-11}$(MKS units) and $I, \sim 10^{12}$ W/cm² $= 10^{16}$ W/m². Consequently,

$$d\sigma_{L\to s}/d\Omega \approx 10^{-47}\ m^2 << \pi a^2 \sim 10^{-9}\ m^2 \qquad\qquad (49)$$

Thus the SBS scattering cross-section is far less than the geometrical (Mie) scattering cross-section. This is not surprising since the propagation of distance of 30 μm within the bead is hardly sufficient for SBS to set in.

Case (b):

Let us now take another tack and say that the frequency of some of the Brillouin photons which will be emitted in a "narrow" continuum around the stokes frequency is such that it hits a "Mie" resonance. Such photons will get trapped within the perfectly spherical bead, and circulate just under the surface. Under such resonance conditions, $I_s \sim 10^6\ I_{noise}$. This amplification factor was obtained by Chylek et al[2] in performing internal Mie field calculations for spherical particles with a size parameter near 40. This factor of $10\S$ is still insufficient to make the SBS cross-section non-negligible.

---

[2] P. Chylek, J.D. Pendleton, R.G. Pinnick, *Internal and near-surface scattered field of a spherical particle at resonant conditions,* App. Optics, 24, 3940 (1985)

Let us now see if we can give these photons the benefit of the doubt and allow them to have the proper phase so that they gain energy each time they go around the droplet. There is a hot spot formed by the incident field due to focusing (see Fig. 2) and one suspects that this hot spot might somehow pump the Brillouin photon as it passes throught the focal area. But the notion of pumping suggests that as the Brillouin photon gains energy in going around, in a clockwise direction, lets say, then a pump/laser field photon propagates in the counter-clockwise direction. But this is impossible, since the laser field, not being on-resonance, does not propagate counter-clockwise under the surface of the sphere, but simply refracts out of the bead (see fig. 3). Thus the Brillouin field cannot gain any more intensity, and the SBS cross-section will remain negligible.

Actually, to account for interference effects, one must add the scattering amplitudes for the linear portion of the scattering and the SBS portion. This yields a cross-term in the differential scattering cross-section which is of the order of $\sqrt{(d\sigma_{SBS}/d\Omega)}$ $\sqrt{(\pi a^2)} \sim 10^{-29}$ m^2 $<< \pi a^2 \sim 10^{-9}$ m^2.

To complete the estimation of whether SBS will shatter the glass bead, we use these intuitive ideas on the behaviour of the SBS field within the bead, to estimate ρ. It turns out that $\rho <<< \rho_0$.

Case (c):

In this case, the both the incident and the stokes field are on a Mie resonance. Then, both fields will resonate in the form of "surface" waves in the bead. The SBS field will then be pumped continuously along its propagation distance of $c_{light} \geq t_{pulse} \sim 3$ m, ($t_{pulse} \sim 10$ ns). The stokes intensity will then be $I_{noise} (\exp(g_B I_{inc} 3) - 1)$. Since the incident field is also on resonance, $I_{inc} \sim I_0 \cdot 10^6$. Thus, even for a low incident flux of $I_0 = 10 W/cm^2$, $I_s \sim e^{(60-25)} \sim e^{35} \sim 10^{15}$ (MKS units). This is a huge amplification, so that $\rho >>$

ρ_0, so that $\Delta P = (R/\mu)T_0\rho \gg P_{critical}$, and the droplet may be expected to shatter very easily.

To estimate the cross-section, we use the above ideas in (33), after modifying (40) and (41) to read:

$$I_S(r) E_L(r) = a \delta(|r|-a) I_S^0 E_L^0 A \tag{50}$$

where $I_S^0 = I_{noise} \exp(g_B I_L^0 A^2 (c_{light} t_{pulse}))$, $I_L^0 = (c/4\pi)(E_L^0)^2$ is the incident flux, A^2 is the amplification factor for the intensity due the fact that we are on resonance.[3] The prefactor a (radius) on the right hand side of (50) helps preserve the dimensions. The incident and the stokes fields are therefore restricted to lie at the surface. The SBS scattering amplitude is then obtained as before:

$$f_{SBS}(\Omega) = (a^3 \nu_L I_S^0 A/4\pi) J_0(\sqrt{\epsilon_0} k_L a) \tag{51}$$

The scattering cross-section is thus:

$$d\sigma_{L\rightarrow S}/d\Omega = (a^3|\nu_L|I_S^0 A/4\pi)^2 \cdot [J_0(\sqrt{\epsilon_0} k_L a)]^2 \tag{52}$$

Notice that the cross-section is isotropic, in contrast to (46), which describes the non-resonant case, and shows a predominant forward angle scattering. The asymptotic expression for $J_0(z)$ is

$$J_0(z) \sim (2/\pi z)^{1/2} \cos(z-\pi/4) \tag{53}$$

This formula is valid since our size parameter ($k_L a$) is greater than 90. We therefore see "damped" oscillations in the scattering cross-section as the size parameter changes. To get an order of magnitude estimate of the scattering cross-section, we write (52) in terms of measurable quantities:

$$d\sigma_{L\rightarrow S}/d\Omega = (a^3 I_S^0 A/4\pi)^2 \cdot (g_B k_L)^2 \cdot [J_0(\sqrt{\epsilon_0} k_L a)]^2 \tag{54}$$

$$\sim 10^{-11} \, m^2 < \pi a^2 \sim 10^{-9} \, m^2 \qquad (55)$$

A cross-term of the sort described in the previous section is of the order $\sim 10^{-10} \, m^2 \sim 10\%$ of the geometric cross-section, and in some sense becomes non-negligible. We must remember that this number was obtained using an extremely low incident flux. The implication is that for higher fluxes, the resonant-SBS effect will become more pronounced. Of course, for higher fluxes, when the incident wavelength is on a Mie resonance, the effective flux that is achieved within the spherical glass bead may very well exceed the breakdown threshold.

We therefore conclude that in this special case (case (c)), SBS may shatter the glass bead. But one must note that our final objective is to describe propagation through a cloud of glass beads which are poly-disperse, and the probability of finding a "resonant" bead is not very high; unless the dispersion is of a very special nature.

Blank

INTERACTION OF EXCIMER LASER RADIATION
WITH SOLID PARTICLES

D.R. Alexander, D.E. Poulain, J.P. Barton, S.A. Schaub, and J. Zhang

Center for Electro-Optics
University of Nebraska-Lincoln
Lincoln, Nebraska 68588-0525

RECENT PUBLICATIONS, SUBMITTALS FOR PUBLICATION AND PRESENTATIONS

A) J.P. Barton, D.R. Alexander, and S.A. Schaub, "Spherical particle irradiated by a tightly-focused laser beam: focal point positioning effects at resonance conditions", submitted for publication in J. Appl. Phys., September 1988.

B) J.P. Barton, D.R. Alexander, and S.A. Schaub, "Internal and near-surface electromagnetic fields for a spherical particle irradiated by a focused laser beam", J. Appl. Phys., **64** (4), 15 August 1988, 1632.

C) S.A. Schaub, D.R. Alexander, and J.P. Barton, "Theoretical model for the image formed by a spherical particle in a coherent imaging system: comparison to experiment", submitted for publication to Opt. Eng., July 1988.

D) D.R. Alexander, D.E. Poulain, J.P. Barton, S.A. Schaub, and J. Zhang, "Nonlinear effects of excimer laser radiation with solid particles in a vacuum", presentation at the 1988 CRDEC Conference on Obscuration and Aerosol Research, June 1988.

E) S.A. Schaub, D.R. Alexander, and J.P. Barton, "Focused laser beam interactions with methanol droplets: effects of relative beam diameter", submitted for publication in Appl. Opt., May 1988.

F) M.A. Emanuel, "Explosive vaporization of spherical and cylindrical aerosols: comparison between experimental results using a CO_2 laser and internal and scattered optical fields", Masters Thesis, Mechanical Engineering Department, Center for Electro-Optics, University of Nebraska-Lincoln, Lincoln, Nebraska, 68588-0525, October 1987.

G) D.R. Alexander, J.P. Barton, S.A. Schaub, and M.A. Fitzwater, "Beam propagation effects resulting from the electric field strengths for spheres and cylinders: internal and near field", presentation at Workshop on the Physics of Directed Energy Propagation in the Atmosphere, U.S. Army Atmospheric Sciences Laboratory (ASL) at New Mexico State University, Los Cruces, New Mexico, January 27-28, 1987.

H) D.R. Alexander and J.G. Armstrong, "Explosive vaporization of aerosol drops under irradiation by a CO_2 laser beam", Appl. Opt., **26** 1987, 533.

I) J.G. Armstrong, "Experimental study of the explosive vaporization of aerosol drops under irradiation by a CO_2 laser", Masters Thesis, Mechanical Engineering Department, University of Nebraska-Lincoln, Lincoln, Nebraska, 68588-0525, May 1986.

J) D.R. Alexander, "Nonlinear effects of high energy CO_2 laser illumination of aerosol drops", presentation at the 1986 CRDEC Conference on Obscuration and Aerosol Research, June 1986.

K) D.R. Alexander, K.J. Wiles, S.A. Schaub, and M.P. Seeman, "Effects of non-spherical drops on a phase doppler spray analyzer", SPIE **573** 1985, 67.

L) D.R. Alexander, "Experimental system for real-time observation of particle dynamics at high energy", presentation at the 1985 CRDEC Conference on Obscuration and Aerosol Research, June 1985.

Abstract

Results have been obtained for the interaction of KrF excimer laser radiation ($\lambda = 248$ nm, FWHM pulse width $= 17$ ns) with solid particles in air and under vacuum conditions down to approximately 10^{-5} Torr. Solid particles of glass spheres, Al spheres, Al_2O_3, W, SiC, ground fused silica (Suprasil), and polystyrene divinylbenzene have been imaged at various stages of the explosive process after interaction with the KrF laser operating at focused irradiance values of approximately 10^{11} W/cm^2. In addition to illustrating the dynamics of the explosive process, the excimer laser imaging system was also used to extract information regarding the velocities of the ejected material by the use of a dual imaging pulse. Although the velocity of the ejected material depends on several parameters, among these being the location of the particle within the focal region, typical velocities ranged from 200 to 2000 m/s. Streak camera images were also taken which revealed that the lifetime of plasma emission ranged from about 40 to 2700 ns depending on the particular material and surrounding pressure.

Introduction

The propagation of high energy lasers through an atmosphere containing an aerosol as well as the penetration of a laser beam through particle clouds in a vacuum are of current interest. Although good progress has been made in understanding the interaction of intense laser radiation with spherical liquid aerosol particles, the open literature on the interaction of high energy laser beams with solid particles less than 100 μm in diameter is not extensive. Most of the work performed thus far appears to have been for the interaction of intense laser beams with a wide variety of thin metal films or foils.[1-6] Bol'shov, et al.[1] points out that the validity of extrapolating the results and conclusions to spherical geometry must be evaluated in each specific case.

The current paper describes experimental work on the interaction of excimer laser radiation at $\lambda = 248$ nm with solid particles in air and in vacuum conditions up to 10^{-5} Torr. Of particular interest in this work, was the observation of the dynamics of the laser beam interaction with several types of solid particles or clumps of solid particles. In addition, the velocity and distribution of material being ejected were also of interest.

Experimental Setup

A schematic of the experimental setup used in the research is shown in Figure 1. The output beam (10 x 20 mm) from the front excimer laser (Questek Model 2860 operating on KrF with unstable optics, $\lambda = 248$ nm) is brought directly into the vacuum chamber where it is focused to a spot size of approximately 10^4 μm^2. The spot size was determined experimentally by moving a razor blade through the focal point and taking a ratio of transmitted energy, E_2, to input energy, E_1. The energies were measured with two Molectron Model J50 detectors whose output was coupled

to an A/D board in an IBM PC AT computer for processing. The FWHM size of the focal spot as shown in Fig. 2 was 95 μm high by 115 μm wide. The maximum irradiance value used in the work reported here was approximately 10^{11} W/cm^2 which is based on a pulse length of 17 ns, pulse energy of 400 mJ, and 10^4 μm^2 spot size. The second excimer laser, identical to the first except for having stable optics, is incident on the vacuum chamber in a direction orthogonal to both the high energy laser pulse used to heat the particles and the motion of the solid particles, serves as the illumination source for imaging studies and velocity measurements. The pulse from the second excimer laser was split into two separate pulses, one of which was sent directly to the vacuum chamber over a minimum optical path length, and the second which was sent over an additional 45 feet of optical path. Consequently, two 17 ns pulses delayed by approximately 45 ns allowed determination of the velocity of the expelled material by measuring the distance the material had traveled during the 45 ns interval. The absolute delay time between the firing of the second excimer (imaging) laser and the first excimer (high energy) laser was controlled by a digital delay generator incorporated into the laser sync unit and could be adjusted over a time range from 10 ns to several microseconds. Jitter in the laser circuitry, however, resulted in the absolute delay times between the two lasers to have an uncertainty of about ± 10 ns (recently reduced to ± 7 ns).

Images of the explosion dynamics were recorded on a vidicon (Cohu camera system) and the data stored on an optical memory disk recorder (Panasonic model TQ-2023F). The streak images were obtained using a Hamamatsu Streak Camera (Model M2548) which was oriented orthogonal to the direction of the high energy pulse and provided information regarding the duration of the plasma emission.

The solid particles were dispersed using a mechanical shaker which consisted of a particle reservoir mounted on an acoustic speaker. The input frequency and amplitude were adjusted using a Tektronixs Model FG 503 function generator and a Nikko Model Alpha 230 power amplifier so that the desired particle concentration was distributed in the focal region of the high energy laser beam.

The vacuum chamber consisted of a stainless steel cylinder (11.5 inches diameter, 6.5 inches high) with 9 optical viewing ports. High vacuum conditions were obtained using a cryogenic pump (CTI Cryogenics, Cryo-torr 100 high vacuum pump) connected to the base of the vacuum chamber through an eight-inch hole in the Newport research optical table. Pressures within the vacuum chamber were monitored using a thermocouple and ion gauge.

Results

Dynamics of Particle Breakup

Using the experimental arrangement described in the previous section, we investigated the laser-induced breakdown of Al_2O_3, W, SiC glass spheres, Al spheres, ground fused silica (Suprasil), and polystyrene divinylbenzene. Since the Al_2O_3, W, SiC, and ground fused silica were not spherical in form, it was difficult to distinguish material being ejected due to high energy laser interaction from additional particles in the field of view. However, the basic interactions were similar to those observed with spherical particles, and we report results only on the spherical materials. Video tapes for the other materials interacting with excimer laser radiation were given to CRDEC project monitors.

Figures 3-5 show the typical interaction of $\lambda = 248$ nm laser radiation at $I \approx 10^{11}$ W/cm^2 with Al spheres at pressures of 760 Torr, 0.1 Torr and 3×10^{-5} Torr. Note the evidence of shock formation under atmospheric conditions shown in Fig. 3 which was absent for both intermediate and high vacuum conditions. The dynamics of the explosion process shown in Fig. 3 are also strongly influenced by the relative location of the particles within the focal region. Fig. 6 shows the elastically scattered $\lambda = 248$ nm radiation from the Al particles and glass spheres during the 17 ns laser heating pulse (no imaging pulse). The bright spots serve as spatial and time reference markers as illustrated in Figs. 3-5. Figures 7 and 8 show the typical interaction of glass microspheres under the same illumination conditions as for Al particles. Again, shock formation is exhibited for the atmospheric pressure case. Figure 9 shows the interaction of a large 230 μm polystrene divinylbenzene particle with $\lambda = 248$ nm radiation in air at 10^{10} W/cm^2. Filamentry formations can be observed extending outward from the plasma corona. Our work also agreed with Dhareshwar, et al.[3] where the high atomic number (Z) targets show much more pronounced plasma jetting. Velocity information of bulk material and plumes were obtained from either single delayed imaging pulses or dual delayed imaging pulses with a 45 ns optical path difference. Table 1 shows typical velocities obtained for either plumes or bulk material.

As illustrated in Figs. 3-5 and 7-8, material is being ejected from the shadow surface of the Al and glass spheres. The ejection of this material from the shadow surface was surprising since the index of refraction of Al, for example, at $\lambda = 248$ nm is $n = 0.19 + 2.942$ i and theoretical Mie calculations indicate extremely high absorption on the illuminated surface. Based on the short

Table 1. Typical Velocities Found by Dual Pulse Imaging

Material	Power (W/cm^2)	Pressure (Torr)	Velocity(m/s)	
			Bulk	Plume
Glass Spheres (5-50 microns)	10^{11}	10^{-5}	NA	440 460 690 760 2000
Glass Spheres (5-50 microns)	10^{11}	760	250 250· 270 300 330	510 550 750
Al Spheres (20 microns)	10^{11}	10^{-5}	NA	450 460 1300 1700 1800

time scales for the appearance of this material, a possible explanation of this material ejection is due to spallation from shock phenomena off the shadow side of the spheres. Bol'shov et al.[1] report shock velocities of 9×10^4 m/sec on the shadow surface of thick aluminum foils at 5×10^{13} W/cm^2.

Lifetimes of Plasma Emissions

Observations of laser induced time dependent plasma formation were made with a Hamamatsu streak camera. The data was obtained using the vacuum chamber with the pressure ranging from 760 Torr to 1×10^{-5} Torr. The streak camera was set at right angles to the excimer laser beam ($\lambda = 248$ nm) used to heat and vaporize the solid particles. The broad band light emission from the plasma was focused through a fused silica lens onto the entrance slit of the streak camera with sensitivity ranging from 200 - 800 nm. Sweeping speeds of the streak camera, which could be adjusted from 10 ns to 1 ms, were used to study plasma emission times.

Figure 10 gives the result of the air breakdown initiated by the excimer laser irradiation. From Fig. 10 we see that the breakdown region extends 3.5 mm along the main beam axis. The plasma emission reached its peak intensity within the first 10-12 ns, and then decayed in time. Broad spectral emission lasted more than 100 ns after the main laser pulse ended. Figure 11 shows the results of the interaction $\lambda = 248$ nm irradiation with 20 μm diameter aluminum spheres. At atmospheric pressure (Figure 11a) with the presence of aluminum spheres, the laser-induced plasma emission was enhanced. The spatial region of the plasma extended over 4.5 mm. The peak intensity was about three times higher than that without the spheres. The emission lasted more than 800 ns after the main pulse had ceased. In vacuum, (Figure 11b) at 0.1 Torr and (Figure 11c) at 5×10^{-5} Torr, the plasma emission showed different characteristics. For example, the spatial emission regions were more confined and the peak intensities decreased. (Note that the data in Figure 11c was taken at higher streak camera sensitivity.) The emissions in vacuum lasted only 30-50 ns, which were much shorter than that at atmospheric pressure. Figure 13 gives the plasma emission time for air, glass, and Al spheres under different pressures.

Under vacuum conditions, shown in Figs. 11 and 12, the plasma emissions showed two-peak structure. By using a band pass filter, the first peak was shown to come from the elastic scattering of the 248 nm incident light, and the second peak was the broad band emission. Batanov, et al.[7] suggest that at certain temperatures metallic conductivity ceases and liquid metal becomes a liquid dielectric and becomes almost transparent to the incident radiation. Figure 12 gives similar

results for interactions of $\lambda = 248$ nm irradiation with 5-50 micron glass spheres. The physical characteristics of the plasma emissions were very similar to aluminum spheres. However, plasma emission lifetimes increased and, in our experiments, the maximum observed lifetime was 2,700 ns.

At atmospheric pressure without particles being present, the air breakdown is initiated by multi-photon ionization (the ionization potential for air is approximately 14 eV), which provides the initial free electrons for the cascade ionization processes.[8] In air breakdown the cascade processes dominated the ionization process and accounts for the major absorption of the incident energy. However, with the presence of aluminum spheres or glass spheres, the ionization processes were enhanced. For the case where particles are also present, the lower energy required for removal of electrons from aluminum atoms where the work function of Al is 4 eV and the ionization potential is 6 eV results in more free electrons for cascade processes to initiate. In fact, the direct ionization through photoelectric effects and multi-photon ionization (for Al only 1 to 2 photons are needed) played an important role in the ionization process, under vacuum conditions since cascade ionization becomes less important[8]. In our experiments, at pressures of 0.1 Torr and lower, no air breakdown could be observed. However, at these same low pressures (0.1 Torr and 4 x 10^{-5} Torr), when aluminum particles were present, strong plasma emissions were observed which indicates that the photoelectric effects and the multi-photon ionization were the main mechanisms of plasma formation in vacuum environments.

Conclusions

The current work reports the interaction of short wavelength $\lambda = 248$ nm excimer radiation at 10^{11} W/cm^2 with solid particles in air and vacuum conditions. Material was shown to be ejected from the shadow surface of all materials studied except for the 230 μm polystyrene divinylbenzene particles. Velocities measured for the ejected material in the plumes were comparable to the sonic velocities in the materials and ranged from 200 to 2000 m/s. Plasma lifetimes decrease as the surrounding gas pressures were reduced. Plasma lifetimes ranging from 40 to 2700 ns were measured and found to decrease as the surrounding gas pressures were reduced and greatly increased with the presence of small solid particles.

Acknowledgements

References

1. L. A. Bol'shov, I. N. Burdonskii, A. L. Velikovich, V. V. Gavrilov, A. Yu. Gol'tsov, E. V. Zhuzhukalo, S. V. Zabyalets, V. P. Kiselev, N. G. Koval'skii, M. A. Liberman, L. S. Mkhitar'yan, M. I. Pergament, A. I. Yudin, and A. I. Yaroslavskii, "Acceleration of Foils by a Pulsed Laser Beam", Sov. Phys. JETP, Vol. 65, No. 6, June 1987.

2. P.D. Gupta, Y.Y. Tsui, R. Popil, R. Fedosejves, and A.A. Offenberger, "Experimental Study of KrF - Laser High -Z- Plasma Interaction Dominated by Radiation Transport," Physical Review A, Vol. 34, No. 5, 1986.

3. L.J. Dhareshwar, P.A. Naik, P.D. Nandwana, and H.C. Pant, "Characteristics of Plasma Flow from Laser Irradiated Thin Foil", J. Appl. Phys., Vol. 61, No. 9, 1987.

4. David Salzmann, Henry Szichmann, Aaron D. Krumbein and C.E. Capjack, "Radiative Preheat in Laser Produced Aluminum Plasma", Phys. Fluids, Vol. 30, No. 2, 1987.

5. G.S. Korshunov, V.V. Ustyuzhin, and V. Ya Ushakov, "Laser-Induced Formation of Long Plasma Jets from Metal Powder Targets", Sov. Phys. Tech. Phys., Vol. 30, No. 4, 1985.

6. Robert B. Raphael, "Review of Impulse Coupling with Materials", SPIE Vol. 476, p. 112, Excimer Lasers, Their Applications and New Frontiers in Lasers, 1984.

7. V. A. Batanov, F. V. Bunkin, A. M. Prokhorov, and B. V. Fedorov, "Evaporation of Matallic Targets Caused by Intense Optical Radiation", Soviet Physics JETP, Vol. 36, No. 2, 1973.

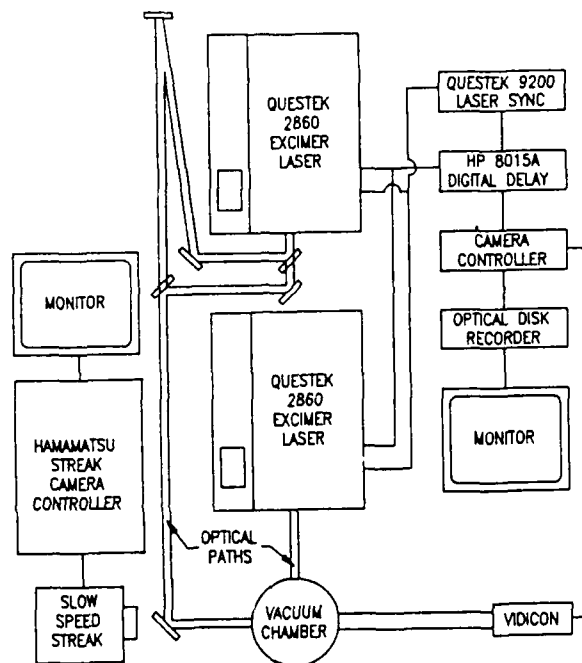8. George Bekefi, "Principles of Laser Plasma", John Wiley and Sons, Inc., 1976.
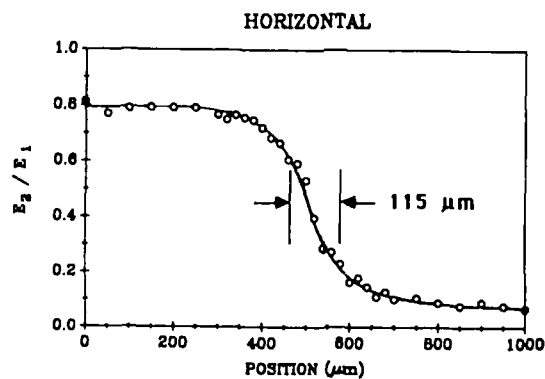
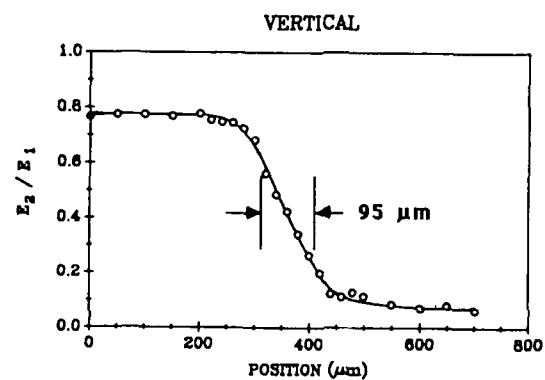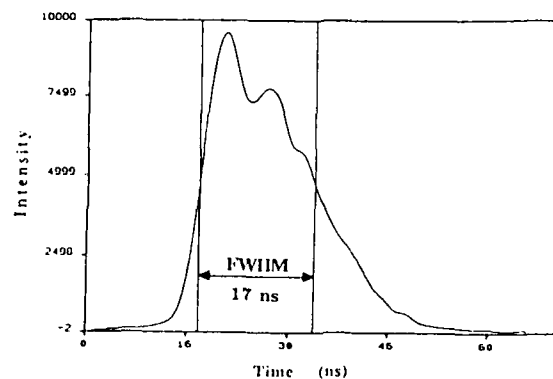Fig. 1. Schematic of experimental setup.

Fig. 2. (Top) Temporal profile of a typical output pulse of a Questek Model 2860 excimer laser using Krypton Fluoride ($\lambda = 248$ nm). (Bottom) Experimental determination of focused beam waist by measurement of pulse energy transmitted past a knife-edge translated through the focal point of the beam (Focusing lens: $\phi = 50$ mm, $f = 250$ mm).

136

20 micron Al spheres

$\lambda_{inc} = 248$ nm

$I \approx 10^{11}$ W/cm^2 (400 mJ/pulse)

P = 760 Torr

Beam propagation

Imaging pulse arrives 200 ns after high energy pulse.

Fig. 3. Interaction of 20 μm aluminum spheres with intense UV radiation (λ = 248 nm, I $\approx 10^{11}$ W/cm^2) in atmosphere 200 ns after arrival of the heating pulse. Note the various dynamics occurring in the probe volume relative to the focal point of the explosive beam. White spots mark the initial heating and scattering of light on illuminated surface.
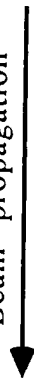
20 micron Al spheres

$\lambda_{inc} = 248$ nm

$I \approx 10^{11}$ W/cm^2 (400 mJ/pulse)

$P = 10^{-1}$ Torr

Imaging pulse arrives 50 ns after high energy pulse.

Beam propagation

Fig 4 Interaction of a 20 μm aluminum sphere with intense UV radiation ($\lambda = 248$ nm, $I \approx 10^{11}$ W/cm^2) in vacuum (0.1 torr) 50 ns after pulse incidence. Note the "jetting" of material from the sphere in the direction of beam propagation.
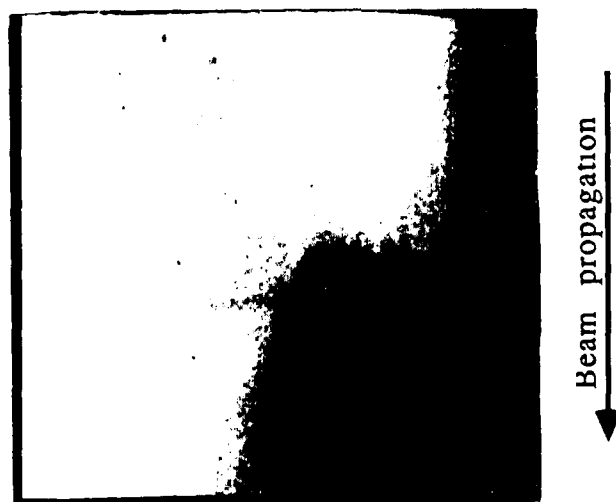
20 micron Al spheres

λ_{inc} = 248 nm

$I \approx 10^{11}$ W/cm^2 (400 mJ/pulse)

$P = 10^{-5}$ Torr

Imaging pulses arrive 50 ns and 95 ns after high energy pulse.

Velocity of upper plume is 1300 m/s and velocity of lower plume is 1700 m/s.

Beam propagation →

Fig. 5. Dual exposure of the interaction of two adjacent 20 μm aluminum spheres with intense UV radiation (λ = 248 nm, $I \approx 10^{11}$ W/cm^2) 50 and 95 ns after pulse incidence. Computed velocity of the upper and lower plumes are 1300 and 1700 m/s, respectively. The bright, white spots locate the initial interaction at time = 0 ns.

139

Beam propagation
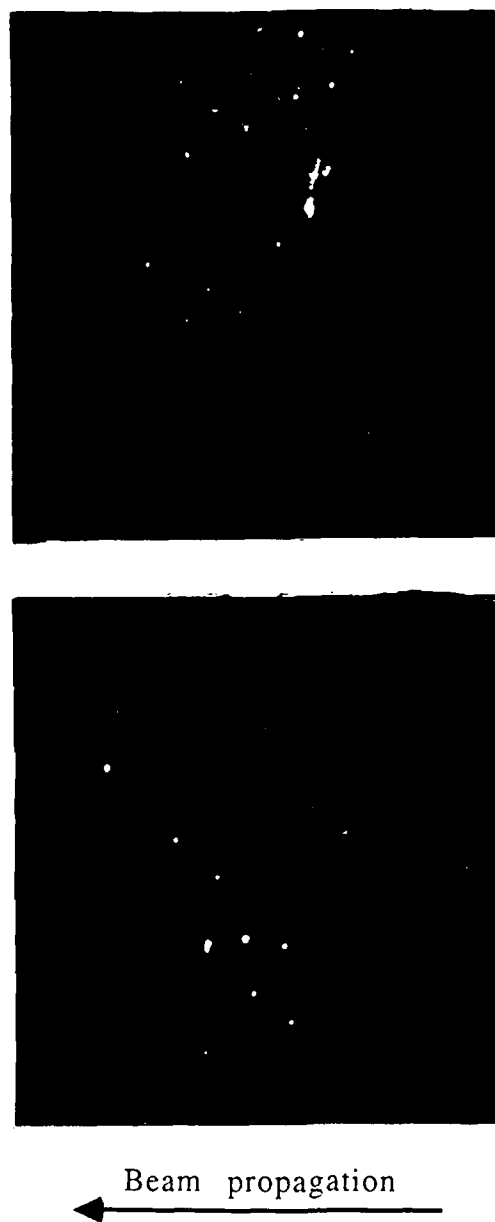
Fig. 6. Images taken without any imaging beam illumination of the interaction of 20 μm aluminum spheres (top) and 5-50 μm glass spheres (bottom) with intense UV radiation ($\lambda = 248$ nm, I $\approx 10^{11}$ W/cm^2). The only light observed is scattered 248 nm light due to the presence of a bandpass filter.

140

5-50 micron glass spheres

$\lambda_{inc} = 248$ nm

$I \approx 10^{11}$ W/cm^2 (400 mJ/pulse)

$P = 760$ Torr

Beam propagation

Imaging pulse arrives 50 ns after high energy pulse.

Fig. 7. Interaction of 5-50 μm glass spheres with intense UV radiation ($\lambda = 248$ nm, $I \approx 10^{11}$ W/cm^2) in atmosphere 50 ns after pulse incidence. Note "jetting" of the material from the shadow hemisphere of the spheres in the direction of beam propagation, and the presence of the shock front behind the spheres.

5-50 micron glass spheres

$\lambda_{inc} = 248$ nm

$I \approx 10^{11}$ W/cm^2 (400 mJ/pulse)

$P = 4.5 \times 10^{-5}$ Torr

Beam propagation
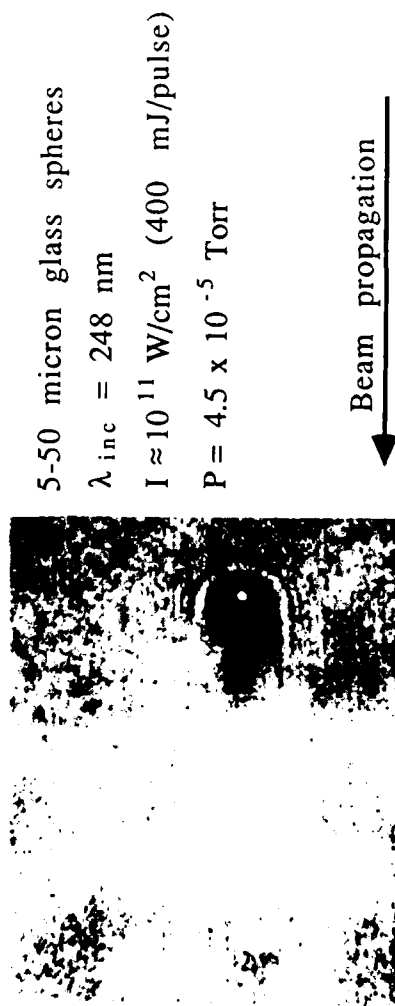
Imaging pulse arrives 0 ns after high energy pulse.

Fig. 8. Interaction of a 5-50 μm glass sphere with intense UV radiation ($\lambda = 248$ nm, $I \approx 10^{11}$ W/cm^2) in high vacuum (5×10^{-5} torr) 20 ns after pulse incidence. Note "jetting" of the material from the shadow hemisphere of the sphere. The estimated velocity of the plume is 2000 m/s.

230 micron polystyrene/DVB

$\lambda_{inc} = 248$ nm

$I \approx 10^{10}$ W/cm^2

$P = 760$ Torr

Imaging pulse arrives 28 ns after high energy pulse.
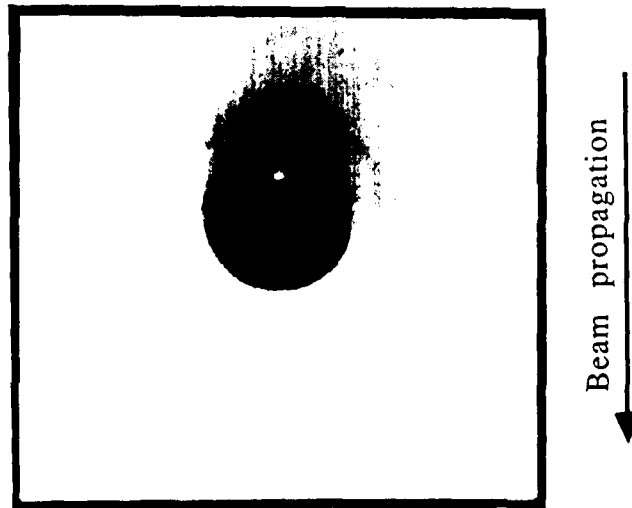
Beam propagation

Fig. 9. Interaction of a 230 μm Polystyrene/DVB sphere with intense UV radiation ($\lambda = 248$ nm, $I \approx 10^{10}$ W/cm^2) in atmosphere 28 ns after pulse incidence. Note the propagation of the shock front and jets/streamers of material from the illuminated hemisphere of the particle in the direction of the incident laser beam.

143

Fig. 10. Air breakdown induced by focused excimer laser radiation ($\lambda = 248$ nm, $I \approx 10^{11}$ W/cm^2).

Fig. 11. 20 μm aluminum spheres irradiated by excimer laser radiation ($\lambda = 248$ nm, $I \approx 10^{11}$ W/cm^2) for (a) P = 760 torr, (b) P = 0.1 torr, (c) P = 4 × 10^{-5} torr.
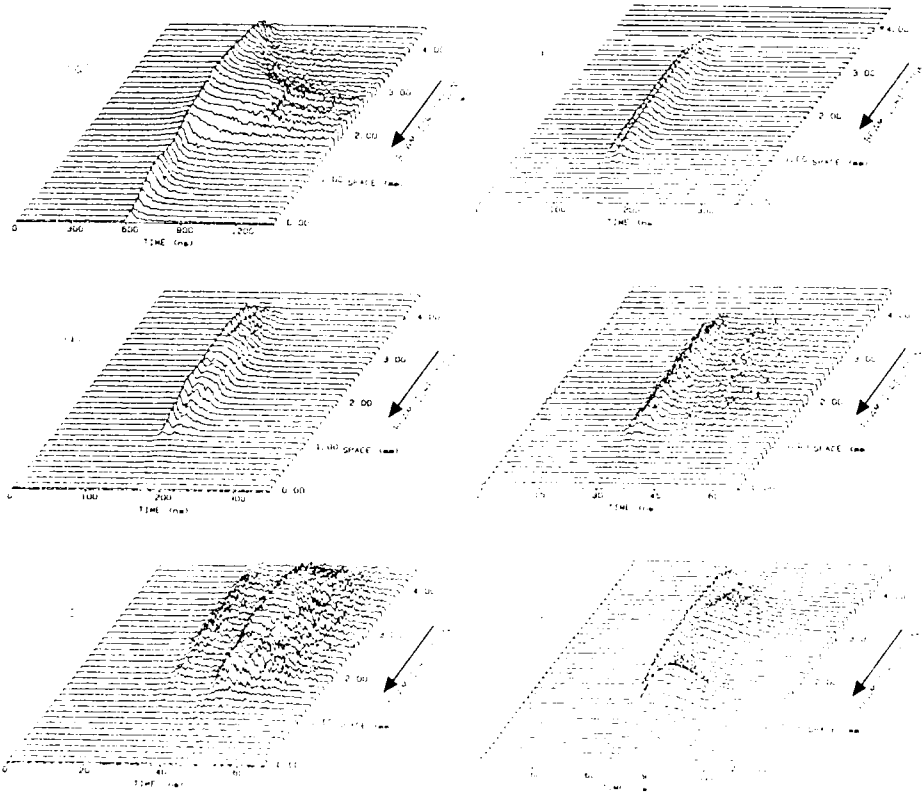
Fig. 12. 10 μm glass spheres irradiated by excimer laser radiation ($\lambda = 248$ nm, $I \approx 10^{11}$ W/cm^2) for (a) P = 760 torr, (b) P = 0.1 torr, (c) P = 4 × 10^{-5} torr.
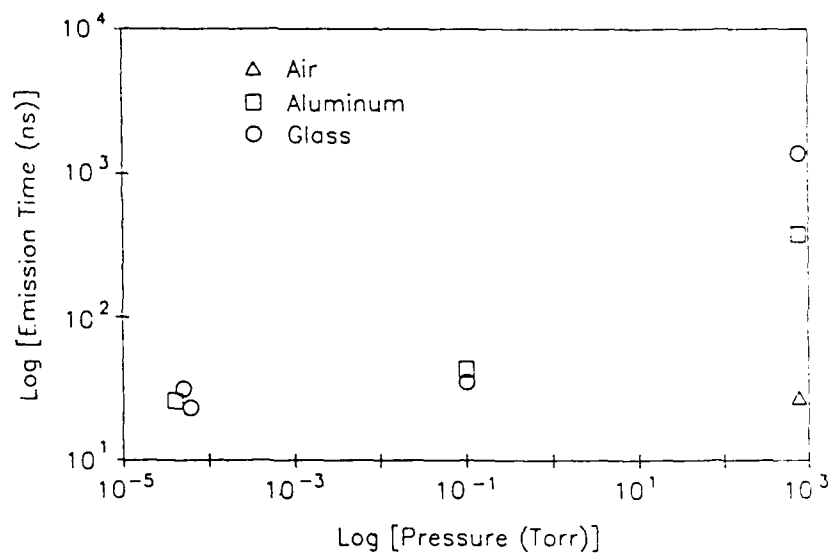
144

Fig. 13.   Plasma emission time as a function of absolute pressure for air
and aluminum and glass spheres.

Blank

PROPAGATION OF HIGH-ENERGY LASER BEAMS THROUGH METALLIC AEROSOLS

A. Zardecki
Theoretical Division, MS K723
Los Alamos National Laboratory
Los Alamos, NM 87545

R. L. Armstrong
Physics Department, Applied Laser Optics Group
New Mexico state University
Las Cruces, NM 88003

ABSTRACT

By combining the results of the hydrodynamic code CON1D and the beam propagation code LASER, we investigate the propagation of high-energy laser beams through vaporizing metallic aerosols in the regime for which the plasma generation becomes important. An effective plasma absorption coefficient allows us to set up a coupled system of equations describing the system consisting of the beam and vapor.

INTRODUCTION

When an aerosol particle is irradiated by a high-flux laser beam, plasma formation is one of many interactions modes that may occur. In this interaction, careful distinction must be made between absorbing aerosols, and aerosols which are minimally absorbing, or even effectively transparent, at the laser wavelength of interest.

In the case of absorbing aerosols,[1-3] deposition of laser energy results in the rapid liberation of high-temperature vapor at the aerosol surface. Free electrons present in this vapor serve as seed electrons for the avalanche ionization process producing a plasma fireball in the neighbourhood of the aerosol. Under suitable conditions, not known in quantitative detail, fireballs around individual aerosols can merge to form a beam-blocking plasma.

The process of plasma formation is slightly different for quasi-transparent aerosols. In this case, the driving mechanism underlying plasma formation is the presence of field inhomogeneities either inside or near its surface.[4,5]

147

Typically, a two-step process of plasma formation is initiated by seed electrons due to multiphoton ionization. In the second step, cascade ionization leads to a rapid growth in the number of ions.

In this paper, we study the initiation of plasma above absorbing, metallic surfaces irradiated with laser fluxes within the range of 10^6-10^9 W/cm^2. As discussed in the work of Pirri et al.[6] and in the work of Weyl et al.[7] the plasmas in an air environment grow rapidly, developing either a laser-supported detonation wave or a laser-supported combustion wave which absorbs the laser radiation and strongly influences the laser coupling to the surface. For moderate fluxes, where the diffusive vaporization regime prevails, a hydrodynamic model of plasma initiation off irradiated metallic aerosols in vacuum has recently been formulated by Chitanvis.[8] For high laser fluxes, convective vaporization is accompanied by production of shock waves in the non-isobaric ambient medium.[9,10] The increase in the ion number density, regarded as a special case of a chemical reaction, allows us to calculate the plasma absorption coefficient of a single metallic aerosol. To this end, the hydrodynamic code CON1D[11] is employed. The CON1D output is then utilized to analyze the nonlinear beam propagation with the aid of the propagation code LASER.

EQUATIONS OF MOTION

Consider an aerosol particle of radius r_d and density ρ_d uniformly irradiated by a time-varying electromagnetic flux F. At $t = 0$, the arrival time of the leading edge of the pulsed beam, the particle is assumed to be in equilibrium with the ambient gas at a temperature T_0 and a pressure p_0. For times, $t > 0$, the particle absorbs energy from the beam, the particle temperature T_d rises, and the particle is no longer in equilibrium with ambient gas. A thin, nonequilibrium region, the Knudsen layer, is created at the particle surface. For low to moderate flux levels, diffusive and convective processes transport mass, momentum, and energy into the surrounding medium whereas, for high flux levels, the aerosol particle vaporizes explosively, creating shock waves.

The region surrounding the particle is a multi component medium consisting of the particle vapor, which we take—for the sake of concreteness—as aluminum: the molecular gases: N_2 and O_2; the ions: Al^+ and e; and the gas of Al^*, excited aluminum atoms. The basic two kinetic ionization reactions are:

$$Al + e = Al^* + e,\tag{1}$$

$$Al^* + e = Al^+ + e + e.\tag{2}$$

If the index $k = 1,\ldots,K$ denote species k, and the index $l = 1,\ldots,L$ numbers the chemical reactions, the ionization process will induce additional chemical source terms in the species continuity and energy equations. In terms of the reaction rates $\dot{\omega}_l$, they are

$$\dot{\rho}_k^c = W_k \sum_{l=1}^{L} (b_{k,l} - a_{k,l}) \dot{\omega}_l \tag{3}$$

and

$$\dot{Q}_c = \sum_{l=1}^{L} \dot{\omega}_l Q_l. \tag{4}$$

Here Q_l is the negative of the heat of reaction l at absolute zero:

$$Q_l = -\sum_{k=1}^{K} (b_{k,l} - a_{k,l})(\Delta H_f^0)_k, \tag{5}$$

where $(\Delta H_f^0)_k$ refers to the heat of formation of species k. The $a's$ and $b's$ in these equations are the stoichiometric coefficients; corresponding to reactions described by Eqs. 1 and 2, they are $a_{k,1} = 1,0,0,0,1,0; b_{k,1} = 0,0,0,0,1,1; a_{k,2} = 0,0,0,0,1,1;$ and $b_{k,2} = 0,0,0,1,2,0$.

Finally, the reaction rates are given as

$$
\begin{aligned}
\dot{\omega}_l = c_{fl} T^{\eta_{fl}} exp(-E_{fl}/T) \prod_{k=1}^{K} \left(\frac{\rho_k}{\mu_k}\right)^{a_{k,l}} \\
- c_{bl} T^{\eta_{bl}} exp(-E_{bl}/T) \prod_{k=1}^{K} \left(\frac{\rho_k}{\mu_k}\right)^{b_{k,l}}
\end{aligned}
\tag{6}
$$

where the μ_k are the molecular weights, whereas the coefficients c, E and η are the appropriate forward and backward reaction constants.

The hydrodynamic equations of motion, supplemented by the source terms due to chemical reactions, now become:

(i) the mass conservation equations

$$\frac{\partial \rho_k}{\partial t} = \frac{1}{r^2} \frac{\partial}{\partial r} (\rho_k u r^2) = \frac{1}{r^2} \left[\rho D r^2 \frac{\partial}{\partial r} \left(\frac{\rho_k}{\rho} \right) \right] + \dot{\rho}_k^c, \tag{7}$$

(ii) the momentum conservation equation

$$\frac{\partial \rho u}{\partial t} + \frac{1}{r^2} \frac{\partial}{\partial r} (\rho u^2 r^2) + \frac{\partial p}{\partial r} = \frac{1}{r^2} \frac{\partial}{\partial r} (r^2 \Sigma_{rr}) - \frac{\Sigma_{\phi\phi} + \Sigma_{\theta\theta}}{r}, \tag{8}$$

(iii) the energy conservation equation

149

$$\frac{\partial \rho \epsilon}{\partial t} + \frac{1}{r^2}\frac{\partial}{\partial r}(\rho \epsilon u r^2) + \frac{p}{r^2}\frac{\partial}{\partial r}(u r^2)$$

$$= \frac{1}{r^2}\frac{\partial}{\partial r}\left(\kappa r^2 \frac{\partial T}{\partial r}\right) + \frac{1}{r^2}\left\{\frac{\partial}{\partial r}r^2 \rho D\left[\sum_{k=1}^{K} h_k \frac{\partial}{\partial r}\left(\frac{\rho_k}{\rho}\right)\right]\right\}$$

$$+ \Sigma_{rr}\frac{\partial u}{\partial r} + \left(\Sigma_{\phi\phi} + \Sigma_{\theta\theta}\right)\frac{u}{r} + \dot{Q}_c. \tag{9}$$

In Eqs. 7-9, $\rho_k, \epsilon, \rho, u, p$, and T are the component mass densities, and the mixture internal energy, density, velocity, pressure, and temperature, respectively. Expressions for the stress tensor components $(\Sigma_{rr}, \Sigma_{\theta\theta}, \Sigma_{\phi\phi})$, and the transport coefficients (D, κ) are given in Ref. 9. Also given there are the expressions for the caloric equation of state for ϵ, the species enthalpy h_k, and the thermal (ideal gas) equation of state. Equations 7-9 need to be solved with appropriate boundary conditions, which are discussed in detail in Ref. 10.

The hydrodynamic equations in the vapor yield the density distribution of each species in the region surrounding the particle. The density of metallic ions determines the plasma absorption coefficient, σ_{plasma}.[12,13] By writing a simple energy balance equation for the plasma, which is seen by the incoming beam as a spherical annulus with area A,

$$\int \sigma_{plasma} dv = A Q_{pl}, \tag{10}$$

we can obtain an effective plasma absorption efficiency factor, Q_{pl}. This is the quantity that accounts for the coupling of plasma to radiation.

In the small-angle approximation, the irradiance at any spatial point is obtained from the transport equation for the intensity distribution function (radiance) I. If ϕ specifies the projection of the unit directional vector on the plane perpendicular to the beam axis, this equation has the form[14]

$$\left(\frac{\partial}{\partial z} + \phi \cdot \frac{\partial}{\partial r} + \sigma_t\right)I(r, z, \phi, t') = \sigma_s \int p(\phi - \phi')I(r, z, \phi', t')d^2\phi'. \tag{11}$$

In Eq. 11, $p(\phi - \phi')$ is the phase function; $t' = t - z/c$ is the retarded time; σ_s is the volume scattering coefficient due to aerosols, whereas σ_t is the total volume extinction coefficient. The small-angle, forward-scattered radiation flux (irradiance) is given as

$$F(r, z, t') = \int I(r, z, \phi, t')d^2\phi'. \tag{12}$$

Equations 11-12 can be solved numerically by advancing from a plane $z = $ const to a neighbouring plane $z + \delta z$, where $\sigma_s \delta z \ll 1$. The effect of plasma absorption is included by modyfing the σ_t on the left-hand-side of Eq. 11. We note that in the absence of the plasma

$$\sigma_t = \sigma_s + \sigma_a, \tag{13}$$

where σ_a is the aerosol absorption coefficient. We thus define the effective absorption coefficient as

$$\sigma_{eff} = \sigma_a + \sigma_{plasma}. \tag{14}$$

In actual computation, the absorption and scattering cross sections vary with space and time, depending on the value of the laser flux. Figure 1 shows the plasma absorption efficiency as a function of time for different flux levels of the laser beam.

NUMERICAL RESULTS

To illustrate our former considerations, we model numerically the propagation of a laser pulse through a 2 m slab filled with monodisperse aluminum particles having the radius of 10 μm. The laser wavelength is assumed to be 10.6 μm, which corresponds to the complex refractive index of $(2.66527 + 0.0519i)$. The pulse, which is Gaussian in time, has the width of 5×10^{-7} s, and the concentration of aluminum particles is adjusted to yield the linear (in the absence of plasma) optical depth of the order of 4 or 8.

In Figs. 2–3, we compare the behavior of the pulse—in the absence and in the presence of plasma—for aerosol concentration corresponding to optical depth of 4.21. It is evident that the plasma absorption quenches the punch-through effect, in which the high-energy pulse propagates through an aerosol cloud virtually unattenuated. A similar situation, for optical depth of 8.41, is illustrated in Figs. 4 and 5. Here, even in the absence of plasma, the punch-through effect is not so pronounced as in the former case, due to higher aerosol density.

CONCLUSIONS

We have investigated the propagation of an intense laser pulse interacting with a cloud of metallic particles, with the inclusion of plasma absorption. The plasma initiated by the laser beam leads to an additional coupling of the radiation to the medium; this is described in terms of a nonlinear absorption coefficient, which leads to enhanced attenuation of the beam. For metallic aerosols, the plasma formation, and its effects on beam propagation, should not be neglected if the pulse flux is of the order of 10^7 W/cm^2 or higher.

REFERENCES

1. D. C. Smith, "Gas Breakdown Initiated by Laser Interaction with Aerosols and Solid Surfaces," J. Appl. Phys. **48**, 2217 (1977).
2. D. E. Lencioni, "The Effect of Dust on 10.6-μm Laser-Induced Air Breakdown," Appl. Phys. Lett. **23**, 12 1973.
3. D. E. Lencioni, "Aerosol-Induced Air Breakdown with CO$_2$ Laser Radiation," Appl. Phys. Lett. **25**, 15 1974.
4. V. A. Pogodaev and A. E. Rozhdestvenskii, "Threshholds of Optical Breakdown in Weakly Absorbing Aqueous Aerosol," J. Sov. Laser Res. **8**, 260 (1984).

5. J. H. Eickmans, W.-F. Hsieh, and R. K. Chang, "Plasma Spectroscopy of H, Li, and Na in Plumes Resulting from Laser-Induced Droplet Explosion," Yale University preprint, 1987.

6. A. N. Pirri, R. G. Root, and P. K. S. Wu, "Plasma Energy Transfer to Metal surfaces Irradiated by Pulsed Lasers," AIAA J. **16**, 1296 (1977).

7. G. Weyl, A. Pirri, and R. Root, "Laser Ignition of Plasma off Aluminum Surfaces," AIAA J. **19** 460 (1980).

8. S. M. Chitanvis, "A Hydrodynamic Model of Plasma Initiation off Irradiated Metallic Aerosols in Vacuum: The Diffusive Regime," Los Alamos National Laboratory report LA-UR-88-522, May 1988.

9. R. L. Armstrong, P. J. O'Rourke, and A. Zardecki, "Vaporization of Irradiated Droplets," Phys. Fluids **29**, 3573 (1986).

10. R. L. Armstrong and A. Zardecki, "Diffusive and Convective Vaporization of Irradiated Droplets," J. App. Phys. **62**, 4571 (1987).

11. R. D. Janssen and P. J. O'Rourke, "CON1D: A Computer Program for Calculating Spherically symmetric Droplet Combustion," Los Alamos National Laboratory Report LA-10269-MS, December 1984.

12. O. N. Krokhin, "Generation of High-Temperature Vapors and Plasmas by Laser Radiation," in *Laser Handbook*, Vol. 2, edited by F. T. Arecchi and E. O. Schultz-Dubois, (North-Holland, Amsterdam, 1972), p.1371.

13. J. J. Duderstadt and G. A. Moses, *Inertial Confinement Fusion*, (Wiley, New York, 1982)

14. R. L. Armstrong, S. A. W. Gerstl, and A. Zardecki, "Nonlinear Pulse Propagation in the Presence of Evaporating Aerosols," J. Opt. Soc. Am. **A2**, 1739 (1985).

$$R_o = 1.0E-03 \text{ cm}$$

$$t_p = 5.0E-07 \text{ sec}$$
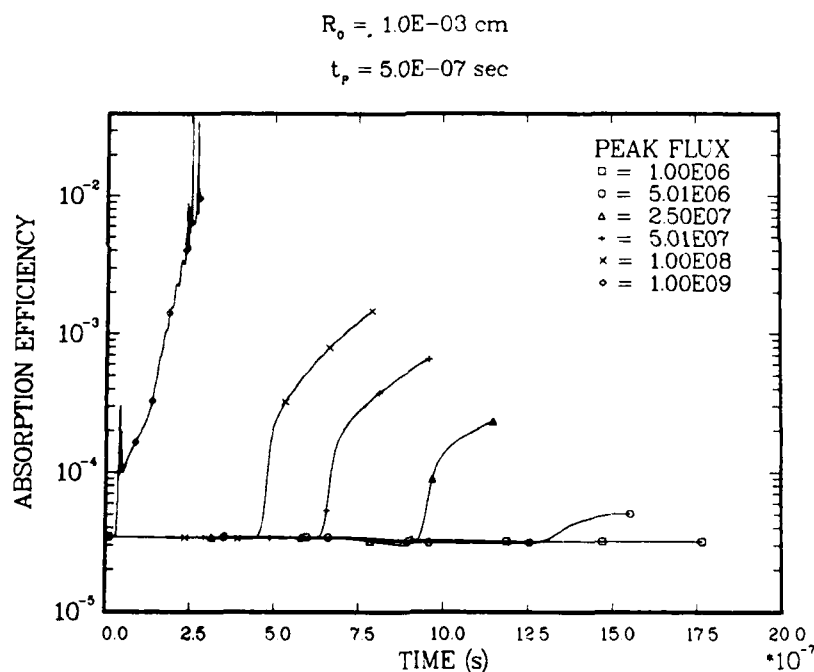
Figure 1. Plasma absorption efficiency as a function of time for different flux levels of the incoming laser pulse.

152

GAUSSIAN PULSE
$F_{MAX} = 2.00E08\ W\ cm^{-2}$
$t_p = 5.00E-07\ sec$
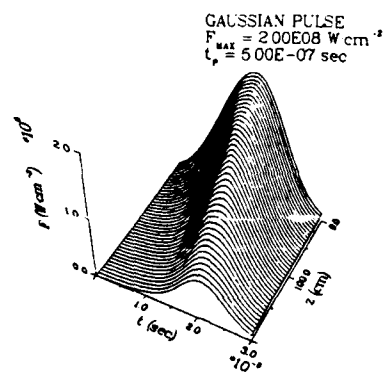
Figure 2. Pulse shape on-axis as a function of time and propagation distance. Optical depth $\tau = 4.21$. Plasma absorption supressed.

GAUSSIAN PULSE
$F_{MAX} = 2.00E08\ W\cdot cm^{-2}$
$t_p = 5.00E-07\ sec$
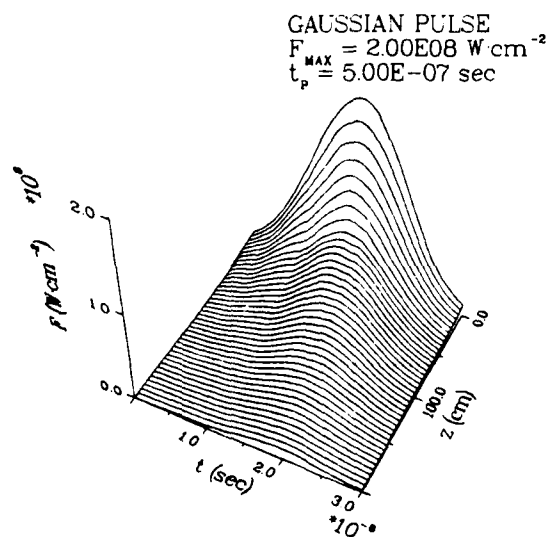
Figure 3. Pulse shape on-axis as a function of time and propagation distance. Optical depth $\tau = 4.21$. Plasma absorption included.

153

GAUSSIAN PULSE
$F_{MAX} = 2.00E08 \ W \ cm^{-2}$
$t_p = 5.00E-07 \ sec$

Figure 4. Pulse shape on-axis as a function of time and propagation distance. Optical depth $\tau = 8.41$. Plasma absorption supressed.

GAUSSIAN PULSE
$F_{MAX} = 2.00E08 \ W \cdot cm^{-2}$
$t_p = 5.00E-07 \ sec$

Figure 5. Pulse shape on-axis as a function of time and propagation distance. Optical depth $\tau = 8.41$. Plasma absorption included.

154

STIMULATED RAMAN SCATTERING FROM MICRON SIZED DROPLETS: TIME RESOLVED AND ANGULAR DEPENDENCE MEASUREMENTS

A. Biswas[1], R. G. Pinnick[2], H. Latifi[1], R. L. Armstrong[1]

V. Srivastava[1], G. Fernandez[2]

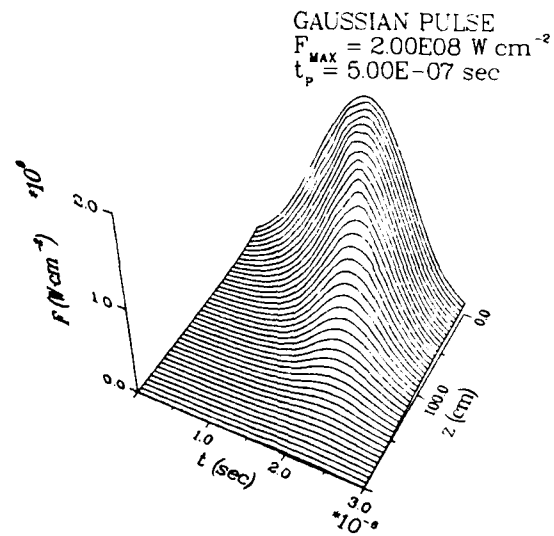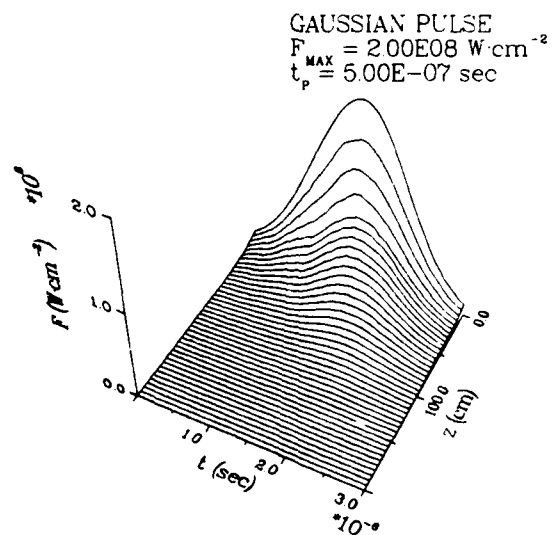1. Applied Laser/Optics, Physics Department, New Mexico State University, Las Cruces, NM 88003

2. U.S. Army Atmospheric Sciences Laboratory, White Sands Missile Range, NM 88002

ABSTRACT

Time-resolved measurements of elastic scattering and stimulated Raman scattering (SRS) in micrometer-sized water and carbon-tetrachloride droplets irradiated with a pulsed, frequency doubled, (λ = 532 nm) Q-switched Nd:YAG laser are reported. Elastic scattering of light is instantaneous within our measurement error, estimated to be $\pm$ 1 nsec. On the other hand, the first Stokes shift in water and multiple order (through ninth order) Stokes shifts in carbon tetrachloride are delayed in initiation with respect to the elastically scattered light. The delay in SRS is apparently a consequence of structure resonances within the droplet, which acts as an optical cavity with relatively high Q. This delay of SRS is not observed in the presence of plasma formation. Furthermore, the angular scattering of the SRS was also measured and the angular fine structure characteristics of the coherent elastic scattering process is lacking in the SRS, regardless of whether it derives from multiple orders of Stokes shifts, multiple resonances within a single Stokes shift, or single resonances within a single Stokes shift.

1. INTRODUCTION

Measurements of the spectral characteristics of SRS from micron-sized drops of water, and carbon-tetrachloride (CCl_4) have been previously reported.[1,2] The spectra show quasi-periodic peaks within the broad Raman bandwidth for water, whereas single peaks appear at the appropriate Raman shifts for CCl_4. A distinctive feature of the emitted SRS radiation is that it is confined to the surface of the drops, thus giving the ring-like appearance when the irradiated drops are viewed under an optical microscope. The SRS observed in these drops is associated with the structure resonances within the drop.[1]

An exact theory to explain the mechanism by which SRS appears is unavailable at this time. We decided to undertake experiments which would provide data for future modelling and understanding of the SRS process in droplets. Two such measurements are discussed in this paper, namely: the temporal behavior of SRS and its angular intensity distribution.

2. EXPERIMENTAL ARRANGEMENT

A. Temporal behavior of SRS:

A schematic diagram of our experimental arrangement is shown in Fig. 1. Green light from a frequency-doubled laser (temporal FWHM = 8 ns) is focused onto droplets emanating from a modified Bergland-Liu orifice generator. The droplets scatter elastic (green) and inelastic (red-shifted SRS) light which is collected through the slit of a spectrometer. Part of this light is reflected onto a one-dimensional photodiode array (PDA) by a beam splitter (BS2) for measurement of its spectral content. The remaining scattered light is combined with a delayed (green) light pulse from the reference beam and passed through the exit slit onto a photomultiplier tube (PMT). The PMT signal is then fed to a transient digitizer, and the resulting signal traces are displayed on a CRT for measurement of time delay between scattered and reference beams.

B. Angular intensity dependence of SRS:

A schematic diagram of our experimental arrangement (Fig. 2) depicts green light from the Nd:YAG laser focused to a 60 μm spot size. A stream of droplets emanating from a vibrating orifice generator is directed through this intensely illuminated

region, where single drops scatter elastic and SRS light. A portion of the scattered light is detected by a one-dimensional PDA mounted a distance of 14 cm from the drop on a rotatable goniometer arm. The PDA assembly is equipped with neutral density filters to attenuate the intense and highly non-isotropic elastically scattered green light, and green blocking filters that eliminate the green light during measurement of the much less intense and more isotropically scattered SRS light. The image intensified portion of the array subtends a 4.7 degree field of view. The laser beam is plane polarized in the plane of scattering. A gear driven shaft encoder is used to measure scattering angle to an accuracy of one degree.

The aforementioned arrangement allows the simultaneous recording of SRS associated with multiple Stokes orders for materials like CCl_4 or multiple resonances of the first Stokes order for materials like water and ethanol. In order to check whether the angular intensity distribution of the scattered light at a single wavelength deviated from the observations using the above arrangement, an alternate scheme was used. Here the PDA was mounted on a spectrometer in a manner such that the individual pixels are lined up parallel to the slit. A dove prism was then used to rotate the light scattered from the droplet stream by ninety degrees so that it too was parallel to the spectrometer slit. The proximity of the droplet stream to the dove prism was such that a very small angular region (4 degrees) was imaged on the PDA. With this arrangement angular scans were not possible but a 4° region centered at discrete angular positions could be measured. Thus a comparison of the elastic and SRS angular distributions at a single wavelength (bandwidth = 0.16 nm) was possible.

3. RESULTS

A. Temporal behavior of SRS:

Figure 3 shows a typical data set of elastic and SRS temporal measurements. Taking into account the speed of light and the path length difference of the reference beam the delay in initiation of the SRS with respect to the elastically scattered light is 7 nsec.[3,4] Measurements made for the first Stokes shift for water and up to nine orders of Stokes shifts for CCl_4 showed similar delays ranging from 5 to 7 nsec. Moreover a variety of droplet sizes ranging from 26 μm diameter to 68 m diameter showed nominally the same delays. However, some of the mixed

Stokes orders for CCl_4 i.e. $\nu_1 + \nu_2$, $2\nu_1 + \nu_2$, $\nu_1 + \nu_4$ and $2\nu_1 + \nu_4$, appeared delayed 1-3 nsec longer. Here ν_1(458 cm^{-1}), ν_2(218 cm^{-1}) and ν_4(314 cm^{-1}) refer to the Raman Stokes shifts for CCl_4.

A second noteworthy feature of Fig. 3 is the temporal narrowing of SRS compared to the elastic. This we believe owes its origin to the fact that only during a fraction of the total duration of the Nd:YAG pulse is the SRS threshold exceeded.

Typical single shot spectra obtained for water droplets are shown in Fig. 4. The periodicity of these peaks can be used to make a precise (within 2%) assessment of the droplet size using an asymptotic relation.[5] Furthermore the appearance of the spectra suggest contributions from a single mode order of the structural resonances.

During these measurements, when the incident irradiance of the Nd:YAG laser was allowed to exceed the breakdown threshold causing small plasma plumes to appear, the observed delay was found to be severely suppressed or completely disappear. Fig. 5 shows typical traces of the elastic scattered light and the SRS, both in the presence and absence of plasma. In the presence of plasma the continuum was subtracted from the respective signals. (Note that the signals shown in Fig. 5 are not intensity corrected for the use of neutral density and green blocking filters, thus giving the false impression that the SRS intensity exceeds that of the elastic.) Fig. 6 shows how the temporal width of the SRS changes as a function of laser irradiance. Note that in this plot only the shaded data point is below plasma formation threshold while the remaining points are at higher irradiances i.e. in the presence of plasma plumes.

B. Angular intensity dependence of SRS:

As a check of our method we first measured elastically scattered light by single CCl_4 drops in each of single angular regions. Typical single laser shot measurements of the familiar angular fine structure are shown in Fig. 7a compared to Mie theory predictions for independently measured drop size and for the appropriate parallel polarization Mie intensity function I_{22}.[6] Considering our 2% error in measurement of drop size, the complication posed by spatial intensity variations of the incident laser beam, and by the fact that we focused the incident beam so that we do not have simple plane-wave scattering by a sphere, the agreement is excellent

demonstrating our capability to measure elastic scattering from droplets with confidence.

Single shot SRS measurements for the corresponding angular regions (Fig. 7b) clearly lacks the angular fine structure. Furthermore upon measuring the angular structure for elastic and SRS using the spectrometer arrangement described no difference in the results were observed. Finally, we placed a polarizer in front of the PDA detector and observed SRS to be weakly polarized.

Measurements of the overall angular variation and magnitude of SRS as compared to elastic scattering were accomplished with the PDA configured in a scanning mode, whereby data was acquired continuously from the PDA while the goniometer was scanned over angle. The resulting 5 degree "running means" of angular averaged scattering for water, ethanol, and CCl_4 are presented in Fig. 8. As for the single laser shot data of Fig. 7, the elastic scattering measurements are normalized for best fit to Mie theoretical predictions. These properly account for a running mean of the angular intensity functions for the appropriate parallel laser polarization, and for the measured sizes and refractive indices of the droplets. Again the angular measurements of elastic scattering and Mie predictions are in good agreement, even though the intensities span several orders of magnitude. Angular scans for the SRS are shown relative to the elastic scans by accounting for the attenuation of neutral density and green blocking filters.

4. DISCUSSIONS AND CONCLUSIONS

A. Temporal behavior of SRS:

We suggest that the delay of SRS initiation in small droplets is a consequence of the finite time required to build up resonances that support SRS. The droplets act as electromagnetic cavities with Q (energy stored/power gain per cycle = time delay of SRS for laser intensity used/period per cycle) $\sim 3 \times 10^6$. The SRS spectra are normally dominated by one set of quasi-periodic peaks, suggesting that for a given droplet size and refractive index, structure resonances of a particular width and mode order dominate over all others.

The fact that the SRS delays are severely diminished with the onset of breakdown is consistent with 1) SRS being generated only during the rising part of the laser pulse, since generation of plasma internal to the drop quenches SRS, and 2) our

conjecture that higher laser intensity causes resonances that support SRS to build up faster, resulting in less time delay of SRS.

B. Angular intensity dependence of SRS:

Several observations can be made from comparison of the elastic and SRS scans: 1) SRS intensity is a factor $\sim 10^4$ less than elastic scattering in the forward direction, and a factor $\sim 10^3$ less at $90°$, 2) SRS is more isotropic than elastic scattering patterns, and 3) the angular scattering characteristics of SRS for ethanol, water, and CCl_4 drops of approximately the same size have a similar form.

In conclusion, SRS emitted from micron-sized droplets of the materials mentioned is more isotropic than the elastic scattering and lacks angular fine structure. Similar observations have been made for fluorescence scattering[7-9] in smaller spheres. The commonality of SRS angular scattering characteristics for water, ethanol and CCl_4 suggests that SRS deriving from single/multiple order Stokes shifts and from single and multiple resonances have the same angular scattering characteristics.

ACKNOWLEDGMENTS

REFERENCES

1. J. B. Snow, S. Qian, and R. K. Chang, Opt. Lett. 10, 37, (1985).

2. S. Qian, and R. K. Chang, Phys. Rev. Lett. 56, 926, (1986).

3. J. Zhang, D. H. Leach and R. K. Chang, Opt. Lett., 13, 270, (1988).

4. W. F. Hsieh, J. Zheng and R. K. Chang, Opt. Lett., 13, 497, (1988).

5. P. Chylek, J. Kiehl, and M. Ko, Phys. Rev. A. 18, 2229, (1978).

6. See for example: C. F. Bohren and D. R. Huffmann, "Absorption and S attering of Light by Small Particles", John Wiley and Sons, 1983.

7. E. Lee, R. E. Benner, J. B. Fenn, and R. K. Chang, Appl. Opt. 17, 1980, (1978).

8. J. P. Kratovil, M. Lee and M. Kerker, Appl. Opt. 17, 1978, (1978).

9. P. J. McNulty, S. D. Druger, M. Kerker and H. W. Chew, Appl. Opt. 18, 1484, (1979).
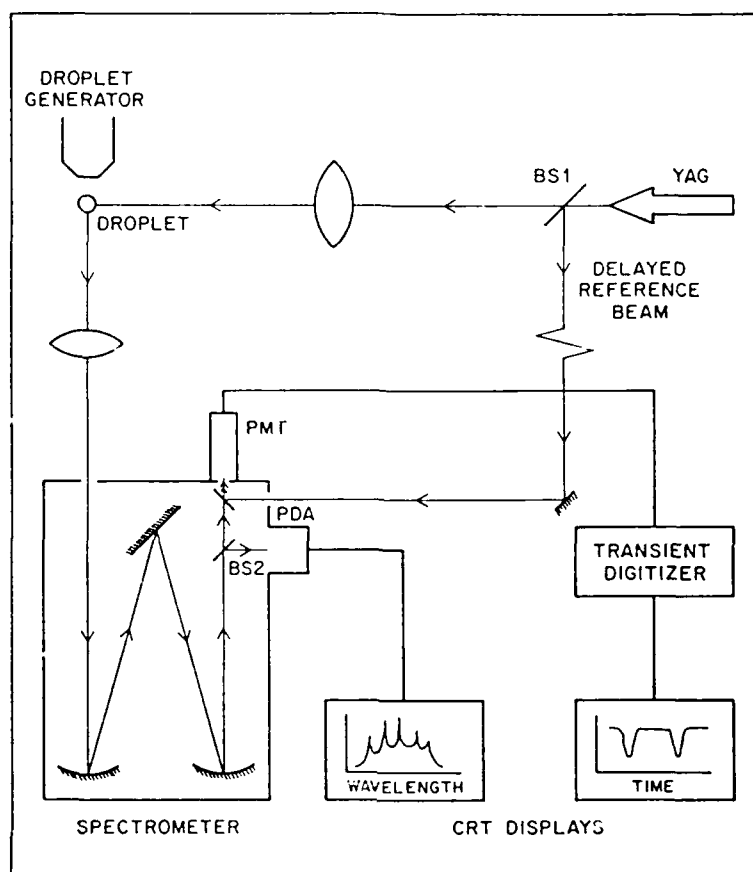
Figure 1. Schematic of the experimental setup used for measuring time
dependence and spectral content of elastic and inelastic (SRS) scattering
in small droplets.
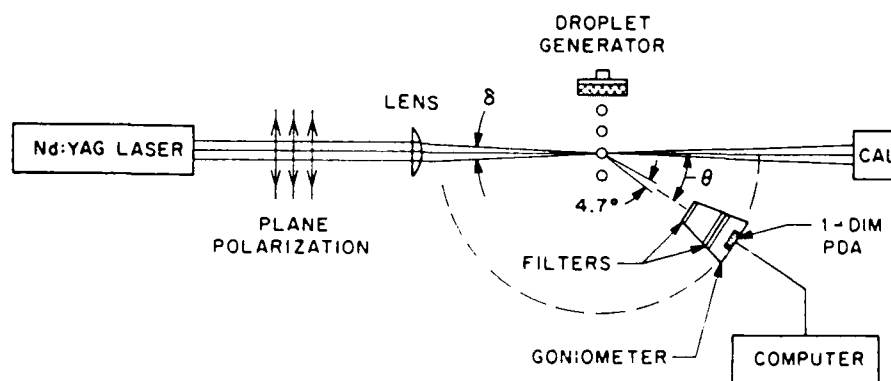
Figure 2. Schematic of experimental setup used to measure angular scattering
characteristics of SRS from single micron-sized droplets.
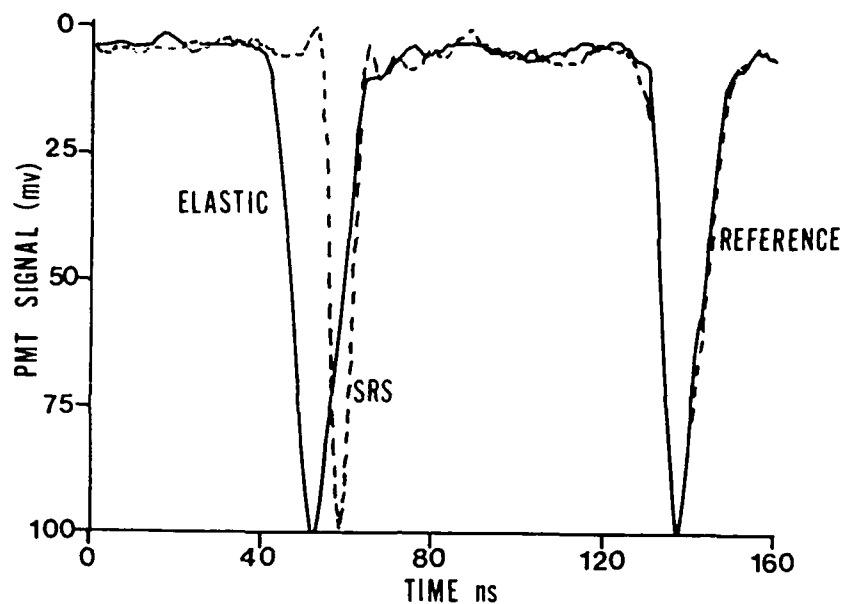
Figure 3. Typical transient digitizer traces of PMT signal. These traces allow measurement of delay for initiation of SRS, full width at half maximum and rise times.
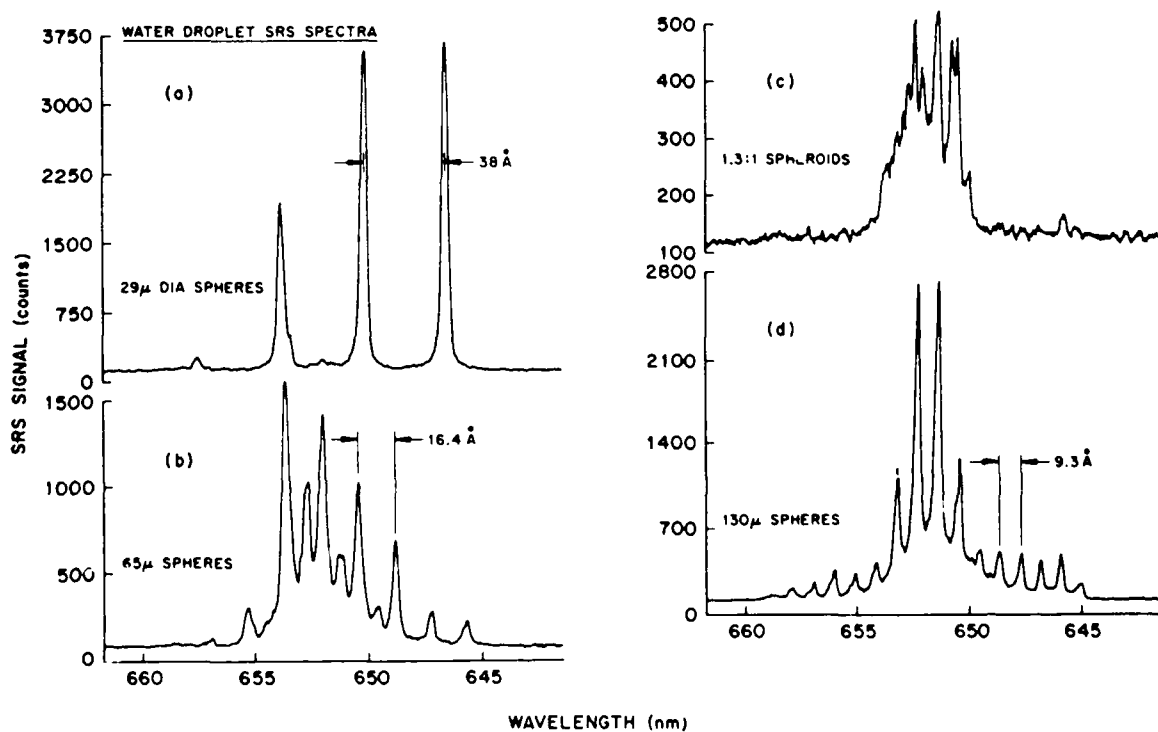
Figure 4. Single shot SRS spectra of water drops irradiated by peak irradiance ~ 1 Gw/cm^2.

ELASTIC & SRS FROM 60μm DIA CCl₄ DROPS
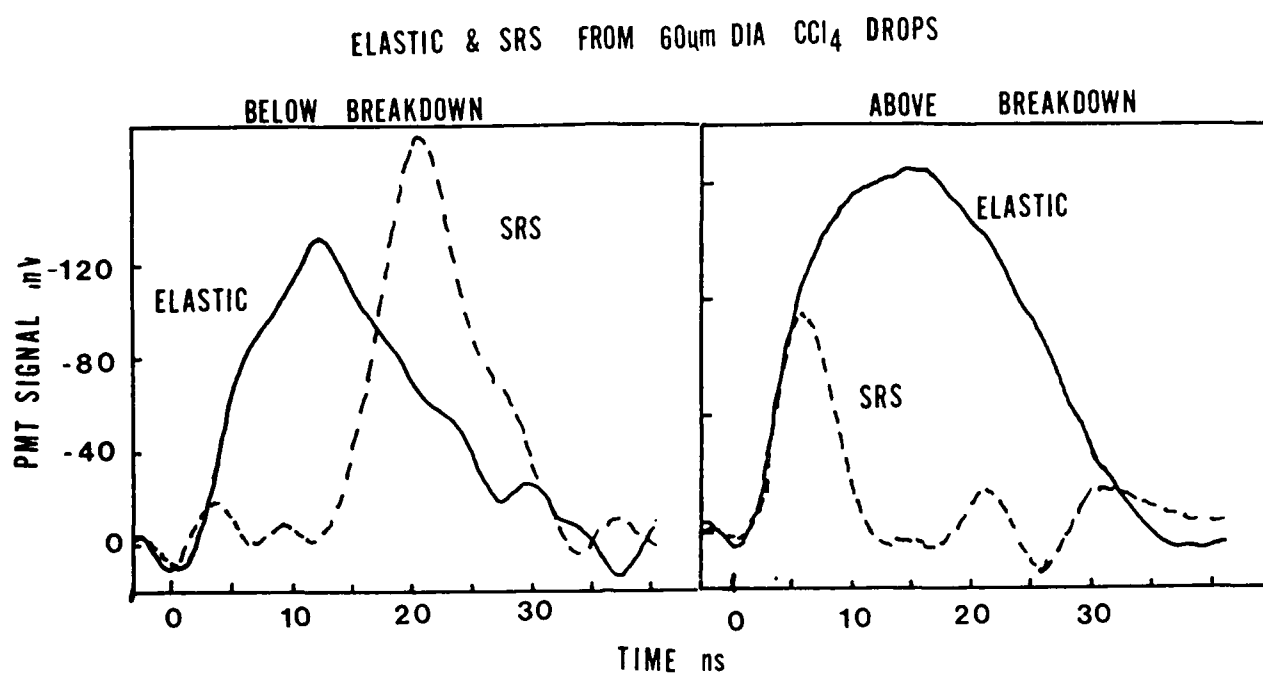
Figure 5. Typical reconstructed traces of elastic and SRS light after correcting for plasma continuum.
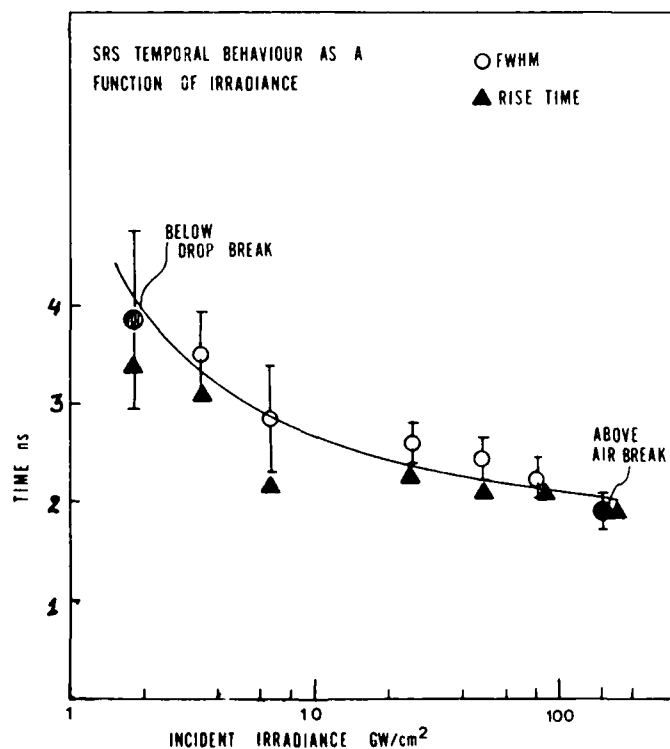
Figure 6. Variation of temporal width and rise time of SRS as a function of irradiance.

163
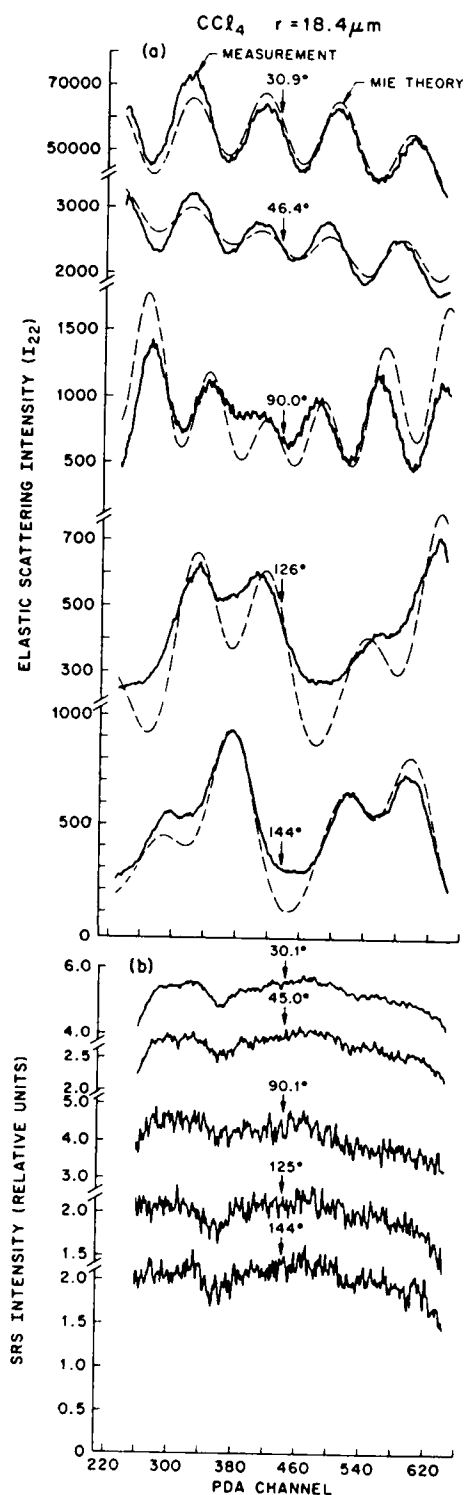
Figure 7. (a) Single shot angular intensity distribution of elastic scattered light compared to Mie theory calculations, (b) corresponding SRS angular distribution.
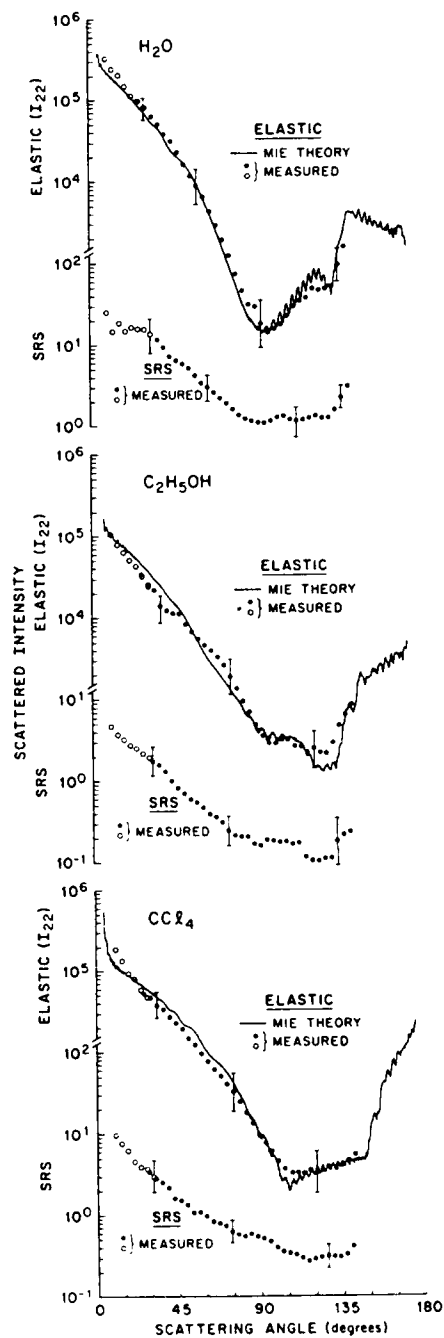
Figure 8. Running means of elastic and SRS from droplets compared to Mie theory calculation averaged over 5°.

IV. OPTICAL PROPERTIES OF AEROSOLS

Blank

Resonances and Near and Internal Fields

of Spheres with Cavities and Coagulated Spheres

Leland Pierce and Herschel Weil

The University of Michigan, Radiation Lab, EECS Dept.

Ann Arbor, MI 48109-2122

Recent Publications:

Pierce, L. E. and Weil, H. (1987), Absorption by Spheres and Aggregates of Spheres. *Proceedings of the 1987 Scientific Conference on Obscuration and Aerosol Research.* to be published.

Weil, H, (1987), Summary of Recent Progress on Aerosol Scattering and Absorption Analysis at the University of Michigan. *Proceedings of the 1987 Scientific Conference on Obscuration and Aerosol Research.* to be published.

Willis, T. and Weil, H. (1987), Verification of Disc Scattering by the CWW (full wave) Method and Range of Validity. *Proceedings of the 1987 Scientific Conference on Obscuration and Aerosol Research.* to be published.

Willis, T., Weil, H., Le Vine, D. M. (1988), Applicability of Physical Optics Thin Plate Scattering Formulas for Remote Sensing. *IEEE Trans. Geosci. Remote Sensing,* **26,** March 1988, p. 153.

Willis, T., Weil, H. (1987), Disc scattering and absorption by an improved computational method. *Appl. Optics,* **26,** Sept. 1987, p. 3987.

ABSTRACT

Work in progress is reported on electromagnetic scattering and absorption from Rayleigh spheres that are coagulated and spheres that have cavities in them. Absorption cross-sections are calculated at frequencies around that of visible light, and static internal and near-field equipotential lines are plotted. Polarizability tensor elements are calculated and modeled for a few specific cases. The significance of these models in the context of absorption cross-sections is explored. Future work will concentrate on specific applications of this work to problems in the physical, chemical, and biological sciences.

I. GENERAL FORMULATION

This paper explains the formulation and implementation of the low-frequency scattering

problem as applied to some axially-symmetric homogeneous dielectric bodies. In particular

two families of shapes are investigated:

1. Two spheres of equal dimension. Their center-to-center separation is variable, and hence produces two coagulated spheres or two complete spheres near each other.

2. Single sphere with a spherical cavity. Here the position and size of the cavity are variable, producing hollow spherical shells, off-center holes in spheres, and holes in the surface of the sphere.

To start with, both theory and practice are introduced for the general case. Later in this section the model for some of our results is presented and discussed. In section two the results for coagulated spheres are presented, while in section three the results for the sphere with cavity are presented. Section four summarizes the results and discusses future plans.

Ia. Theory

The work we present is an extension of the investigation described by Weil [1986]. It follows the formulation of Rayleigh theory given by Senior [1976] (see fig. 1.1). The polarization tensor P_{ij} and the dipole moments p_i of the induced fields:

$$p_i = \epsilon_o P_{ij} E_j$$

are found by considering the fields in the limit as $k_o \rightarrow 0$. Hence one solves the *statics* problem of figure 1.1.

Let Φ_j^s be the scattered, exterior potential and Φ_j be the total, interior potential. Then the conditions governing Φ_j^s and Φ_j for a unit electric field excitation of a scatterer of boundary B and unit outward normal $\hat{n}$ are:

$$\nabla^2 \Phi_j^s = 0 \quad \text{Outside B}$$

$$\Phi_j^s = O(r^{-2}) \text{ as } r \rightarrow \infty$$

$$\nabla^2 \Phi_j = 0 \quad \text{Inside B}$$

$$\Phi_j^s = \Phi_j + x_j \quad \text{On B}$$

$$\frac{\partial}{\partial n} \Phi_j^s = \epsilon \ \frac{\partial}{\partial n} \Phi_j + \hat{n} \cdot \hat{x}_j \quad \text{On B}$$

By using Green's Theorem twice, once inside and once outside B, and combining the results,
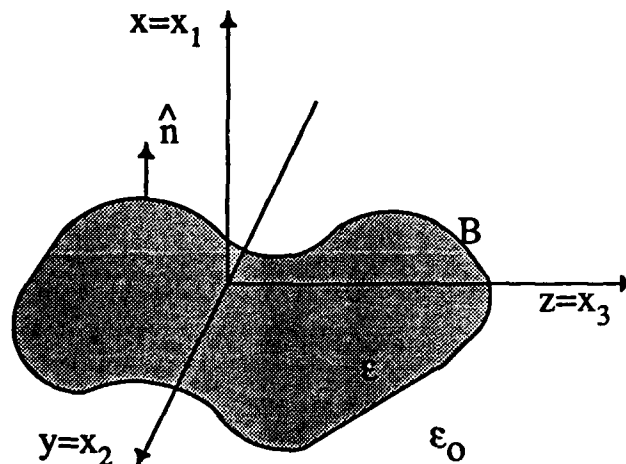
Figure 1.1 — Geometry of the Scattering Problem.

Senior obtained: *

$$\Gamma[\ \Phi_j^t + x_j] + (1 - \Gamma)[\epsilon\ \Phi_j + x_j] = \frac{(1 - \epsilon)}{4\pi} \int_B (\Phi_j^t - x_j')\frac{\partial}{\partial n'}\left(\frac{1}{R}\right)dS'$$

where $R = |\bar{r} - \bar{r}'|$, and

$$\Gamma = \begin{cases} 1, & \text{if } \bar{r} \text{ is external to B} \\ \frac{1}{2}, & \text{if } \bar{r} \text{ is on B} \\ 0, & \text{if } \bar{r} \text{ is interior to B} \end{cases}$$

Now specialize to a body of revolution in cylindrical coordinates ρ, ϕ, z:

$$dS' = \rho' d\phi' ds'$$

where s' is length along the body perimeter, S.

For an x–directed $\bar{E}$ field the right hand side becomes:

$$= \frac{(1 - \epsilon)}{4\pi} \int_0^{2\pi} \int_S (\Phi_1^t - x')\frac{\partial}{\partial n'}\left(\frac{1}{R}\right)\rho' d\phi' ds'$$

Since the total field will vary as $\cos\phi'$, along the body's perimeter it can be written in the

form:

$$\Phi_1^t = \Phi_1^t - x' = \frac{-1}{1 - \epsilon}W_1(s')\ \cos\phi'$$

---

* This is the correct form of the corresponding equation which is given following eq. 19 in Senior (1976)

169

so the right hand side becomes

$$= -\frac{1}{4\pi} \int_S \left[\int_0^{2\pi} \cos\phi' \frac{\partial}{\partial n'} \left(\frac{1}{R} \right) d\phi' \right] W_1(s') \rho' ds'$$

Senior and Ahlgren [1972, eqn. 63, p. 20] put this expression into the form:

$$= -\frac{1}{4\pi} \int_S 2\cos\phi \left\{ \rho \cos\alpha' \Omega_2 + [(z'-z)\sin\alpha' - \rho'\cos\alpha']\Omega_1 \right\} W_1(s') \rho' ds'$$

At $\phi = 0^\circ$ this gives:

$$\left. \begin{array}{ll} \text{outside:} & -\Phi_1^t(\bar{r}) \\[2ex] \text{bndry:} \dfrac{1}{2}\dfrac{(1+\epsilon)}{(1-\epsilon)} W_1(s) \\[2ex] \text{inside:} & -\epsilon\Phi_1(\bar{r}) \end{array} \right\} = \rho + \frac{1}{2\pi} \int_S W_1(s') \left\{ \rho\cos\alpha'\Omega_2 + [(z'-z)\sin\alpha' - \rho'\cos\alpha']\Omega_1 \right\} \rho' ds'$$

This is an integral equation for W_1 when $\bar{r}$ is on the surface B. Similarly for the z–directed $\bar{E}$ field excitation, the field along the body's perimeter can be written in the form:

$$\Phi_3^t = \frac{-1}{1-\epsilon} W_3(s')$$

$$\left. \begin{array}{ll} \text{outside:} & -\Phi_3^t(\bar{r}) \\[2ex] \text{bndry:} \dfrac{1}{2}\dfrac{(1+\epsilon)}{(1-\epsilon)} W_3(s) \\[2ex] \text{inside:} & -\epsilon\Phi_3(\bar{r}) \end{array} \right\} = z + \frac{1}{2\pi} \int_S W_3(s') \left\{ \rho\cos\alpha'\Omega_1 + [(z'-z)\sin\alpha' - \rho'\cos\alpha']\Omega_0 \right\} \rho' ds'$$

In these equations

$$\Omega_n = \int_0^\pi \frac{\cos^n(\Psi)}{R^3} d\Psi \qquad n = 0, 1, 2$$

and

$$R = \left[(\rho + \rho')^2 + (z - z')^2 \right] \left[1 - m\sin^2\theta \right]$$

where

$$m = \frac{4\rho\rho'}{(\rho + \rho')^2 + (z - z')^2}$$

$$\theta = \frac{1}{2}(\pi - \Psi)$$

Senior and Ahlgren (p. 61) show that

$$\Omega_0 = \frac{1}{4}\left(\frac{m}{\rho\rho'}\right)^{3/2}\left[K(m) + 2m\frac{d}{dm}K(m)\right]$$

$$\Omega_1 = \left(\frac{m}{\rho\rho'}\right)^{3/2}\left[(1-\frac{m}{2})\frac{d}{dm}K(m) - \frac{1}{4}K(m)\right]$$

$$\Omega_2 = \frac{1}{m^2}\left(\frac{m}{\rho\rho'}\right)^{3/2}\left[2m(1-\frac{m}{2})^2\frac{d}{dm}K(m) - (1-\frac{m^2}{4})K(m) + E(m)\right]$$

where K and E are Elliptic Integrals.

The Electric Polarizability Tensor is

$$P_{ij} = (1-\epsilon_r)\int_B \hat{n}\cdot \pounds_i \quad \Phi_j dS$$

For the case of rotational symmetry about the z–axis $P_{11} = P_{22} \neq 0$;

$P_{33} \neq 0; P_{ij} = 0, i \neq j$. Hence we need only find P_{11} and P_{33}.

The absorption cross–section can be expressed in terms of P_{ii} , and by averaging over all possible scatterer orientations (all assumed equally likely) one gets the average absorption cross–section:

$$<\sigma_A> = \frac{k_0 V}{3}\text{Im.}(2P_{11} + P_{33})$$

where k_0 is the free–space wavenumber of the incident light, and V is the volume of one scatterer. The dimensionless quantity $<\sigma_A>/k_0 V$ is used in the plots of absorption vs. wavelength presented later.

Ib. Practice

The integral equations for W_1 and W_3 are solved using the moment method. We choose pulse basis functions and delta–function weighting functions to get a point–matching solution.

The body perimeter is broken up into equal–length arcs and the W's are determined at the center of each arc. The integral becomes:

$$\int_{s'} W_i(s') K_i(\bar{r}, \bar{r}') \rho' ds' = \sum_{j=1}^{N} W_i(s_j) \int_{s_j - \Delta/2}^{s_j + \Delta/2} K_i(\bar{r}, \bar{r}') \rho' ds'$$

where j runs over every segment of the perimeter, and i is either 1 or 3.

A simple six–point integration scheme works well if $\bar{r}$ is on the surface, and the surface has no cusps. However, to get the near fields, and accurate surface values for complicated shapes, a more sophisticated method must be used. This is because for $\bar{r}$ near the surface $K(\bar{r}, \bar{r}')$ varies rapidly, hence a 6–point integration scheme will not capture it sufficiently.

Our method removes the rapidly–varying terms and integrates them analytically over the appropriate very small sub–segment (approximating it as straight, no longer curved) This can give us accurate field values near the surface and elsewhere.

The numerically troublesome terms are in the Ω_n's . Specifically a $\frac{1}{m_1}$ term and a $\ln(\frac{1}{m_1})$ term. Both blow up as the field point approaches the surface (source point) in our integral equations. Since

$$K(m) \simeq (a_0 + a_1 m_1 + \cdots a_4 m_1^4)$$

$$+ (b_0 + b_1 m_1 + \cdots b_4 m_1^4) \ \ln(\frac{1}{m_1})$$

$$\frac{d}{dm} K(m) \simeq (\frac{b_0}{m_1} + (b_1 - a_1) + (b_2 - 2a_2) m_1 + \cdots (b_4 - 4a_4) m_1^3)$$

$$- (b_1 + 2b_2 m_1 + \cdots 4b_4 m_1^3) \ \ln(\frac{1}{m_1})$$

$$E(m) \simeq 1 - \frac{1}{4} m_1 + \frac{1}{4} \ m_1 \ln(\frac{1}{m_1})$$

172

where $m_1 = 1 - m$. The troublesome terms are:

$$\frac{b_0}{m_1} \quad \text{in the} \quad \frac{d}{dm}K(m) \text{ term,}$$

$$-b_1\ln(\frac{1}{m_1}) \quad \text{in the} \quad \frac{d}{dm}K(m) \text{ term,}$$

$$\text{and} \quad b_0\ln(\frac{1}{m_1}) \quad \text{in the} \quad K(m) \text{ term.}$$

The constants a_i and b_i can be found in Abramowitz and Stegun [1964] . We pulled these terms out of the expressions for $K_i(\bar{r}, \bar{r}')$, integrated them analytically, then added them back in to the numerical integration which was done with the remaining terms.

The geometry to explain the following formulas for the analytic evaluations is shown in figure 1.2.
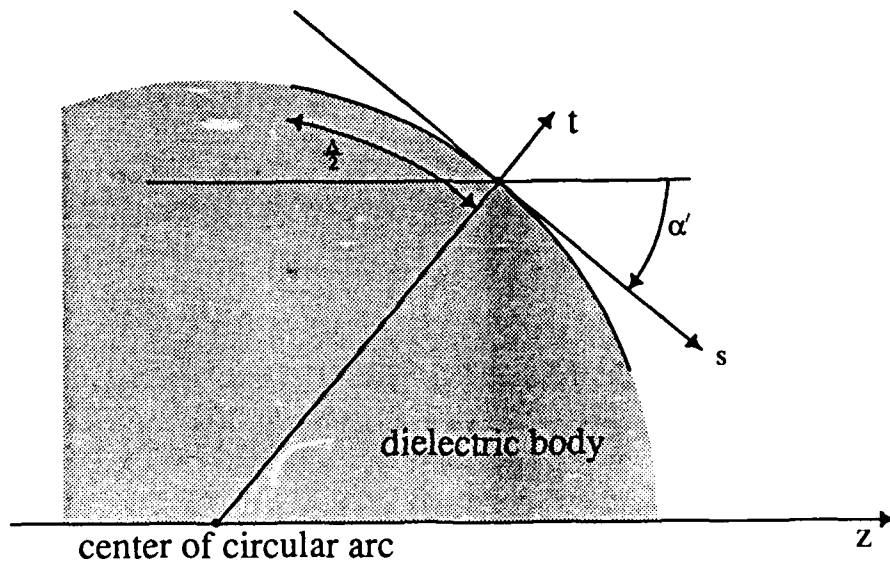

Figure 1.2 — Coordinates used for Surface Integration.

173

We need to evaluate two integrals involving b_o/m_1:

$$I_1 = \int_{-\frac{\Delta}{2}}^{\frac{\Delta}{2}} \frac{1}{m_1} ds' = 2\sin\alpha'(s\sin\alpha' + t\cos\alpha') \ln\left[\frac{\Delta^2/4 - s\Delta + s^2 + (t'-t)^2}{\Delta^2/4 + s\Delta + s^2 + (t'-t)^2}\right] + \Delta$$

$$+ \frac{4(s\sin\alpha' + t\cos\alpha')(s\sin\alpha' + t'\cos\alpha')}{t'-t}\left[\tan^{-1}\left(\frac{\Delta - 2s}{2(t'-t)}\right) + \tan^{-1}\left(\frac{\Delta + 2s}{2(t'-t)}\right)\right]$$

$$I_2 = \int_{-\frac{\Delta}{2}}^{\frac{\Delta}{2}} \frac{s'}{m_1} ds' =$$

$$(s\sin\alpha' + t\cos\alpha')\left\{(4s\sin\alpha' + 2t'\cos\alpha')\ln\left[\frac{\Delta^2/4 - s\Delta + s^2 + (t'-t)^2}{\Delta^2/4 + s\Delta + s^2 + (t'-t)^2}\right] + 4\Delta\sin\alpha'\right.$$

$$+ \frac{4[st'\cos\alpha' + s^2\sin\alpha' - (t'-t)^2\sin\alpha']}{t'-t}\left.\left[\tan^{-1}\left(\frac{\Delta - 2s}{2(t'-t)}\right) + \tan^{-1}\left(\frac{\Delta + 2s}{2(t'-t)}\right)\right]\right\}$$

These integrals are combined with the other terms in the expressions for the Ω_n's and then with others to make the K_i's. The following expressions are for that part of each K_i that is singular:

$$K_{1,extra} = \frac{2[s^2 + t^2 + t'^2 + 2t'\sin\alpha'(s\cos\alpha' - t\sin\alpha')]}{t'[s^2 + (t + t')^2 + 4t'\sin\alpha'(s\cos\alpha' - t\sin\alpha')]^{5/2}}$$

$$\cdot(s^2 + t^2 - t'^2)\left[t'\cos\alpha' I_1 + \sin\alpha' I_2\right]$$

$$K_{3,extra} = \frac{4\cos\alpha'[s\sin\alpha' + t\cos\alpha'][s^2 + t^2 - t'^2]}{[s^2 + (t+t')^2 + 4t'\sin\alpha'(s\cos\alpha' - t\sin\alpha')]^{5/2}}\left[t'\cos\alpha' I_1 + \sin\alpha' I_2\right]$$

The analysis is similar for the $\ln(m_1)$ term.

174

Ic. Polarizability Tensor Elements

The calculation of absorption spectra is useful and desirable by itself, however, a more theoretically satisfying calculation that can yield much deeper insight into absorption spectra of irregularly shaped particles is that of P_{ii} as a function of ϵ, instead of frequency and material. Cast in this way, there is a direct analogy with the analytical formula for a sphere. For a Rayleigh sphere we have:

$$\text{Im.}(P_{11}) = \frac{9\epsilon_r''}{(\epsilon_r' + 2)^2 + \epsilon_r''^2}$$

where ϵ_r' and ϵ_r'' are the real and imaginary parts, respectively, of the complex relative permittivity of the sphere. This can intuitively be seen as a sharp resonance of "strength" 9 at $\epsilon_r' = -2$, which stands out against a more uniform background; see fig 1.3. Physically, this resonance can be explained as a coupling of electromagnetic energy into an internal, non–electromagnetic vibrational mode of the material: the electromagnetic energy is used to drive the lattice vibrations. In dielectric materials this mode is called a polariton, whereas in metals a similar excited mode is called a surface plasmon [Nelsor., 1979].

Expressions similar to those for the sphere be given f°. ellipsoids [see Bohren and Huffman, p.350]. Using this idea, we can reformulate the numerical procedure to give us the eigenvalues of the integral equation. The resonant positions (ϵ_r' to give infinite absorption when $\epsilon_r'' = 0$) are then simple functions of these eigenvalues. Using these resonant ϵ's and some numerically-generated Im.$P_{ii}(\epsilon)$, we can fit this data with a generalization of the preceding formula; ie:

$$\text{Im.}P_{ii}(\epsilon) = \sum_{k=1}^{N} \frac{A_k \epsilon_r''}{(\epsilon_r' - \epsilon_{res,k})^2 + \epsilon_r''^2}$$

This procedure works quite well. The only problem with it is that the decision concerning N is difficult: the discretized version of the integral equation has as many eigenvalues as the size of the matrix we create. Which of these are "real" ? So far, we have chosen those resonances that are most prominent for large ϵ_r''. Sometimes this leaves out certain resonances that are numerically quite prominent when ϵ_r'' is small, but decay rapidly with increasing ϵ_r''. However, most of the resonances don't even get this far: they have no peak near the negative real ϵ axis; hence, they are assumed to be due to the discretization process.

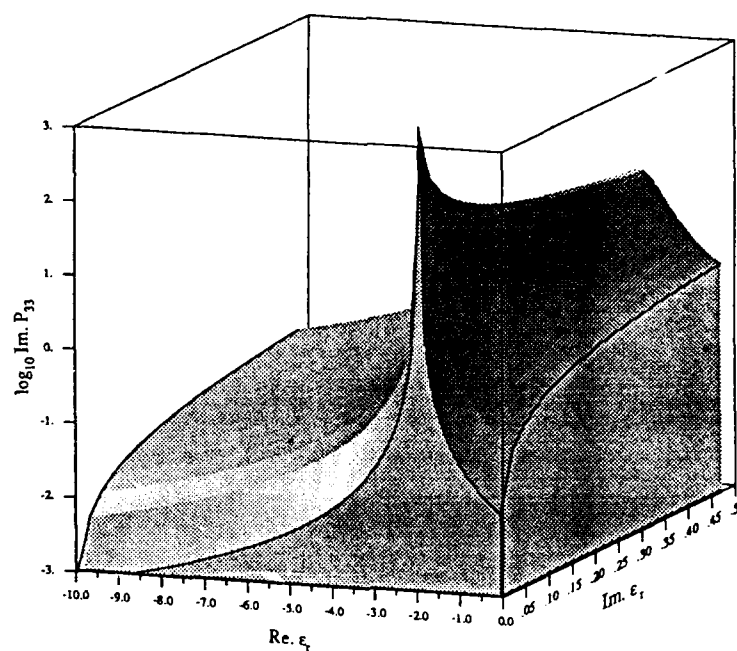Absorption as a function of Complex Relative Permittivity (ϵ_r), sphere

Figure 1.3 — **Analytical Im.(Polarizability) for a Sphere**

So far, the resonances that decay quickly are also thought of as spurious, but more analysis in the future may reveal a different explanation. Illustrations of this for the particular shapes investigated here are included in sections two and three.

II. COAGULATED SPHERE RESULTS

We simulated two spheres, both separate and coagulated. Two examples are the following:

separate   coagulated

Figure 2.1 – Two examples from the family of sphere pairs

The center–to–center separation of the two spheres is given in terms of the sphere diameter. For example, the separate spheres above have a center–to–center separation of about 2, whereas the two coagulated spheres have a center–to–center separation of about 0.8 . This is made more plain in figure 2.2.

The fields were plotted with a variety of separations and also at many different frequencies; each different frequency corresponds to a different ϵ for gold, tabulated in Physik Daten [1981]. Due to symmetry, only a portion of the field structure is shown. That part of the field that intersects the plane through the symmetry axis (see fig 2.3) and is in the first quadrant (darkened piece of the plane) is displayed in the field plots. The wire mesh is meant to represent the surface of the (see–thru) particle that is being halved by the cutting plane.

Typical field plots are shown in figs 2.4–2.7 for the near–resonance case and for the off–resonance case. Each of the field plots has the real part and imaginary part of the potential for a particular shape, frequency and ' incident ' E-field direction:

x-directed means E is vertical at infinity.

z-directed means E is horizontal at infinity.

Each plot has 4–6 equipotential lines, while ΔV (or "spacing in volts" on the plots) between them varies from plot-to-plot. Hence a large value for ΔV means that we have high local E-field concentrations.

Tau in each plot is the value for the relative dielectric constant.
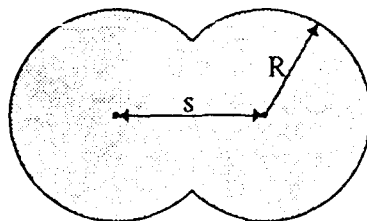
R = 0.5 - radius of solid sphere
s = center-to-center separation

EXAMPLES
s=0.0 -- a sphere: ◯
s=0.5 -- 2 intersecting spheres: ◯◯
s=1.0 -- 2 just-touching spheres: ◯◯
s=2.0 -- 2 separate spheres: ◯ ◯
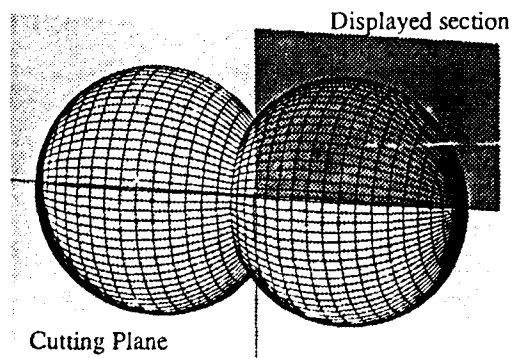
Figure 2.2 — The coagulated sphere geometry

Figure 2.3 -- Position of field plots in relation to the particle

The dimensionless average absorption cross section, as described earlier, was plotted for each geometry as a function of free space wavelength. Typical spectra are shown in figs 2.8-2.17.

X DIRECTED EXCITATION REAL PART   ***** ISO-RV CURVES *****
TAU = -8.515 +J 0.960   RV=-0.666,-0.420,-0.174,.07204,
SPACING IN VOLTS = 0.24605
RVMIN(VOLT) = -0.78913   Center-to-Center Spacing: 0.8000
RVMAX(VOLT) = 0.19507

X DIRECTED EXCITATION IMAGINARY PART   ***** ISO-IV CURVES *****
TAU = -8.515 +J 0.960   IV= .00345,.01036,.01727,.02417,
SPACING IN VOLTS = 0.00691
IVMIN(VOLT) = 0.00000   Center-to-Center Spacing: 0.8000
IVMAX(VOLT) = 0.02763
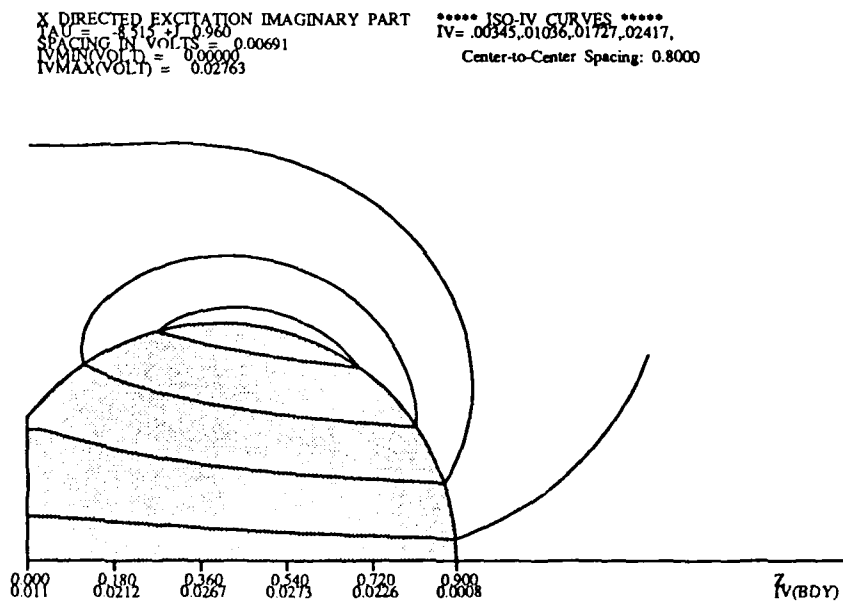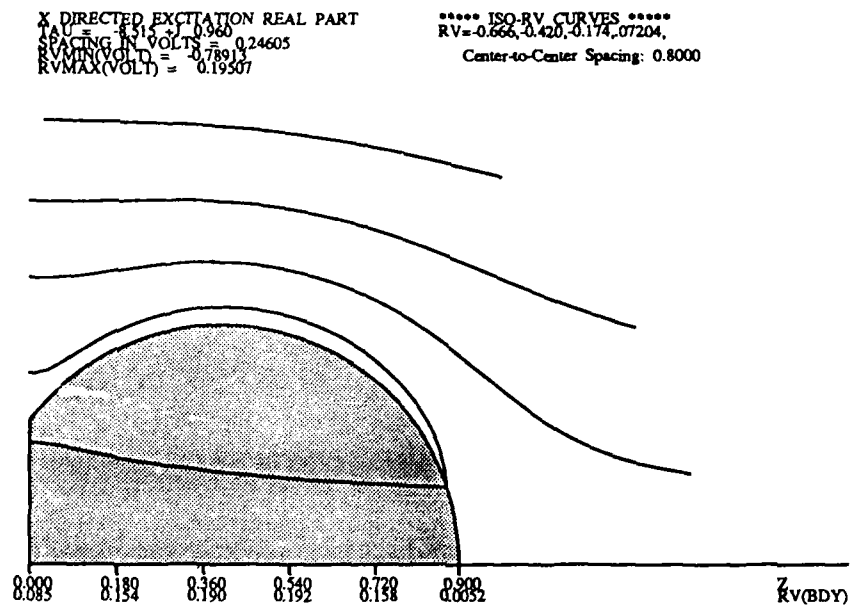
Figure 2.4 — Iso-Potential Lines for Near-Resonance Case (x-inc.)

Z DIRECTED EXCITATION REAL PART
TAU = -8.515 + J 0.960
SPACING IN VOLTS = 0.26971
RVMIN(VOLT) = -1.01312
RVMAX(VOLT) = 0.33545

***** ISO-RV CURVES *****
RV= -0.878, -0.609, -0.339, -.0691, 0.2006,

Center-to-Center Spacing: 0.8000

Z DIRECTED EXCITATION IMAGINARY PART
TAU = -8.515 + J 0.960
SPACING IN VOLTS = 0.89864
IVMIN(VOLT) = 0.00000
IVMAX(VOLT) = 4.49318

***** ISO-IV CURVES *****
IV= 0.4493, 1.3480, 2.2466, 3.1452, 4.0439,

Center-to-Center Spacing: 0.8000

Figure 2.5 — Iso-Potential Lines for Near-Resonance Case (z-inc.)

180

X DIRECTED EXCITATION REAL PART   ***** ISO-RV CURVES *****
TAU =   -4.390 +J 1.480   RV=-0.621,-0.397,-0.173,.05132,0.2755,
SPACING IN VOLTS =   0.22419
RVMIN(VOLT) = -0.73333   Center-to-Center Spacing: 0.8000
RVMAX(VOLT) =   0.38761


```
0.000   0.180   0.360   0.540   0.720   0.900              Z
0.16    0.302   0.378   0.382   0.315   0.0104             RV(BDY)
```

X DIRECTED EXCITATION IMAGINARY PART   ***** ISO-IV CURVES *****
TAU =   -4.390 +J 1.480   IV= .02165,.06494,0.1082,0.1515,0.1948,
SPACING IN VOLTS =   0.04329
IVMIN(VOLT) =   0.00000   Center-to-Center Spacing: 0.8000
IVMAX(VOLT) =   0.21646


```
0.000   0.180   0.360   0.540   0.720   0.900              Z
0.080   0.138   0.287   0.215   0.180   0.0060             IV(BDY)
```

Figure 2.6 — Iso-Potential Lines for Off-Resonance Case (x-inc.)

181

Z DIRECTED EXCITATION REAL PART
TAU = -4.390 +J 1.480
SPACING IN VOLTS = 0.22190
RVMIN(VOLT) = -1.3314)
RVMAX(VOLT) = 0.00000

***** ISO-RV CURVES *****
RV=-1.220,-0.999,-0.777,-0.555,-0.333,
    -0.111,

Center-to-Center Spacing: 0.8000

Z DIRECTED EXCITATION IMAGINARY PART
TAU = -4.390 +J 1.480
SPACING IN VOLTS = 0.15359
IVMIN(VOLT) = -0.19435
IVMAX(VOLT) = 0.72720

***** ISO-IV CURVES *****
IV= -0.118,.03604,0.1896,0.3432,0.4968,
    0.6504,

Center-to-Center Spacing: 0.8000

Figure 2.7 — Iso-Potential Lines for Off-Resonance Case (z-inc.)

In comparing the near– and off–resonance fields, note that the resonance itself is numerically apparent in the voltage magnitudes of the resonant z–directed imaginary part: an increase of slightly less than five times. This resonance is for the z–directed excitation only. The field structure for the x–directed cases changes very little. One notable difference is that the field strength in the imaginary parts (x–dir) becomes about ten times smaller as compared to the off–resonance case. This is interesting and deserves further investigation to determine if it is a general feature or just a specific occurrence.

Moving on to a comparison of the z–directed field plots, the most striking difference is in the field structure: the resonant field lines are much more curved. A consequence of this is that the near–surface electric field is much stronger and the internal field is much weaker: hence the term "surface mode" for this kind of resonance behavior. There are a number of other distinguishing features of these field plots, but their significance in undetermined at this time: the "chimney" in the real part has moved from an off–center position off–resonance to, apparently, the central position of the particle; the field concentration at the central cusp of the particle has moved from the real part off–resonance to the imaginary part near–resonance.

The following pages show the absorption spectrum of coagulated gold particles in the frequency range near that of visible light. Note that the vertical scales are different, and that the absorption spectrum for a single sphere is included in each plot for comparison. Recall that 'sep' in these plots stands for the center–to–center separa ion between the two spherical particles that make up the coagulated particle. A separation of 1.0 indicates that the two spheres are just barely touching one another, while a separation of 0.8 indicates that the two spheres are overlapping and are coagulated. A separation greater than one indicates that the two spheres are near each other but not touching.
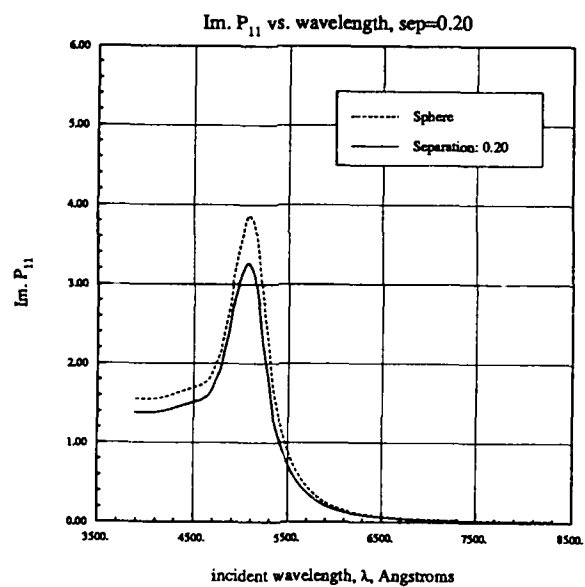
Im. P$_{11}$ vs. wavelength, sep=0.20

Figure 2.8 — X–Incidence Absorption Spectrum, sep=0.2

Im. P$_{33}$ vs. wavelength, sep=0.20
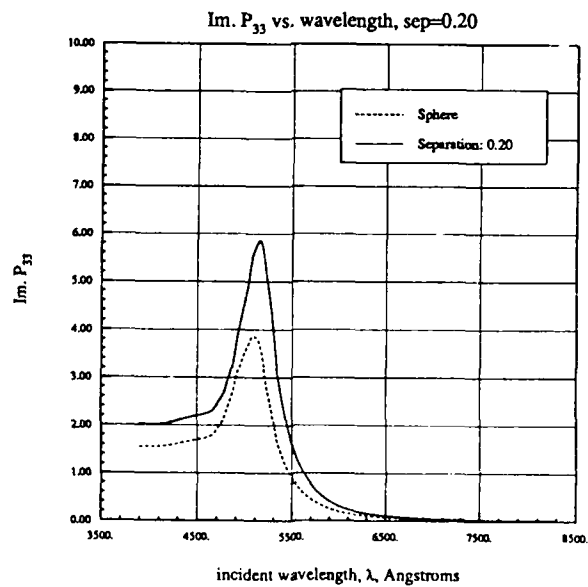
Figure 2.9 — Z–Incidence Absorption Spectrum, sep=0.2

Im. P_{11} vs. wavelength, sep=0.80
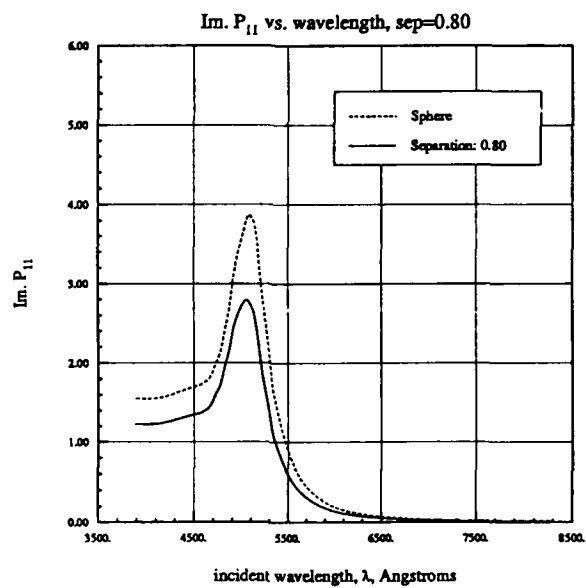
Figure 2.10 — X-Incidence Absorption Spectrum, sep=0.8

Im. P_{33} vs. wavelength, sep=0.80

Figure 2.11 — Z-Incidence Absorption Spectrum, sep=0.8

Im. P_{11} vs. wavelength, sep=1.00

Figure 2.12 — X-Incidence Absorption Spectrum, sep=1.0
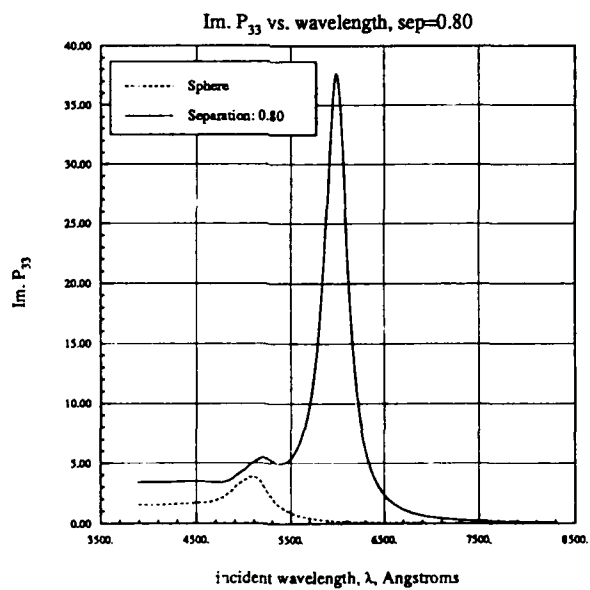

Im. P_{33} vs. wavelength, sep=1.00

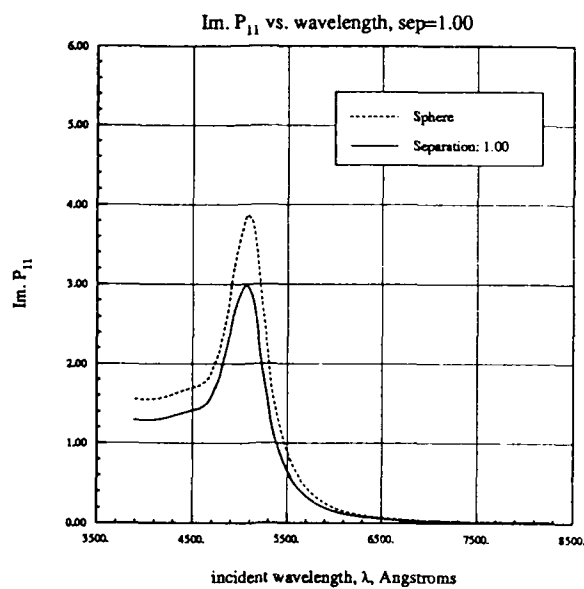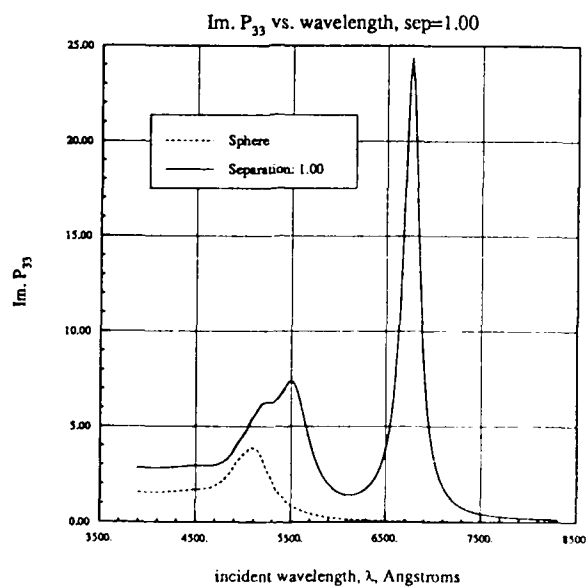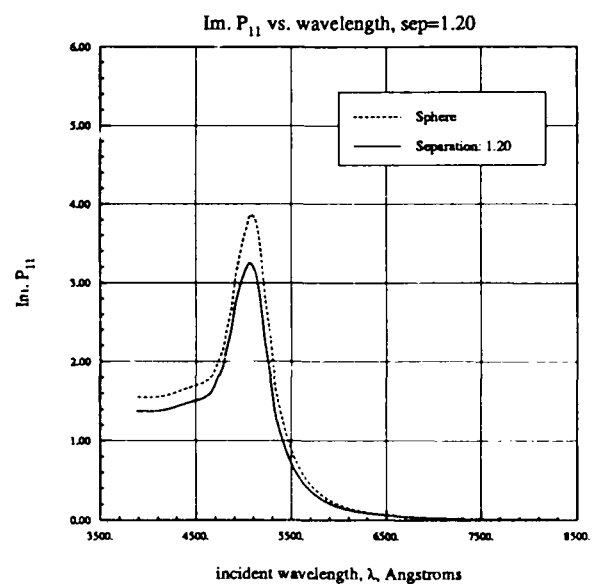**Figure 2.13 — Z-Incidence Absorption Spectrum, sep=1.0**

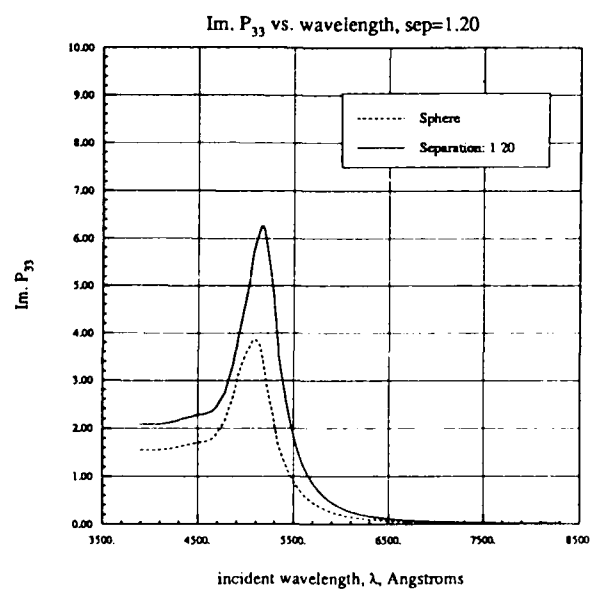Figure 2.14 — X–Incidence Absorption Spectrum, sep=1.2

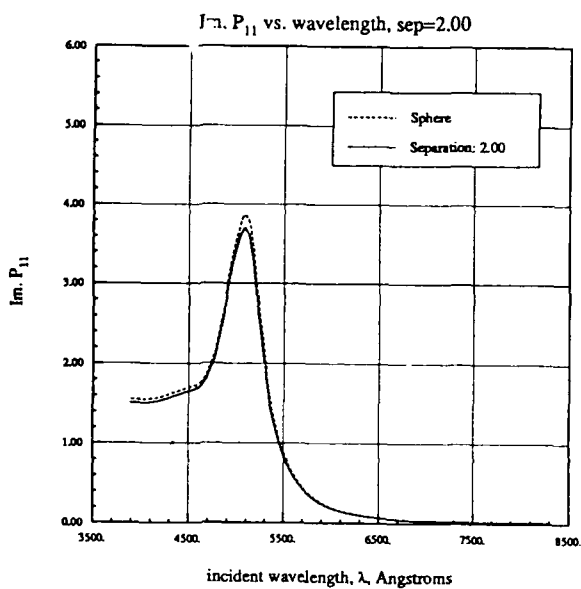Figure 2.15 — Z–Incidence Absorption Spectrum, sep=1.2

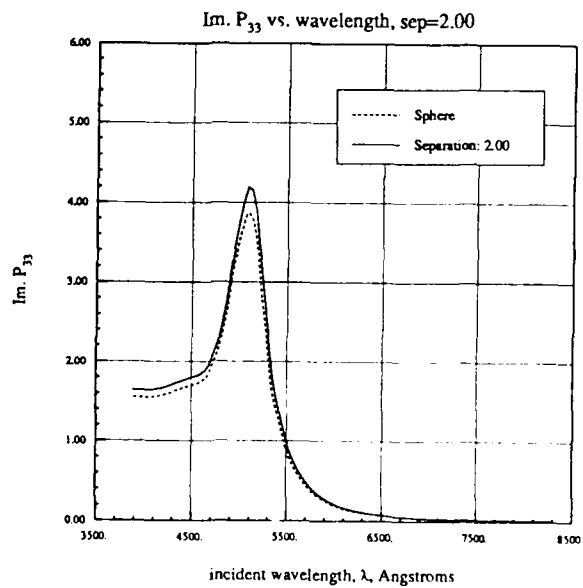Figure 2.16 — X-Incidence Absorption Spectrum, sep=2.0

Figure 2.17 — Z-Incidence Absorption Spectrum, sep=2.0

The absorption cross–section plots are done for gold particles at approximately optical wavelengths. The most apparent similarity among these spectra is the only slight variability of the x–directed absorption: the single absorption peak is retained, with respect to its wavelength of occurrence, over the entire family of geometries. The magnitude of this absorption peak varies between 3 and 6 compared to the sphere's 4.

The variation of the z–directed spectra is greater, as one might expect from the previous field comparisons. The single–sphere peak appears to be retained, although it moves slightly (about 200 Angstroms) and its magnitude varies between 4 and 6. The most interesting feature, however, is the appearance of new absorption peaks. These peaks only occur for coagulated spheres that are nearly–whole spheres. In our examples, this is shown for separations of 0.8 and 1.0; ie. for nearly–whole, but coagulated spheres (0.8), and for whole but touching spheres (1.0). In each case the absorption peak is 6 to 10 times as strong as the single–sphere peak, and both are also shifted to longer wavelengths. The positions and strengths of these absorption peaks are highly dependent on geometry. Also of note, for the just–touching spheres case (sep = 1.0) is a more complicated absorption spectrum in the region of the single–sphere peak: there appears to be two overlapping absorption peaks, each at a longer wavelength than the single–sphere peak.

The implications of these spectra for the colors of colloidal gold will be discussed later.

IIa. Polarizability Tensors

The Polarizability Tensor elements are functions of complex ϵ. Hence they are best displayed as surfaces in three–dimensional space. The following two figures (figs. 2.18 and 2.19) show a numerically–generated surface, and its fit, using the major resonances and their strengths.

A comparison of figures 2.18 and 2.19 shows that the fit (2.19), as far as it goes, does an excellent job. The error in regions not near Re. $\epsilon_r = -1$ is on the order of 1%. This shows that in those regions the simple, intuitive, and physically meaningful model presented earlier is valid. In the region near Re. $\epsilon_r = -1$, however, the fit does not agree well with the numerically–generated data. The major reason for this is that the model chosen used only the three largest resonances. When the other, weaker, resonances are added to the model, the fit, of course, improves in that region. However, I personally am suspicious of the reality of these minor resonances and further work is planned to better understand them.

Absorption as a function of Complex Relative Permittivity (ϵ_r), sep=0.8
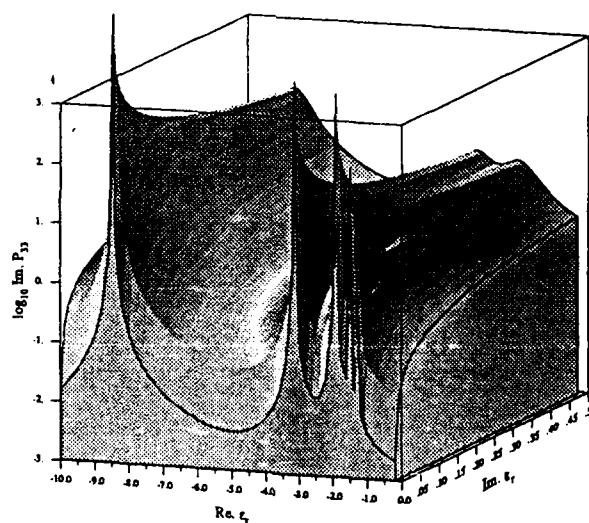
Figure 2.18 — Z–Incidence, Im. Polarizability, sep=0.8, numerical.

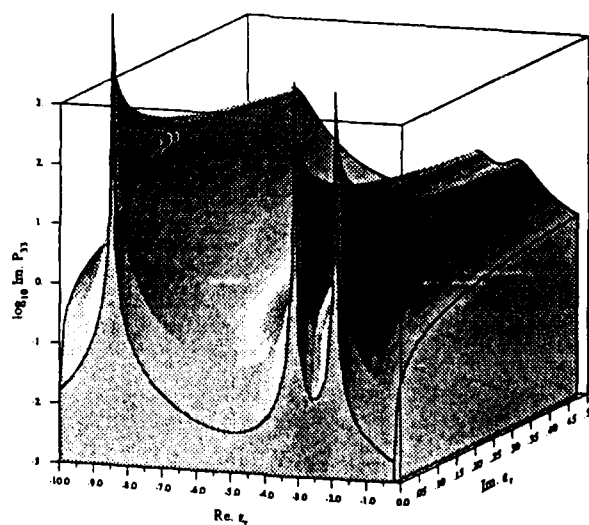Absorption as a function of Complex Relative Permittivity (ϵ_r), sep=0.8

Figure 2.19 — Z–Incidence, Im. Polarizability, sep=0.8, least–squares fit.

IIb. Resonances

As discussed in section one, the resonances, and associated strengths, of a particle completely determine the behavior of its Polarizability Tensor elements, as a function of relative permittivity. Hence, the resonances were investigated for the coagulated sphere family of shapes. Figures 2.20 and 2.21 show the behavior of the major resonances; major as determined by their strength. The strength was measured using the absorption cross-section of the particle with a dielectric constant equal to that of the resonant value with .1 added to it's imaginary part to give it some loss. The movement of these resonances in the ϵ-plane can be seen as a cause for the variability in the color of a suspension of such particles when observed in white light: different particle shapes will cause the suspension to appear to have different colors than other shapes would.

These figures present the magnitude and position for the resonances observed in this family of geometries in a very complete way. The positions are clearly shown in fig. 2.20 for both x- and z-incidence (note the difference in the x-scales). The relative magnitudes of these resonances are displayed in fig. 2.21.

In these figures on can easily see the movement of the resonances away from that of the sphere (-2), and their eventual return for the case of two separated spheres. Between these two extremes the behavior is quite different for the x- and z-directed cases: the x-directed resonance remains very close to $\epsilon_r = -2$ and moves closer to $\epsilon_r =$zero during its deviation while the z-directed case spawns many resonances all increasing rapidly near separation= 1 (2 touching whole spheres). The major z-resonance is also much larger in magnitude than the x-resonance.

Please note that a previous paper (Weil, 1985) gave a plot similar to fig 2.20 here, but that the lines were drawn in the wrong direction due to insufficient data. That has been corrected here.

192

Major Resonances of 2-Sphere System: x-inc.

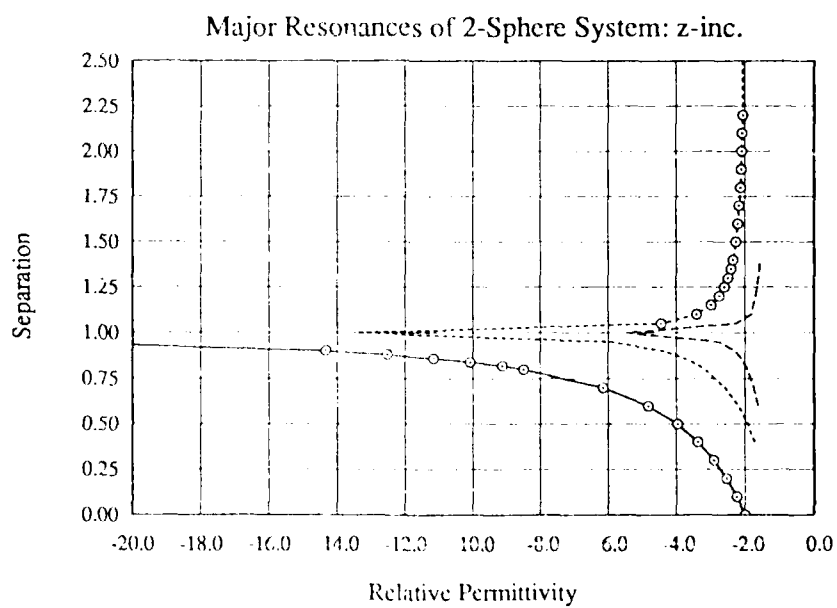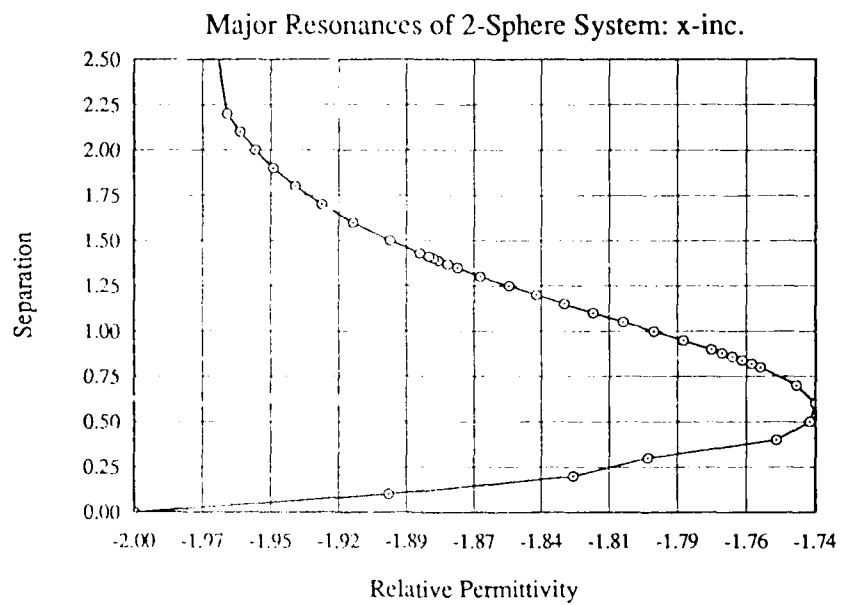Major Resonances of 2-Sphere System: z-inc.

Figure 2.20 — Major Resonances for Coagulated Spheres

193

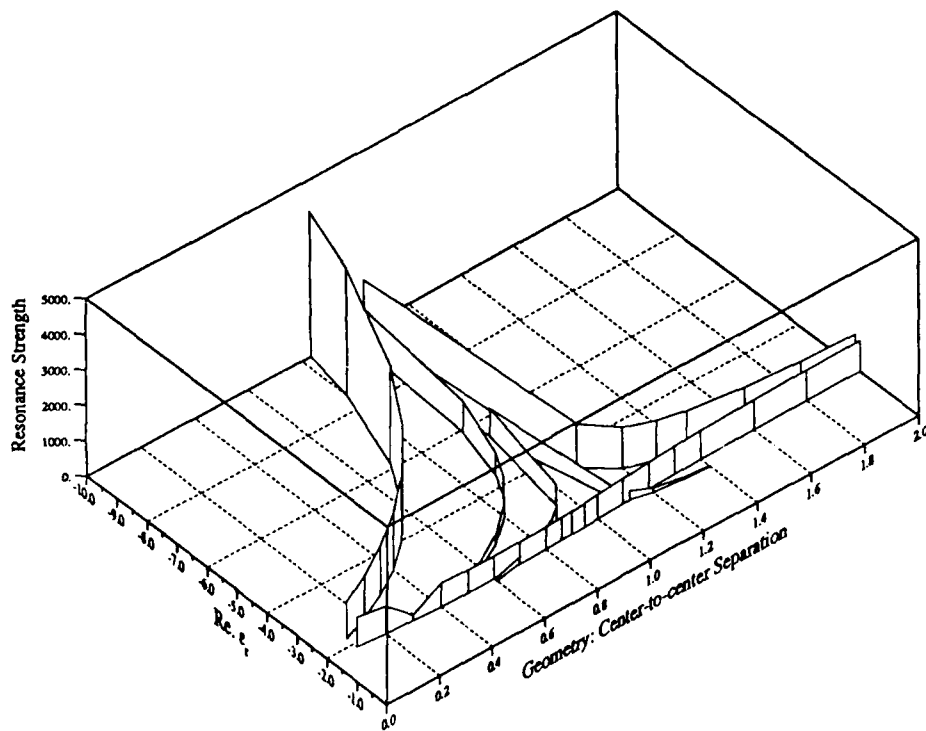Resonance Strength as function of Geometry

Figure 2.21 — Strengths of Major Resonances for Coagulated Spheres

A very intuitive method for understanding absorption spectra is to use the numerically-generated or modeled Polarizability Tensor elements and merely superimpose the plot of the relative permittivity on it. This gives a line on the wavy surface which can be visualized as a particular wavy slice through this surface to give rise to an absorption spectrum. This concept is shown in figures 2.22 and 2.23. Figure 2.22 shows the line on the surface of the Polarizability Tensor, while figure 2.23 shows the equivalent absorption cross-section, which in this case is the Im.P_{33}.

Looking at figure 2.22, note that the value of the bulk relative permittivity for gold at about 4000 Angstroms is about $-2 + j6$., and so the spectrum begins in the upper right corner. In comparing these two figures keep in mind that the surface is plotted with a logarithmic vertical scale, while the absoroption spectrum uses a linear vertical scale. Despite this, we can still observe the two prominent absorption peaks in fig. 2.22. This is an intuitively pleasing way of thinking about absorption spectra for particular materials and particle shapes.

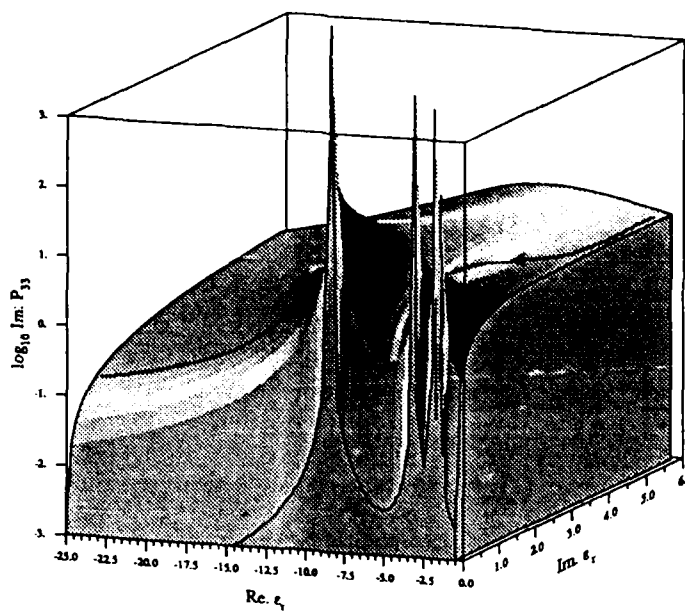Absorption as a function of Complex Relative Permittivity (ϵ_r), sep=0.8

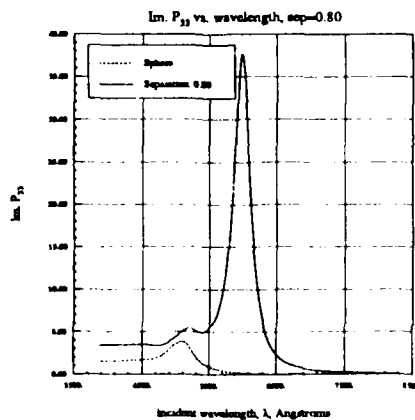Figure 2.22 — Z–Incident, Im. Polarizability, sep=0.8, with ϵ(freq) for gold superimposed.

Figure 2.23 — Absorption Spectrum of Coagulated Gold Spheres, sep=0.8.

The model of the Polarizability Tensor elements can be used to generate a fit to the absorption cross–section as a function of geometry as well as wavelength. This scheme was used to generate figure 2.24, which is in fact a good fit to the available numerical data.

This figure shows the z–directed absorption spectrum for coagulated gold spheres as a function of separation. This data is a pretty good fit to the computer–generated numbers; we use a fit to generate this plot in order to save time. The features in this figure are the same as those noted for figures 2.9, 2.11, 2.13, 2.15, and 2.17: the z–directed absorption spectra. In this figure however, the continuous variation in the absorption peak's position and magnitude gives a better picture of their variability. As the separation increases toward 1 (from 0), and hence from a single sphere, through two coagulated spheres, and on to two just–touching spheres, we see that the single–sphere absorption peak "spawns" other peaks as the geometry becomes more concave. The first, and by far strongest, extra absorption peak begins to form at a separation of 0.4 or so. This peak then moves to progressively larger wavelengths, and increases in magnitude sharply after a separation of about 0.9, also spawned by the persistent single–sphere absorption peak. It moves toward longer wavelenths and increases slightly in magnitude by the time the two spheres are just touching.
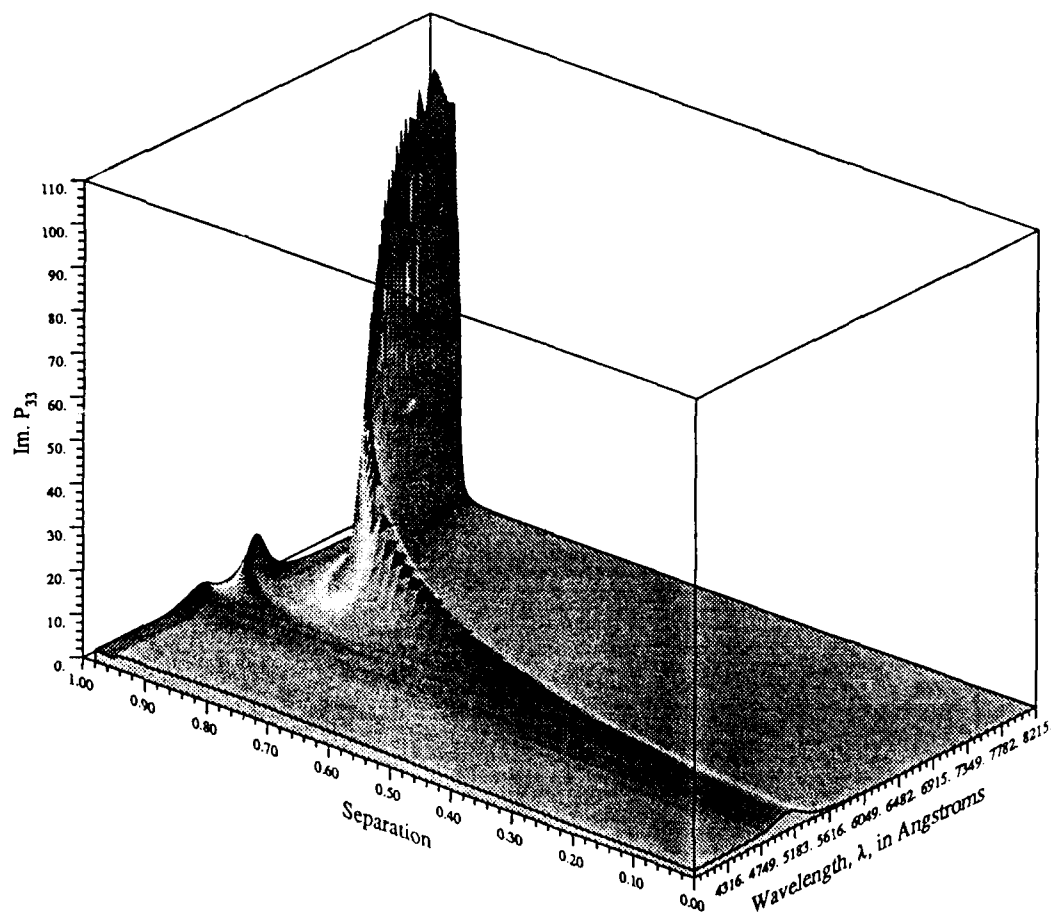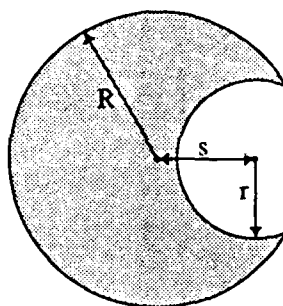
Optical Absorption Spectrum of gold vs. Separation

Figure 2.24 — Z-Incident Absorption Spectrum as function of Geometry.

III. SPHERE–WITH–CAVITY RESULTS

The geometry of this case is addressed in fig 3.1.

R = 0.5 -- radius of solid sphere
s = center-to-center separation
r = radius of spherical hole

EXAMPLES
s=0.0, r=0.3 -- a hollow spherical shell: ◎
s=0.2, r=0.2 -- off-center spherical hole inside sphere: ⊙
s=0.3, r=0.4 -- a spherical bite out of side of sphere: ☾

Figure 3.1 — The Sphere–with–Cavity Geometry

The fields were plotted with a variety of separations and also at many different frequencies; each different frequency corresponds to a different ϵ for gold, tabulated in Physik Daten [1981]. Due to symmetry, only a portion of the field structure is shown. That part of the field that intersects the plane through the symmetry axis (see fig 3.2) and is in the first two quadrants (darkened piece of the plane) is displayed in the field plots. The wire mesh is meant to represent the surface of the (see–thru) particle that is being halved by the cutting plane.

Typical field plots are shown in figs 3.3–3.8 for the three typical geometries, and an arbitrary relative permittivity. Each of the field plots has the real part and imaginary part of the potential for a particular shape, frequency and ' incident ' E-field direction:

x-directed means E is vertical at infinity.
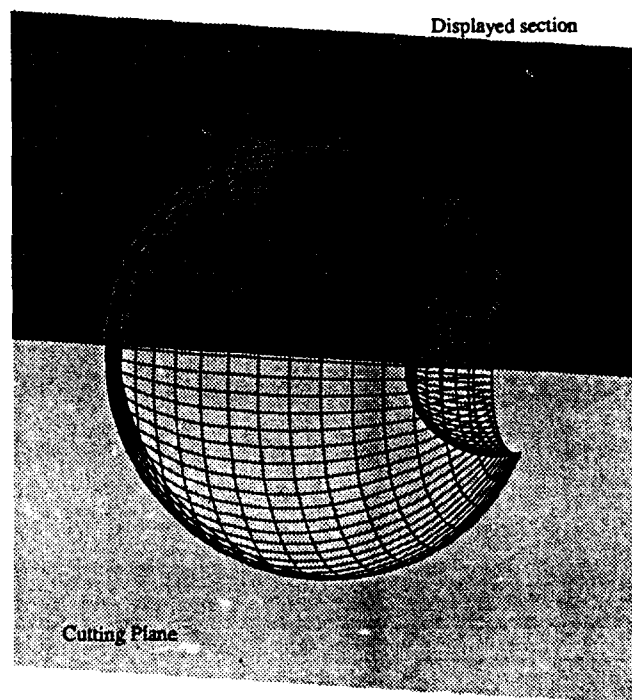
Figure 3.2 — Position of Field Plots in relation to the particle

z-directed means E is horizontal at infinity.

Each plot has 4–6 equipotential lines, while ΔV (or "spacin_ in volts" on the plots) between them varies from plot-to-plot. Hence a large value for ΔV means that we have high local E-field concentrations.

Tau in each plot is the value for the relative dielectric constant.

The dimensionless average absorption cross-section, as described earlier, was plotted for each geometry as a function of free-space wavelength. Typical spectra for each of the three typical geometries previously used are shown in figs 3.9–3.13.

X DIRECTED EXCITATION REAL PART   ***** ISO-RV CURVES *****
TAU =   -3.000 +J 0.500   RV=-1.794,-1.289,-0.785,-0.280,
SPACING IN VOLTS =   0.50460
RVMIN(VOLT) =   -2.04610   Offset: 0.0, Sradius: 0.3000
RVMAX(VOLT) =   -0.02771

0.000   0.400   0.800   1.200   1.600   2.000   Z

X DIRECTED EXCITATION IMAGINARY PART   ***** ISO-IV CURVES *****
TAU =   -3.000 +J 0.500   IV= 0.2992,0.8746,1.4499,2.0253,
SPACING IN VOLTS =   0.57536
IVMIN(VOLT) =   0.01154   Offset: 0.0, Sradius: 0.3000
IVMAX(VOLT) =   2.31300

0.000   0.400   0.800   1.200   1.600   2.000   Z

Figure 3.3 — X-Incident Equi-Potential lines for a Hollow Shell.

201

Z DIRECTED EXCITATION REAL PART
TAU = -3.000 +J 0.500
SPACING IN VOLTS = 0.57306
RVMIN(VOLT) = -3.00628
RVMAX(VOLT) = 1.00514

***** ISO-RV CURVES *****
RV=-2.720,-2.147,-1.574,-1.001,-0.428,
0.1455,0.7186,

Offset: 0.0, Sradius: 0.3000

0.000   0.400   0.800   1.200   1.600   2.000   Z

Z DIRECTED EXCITATION IMAGINARY PART
TAU = -3.000 +J 0.500
SPACING IN VOLTS = 0.64668
IVMIN(VOLT) = -2.26324
IVMAX(VOLT) = 2.26353

***** ISO-IV CURVES *****
IV= -1.940,-1.293,-0.647,.00014,0.6468,
1.2935,1.9402

Offset: 0.0, Sradius: 0.3000

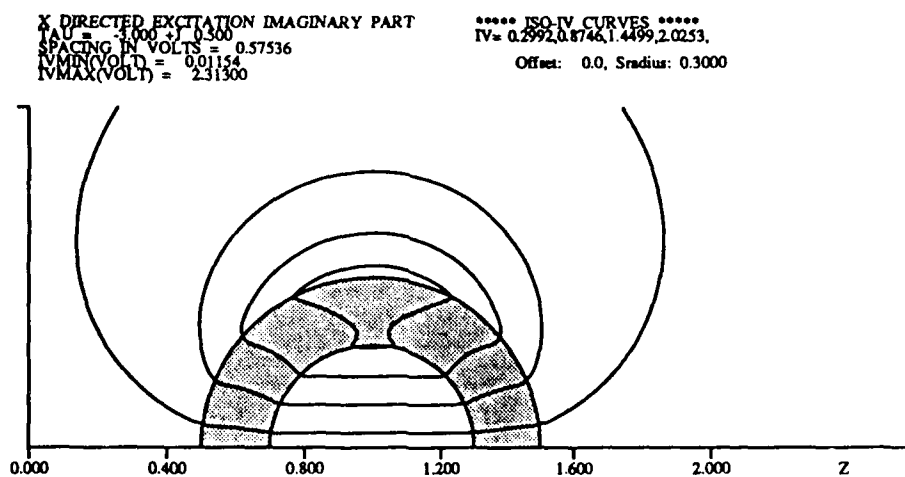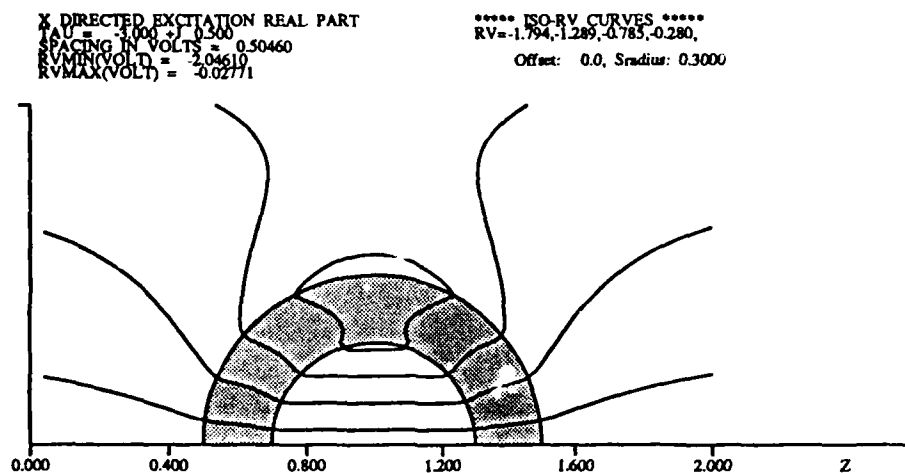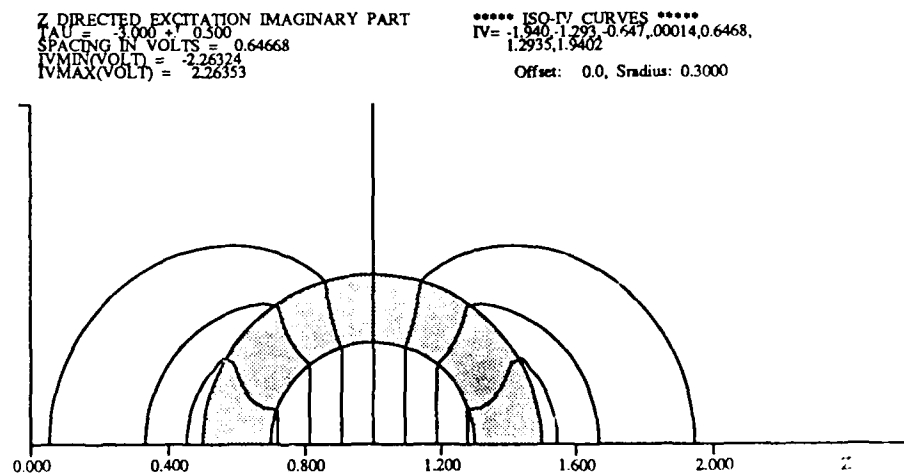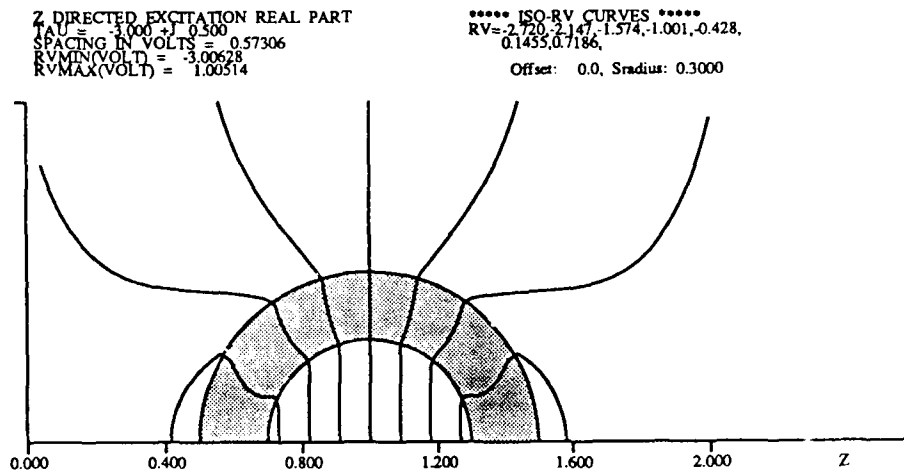0.000   0.400   0.800   1.200   1.600   2.000   Z

Figure 3.4 — Z-Incident Equi-Potential lines for a Hollow Shell.

202
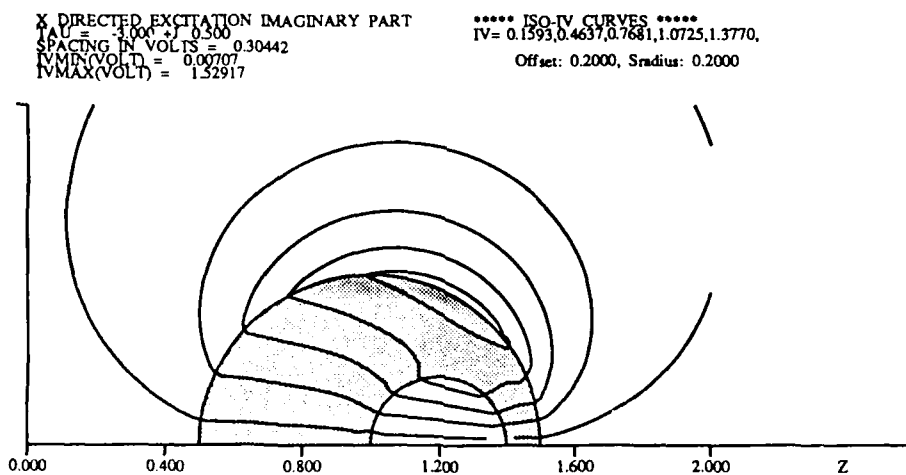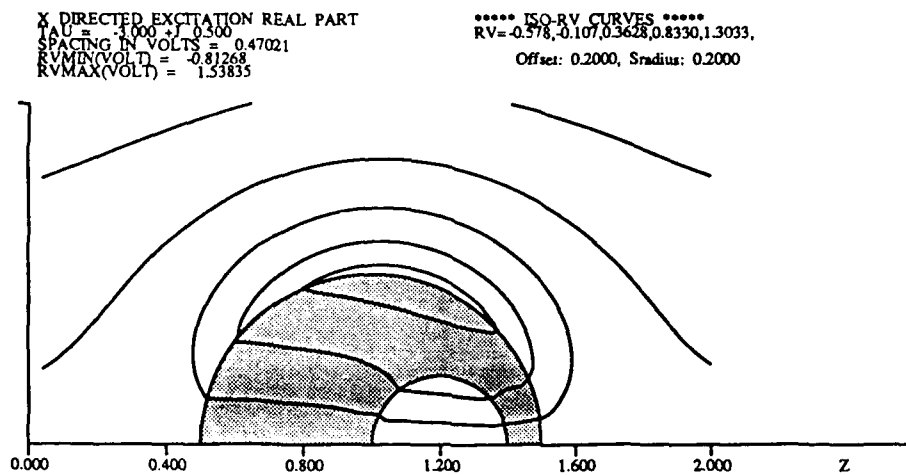
Figure 3.5 — X-Incident Equi-Potential lines for an Off-center Hole.

***** ISO-RV CURVES *****
RV=-2.012,-1.342,-0.671,.00014,0.6710,

Offset: 0.2000, Sradius: 0.2000

Z DIRECTED EXCITATION IMAGINARY PART
TAU = -3.000 +J 0.500
SPACING IN VOLTS = 0.77096
IVMIN(VOLT) = -1.24370
IVMAX(VOLT) = 2.61109

***** ISO-IV CURVES *****
IV= -0.858,-.0873,0.6837,1.4547,2.2256,

Offset: 0.2000, Sradius: 0.2000
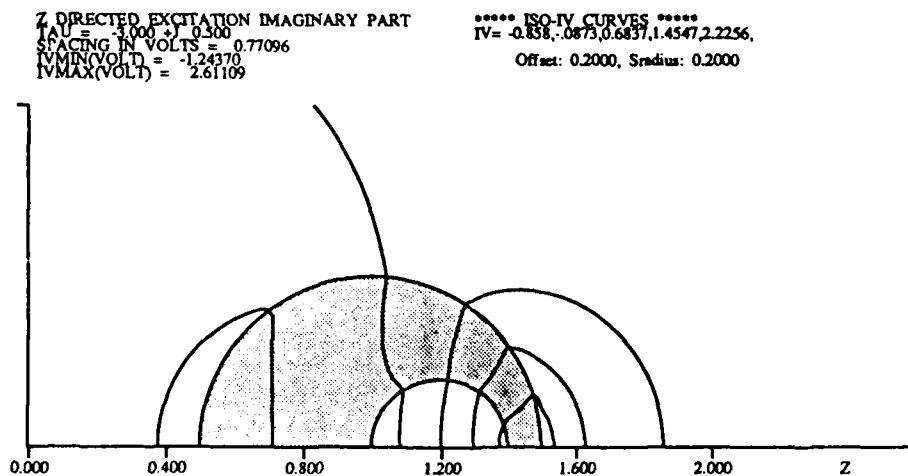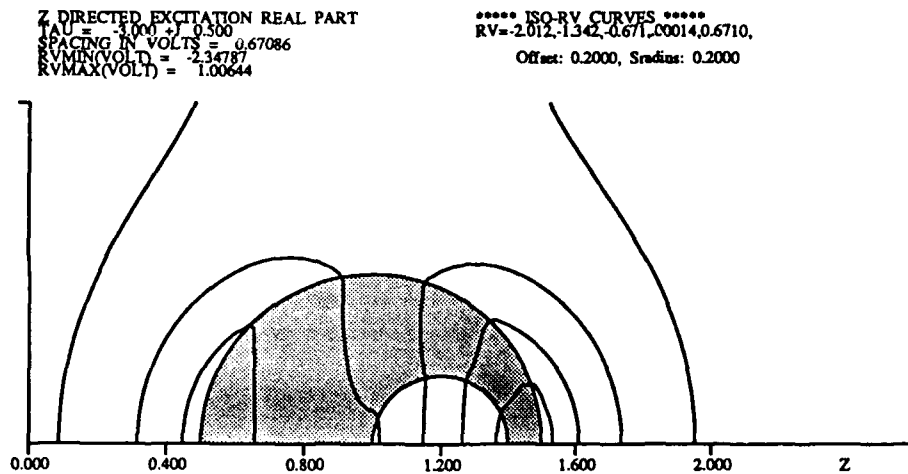
Figure 3.6 — Z-Incident Equi-Potential lines for an Off-center Hole.

X DIRECTED EXCITATION REAL PART
TAU = -1.000 +J 0.500
SPACING IN VOLTS = 0.54172
RVMIN(VOLT) = -1.69187
RVMAX(VOLT) = 1.01672

***** ISO-RV CURVES *****
RV=-1.421,-0.879,-0.338,0.2041,0.7459,

Offset: 0.4000, Sradius: 0.2000

X DIRECTED EXCITATION IMAGINARY PART
TAU = -1.000 +J 0.500
SPACING IN VOLTS = 0.17067
IVMIN(VOLT) = 0.00419
IVMAX(VOLT) = 0.85753

***** ISO-IV CURVES *****
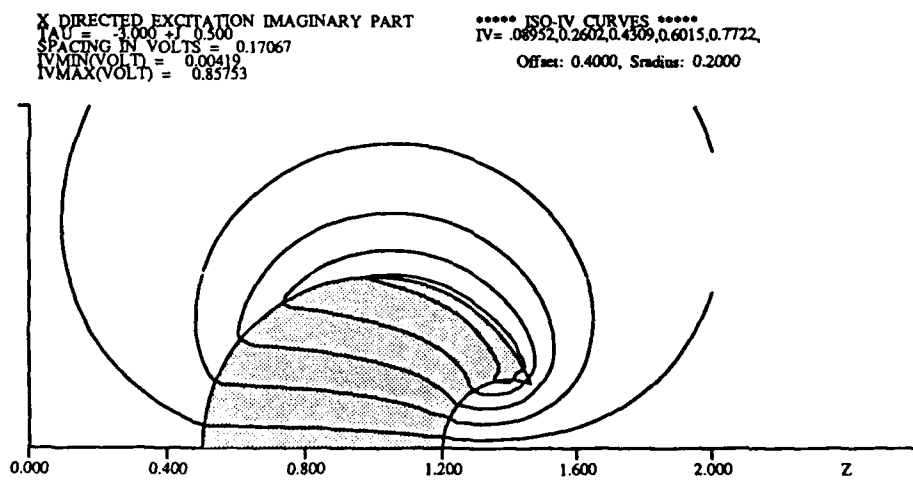IV= .08952,0.2602,0.4309,0.6015,0.7722,

Offset: 0.4000, Sradius: 0.2000
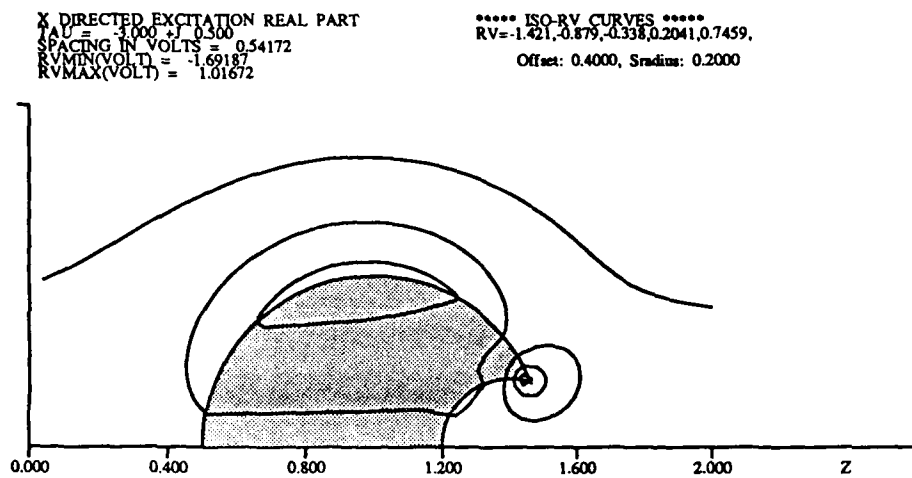
Figure 3.7 — X–Incident Equi–Potential lines for a Spherical Aperture in a Sphere.

Z DIRECTED EXCITATION REAL PART
TAU = -3.000 +J 0.500
SPACING IN VOLTS = 0.35412
RVMIN(VOLT) = -1.93479
RVMAX(VOLT) = -0.16420

***** ISO-RV CURVES *****
RV=-1.758,-1.404,-1.049,-0.695,-0.341,

Offset: 0.4000, Sradius: 0.2000

Z DIRECTED EXCITATION IMAGINARY PART
TAU = -3.000 +J 0.500
SPACING IN VOLTS = 0.73221
IVMIN(VOLT) = -0.92716
IVMAX(VOLT) = 2.73389

***** ISO-IV CURVES *****
IV= -0.561,0.1712,0.9034,1.6356,2.3678,
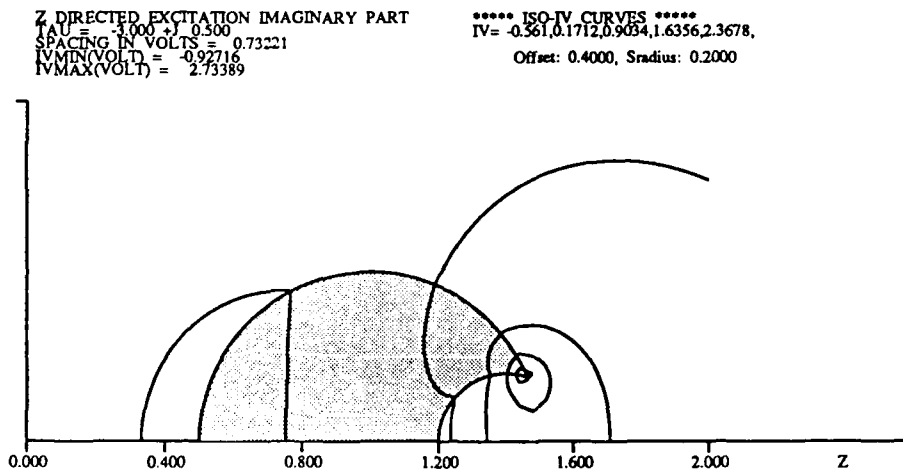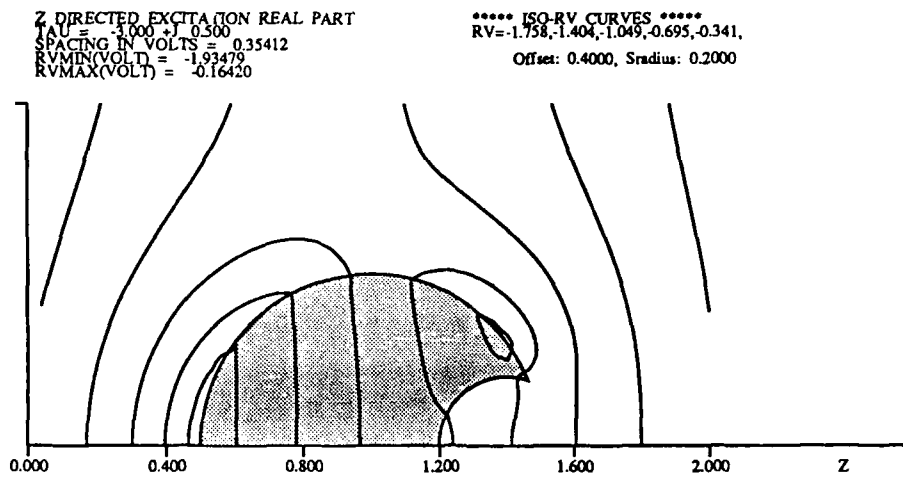
Offset: 0.4000, Sradius: 0.2000

Figure 3.8 — Z-Incident Equi-Potential lines for a Spherical Aperture in a Sphere.

206

The typical field plots shown in the preceding figures (3.3–3.8) are meant to show the different geometries and typical field lines. All are for $\epsilon_r = -3. + j0.5$. No detailed study has yet been made of resonant field structures as was done for the coagulated spheres. Some features that one would intuitively expect are apparent: the spherical shell has a uniform field inside the hole and has x–directed and z–directed fields that are the same but for a rotation; the non–symmetric shapes show the general tendency to have larger field strengths in their regions of highest structural variability. Specifically, the off–center hole geometry has a higher field in the thinner part of the shell, and the sphere with the surface hole has a large concentration near the cusp caused by this hole.
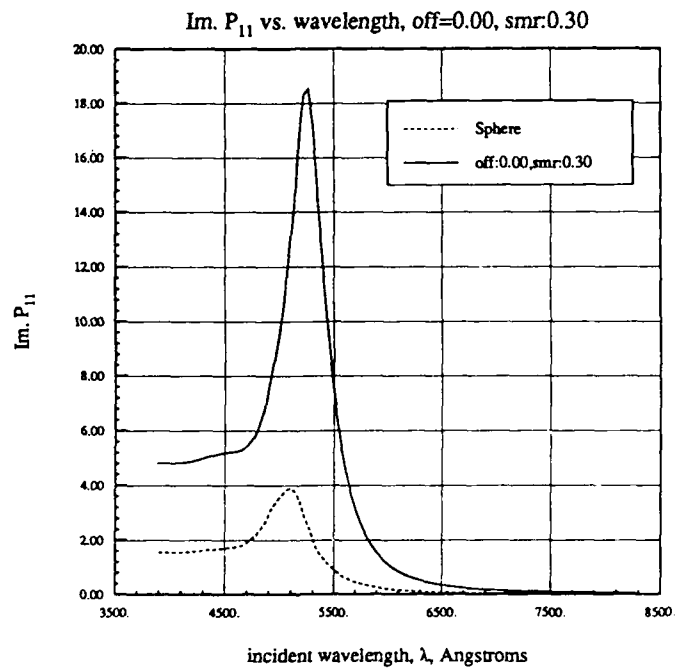
Im. P_{11} vs. wavelength, off=0.00, smr:0.30

incident wavelength, λ, Angstroms

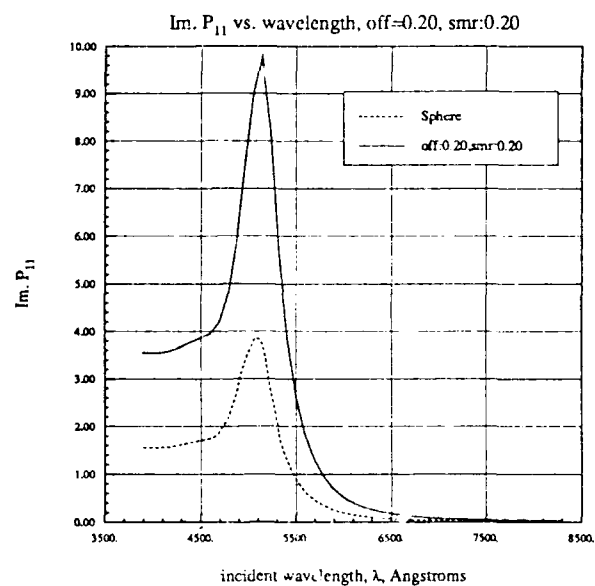Figure 3.9 — Absorption Spectrum for a Hollow Shell.

207

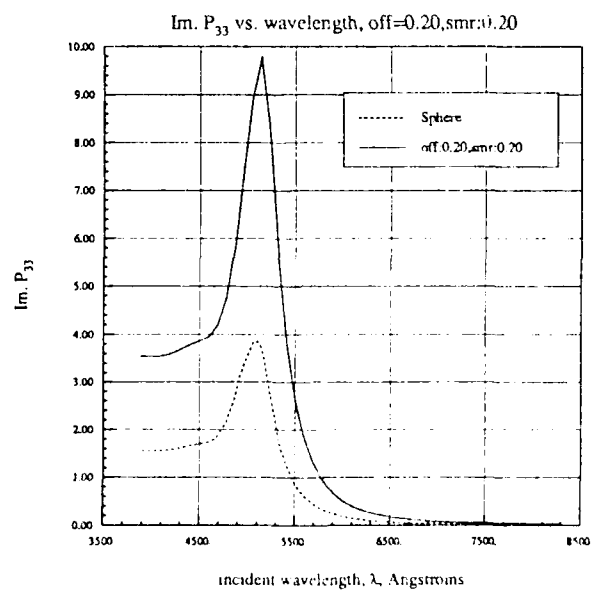Figure 3.10 — X-Incident Absorption Spectrum for an Off-center Hole.

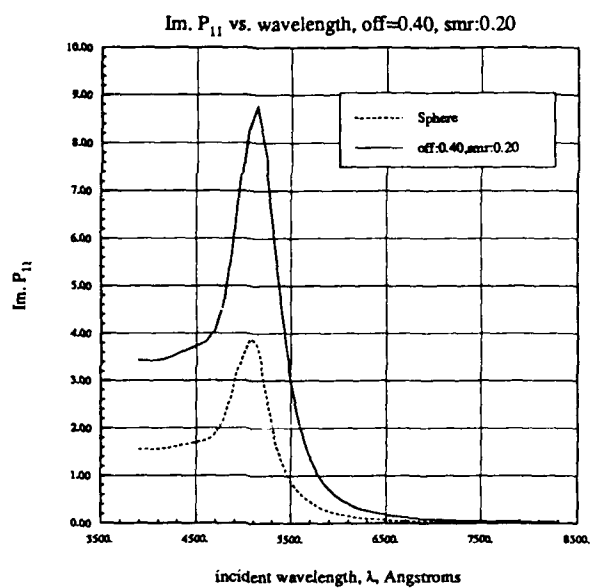Figure 3.11 — Z-Incident Absorption Spectrum for an Off-center Hole.

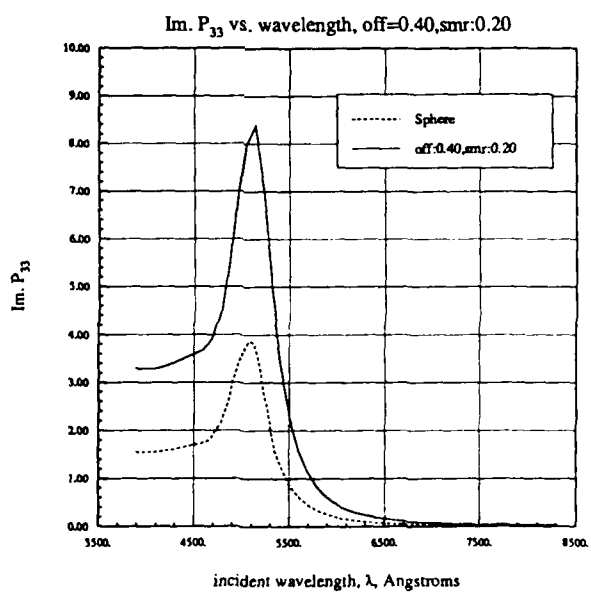**Figure 3.12 — X-Incident Absorption Spectrum for a Spherical Aperture in a Sphere.**

Figure 3.13 — Z-Incident Absorption Spectrum for a Spherical Aperture in a Sphere.

209

Some typical absorption spectra for gold particles are shown in figs 3.9–3.13. The spectra are remarkably similar. In each case the one absorption peak occurs at nearly the same wavelength as for a single sphere. Also, in each case the absorption magnitude is 2.5 to 5 times that of a single sphere. Lastly, the difference between x– and z–directed absorption was very small, almost non–existent, amounting to a small change in absorption magnitude. These results are surprising in light of the extreme differences seen for different geometries and incidence directions for the coagulated spheres in the previous section.

IIa. Polarizability Tensors

The Polarizability Tensor elements are functions of complex ϵ. Hence they are best displayed as surfaces in three–dimensional space. Specifically the $\text{Im}.P_{33}$ is shown for each of the three typical shapes in figures 3.14 through 3.16

These three surfaces point up to us why the absorption spectra are similar. Each surface shows complicated resonance behavior for Re. $\epsilon_r \in (0,-4)$ but are uniformly decaying outside that range. (Note: the surfaces for Im. P_{11} are similarly complicated and clustered between 0 and -4.) When the imaginary part of ϵ_r gets larger than about 0.4 the surfaces are similar and difficult to distinguish. Hence for a permittivity trace in the ϵ_r–plane that doesn't enter this region, or which only goes through slightly, the spectra will be difficult to distinguish. That is what happened in the previous plots. Also note that the hollow spherical appears to have the same resonance as the single sphere, except shifted, and to have another small resonance near zero. The other two geometries have very similar, but complex, surfaces. Further work in this area, especially modeling, is continuing.

Absorption as a function of Complex Relative Permittivity (ϵ_r), off=.0, smr=.3
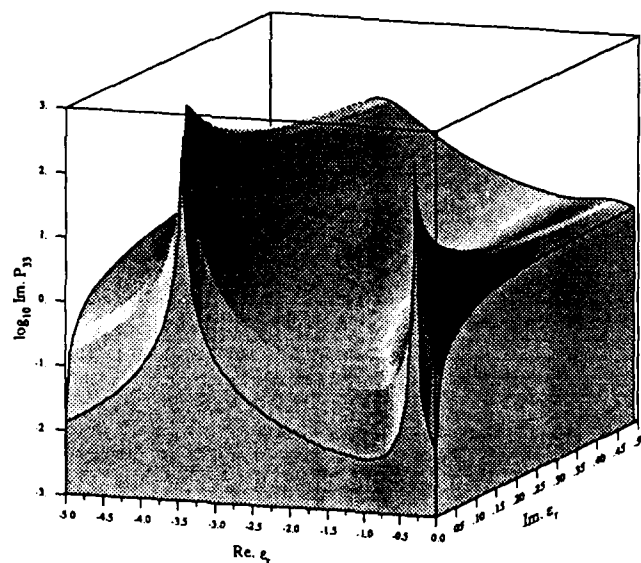

Figure 3.14 — Im. Polarizability for a Spherical Shell.

Absorption as a function of Complex Relative Permittivity (ε_r), off=.2, smr=.2
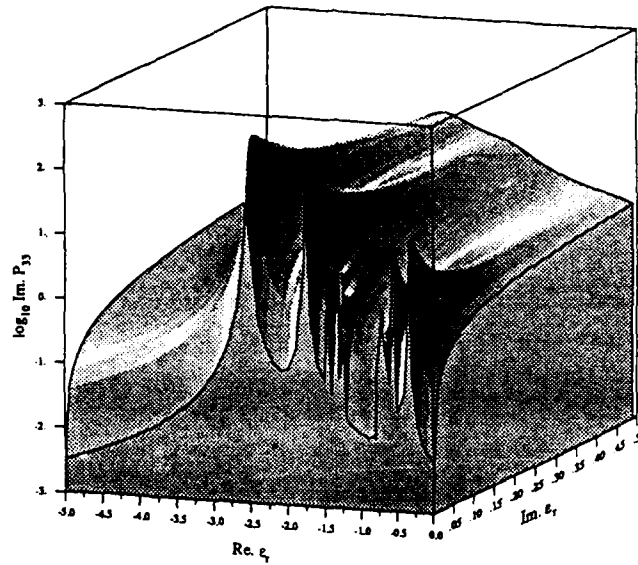

Figure 3.15 — Im. Polarizability for an Off-center Hole.

Absorption as a function of Complex Relative Permittivity (ε_r), off=.4, smr=.2
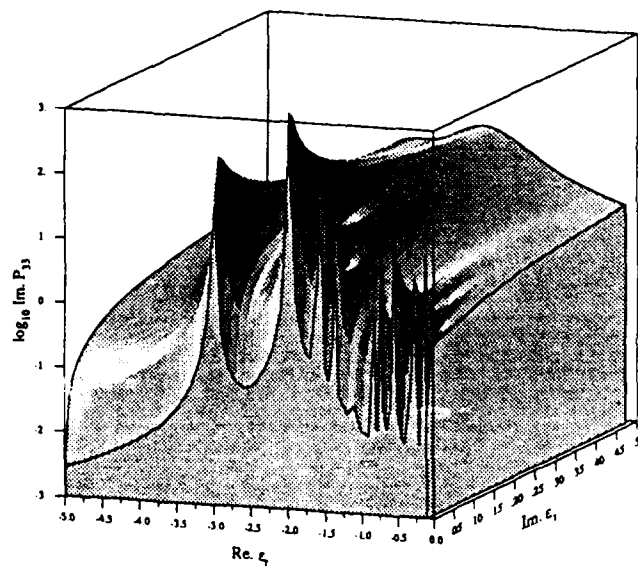

Figure 3.16 — Im. Polarizability for a Spherical Aperture in a Sphere.

212

IIIb. Resonances

As discussed in section one, the resonances, and associated strengths, of a particle completely determine the behavior of its Polarizability Tensor elements, as a function of relative permittivity. Hence, the resonances were investigated for the three typical cavity shape families. Figures 3.17, 3.18, and 3.19 show the behavior of the major resonances; major as determined by their strength. The movement of these resonances in the cause for the variability in the color of a suspension of such particles when observed in white light: different particle shapes will appear to have different colors than others.

Further insight into the absorption spectra of this family of shapes can be gleaned from these figures. They show the positions of the major resonances of each of the three canonical shapes. The resonances of the hollow spherical shell are shown in fig. 3.17. They follow the familiar track, starting near -2 and diverging to $-\infty$ as the shell gets thinner. The other cases were quite different. The off–center hole family (position of hole was varied) had a major resonance near -2 and stayed there, for both x– and z–incidence. The hole–in–surface family varied the hole size, and for x–incidence the resonance stayed relatively near -2, although it began to diverge as the hole size increased. For z–incidence the resonance diverged more rapidly, but for both x– and z–incidences the resonances diverged very slowly in comparison to those for the hollow sphere or for the coagulated sphere.
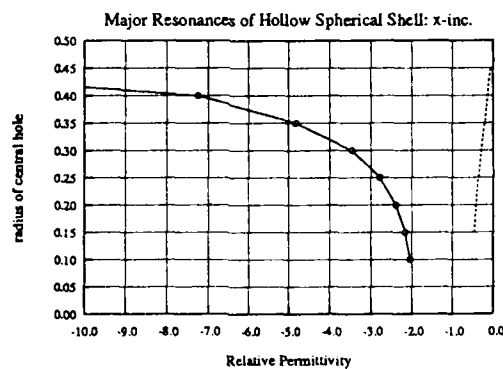
Figure 3.17 — Major Resonances of Spherical Shell as function of Hole Radius.

Major Resonances of Sphere with Off-Center Hole (r=.1): x-inc.

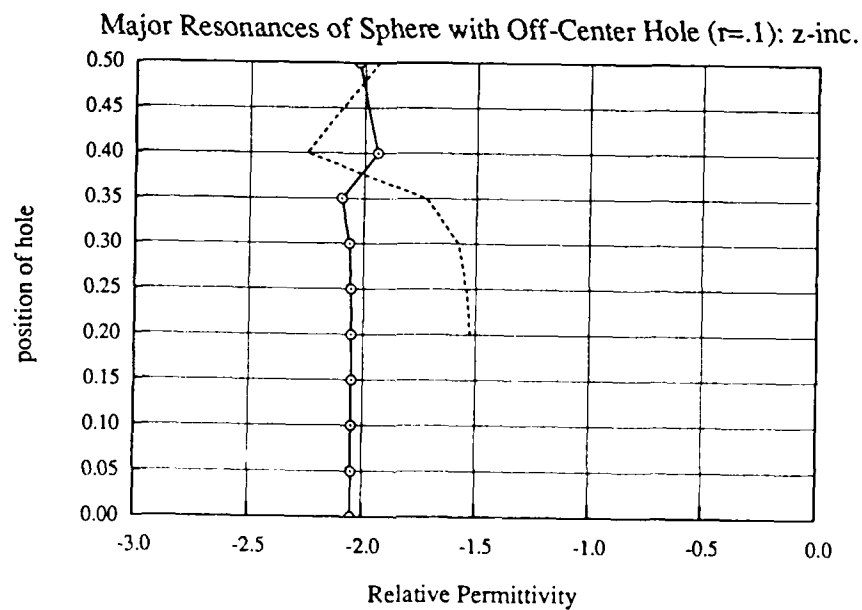
Major Resonances of Sphere with Off-Center Hole (r=.1): z-inc.
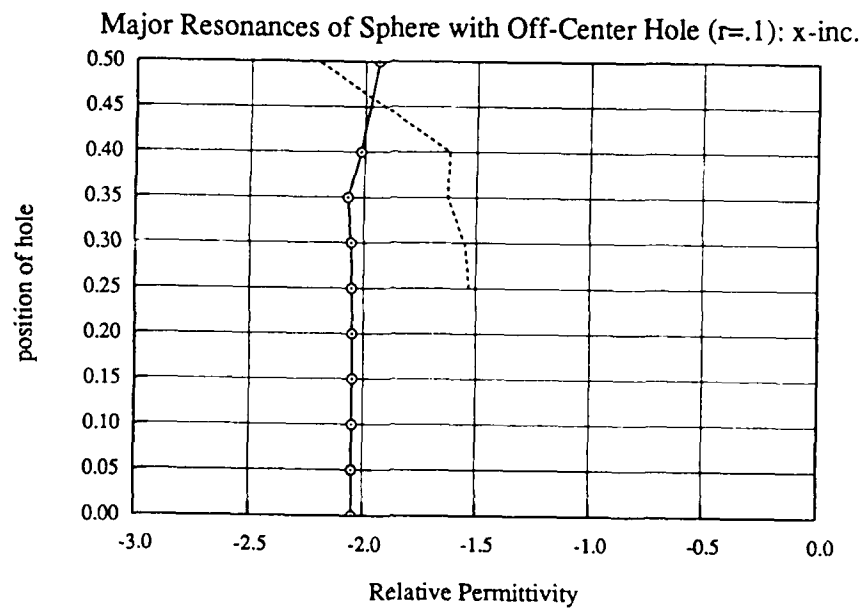
Figure 3.18 — Major Resonances of Off-center Hole as function of Hole Position.

Major Resonances of Sphere with Hole in Surface: x-inc.

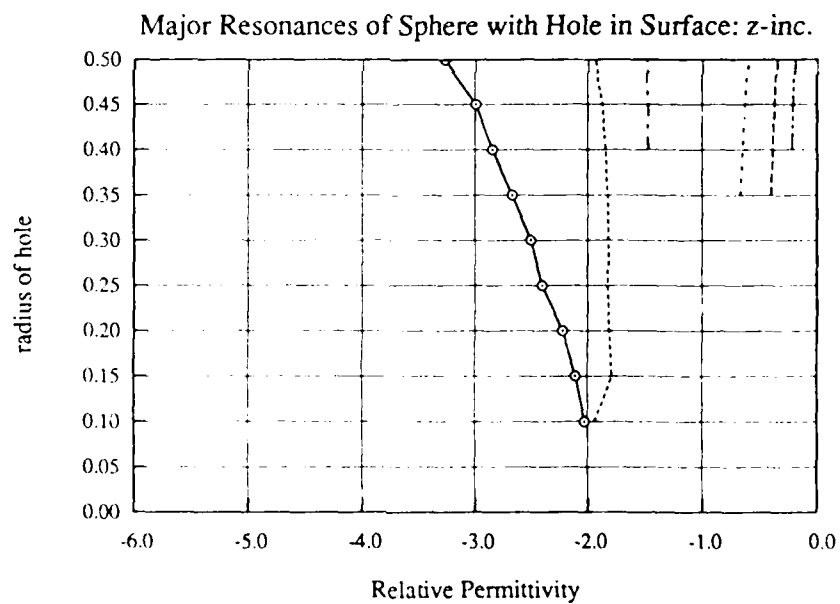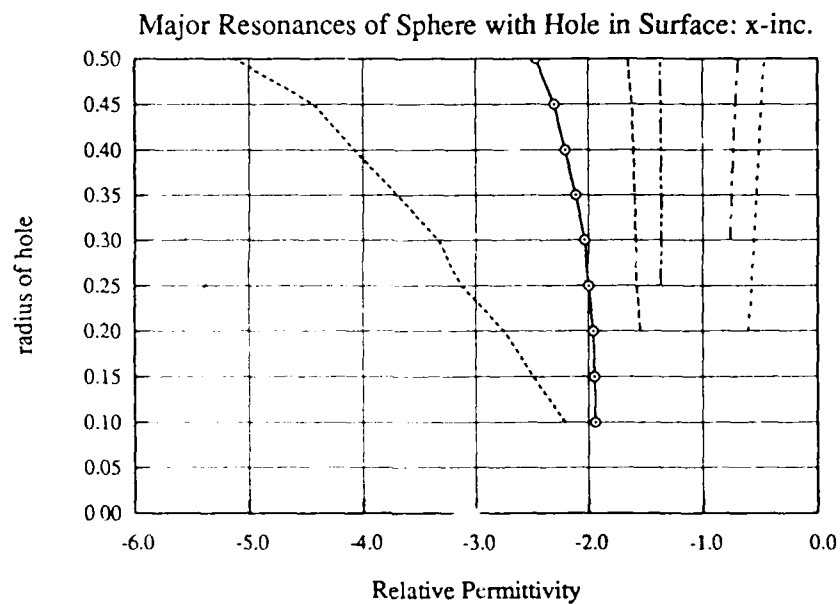## Major Resonances of Sphere with Hole in Surface: z-inc.

Figure 3.19 — Major Resonances of Spherical Aperture in Sphere as function of Hole Radius.

IV. CONCLUSION

A great deal can be learned about small particle absorption with the use of calculated near fields and polarizability tensor elements (as a function of ϵ_r) for different shapes. The shape effects can be quite striking for materials that have bulk permittivities with negative real parts and small (< 3 or so) imaginary parts. Gold in the visible is one such material and we used it extensively in our calculations.

The model of the polarizability tensor elements is very simple and allows clear, physical interpretation of it's few free parameters, while fitting our numerically–generated data quite well.

Extensive work still remains in a number of areas, included in these are:

(1) Finding better ways of choosing the "major" resonances of a particle.

(2) Understanding the variation of resonance position and strength with geometry, for each family of shapes.

(3) Understanding the near and internal field structure near a resonance.

Work is continuing on these and other topics.

BIBLIOGRAPHY

Abramowitz, M. and Stegun, I. A. (1964), *Handbook of Mathematical Functions.* National Bureau of Standards.

Bohren, C. F. and Huffman, D. R. (1983), *Absorption and Scattering of Light by Small Particles,* Wiley, NY.

Nelson, D. F. (1979), *Electric, Optic, and Acoustic Interactions in Dielectrics,* (esp. Ch. 9) John Wiley and Sons, New York.

Physik Daten Part II (1981), Fachinformationzentrum Energie, Physik, Mathematik, GMBH, Karlsruhe.

Senior, T. B. A. and Ahlgren, D. J. (1972), The Numerical Solution of Low Frequency Scattering Problems. *Rad Lab Report,* **103630 3–T.**

Senior, T. B. A. (1976), Low- Frequency Scattering by a Dielectric Body. *Radio Sci,* **11,** 477.

Weil, H. (1986), Surface Roughness, Clustering and Material Effects in Absorption and Scattering by Electrically Small Particles. *Proceedings of the 1985 Scientific Conference on Obscuration and Aerosol Research,* CRDEC-SP-86019, p. 547.

NEAR FIELD VARIATIONAL PRINCIPLE:
SCATTERING FROM SPHERES

D. E. Freund and R. A. Farrell
The Milton S. Eisenhower Research Center
The Johns Hopkins University Applied Physics Laboratory
Laurel, MD 20707

RECENT PUBLICATIONS, SUBMITTALS FOR PUBLICATION AND PRESENTATIONS:

A) J. A. Krill, J. F. Bird, and R. A. Farrell, "Trial Functions in Variational Calculations," in Proceedings of the 1982 CSL Scientific Conference on Obscuration and Aerosol Research (ed. by R. H. Kohl and Assoc., Tullahoma, TN, 1983), pp. 201-209.

B) J. A. Krill and R. A. Farrell, "The Development and Testing of a Stochastic Variational Principle for Electromagnetic Scattering," in Wave Propagation and Remote Sensing, Proceedings of URSI Commission F 1983 Symposium (European Space Agency, Noordwijk, The Netherlands, 1983), pp. 299-307.

C) B. J. Stoyanov and R. A. Farrell, "On the Asymptotic Evaluation of $\int_0^{\pi/2} J_0^2(\lambda \sin x) dx$," Math. Comp. 49, 275-279 (1987).

D) B. J. Stoyanov, J. A. Krill, J. F. Bird, and R. A. Farrell, "Broadband Trial Functions for Surface Scattering with Detailed Analysis for a Simple Model," in Proceedings of the 1986 CRDEC Scientific Conference on Obscuration and Aerosol Research (ed. by Kohl and Assoc., Tullahoma, TN, 1987), to appear.

E) J. F. Bird, R. A. Farrell, E. P. Gray, and B. J. Stoyanov, "Trial Functions for Scattering from Surfaces of Arbitrary Roughness and Variational Test Calculations," in Proceedings of the 1986 CRDEC Scientific Conference on Obscuration and Aerosol Research (ed. by Kohl and Assoc., Tullahoma, TN, 1987), to appear.

F) B. J. Stoyanov and R. A. Farrell, Effects of Simple Shadowing on Variational Calculations," presentation at the 1987 CRDEC Conference on Obscuration and Aerosol Research, June 1987.

ABSTRACT

A Schwinger-type variational principle is presented for the scattered wave in the case of scalar wave scattering with an arbitrary field incident on an object of arbitrary shape with homogeneous Dirichlet boundary conditions. If the distance from the scatterer to the observer is designated by r, then the result is variationally invariant for all values of r ranging from the surface of the scatterer to the far field. This result is an important extension of the usual Schwinger variational principle for the scattering amplitude, and it paves the way for the computation of accurate near field results to scattering problems. Also, a generic procedure is presented for constructing simple trial functions to approximate the fields. Variational calculations using these functions for the test case of a spherical scatterer yield accurate answers over a wide frequency range. This procedure is physically motivated by the general principles of boundary conditions and shadowing, which apply to all scattering problems. The results are markedly degraded if either the boundary condition or shadowing are ignored in constructing the trial function.

Introduction

It is well known that Schwinger's variational principle provides an invariant expression for the scattering amplitude, T.[1-3] What is not so well known is that Schwinger's principle can be generalized and used to construct variationally invariant expressions for ψ_{sc}, the scattered wave.[4,5] This generalization might be expected since the scattering amplitude is a far field quantity that, in three dimensions, is related to the scattered field by $\lim_{r \to \infty} \psi_{sc} = \frac{T e^{ikr}}{r}$, with r being the distance from the

scatterer to the observer.[3-5] The generalized principle provides an expression for the scattered wave that is variationally invariant for all values of the distance parameter, kr, such that $kr \geq ka$, where $k = 2\pi/\lambda$ is the wavenumber and a is a length of the order of the size of the scatterer. However, this generalization is usually only alluded to with no explicit development or discussion or, in the cases when a variationally invariant expression is derived for the scattered wave, no numerical results are given.[6] Numerical calculations require initial trial fields that the variational principle is to improve, and the principle has not been particularly successful in extending the range of validity of the classic long-wavelength approximations, which might explain the absence of numerical results. Recent studies have shown that far-field variational calculations using other trial fields that incorporate certain physical concepts can lead to results that are accurate at essentially all size parameters (wavelengths).[7-10] The physical concepts are that the form of the trial field should be capable of satisfying the boundary condition, and the fact that shadowing occurs for large objects should be incorporated (approximately) in the trial function. The main purpose of this paper is twofold: first, to demonstrate a procedure that can be used to derive a variationally invariant expression for the scattered wave; and second, to show that good numerical results are obtained for a wide range of the size parameter, the distance parameter and for all scattering angles when the above two physical concepts are incorporated into simple variational trial fields.

A Scattered Wave Variational Principle

The general procedure that Jones used to obtain the scattered wave variational principle will first be briefly reviewed.[6] It begins by considering a function (Hilbert) space $\mathcal{H}$. If ψ_1 and ψ_2 are any two functions in $\mathcal{H}$, then their inner product is denoted by $\langle \psi_1, \psi_2 \rangle$. Next, assume that an equation to be solved can be written in the form $\mathcal{L}\psi = \psi_i$, where $\mathcal{L}$ is a known linear operator, ψ is an unknown function and ψ_i is a known function. The adjoint equation is defined such that $\tilde{\mathcal{L}}\tilde{\psi} = \tilde{\psi}_i$, where $\tilde{\mathcal{L}}$ is the operator adjoint to $\mathcal{L}$, $\tilde{\psi}$ is the unknown adjoint function that depends on the choice of $\tilde{\psi}_i$. Recalling that the definition for the adjoint operator is $\langle \psi, \tilde{\mathcal{L}}\tilde{\psi} \rangle = \langle \mathcal{L}\psi, \tilde{\psi} \rangle$, it follows that

$$\langle \psi, \tilde{\psi}_i \rangle = \langle \psi, \tilde{\mathcal{L}}\tilde{\psi} \rangle = \langle \mathcal{L}\psi, \tilde{\psi} \rangle = \langle \psi_i, \tilde{\psi} \rangle .$$ (1)

From the various relations in Eq. (1), one can write immediately

$$\langle \psi, \tilde{\psi}_i \rangle = \frac{\langle \psi, \tilde{\psi}_i \rangle \langle \psi_i, \tilde{\psi} \rangle}{\langle \mathcal{L}\psi, \tilde{\psi} \rangle} .$$ (2)

If, on the right hand side of Eq. (2), the exact function ψ and $\tilde{\psi}$ are replaced with trial functions $\psi_t \equiv \psi + g_0\delta$ and $\tilde{\psi}_t \equiv \tilde{\psi} + \tilde{g}_0\tilde{\delta}$, then it is readily shown[*] that Eq. (2) is a variationally invariant expression for $\langle\psi,\tilde{\psi}_i\rangle$. That is, first order errors in the trial functions cancel, giving an approximation for the quantity $\langle\psi,\tilde{\psi}_i\rangle$ that is correct to second order in the small quantities δ and $\tilde{\delta}$. For example, if one substitutes $\psi_t = \psi + g_0\delta$, then

$$\langle\psi_t,\tilde{\psi}_i\rangle = \frac{[\langle\psi,\tilde{\psi}_i\rangle+\delta\langle g_0,\tilde{\psi}_i\rangle]\langle\psi_i,\tilde{\psi}\rangle}{[\langle\mathscr{L}\psi,\tilde{\psi}\rangle+\delta\langle\mathscr{L}g_0,\tilde{\psi}\rangle]} , \tag{3}$$

where we have used the linearity of the inner product and the fact that $\mathscr{L}$ is a linear operator. From Eq. (1) it follows that $\langle\mathscr{L}g_0,\tilde{\psi}\rangle = \langle g_0,\tilde{\mathscr{L}}\tilde{\psi}\rangle$, which when inserted in Eq. (3) yields

$$\langle\psi_t,\psi_i\rangle = \frac{\langle\psi_i,\tilde{\psi}\rangle\langle\psi,\tilde{\psi}_i\rangle}{\langle\mathscr{L}\psi,\tilde{\psi}\rangle} + \frac{\langle\psi_i,\tilde{\psi}\rangle}{\langle\mathscr{L}\psi,\tilde{\psi}\rangle}\left[\langle g_0,\tilde{\psi}_i\rangle - \frac{\langle\psi,\tilde{\psi}_i\rangle}{\langle\mathscr{L}\psi,\tilde{\psi}\rangle}\langle g_0,\tilde{\mathscr{L}}\tilde{\psi}\rangle\right]\delta + \mathcal{O}(\delta^2) , \tag{4}$$

where $[1+\phi\delta]^{-1}$ has been expanded as $[1-\phi\delta+\mathcal{O}(\delta^2)]$. The final step is to recognize that $\langle\psi,\tilde{\psi}_i\rangle = \langle\mathscr{L}\psi,\tilde{\psi}\rangle$ from Eq. (1) so that the coefficient of δ vanishes provided $\langle g_0,[\tilde{\psi}_i-\tilde{\mathscr{L}}\tilde{\psi}]\rangle$ is zero, which follows from the adjoint equation. A similar proof holds if one substitutes $\tilde{\psi}_t = \tilde{\psi} + \tilde{g}_0\tilde{\delta}$. For our application, it is important to note that linearity and the ability to define an operator $\tilde{\mathscr{L}}$ are the only properties of the inner product operation needed in the invariance proof. Thus, the $\langle \rangle$ symbol could denote any bilinear operation that permits an operator $\tilde{\mathscr{L}}$ (not necessarily the adjoint) to be defined by the relation $\langle\psi\tilde{\mathscr{L}}\tilde{\psi}\rangle = \langle\mathscr{L}\psi,\tilde{\psi}\rangle$.

For Eq. (2) to be useful, the quantity $\langle\psi,\tilde{\psi}_i\rangle$ must be of interest. Fortunately $\tilde{\psi}_i$ can be any well-defined function, and we will choose it such that $\langle\psi,\tilde{\psi}_i\rangle$ is the scattered field. Because our choice of trial field for $\tilde{\psi}$ is guided by physical insight, it is also important that the adjoint equation $\tilde{\mathscr{L}}\tilde{\psi} = \tilde{\psi}_i$ permit a physical interpretation of $\tilde{\psi}$. We illustrate these remarks by considering the scattering from an object upon which the total field, ψ, satisfies the homogeneous Dirichlet boundary conditions and is a solution to the Helmholtz equation. Thus, the initial scattering problem is given by[3,11]

$$\psi(r_f;k_i) = \psi_i(r_f;k_i) - \oint G(r_f,r^s) \frac{\partial\psi(r^s;k_i)}{\partial n}dS , \tag{5}$$

where ψ_i is the incident field, $G(r,r') \equiv e^{ik|r-r'|}/4\pi|r-r'|$ is the free space Greens function, k_i is a vector parameter of the incident field which becomes the incident wavevector for the special case of a plane wave, r_f is the field point where the observer is located, the integration is over the closed

219

surface S bounding the scatterer and $\hat{n}$ is the unit normal directed outward from the surface S; hence $\partial\psi/\partial n$ is the normal derivative of the total field ψ. The incident field is an arbitrary solution of the homogeneous Helmholtz equation.[3] The notation used in Eq. (5) is chosen in anticipation of forthcoming results. In particular, the fields have been explicitly written as functions of the parameter k_i and a subscript f has been placed on the field point r in order to clearly distinguish it from other r's. Also, in accordance with the notation of reference 11, points on the surface of the scatterer have been designated with a superscript s. With the scattering problem defined by Eq. (5), the next step is to choose a specific bilinear operation $\langle\ \rangle$ between two functions ψ_1 and ψ_2. From the form of Eq. (5), a convenient choice is $\langle\psi_1,\psi_2\rangle \equiv \oint \psi_1(r^S)\psi_2(r^S)dS$. Strictly speaking, this operation is not an inner product, since $\langle\psi,\psi\rangle$ is not a positive real number for complex functions ψ. However, $\langle\ \rangle$ is a bilinear operation which permits an $\tilde{\mathscr{L}}$ to be defined through $\langle\mathscr{L}\psi,\tilde{\psi},\rangle = \langle\psi,\tilde{\mathscr{L}}\tilde{\psi}\rangle$, so that using it in Eq. (2) produces an invariant expression for $\langle\psi,\tilde{\psi}_i\rangle$.

The scattered wave ψ_{sc} is defined as

$$\psi_{sc}(r_f;k_i) \equiv - \oint G(r_f,r^S) \frac{\partial\psi(r^S;k_i)}{\partial n}dS , \qquad (6)$$

and is a quantity of interest in so-called direct scattering problems where the incident field and the scatterer are specified. Thus, we will derive a variationally invariant expression for ψ_{sc} that will be valid for all values of the distance parameter kr_f. The boundary condition is $\psi(r_f^S;k_i) = 0$, so that evaluating Eq. (5) for r_f on the surface of the scatterer one finds

$$0 = \psi_i(r_f^S;k_i) + \psi_{sc}(r_f^S;k_i) . \qquad (7)$$

If $\Phi(r;k_i)$ is a function in the Hilbert space, then we elect to define the integral operator, $\mathscr{L}$, by

$$\mathscr{L}\Phi \equiv \oint G(r_f^S,r^S)\Phi(r^S;k_i)dS . \qquad (8)$$

It follows that Eq. (7) can be written in the form

$$\mathscr{L}\frac{\partial\psi}{\partial n} = \psi_i^S , \qquad (9)$$

where ψ_i^S designates the incident field evaluated on the surface of the scatterer. Note, the operator defined in Eq. (8) becomes singular when $r^S = r_f^S$. However, it is an integrable singularity that can be dealt with.[12-14] Introduce the "adjoint" problem by

$$\tilde{\mathscr{L}} \frac{\partial \tilde{\psi}}{\partial n} = \tilde{\psi}_i^s \ , \tag{10}$$

where $\tilde{\mathscr{L}}$ is the integral operator "adjoint" to $\mathscr{L}$ in the sense that $\langle \mathscr{L}\psi, \tilde{\psi}\rangle = \langle \psi \tilde{\mathscr{L}} \tilde{\psi}\rangle$, $\partial\tilde{\psi}/\partial n$ is the normal derivative of the unknown "adjoint" field and $\tilde{\psi}_i^s$ is the incident "adjoint" field evaluated on the surface of the scatterer.[11] The quotation marks around adjoint will be dropped, but it must be kept in mind that the $\langle \ \rangle$ used to define a $\tilde{\mathscr{L}}$ is not an inner product. However, from the definition of $\mathscr{L}$ one can show that $\tilde{\mathscr{L}} = \mathscr{L}$ satisfies the defining equation.[11] Following the procedures used in deriving Eq. (2), one can immediately write a variationally invariant expression for the quantity $\langle \partial\psi/\partial n, \tilde{\psi}_i \rangle$:

$$\langle \frac{\partial\psi}{\partial n}, \tilde{\psi}_i \rangle = \frac{\langle \frac{\partial\psi}{\partial n}, \tilde{\psi}_i \rangle \langle \psi_i, \frac{\partial\tilde{\psi}}{\partial n} \rangle}{\langle \mathscr{L}\frac{\partial\psi}{\partial n}, \frac{\partial\tilde{\psi}}{\partial n} \rangle} \tag{11}$$

So far we have merely followed the results that were sketched previously for a particular scattering problem with a specific choice of the linear operator $\mathscr{L}$ and a specific choice for $\langle \ \rangle$, which is linear in both arguments. It follows from the definition of $\langle \ \rangle$ and Eq. (6) that $\langle \frac{\partial\psi}{\partial n}, \tilde{\psi}_i \rangle$ will be the negative of the scattered field, ψ_{sc}, provided the function $\tilde{\psi}_i$ is chosen to be

$$\tilde{\psi}_i(\tilde{r};r_f) \equiv G(\tilde{r},r_f) \equiv \frac{e^{ik|\tilde{r}-r_f|}}{4\pi|\tilde{r}-r_f|} \ . \tag{12}$$

Notice that r_f is the field point (the point where the observer is located) which, analogous to k_i for the initial (non-adjoint) fields, is a parameter that all adjoint fields depend on. With this choice for $\tilde{\psi}_i$ Eq. (11) becomes an invariant expression for ψ_{sc}. Note, if $\tilde{\psi}_i$ is chosen to be something other than a Green's function point source and then if this different choice is used in Eq. (11), we still would have a variationally invariant expression, but not for the negative of the scattered wave. That is, the only choice for $\tilde{\psi}_i$ that makes $\langle \frac{\partial\psi}{\partial n}, \tilde{\psi}_i \rangle$ equal to the (negative of the) scattered wave (defined in Eq. (6)) is the choice of $\tilde{\psi}_i$ that we made in Eq. 12. In order to write Eq. (11) in a more common notation[7-10] we make the following definitions

$$N_1(r_f, k_i) \equiv \langle \frac{\partial\psi}{\partial n}, \tilde{\psi}_i \rangle \equiv \oint G(r^s, r_f) \frac{\partial\psi}{\partial n}(r^s; k_1) dS \tag{13}$$

$$N_2(r_f, k_i) \equiv \langle \psi_i, \frac{\partial\tilde{\psi}}{\partial n} \rangle \equiv \oint \frac{\partial\tilde{\psi}}{\partial n}(r^s; r_f)\psi_i(r^s; k_1) dS \tag{14}$$

and

$$D(r_f,k_i) \equiv \left\langle \mathcal{L}\frac{\partial\psi}{\partial n}, \frac{\partial\tilde{\psi}}{\partial n} \right\rangle \equiv \oint d\tilde{S} \oint dS \left[\frac{\partial\psi}{\partial n}(r^S;r_f) G(r^S,\tilde{r}^S) \frac{\partial\tilde{\psi}}{\partial n}(\tilde{r}^S;k_i) \right] . \tag{15}$$

With this choice of notation Eq. (11) can be written in the more convenient form that explicitly displays the functional dependence on r_f and k_i,

$$\psi_{sc}(r_f,k_i) = \frac{-N_1(r_f,k_i)N_2(r_f,k_i)}{D(r_f,k_i)} . \tag{16}$$

The Euler equations can be obtained from Eq. (16) in the usual way.[2] In particular: the exact fields ψ and $\tilde{\psi}$ are replaced by trial fields $\psi_t = \psi + g_0\delta$ and $\tilde{\psi}_t = \tilde{\psi} + \tilde{g}_0\tilde{\delta}$, respectively; these trial fields are inserted into Eq. (16); and first order errors are required to vanish. As expected, this condition yields Eq. (7) for the Euler equation that ψ must satisfy, while the Euler equation for $\tilde{\psi}$ is

$$0 = G(\tilde{r}_f^S,r_f) - \oint G(\tilde{r}_f^S,r^S) \frac{\partial\tilde{\psi}}{\partial n}(r^S;r_f)dS . \tag{17}$$

Note that this result could have been anticipated too, since Eq. (17) is basically the integral form of Eq. (10).

The physical interpretations of the initial and adjoint scattering problems are obvious. Specifically, with the aid of Figure 1 it is clear that Eq. (5), the integral equation that represents the initial scattering problem, can be interpreted in the usual way. That is, an incident field is deflected by the surface of the scatterer. An observer located at an arbitrary, but fixed, field point r_f measures the relative amounts of the incident and scattered wave given by the two terms on the right-hand side of this equation.[3] The interpretation of the adjoint scattering problem will be facilitated by first writing down an integral equation for a function $\tilde{\psi}$ at an arbitrary point r_f which is analogous to Eq. (5) and reduces to Eq. (17) for $\tilde{r}_f$ on the surface. In view of Eq. (17) we see that a reasonable candidate for such an equation is

$$\tilde{\psi}(\tilde{r}_f;r_f) = G(\tilde{r}_f,r_f) - \oint G(\tilde{r}_f,\tilde{r}^S) \frac{\partial\tilde{\psi}}{\partial n}(\tilde{r}^S;r_f)d\tilde{S} , \tag{18}$$

with $\tilde{r}_f$ being the adjoint field point where the adjoint observer is located and $\tilde{\psi}$ satisfies homogeneous Dirichlet boundary conditions on S. With the aid of Figure 2 and Eq. (18) one can now interpret the adjoint scattering problem. We see that the adjoint incident field is that of a point source Green's function located at r_f (recall r_f is the location of the observer in the initial scattering problem), which produces a spherical wave incident field that is deflected by the surface of the scatterer. The

scatterer is the one that appears in the initial problem. The adjoint observer is located at an arbitrary point $\tilde{r}_f \neq r_f$ and measures the relative amounts of the adjoint incident and adjoint scattered wave.

Selection of Trial Functions

As stated in the introduction, the selection of trial functions to approximate the fields is an important consideration if one wishes to obtain good numerical results. It has recently been shown that by considering shadowing and the boundary conditions one can construct simple trial functions that yield excellent results for a wide range of the size parameter ka using the far field variational principle.[9,10] We will show that these same general considerations (shadowing and the boundary conditions) will also yield good numerical results for the scattered wave not only for a wide range of the size parameter $(.01 \leq ka \leq 100)$, but also for a wide range of the distance parameter $(ka \leq kr < \infty)$ and for all scattering angles $(0 \leq \theta_s \leq \pi)$. Furthermore, it will be shown that if shadowing or the boundary conditions or both are omitted from consideration in the selection of the trial functions, then one obtains poor results, thus showing the importance of incorporating the basic physics of a problem into the starting approximations.

The trial functions we will use are analogous to the so-called boundary Born trial functions with shadowing used in the far field calculations of Reference 9. They are intended to approximate the field for field points in the immediate vicinity of the scatterer. The surface of the scatterer is assumed to be smooth enough that each field point r has a unique surface point r_s associated with it such that the unit vector $\lim_{|r-r_s| \to 0} [(r-r_s)/|r-r_s|]$ is normal to the scatterer surface at the point r_s. In that event, we write

$$\psi_t(r,k_i) \equiv \{\psi_i(r,k_i) - f(r-r_s)\psi_i(r^s,k_i)\}S(\theta) \tag{19a}$$

and

$$\tilde{\psi}_t(\tilde{r},k_i) \equiv \{G(\tilde{r},r_f) - \tilde{f}(\tilde{r}-\tilde{r}_s)G(\tilde{r}^s,r_f)\}S(\tilde{\theta}) . \tag{19b}$$

It is obvious that these trial fields would obey the boundary conditions if $f(0) = \tilde{f}(0) = 1$. In order to get something different from the usual Born approximation, it is assumed that the normal derivatives of f and $\tilde{f}$ do not vanish on the surface of the scatterer. As a first approximation, these derivatives are taken to be independent of position on the surface. Denoted by f' and $\tilde{f}'$, they may depend on the wavelength of the incident beam. The functions f' and $\tilde{f}'$ are optimally determined by setting $\partial\psi_{sc}/\partial f' = \partial\psi_{sc}/\partial\tilde{f}' = 0$.[7-10]

The functions $S(\theta)$ and $\tilde{S}(\tilde{\theta})$ are the "shadow functions" defined by $S(\theta) \equiv (1-\beta\cos\theta)$ and $\tilde{S}(\tilde{\theta}) \equiv (1+\beta\cos\tilde{\theta}")$, where β is a real number such that $0 \leq \beta \leq 1$ and $\cos\tilde{\theta}" \equiv \cos\theta_f\cos\tilde{\theta}_f + \sin\theta_f\sin\tilde{\theta}_f\cos(\tilde{\phi}_f-\phi_f)$. (See Figure 2.) The real parameter β is determined by realizing that shadowing effects are important for large ka but are negligible for small ka. Therefore, we will choose $\beta = 0$ (no shadowing) for small ka and $\beta = 1$ for large ka. The value of β between ka small and ka large is found by linear interpolation. That is,

$$\beta \equiv \begin{cases} 0 & ka \leq (ka)_0 \\[2mm] \dfrac{ka-(ka)_0}{(ka)_1-(ka)_0} & (ka)_0 \leq ka \leq (ka)_1 \ , \\[2mm] 1 & ka \geq (ka)_1 \end{cases} \tag{20}$$

where $(ka)_0$ is the value of ka for which the scatterer can be considered small and $(ka)_1$ is the value of ka for which the scatterer is considered large. The determination of $(ka)_0$ and $(ka)_1$ is facilitated by the use of Fock's theory, which provides an estimate of the width of the penumbra region.

Specifically, Fock showed that the width of the penumbra region is given by $w = R(2/kR)^{1/3}$, where R is the radius of curvature at the geometric optics boundary.[1,15] This estimate is valid for arbitrary convex perfectly conducting objects with continuously varying curvature. For example, for a sphere of radius a, it is known from Fock's theory[1] that the arclength of the penumbra region is given by $\ell = 2a(2/ka)^{1/3}$. Thus, it is clear that shadowing is negligible when $(2/ka)^{1/3} = \pi/2$; this corresponds to ka $\approx .52$. It seems reasonable that the illuminated side and the shadow side of the scatterer become well defined when the arclength of the penumbra region is less than the arclength of the illuminated and shadow region. This corresponds to the case $(2/ka)^{1/3} = \pi/4$ which is realized when ka ≈ 4.2. Thus, for a sphere we would let $(ka)_0 = .52$ and $(ka)_1 = 4.2$.

A Test Case

We will test the results of the previous sections for the special case when the scatterer is a sphere of radius a and the incident field is a plane wave of unit amplitude. Thus the vector parameter k_i is the incident wavevector. The direction of propagation is chosen as the z-axis of the coordinate system, i.e., $\hat{z} = \hat{k}_i$, whose origin is at the center of the sphere. The exact solution for this problem is known[3] and will be used as a test of the accuracy of the variational results.

Figures 3a-3c illustrate the importance of selecting appropriate trial functions in variational calculations. Figure 3a gives the variational results obtained using the classic Born approximation for the trial fields. These trial fields lead to especially poor results at all values of ka, even ka

small. Figure 3b incorporates the boundary conditions but not shadowing. There is marked improvement over the variational Born results, especially at small values of ka (not shown), but the 40 percent error at ka ~ 4 is unacceptable, as are the ~15% errors due to the oscillations at larger ka values. Figure 3c incorporates shadowing but not the boundary conditions, and oscillates about the exact result with steadily increasing amplitude as ka increases. These trial fields should not be used in practical applications and are presented to illustrate the importance of including both shadowing and the boundary conditions. Figure 3d shows the surprisingly good improvements obtained by incorporating both of these physical considerations in the trial function design as described in the previous section. In particular, when the trial functions given by Eq. (19) of the previous section are used, where f' and $\tilde{f}'$ are determined optimally, β is given by Eq. 20 with $(ka)_0 = .52$ and $(ka)_1 = 4.2$, remarkably good results are obtained for all the values of ka shown in Figure 3d. Note, it is important to point out that the results of Figure 3d are not sensitive to the choice of $(ka)_0$ and $(ka)_1$ in Eq. (20). This was tested numerically by setting $(ka)_0 = 1$ and $(ka)_1 = 10$; the changes in accuracy were nominal. Thus, boundary Born trial functions with shadowing are far superior to trial fields that neglect shadowing, the boundary conditions, or both. Note, these results are not restricted to the implementation of variational principles; one should always try to make their initial approximation contain as much of the relevant physics as possible, irrespective of the computational method being employed.

Figures 4 through 7 show plots comparing the variational results with the exact results. The boundary Born trial functions with shadowing are used in each case. In all these figures the solid line represents the exact results and the dashed line represents the variational results. The range and increments for the abscissa in these figures is the following: In Figure 4 and Figure 7, the value of ka runs from $.01 \le ka \le 100$. The increments are in steps of $\Delta ka = .01$ until $ka = .1$ at which time the step size is changed to $\Delta ka = .1$. In Figure 5, kr_f runs from $ka \le kr_f \le 100ka$. The increments are in steps of $\Delta kr_f = ka/10$. In Figure 6 θ_f runs from $0 \le \theta_f \le \pi$ in increments of $\Delta\theta_f = \pi/180$ ($=1°$). In all figures, the quantity plotted along the ordinate is $|2\psi_{sc}r_f/a|^2$. The factor $(2r_f/a)$ is chosen so that the quantity being plotted becomes the well-known normalized differential scattering cross section in the far-field limit.[1,3]

It is apparent from the figures that the variational results are in excellent agreement with the exact results. The largest percent error for each of the plots is given in the figure captions and, except for Figures 6b, 7a and 7b, the maximum percent error was always less than 12% and usually less than 3%. The rare anomalous spikes near $\theta = 72°$ in Figure 6b and near $ka = 80$ in Fig. 7b are in error by about 25%. Finally we note that in Figure 7a the much less pronounced spikes near $ka = 32$ and $ka =$

58 are not such serious problems as in Figures 6b and 7b. However, it is clear that for ka $\geq$ 35 the variational result starts getting out of phase with the exact result. This problem is not so easy to remedy and it is indicative of the fact that some physics has been left out of the trial functions that were discussed in the previous section. One possible solution would be to let the parameters of the shadow function in the adjoint trial field be not only a function of ka but also a function of kr_f.

In conclusion, we have used known techniques to explicitly derive a variationally invariant expression for the scattered field for scalar wave scattering with an arbitrary incident field from an arbitrarily shaped scatterer obeying homogeneous Dirichlet boundary conditions. This result is embodied in Eq. (11) and Eq. (16) and it represents a generalization of the well-known Schwinger variational principle for the scattering amplitude, which is a far field quantity. This generalization allows one to compute the scattered field from a variationally invariant expression which is valid for all values of kr_f ranging from the surface of the scatterer to infinity. In the limit $kr_f \rightarrow \infty$ the present result reduces to the usual Schwinger variational principle for the scattering amplitude. It is clear from Figures 4-7 that one does indeed obtain excellent numerical results for a wide range of the distance parameter kr_f as well as a wide range of the size parameter ka. Furthermore, it is clear from Fig. 3 that lack of a good trial field gives poor results. Thus we see that the computational usefulness of variational principles hinges on a good choice of trial fields.

References

1. Electromagnetic and Acoustic Scattering by Simple Shapes, J. J. Bowman, T. B. A. Senior, P. L. E. Uslenghi, editors (North-Holland Publishing Company, Amsterdam, 1969) pp. 31-41 and 362-369.

2. J. A. Krill and R. H. Andreo, "Vector Stochastic Variational Principles for Electromagnetic Wave Scattering," IEEE Trans. Antennas. Propagat., Vol. AP-28, pp. 770-776 (1980).

3. P. M. Morse and H. Feshbach, Methods of Theoretical Physics, Part II (McGraw-Hill, New York, 1953), pp. 1068-1070, 1134-1136 and 1483-1486.

4. D. S. Jones, <u>Methods in Electromagnetic Wave Propagation</u> (Clarendon Press, Oxford, 1979), pp. 166-176 and 304-309.

5. D. S. Jones, "A Critique of the Variational Method in Scattering Problems," IRE Trans. Antennas Propagat., Vol. AP-4, pp. 297-301 (1956).

6. H. Levine, "Variational Methods for Solving Electromagnetic Boundary Value Problems," Notes of lectures, 1954, Sylvania Products Co., Mountain View, California and S. Altshuler, "Variational Principles for the Wave Function in Scattering Theory," Phys. Rev., Vol. 109, pp. 1830-1836 (1958). In this second reference the author is investigating quantum mechanical scattering from point sources.

7. J. A. Krill and R. A. Farrell, "The Development and Testing of a Stochastic Variational Principle for Electromagnetic Scattering," in <u>Wave Propagation and Remote Sensing, Proc. URSI Commission F 1983 Symposium</u> (European Space Agency, Noordwijk, The Netherlands, 1983), pp. 299-307.

8. J. A. Krill, J. F. Bird, and R. A. Farrell, "Trial Functions in Variational Calculations," Proc. 1982 CSL Scientific Conf. on Obscuration and Aerosol Research (R. H. Kohl and Assoc., Tullahoma, TN, 1983), pp. 201-209.

9. B. J. Stoyanov and R. A. Farrell, "Effects of Simple Shadowing on Variational Calculations," Proc. 1987 CRDEC Scientific Conference on Obscuration and Aerosol Research.

10. B. J. Stoyanov and R. A. Farrell, "A Physical Approach to Developing All-Frequency Trial Functions in Variational Wave-Scattering Calculations," in preparation.

11. P. M. Morse and H. Feshbach, <u>Methods of Theoretical Physics,</u> Part I (McGraw-Hill, New York, 1953), pp. 791-808 and pp. 877-878.

12. J. A. Krill, R. H. Andreo, and R. A. Farrell, "A Computational Alternative for Variational Expressions that Involve Dyadic Green Functions," IEEE Trans. Antennas Propagat., Vol. AP-30, pp. 1003-1005 (1982).

13. H. A. Schenck, "Improved Integral Formulation for Acoustic Radiation Problems," J. Acoust. Soc. Am., Vol. 44, pp. 41-58 (1967).

14. L. G. Copley, "Integral Equation Method for Radiation from Vibrating Bodies," J. Acoust. Soc. Am., Vol. 41, pp. 807-816 (1966).

15. V. A. Fock, <u>Electromagnetic Diffraction and Propagation Problems</u> (Pergamon Press, New York, 1965).
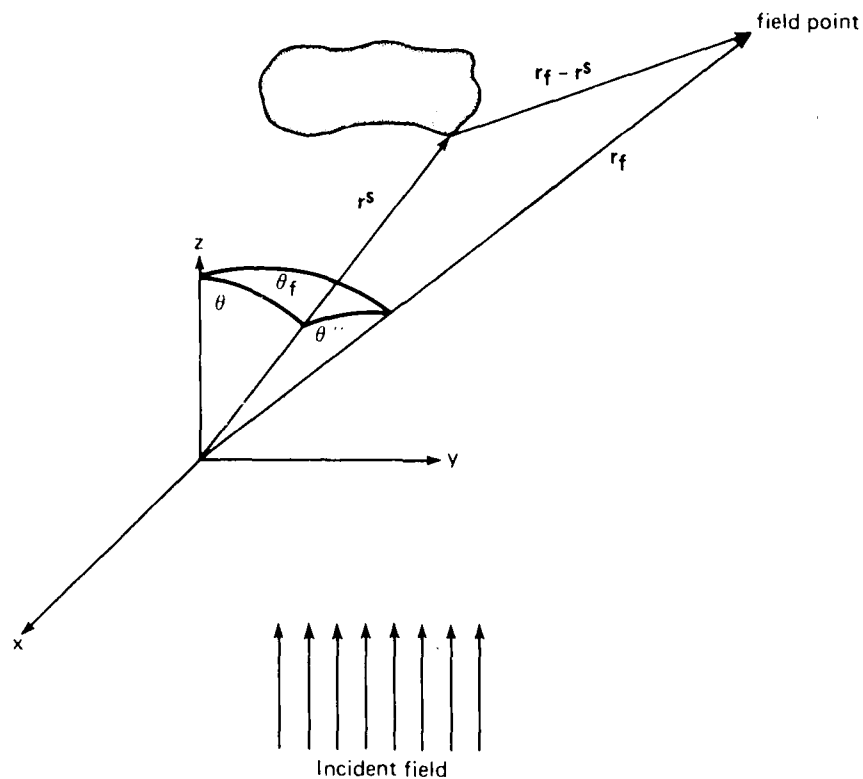
FIGURE 1. Schematic representation of the initial (non-adjoint) scattering problem. The shaded region represents an arbitrary scatterer with an incident field impinging upon it. The observer is at the field point which is located by r_f. An arbitrary point on the scatterer is given by r^S. The "spherical triangle" defines the relevant polar angles: $\cos\theta \equiv \hat{r} \cdot \hat{z}$, $\cos\theta_f \equiv \hat{r}_f \cdot \hat{z}$ and $\cos\theta'' \equiv \hat{r}_f \cdot \hat{r}$ where $\hat{r}_f$ is a unit vector in the direction of r_f and $\hat{r}$ is a unit vector in the direction of r^S.
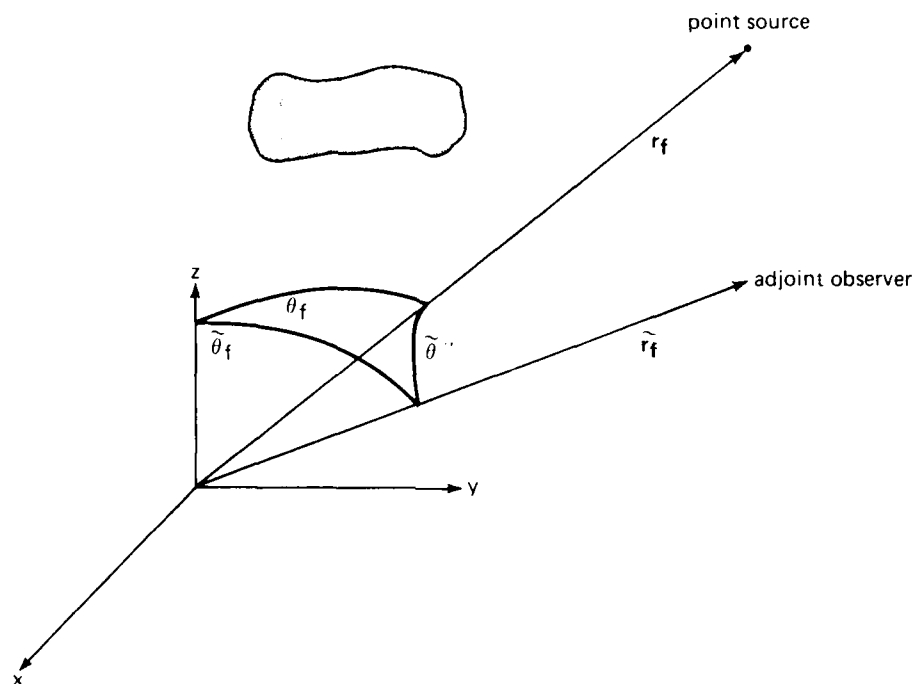
FIGURE 2. Schematic representation of the adjoint scattering problem. The shaded region is the scatterer and the source is a point source located at r_f, where r_f is the location of the field point (observer) for the initial scattering problem. The vector $\tilde{r}_f \neq r_f$ locates the adjoint observer. The "spherical triangle" defines the relevant polar angles: $\cos\tilde{\theta}_f \equiv \tilde{r}_f \cdot \hat{z}$, $\cos\theta_f \equiv \hat{r}_f \cdot \hat{z}$ and $\cos\tilde{\theta}'' \equiv \hat{r}_f \cdot \hat{\tilde{r}}_f$, where $\hat{r}_f$ is a unit vector in the direction of r_f and $\hat{\tilde{r}}_f$ is a unit vector in the direction of $\tilde{r}_f$.

(a)

(b)

(c)

(d)

$f = 0$
$\beta = 0$

$f \neq 0$
$\beta = 0$

$f = 0$
$\beta \neq 0$

$f \neq 0$
$\beta \neq 0$

$|(2\psi_{SC}/ka)kr_f|^2$

ka
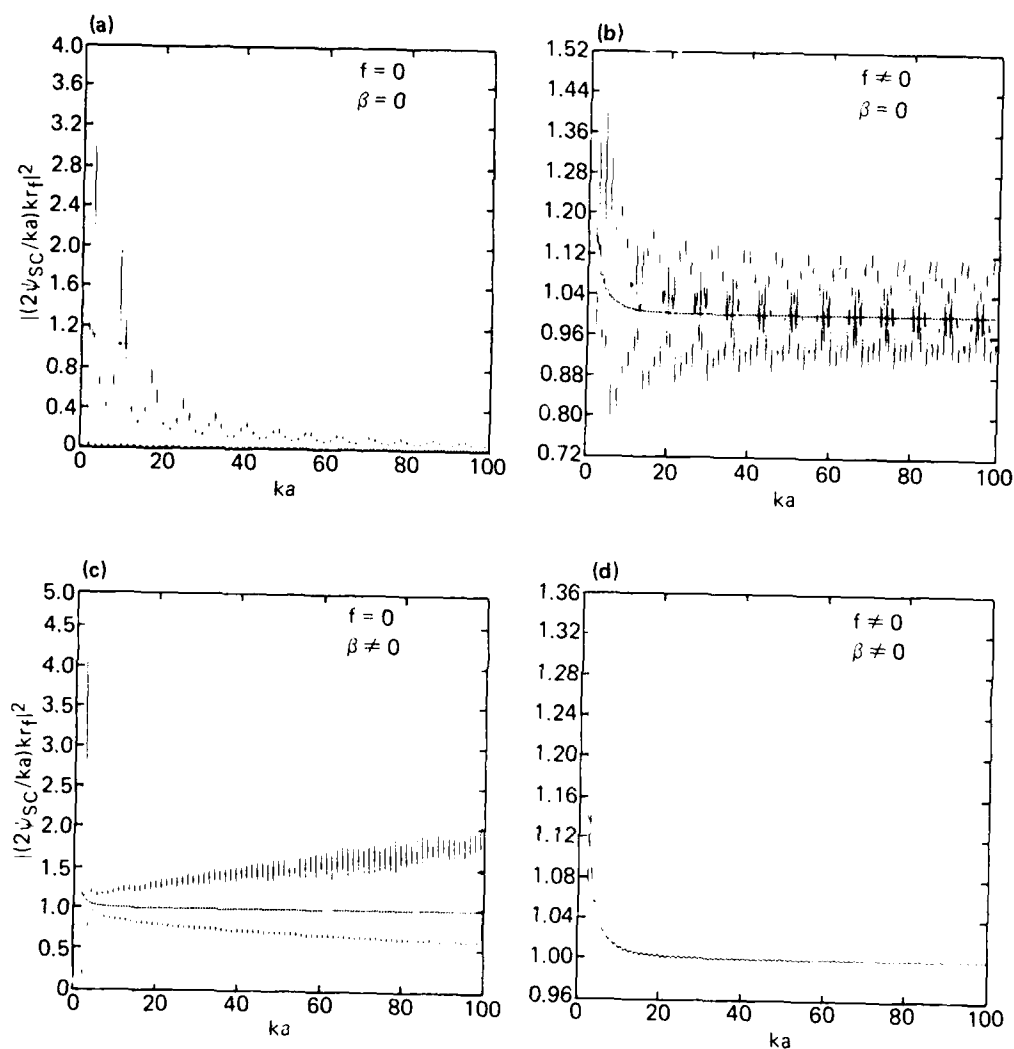
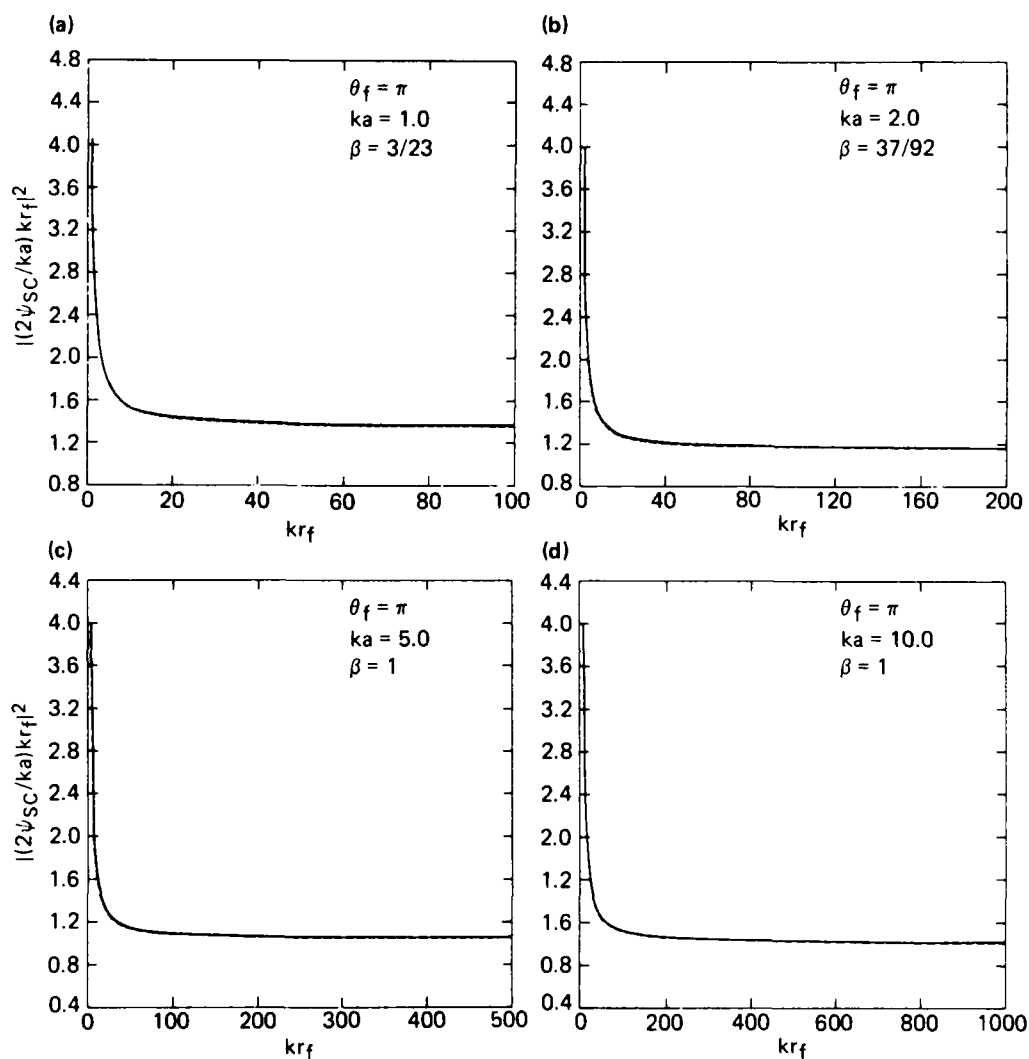FIGURE 3. Plots of $|(2\psi_{SC}/ka)kr_f|^2$ for far field backscattering from an acoustically soft sphere as a function of ka for four selected trial fields. The smooth curve represents the exact answer and the oscillatory curves show the variational result. Note $f \neq 0$ means that the boundary Born nature of the trial field was included and $\beta \neq 0$ means shadowing was accounted for. The maximum percent error in each case is: (a) 400% at ka = 1.5; (b) 43% at ka = 4.0; (c) 254% at ka = 2.7; (d) 6.1% at ka = 2.3.
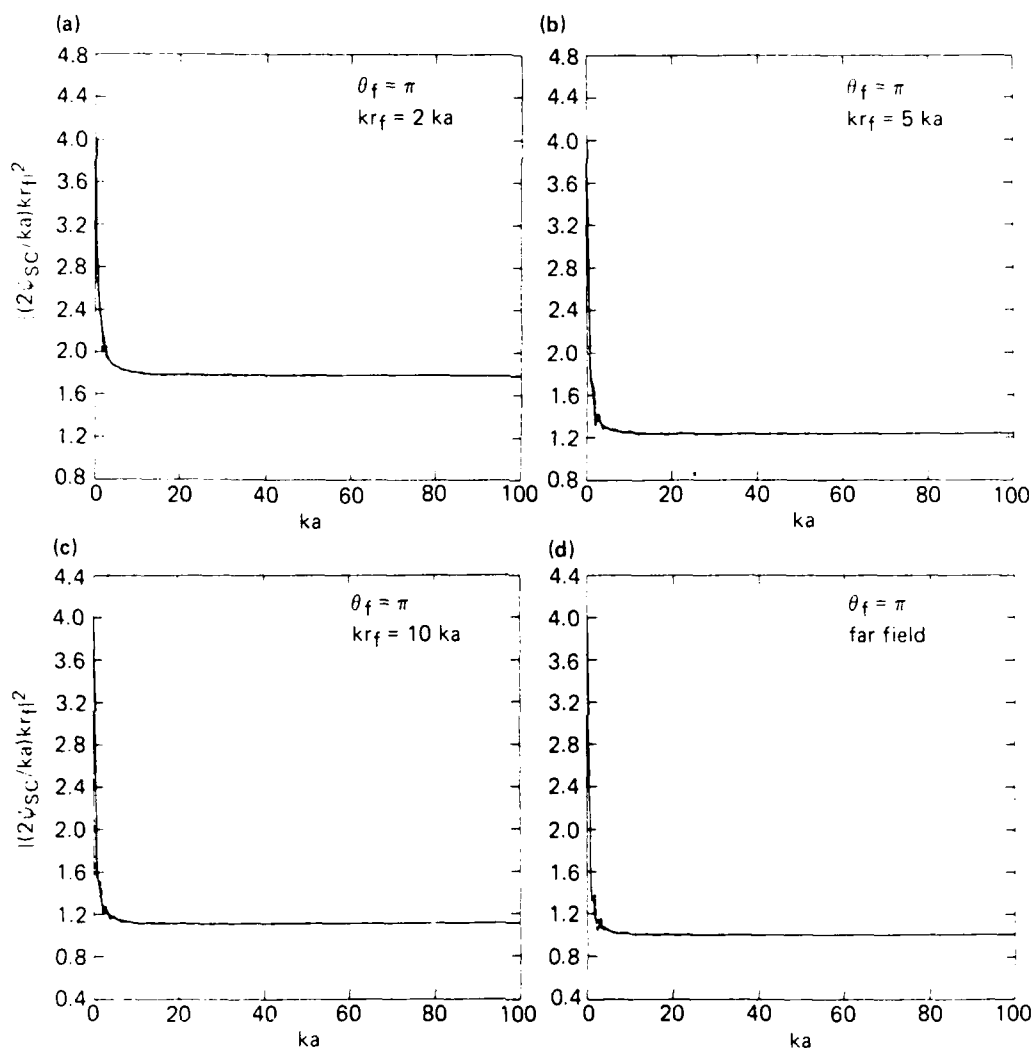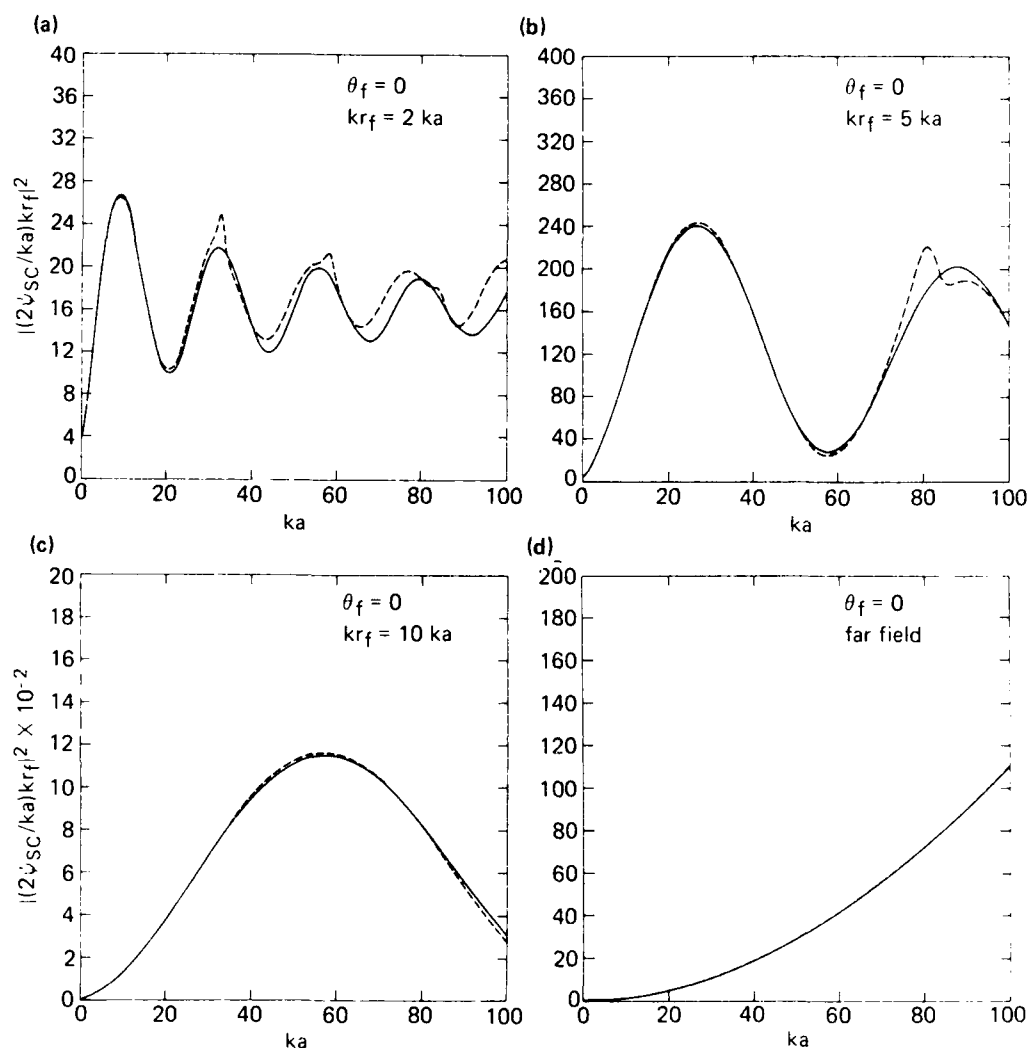
FIGURE 4. Plots of $|(2\psi_{sc}/ka)kr_f|^2$ for backscattering from an acoustically soft sphere as a function of ka for four selected values of kr_f. Plots (a)-(d) show that the variational results (-----) are in good agreement with the exact answer (———) for all values of ka. The maximum percent error for each case is: (a) 3.1% at ka = 2.1. (b) 4.3% at ka = 2.2. (c) 5.1% at ka = 2.3. (d) 6.1% at ka = 2.3.

FIGURE 5. Plots of $|(2\psi_{SC}/ka)kr_f|^2$ for backscattering from an acoustically soft sphere as a function of kr for four selected values of ka. Plots (a)-(d) show that the variational results (-----) are in good agreement with the exact answer (———) for all values of kr_f. The maximum percent error for each case is: (a) 1.3% at kr_f = 1.0. (b) 2.7% at kr_f = 3.2. (c) .5% at kr_f = 5.0. (d) .2% at kr_f = 1000.
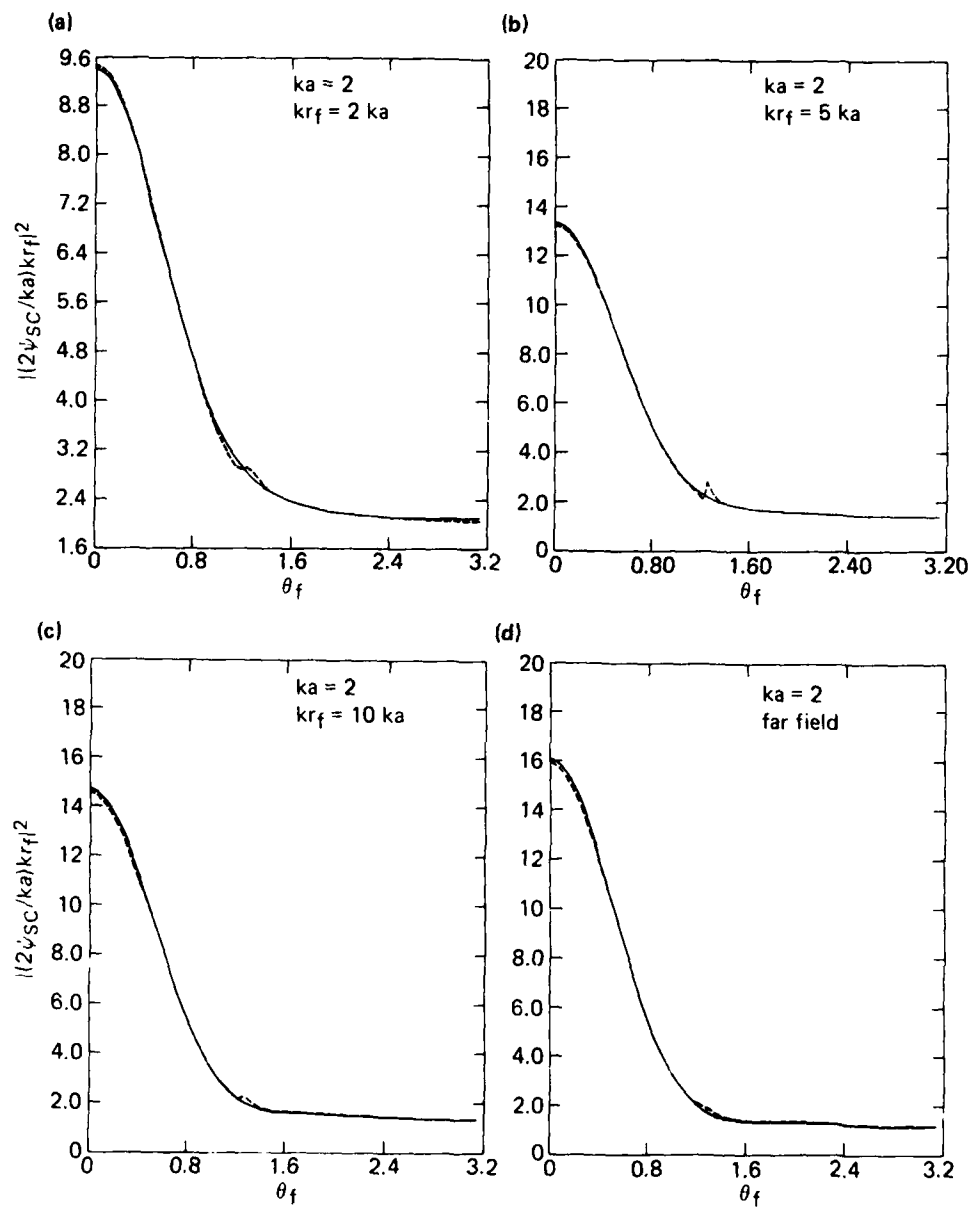
FIGURE 6. Plots of $|(2\psi_{SC}/ka)kr_f|^2$ for scattering from an acoustically soft sphere with size parameter equal to 2 as a function of θ_f for four selected values of kr_f. Plots (a)-(d) show that the variational results (-----) are in good agreement with the exact answer (———) for most values of θ_f. The maximum percent error for each case is: (a) 4.0% at $\theta = 1.27$ radians. (b) 28% at $\theta = 1.26$ radians. (c) 12% at $\theta = 1.27$ radians. (d) 8.6% at $\theta = 1.29$ radians.

FIGURE 7. Plots of $|(2\psi_{sc}/ka)kr_f|^2$ for forward scattering from an acoustically soft sphere as a function of ka for four selected values of kr_f. Plots (a) - (d) show that the variational results (-----) are in reasonable agreement with the exact answer (————) for all values of ka. The maximum percent error for each case is: (a) 26% at ka = 96.3; (b) 23% at ka = 80.3; (c) 6.9% at ka = 100; (d) 1.3% at ka = 1.7.

234

CALCULATION OF TIME-RESOLVED SCATTERING OF FEMTOSECOND LIGHT PULSES FROM DIELECTRIC SPHERES

Chia-Ren Hu, Gregory H. Rose, and George W. Kattawar
Department of Physics. Center for Theoretical Physics
Texas A&M University. College Station. Texas 77843

RECENT PUBLICATIONS, SUBMITTALS FOR PUBLICATION, AND PRESENTATIONS:

A) C.-R. Hu. G. W. Kattawar. M. E. Parkin. and P. Herb. "Symmetry Theorems on the forward and Backward scattering Mueller Matrices for Light Scattering from a Nonspherical dielectric Scatterer", Appl. Opt. 26. 4159 (1987)

B) G. W. Kattawar, C.-R. Hu, M. E. Parkin, and P. Herb. "Mueller Matrix Calculations for Dielectric Cubes", Appl. Opt. 26, 4174 (1987).

C) K. A. Fuller and G. W. Kattawar, "Consummate solution to the Problem of Classical electromagnetic Scattering by an Ensemble of spheres. I: Linear Chains", Opt. Lett. 13, 90 (1988).

D) K. A. Fuller and G. W. Kattawar, "A Consummate solution to the Problem of Classical electromagnetic Scattering by Ensembles of spheres. Part II: Clusters of arbitrary configuration", Accepted for publication in Opt. Lett.

E) W. White, E. Fry, and G. W. Kattawar. "Scattering of Femtosecond Pulses from Diectric Spheres", Presentation at the 1988 CRDEC Conference on Obscuration and Aerosol Research, June 1988.

F) G. H. Rose, C.-R. Hu, and G. W. Kattawar. "Calculations of Time-Resolved Scattering of Femtosecond Pulses from Diectric Spheres", Presentation at the 1988 CRDEC Conference on Obscuration and Aerosol Research. June 1988.

G) C.-R Hu. G. H. Rose, and G. W. Kattawar. "Calculations of Time-Resolved Scattering of Femtosecond Light Pulses from Diectric Spheres", in preparation for publication.

H) C.-R. Hu. "Quantum topological Phases from Cyclic sequences of Projections and General Validity of Geodesic constructions in some Optical Tests", in preparation for publication.

I)Four additional items under this contract are listed with the paper by W. E. White, C. Wang and E. S. Fry

ABSTRACT

We have written and tested a program to calculate the time resolved scattering of ultra-short pulses from dielectric spheres at any scattering angle. Preliminary results to compare with the earlier results of Rheinstein are presented. Several interesting features have been noted in our calculation and some of them are explained herein.

I. INTRODUCTION

One of the most-important frontiers of optical research today is the generation and the applications of ultra-short light pulses.Our experimental group, headed by E. S. Fry. have recently constructed an apparatus which is capable of generating light pulses

with temporal width as short as 27 femto-seconds. They are presently performing an experiment measuring the time-resolved scattering of such pulses from a dielectric cylinder or a sphere (using pulses with 35-40 femtosecond width.) In order to eventually have a comparison between theory and experiment, we have developed a program to calculate the time-resolved scattering amplitudes and intensities (at any scattering angle) of a femtosecond light pulse from a dielectric sphere. (The case of scattering from a cylinder will be considered in the future.) In order to test our program, we first duplicated some of the cases studied previously by Rheinstein,[1] except that he considered only backscattering, whereas we have studied the time-resolved scattering amplitude and intensity for several scattering angles. (In this paper we shall only present our results for backscattering and forward scattering.) Another minor difference between the two works is that Rheinstein used a truncated cosine pulse profile, while we have used a Gaussian profile. We have also allowed the possibility of chirping in the pulse because the actual pulses generated in the laboratories do have some amount of chirping, which might affect the scattering result. (The effect of chirping will not be presented in this paper.) The output of such a scattering of a single incident pulse is a sequence of scattered pulses with various time delays and intensities (at any fixed scattering angle). We have obtained good agreement on most of the main peaks obtained in Rheinstein's calculation, except that (1)there are a few weaker peaks that he obtained but we didn't, which may have been due to the different pulse profiles adopted, which can obscure some minor peaks, and (2)we obtained some additional weaker peaks which he may have neglected to report. In any case, we can say that the comparison has established the essential correctness of our program, and we are presently in the process of systematically studying the accuracy of our program by varying the discretization step sizes and the cut-offs in the k-integrals. etc. On the other hand, using the program we presently have, we have already discovered some new physics not reported before, and will briefly discuss later in this paper. A full understanding of these new features will require more extensive study and analyses, which will be published in the future. As a matter of fact, some of the puzzles discovered might need the brainstorming of other experts in the area of light-scattering in order to fully understand them. This study, therefore, when completed, can lead to a much better understanding of the scattering of ultra-short light pulses by aerosal particles, (or by defects in an optical fiber as a variation). The results should be useful in a wide range of applications, such as in LIDAR and optical communication, etc.

II. THEORY AND METHOD OF COMPUTATION

The basic theory of scattering of a light pulse from a dielectric sphere is very simple. The incident pulse is taken to have a Gaussian profile:

$$\mathbf{E}_i(z - ct) = E_0 \hat{e}_x \exp[-a(z - ct)^2/2 + ik_c(z - ct)]$$

$$= \int_{-\infty}^{\infty} E_{ki} \hat{e}_x e^{ik(z-ct)} dk/2\pi,$$

where $a = a_r + ia_i$, and a_i is the chirping parameter, and

$$E_{ki} = E_0 \left(\frac{2\pi a^*}{|a|^2} \right)^{1/2} \exp\left[-\frac{a^*(k - k_c)^2}{2|a|^2} \right]$$

Then the time-resolved scattered field is given by

$$E_{sc,\theta} = E_0 \frac{\cos\phi}{-ir} \int_{-\infty}^{\infty} \frac{dk}{k} \left(\frac{a^*}{2\pi|a|^2} \right)^{1/2} \exp\left[-\frac{a^*(k - k_c)^2}{2|a|^2} + ik(r - ct) \right] S_2(k,\theta),$$

$$E_{sc,\phi} = E_0 \frac{\sin\phi}{ir} \int_{-\infty}^{\infty} \frac{dk}{k} \left(\frac{a^*}{2\pi|a|^2} \right)^{1/2} \exp\left[-\frac{a^*(k - k_c)^2}{2|a|^2} + ik(r - ct) \right] S_1(k,\theta),$$

where S_1 and S_2 are the Mie scattering amplitudes. (See Bohren and Huffman[2].)

To numerically calculate these quantities, we have truncated the k-integral to a range covering four standard deviations of the Gaussian profile on each side of the peak, and then discretize this k-range into four hundred points. Thus far we have used Simpson's rule in the numerical integration, and have not investigated any possible improvement over this method. For the value of $\lambda_0 \equiv 2\pi/k_c$, we have used 6300Å, which roughly corresponds to the wavelength of the laser used in Fry's laboratory. To duplicate some of the cases studied by Rheinstein, we had to note that the quantity τ in his theory is the FWHM of the electric field of the incident pulse. So the FWHM of the *intensity* of his incident pulse is only 0.72811τ. This leads to somewhat odd choices for the values of the FWHM in the results presented below, since for τ his choices were simply $d/4$ and $d/8$, where d stands for the diameter of the spherical scatterer. Using his notation we have taken the complex index of refraction to be $m = 1.60 + i0.01$ and $m = 2.50 + i0.01$. The sphere diameter d is taken to be $2\lambda_0$, $3\lambda_0$, and $4\lambda_0$ (and other values which we will not report here). To present a time-resolved scattering result, we need to define the zero of time. Rheinstein considered only backscattering, so for him it was convenient to take the zero of time to be the time a backscattered pulse from the front surface of the scatterer arives at the

detector. (Rheinstein called this "the front axial return".) We wish to eventually consider all angles of scattering. This makes his choice of the zero of time no longer convenient, so we take the zero of time to be when the pulse, traveling at the speed of light in vacuum, c, first arrives at the origin on a straight path, and then turn abruptly to the scattering direction in order to reach the detector on another straight path. For backscattering this choice for the zero of time is later than Rheinstein's choice by d/c. Rheinstein actually measured time in units of $d/2c$, or, in his words, "position of observed return in sphere radii". Then our "dimensionless time" is Rheinstein's "dimensionless time" minus two. Thus for our zero of time, the front axial return for backscattering occurs at $-d/c$ (or -2 in dimensionless units), and is not presented below, since our plots are all for $t > 0$ only. In the plots, we have also indicated "the transit time" which is defined to be d/c times the real part of m. We now present briefly some of our results in the next section, with a fuller account of our results to be given in a future publication.

III. RESULTS AND DISCUSSION

Figures 1-3 show the time-resolved scattered intensity I_l as a function of time, for three values of the sphere diameter, namely, $d/\lambda_c = 4$, 6, and 8. Dividing the abscissa scale by $(d/2c)$ and then adding two to it converts it to Rheinstein's abscissa scale. The index of refraction is $1.60 - i0.01$ for all three cases, and the FWHM for the intensity of the incident pulse is fixed relative to d, corresponding to Rheinstein's choice of $\tau = 0.5a$. Solid lines give backscattering, and the dotted lines give forward scattering. The subscript l in I_l refers to the parallel component, meaning that both the incident and the scattered electric fields are in the scattering plane. For forward and backward scattering from a spherical scatterer this component is trivially equal to the other (perpendicular) component,[3] I_r, (for which both the incident and the scattered electric fields are perpendicular to the scattering plane,) so there is no need to present the other component. In Fig.4, we have shown one case for $m = 2.50 - i0.01$. The other parameters are such that it corresponds to Rheinstein's case with $a/\lambda_c = 2$ and $\tau = 0.5a$. Fig.4 and Fig.1 should be compared with Rheinstein's Fig.11 and Fig.12, except that his plots are on a linear scale, whereas ours are semi-log, which reveals the weaker peaks more clearly.

In Tables I and II we have compared the positions of the major backscattering peaks in Figs.1 and 4 with those found by Rheinstein. It is clear that the agreement is quite good except that a few of the minor peaks found by Rheinstein are not obtained in our calculation. However, examining the plots reveal that these 'missing' peaks are

probably hidden in the shoulders of the neighboring more major peaks, and are simply not resolved. Although we have deliberately chosen the same FWHM for the incident pulse as in Rheinstein's calculation. the different pulse shapes adopted in the two calculations can still occationally lead to different minor peaks being obscured by the nearby major peaks.

Rheinstein tried to understand the positions of the larger-intensity backscattering peaks in terms of the axial rays (back-and-forth reflection one or more times along the axis), the bounce rays (two refractions with one or more internal reflections in betwreen), the stationary rays (not exactly backscattering bounce rays which happen to be a stationary function of the exit angle near the backward direction). and the surface waves (waves travering along the surface of the sphere but can make any number of critical angle short-cuts into the sphere allowed by the path length). All of these are the result of simple geometrical optics considerations. except for the conceptual existence of a surfave wave. For the sake of convenience. We shall refer to all of them as the 'classical' peaks. The idenfications of these 'classical' peaks are given in Table I and II. As may be seen from these tables, the difference between these predicted positions and the calculated ones based on such simple 'classical' pictures appears to be much larger than can be explained in terms of the inaccuracies of the calculations. (Our calculated positions of the peaks also differ slightly from Rheinstein's results, but this difference is much smaller than with the theoretical predictions based on the 'classical' picture.) This is particularly true with the higher-order surface waves occuring at larger delays. which strongly suggests that the surface wave velocity may not be simply the speed of light in vacuum,[4] as was assumed by Rheinstein in his determination of the positions of such returns. A closer theoretical look into this question will be made in the future. Rheinstein did not look into other scattering angles. Comparing the backscattering results (solid lines) with the forward-scattering results (dotted lines) in Figs.1-4. we notice one important difference: The back-scattering time-resolved intensities appear to be all made of only those 'classical' peaks (possibly with small 'non-classical' corrections to their positions). whereas the forward-scattering time-resolved intensities appear to be given by similar 'classical peaks' *plus a nearly time-independent background.* We think that this background is due to diffraction. One way to see this is by increasing the absorptive (or imaginary) part of the index of refraction to essentially metallic values. One such case is shown in Fig.5. where one finds that almost all 'classical' peaks are suppressed. and one is left with only the background in the forward scattering due to diffraction. We think that we know why this background is essentially

239

independent of time — it is truely a constant of time only if the pulse is not confined at all in the directions transverse to the direction of propagation — but we are still in the process of understanding some quantitave aspects of this background contribution, such as (1)why it appears to be an oscillatory function of the sphere diameter (see Fig.1-3), (2)what is the origin of the small oscillations that appear to be superposed on this background (see especially Fig.4), and (3)how do the frequencies of these oscillations depend on the parameters, etc.

The parameters in Figs.1-4 were all chosen to duplicate some of the cases investigated by Rheinstein. Actually the FWHM's chosen there are not practical. For example, the FWHM of the case presented in Fig.3 corresponds to an incident pulse of roughly 3fs pulse width. This pulse width is clearly too small to be realizable even in the near future. Fig.6 corresponds to the same choice of all parameter values as in Fig.3, except that the incident pulse width is increased by a factor of four — to about 12fs, which is still small in comparison with that of the pulse generated in Fry's laboratory. Yet it is clear from this figure that practically all of the detailed 'classical peaks' have merged into one set of broad peaks, which appear to have a single principal period. It is clearly interesting to know what physics governs this period. We find that it can be explained in terms of the surface waves with the maximum number of short cuts at the critical angle into the dielectric sphere. Based on this idea we have derived the following formula for the period:

$$\{\pi + \frac{2\pi}{\pi - 2\sin^{-1}(1/m)}[(m^2 - 1)^{1/2} - \cos^{-1}(1/m)]\}d/c.$$

For the parameter values in Fig.6, this formula predicts the period to be $7.36 \cdot 10^{-14}s$, whereas from Fig.6 we can read off an average period of $7.42 \cdot 10^{-14}s$ (by using the total time elapsed between the first and the sixth peaks). The agreement is clearly very good, especially in view of the fact that the formula is supposed to be valid only in the asymptotic regime, i.e., as time approaches infinity, whereas Fig.6 shows only the first six 'broad peaks'. Furthermore, in the asymptotic regime the broad peaks are expected to occur rather regularly. This is clearly not quite the case near the sixth peak.

IV. EXPECTED DIRECTION OF FUTURE WORK

This short paper is only a progrss report of an on going research. However, from what we have presented in the previous sections, it should be clear that we have already made substantial progress in the understanding of the problem at hand, and have

found quite an amount of new physics in it. We also find that many unanswered questions exist about this problem, in spite of the fact that there exist several excellent earlier investigations. We believe that many of these unanswered questions can lead to very fundamental new perspectives on the scattering of a ultra-short light pulse by a small dielectric particle, and we plan to thoroughly investigate them. This includes: (1) understanding the origin of the discrepancies between the positions of the observed 'classical' peaks and their theoretically predicted values; (2) investigating the general appearances of the output pulse-trains as one varies the various parameters of the problem, including the size parameter of the scatterer, the real and imaginary parts of the index of refraction of the scatterer, the amount of chirping in the incident pulse, and the FWHM of the incident pulse, etc.; (3)investigating the scattering output at other scattering angles, and their possible interpretation; (4) studing the physical origin of the nearly constant background in the forward scattering intensity, and its quantitative aspects such as its apparent oscillatory dependence on the size parameter, how far in time will it remain 'constant', and the reason for the small oscillations that are superposed on the nearly constant background, etc. (5)studying the relative intensities of the various output peaks and their dependence on the various parameters; and finally and probably most importantly, (6)studying the intermediate pulse-width regime where the individual 'classical' peaks are not resolved, and the output is a much simpler structure of a set of broad peaks. It should be a fundamental contribution to the theory of scattering of ultra-short light pulses by dielectric particles if a simple theoretical picture could be developed in understanding this intermediate regime.

References

1. J. Rheinstein, IEEE trans. Antennas and Propagation, AP-16, 89 (1968).

2. C. F. Bohren and D. R. Huffman, *Absorption and Scattering of Light by Small Particles*,(Wiley, New York, 1983).

3. C.-R. Hu, G. W. Kattawar, M. E. Parkin, and P. Herb, Appl. Opt. 26, 4159 (1987).

4. The surface wave has been extensively discussed in V. de Hulst, *Light scattering by Small Particles*, (Dover, New York, 1957). This reference did point out that the speed of a surface wave on a conducting sphere is less than c, (c.f., p.368 of V. de Hulst,) but the corresponding speed of a surface wave on a dielectric sphere was not discussed.

Table I. Comparison of the positions of the major backscattering peaks obtained in this calculation with those obtained by Rheinstein (Ref. 1) for the case depicted in Fig. 1.

Position of Observed Return (as is given by Rheinstein)		Identification	Predicted Position
From this work	From Rheinstein		
	5.95	surface wave N=1, M=1	5.848
		stationary ray p=2 (?)	6.17
6.498 (*)	6.525	rear axial	6.400
		bounce ray (glory) N=1, p=2	6.560
12.779		axial ray (3 internal refl.)	12.800
		surface wave N=2, M=3	13.544
	14.45	surface wave N=2, M=4	14.251
		bounce ray N=2, p=5	14.841
15.091 (*)	15.05	surface wave N=2, M=5	14.958
	15.6	?	
		axial ray (5 internal refl.)	19.200
		surface wave N=3, M=5 (?)	21.241
		surface wave N=3, M=6 (?)	21.948
22.972	22.975	surface wave N=3, M=7 (?)	22.655
24.253 (*)	24.525	surface wave N=3, M=8 (?)	23.361
		axial ray (7 internal refl.)	25.600
		surface wave N=4, M=8 (?)	29.645
		surface wave N=4, M=9 (?)	30.351
		surface wave N=4, M=10 (?)	31.058
32.685 (*)	32.675	surface wave N=4, M=11 (?)	31.765
33.930		surface wave N=4, M=12 (?)	32.471
		surface wave N=5, M=12 (?)	38.754
		surface wave N=5, M=13 (?)	39.461
		surface wave N=5, M=14 (?)	40.168
42.154 (*)		surface wave N=5, M=15 (?)	40.874
		surface wave N=6, M=15 (?)	47.158
		surface wave N=6, M=16 (?)	47.864
		surface wave N=6, M=17 (?)	48.571
49.915		surface wave N=6, M=18 (?)	49.278
51.734 (*)		surface wave N=6, M=19 (?)	49.984
		surface wave N=7, M=19 (?)	56.267
		surface wave N=7, M=20 (?)	56.974
		surface wave N=7, M=21 (?)	57.681
59.860 (*)		surface wave N=7, M=22 (?)	58.387
		surface wave N=8, M=22 (?)	64.671
		surface wave N=8, M=23 (?)	65.377
		surface wave N=8, M=24 (?)	66.084
		surface wave N=8, M=25 (?)	66.791
69.501 (*)		surface wave N=8, M=26 (?)	67.497

(*) The locally largest intensity peaks

Table II. Same as Table I except that it is for the case depicted in Fig. 4.

Position of Observed Return (as is given by Rheinstein)		Identification	Predicted Position
From this work	From Rheinstein		
4.647			
5.364	5.35	surface wave N=1, M=0 (?)	5.142
7.414	7.45	surface wave N=1, M=1	7.406
10.022 (*)	9.975	rear axial	10.000
		surface wave N=2, M=1	13.689
		surface wave N=2, M=2	15.923
16.384			
18.424	18.45	surface wave N=2, M=3	18.217
	19.925	axial ray?(3 internal refl.)	20.000
20.513 (*)	20.525	surface wave N=2, M=4	20.481
22.615	22.55		
27.567		surface wave N=3, M=4 (?)	26.764
29.506	29.40	surface wave N=3, M=5 (?)	29.028
	29.775	axial rays?(5 internal refl.)	30.000
31.581	31.60	surface wave N=3, M=6 (?)	31.292
33.627 (*)	33.625	stationary ray p=7 (?)	33.9
35.673		surface wave N=4, M=5 (?)	35.311
		surface wave N=4, M=6 (?)	37.575
	39.25	surface wave N=4, M=7 (?)	39.839
40.565		axial rays?(7 internal refl.)	40.000
42.589	42.625	surface wave N=4, M=8 (?)	42.103
	43.125	bounce ray (?)	
44.887	44.775	surface wave N=4, M=9 (?)	44.367
46.726 (*)	46.70	surface wave N=5, M=7 (?)	46.122
48.448		surface wave N=5, M=8 (?)	48.386
		surface wave N=5, M=9 (?)	50.650
53.777		surface wave N=5, M=10 (?)	52.915
55.720		surface wave N=5, M=11 (?)	55.179
57.504		surface wave N=5, M=12 (?)	57.443
59.735 (*)		surface wave N=6, M=10 (?)	59.198
61.451		surface wave N=6, M=11 (?)	61.462
62.479		surface wave N=6, M=12 (?)	63.726
66.982		surface wave N=6, M=13 (?)	65.990
68.883		surface wave N=6, M=14 (?)	68.254
70.679 (*)		surface wave N=7, M=12 (?)	70.009
72.752		surface wave N=7, M=13 (?)	72.273
74.514		surface wave N=7, M=14 (?)	74.537
75.702			
		surface wave N=7, M=15 (?)	76.801
79.968		surface wave N=7, M=16 (?)	79.065
		surface wave N=7, M=17 (?)	81.329
		surface wave N=8, M=14 (?)	80.820
82.139			
83.812 (*)		surface wave N=8, M=15 (?)	83.084
		surface wave N=8, M=16 (?)	85.348
87.583		surface wave N=8, M=17 (?)	87.612
88.914			
		surface wave N=8, M=18 (?)	89.876
		surface wave N=8, M=19 (?)	92.140
		surface wave N=8, M=20 (?)	94.404
95.422			
96.921 (*)			
98.810			

(*) The locally largest intensity peaks.
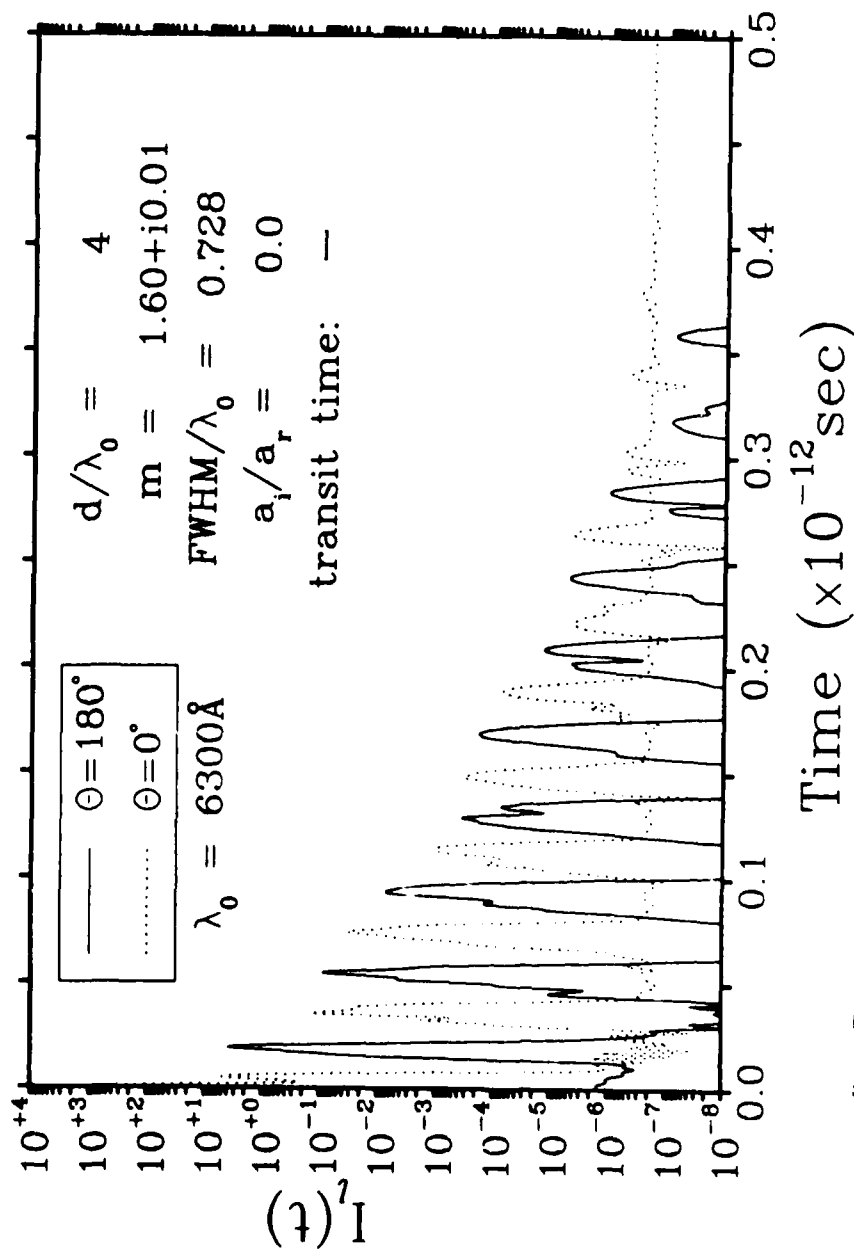
Fig 1 Time-resolved forward (dotted line) and backward (solid line) scattering intensity for $d/\lambda_0 = 4$. The other parameters are: $m = 1.60 + i0.01$, FWHM (of the incident pulse intensity) $= 0.182d$, $a_i = 0$, and $\lambda_0 = 6300\text{Å}$. The chosen FWHM corresponds to Rheinstein's choice of $\tau = 0.5a$.
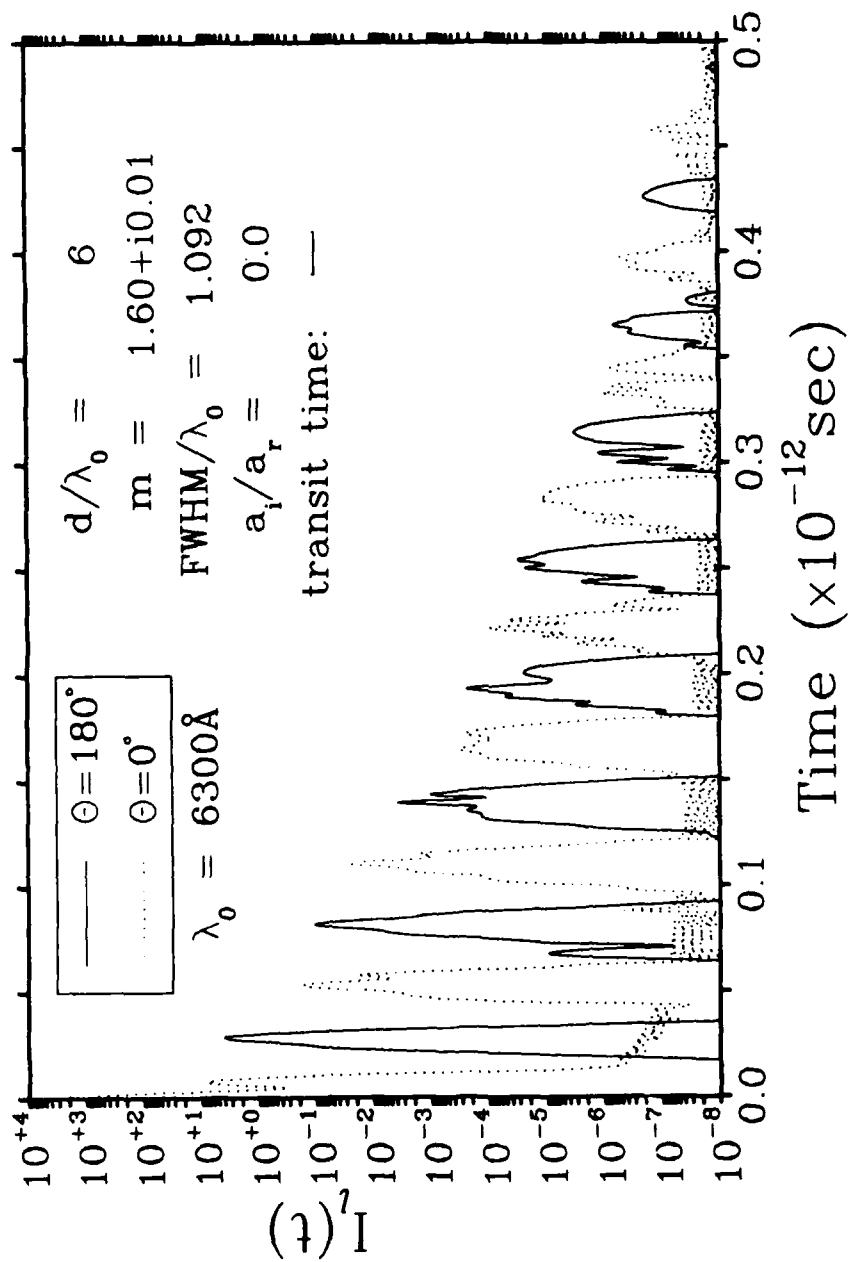
Fig.2 Same as Figure 1, except that $d/\lambda_0 = 6$.
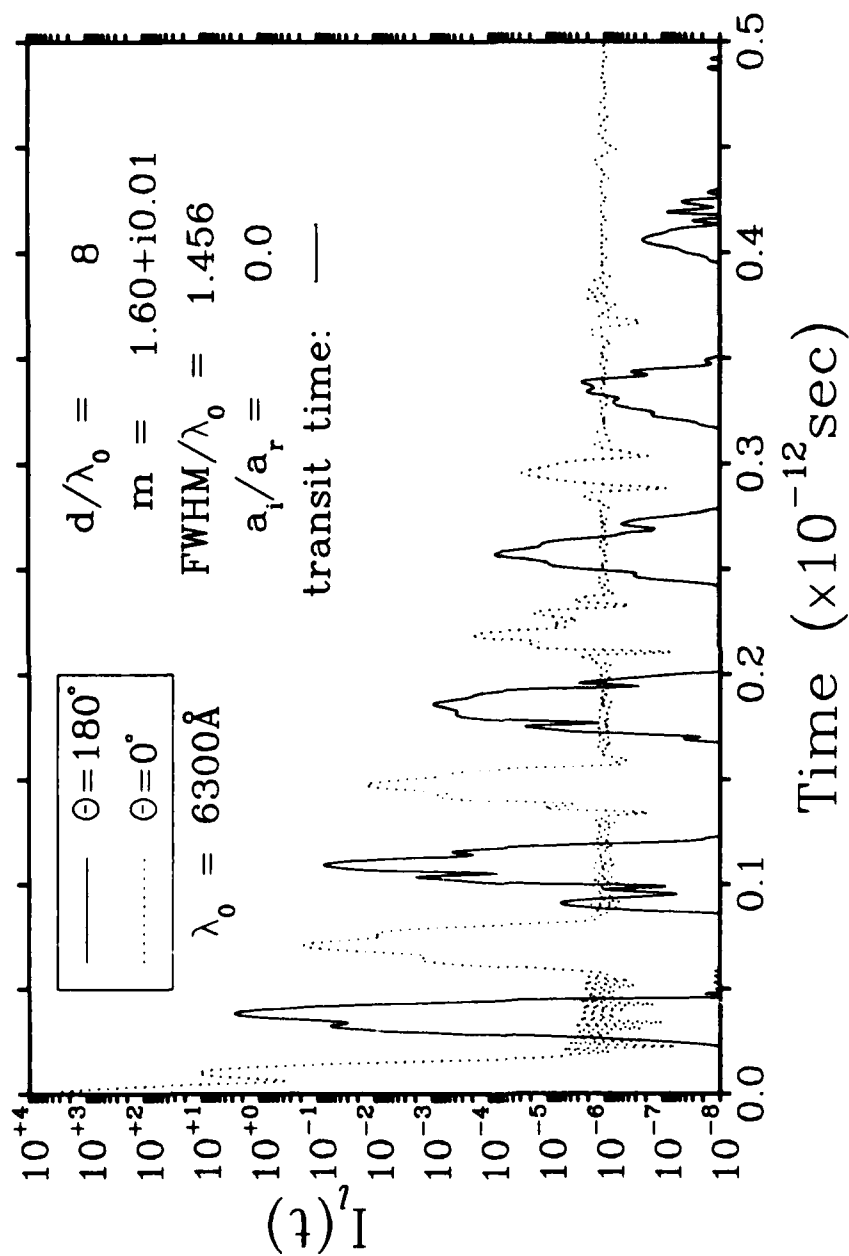
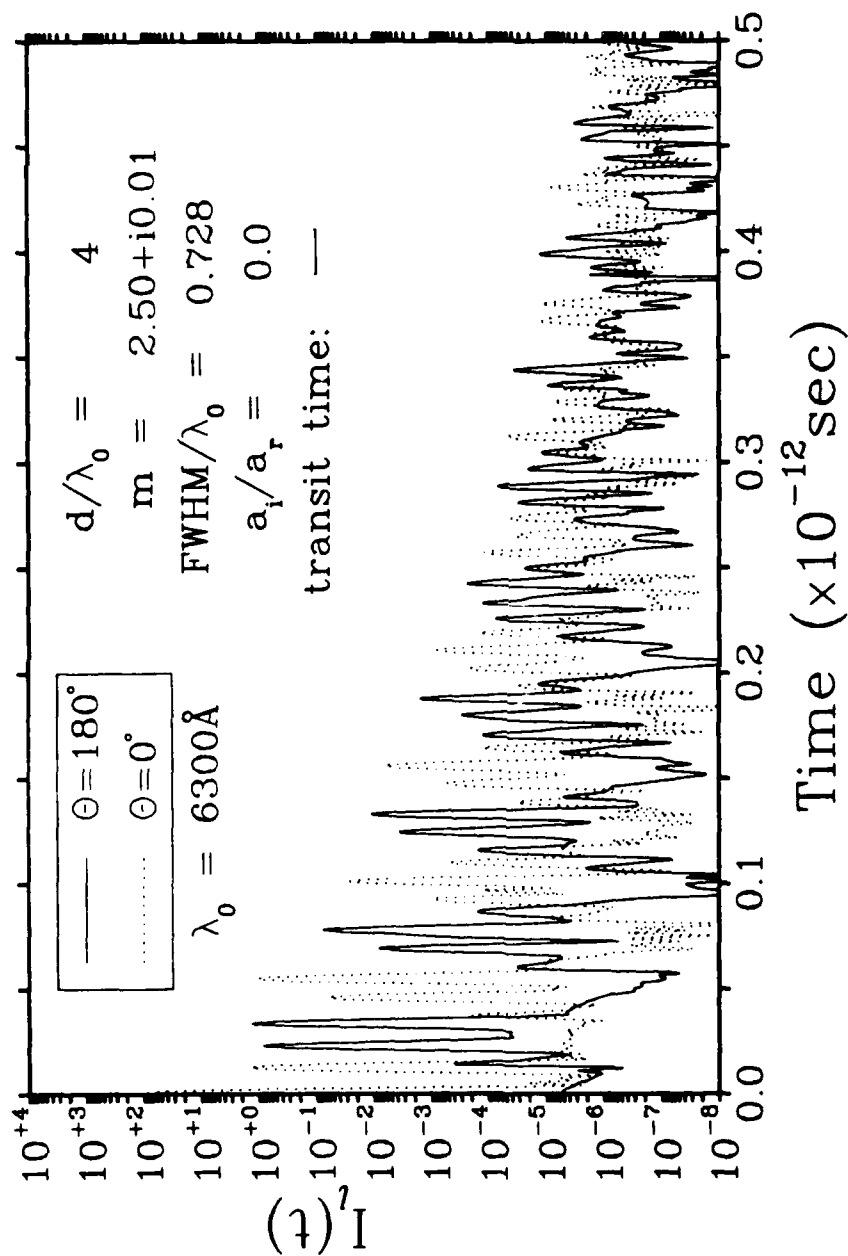Fig.3 Same as Figure 1, except that $d/\lambda_0 = 8$.
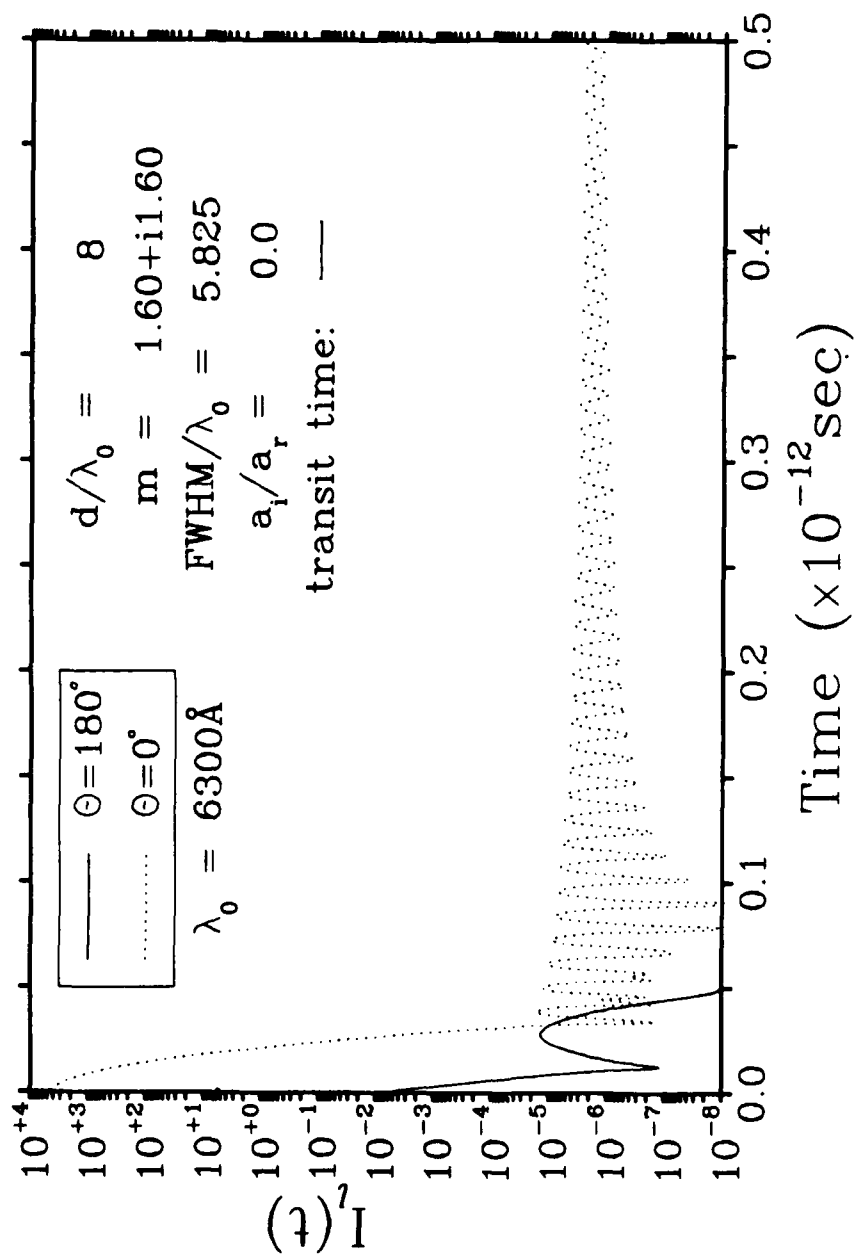
Fig.4 Same as Figure 1, except that $m = 2.50 + i0.01$.

Fig.5 Same as Figure 3. except that $m = 1.60 + i1.60$. and that the FWHM is a factor of four larger (as in Fig.6).
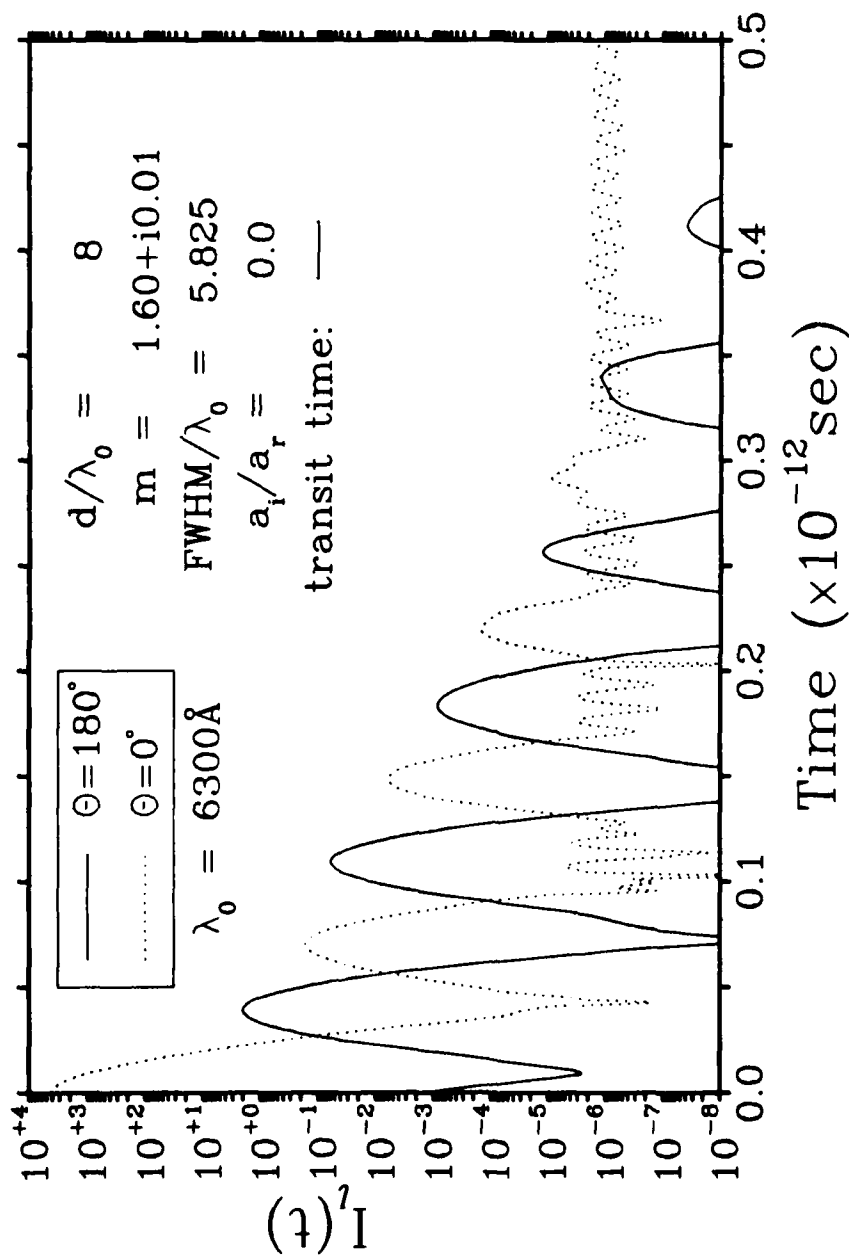
Fig.6 Same as Figure 3, except that the FWHM is increased by a factor of four to 0.728d.

Blank

CAN REPRODUCIBILITY BE ESTABLISHED FOR S_{34} SCATTERING IN A MICROBIAL SYSTEM?

WILLEM P. VAN DE MERWE, DONALD H. HUFFMAN, BURT V. BRONK

UNIFORMED SERVICES UNIVERSITY OF THE HEALTH SCIENCES
UNIVERSITY OF ARIZONA
CHEMICAL RESEARCH DEVELOPMENT AND ENGINEERING CENTER

ABSTRACT

This paper describes our effort to establish a "standard" for polarized light scattering from microorganisms. Specifically, we report conditions under which the S_{34} Mueller matrix element as a function of scattering angle was reproducible for E. Coli K12 grown on different occasions and is expected to be reproducible from laboratory to laboratory.

We also give an example where a change in preparation of the same organism (i.e. the stage of growth) gives a substantial change in the signal observed. Experiments to be performed in the coming year include the study of wavelength-dependence of the signals and the search for conditions to ensure the uniqueness of the signal. We will also measure changes in signal or the lack thereof during modification of internal structure of a bacterium during phage induction.

INTRODUCTION

Since the mid-seventies several investigators have reported "organism-unique" polarized light scattering signals as a function of scattering angle. It was suggested that one could identify (fingerprint) micro-organisms by the signal. However, after these many years of investigation, no-one has yet published a unique scattering signal that was reproduced in other laboratories. Nor has anyone reported the effects of various parameters on the signal so that one might understand the sensitivity of the signal to slight variations, such as; size distribution, DNA content, growth conditions, etc. In this report we give an example in which a small change in growth conditions (i.e. the stage of growth) produces changes in the scattering signal which

are larger than changes which others have indicated can distinguish between similar organisms. The signals reported are the angular-dependent Mueller matrix elements that describe the scatterer. The matrix transforms the Stokes vector which completely characterizes the intensity and polarization state of the light.

To obtain reliable signals one has to understand the experimental set-up very well and recognize the various artifacts that could impact the final signal. In addition, one has to understand the biological parameters very well and recognize the effects of different preparation procedures. In other words, in order to establish whether or not one can "uniquely" identify a micro-organism by measuring a Mueller matrix element one needs expertise in experimental physics as well as in microbiology. If it turns out that the signal does not uniquely identify the organism, one must establish what the limitations are. In that case, maybe one can distinguish groups of organisms that, as far as the scattering signals are concerned, are look-alikes.

EXPERIMENTAL SET-UP

At the University of Arizona we used the experimental apparatus set up several years ago by Huffman which is described in detail elsewhere (1,2). A similar apparatus was set up recently at the Uniformed University of the Health Sciences (USUHS). In it, a HeNe laser beam is modulated by a time-varying retarder that converts the linearly polarized beam into a beam that alternates between left and right circular-polarized light at a frequency of 50 kHz. The scattered light passes through a linear polarizer at 45 degrees to the scattering plane, and is detected by a photomultiplier tube. With a lock-in amplifier the 50 kHz component is measured. By electronically keeping the dc component of the PMT-signal constant in the particular configuration, one measures the following combination of matrix elements:

$$(S_{14} + S_{34})/(S_{11} + S_{31})$$

Since for our system S_{14} and S_{31} are negligible, this may be approximated by:

$$S_{34}/S_{11}$$

The signal is calibrated by forcing the signal into a pure polarization state (in our case with the aid of a quarter-wave plate) and expressing the measured signals as a percent of the pure-state signal.

252

BIOLOGICAL PREPARATIONS

BIOLOGICAL PREPARATIONS

For our standard scattering organism we chose Escherichia Coli K(12) with heat-inducible lambda virus incorporated in the main chromosome. Some of the advantages of this bacterium are that one can easily induce the expression of the virus, thus ensuring (with a large probability) that indeed one has the correct bacterium and not a look-alike contaminant that was grown instead. In addition, one can upon induction change the contents of the bacterium in a predictable way. Upon induction the lambda virus genes are transcribed and within a known time (about 30-50 minutes, depending the temperature) 100 to 200 viruses have been formed in the bacterium and burst open the cell. This last step is easy to "eyeball" since it gives rise to a sharp change from a cloudy suspension to a clear one.

It is well-known that the volume and contents of an E. Coli cell can be modified greatly by simply changing the medium in which it is grown (3). Some other simple modifications giving rise to measurable changes in the cell include the stage of growth, the growth medium, the growth temperature, etc.

In general when one starts growing bacteria the cells are in a "lag" phase, that is they are not directly dividing. After this initial phase the bacteria enter into the "log" phase where the bacteria are actively dividing with the number of bacteria growing exponentially (the rate of growth is characterized by the "doubling time"). After the concentration of bacteria reaches a certain value, the bacteria start to interact and the growth rate decreases, until the bacteria stop dividing and the bacteria are said to have entered the "stationary" phase. Figure 1 pictures a typical growth curve.

The E.Coli was grown at 30 degrees C, in LB broth with vigorous shaking.

The stationary phase was generally harvested after growing the culture overnight. The late-log phase would be harvested when the optical density (OD) of the sample was about 0.3, and the mid-log phase when the bacteria are actively dividing at an OD of 0.1. The cells were spun down at a moderate speed at resuspended in 0.9% NaCl at an OD of 0.05.

EXPERIMENTAL RESULTS

The E. Coli K12 was used as described above, at the USUHS and the University of Arizona.

Figure 2 shows the results of a reproducible signal between the two laboratories.

Figure 3 shows the reproducibility within the USUHS.

Figure 4 shows the comparison of the signal obtained during log and stationary phase.
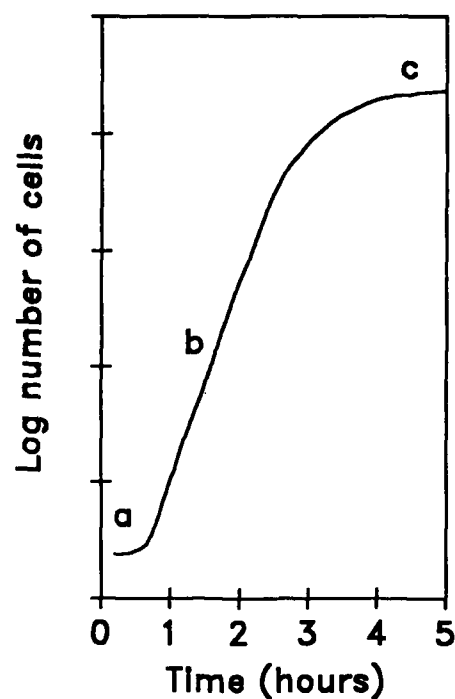
FIGURE 1. TYPICAL BACTERIAL GROWTH CURVE. Phase a, the bacteria are not yet actively dividing (lag phase). Phase b, the number of bacteria increases exponentially (log phase). Phase c, the bacteria stop dividing (stationary phase).
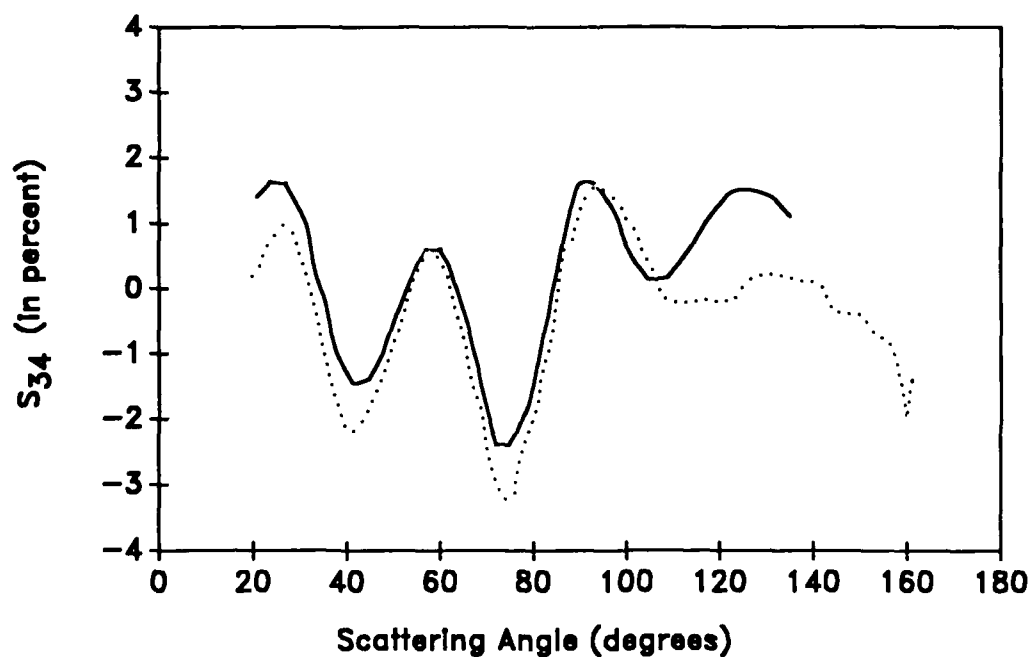
FIGURE 2. LATE-LOG PHASE E.COLI S_{34} AS A FUNCTION OF SCATTERING ANGLE. The solid line represents data obtained at the USUHS and the dotted line data obtained at the UofA. The figure exemplifies the reproducibility between laboratories.
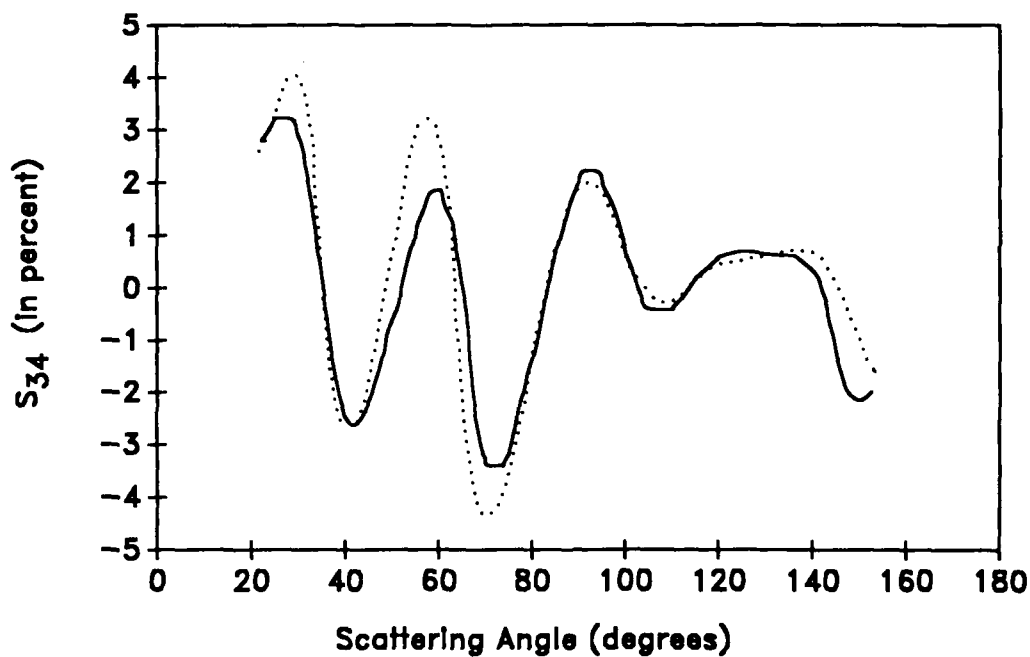
FIGURE 3. STATIONARY PHASE E.COLI S_{34} AS A FUNCTION OF SCATTERING ANGLE. Both solid and dotted lines represent data obtained at the USUHS on separate occasions from different batches. The figure exemplifies the reproducibility within the same laboratory.
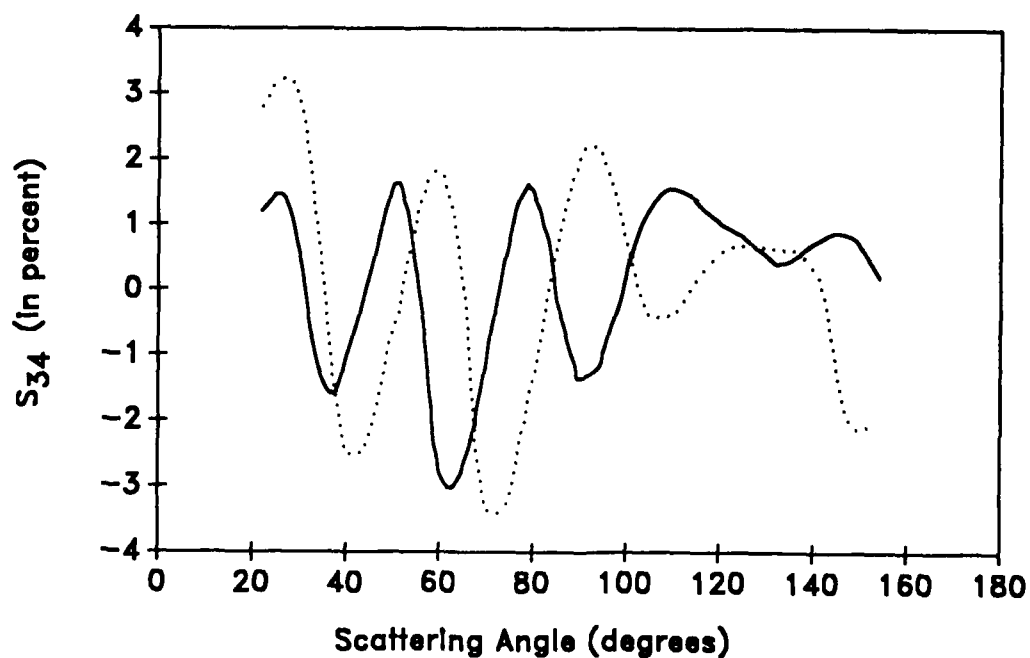
FIGURE 4. MID-LOG AND STATIONARY PHASE E.COLI S_{34} AS A FUNCTION OF SCATTERING ANGLE. The solid line represents the mid-log phase and the dotted line the stationary phase.

Additional experiments were performed using different wavelengths, dilution and growth media, during induction of the E. Coli, amongst others, as well as organisms of different shape. From these experiments it is becoming clear that the location of the peaks as well as the overall shape of the graph is very reproducible, given the same biological parameters. The height of the peaks depends more on the optics as well as the OD of the sample.

DISCUSSION

From the data collected this far we may conclude that under very well defined conditions one can expect a reproducible angular-dependent scattering signal S_{34}. Ongoing studies indicate that, in the visible wavelength region, the signal depends strongly on the size and shape of the organism, rather than on the contents. This is evidenced by the fact that the signal barely changed upon induction of the virus until the E. Coli burst open, after which the signal was reduced to zero and the S_{12} became identical to the Rayleigh signal for the virus alone. Also, comparing the signals obtained with green and red HeNe lasers, using different size distributions indicate that slightly smaller E. Coli measured with green light are identical to somewhat larger E. Coli measured with red. Studies will have to be undertaken, therefore, in the blue and ultra-violet region of the spectrum, where more interaction between the radiation and macromolecules takes place.

Evaluating our current results, we are left with the impression that,as far as the S_{34} signal is concerned, we may be able to "footprint" rather than "fingerprint" microorganisms.

REFERENCES

Hunt, A.J. and Huffman, D.R., A new polarization-modulated light scattering instrument
Rev. Sci. Instrum., 44, 1753, (1973)

Bickel, W.S., et.al., Application of polarization effects in light scattering: A new
biophysical tool
PNAS, 73, 486, (1976)

Bronk, B.V. and Walbridge, D., Sensitivity to UV radiation as a function of DNA content in E-
Coli B/r
Bioph.J. 31, 381, (1980)

SCATTERING OF LINEARLY POLARIZED LIGHT
FROM A DIELECTRIC HELIX AND SPHEROID
INCLUDING SELF-INTERACTION

Richard D. Haracz, Leonard D. Cohen, Alice R. W. Presley
and
Ariel Cohen

Department of Physics and Atmospheric Science
Drexel University, Philadelphia, Pa. 19104

ABSTRACT

A new technique for determining the scattering intensities for
dielectric targets of arbitrary shape is described, and applications to a
helical and a spheroidal target are presented. The method involves including
self-interactions within the target by approximating the polarization matrix
inside the target by non-perturbative means. The results are compared with
perturbation theory (the Shifrin method).

THE INTEGRAL EQUATION FOR THE POLARIZATION MATRIX

The Shifrin condition for the scattering of light from a dielectric target is

$$2ka(m-1) < 2, \tag{1}$$

where $k_o = 2\pi/\lambda$, and "a" is a critical dimension of the target, for example the diameter of a circular cross section. This condition limits the size of the target relative to the wavelength of the incident light, and it physically means that the target cannot be so large that internal standing waves can be established. The perturbation theory uses an expansion that relies on the small size of k_o a.

We are presenting an approach that is nonperturbative, but which still requires that internal resonances will not occur. The starting point is the integral equation for the scattered wave:

$$E(r) = E_o\, e^{ik\, r} + \nabla \times \nabla \times \int dV'\, (m^2 - 1)/(4\pi)$$
$$[e^{ik\,|r-r'|}/\,|r-r'|]\ E(r') \quad + (1-m^2)\, E(r) \tag{2}$$

The effective field is defined by

$$E_{eff}(r) = (m^2 + 2)/3 \quad E(r), \tag{3}$$

and substitution of this into eq. (2) gives the equation

$$\mathbf{E}_{\text{eff}}(\mathbf{r}) = \mathbf{E_o}\, e^{ik\,\mathbf{r}} + \alpha\, \nabla \times \nabla \times \int dV'\; e^{ik\,|r-r'|}/\,|r-r'|$$

$$\mathbf{E}_{\text{eff}}(\mathbf{r}')\; -8\pi/3\;\alpha\, U(\mathbf{r})\;\mathbf{E}_{\text{eff}}(\mathbf{r}), \tag{4}$$

where

$$\alpha = 3/(4\pi)(m^2-1)/(m^2+2)$$

and $U(\mathbf{r})$ is one if $\mathbf{r}$ is inside the target and zero otherwise. The singularity is accounded for by separating out an infinitesimal region surrounding $\mathbf{r} = \mathbf{r}'$ as described in Appendix V of Born and Wolf with the result:

$$\mathbf{E}_{\text{eff}}(\mathbf{r}) = \mathbf{E_o}\, e^{ik\,\mathbf{r}} + \alpha\,\lim_{\sigma \to 0}\int_\sigma dV'\; (\nabla.\nabla + k^2)$$

$$[e^{ik\,|r-r'|}/\,|r-r'|\;]\;\mathbf{E}_{\text{eff}}(\mathbf{r}')\;, \tag{5}$$

where σ is a small sphere surrounding the point $\mathbf{r}'=\mathbf{r}$.

THE POLARIZATION MATRIX

We next extract an equation for the polarization matrix from eq.(5) by defining the polarization matrix A:

$$(\mathbf{E}_{\text{eff}}(\mathbf{r}))_i = A_{ij}\,[\mathbf{E}_{\text{inc}}(\mathbf{r})]_j \tag{6}$$

Substitution into eq. (5) gives

$$A_{ij}(r) = \delta_{ij} + \alpha \int_\sigma dV' \, [e^{ik\,R}/R \,] \, [r_1 \, \delta_{ik} + (h_i + x'_i)(h_k + x'_k)$$

$$r_2] \; A_{kj}(r') \; e^{ik\,(r'-h)} \tag{7}$$

The geometry for this equation, specialized to a helical target, is shown in Figure 1. The vector **r'** locates a point in the target, and the vector **h** locates a point on the helical axis (or the center of a cross sectional disk, as the helix is formed by turning a cylinder into the shape of a helix).

Also, R is the distance from the source point **r'** to the field point **r**, and

$$r_1 = (k_2 - (1/R)^2 + i\,k/R\,),$$

$$r_2 = (-(k/R)^2 + 3/R^4 - 3ik/R^3). \tag{8}$$

The vector **h** shown in Figure 1 is directed from the common origin of the reference frame (x_0, y_0, z_0) target frame (x_t, y_t, z_t), where where z_0 is in the direction of incidence, and z_t is the symmetry axis of the helix. The x_t axis is in the plane formed by z_t and the incident direction specified by k_0.

Up to this point, no approximations have been made. If the integral equation (7) for A is solved, perhaps using an iterative approach starting with A being the unit matrix, the matrix A and hence the internal electric field would be known as accurately as the method of solution would allow. However, that is a very difficult problem.

THE MODEL ASSUMPTION AND APPLICATIONS

We first restrict the allowed target shapes to those that can be formed by turning a cylinder into any arbitrary shape. The radius of the cylinder can vary, but the applications that follow have a uniform radius.

The model assumption is that the polarization matrix A is constant

throughout each disk that composes the target, but A can vary from disk to disk as demanded by eq. (7). This flexibility accounts for self interactions. Figure 2 shows two such disks located by $h(\phi)$ and $h'(\phi')$, where the angular variables ϕ and ϕ' locate a position in the target (assumed a helix in Figure 2).

We consider two applications:

1. THE HELIX.

The vector h for a helical target has the specific form

$$h(\phi) = a \cos (\phi) \; i_t + a \sin (\phi) \; j_t + P/(2\pi) \; \phi \; k_t \qquad (9)$$

where i_t, j_t, k_t are unit vectors that define the target frame of reference.

The integral equation for the polarization matrix for a helix then takes the form

$$A_{ij} (\phi) = \delta_{ij} + \alpha \int_0 \; \sqrt{(a^2 + (P/(4\pi))^2} \; d\phi'$$

$$x \int_\epsilon (\phi) \; \rho \; d\rho \quad e^{-ik \; d(\phi,\phi')} \; x \int_0 \quad d\theta \; e^{ik \; R}/R$$

$$e^{i\rho\tau(\phi') \cos(\theta)} \quad T(\phi'->t)_{il} \; [r_1 \; \delta_{lm} \; A(\phi')_{mn}$$

$$+ \; [d(\phi,\phi')_l \; - \; \rho_l] \; [d(\phi,\phi')_m \; - \; \rho_m]$$

$$A(\phi')_{mn} \; r_2]\phi' \; T(t->\phi')_{nj} \qquad (10)$$

where the vector d locates the center of one disk relative to anoher as shown in Figure 2, "a" is the radius of the cylinder that forms the helix, "P" is the pitch of the helix, ρ is a vector from the center of a disk that locates points in the disk, and $T(t->\phi)$, for example, is the transfromation matrix from the target frame to a disk frame of reference. The disk frame of

reference has its z-axis perpendicular to the disk and its z axis in the plane formed by $\mathbf{k_o}$, direction of incidence, and the disk z axis. Each disk in the target has its own disk frame, and the above integral requires continual transformation from these frames of reference back to and from the target frame. The singularity region is accounted for by an integration on a disk from

$$\epsilon(\phi') = [\epsilon^2 - (a^2 + (P/(2\pi))^2 \, |\phi - \phi'|^2 \,)]1/2$$

to ϵ, the radius of the sphere surrounding the singularity, as long as the condition $(a^2 + [P/(2\pi)]^2 \, |\phi - \phi'|^2 \,) < \epsilon$ is satisfied. The separation distance for the helix is

$$R^2 = 2 \, a^2 \, (1 - \cos(\phi - \phi')) + [P/(2\pi)]^2 \, (\phi - \phi')^2 + \rho^2$$
$$- 2 \, d(\phi, \phi') \, \rho(\theta) \quad . \tag{11}$$

An iterative approach is use to solve eq. (10). The matrix is first written in polynomial form:

$$A_{ij}(\phi') = c0_{ij} + c1_{ij} \, z + c2_{ij} \, z^2 + \ldots + cn_{ij} \, z^n \,, \tag{12}$$

where $z = \sqrt{[a2 + (P/(4\pi))]^2} \, \phi'$. The iterative solution is then initiated by the values

$$c0_{11} = c0_{22} = c0_{33} = 1.0 \quad .$$

with all other components of $c0(i,j)$ zero. These are substituted into eq. (10), and the resulting matirx A is re-circulated until convergence is obtained.

Once the polarization matrix is obtained, the electric field in the far field is easily evauated by solving the one-dimensional equation

$$E(r)_i = E_{o\ i}\ \exp^{ik\ r} + \alpha \int d\phi\ [a^2 + [P/(2\pi)]^2]^{1/2}$$

$$J_1(q_{per}\ a)/\ (q_{per})$$

$$x\ \exp^{(q\ h(\phi))}\ \{T(\phi->ref)\}_{mn}\ \{A(\phi)_{no} - xn\ xo\ A(\phi)_{op}\}\phi$$

$$E_{op} \tag{12}$$

Here, $q = (r - k_o)/k_o$, and q_{per} is the component of q perpendicular to the disk located by the angular variable ϕ.

The specific helix used has seven turns, a wire radius of rw = 0.24 cm, a helix radius a = 1.83 cm, and a pitch P = 0.553 cm. The complex index of refraction is m = 1.626 + i 0.012. By way of contrast, the polarization matrix for an infinite cylinder of he same radius and material is

$$A_{inf} = \begin{matrix} 0.850, -0.002 & 0 & 0 \\ 0 & 0.850, -0.002 & 0 \\ 0 & 0 & 1.548, 0.013 \end{matrix}$$

The result of solving for A using the approach just described is

$$A_0 = \begin{matrix} 1.084, 0.075 & 0.199, -0.094 & 0 \\ 0.014, -0.011 & 0.819, -0.268 & 0.027, 0.009 \end{matrix}$$

$$0.097, -0.043 \quad 0.089, 0.017 \quad 2.052, 1.367,$$

and

$$A_{90} = \begin{array}{ccc} 0.500, -0.096 & 0 & 0 \\ 0 & 0.551, 0.404 & 0.101, 0.069 \\ 0 & 0.079, 0.128 & 0.576, 0.461 \end{array}$$

for the helical axis oriented along and perpendicular to the direction of incident light, respectively.

Results for the intensity $I_{11}(0,0)$ and $I_{22}(90,90)$ are shown in Figures 3 and 4, respectively. In the first case, the helical axis is along the direction of incidence, and in the second case, the helical axis is perpendicular to the scattering plane. The experimental points of Ru Wang[1] are shown as crosses, the results using the infinite cylinder polarization matrix is shown as a solid line, and the new results are shown with a solid line with solid circles. In each of these cases, the more accurate determination of the polarization matrix improves agreement with experiment.

2. THE SPHEROID (ASANO AND YAMAMOTO[2]).

The spheroid under study has the parameters: m = 1.33, C(size parameter) = 6, a/b (aspect ratio) = 5, and k_o = 1.0. In arbitrary units, the volume of this spheroid is 61.1, which is much larger than we were able to handle in our previous perturbation calculation[3].

In fact, the results of our present calculation for the intensities I_1 and I_2 are shown in Figure 5. The crosses that appear here are the results of

Asano and Yamamoto. We see that agreement is excellent.

REFERENCES

1. "Scattering of linearly polarized microwave radiation from a dielectric helix", R. D. Haracz, L. D. Cohen, A. Cohen, and Ru. T. Wang, Applied Optics **26**, 4632 (1987).

2. "Light scattering by spheroidal particles", S. Asano and G. Yamamoto, Applied Optics **14**, 29 (1975).

3. "Perturbation theroy for scattering from dielectric spheroids and short cylinders", R. D. Haracz, L. D. Cohen, and A. Cohen, Journal of Applied Physics **58**, 3322 (1985).
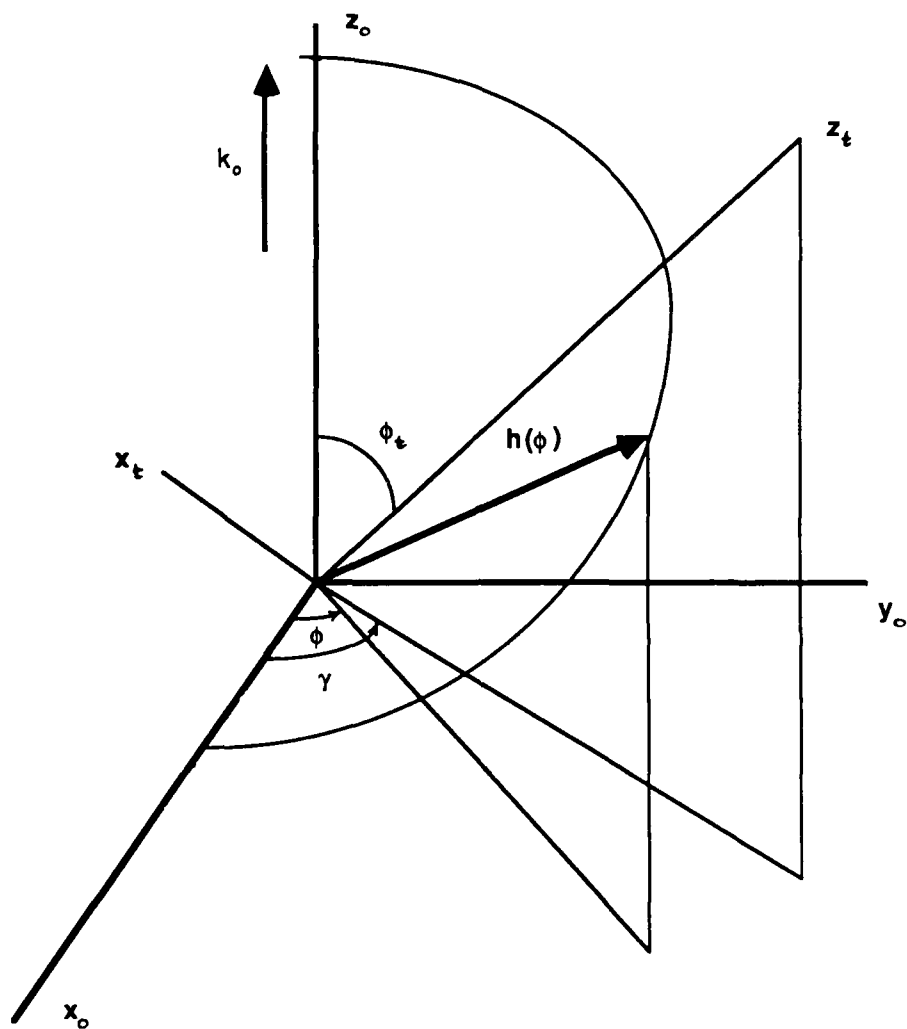
Figure 1. The reference frame (x_o, y_o, z_o) is shown along with the target frame (x_t, y_t, z_t). The z_o axis is along the direction of incidence, and x_o-z_o is the scattering plane. The z_t axis is the symetry axis of the target. The vector **h** traces out the central line of the turned cylinder that forms the target.

266
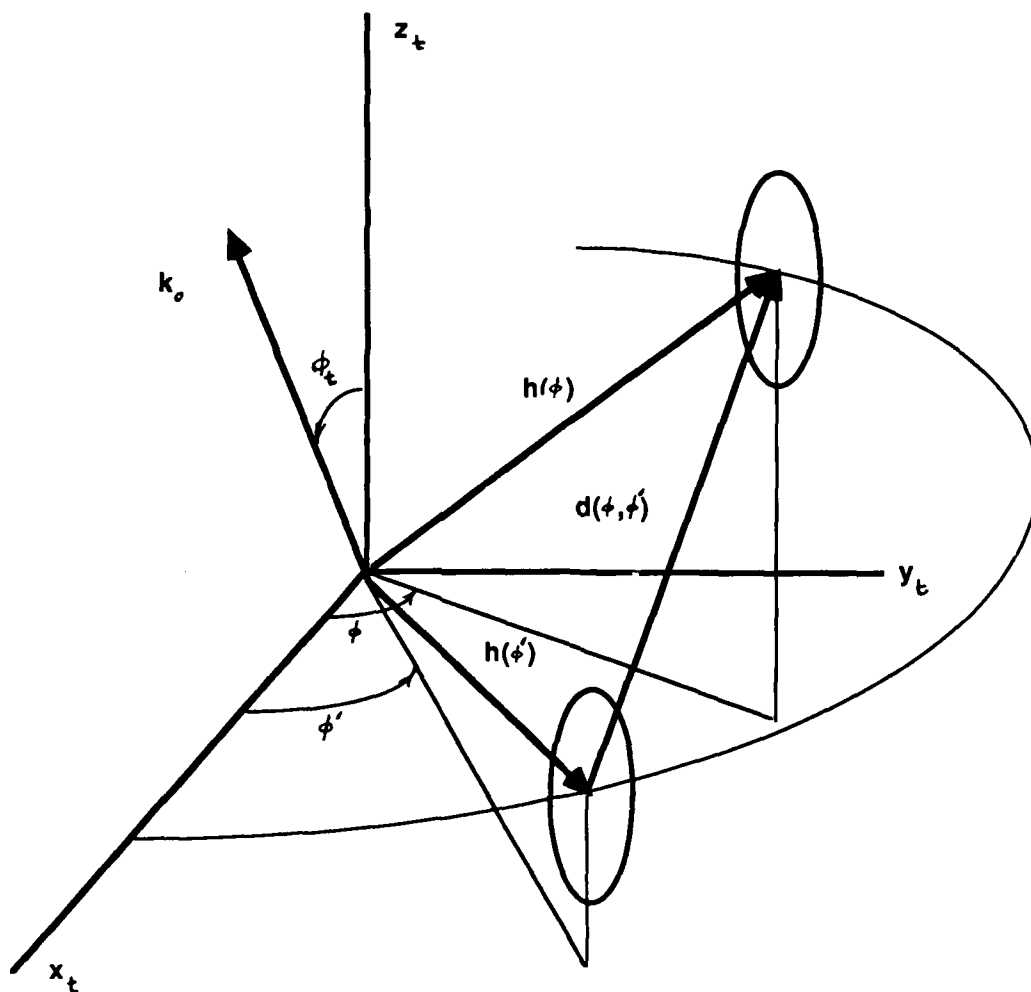
Figure 2. Two cross sectional disks in the target are shown in the target frame.
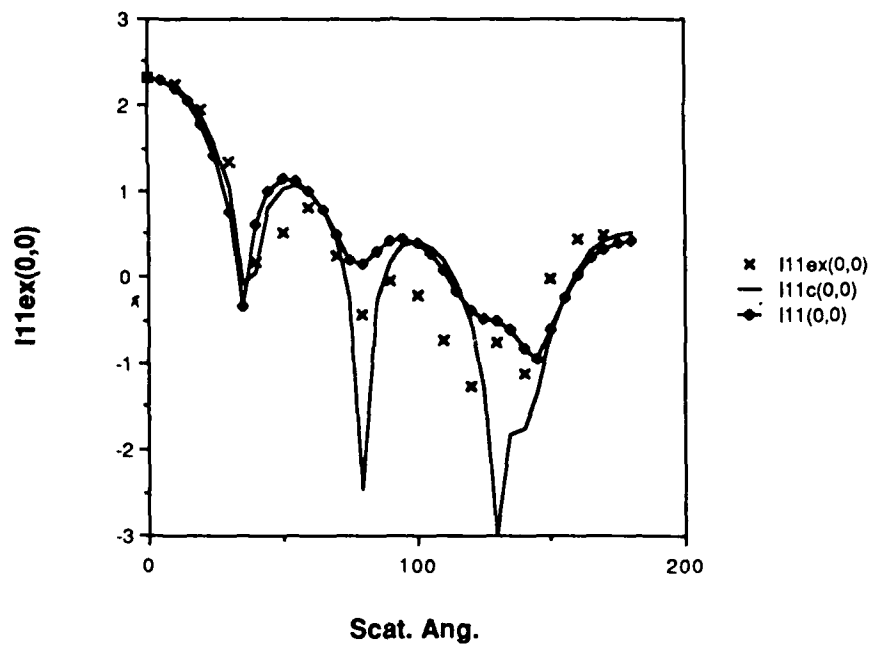
Figure 3. The intensity I_{11} with the symmetry axis of the spiral along the z_0 axis. The solid lines are the perturbative results, the lines with solid diamonds include self interaction, and the crosses are the experimental points of Ru Wang.
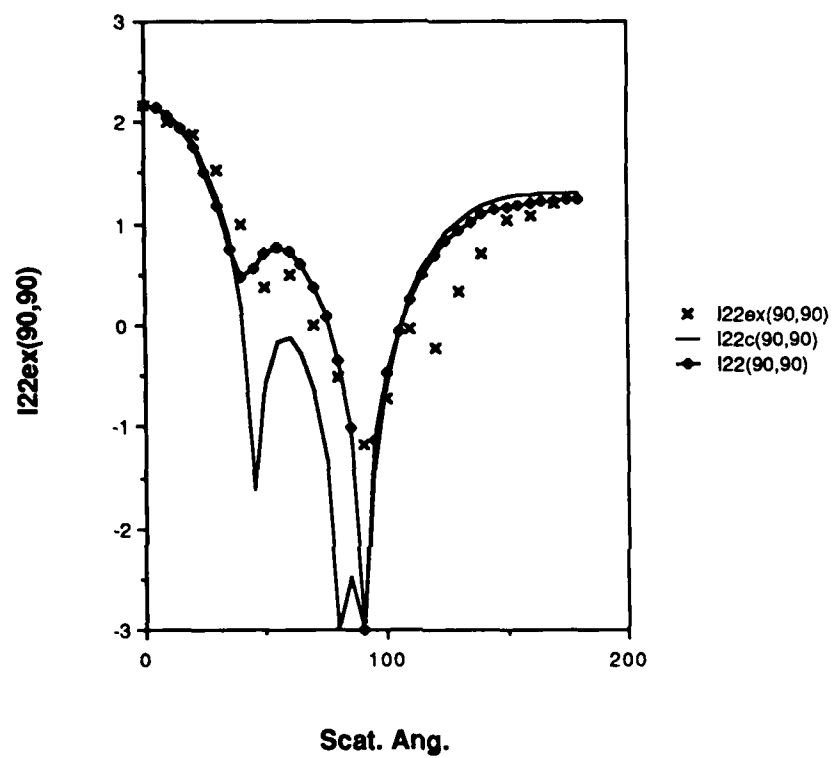
Figure 4. The intensity I_{22} with the symmetry axis of the spiral along the y_0 axis.
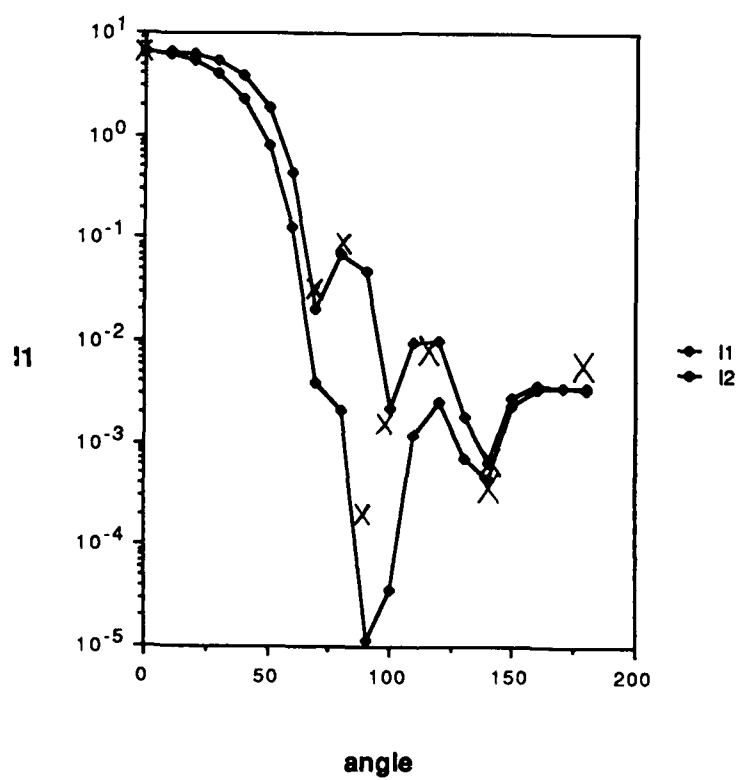
Figure 5. The intensities I_1 and I_2 for a spheroidal target. The solid lines are the results of the present calculation while the crosses are taken from Asano and Yanamoto.

A NEW ALGORITHM FOR
EXACT SCATTERING CALCULATIONS USING RATIOS

R. T. WANG
Space Astronomy Laboratory, University of Florida,
Gainesville, FL 32609

ABSTRACT

A simple algorithm using *ratios* between successive-order Bessel and/or Neumann functions was
found to be well-suited for the efficient, accurate calculations needed in light-scattering problems
when the exact analytical solutions are available, e.g., for homogeneous spheres (Mie theory), con-
centric spheres, and oblique infinite cylinders.   The advantage of this *ratio algorithm* over
other currently available routines is the mathematical simplicity and the numerical stability with

which it evaluates all partial-wave expansion coefficines of the excited exterior/interior fields
of a particle under an incident EM field.   The particle can span in size from the Rayleigh to the
geometrical optics regions($10^{-5} \lesssim x=2\pi a/\lambda \lesssim 3\times10^4$) and its complex refractive index is virtually
unrestricted.   A number of such computer routines have already been prepared not only to facilitate
our microwave measurement procedures — especially in *absolute magnitude calibrations* — but also for
practical applications where the exact evaluation of EM fileds is needed. This paper outlines the
algorithm and presents a few graphical examples for application to rainbow,glory and resonance
phenomena exhibited by large homogeneous spheres.   Detailed discussions and further extension to
other problems will be submitted, in an orderly sequence, to public journals.

OUTLINE OF THE ALGORITHM

It is well known that the most crucial but laborious task in Mie scattering calculations is to
accurately evaluate all partial-wave expansion coefficients a_n's and b_n's (the Mie coefficients) in
the series expansion of scattered fields. These coefficients are the functions of Riccati-Bessel
($\psi_n(z)$), Riccati-Neuamnn ($\chi_n(x)$), and Riccati-Hankel ($\zeta_n(x)=\psi_n(x)+i\chi_n(x)$) functions, where z can
be either complex ($z=(m'-im'')x$) or real ($z=x= 2\pi a/\lambda$=size parameter); and their accurate calculations
have been most difficult and time-consuming. The *ratio algorithm* alleviates this basically through
two precomputed arrays of ratios: $p_n(z)=\psi_n(z)/\psi_{n-1}(z)$ and $q_n(x)=\chi_n(x)/\chi_{n-1}(x)$.   These ratios are
generated by the following recurrence formulae as derived from those for $\psi_n(z)$, $\chi_n(x)$ themselves:

$$p_n(z) = \psi_n(z)/\psi_{n-1}(z) = 1 / \{ (2n+1)/z - p_{n+1}(z) \}$$

$$q_n(x) = \chi_n(x)/\chi_{n-1}(x) = (2n-1)/x + 1/q_{n-1}(x) \tag{1}$$

Although the recurrence relations are the same for generating both $p_n(z)$'s and $q_n(x)$'s, they are written separately to emphasize that *downward* recurrence must be employed for $p_n(z)$, but *upward* recurrence be used for $q_n(x)$ to insure the numerical stability in computing for all orders n, especially when z is complex. With these two basic ratio arrays, other ratios commonly known as *logarithmic derivatives* can also be computed:

$$A_n(z) = \psi_n'(z)/\psi_n(z) = -n/z + 1/p_n(z) \quad ; \quad B_n(x) = \chi_n'(x)/\chi_n(x) = -n/x + 1/q_n(x) \quad . \tag{2}$$

The explicit expressions for the expansion coefficients can then be written in the following:

Expansion Coefficients a_n & b_n (exterior field) and

c_n & d_n (interior field) for a Homogeneous Sphere

(1) Boundary Conditions:

$$a_n \zeta_n(x) + m c_n \psi_n(y) = \psi_n(x)$$

$$a_n \zeta_n'(x) + c_n \psi_n'(y) = \psi_n'(x)$$

$$b_n \zeta_n(x) + d_n \psi_n(y) = \psi_n(x)$$

$$b_n \zeta_n'(x) + m d_n \psi_n'(y) = \psi_n'(x)$$

where $m = m' - im''$ = complex refractive index, $x = 2\pi a/\lambda$, and $y = mx$. Solving these boundary conditions, we obtain the explicit formulae for a_n, b_n, c_n, and d_n:

$$a_n = \{\psi_n'(y)\psi_n(x) - m\psi_n(y)\psi_n'(x)\} / \{\psi_n'(y)\zeta_n(x) - m\psi_n(y)\zeta_n'(x)\}$$

$$b_n = \{ m\psi_n'(y)\psi_n(x) - \psi_n(y)\psi_n'(x)\} / \{ m\psi_n'(y)\zeta_n(x) - \psi_n(y)\zeta_n'(x)\}$$

$$c_n = i / \{\psi_n'(y)\zeta_n(x) - m\psi_n(y)\zeta_n'(x)\}$$

$$d_n = i / \{ m\psi_n'(y)\zeta_n(x) - \psi_n(y)\zeta_n'(x)\}$$

(2) Expansion Coefficients in terms of Ratios

$$a_n = 1 / \left[1 + i\chi_n(x)\{A_n(y) - mB_n(x)\} / \left(\psi_n(x)\{ A_n(y) - mA_n(x)\}\right) \right]$$

$$b_n = 1 / \left[1 + i\chi_n(x)\{mA_n(y) - B_n(x)\} / \left(\psi_n(x)\{ mA_n(y) - A_n(x)\}\right) \right]$$

$$c_n = i / \left[\psi_n(y) \psi_n(x)\{ A_n(y) - mA_n(x)\} + i\chi_n(x)\{ A_n(y) - mB_n(x)\} \right]$$

$$d_n = i / \left[\psi_n(y) \psi_n(x)\{ mA_n(y) - A_n(x)\} + i\chi_n(x)\{ mA_n(y) - B_n(x)\} \right] \tag{3}$$

where

$$\psi_n(y) = \psi_1(y)\prod_{i=2}^{n} p_i(y) \quad , \qquad \psi_n(x) = \psi_1(x)\prod_{i=2}^{n} p_i(x) \quad ,$$

$$\chi_n(x) = \chi_1(x)\prod_{i=2}^{n} q_i(x) \quad ,$$

and

$$\psi_1(x) = \sin x/x - \cos x \quad , \quad \chi_1(x) = \cos x/x + \sin x \quad .$$

Evaluation of all exterior-field Mie coefficients a_n and b_n , for example, is thus reduced to finding

mathematically simple and numerically stable *ratio arrays* $p_n(z)$ and $q_n(x)$ $(n=1,2,\cdots,n_m)$ given by

Eqs.(1) (which in turn yield *logarithmic derivative arrays* $A_n(z)$ and $B_n(x)$ through Eqs.(2)), plus *only*

two transcendental functions sinx and cosx appearing in Eqs.(3). $\psi_1(x)$ and $\chi_1(x)$ there are seen to

be the two basic functions from which all higher-order Riccati-Bessel and -Neumann functions are genera-

ted by successive multiplications. As x gets very small (Rayleigh region), only $\psi_1(x)$=sinx/x-cosx is

needed. However, a serious loss of accuracy was found to result in such case, after *machine-subtracting*

the right hand side terms. The difficulty was removed by employing power series expansion formulae

for sinx and cosx:

$$\psi_1(x) \xrightarrow{x \to 0} \sim \sum_{n=1}^{4} (-1)^{n+1} x^{2n}\, 2n\, /(2n+1)! \tag{4}$$

Finally, these ratios were found to be more *bounded* when the argument z is *complex* than it is real,

i.e., Mie calculation is more stable for absorbing spheres than for non-absorbing ones, which is oppo-

site to many other Mie routines. Extensive comarison of the outcome of this Mie algorithm to other

authors' were made, particulary to those by J.V. Dave [Refs. 2,3] , and excellent agreement were

obtained.

APPLICATION TO RAINBOW/GLORY/RESONANCE

The development of this algorithm started circa 1973 and was primarirly motivated by the necessity

of calibrating the *absolute magnitudes* of scattering in our microwave experiment [8] , and further

stimulated by the systematic understanding of ubiqutous light-scattering phenomena wherein the sizes of

scattering particles were either too large or too small for our $\lambda \simeq 3$ cm microwave technique to

simulate. The progress made was reported much later [9] and continued to this date. From the

beginning, it was intended for practical applications where exact evaluations of the necessarily

complex scattering formulae were mandated. Few *exact* calculations dealing with *very large particles*

compared to the incident wavelengths have been published in literature, especially those with compari-

son to experimental/observational evidence. Therefore the author looked also for natural/experimental

phenomena to test the validity of this ratio algorithm. The best candidates found are rainbow, glory

and resonance where the familiar laws of geometrical optics break down [7] and the application of

physical optics remains controversial. In this article only a few are selected out of a number of

the computational results, and displayed graphically with brief explunations attached.

Rainbow Figures

Figs. 1A-1C display the *absolute magnitudes* of S_{11} (the 1,1 element of the Mueller scattering

matrix represnting the total intensity) and polarization of scattered solar light at wavelengths

λ = 0.4 (violet), 0.55 (yellow-green) and 0.65 (red), respectively, versus the scattering angle

by a 800μ-diam. water droplet in atmosphere.   The Θ range covers the familiar primary/secondary and

their supernumeray bow regions separated by a dark band called the *Alexander's dark band* 6   where the

sky brightness is dimmer than the surrounding bow regions.   The Mie theory results using ratio techni-

que are consistent with familiar rainbow features: the angular positions, widths and brightness of bows,

color sequence, etc.   Furthermore, the theory predicts *not-so-familiar* polarization characteristics:

Except for the dark band the polarization is in *perfect phase* with S_{11}, e.g., near primary bow peaks

the rainbow light is strongly polarized along the arcs of rainbow (i.e., perpendicular to the scattering

plane formed by sun-droplet-observer), while near troughs, the polarization is strong in the scattering

plane.   The classical Airy theory [5,7] results for S_{11} are also shown in each figure, magnified by

a factor of 10 for readability.   As seen, it gives striking similarities (angular positions of peaks/

troughs, widths and peak magnitudes of bows) as well as differences (lack of fine fringe structures,

zero S_{11} at troughs, etc.) to the Mie theory prediction.   In Fig.1B the effect of very narrow droplet-

size distribution (b=0.005 in Hansen-Travis' standard size distribution, Space Science Reviews, 16,

527-610, 1974; abbreviated as *Gamma Distribution*) on the rainbow S_{11}/polarization profiles is also shown.

Glory Figures

Compared to rainbow phenomena, glory phenomena [4,6,7] are less well-known/studied, but no less

important in physics because they pack enormous information on particle size, refractive index, shape

(assumed spherical in this article), surface wave behavior, etc.   Glory is a back-scattering phenomenon

the correct explanation of which is feasible via exact Mie theory, and Figs.2A & 2B show again the

total brightness S_{11} and polarization, respectively, for a 100μ-diam. water droplet scattering incident

solar light in $175^{\circ} \leq \Theta \leq 180^{\circ}$.   Bluish circular rings surrounding the anti-solar point ($\Theta = 180^{\circ}$)

would be visible, according to the Mie calculation results in Fig.2A.

Resonance Figures

The ratio algorithm can also be efficiently employed to study the resonance interaction between

a propagating EM wave and a large aerosol, which is a hot topic in recent years.   The theoretical

study also requires the exact calculation by which one can and must also study both the exterior and

interior excited fields.   Eqs.(3) are written in ratio forms for this convenience.   Fig.3A - 3D depict

the Mie coefficients pairs (a_n,c_n) and (b_n,d_n) for n=38 and n=39 as a m=1.40-i0.0 particle changes its

size across *first-order resonance* points [1].   Inspection of these figures suggests that the resonan-

ce can be more easily studied experimentally on *interior* fields rather than on exterior fields.

SUMMARY

The ratio algorithm which has been developed over the years is now beyond doubt applicable for efficient, accurate evaluations of a variety of scattering problems whenever exact/reliable analytical formulae are availabe and the pertaining Bessel/Neumann functions can be feasibly expressed in ratio forms.   Indeed, the similar technique to sphere problems has been extended to oblique infinite cylinder and core-mantle sphere problems.   A perpendicularly illuminated infinite cylinder, for example, would exhibit essentially the same rainbow patterns as the equal-diameter sphere. A water bubble with a spherical cavity as large as half of the bubble diameter would also have the similar rainbow profiles as the same sized full water sphere.   Current routines, written in no more sophistication than Fortran IV-plus level, and in separate real and imaginary parts when complex variables are encountered, are expected to be very useful even with less expensive personal computers.

REFERENCES

1. Conwell, P.R., Barber, P.W. and Rushforth, C.K., Resonance spectra of dielectric spheres, J. Opt. Soc. Am. A-1, 62-67 (1984).

2. Dave, J.V., Subroutines for Computing the Parameters of the Electromagnetic Radiation Scattered by a Sphere (Rept. No.320-3237, IBM Scientific Center, Palo Alto, Calif. 1968).

3. ibid, Scattering of Visible Light by Large Water Spheres, Appl. Opt. 8, 155-164 (1969).

4. Kerker, M., The Scattering of Light and other Electromagnetic Radiation , Academic Press, N.Y., (1969).

5. Humphreys, W.J., Physics of the Air, McGraw-Hill, N.Y. (1929).

6. Nussenzveig, H.M., Complex angular momentum theory of the rainbow and the glory, J. Opt. Soc. Am. 69, 1068- 1079 (1979). See also plate 107 in p. 1193.

7. van de Hulst, H.C., Light Scattering by Small Particles, Wiley, N.Y. (1957). See pp.240-258 for rainbow/glory.

8. Wang, R.T. and Greenberg, J.M., Scattering by spheres with nonisotropic refractive indices, Appl. Opt. 15, 1212-1217 (1976).

9. Wang, R.T. and, Wang, W.X., Scattering by arbitrarily large homogeneous/concentric spheres – exact theory with use of new efficient algorithms, Proc. of the 1985 Scientific Conference on Obscuration and Aerosol Research, R. Kohl, ed., Army CRDEC-SP-86019, 381-409, (1986).

FIGURES
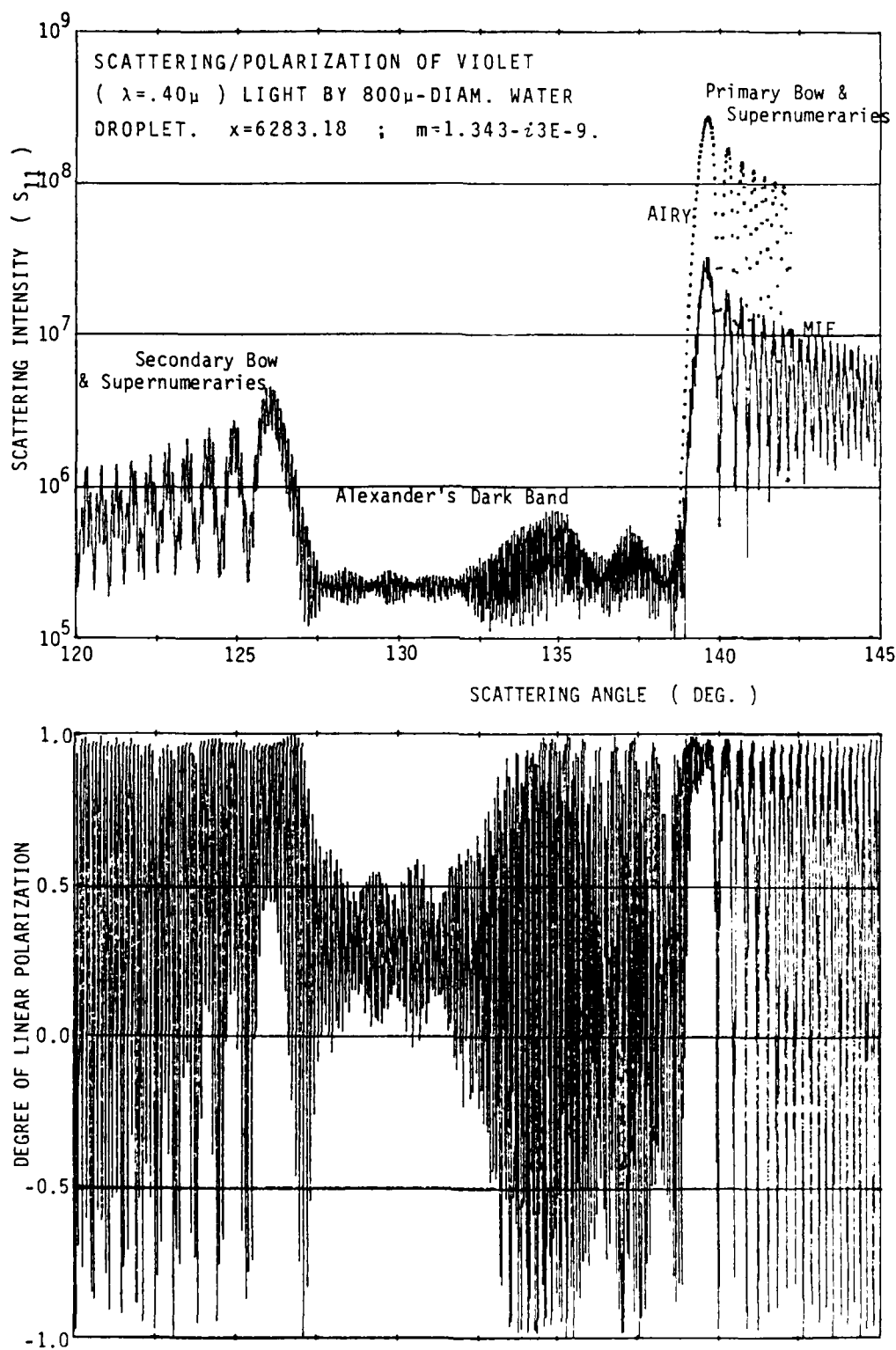
FIGURE 1A.   RAINBOW PROFILE BY MIE THEORY USING THE RATIO ALGORITHM
Airy theory results in the primary bow regions are shown by dotted curve.

276
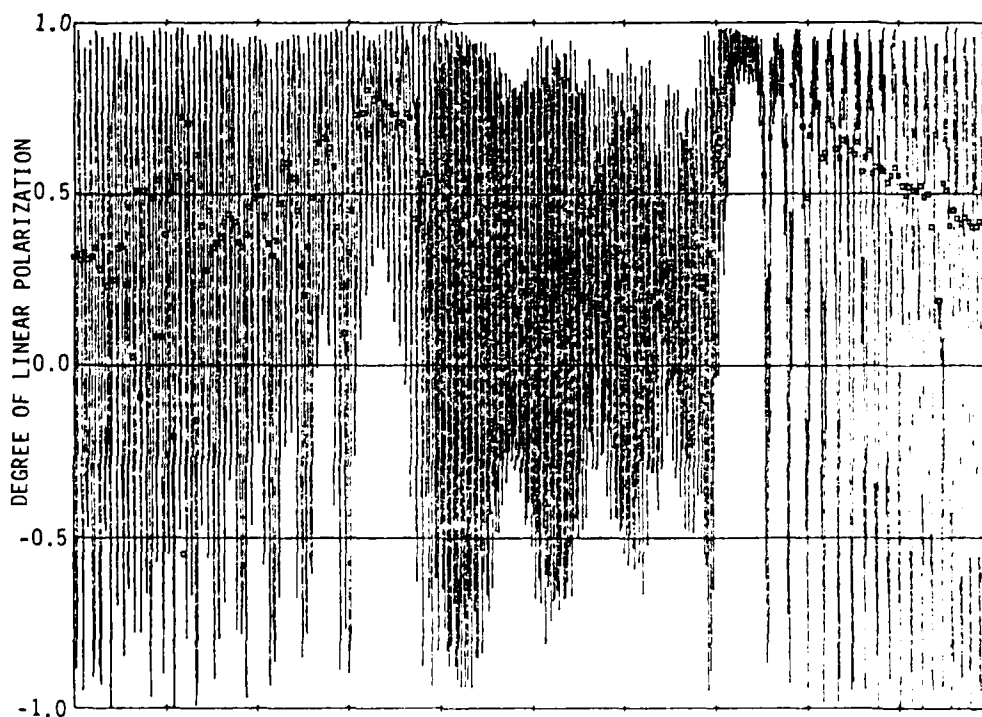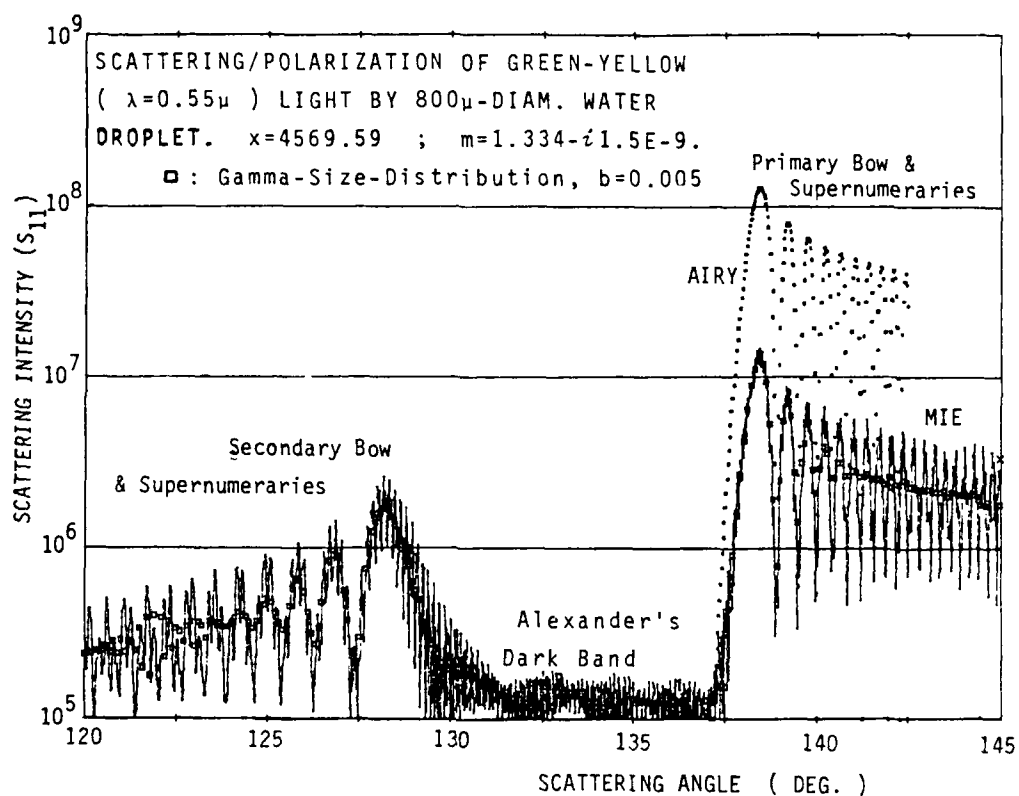
FIGURE 1B.   RAINBOW PROFILE BY MIE THEORY USING THE RATIO ALGORITHM
Airy theory result in the primary bow regions is shown by a dotted curve.

277
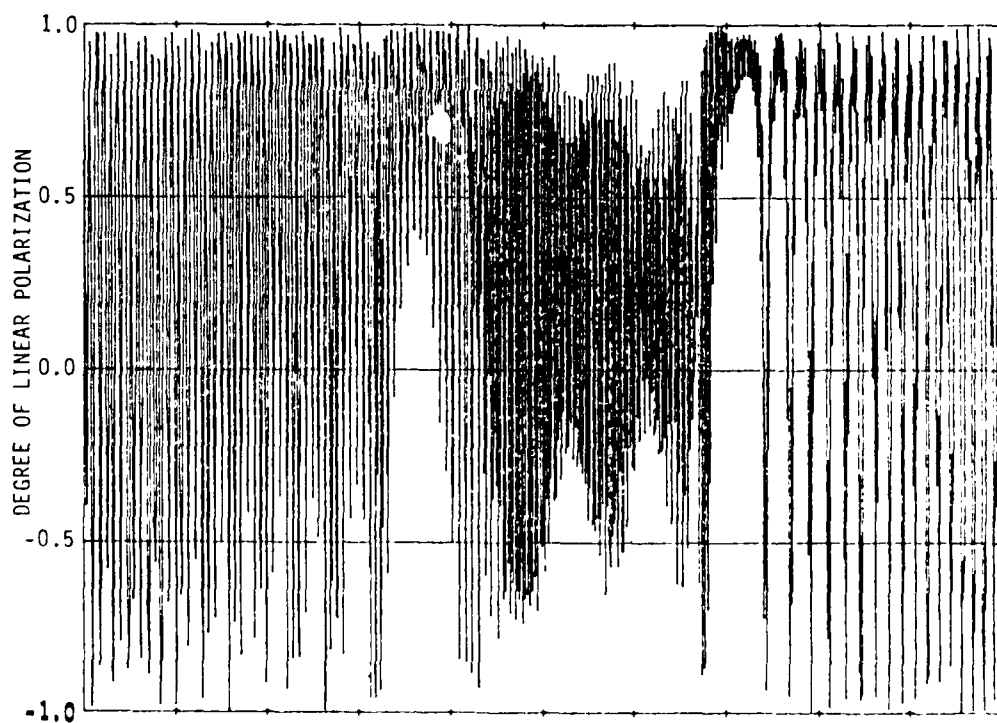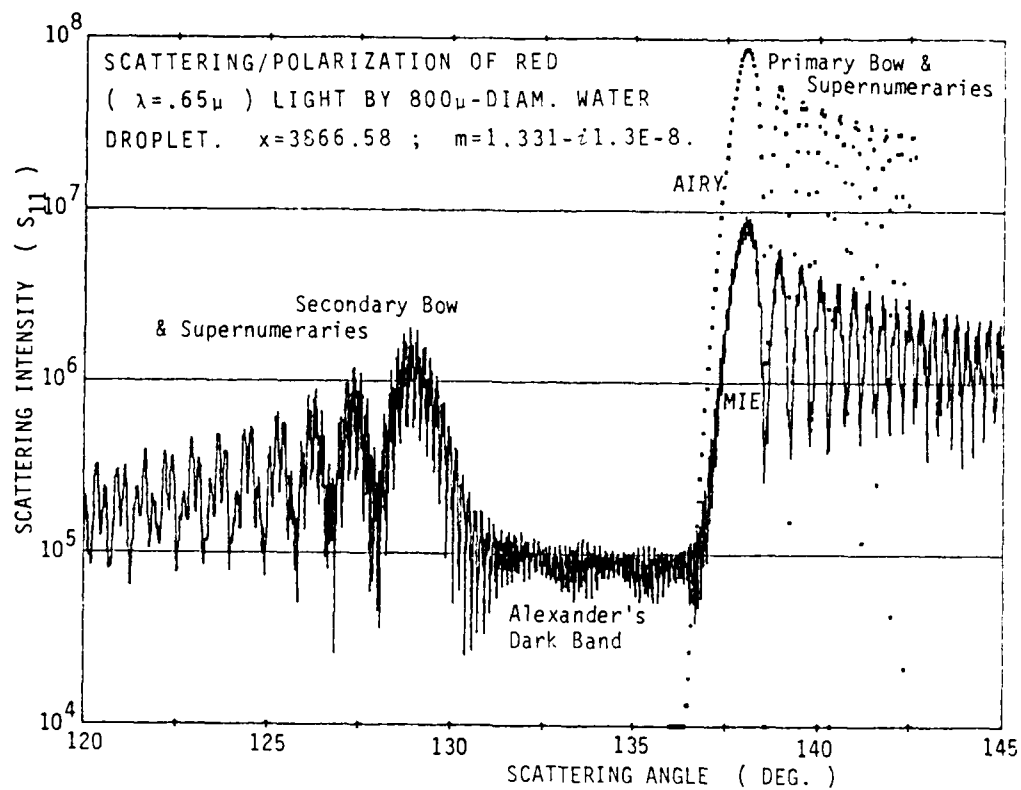
FIGURE 1C.   RAINBOW PROFILE BY MIE THEORY USING THE PATTO ALGORITHM

Airy theory result in the primary bow regions is shown by a dotted curve.

Mie Theory in the Glory Region for D=10μ H₂O:

□ : λ=0.40μ ; x=785.3982; m=1.343-i3E-9;
● : λ=0.55μ ; x=571.1987; m=1.334-i1.5E-9;
✕ : λ=0.65μ ; x=483.3220; m=1.331-i1.3E-8;

FIGURE 2B.   GLORY POLARIZATION BY MIE THEORY

Mie Theory in the Glory Region for D=100μ H₂O:

□ : λ=0.40μ ; x=785.3982; m=1.343-i3E-9;
● : λ=0.55μ ; x=571.1987; m=1.334-i1.5E-9;
✕ : λ=0.65μ ; x=483.3220; m=1.331-i1.3E-8

FIGURE 2A.   GLORY INTENSITY BY MIE THEORY

279

RESONANCES OF MIE COEFFICIENTS a_{39} AND c_{39} (Cf. also JOSA A-1,62 (1984))
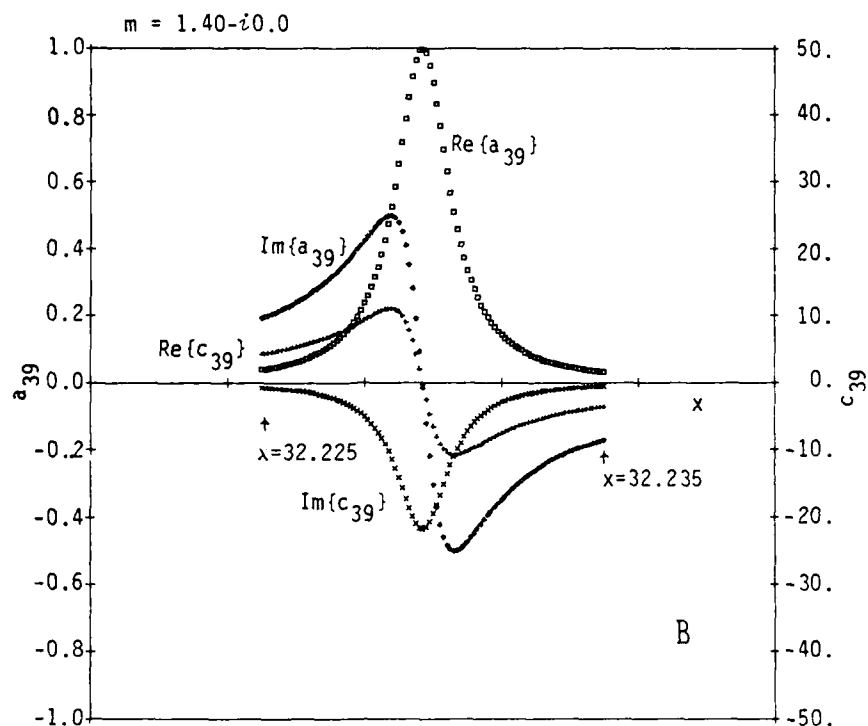
RESONANCES OF MIE COEFFICIENTS a_{38} AND c_{38} (Cf. also JOSA A-1,62 (1984))
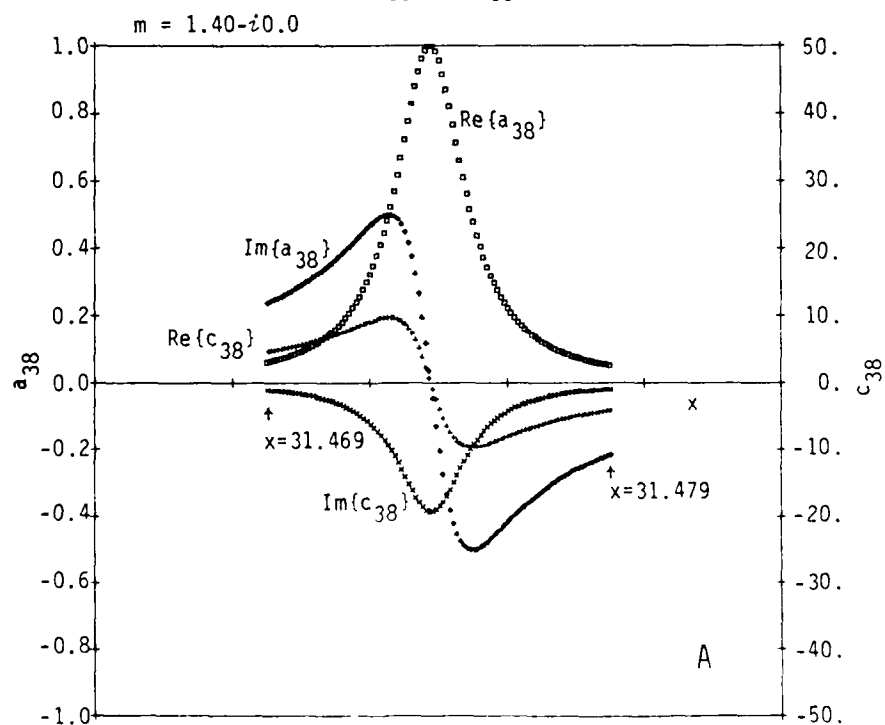
FIGURES 3A & 3B. RESONANCES OF MIE COEFFICIENTS (a_{38}, c_{38}) & (a_{39}, c_{39})

RESONANCES OF MIE COEFFICIENTS b_{39} AND d_{39} (Cf. also JOSA A-1,62 (1984))

$m = 1.40 - i0.0$
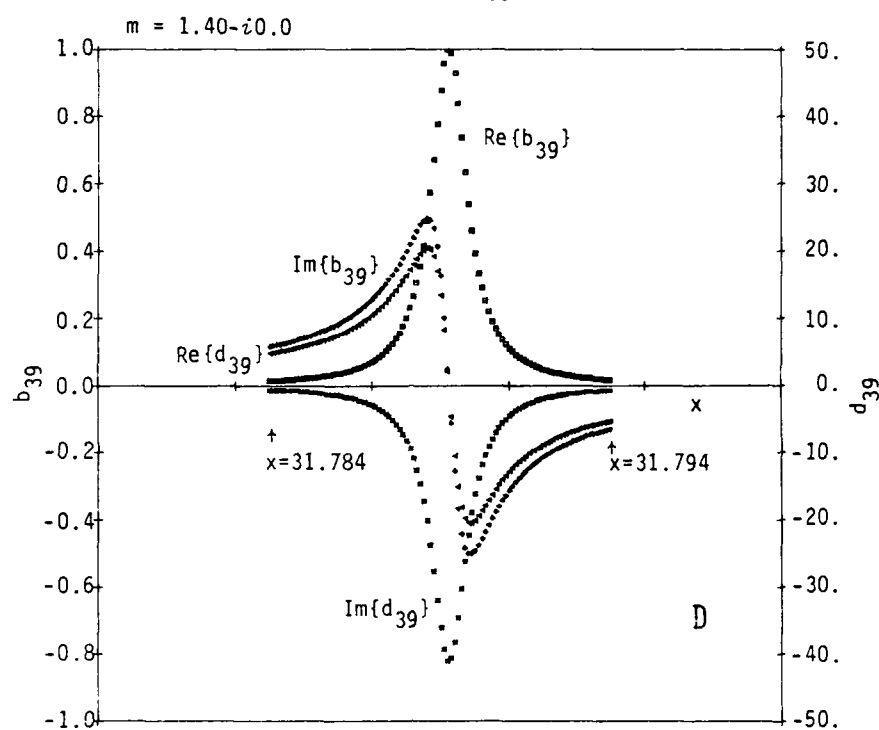
RESONANCES OF MIE COEFFICIENTS b_{38} AND d_{38} (Cf. also JOSA A-1,62 (1984))

$m = 1.40 - i0.0$
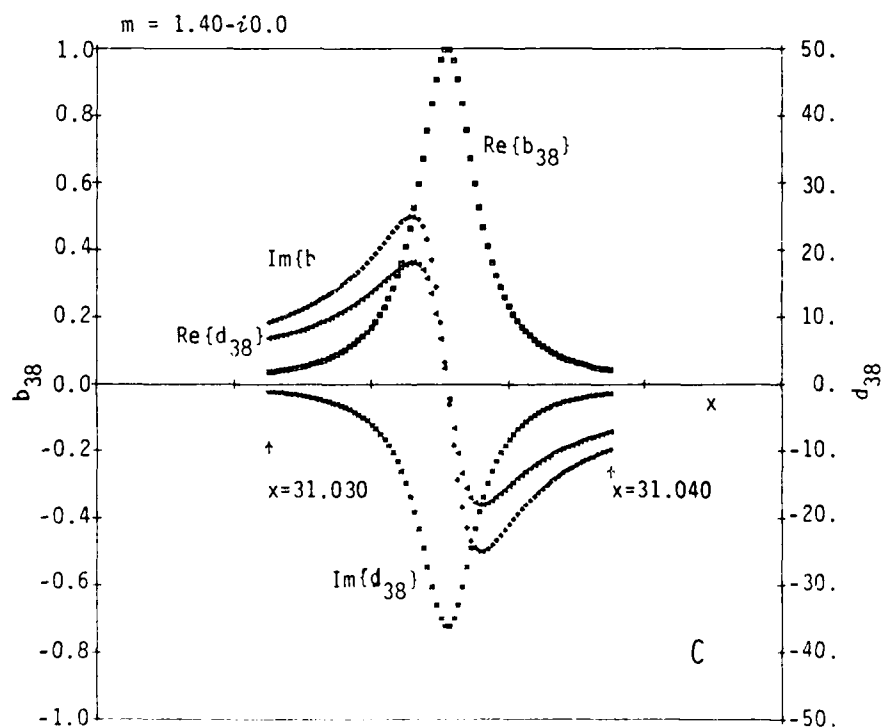
FIGURES 3C & 3D.   RESONANCE OF MIE COEFFICIENTS (b_{38}, d_{38}) & (b_{39}, d_{39})

Blank

SPECULAR SCATTERING BY
MULTIPLE SPHERES, SPHEROIDS AND A SQUARE PLATE

R. T. Wang
Space Astronomy Laboratory, University of Florida,
Gainesville, FL 32609

RECENT PUBLICATIONS, SUBMITTALS FOR PUBLICATION AND PRESENTATIONS:

A) R.T. Wang and Y.L. Xu, "Specular Scattering by Oriented Finite Cylinders," Proc. of the 1985 CRDEC Scientific Conference on Obscuration and Aerosol Research, R.Kohl, ed., Army CRDEC-SP-86019, pp 475-485 (1986).

B) K.A. Fuller, G.W. Kattawar and R.T. Wang, "Electromagnetic scattering from two dielectric spheres: further comparisons between theory and experiment," Appl. Opt. 25, 2521-2529 (1986).

C) R.T. Wang, "Status of the Microwave Facility (MSF) Upgrade," submitted to Proc. of the 1987 CRDEC Scientific Conference on Obscuration and Aerosol Research,"(in press).

D) W.X.Wang and R.T. Wang, "Light Scattering by Spheroidal Particles with High Aspect Ratio," J. Wave-Material Interaction 3, 151-161 (1988), and the 3 references cited therein.

E) R.T. Wang, "Specular Scattering by Multiple Spheres and Spheroids," presented at the 1988 CRDEC Scientific Conference on Obscuration and Aerosol Research, Aberdeen, MD (June 1988).

EXTENDED ABSTRACT

This article presents a few selected microwave data, and display them in *absolute-magnitude-calibrated* graphical form, the most recent measurement results on particle-orientation-dependent angular scattering by 2-spheres, 4-spheres, prolate/oblate spheroids and a square plate. All particles exhibit highly intriguing resonces/anti-resonances as each of them is rotated azimuthally throgh 180^{0} in 1^{0} steps in the beam, and observed at a fixed scattering angle Θ with fixed transmitteing/receiving polarizations. Presently, such a detailed experimental investigation can only be carried out using our microwave analog technique, and the recent continued facility upgrade [Ref. 5] has considerably improved the speed, accuracy and analysis/display of data gathering.

Reliable theoretical interpretation of such data is still very difficult, and yet is very important not ony for basic physics but also for properly linking to practical applications. For this reason, in addition to our in-house theoretical studies Refs. 6,7 we have also provided a number of such experimental data to other Army-supported theorists for comparison [Refs 1,2,3]. Only brief discussions on the interesting features are made:

Figs.1A-1D show the scattering profiles versus particle azimuth for a pair of nearly touching identical spheres and a 2:1 prolate spheroid, both are axially symmetric and have nearly the same total volume. Particle parameters are shown in the captions. Being axially symmetric in particle shape, all profiles are symmetrical about the bisectrix: (π-Θ)/2 [Ref. 4]. Specular scattering occurs when the particle axis bisects the scattering angle Θ, where the sphere-dumbbell is seen to scatter as much as ∿25 times that by a single isolated sphere (Fig. 1A). The width of such a resonant spike is related to the diameter of single sphere, similar to finite cylinder cases [Ref. 4], and 2-spheres are seen to peak higher than the same-volumed, 2:1 prolate spheroid. Outside of this resonance, both particles exhibit anti-resonance where the scattering intensity is rather low, and the averaged intensity over all azimuth positions is also indicated.

Recently we added in our inventory two 7:1 prolate and two 7:1 oblate spheroids made of aluminum and delrin plastics, respectively. All were machined to have the same volume, and were intended to serve as *calibration stanlards for absolute-magnitude measurements*. Comparisons of extinction measurements with our in-house spheroid theory have already been published [Ref. 7] and the theory is

being extended to study angular scattering, especially the Mueller Scattering Matrix so that these *high-aspect-ratio* spheroids can be employed as *cross-polarization-components* calibration standards. Figs. 2A-2H depict the measurement results.   Although all profiles are symmetrical about $(\pi-\theta)/2$ as in Figs. 1A-1D, the peaks of the delrin prolate spheroid observed at $\theta=30°$ are not located at $\theta/2$ (very few exceptional cases observed thus far).

Figs. 3A-3C are for 4 identical spheres froming a contacting tetraheron, and the array was rotated through $180°$ from the azimuth angle $0°$ where the incident beam direction was perpendicular to a two-sphere axis in the tetrahedron base.   This array is *not axisymmetric*, and compared to an axisymmetric dumbbell array in Figs.1A-1D the intensity profiles are rather smeared out, as seen by the single-sphere magnitudes indicated in each figure.   See [Refs. 2,3] for additional 3-, 4-sphere data as compared to theoretical work.

Finally, Fig.4 displays the intensity profile by a single square plate made recently of expanded polystyrene.   Despite its small size, it has an enormously high peak when the plate face is near $\theta/2$, i.e., the plate acts like a *reflecting mirror*!   The slight shift of the peak position from $\theta/2$ is presently estimated due to the finite plate thickness.   The plate face is kept perpendicular to the horizontal scattering plane during the azimuth rotation.   Notice, furthermore, outside of this specular reflection region the intensity is so low that the plate becomes practically *invisible*.   Theoretical explanation of this intriguing phenomenon is being pursued.

The study of *specular scattering* over the years is based on our belief that through such phenomena one can most critically and perhaps feasibly test the necessarily complex theoretical codes, which may inturn improve the experiment, ultimately leading to systematic understanding of light scattering itself.   These phenomena have been observed to occur predominantly in the forward directions ($\theta \lesssim 90°$) but have *never been studied* near $\theta = 180°$.   Future studies will be directed to such *backscattering* where as yet unknown. intriguing phenomena may exist.

ACKNOWLEDGMENT

REFERENCES

1. K.A. Fuller, G.W. Kattawar and R.T. Wang, "Electromagnetic scattering from two dielectric spheres: further comparisons between theory and experiment," Appl. Opt. 25, 2521-2529 (1986).

2. K.A. Fuller and G.W. Kattawar, "Consummate solution to the problem of classical electromagnetic scattering by an ensemble of spheres. I: Linear chains," Opt. Lett. 13, 90-92 (1988).

3. K.A. Fuller and G.W. Kattawar, "A consummate solution to the problem of classical electromagnetic scattering by ensembles of spheres part II: clusters of arbitrary configuration," to appear in Opt. Lett. (1988).

4. R.T. Wang and Y.L. Xu, "Specular Scattering by Oriented Finite Cylinders," Proc. of the 1985 CRDEC Scientific Conference on Obscuration and Aerosol Research, R. Kohl, ed., Army CRDEC-SP-86019, pp 475-485 (1986).

5. R.T. Wang, "Status of the Microwave Scattering Facility (MSF) Upgrade," submitted to Proc. of the 1987 CRDEC Scientific Conference on Obscuration and Aerosol Research (in press).

6. W.X. Wang and R.T. Wang, "Corrections and developments on the theory of scattering by spheroid-comparison with experiments," J. Wave-Material Interaction 2, 227-241 (1987).

7. W.X. Wang and R.T. Wang, "Light Scattering by Spheroidal Particles with High Aspect Ratio," J. Wave-Material Interaction 3, 151-161 (1988).
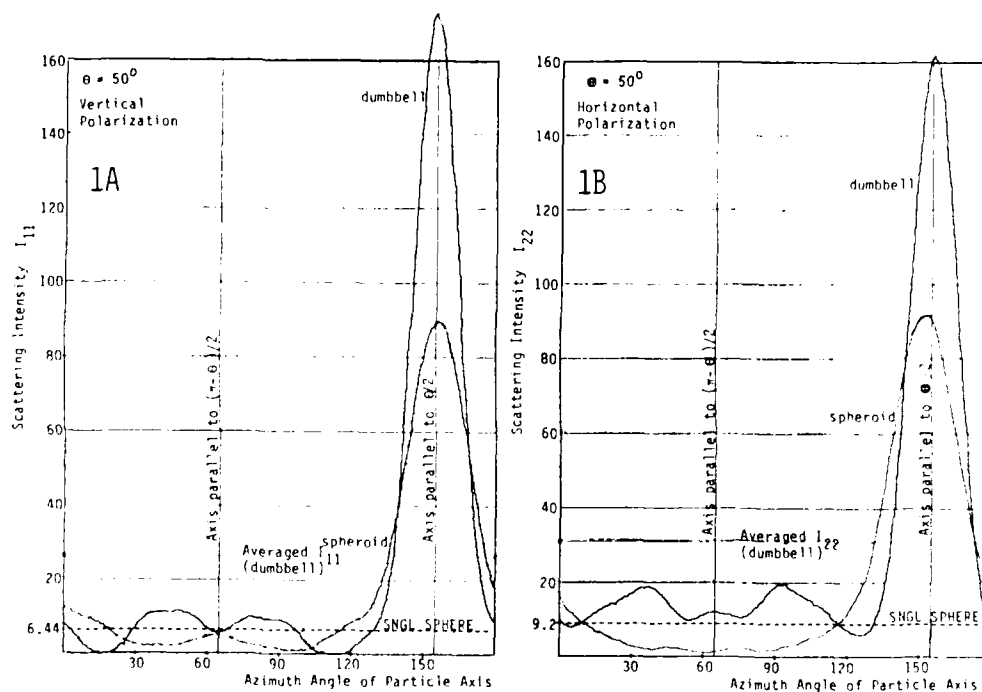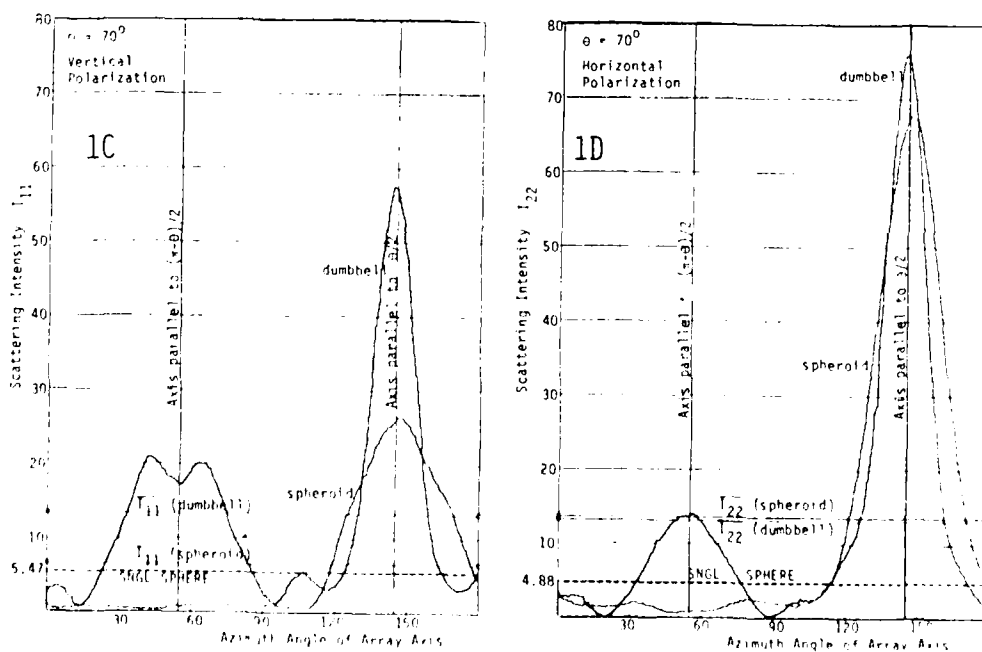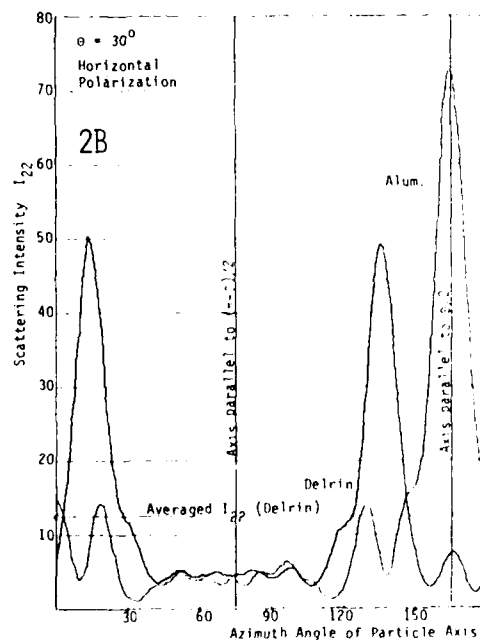
FIGURES 1A-1D.   COMPARISON OF SCATTERING BY A 2:1 PROLATE SPHEROID (x_v=5.811, m=1.374-i0.005)

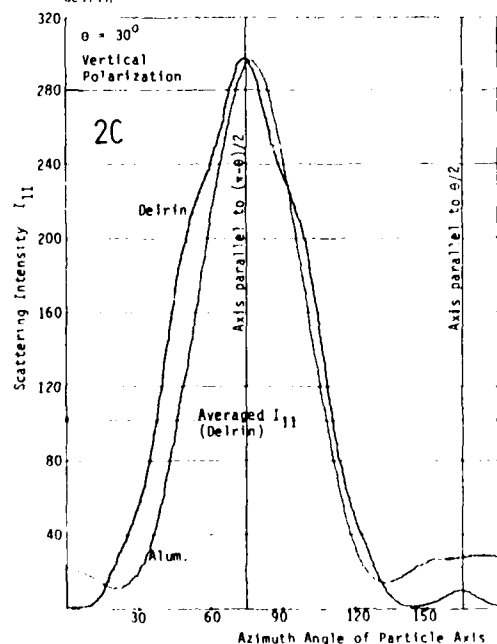AND A 2-SPHERE DUMBBELL (x_1=x_2=4.665, x_v=5.878, m=1.365-i0.005)

FIGURES 2A-2D.   SCATTERING INTENSITY VS. AZIMUTH ANGLE θ θ = 30° FOR 7:1 ALUMINUM/DELRIN
PROLATE SPHEROIDS (FIGS. 2A & 2B), AND FOR 7:1 ALUMINUM/DELRIN OBLATE SPHEROIDS (FIGS. 2C & 2D).

286

VAZRSN runs: 9-3-87; R71111.H50
(7:1 Delrin Prolate Sphrd)
9-3-87; R71211.H50
(7:1 Aluminum Prolate Sphrd)
Both particles have nearly the same volume: x_v=4.719.
m_{delrin}=1.70-i0.022.

$\theta = 50^0$

Vertical Polarization

2E

Scattering Intensity I_{11}

Axis parallel to $(\pi-\theta)/2$

Axis parallel to $\theta/2$

Alum.

Averaged I_{11} (Delrin)

Delrin

30   60   90   120   150
Azimuth Angle of Particle Axis

VAZRSN runs: 9-3-87; R71122.D50
(7:1 Delrin Prolate Sphrd)
9-3-87; R71222.D50
(7:1 Aluminum Prolate Sphrd)
Both particles have nearly the same volume: x_v=4.719.
m_{delrin}=1.70-i0.022.

$\theta = 50^0$

Horizontal Polarization

2F

Scattering Intensity I_{22}

Axis parallel to $(\pi-\theta)/2$

Axis parallel to $\theta/2$

Alum.

Averaged I_{22} (Delrin)

Delrin

30   60   90   120   150
Azimuth Angle of Particle Axis

VAZRSN runs: 9-3-87; R17111.H50
(1:7 Delrin Oblate Sphrd)
9-3-97; R17211.H50
(1:7 Aluminum Oblate Sphrd)
Both particles have nearly the same volume: x_v= 4.719.
m_{delrin}=1.70-i0.022.

$\theta = 50^0$

Vertical Polarization

2G

Scattering Intensity I_{11}

Axis parallel to $(\pi-\theta)/2$

Axis parallel to $\theta/2$

Alum.

Averaged I_{11} (Delrin)

Delrin

30   60   90   120   150
Azimuth Angle of Particle Axis

VAZRSN runs: 9-3-87; R17122.D50
(1:7 Delrin Oblate Sphrd)
9-3-97; R17222.D50
(1:7 Aluminum Oblate Sphrd)
Both particles have nearly the same volume: x_v=4.719.
m_{delrin}=1.70-i0.022.

$\theta = 50^0$

Horizontal Polarization

2H

Scattering Intensity I_{22}

Axis parallel to $(\pi-\theta)/2$

Axis parallel to $\theta/2$

Alum.

I_{22} (Delrin)

Delrin

30   60   90   120   150
Azimuth Angle of Particle Axis

FIGURES 2E-2H.   SCATTERING INTENSITY VS AZIMUTH ANGLE @ $\theta = 50^0$ FOR 7:1 ALUMINUM/DELRIN PROLATE SPHEROIDS (FIGS. 2E & 2F), AND FOR 7:1 ALUMINUM/DELRIN OBLATE SPHEROIDS (FIGS. 2G & 2H).
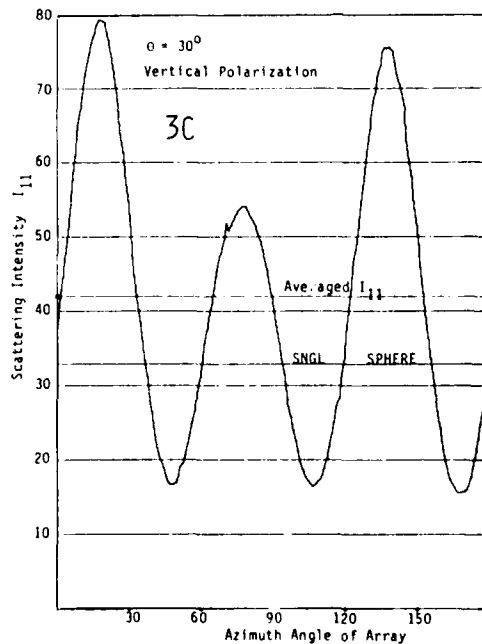
VAZRSN run: R4TH11.H50; 9-3-87:

4 Spheres Forming a Contacting Tetrahedron:
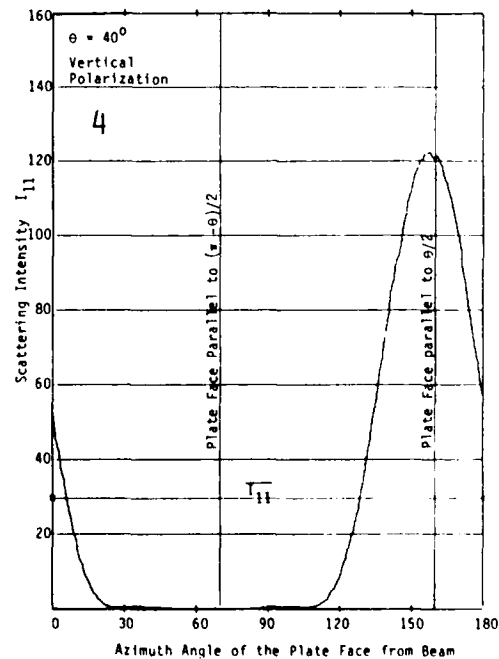$x_1 = x_2 = x_3 = x_4 = 3.114$, $m_1 = m_2 = m_3 = m_4 = 1.366 - i0.005$.
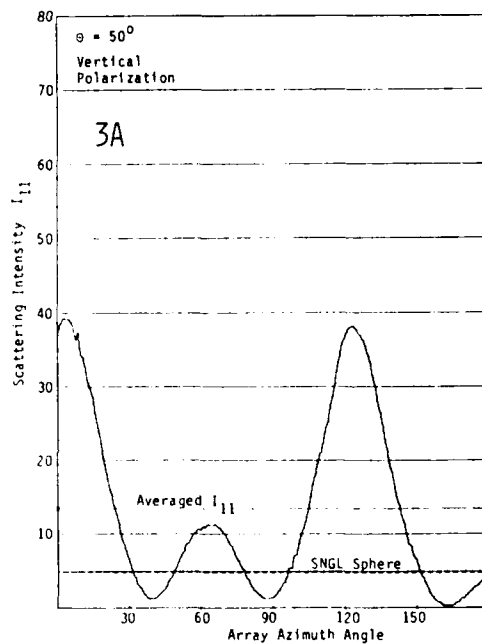
VAZRSN run: 9-3-87; R4TH22.D50;

4 Spheres Forming a Contacting Tetrahedron;
$x_1 = x_2 = x_3 = x_4 = 3.114$, $m_1 = m_2 = m_3 = m_4 = 1.366 - i0.005$.
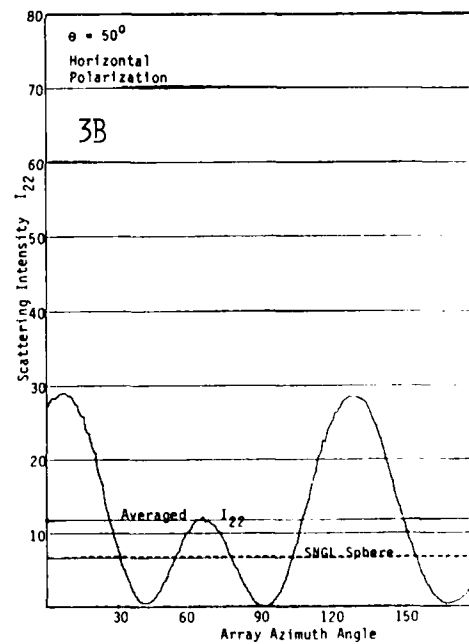
VAZRSN run: 8-4-87; R3TG11.C30

3 Spheres Forming a Contacting Triangular Array:
$x_1 = x_2 = x_3 = 3.114$, $m_1 = m_2 = m_3 = 1.365 - i0.005$.

VAZRSN run: 8-24-88; R13111.040

Square Plate: 4.7612cm X 4.7612cm X .9492cm

$x_v = 3.405$; $m = 1.366 - i0.005$.

FIGURES 3A-3C.   SCATTERING INTENSITY VS
AZIMUTH FOR A TETRAHEDRON ARRAY OF 4 SPHERES

FIGURE 4.   SCATTERING INTENSITY VS AZIMUTH
FOR A SQUARE PLATE

288

Computations of the Absorption Coefficient of a Dispersion of Clusters — Comparison of Computed Data with Experimental for Small Clusters.

Orazio I. Sindoni

Chemical Research, Development and Engineering Center
Aberdeen Proving Ground, Md 21010- 5423

Ferdinando Borghese, Paolo Denti, Rosalba Saija, Giuditta Toscano

Istituto di Struttura della Materia, University of Messina
98100 Messina, Italy

ABSTRACT

A selection of clusters composed of 20 spheres, simulating irregularly shaped particles often observed in powders, are used to model a low density monodispersed aerosol for which the absorption coefficient is calculated. Also calculations will be shown for small clusters (composed of 2 spheres) having the same optical characteristics as those of existing experimental data with which comparison will be made.

1. Introduction.

The fact that aerosol particles, but for few exceptions, are not spherical, nor can be described as spherical in consideration of their optical properties, is well known. It is not surprising that the optical behaviour of aerosol particles as calculated using Mie Theory is seldom consistent with the experimentally observed data, since the Mie theory is based upon the sphericity of the scatterer. It is however important to achieve a reasonable confidence in solving the problem of scattering by an irregularly shaped particle. The problem is not easily solved and special difficulties arise when the scatterer is equal to or larger than the wavelength of the incident light and when the index of refraction of the surrounding medium differs more than for a small amount. We have developed a formalism which allows us to describe an irregularly shaped particle[1-5], and the calculation of the properties of such a complex scatterer can be performed following the approach outlined in previous works[6-8] Having obtained in this manner the optical properties of a single scatterer then the next step is to calculate the macroscopic optical constants for the propagation through a model aerosol. We will show that our computation for two spheres agree with experimental results[9], then we will discuss the case of some complex structures which are types found commonly in powders[10-12]

2. Theory.

We refer you to other papers for the details of the computations and their justifications, see[13-17] , here simply accept that we can write the extinction cross section of a whole cluster, where a cluster is the geometrical description of a particle, in the form

$$\sigma_{ext} \; = \; < \mathbf{V}^\dagger | S | \mathbf{V} > \qquad (1)$$

where the matrix S depends only on the structure of the cluster:

$$S \equiv |\mathbf{I}| \times |\mathbf{T}| \times e^{i\mathbf{k} \cdot \mathbf{R}} \qquad (2)$$

The matrix S includes all the information on the scattering power of the cluster as a whole (its elements depend only on the scattering power of the spheres of the cluster and on the relative positions of their centers). In eq.(2), the matrices I and T were defined previously[7]. Matrix I has the role of referring the amplitudes of the multipole fields scattered by each sphere to the origin of the coordinates. The matrix T of the form:

$$\mathbf{T} = \begin{vmatrix} \mathbf{T}^{(1,1)} & \mathbf{T}^{(2,1)} \\ \mathbf{T}^{(1,2)} & \mathbf{T}^{(2,2)} \end{vmatrix} \qquad (3)$$

which must be calculated as the inverse of the matrix :

$$\mathbf{M} = \begin{vmatrix} [\mathbf{R}^{(1)}]^{-1}+\mathbf{H} & \mathbf{K} \\ \mathbf{I} & [\mathbf{R}^{(2)}]^{-1}+\mathbf{H} \end{vmatrix} \qquad (4)$$

and which is *determined by the strucure of the cluster* . The matrix V represents the amplitudes of the multipole fields and its elements make eq.(1) dependent on the direction of incidence. The matrix H describes in the vicinity of the surface of each sphere the multipole fields scattered by the other spheres of the cluster. The matrix K represents the cross terms of the multipole fields. And finally the matrices $\mathbf{R}^{(1)}$ and $\mathbf{R}^{(2)}$ are the *scattering power* of the single spheres composing the cluster (identical in physical meaning to the terms A and B in Van De Hulst[18]).

3. Results and Discussion

Two spheres – touching. The first set of data will be that of the two spheres, which will be compared with the experimental data of Shuerman and Wang[9]. The spheres are touching, the quantities which we have computed are the complex forward scattering amplitude $|S(0)|$ as a function of the size parameter $ks = 2\pi s/\lambda$ of the cluster. The geometry and all the parameters we have used and that we report are the same as the experi-

ments for which we compare. Following we reproduce the experimental setup:
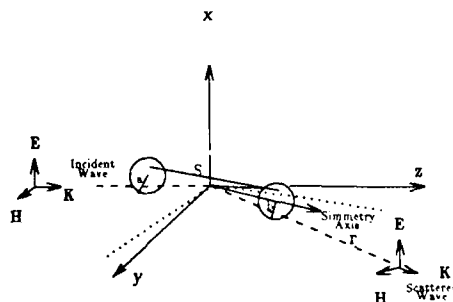
the following graph shows our calculated data (solid line) and the experimental data (dotted line).
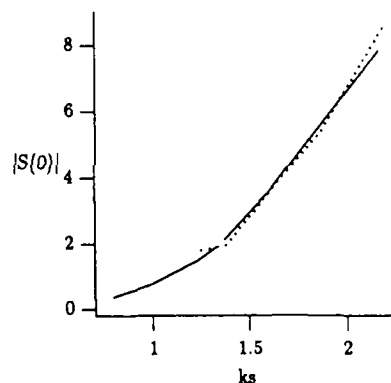
20 Spheres. We will now consider clusters composed of 20 spheres in order to simulate some irregularly shaped aggregations often found in powders[10-12] In the figures we report the quantities $\Gamma = \gamma/\gamma_{sp}$ and $\Gamma_{or} = \gamma_{or}/\gamma_{sp}$ for several direction of incidence as a function of χ the size parameter ; where γ_{sp} is the absorption coefficient of a dispersion of spheres of size parametr $\chi_{sp} = 20^{1/3} \chi$, whose number density equals that of the dispersion of clusters. The quantity γ is the absorption coefficient for the cluster randomly oriented and γ_{or} depends on the orientation of the clusters with respect to the incident plane–wave. The material of the spheres composing the cluster in all cases was chosen to be homogeneous isotropic, dielectric, and nondispersive with refractive index $n = 1.3$ and finally all the spheres in the clusters are identical.
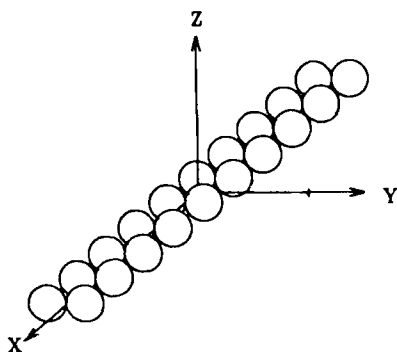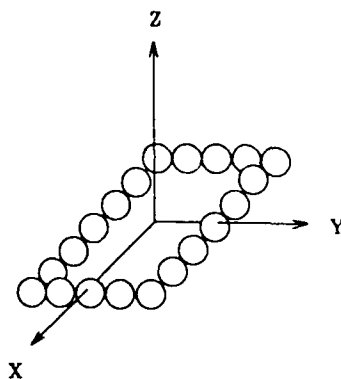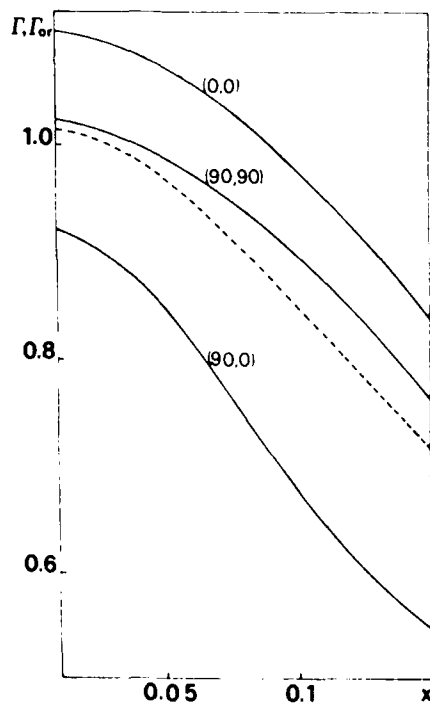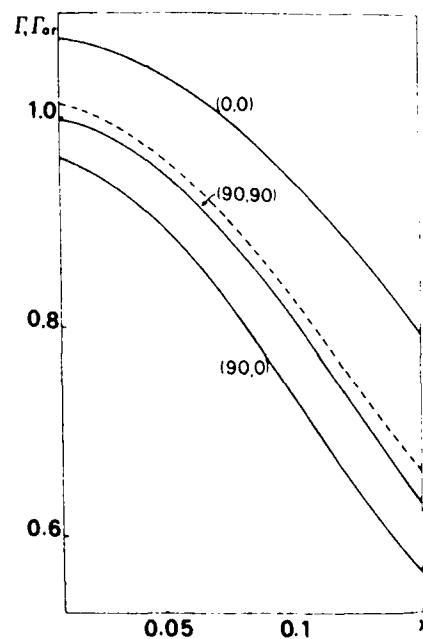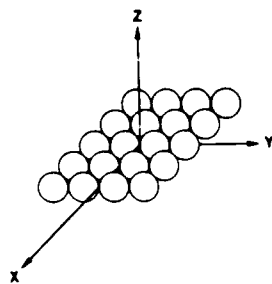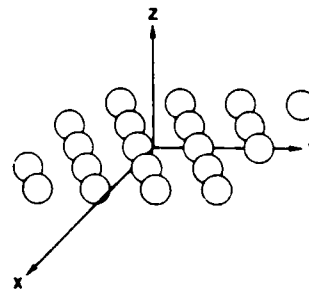
figure 3

The cluster is defined as a *Strip* and its geometric features are shown above. In the graph below the cluster Γ (broken curve) and Γ_{or} (solid lines) versus χ for several directions of incidence for a dispersion of strips. The incident plane wave is circularly polarized. The angles of incidence (teta,ϕ) , in degrees, labeling the Γ_{or} curves are related to the common orientation of the clusters.
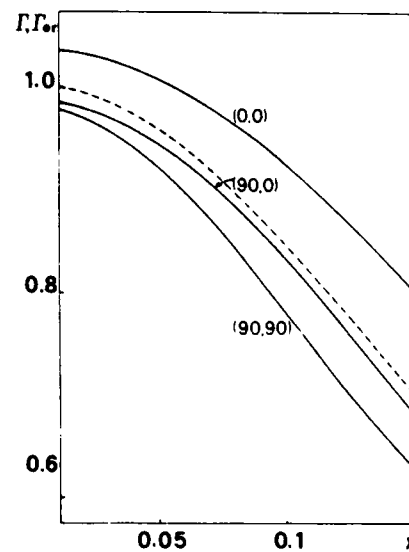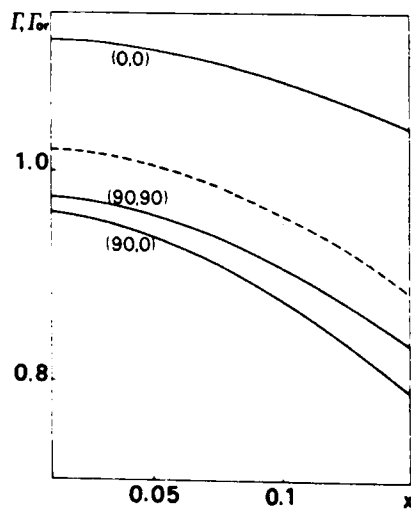

figure 4

The cluster is defined as a *Empty rectangle* and its geometric features are shown above. In the graph below the cluster Γ (broken curve) and Γ_{or} (solid lines) versus χ for several directions of incidence for a dispersion of empty rectangles. The incident plane wave is circularly polarized. The angles of incidence (teta,ϕ) , in degrees, labeling the Γ_{or} curves are related to the common orientation of the clusters.
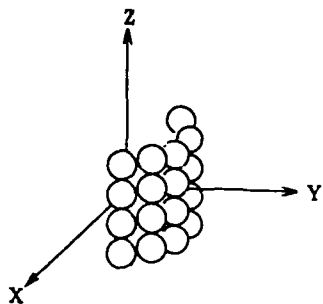

291

figure 5

The cluster is defined as a *Rectangle* and its geometric features are shown above. In the graph below the cluster Γ (broken curve) and Γ_{or} (solid lines) versus χ for several directions of incidence for a dispersion of rectangles. The incident plane wave is circularly polarized. The angles of incidence $(teta, \phi)$, in degrees, labeling the Γ_{or} curves are related to the common orientation of the clusters.
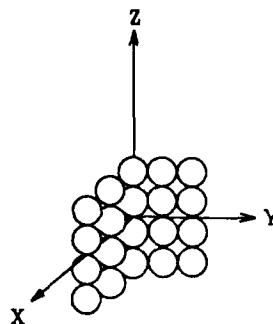
figure 6

The cluster is defined as a *Network* and its geometric features are shown above. In the graph below the cluster Γ (broken curve) and Γ_{or} (solid lines) versus χ for several directions of incidence for a dispersion of networks. The incident plane wave is circularly polarized. The angles of incidence $(teta, \phi)$, in degrees, labeling the Γ_{or} curves are related to the common orientation of the clusters.

figure 7

The cluster is defined as a *Roofing tile* and its geometric features are shown above. In the graph below the cluster Γ (broken curve) and Γ_{or} (solid lines) versus χ for several directions of incidence for a dispersion of roofing tiles. The incident plane wave is circularly polarized. The angles of incidence (teta,ϕ), in degrees, labeling the Γ_{or} curves are related to the common orientation of the clusters.

figure 8

The cluster is defined as a *Angular strip* and its geometric features are shown above. In the graph below the cluster Γ (broken curve) and Γ_{or} (solid lines) versus χ for several directions of incidence for a dispersion of angular strips. The incident plane wave is circularly polarized. The angles of incidence (teta,ϕ), in degrees, labeling the Γ_{or} curves are related to the common orientation of the clusters.
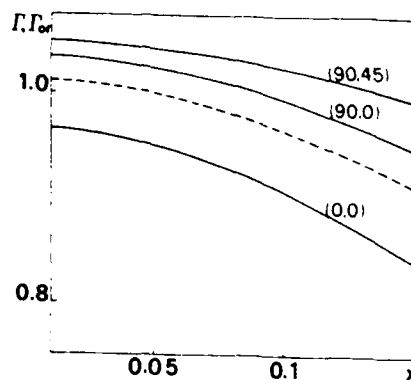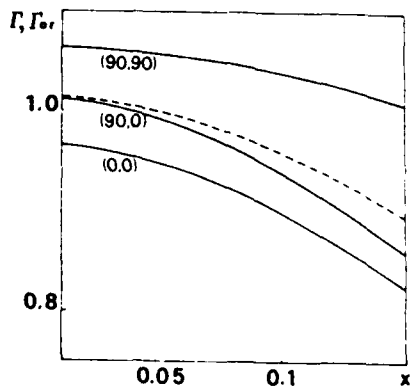
On the basis of the results shown, we can conclude that the aborption efficiency of a random dispersion of identical scatterers appreciably depends on the degree of anysotropy of the single scatterers. Within large limits of the size parameter, however, several kinds of anysotropy give very similar results, as far as the compactness is comparable. Ultimately, in a random dispersion the size distribution of the scatterers as inferred from optical data should not be considered reliable if the single scatterers are appreciably anisotropic[19,20].

REFERENCES

1. Borghese F., Denti P., Toscano G., and Sindoni O. I., (1981). *Chemical Systems Laboratory Special Publication*, ARCSL–SP–81008.

2. Sindoni O. I., Borghese F., Denti P., and Toscano G., (1981). *Chemical Systems Laboratory Special Publication*, ARCSL–SP–81009.

3. Borghese F., Denti P., Toscano G., and Sindoni O. I., (1981). *Chemical Systems Laboratory Technical Report*, ARCSL–TR–81048.

4. Borghese F., Denti P., Saija R., Toscano G., and Sindoni O. I., (1984). *Aerosol Sci. Technol.* 3:227.

5. Sindoni O. I., Borghese F., Denti P., Saija R., Toscano G., (1984). *Aerosol Sci. Technol.* 3:237.

6. Borghese F., Denti P., Saija R., Toscano G., and Sindoni O. I., (1984). *J. Opt. Soc. Am.* A 1:183.

7. Borghese F., Denti P., Saija R., Toscano G., and Sindoni O. I., (1984). *Il Nuovo Cimento* B 81:29.

8. Borghese F., Denti P., Saija R., Toscano G., and Sindoni O. I., (1985). *Il Nuovo Cimento* 6:545.

9. Schuerman D. W., Wang T. Ru, (1981). *Chemical Systems Laboratory Contractor Report* ARCSL–CR–81003.

10.Kerker M., (1963). *Electromagneti Scatter-*
ing Pergamon Press, Oxford England.

11.Kerker M., (1969). *The scattereing of Light.* Academic Press, New York.

12.Liu B. Y. H., Pui D. Y. H., Fissan H. J., (1984). *Aerosol. Proceedings of the First International Aerosol Conference.* Elsevier, New York.

13.Sindoni O. I., Borghese F., Denti P., Saija R., and Toscano G., (1984). *Aerosol. Proceedings of the First International Aerosol Conference.* pg.810, Elsevier, New York.

14.Saija R., Sindoni O. I., Toscano G., Denti P., and Borghese F., (1984). *Aerosol. Proceedings of the First International Aerosol Conference.* pg.817, Elsevier, New York.

15.Saija R., Toscano G., Sindoni O. I., Borghese F., and Denti P., *Il Nuovo Cimento* B 85:79.

16.Sindoni O. I., Borghese F., Denti P., Saija R., and Toscano G., (1987). *Proccedings of The 1985 Symposium on Multiple Scattering of Waves in Random Media and Random Rough Surfaces* The Pennsylvania State University.

17.Borgese F., Denti P., Saija R., Toscano G., and Sindoni O. I., (1988). *Proceedings of the Intrnational Conference On Scattering and Propagation in Random Media* 419 40–1 AGARD Pub. Neully Sur Seine, France.

18. Van de Hulst H. C. (1957). *Light Scattering by Small Particles.* Wiley, New York.

19. Gallily I., Eisner A. D., and Krushkal E. M., (1983). ARCSL–SP–8301.

20. Milham M., (1976). *Edgewood Arsenal Special Publication.* ED–SP–77002.

THE EFFECT OF COOPERATIVE SCATTERING ON MORPHOLOGY – DEPENDENT RESONANCES OF SPHERES

K. A. Fuller
Atmospheric Sciences Laboratory
SLCAS-AR-A
WSMR, NM 88002

RECENT PUBLICATIONS, SUBMITTALS FOR PUBLICATION, AND PRESENTATIONS:

(A) K. A. Fuller and G. W. Kattawar, "Light Scattering by an Arbitrarily Configured Cluster of Spheres," in *Proceedings of the 1987 CRDEC Scientific Conference on Obscuration and Aerosol Research*.

(B) K. A. Fuller and G. W. Kattawar, "Light Scattering by Ensembles of Interacting Spheres," presented to the Life Sciences Division of Los Alamos National Laboratory, Los Alamos NM, July 20, 1987.

(C) K. A. Fuller, *Cooperative Electromagnetic Scattering by Ensembles of Interacting Spheres*, PhD Dissertation, Texas A&M University, Dec., 1987.

(D) K. A. Fuller and G. W. Kattawar, "A Consummate Solution to the Problem of Classical EM Scattering by an Ensemble of Spheres Part I: Linear Chains," Opt. Lett. **13**, 90(1988).

(E) K. A. Fuller and G. W. Kattawar, "A Consummate Solution to the Problem of Classical EM Scattering by an Ensemble of Spheres Part II: Clusters," accepted for publication in Optics Letters.

(F) K. A. Fuller, "On the Spectra of Cooperatively Scattering Gold Spheres," in preparation for submission to Phys. Rev. Lett.

(G) K. A. Fuller, "Internal Fields of Two Cooperatively Scattering Spheres," to be presented to the Optical Society of America, 1988 Annual Meeting, Nov. 2.

ABSTRACT

This is the fourth in a series of reports appearing in these proceedings on the study of cooperative scattering by clusters of spheres. The second and third reports in this series established, through comparisons with experimental data, the validity of an order-of-scattering (OS) method of calculating the fields scattered by clusters of spheres. The theory was applied first to the case of linear chains, then to more arbitrarily configured clusters. In the present study, the resonant spectra of pairs of dielectric spheres are considered, with an emphasis being placed on the influence that coupling between the individual spheres plays in altering the spectra that would be observed if no interactions took place. The effects of coupling between specific multipole modes and the contribution of particular orders of scattering to the spectra of interacting Au spheres are also discussed.

DISCUSSION

The development of the theory of cooperative scattering that is used here has been presented elsewhere.[1-3] Parameters of the form $kx = 2\pi x/\lambda$, where λ is the wavelength of the incident radiation, will be used henceforth to describe the dimensions of the system. The constituent spheres are assumed to be of identical size and composition, with size parameter ka (radius a), complex refractive index $N1$, and dimensionless center-to-center separation kd. Linearly polarized plane wave radiation with wave vector $\mathbf{k}_0$ impinges on these bispheres, with the angle between $\mathbf{k}_0$ and the common axis of the two spheres (designated as the z-axis) specified by α. The polarization angle γ of the incident electric field $\mathbf{E}_0$ will be allowed to take on only the values $0°$ and $90°$ for $\mathbf{E}_0$ lying in or perpendicular to the xz-plane, respectively. The scattering angle is β.

Figs. 1-4 show results of calculations made for the forward scattering resonance spectra of two dielectric spheres illuminated at endfire incidence ($\alpha = 0°$) for various separations. The refractive index of the constituent spheres was chosen to be 2 because such a value is large enough to produce a rich spectrum at values of $ka < 10$ (making the calculations less time-consuming) and yet small enough to still be realistic. (For example, this refractive index is very close to that of cryptocrystaline and amorphous sulfur, which is of current interest in the field of planetary astronomy, throughout most of the visible and infrared region of the spectrum.)

Fig. 5 represents a study of the effect of separation (kd) on a particular resonance in the spectrum. It should be pointed out that, due to some difficulties in obtaining convergence for the OS method, the matrix inversion method was used for these calculations. (Comparisons of these two methods are given in the above references.) A more complete discussion of the results displayed in Figs. 1-5 is intended for a future publication.

Another topic of current interest involves the scattering properties of ordered arrays of metalic spheres. A question crucial to the analysis of measurements of these properties is the effect of coupling between the individual particles in the arrays. To provide some insight into these effects the spectrum of two gold spheres illuminated at broadside ($\alpha = 90°$) incidence has been studied and some of the results are shown in Fig. 6. The parameters used in this calculation correspond to those used in an experiment by Acker et al.[4] and the calculation itself is intended to address certain points raised in the authors' discussions of their results. Results for calculations involving a planar array of five Au spheres have been obtained and will be discussed, along with the two-sphere results, in item F under the Recent Publications section. In all cases considered in the Au sphere study, the OS method was found to converge quite rapidly. The value of the physical insight obtained when this method is employed is well represented by the results displayed in Fig. 6.

This work was conducted while the author was on a postdoctoral research associateship administered by the National Research Council and hosted by the U. S. Army Atmospheric Sciences Laboratory.

REFERENCES

1. K. A. Fuller and G. W. Kattawar, Opt. Lett. **13**, 90(1988).

2. K. A. Fuller and G. W. Kattawar, accepted for publication, Opt. Lett.

3. K. A. Fuller, *Cooperative Electromagnetic Scattering by Ensembles of Interacting Spheres*, PhD Dissertation, Texas A&M University, Dec., 1987.

4. W. P. Acker, B. Schlicht, R. K. Chang, and P. W. Barber, Opt. Lett. **12**, 465(1987).

Forward-scattered intensity vs ka; kd=2ka; Endfire incidence
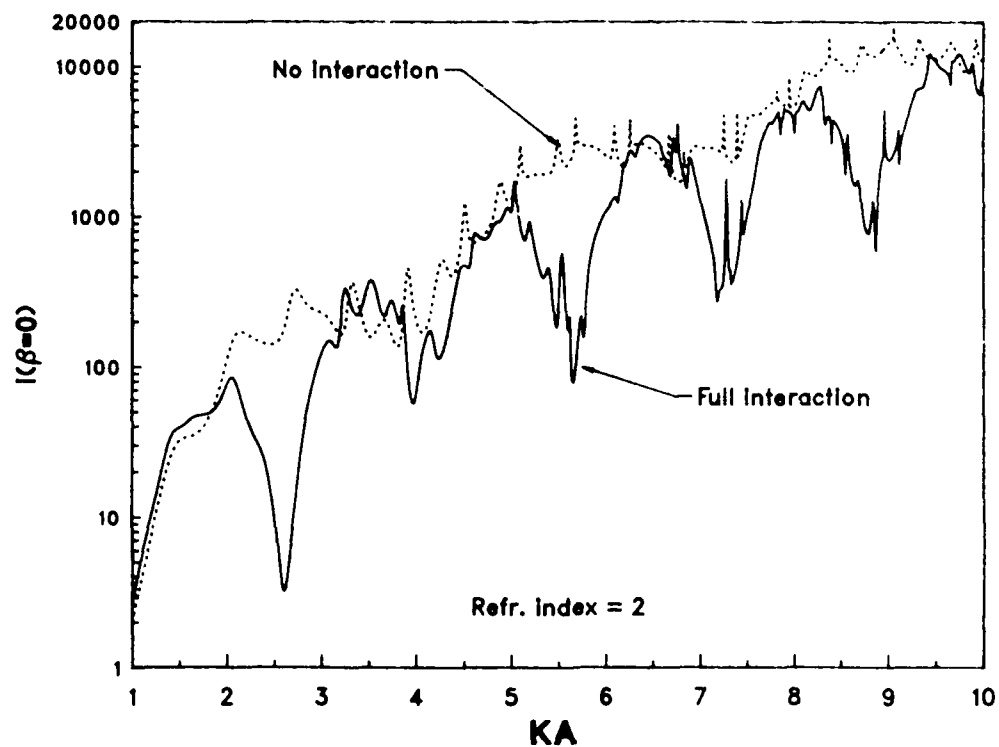

Fig. 1 The forward scattering spectrum of a pair of spheres illuminated at endfire incidence. Both spheres have a refractive index of 2.0 and it is assumed that there is no dispersion. Note that at $kd = 2ka$, the spheres are in contact.

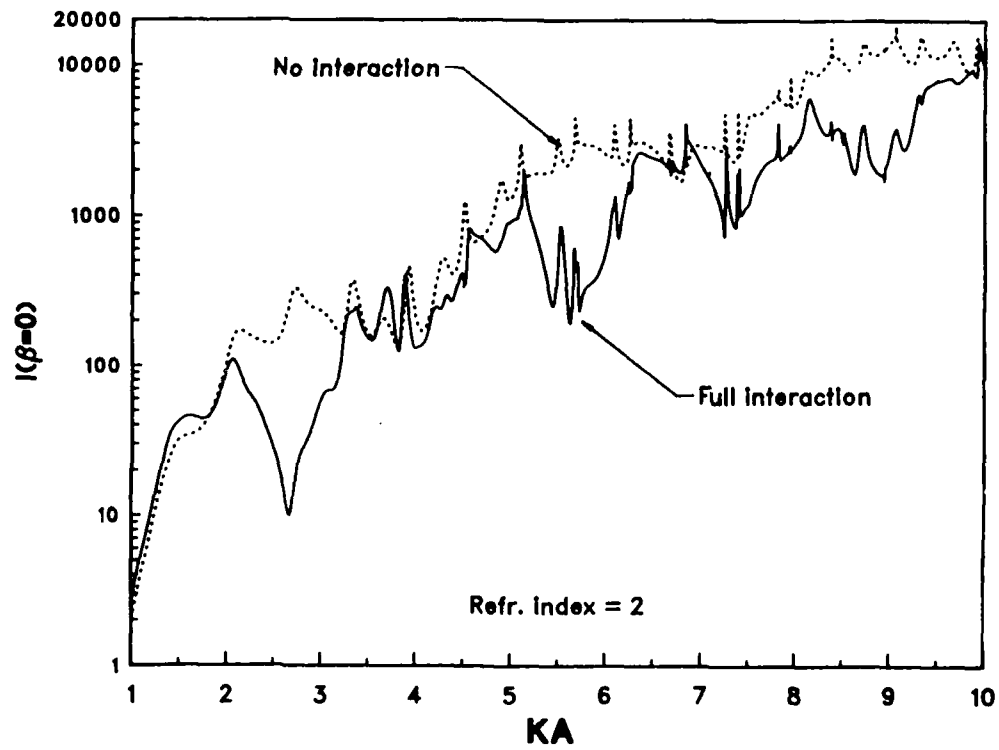# Forward-scattered intensity vs ka; kd=2.25ka; Endfire incidence

Fig. 2 The same as Fig. 1 except $kd = 2.25ka$.
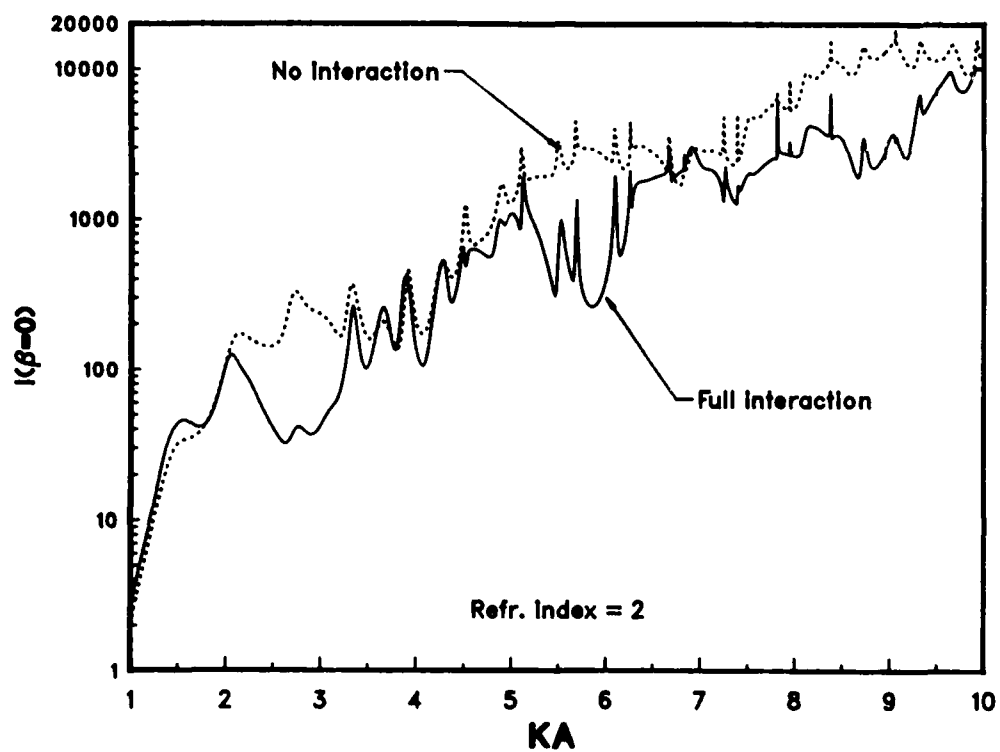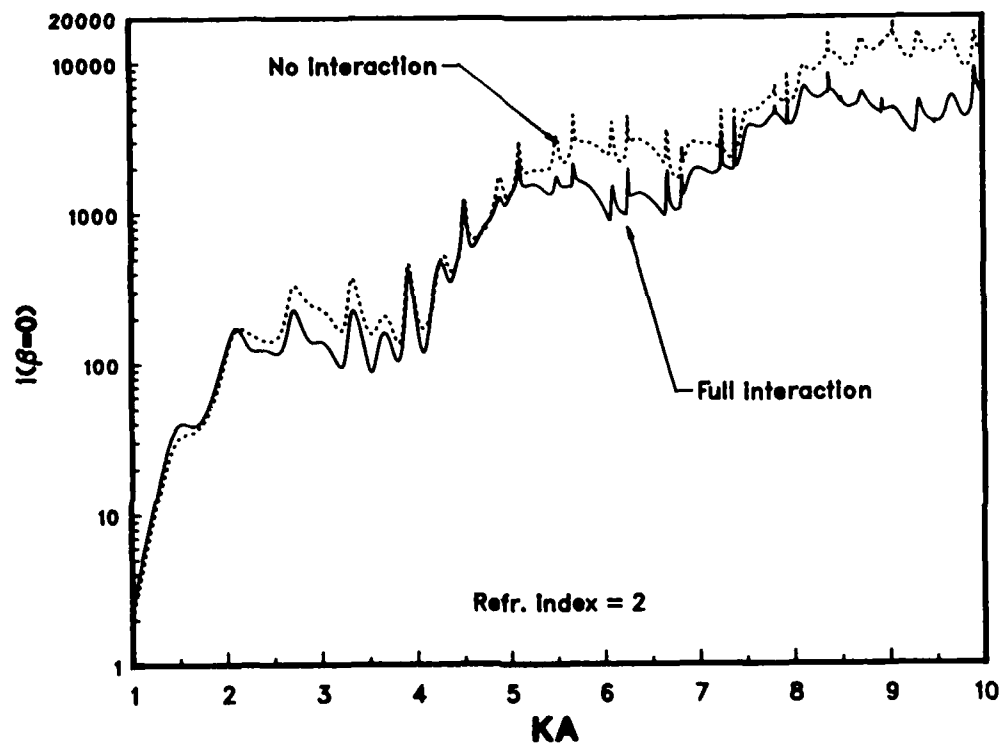
Forward-scattered intensity vs ka; kd=2.5ka; Endfire incidence

Fig. 3 The same as Fig. 1 except $kd = 2.5ka$.

Forward-scattered intensity vs ka; κd=5.0ka; Endfire incidence

Fig. 4 The same as Fig. 1 except $kd = 5.0ka$.

The ka=7.25 region for various seperations

No Interaction

5ka

3ka

2.75ka

2.5ka

2.25ka

2ka

$I(\beta=0)$

KA
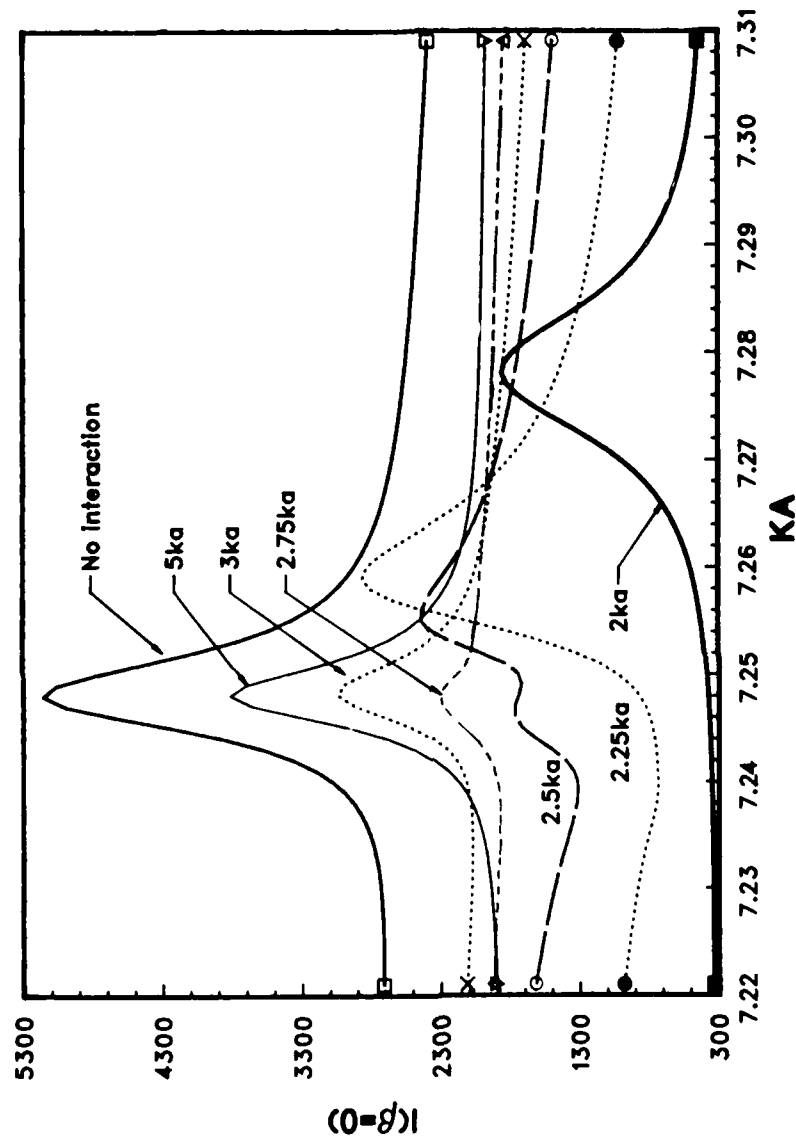
Fig. 5 The effect of sphere separation on the structure of a particular resonance.

302

Two Au spheres in toluene
Interaction between nth and νth multipoles
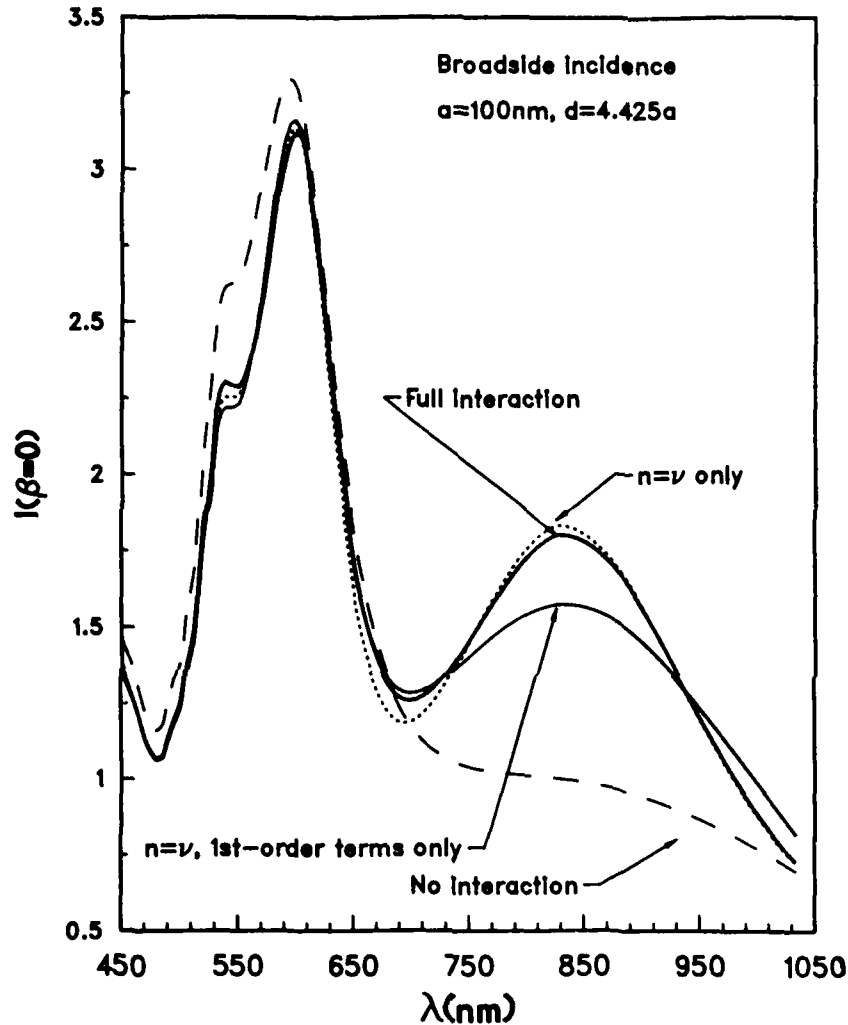
Fig. 6 The resonance spectrum of two gold spheres illuminated at broadside incidence. The incident field is polarized perpendicular to the common axis of the spheres, i.e., $\gamma = 90°$. The effects of dispersion have been accounted for. The expression $\nu = n$ means that only dipole-dipole, quadrupole-quadrupole, etc. interactions have been incorporated into the calculation; effects such as the coupling of a dipole mode of one sphere to the quadrupole modes of the other have been left out in this case. The phrase '1st-order terms' means that only the 1st order, coherent multiply scattered fields have been included in the calculation.

Blank

SCATTERING DEGRADATION OF IR ABSORPTION SPECTRA

Mark L.G. Althouse

U.S. Army CRDEC

A.P.G., MD 21014

1. Introduction:

For analysis of various air pollutants, it is often difficult to collect more than just a few tenths of a microgram of material. To get useful infra-red spectra of such an amount of material it must be in fairly high concentration relative to the background media. Looking at a small area is one way of doing this and an infra-red microspectrophotometer is the instrument that we use. In the course of impaction sampling a substance in the air many particles other than those of interest are collected and they vary widely in size and shape. We found that the presence of airborne dirt in even a small percentage caused a marked degradation of spectral content in our samples. To explore this scattering loss, a set of experiments was set up to measure the effects of particle size and spacing on IR spectra.

2. Instrumentation:

A Nanometrics, Inc., Nanospec 20/IR infrared microspectrophotometer was used to obtain all the spectra in this study. It consists of an IR microscope with reflecting optics, a Nernst glower source, a monochrometer, and a liquid nitrogen cooled mercury cadmium telluride detector. The Nanospec is controlled by a microprocessor that has several scan modes, and can add or subtract spectra and compute derivatives. The wavelength range is from 2.5 - 14.5 um and it can view an area as small as 20 um x 20 um.

3. Experimentation:

For sample material, polystyrene spheres of various radii manufactured by Dow Chemical and Duke Standards were used. The spheres were put as a droplet on a small barium fluoride window and the suspending liquid was allowed to evaporate. A concentration of particles was used such that when the droplet dried it would leave a contiguous mono or multi-layer of spheres near the droplet edge and a randomly spaced monolayer in the interior of the droplet. Data is shown from cases where the spacing

was equal to the sphere diameter in area average. Slit settings used were 37.5 X
62.5 um and 50 X 125 um depending on sphere diameter. Spectra were then taken of
both the randomly spaced area and the contiguous monolayer over the range of particle
diameters (Figures 1,2). We expected to find that the spectra of the randomly spaced
spheres would appear of poorer quality in comparison to the spectra of a contiguous
monolayer. For those samples that had a sphere diameter that fell within or close to
the wavelength range of the instrument (2.5 - 14.5 um), it was observed that the
spectrum for the randomly spaced spheres was badly degraded in spectral content at
wavelengths less than the sphere diameter. The phenomena appeared in more widely
spaced samples but the features became so small due to the lack ok material in view
that consistant numbers were difficult to achieve. At a point close to the
wavelength equal to the sphere diameter the spectrum of the randomly spaced particles
recombines with the spectrum for the contiguous monolayer. As a check on the
spectral data, the absorption coefficients were calculated for the 3.45, 7.0, and
13.5 um features (Table 1). The absorption coefficients were calculated by the
Beer-Lambert law as follows:

$$2.303 \ A = \ln (Io/I) = a \ CL$$

$$A = \log (Io/I)$$

where A = absorbance, Io = incident intensity, I = transmitted intensity, a =
absorption coefficient (m^2/mg), C = concentration (mg/m^2), and L = absorption path
length (m).

$$a = 2.303 \ A \ / \ CL$$

$$C = \frac{(number\ of\ spheres\ viewed)\ x\ (volume\ of\ a\ sphere)}{(total\ area\ viewed)\ x\ L} \quad (.909 \times 10^9 \ mg/m^3)$$

where (.909 X 10^9 mg/m) is the mass density of polystyrene, and the slit area and
number of spheres viewed are observables.
Absorption coefficients at wavelengths smaller than the diameter of the sphere were
from six to ten times greater for the contiguous monolayer, yet at wavelengths nearly
equal to or greater than the sphere diameter coefficients for the two cases were
approximately equal.

4. Conclusion:

An IR spectrum of spherical particles is subject to a degradation of spectral content that is dependent on the size and spacing of the particles. Spectral degradation is present for non-contiguous monolayers of particles at wavelengths smaller than the particle diameter. The resultant loss is opposite that which would occur from diffraction limiting due to the spacing. This phenomenon must be considered when producing spectra of microsamples of particulates that are not densely packed.
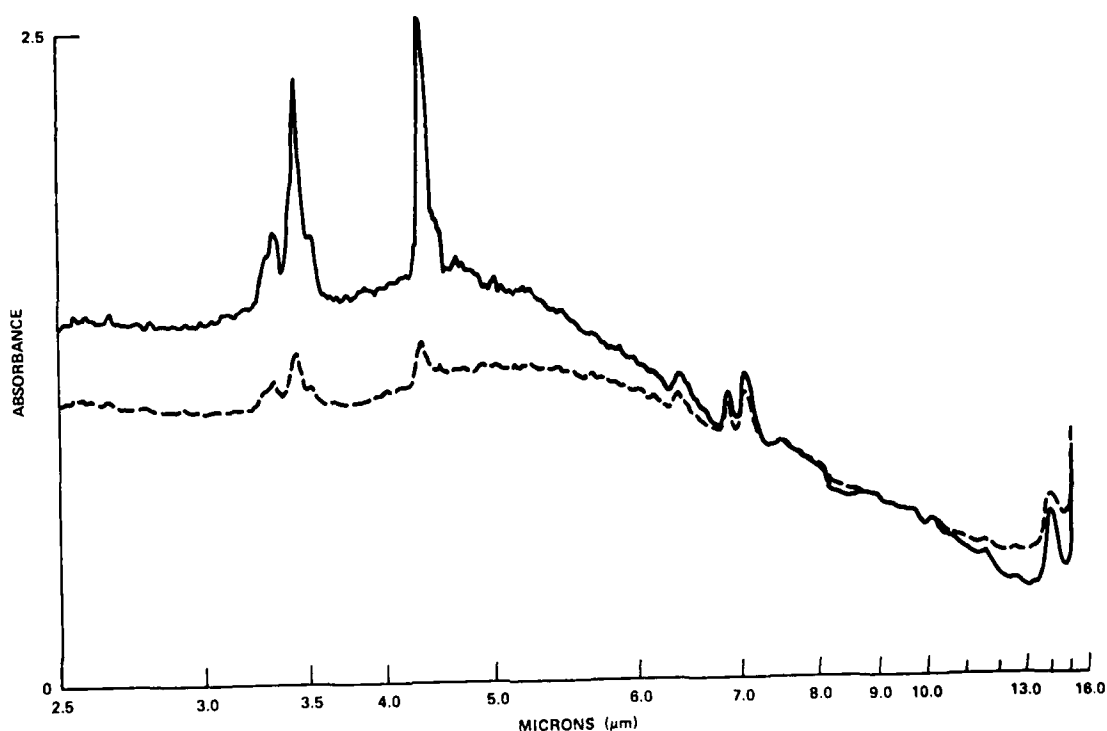

FIGURE 1. 7.6 MICRON POLYSTYRENE SPHERES. The solid curve is from a densly packed monolayer and the dashed curve is from an irregularly distributed monolayer.
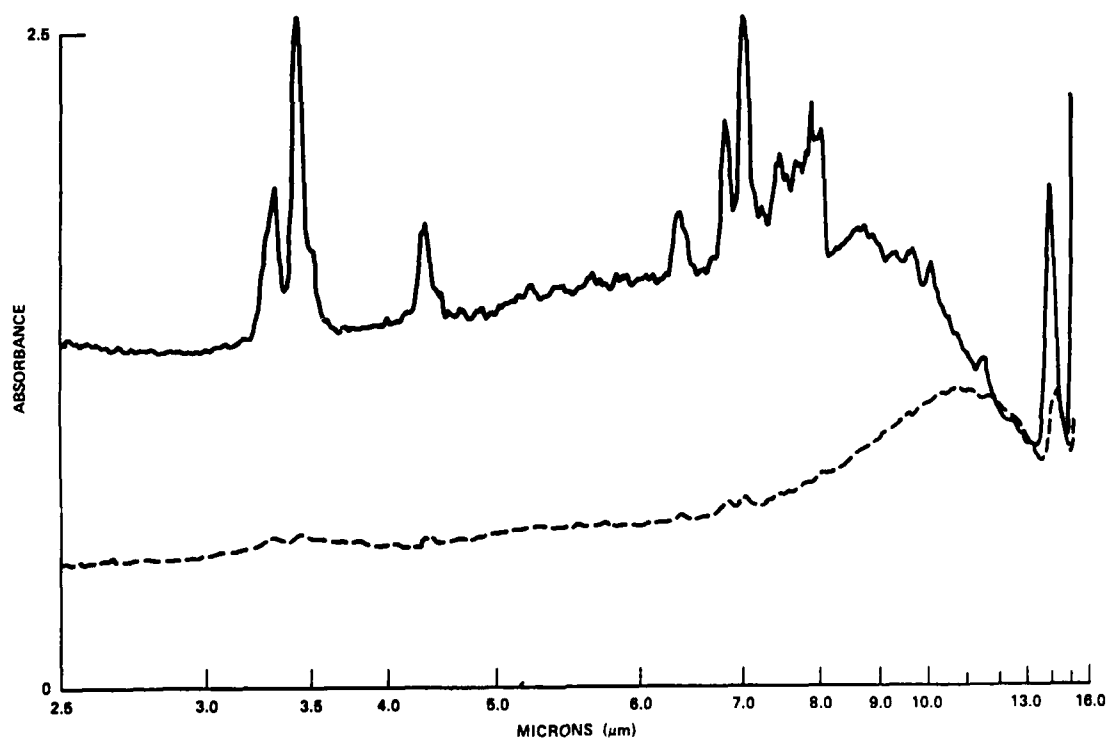
FIGURE 2. 11.3 MICRON POLYSTYRENE SPHERES.

diameter (μm)	slit area (X10^{-9} m^2)	number of spheres viewed	λ = 3.45 μm		λ = 7 μm		λ = 13.5 μm	
			A	a	A	a	A	a
0.81	2.34	4860	.061	26.73	.040	17.53	.056	24.54
0.81	2.34	1600	.029	26.62	.014	18.63	.014	18.63
2.956	2.34	450	.55	23.24	.07	2.96	.10	4.23
2.956	2.34	150	.12	15.2	.03	3.80	.04	5.07
5.1	2.34	95	.29	26.05	.12	10.78	.09	8.086
5.1	2.34	40	.02	4.268	.05	10.66	.03	6.401
5.7	2.34	84	.52	37.85	.17	12.37	.20	14.56
5.7	2.34	40	.075	11.46	.10	15.28	.11	16.81
7.6	2.34	45	.87	49.88	.24	13.76	.24	13.76
7.6	2.34	20	.20	25.80	.17	21.93	.13	16.77
9.8	6.25	70	.50	22.95	.22	10.10	.34	15.61
9.8	6.25	30	.02	2.142	.06	6.426	.14	14.99
11.33	2.34	20	1.25	47.65	.85	33.08	.97	37.76
11.33	2.34	10	.05	3.893	.05	3.893	.25	19.46
13.5	6.25	38	.87	28.14	.39	12.62	.87	28.14
13.5	6.25	16	.05	3.842	.07	5.379	.35	26.89
15.8	6.25	26	.62	18.29	.33	9.735	.57	16.81
15.8	6.25	12	.06	3.83	.06	3.83	.45	28.76

TABLE I. ABSORPTION COEFFICIENTS. Data above the dashed line represents undegraded areas of the spectra and that below the line the degraded cases.

Time Resolved Measurements of the Scattering of Femtosecond Laser Pulses

W. E. White, C.Wang and E. S. Fry
Texas A&M University, Physics Department
College Station, Texas, 77843

Abstract

The scattering of ultrashort laser pulses by Mie size dielectric particles is currently being investigated in the time domain. Time resolved measurements, resulting from use of an interferometric technique, are presented for planar and cylindrical scatterers. In both cases the spatial

length of the pulse is less than the thickness of the scatterer. Work is underway on a fast Kerr cell "shutter" system that will deliver lower noise, time resolved measurements with femtosecond time resolution. This will allow the investigation to be extended to the cases of (1) a sphere, and (2) coherent backscatter by an ensemble of scatterers.

Introduction

The time averaged scattering of electromagnetic radiation by microscopic particles has been studied extensively for the cases of incident plane waves[1] and Gaussian beams.[2-3] However, an interesting case occurs when the time duration of a pulse is so short that the spatial length of the pulse is less than the thickness of the scatterer. Thus, at any given instant in time, different sections of the scatterer will experience different radiation fields. This case has been studied with relatively large spheres at radar wavelength pulses;[4-5] however, prior to the advent of femtosecond lasers, it was not possible at visible wavelengths where the corresponding particle size is much smaller. While our previously reported[6] study confirmed the expectation that time averaged scattering of femtosecond pulses depends on pulse bandwidth, not pulse duration, the time resolved case remains likely to produce some very interesting results.

Experiment

The ultrashort optical pulses used in this experiment are produced in a Colliding Pulse Mode-locked (CPM) laser following the design of Valdmanis, et al.[7] This laser is capable of producing 630 nm pulses with widths as short as 28 fsec. at a repetition rate of 100 MHz. Throughout the experiment, an autocorrelator is used to monitor pulse width, while an optical multichannel analyzer monitors pulse bandwidth and power. Measurement of the scattered light with a time resolution of the order of femtoseconds is achieved through the use of the interferometric technique outlined in Fig. 1.
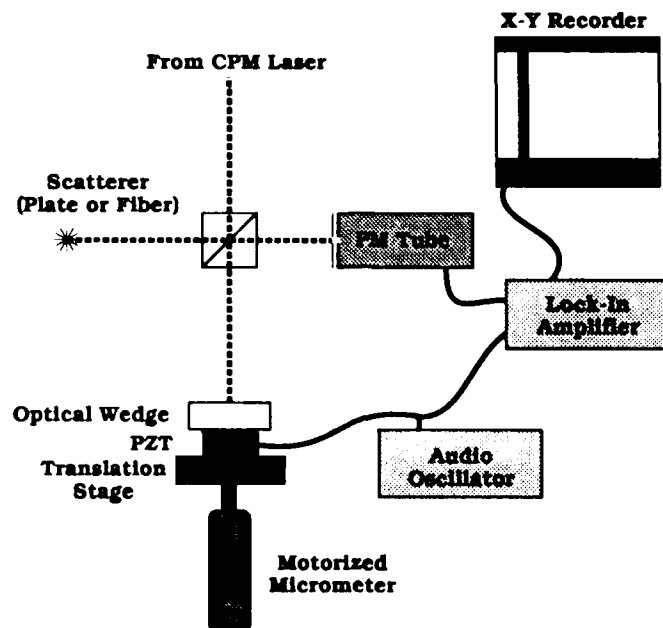
Figure 1. Schematic representation of the apparatus used for measurement of time resolved scattering.

The apparatus is based on a standard Michelson interferometer in which one leg is continuously swept in length in order to produce a time delay while the scattering takes place in the other leg. A slight modulation in length is applied to the time delay leg by means of a PZT, thus allowing for lock-in detection of the interference signal at the photomultiplier tube. The mirror in the time delay leg is replaced by an uncoated optical wedge in order to produce an intensity similar to the backscattered light from the plate or fiber used for the present data.

Results

Results of the time resolved scattering from a 9.5 mil glass plate are shown in Figure 2(b). As one would expect (see Fig. 2a), peaks are observed with time delays corresponding to the delay produced by multiple reflections from the front and rear surfaces of the plate ($\frac{2nd}{c}$, $\frac{4nd}{c}$, etc.). The measured time delays agree with the calculated values to all of the significant digits available when measuring the thickness of the plate (d).
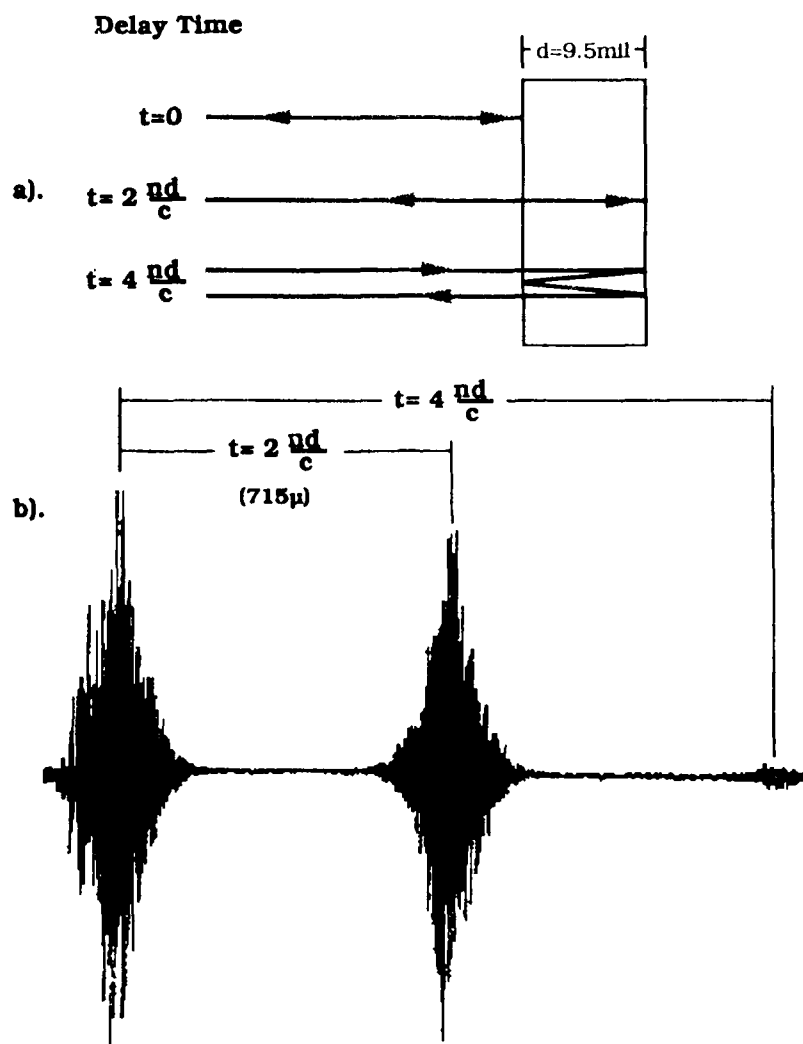
Delay Time

$\vdash d=9.5\text{mil} \dashv$

t=0

a). $t = 2\frac{nd}{c}$

$t = 4\frac{nd}{c}$

$t = 4\frac{nd}{c}$

$t = 2\frac{nd}{c}$

(715µ)

b).

Figure 2. Results of time resolved scattering measurements of a 9.5 mil glass plate. a) graphical explanation of expected results. b) actual scattering data (intensity vs. time).

Time resolved measurements of the scattering from a 75 µ glass fiber shown in figure 3(b) also agree with the time delays expected on the basis of geometric path differences. This is slightly complicated by the fact that for glass with index of refraction n=1.5, the time delay of the "Glory" is almost

equal to the time delay of the direct reflection from the back side of the fiber (as indicated in Fig. 3a). Thus, the larger second peak contains contributions from both modes of scattering. It should also be noted that the small first peak followed by a larger composite second peak bears a striking resemblance to Rheinstein's[4] theoretical predictions of the radar backscatter of a sphere.
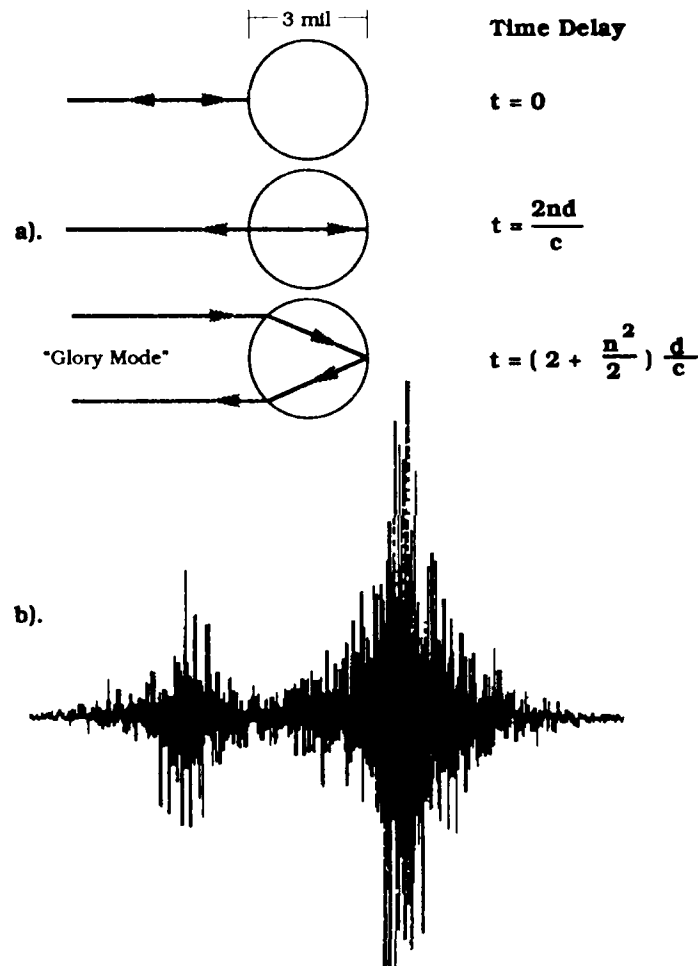

Figure 3. Results of time resolved scattering measurements of a 3 mil glass fiber. a) graphical explanation of expected results. b) actual scattering data (intensity vs. time).

Conclusions

These preliminary results demonstrate that it is possible to measure scattering with a time resolution of the order of femtoseconds. With the addition of the fast Kerr cell shutter, sensitivity will then become high enough to measure a Mie sized sphere. This will allow a comparison to the theoretical results of Hu, et al.,[8] who have developed a technique for predicting the time resolved optical scattering from a Mie sized sphere. The higher sensitivity will also allow an investigation into the temporal behavior of coherent backscatter by an ensemble of scatterers.

References

1. M. Kerker, The Scattering of Light and Other Electromagnetic Radiation, (Academic, New York, 1969).

2. L. W. Casperson, C. Yeh, and W. F. Yeung, Appl. Opt. 16, 1104 (1977).

3. W. G. Tam and R. Corriveau, J. Opt. Soc. Am. 68, 763 (1978).

4. J. Rheinstein, IEEE Trans. Ant. Prop. AP-16, 89 (1968)

5. S. K. Chaudhuri, F. B. Sleator, W. -M. Boerner, Radio Sci. 19,987 (1984).

6. G. T. Bennett, E. S. Fry, W. E. White, P. Herb, G. W. Kattawar, and W. Xu, "The Scattering of Femtosecond Optical Pulses by Small Dielectric Spheres," Proceedings of the 1987 Conference on Obscuration and Aerosol Research, submitted Sept. 1987.

7. J. Valdmanis, R. L. Fork, and J. P. Gordan, Opt. Lett.10,131 (1985).

8. C.-R. Hu, G. H. Rose, and G. W. Kattawar, "Calculation of Time Resolved Scattering of Femtosecond Light Pulses from Dielectric Spheres," submitted for publication in Proceedings of the 1988 Conference on Obscuration and Aerosol Research, submitted Sept. 1988.

NONSPECULAR SCATTERING BY IRREGULAR LAYERED MEDIA--FULL WAVE APPROACH

Ezekiel Bahar
Electrical Engineering Department
University of Nebraska--Lincoln
Lincoln, Nebraska 68588-0511

RECENT PUBLICATIONS, SUBMITTALS FOR PUBLICATION AND PRESENTATIONS:

A) E. Bahar, "Enhancement of Backscatter from Random Rough Surfaces-Full Wave Solution," 1987 IEEE AP-S International Symposium and URSI Radio Science Meeting, Virginia Tech., Blacksburg, Virginia, June 15-19, 1987.

B) E. Bahar, "Backscatter Enhancement of Infrared and Optical Radiation from Finitely Conducting Particles with Smooth and Very Rough Surfaces--First Order and Multiple Scatter," 1987 CRDEC Scientific Conference on Obscuration and Aerosol Research, Aberdeen, Maryland, June 22-26, 1987.

C) E. Bahar, "Radar Cross Section of Rough Terrain and Vegetation Covered Terrain," Member of U.S. National Research Council Delegation, XXIInd General Assembly of the International Union of Radio Science, Tel Aviv, Israel, August 24 - September 2, 1987.

D) E. Bahar, "Backscatter Enhancement from Sparsely Distributed Large Particles with Rough Surfaces," with M. A. Fitzwater, International Union of Radio Science (URSI) Meeting at the University of Colorado, Boulder, January 5-8, 1988.

E) E. Bahar, "Scattering and Depolarization by Two-Dimensional Random Rough Surfaces of Finite Conductivity - Theory and Experiment," with M. A. Fitzwater, 1988 SPIE Technical Symposium on Optics, Electro-Optics and Sensors - Wave Propagation and Scattering in Varied Media, Orlando, Florida, April 4-8, 1988.

F) E. Bahar, "Conditions for Coalescence of the Full Wave Solution for Rough Surface EM Scattering with Perturbation and Physical Optics Solutions in the Low and High Frequency Limits - Theory and Experiment," 1988 IEEE AP-S International Symposium and URSI Radio Science Meeting, Syracuse University, Syracuse, N.Y , June 6-11, 1988.

G) E. Bahar, "Nonspecular Scattering by Irregular Layered Media - Full Wave Approach," 1988 CRDEC Scientific Conference on Obscuration and Aerosol Research, Aberdeen, MD, June 20-24, 1988.

H) E. Bahar, "The Incoherent Like and Cross Polarized Backscatter Cross Sections of an Aniso-tropic Rough Sea Surface with Swell," (FRA2-11), 1988 International Geoscience and Remote Sensing Symposium, Edinburgh University, Edinburgh, United Kingdom, September 13-16, 1988.

I) E. Bahar, "Stokes Parameters for Propagation Media with Random Distributions of Irregular Shaped Particles," International Working Group Meeting on "Wave Propagation in Random Media," Tallin, U.S.S.R., September 19-23, 1988.

J) E. Bahar, "Scattering, Depolarization and Enhanced Backscatter from Random Rough Surfaces," International Working Group Meeting on "Wave Propagation in Random Media," Tallin, U.S.S.R., September 19-23, 1988.

K) E. Bahar, "Scattering and Depolarization by Random Rough Surfaces, Unified Full Wave Approach - An Overview," Proceedings of the International Symposium on Multiple Scattering of Waves in Random Media and Random Rough Surfaces, Editors V.V. Varadan and V.K. Varadan, pp. 715-733, Pennsylvania State University, 1987.

L) E. Bahar, "Comparison of Unified Full-Wave Solutions for Normal-Incidence Microwave Back-scatter from Sea with Physical Optics and Hybrid Solutions," with D.E. Barrick and M.A. Fitzwater, International Journal of Remote Sensing, Vol. 9, No. 3, pp. 365-377, 1988.

M) E. Bahar, "Full Wave Theory Applied to Computer Aided Graphics for Three-Dimensional Objects," with S. Chakrabarti, IEEE Computer Graphics and Applications, Special Issue, Supercomputers for Graphics, Vol. 7, No. 7, pp. 46-60, July 1987.

N) E. Bahar, "Review of the Full Wave Solutions for Rough Surface Scattering and Depolarization - Comparisons with Geometric and Physical Optics, Perturbation and Two-Scale Solutions," Journal of Geophysical Research, Vol. 92, No. 65, pp. 5209-5224, May 15, 1987.

O) E. Bahar, "Application of Full Wave Theory to Computer Aided Geometric Design," with S. Chakrabarti, Proceedings of the 29th Midwest Symposium on Circuits and Systems, Editor, M. Ismail, pp. 911-915, North Holland, N.Y., 1987.

P) E. Bahar, "Incoherent Diffuse Scattering by Irregular Shaped Particles of Finite Conductivity," with M.A. Fitzwater, Invited Paper in Special Issue of Radio Science, Vol. 22, No. 6, pp. 889-898, November 1987.

Q) E. Bahar, "Multiple Scattering Effects of Random Distributions of Irregularly Shaped Particles on Infrared and Optical Propagation," with M.A. Fitzwater, Proceedings of the Advisory Group for Aerospace Research and Development (NATO) Spring 1987 Electromagnetic Wave Propagation Panel Symposium "Scattering and Propagation in Random Media," AGARD-CPP-419, pp. 12-1, 12-15, May 1987.

R) E. Bahar, "Enhancement of the Backscattered Diffuse Specific Intensities from Random Distributions of Finitely Conducting Particles with Rough Surfaces," with M.A. Fitzwater, Journal of the Optical Society of America, A, Vol. 5, pp. 89-98, January 1988.

S) E. Bahar, "Full Wave Theory and Controlled Optical Experiments for Enhanced Scattering and Depolarization by Random Rough Surfaces," with M.A. Fitzwater, Optics Communications, Vol. 63, No. 6, pp. 355-360, September 1987.

T) E. Bahar, "Physical Interpretation of the Full Wave Solutions for the Electromagnetic Fields Scattered from Irregular Stratified Media," Radio Science, in press.

U) E. Bahar, "Full Wave - Co-Polarized Non-Specular Transmission and Reflection Scattering Matrix Elements for Rough Surfaces," with M.A. Fitzwater, Journal of the Optical Society of America, in press.

V) E. Bahar, "Full Wave Physical Models of Nonspecular Scattering in Irregular Stratified Media," with M.A. Fitzwater, IEEE Transactions on Antennas and Propagation, in press.

W) E. Bahar, "Backscatter Enhancement of Infrared and Optical Radiation from Finitely Conducting Particles with Smooth and Very Rough Surfaces - First Order and Multiple Scatter," with M.A. Fitzwater, Proceedings of the 1987 Scientific Conference on Obscuration and Aerosol Research, in press.

X) E. Bahar, "Unified Full Wave Approach Applied to Scattering and Depolarization by Random Rough Surfaces - An Overview," Journal of wave-Material Interaction, Vol. 2, No. 2, pp. 161-180. April 1987.

Y) E. Bahar, "Depolarization and Backscatter Enhancement in Light Scattering from Random Rough Surfaces - Theory and Experiment," with M.A. Fitzwater, Journal of the Optical Society of America, in press.

Z) E. Bahar, "The Incoherent Like and Cross Polarized Backscatter Cross Sections of an Anisotropic Rough Sea Surface with Swell," with C.M. Herzinger and M.A. Fitzwater, Journal of Geophysical Research - Oceans, in press.

AA) E. Bahar, "Scattering and Depolarization by Two-Dimensional Random Rough Surfaces of Finite Conductivity - Theory and Experiment," with M.A. Fitzwater, Proceedings of the SPIE 1988 Technical Symposium on Wave Propagation and Scattering in Varied Media, Vol. 927, pp. 78-87, April 6-8, 1988.

BB) E. Bahar, "Bistatic Incoherent Scattering Cross Sections for Two-Dimensional Random Rough Surfaces of Finite Conductivity," with M.A. Fitzwater, Journal of Wave-Material Interaction, Vol. 3, No. 2, pp. 173-187, April 1988.

CC) E. Bahar, "Scattering Cross Sections for Two-Dimensional Rough Surfaces with Different Correlation Lengths," with M.A. Fitzwater, Journal of Wave-Material Interaction, in press.

ABSTRACT

The full wave solutions for the vertically and horizontally polarized electromagnetic fields scattered by irregular stratified media are expressed in terms of double infinite sums. These full wave solutions satisfy the reciprocity relationships in electromagnetic theory. The physical interpretation of each term in the double infinite series provides insights into the nonspecular scattering phenomena for irregular stratified media. It is shown that n+1 different terms of the full wave expansion replace the single nth term of the corresponding geometric optics series. From scattering in the specular direction these n+1 terms become analytically indistinguishable, and the full wave solution reduces to the geometric optics solution. The full wave solutions are also consistent with Rice's perturbation solution for rough surface scattering in the low-frequency limit. The physical interpretation of the full wave solutions which are based on complete spectral expansions of the fields could be used to construct solutions for the nonspecularly scattered fields in complex problems involving irregular stratified media.

1. INTRODUCTION

Rigorous solutions for the reflection and transmission of electromagnetic waves have been derived

for multilayered media of uniform thickness [Wait, 1962]. However, in a broad class of important

radio wave communications and remote sensing problems, the height of the interface between two adjacent media is a random function, and the thicknesses of the layers are not uniform. In these cases the incident waves are depolarized and scattered into complete spectra of propagating and evanescent waves. Thus an incident plane wave may also be coupled into the surface and lateral waves supported by the layered medium [Brekhovskikh, 1960].

To facilitate the solution to these problems, several simplifying assumptions are made. Thus on adopting a physical optics approach, the Kirchhoff approximations are made for the surface fields, and the fields scattered by an element of the rough surface are proportional to the Fresnel reflection coefficient for the incident wave [Beckmann and Spizzichino, 1963]. However, for nonperfectly conducting surfaces these physical optics solutions for the fields scattered in the nonspecular direction do not satisfy the reciprocity relationships in electromagnetic theory. For perfectly conducting surfaces (for which the Fresnel reflection coefficients are of unit magnitude), the physical optics solutions for the nonspecular scattered field intensities do satisfy reciprocity [Beckmann and Spizzichino, 1963]; however, they are independent of polarization, in contradiction to well-documented experimental evidence [Barrick, 1970]

Similarly, in order to make the problem of propagation over a wedge-shaped overburden more tractable, the concept of the "effective surface impedance" has been introduced [Schlak and Wait, 1967, 1968]. In this case a physical optics approach is used to describe the fields in the wedge-shaped overburden as a sum of multiply reflected waves at the two interfaces of the wedge-shaped overburden. By making judicious use of the compensation theorem, the effective surface impedances (which depend upon position and the direction of propagation) are used to determine the fields at the observation point [Schlak and Wait, 1967, 1968]. It is shown by Schlak and Wait that when the location of the transmitter and receiver are interchanged the results are not in agreement with the reciprocity relationships in electromagnetic theory. Since the experimental results obtained by Schlak [1967] were not considered sufficiently accurate to resolve this problem, it was conjectured that the effective surface impedance calculations based on the physical optics approach were more reliable when propagation is in the direction of increasing overburden depth. However, the results of controlled laboratory experiments at 4.75 GHz conducted by King and Hustig [1971] contradict their conclusions.

These shortcomings of the physical optics approach to scattering in the nonspecular direction have motivated the author to develop a "full wave" approach to scattering in irregular layered structures. The full wave approach is based on a complete expansion of the fields in irregular layered structures (see Figure 1). The vertically and horizontally polarized wave spectra include the radiation fields and the lateral waves (associated with two different branch cuts) as well as the waveguide modes (associated with the poles of the reflection coefficient) of the layered structure. When these

complete expansions for the electric and magnetic fields are substituted into Maxwell's equations and exact boundary conditions are imposed upon the total fields, a set of first-order coupled differential equations is derived for the field transforms. These generalized telegraphists' equations [Schelkunoff, 1955] for the wave amplitudes decouple when the layers of the medium are uniform (constant electromagnetic parameters and plane parallel interfaces). In general, however, these generalized telegraphists' equations can be solved iteratively. The results of a second-order iteration are presented in the form of an integral (not integral equation) whose integrand represents the nonspecular scattering by an element of the irregular surface. Contrary to the physical optics solutions the corresponding full wave solutions for the scattered fields in the nonspecular direction are expressed in terms of double infinite sums that are completely reciprocal for arbitrary incident and scatter angles.

The full wave solutions are shown here to reduce to the familiar geometric optics series for the specular case. In addition, a precise physical interpretation is given to each of the terms of the double infinite series of the full wave solution. This provides additional insight into the phenomenon of electromagnetic wave scattering and facilitates the construction of solutions to more complex scattering problems that are based on spectral expansions of the fields. These reciprocal full wave solutions are not restricted to the far-field regions.

2. FORMULATION OF THE PROBLEM

To obtain full wave solutions for the electromagnetic fields scattered by irregular layered media (see Figure 1), generalized field transforms [Bahar, 1973a] are used. These field transforms provide a basis for the complete expansion of the transverse components of the vertically and horizontally polarized electric and magnetic fields in terms of the radiation fields, lateral waves, and guided surface waves of the layered structure [Brekhovskikh, 1960]. The complete field expansions are substituted into Maxwell's equations for the transverse field components, and use is made of the biorthogonal properties of the basis functions together with the exact boundary conditions for the electric and magnetic fields at each interface. Since the basis functions do not individually satisfy the boundary conditions, it is necessary to use Green's theorems to avoid the interchange of order of summation/integration (over the complete wave spectrum) and differentiation. On expressing the field transforms E^P and H^P (P=V,H) in terms of the forward and backward wave amplitudes a^P and b^P, sets of first-order coupled ordinary differential equations are obtained [Bahar, 1973b, 1974]. These equations are referred to as generalized telegraphists' equations [Schelkunoff, 1955].

For simplicity it is assumed here that the electric permittivity ε_i and magnetic permeability μ_i are constants for each of the three media (i=0,1, and 2) and that the interface between medium 0 and 1 is the plane y=0 while the interface between medium 1 and 2 is given by the continuous function

$$y = h(x) \quad -L < x < L \qquad y = h_{12} = \text{const.} \qquad |x| > L \qquad (1)$$

318

Furthermore, the excitation is assumed to be a plane wave incident from free space $(y > 0)$ with its wave normal in the direction

$$\bar{n}_0^i = \sin\theta_0^i \, \bar{a}_x - \cos\theta_0^i \, \bar{a}_y = \bar{k}_0^i / k_0 \tag{2}$$

Thus for $\exp(i\omega t)$ time harmonic excitations, the incident field is

$$\bar{E}_P^i = E_0^i \exp(-ik_0 \bar{n}_0^i \cdot \bar{r}) \bar{a}^P \qquad P = V, H \tag{3}$$

where k_0 is the free space wavenumber, $\bar{r}$ is the position vector and P is the polarization of the wave (Vertical or Horizontal). The first-order iterative solutions for the wave amplitudes are obtained by neglecting the scattering terms and solving the resulting uncoupled differential equations. These first-order solutions for the wave amplitudes (associated with the primary fields) are substituted in the right-hand side of equations to obtain the second-order iterative solutions. Thus, it can be shown that the second-order expression for the scattered radiation field can be rewritten as follows:

$$E_P^S(x,y,z) = E_{P1}^S(x,y,z) - E_{P2}^S(x,y,z) \tag{4}$$

where E_{P2}^S is expressed as the double infinite sum which can be shown to reduce to

$$E_{P2}^S(x,y,z) = \frac{E_0^i \exp(-ik_0^i \cdot \bar{r}) T_{91}^{Pi} R_{21}^{Pi} \exp(i2v_1^i h_{12}) T_{10}^{Pi}}{1 - R_{01}^{Pi} R_{21}^{Pi} \exp(i2v_1^i h_{12})} \tag{5}$$

where R_{01}^{Pi} and R_{21}^{Pi} are the Fresnel reflection coefficients (for polarization P = Vertical or Horizontal) at the interfaces between medium 1 and 0 and between medium 1 and 2, respectively and T_{01}^{Pi}, T_{10}^{Pi} are the Fresnel transmission coefficients from medium 1 to medium 0 and vice versa. Furthermore $v_1^i = k_1 C_1^i = k_1 \cos\theta_1^i$ The primary, reflected wave from the unperturbed layered structure $(h(x) = H_{12} = \text{const.})$ is

$$E_P^P(x,y,z) = E_0^i \exp(-i\bar{k}_0^i \cdot \bar{r}) \cdot \left[R_{10}^{Pi} + \frac{T_{01}^{Pi} R_{21}^{Pi} \exp(iv_1^i h_{12}) T_{10}^{Pi}}{1 - R_{01}^{Pi} R_{21}^{Pi} \exp(i2v_1^i h_{12})} \right] \tag{6}$$

The second term in (6) is exactly equal to E_{P2}^S. Thus, the total field is given by

$$E_P^T(\bar{r}) = E_P^P(\bar{r}) + E_P^S(\bar{r}) = E_0^i \exp(-i\bar{k}_0^i \cdot \bar{r}) R_{10}^{Pi} + E_{P1}^S \tag{7}$$

where E_{P1}^S is expressed as the double sum:

$$E_{P1}^S(\bar{r}) = E_0^i G_0 \sum_{p,q=0}^{\infty} \int_{-L}^{L} C_1^i F_{11}^P(\bar{k}^f, \bar{k}^i) \cdot T_{10}^{Pf} T_{10}^{Pi} (I_1^P / I_0^P) [R_{01}^{Pf} R_{21}^{Pf} \exp(i2v_1^f h)]^P$$

$$[R_{01}^{Pi} R_{21}^{Pi} \exp(i2v_1^i h)]^q \frac{(C_1^f + C_1^i)}{(2p+1)C_1^f + (2q+1)C_1^i} \cdot \exp[ik_1(\bar{n}_1^f - \bar{n}_1^i) \cdot (x_s \bar{a}_x + h \, \bar{a}_y)] dx_s \tag{8}$$

in which at the stationary point $\theta_1 \to \theta_1^f$ and

$$\bar{k}_1 \to \bar{k}_1^f = k_1 \, \bar{n}_1^f = k_1 (\sin\theta_1^f \, \bar{a}_x + \cos\theta_1^f \, \bar{a}_y) \tag{9}$$

and $\bar{k}_1^f$ is related to $\bar{k}_0^f = k_0 \bar{n}_0^f$, the scattered wave vector in free space through Snell's law. The constant G_0 is

$$G_0 = \frac{k_0 \exp(-ik_0 \rho)}{(2\pi k_0 \rho)^{1/2}} \exp(i\pi/4) \tag{10}$$

and

$$\rho = (x^2 + y^2)^{1/2} \qquad x = \rho\cos\theta_0^i \qquad y = \rho\sin\theta_0^i \tag{11}$$

In equation (8) F_{11}^P is the rough surface element scattering coeffient and I_0, I_1 are related to the

wave impedances in medium 0 and 1. It is interesting to note that in the small perturbation limit

(namely, $k_1 h \ll 1$), equation (8) is in complete agreement with Rice's [1951] solution.

3. PHYSICAL INTERPRETATION OF FULL WAVE RESULTS

To facilitate the analytical presentation in this section, the following abbreviated notations
are introduced

$$E^{Pi} \equiv R_{21}^{Pi} \exp(i2v_1^i h)R_{10}^{Pi} \qquad (12a)$$

$$R^{Pf} = R_{21}^{Pf} \exp(i2v_1^f h)R_{10}^{Pf} \qquad (12b)$$

Thus R^{Pi} and R^{Pf} correspond to complete round trip transitions of trapped waves in medium 1 (ϵ_1, μ_1)
at the incident (θ^i) and scatter (θ^f) angles, respectively. Furthermore, the expression for E_{P1}^S in (4)
is rewritten upon collecting all the terms in the double sum such that p+q=n (since it is absolutely
summable for $|R^{Pf}| < 1$ and $|R^{Pi}| < 1$). Thus

$$E_{P1}^S(x,y,z) = E_0^i G_0 \int_{-L}^{L} C_1^i F_{11}^P(\bar{k}^f, \bar{k}^i) T_{10}^{Pf} T_{10}^{Pi}(I_1^P/I_0^P)$$

$$\sum_{n=0}^{\infty} \frac{(R^{Pi})^n}{n+1} \sum_{p=0}^{n} (R^{Pf}/R^{Pi})^p f_{np}(C_1^f, C_1^i) \cdot \exp[ik_1(\bar{n}_1^f - \bar{n}_1^i) \cdot (x_s \bar{a}_x + h \bar{a}_y)]dx \qquad (13)$$

where

$$f_{np}(C_1, C_1^i) = \frac{(n+1)(C_1^i + C_1)}{2(n+1)C_1^i + (2p+1)(C_1 - C_1^i)} - 1 + \frac{(n-2p)(C_1 - C_1^i)}{2(n+1)C_1^i + (2p+1)(C_1 - C_1^i)} \qquad (14)$$

Thus, the integrand of the term n=0(p=q=0) in (13) corresponds to a wave that is incident at an angle
θ_0^i on the interface $y=h_{01}=0$ and transmitted (T_{10}^{Pi}) at the angle of refraction θ_1^i to the surface element
dx on $y=h_{12}$ where it is scattered $(C_1^i F_{11}^P)$ at an angle θ_1^f before it is transmitted (T_{01}^{Pf}) through
the interface $y=h_{01} = 0$ at the angle of refraction θ_0^f (see Figure 2). Note that this term (n=0)
is reciprocal in the incident and scatter angles. The corresponding physical optics expression in
which $F_{11}^P(\bar{k}^f, \bar{k}^i)$ is replaced by R_{21}^{Pi} is not reciprocal. The physical optics expression is equal to
the full wave expression only for the specular case where $F_{11}^P(\bar{k}^f, \bar{k}^i) = R_{21}^{Pi}$.

In general the integrand of the nth term (p=0, 1,...,n) in (13) corresponds to n+1 different
waves. Typically, each one corresponds to a wave that makes q=n-p complete round trips $((R^{Pi})^{n-p})$
in medium 1 at the incident angle θ_1^i before it is scattered by the surface element dx on $y=h_{12}$,
$(C_1^i F_{11}^P)$ and emerges through the interface $y=h_{01}$ only after it makes p round trips $((R_f^{Pf})^p)$ in medium 1
at the scatter angle θ_1^f (see Figure 2). These n+1 waves taken together are completely reciprocal in
θ_0^i and θ_0^f. For the specular case these n+1 different waves become analytically indistinguishable,
and they add up to the single term in the corresponding physical optics solution, since

$$\frac{(R^{Pi})^n}{n+1} \sum_{p=0}^{n} (R^{Pf}/R^{Pi})^p f_{np}(C_1^f, C_1^i) \rightarrow (R^{Pi})^n \qquad (15)$$

There are two important factors that make the full wave solution completely reciprocal:
Nonspecular scattering at each surface element dx is characterized by the coefficient $C_1^i F_{11}^P$ and not

320

by its physical optics counterpart $C_1^f R_{21}^{Pi}$. Furthermore, for the nonspecular case there are a total

of $n+1$ different waves ($p=0, 1,\ldots,n$; $q=n, n-1,\ldots,0$) associated with the corresponding physical optics

term $T_{01} R_{21} T_{10} [R_{21}\exp(iv_1 h) R_{01}]^n$.

4. CONCLUDING REMARKS

A full wave solution for the electromagnetic fields scattered from irregular stratified media

has been analyzed. These full wave solutions are based on the use of complete spectral expansions of

the fields and the imposition of exact boundary conditions. The full wave solutions for the scattered

fields are expressed as a double infinite sum of terms which, unlike the physical optics solutions,

are completely reciprocal. A physical interpretation is given to each term of the double infinite

series, and it is shown that $n+1$ terms in the full wave expansion are associated with the single nth

term of the corresponding physical optics solution. It is also shown that for scattering in the

specular direction the full wave and physical optics solution are identical for uniform stratified

structures.

ACKNOWLEDGMENTS

REFERENCES

1. Bahar, E., "Depolarization of Electromagnetic Waves Excited by Distributions of Electric and Magnetic Sources in Inhomogeneous Multilayered Structures of Arbitrarily Varying Thickness--Generalized Field Transforms," J. Math. Phys., 14, (11), 1502-1509, 1973a.
2. Bahar, E., "Depolarization of Electromagnetic Waves Excited by Distributions of Electric and Magnetic Sources in Inhomogeneous Multilayered Structures of Arbitrarily Varying Thickness--Full Wave Solutions," J. Math. Phys., 14, (11), 1510-1515, 1973b.
3. Bahar, E., "Depolarization in Nonuniform Multilayered Structures--Full Wave Solutions," J. Math. Phys., 15, (2), 202-208, 1974.
4. Beckmann, P., and A. Spizzichino, The Scattering of Electromagnetic Waves from Rough Surfaces, Pergamon, New York, 1963.
5. Brekhovskikh, L. M., Waves in Layered Media, Academic, San Diego, California, 1960.
6. King, R. J. and C. H. Hustig, "Microwave Surface Impedance Measurements of a Dielectric Wedge on a Perfect Conductor," Can. J. Phys., 49, 820-830, 1971.
7. Rice, S. O.,"Reflection of Electromagnetic Waves from a Slightly Rough Surface," Commun. Pure Appl. Math., 4, 351-378, 1951.
8. Schelkunoff, S. A., "Conversion of Maxwell's Equations into Generalized Telegraphists' Equations," Bell Sys. Tech. J., 34, 999-1043, 1955.
9. Schlak, G. A., "An Investigation of Electromagnetic Wave Propagation Over Inhomogeneous Ground," Ph.D. thesis, Univ. of Colo., Boulder, 1967.
10. Schlak, G. A., and J. R. Wait, "Electromagnetic Wave Propagation Over a Nonparallel Stratified Conducting Medium," Can. J. Phys., 45, 3697-3720, 1967.
11. Schlak, G. A., and J. R. Wait, "Attenuation Function for Propagation Over a Nonparallel Stratified Ground," Can. J. Phys., 46, 1135-1136, 1968.
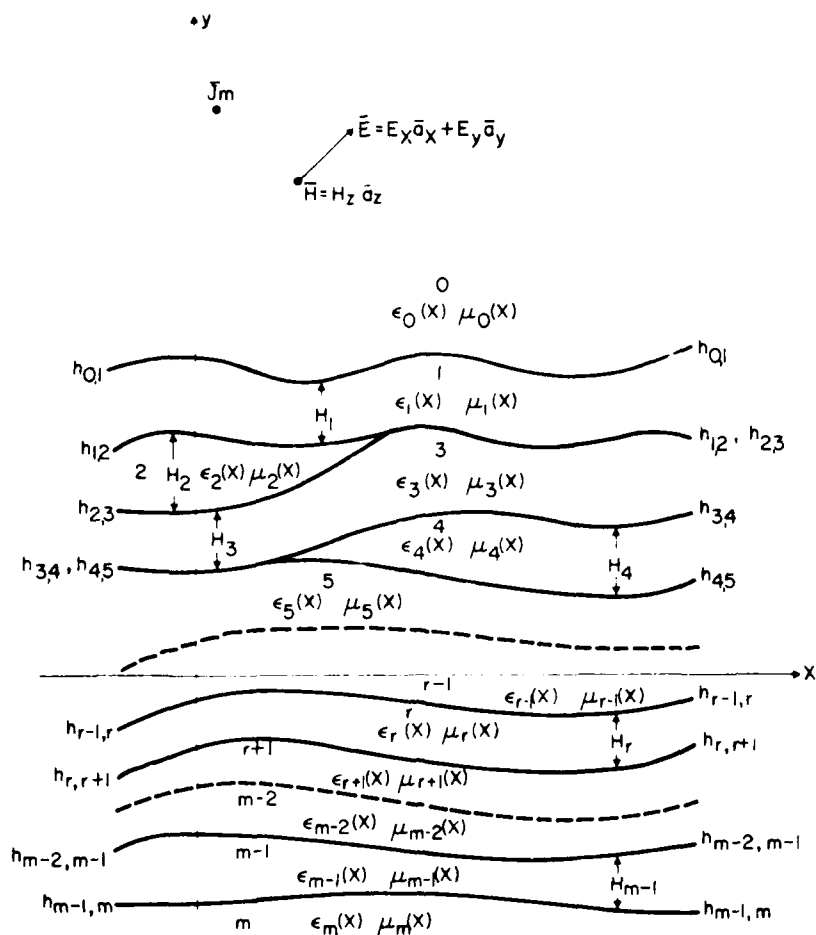12. Wait, J. R., Electromagnetic Waves in Stratified Media, Pergamon, New York, 1962.

FIG. 1. Line source over a nonuniform multilayered structure.
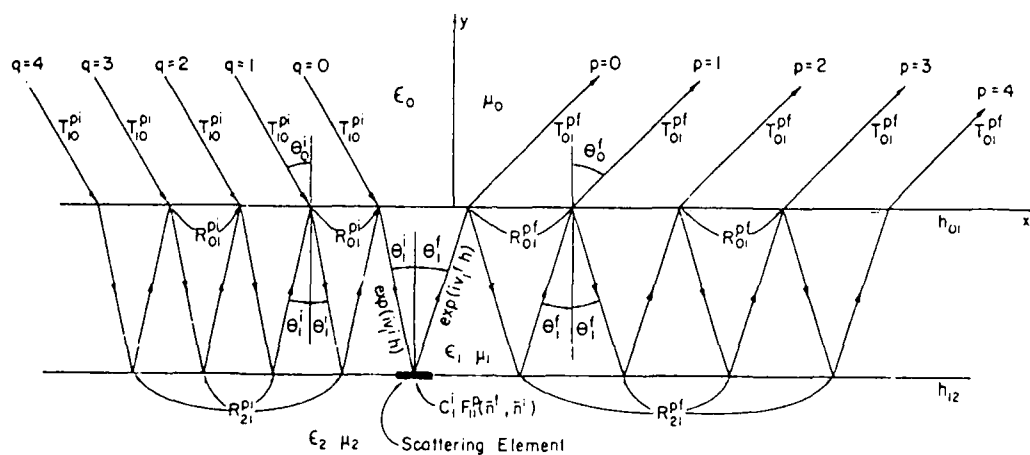

FIG. 2. Physical interpretation of double infinite terms of the full wave solutions; p and q are associated with the scattered and incident waves, respectively.

POLARIZED LIGHT-SCATTERING MUELLER MATRIX ELEMENTS
FOR SOME INTERESTING SCATTERERS

W. S. Bickel, D. Abromson, S.-C. Chiao, P. Bandu, S. Y. Shu and T. Wentzel
Physics Department, University of Arizona
Tucson, AZ 85721

ABSTRACT

Mueller matrix elements of some interesting scatterers are presented to show their importance as signatures and probes for change.

INTRODUCTION

The polarized light-scattering signals (Mueller matrix elements) can be used as a signature for a scatterer and as a probe for a change in its optical and geometrical properties. Light-scattering signals used to quantify scatterers should be unique, specific and sensitive to change. The following experimental and theoretical matrix elements are signatures for some fundamental (ideal) systems. Small changes in optical or geometrical properties of these systems affect the matrix elements and demonstrate their sensitivity to change.

DISCUSSION

Figure 1 compares four experimental and theoretical matrix elements, S_{11}, S_{12}, S_{33} and S_{44}, for a "perfect" 0.999-micron-radius quartz fiber. The almost-exact coincidence of the two curves shows that the fiber is of high quality and that theory is correct. Experiments with quartz fibers show that radius changes less than a nanometer in a one-micron fiber can be detected.
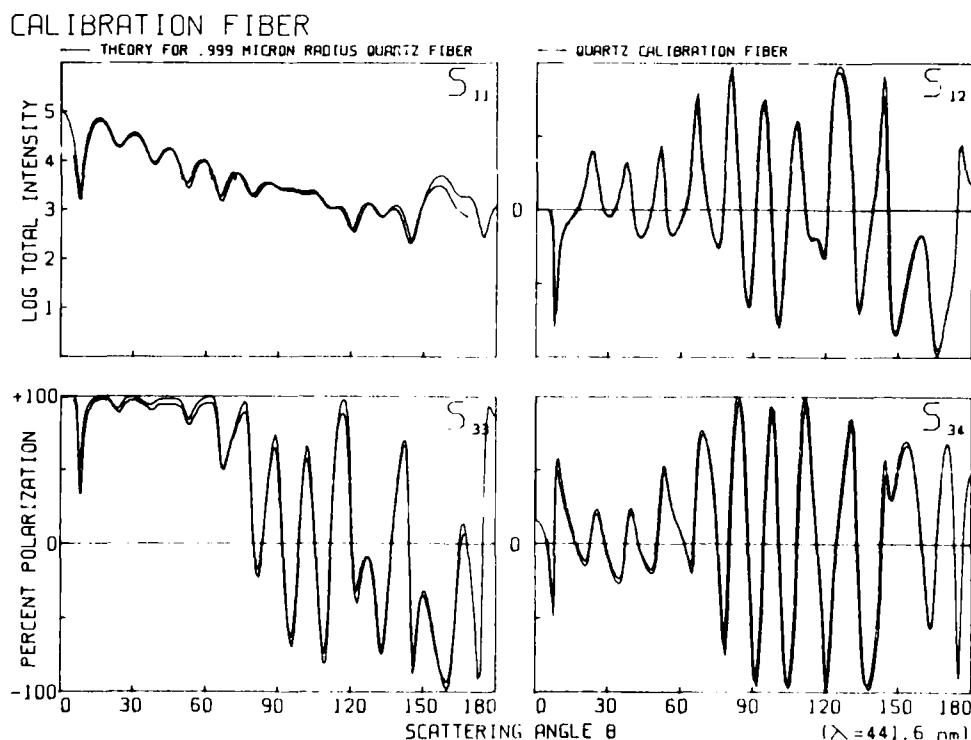
FIGURE 1. MATRIX ELEMENTS FOR A QUARTZ CALIBRATION FIBER

Figure 2 shows four matrix elements for a Rayleigh-Gans sphere when the sphere refractive index is slightly greater (1.008) and slightly less (0.992) than the index of the surrounding medium (1.000). As the refractive index approaches that of the medium, the particle disappears (S_{11} goes to zero at all angles), while the other matrix elements approach the Rayleigh limit. Sharp spikes, which are remnants of Mie phase structure, occur on all S_{ij}. As S_{34} goes to zero, the inflections that remain at certain angles go through a phase change when the sphere index passes through 1.000. Although no material has a refractive index of 1.000, biological cells (and other particles) with high index suspended in solutions with high index become Rayleigh-Gans particles as their indices become equal. These four matrices are calculated from exact Mie theory and therefore show the sharp inflections that are absent in the Rayleigh-Gans approximation.
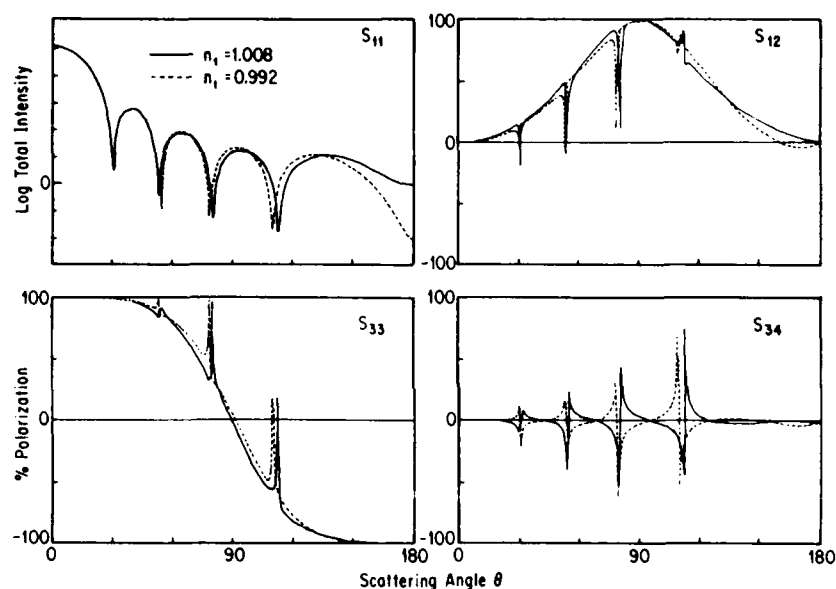
FIGURE 2.   MATRIX ELEMENTS FOR A RAYLEIGH-GANS SPHERE.

Figure 3 shows the theoretical response of matrix element S_{12} as a 0.652-micron-radius quartz fiber is coated with a water layer (n = 1.333) of various thickness. Most significant changes occur in the forward and backscatter as the cladding thickness changes from 0.00 to 0.016 microns. We found that the S_{12} matrix element was the most sensitive indicator of changes of cladding thickness.

Figure 4 shows the experimental response of matrix element S_{12} as the relative humidity of the air surrounding a 0.652-micron-radius quartz fiber is changed from 0 percent RH to 98.9 percent RH. We compared this curve to the one in Fig. 3. Assuming the theory is correct and that the cladding was water, we determined that at 98.0 percent RH, the water cladding was 0.016 microns thick. Using data from all matrix elements, light-scattering measurements can detect cladding thickness as small as 4×10^{-4} microns and possibly monolayers. The theory yielding Fig. 3 has not been experimentally tested yet.

FIBER SCATTERING
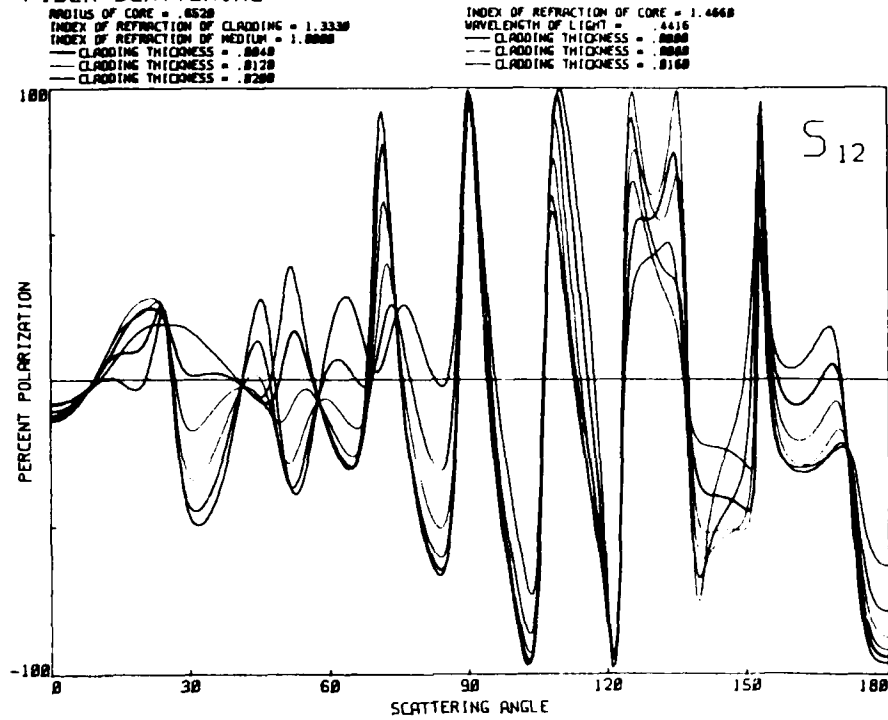
FIGURE 3. MATRIX ELEMENT S_{12} FOR A CLADDED FIBER (THEORY).
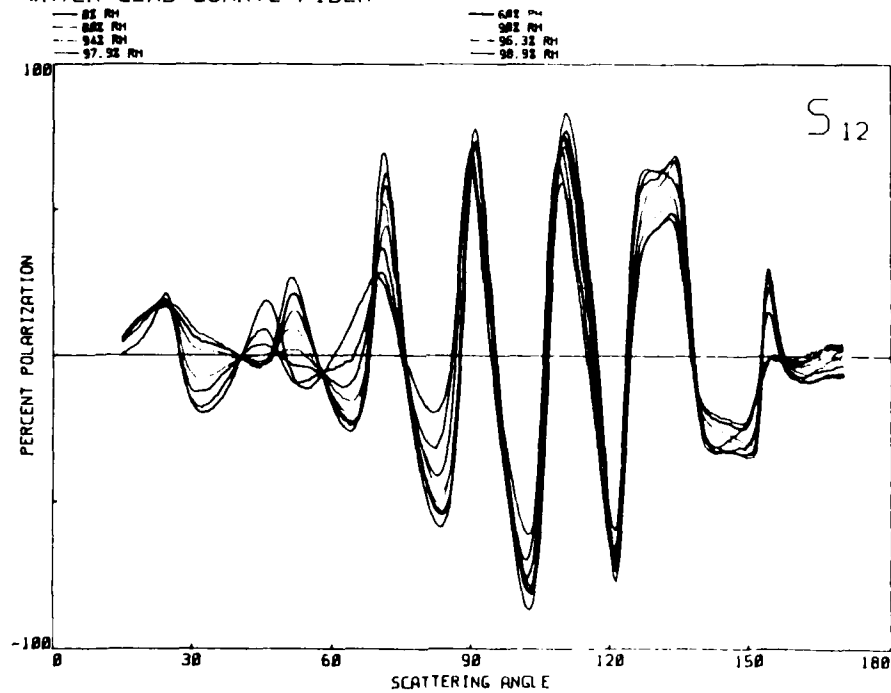
WATER-CLAD QUARTZ FIBER

FIGURE 4. MATRIX ELEMENT S_{12} FOR A CLADDED FIBER (EXPERIMENT).

Figure 5 shows the experimental response of matrix element S_{33} as a 0.610-micron-radius cylindrical quartz fiber is moved toward and parallel to a perfect aluminum mirror until contact is made. The system is illuminated at grazing incidence (α = 0). The initial separation d (fiber-mirror) is 234 microns. As d decreases to 0.0 microns (contact), high-frequency phase information starts at θ = 90° and moves to the forward and backscatter. Near and at contact, the 90-degree region is relatively free of high-frequency oscillations. These experiments show that the matrix elements for the fiber-mirror combination at large and small separation are different, and they are different from the matrix elements of the single fiber with no mirror.
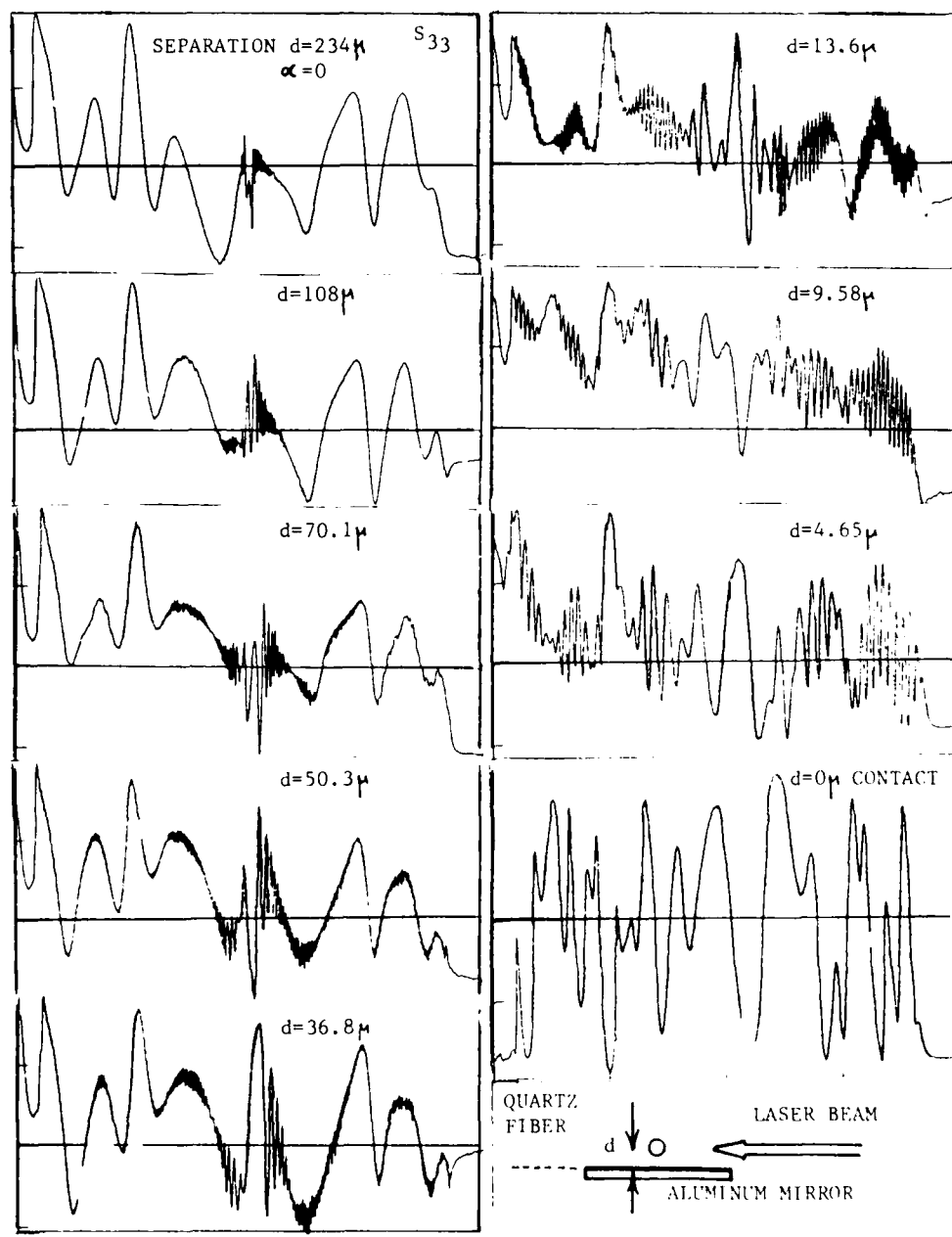
FIGURE 5. MATRIX ELEMENT S_{33} FOR A 0.610 MICRON FIBER NEAR A REFLECTING PLANE.

Figure 6 shows the loss of phase information that occurs in four matrix elements as a 2.8-micron-radius quartz fiber is coated with small (<1.0 micron) MgO crystals. The crystals "roughen" the fiber to create out-of-plane scattering and destroy virtually all the phase information needed to determine the fiber size. The residual high-frequency signal is reproducible "noise" due to localized roughness of the fiber. The matrix elements for this complex scattering system cannot be predicted by exact theory as can the matrix elements for the fundamental systems shown in Figs. 1-5.

QUARTZ FIBER COATED WITH MGO CRYSTALS
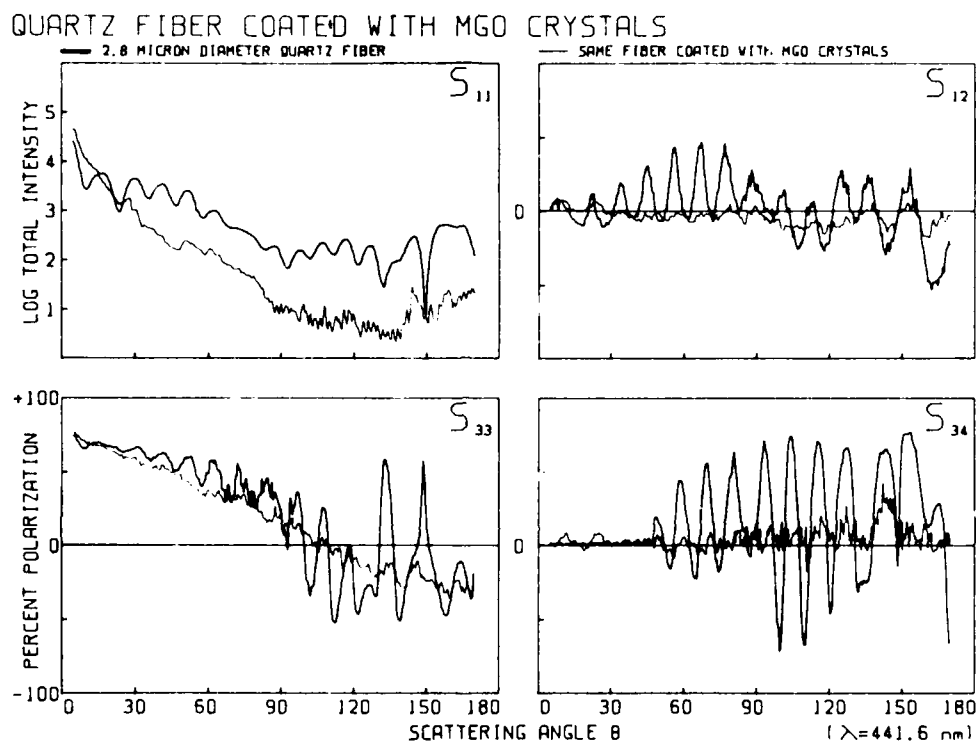
FIGURE 6. MATRIX ELEMENTS FOR A PERFECT AND PERTURBED QUARTZ FIBER.

Figure 7 shows the well-known Fresnel reflection curves for three smooth perfect surfaces of glass, copper and aluminum. These curves are the starting point for scattering from more complex surfaces -- layered, coated with perfect spheres or fibers, scratched or otherwise imperfect. These Fresnel curves for polarized intensities can be transformed into percent polarization curves and displayed as matrix elements.

Figure 8 shows four matrix element curves for the surfaces of Fig. 7. The horizontal scale for each curve gives the incident angle of illumination in degrees. Since a perfect surface "does not scatter," the Fresnel curves and their corresponding matrix elements exist only at the specular reflectance angle, which equals the angle of incidence. These studies show that grazing incidence gives the largest differences in S_{11} and S_{33}, whereas near-normal incidence $60° \gtrsim \theta \gtrsim 85°$ gives the largest differences in S_{12} and S_{34}.

INTENSITY REFLECTED FROM SURFACES
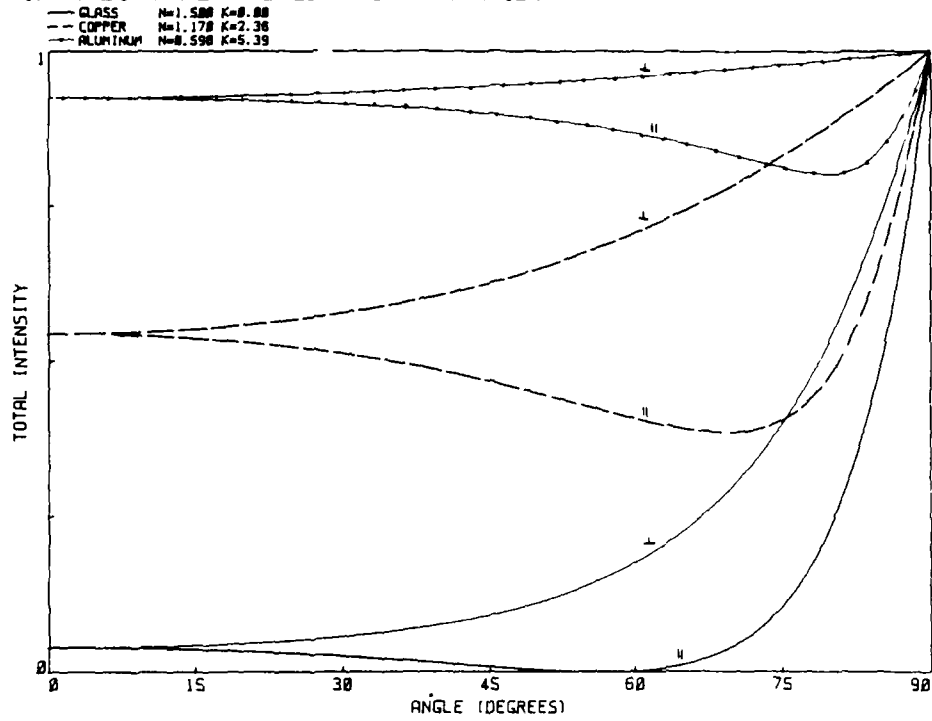
FIGURE 7. FRESNEL CURVES FOR GLASS, COPPER AND ALUMINUM.

REFLECTION FROM SURFACES
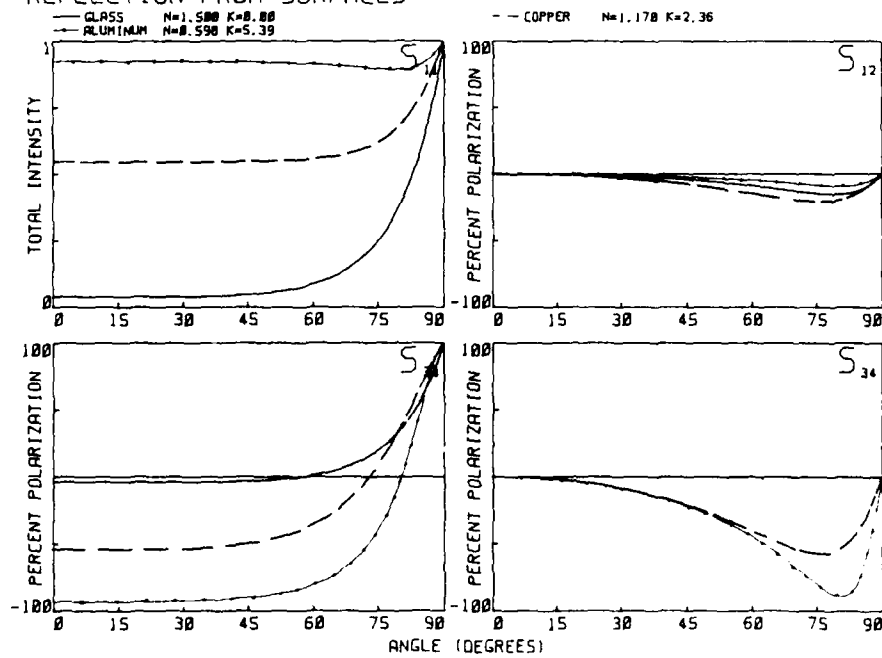
FIGURE 8. MATRIX ELEMENT REPRESENTATIVE OF THE FRESNEL CURVES FOR GLASS, COPPER AND ALUMINUM.

328

Figure 9 shows how the matrix elements respond to changes of water-layer thickness on an aluminum surface. As the thickness increases, the well-known thin film interference patterns appear. These studies show that for water layers (dielectrics) on aluminum, the greatest sensitivity to increasing water thickness lies near normal incidence for all matrix elements.

REFLECTION FROM WATER LAYERS ON ALUMINUM

--- WATER LAYER THICKNESS 0.0002 MICRONS   ··· WATER LAYER THICKNESS 0.0020 MICRONS
--- WATER LAYER THICKNESS 0.0200 MICRONS   --- WATER LAYER THICKNESS 0.2000 MICRONS
--- WATER LAYER THICKNESS 2.0000 MICRONS
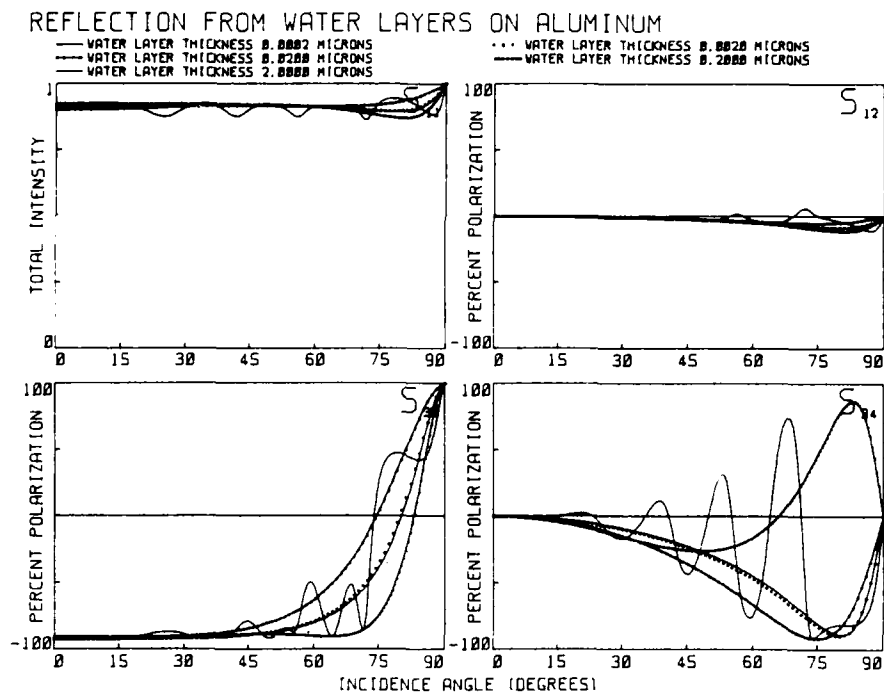
FIGURE 9.   MATRIX ELEMENTS FOR A WATER LAYER ON ALUMINUM.

Figure 10 emphasizes the differences and sensitivity indicated in Fig. 9. Here the water-layer thickness is very small, varying from 0.0002 to 0.008 microns. S_{33} and S_{34} are most sensitive near normal incidence showing from 50 to 200 percent polarization changes for thickness changes of 8 Angstroms. Thicknesses close to a monolayer can be detected with these techniques.

Figure 11 shows how four matrix-element curves respond to a perfect aluminum mirror surface "perturbed" by a 0.26 micron quartz fiber in contact with the surface. The important observation is that the S_{ij} for a fiber on a surface are significantly different than for the fiber alone. No satisfactory theory exists to predict these S_{ij}. The signals depend on the angle of surface illumination which, in this case, was 11 degrees.

Figure 12 shows the response of four matrix elements to a rough, sanded aluminum surface as a function of illuminating angle $\theta_r/2$. Similar data from different metal surfaces and different roughness show that, generally, S_{34} is independent of the illumination angle for all θ_r. S_{33} depends on θ_r in the backscatter, but not in the forward scatter, while S_{34} depends on θ_r over the entire range of illumination angle. S_{11}, the total intensity scattering signal, also shows a strong dependence on θ_r. This dependence often can be removed by appropriate geometrical scaling giving the BRDF (bidirectional relfection distribution function). The scaling is not valid, however, for all types of surfaces and surface roughness.
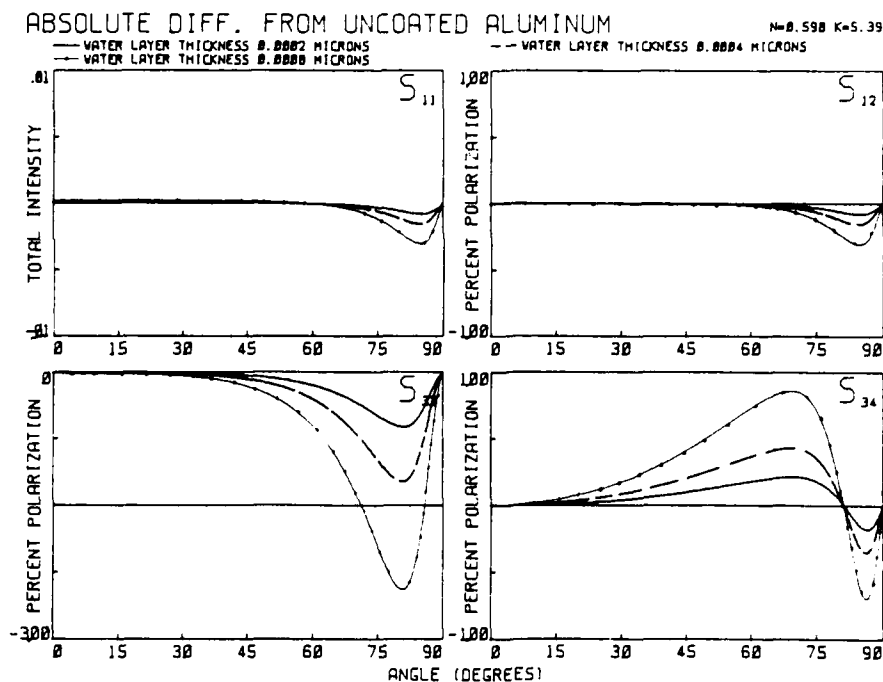
329

ABSOLUTE DIFF. FROM UNCOATED ALUMINUM   N=0.598 K=5.39
— WATER LAYER THICKNESS 0.0002 MICRONS   — — WATER LAYER THICKNESS 0.0004 MICRONS
—+— WATER LAYER THICKNESS 0.0008 MICRONS

FIGURE 10.   SIGNAL DIFFERENCES BETWEEN WATER COATED AND UNCOATED ALUMINUM.

FIBER ON SURFACE STUDY
⋯⋯ 0.26 MICRON QUARTZ FIBER   — 0.26 MICRON QUARTZ FIBER ON PERFECT SURF

SCATTERING ANGLE
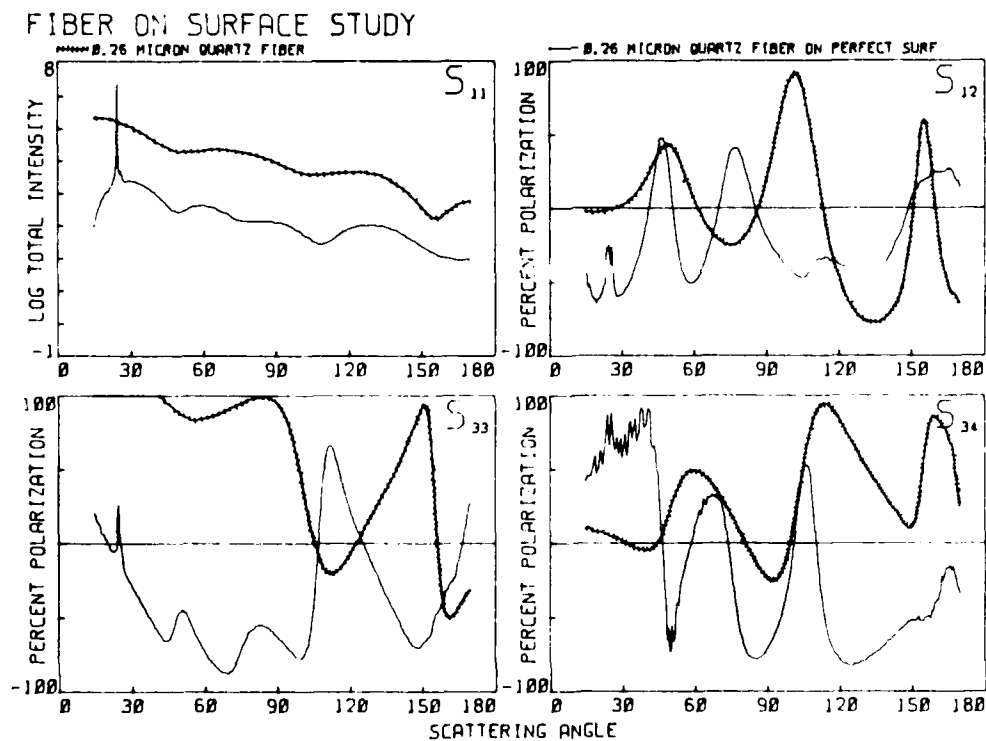
FIGURE 11.   MATRIX ELEMENTS FOR A QUARTZ FIBER ON AN ALUMINUM SURFACE.

330
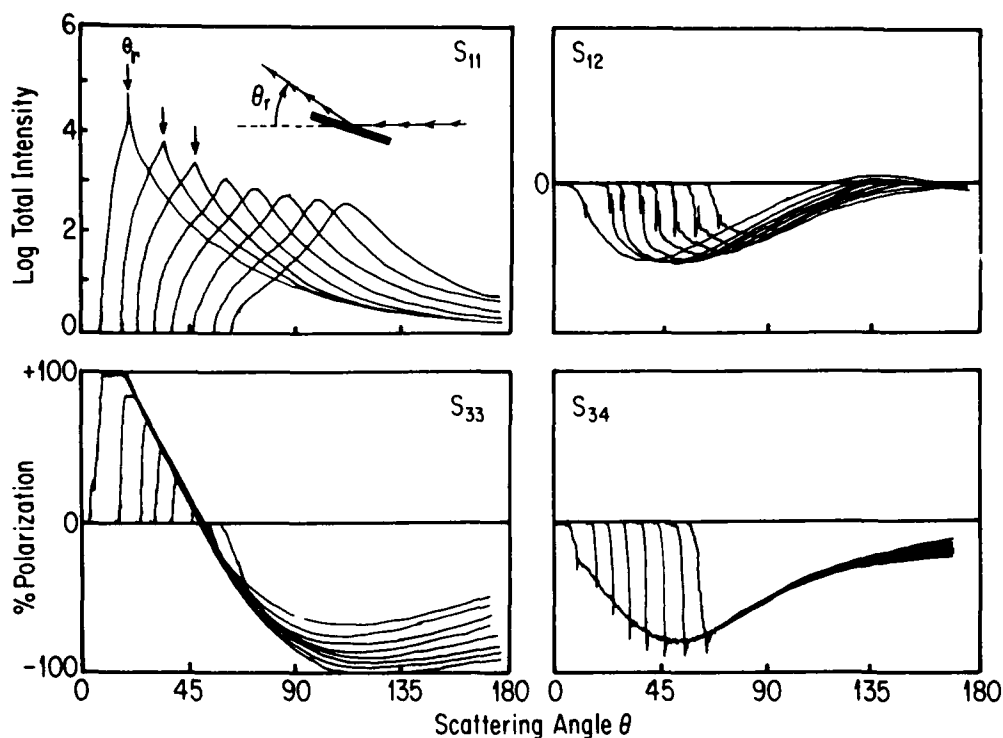
FIGURE 12.   MATRIX ELEMENTS FOR A ROUGH ALUMINUM SURFACE.

Figure 13 shows the response of S_{34} to a rectangular line (h = 0.06 μ, w = 2.2 μ) on an aluminum surface illuminated at two different angles (near grazing α = 15° and near normal α = 81°).   At near-grazing incidence, all phase information disappears.   We find that none of the polarization matrix elements scale with illumination angle α.   This means that data taken at α = 81° cannot predict what the S_{ij} will look like at α = 15° -- and, in general, the S_{ij} taken at one angle cannot be useful to predict the S_{ij} at another angle.
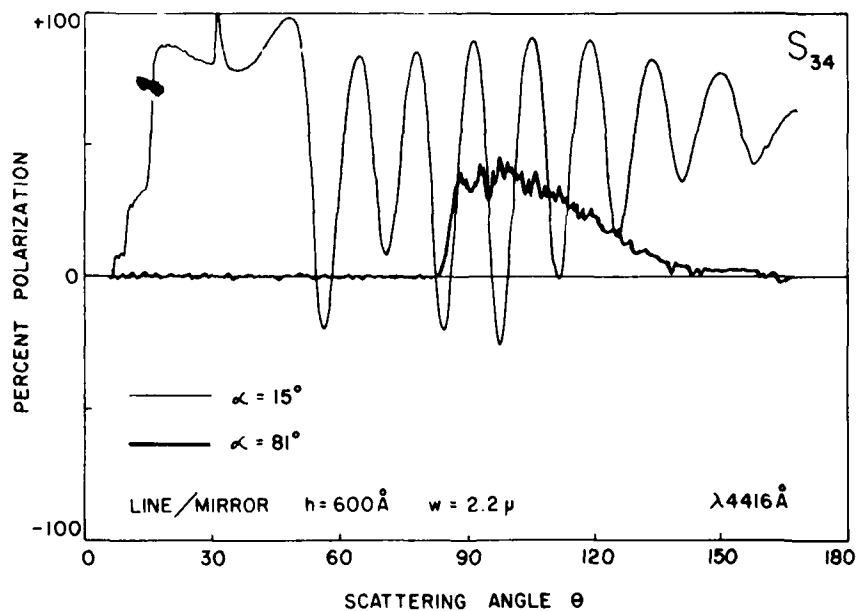
FIGURE 13.   MATRIX ELEMENT S_{34} FOR A RECTANGULAR LINE ON A MIRROR AS A FUNCTION OF ILLUMINATION ANGLE.

Blank

Determination of the Photon Lifetime in an Aerosol
Particle using Energy Transfer

S. Arnold and L.M. Folan

Microparticle Photophysics Laboratory(MP3L)
Department of Physics
Polytechnic University
333 Jay St., Brooklyn, N.Y. 11201

RECENT PUBLICATIONS, SUBMITTALS FOR PUBLICATION AND PRESENTATIONS:

A. L.M. Folan, S. Arnold and S.D. Druger, Enhanced Energy Transfer within a Microparticle,
   Chem. Phys. Lett.118, 322(1985).

B. S.Arnold and L.M. Folan, A Fluorescence Spectrometer for a Single Electrodynamically
   Levitated Microparticle, Rev.Sci.Inst.57, 2250(1986).

C. L.M. Folan, Optical depth probing in a microparticle, Bull. Amer. Phys. Soc. 32, 605
      (1987).

D. S.D. Druger, S.Arnold, and L.M. Folan, Theory of Enhanced Energy Transfer between
      Molecules Embedded in Spherical Dielectric Microparticles, J. Chem. Phys. 87,2649
      (1987).

E. S. Arnold, and L.M.Folan, A Spherical Void Electrodynamic Levitator,
   Rev.Sci.Inst.58, 1732(1987).

F. L.M. Folan and S. Arnold, Determination of Molecular Orientation at the Surface of an
      Aerosol Particle by Morphology Dependent Photoselection, Opt. Lett. 13, 1 (1988).

G. S. Arnold and L.M. Folan, Energy Transfer and the Photon Lifetime within an Aerosol
   particle, Opt.Lett.(Submitted, Sept.1988).

ABSTRACT

The theory of enhanced energy transfer within an aerosol particle based on donor coupling to
morphological dependent resonances(MDR) is tested for the first time. The correspondence
between theory and experiment allows one to obtain the photon lifetime within the longest lived
resonance. A comparison between this lifetime and the lifetime as obtained by Mie theory is
discussed.

Recently it has been found that energy transfer between donor and acceptor molecules in an aerosol particle may be enhanced by orders of magnitude over conventional long range energy transfer(Forster transfer).[1] It was hypothesized in the original article that the enhanced transfer was the result of coupling of donor excitation to morphological resonances of the particle. More recently a number of detailed theories have evolved for explaining this effect based on the original hypothesis. In what follows we provide, for the first time, a verification of the recent theories. In addition we show that the correspondence between experiment and theory enables one to determine the photon lifetime of the longest lived resonances. This is a particularly useful method since other recent determinations of photon lifetime have been based on the buildup of Stimulated Raman Scattering[2,3] for which there have been no corresponding theoretical calculations.

Recently Folan et al[1] have shown that energy transfer (between donor and acceptor molecules) within an aerosol particle(at dilute concentrations) may be enhanced by orders of magnitude over conventional long range transfer(Forster transfer). Aside from the enhancement the most distinct characteristic in these experiments was the independence of the transfer on acceptor concentration from $4 \times 10^{-5}M$ to $10^{-6}M$ in comparison to the linear concentration dependence predicted for Forster transfer. A semiclassical model by Druger et al[4] attributes the large increase in energy transfer to an enhancement in the donor-dipole induced electromagnetic field within the particle at frequencies corresponding to morphological resonances of the particle. Transfer takes place as this field stimulates acceptor absorption. More recently Leung and Young[3] have constructed a quantum mechanical model in which the energy transfer may be considered a two step process. In the first step the enhancement in the local density of photon states near a morphological resonance causes emission to take place preferentially into such a mode. In the second step the energy in this mode is absorbed by an acceptor molecule, or a photon is radiated externally. Both models essentially give the same results, however, the quantum model provides one with a simple equation for describing the concentration dependence. Moreover, as we will show, the correspondence between the predicted and measured concentration dependence enables one to determine the photon lifetime of the longest lived resonant mode. In what follows we will briefly describe the relevant theoretical results of Leung and Young[5], compare this theory with experiment, extract the photon lifetime from this comparison, and attempt to compare this photon lifetime with that predicted from Mie theory.

The rate of transfer $<\Gamma_{tr}>$ as determined by Leung and Young[5] has a particularly simple form

$$\langle \Gamma_{tr} \rangle = \left[\frac{\pi^2 c^3}{\tau V n^3} \frac{D}{\omega_0^2} \phi(\omega_0) \right] \frac{(c/n)\ \sigma_a \rho_a}{\gamma + (c/n)\ \sigma_a \rho_a} \tag{1}$$

where, D is the angular momentum degeneracy(i.e., $D = 2l + 1$) of the resonance, V is the particle volume, τ is the molecular lifetime, n is the refractive index, ω_0 is the frequency of the resonance, $\phi(\omega_0)$ is the normalized intensity of the donor fluorescence spectrum evaluated at ω_0, γ is the photon loss rate of the resonant mode without acceptors, σ_a is the cross section for acceptor absorption and ρ_a is the volume density of acceptors. Although the term in the brackets in Eqn.1 represents the rate at which energy is coupled into the particle at ω_0, the term outside the brackets,

$$P = \frac{(c/n)\ \sigma_a \rho_a}{\gamma + (c/n)\ \sigma_a \rho_a}, \tag{2}$$

is the probability that this energy is absorbed by acceptors. Since only P is dependent on acceptor concentration, the energy transfer efficiency vs. concentration is expected to fit this form.

P has a simple physical interpretation. First it should be noted that the overall energy transfer rate at low concentrations [i.e., $(c/n)\rho_a\sigma_a \ll \gamma$] is proportional to the photon lifetime, γ^{-1}. Thus the overall rate of transfer is principally through the longest lived modes in this region. One can think of the energy responsible for this transfer in terms of rays that skip along the interior of the particle. During this circulation energy is lost by processes other than absorption by acceptor molecules. These loss processes at a rate γ compete against the absorption rate by acceptors, $(c/n)\sigma_a\rho_a$, for the energy deposited into these long lived modes. Thus the probability of transfer is the rate of absorption by acceptors divided by the sum of this rate and and the intrinsic rate of energy loss. If absorption by acceptors dominates this competition then all energy in these modes will be transferred and consequently the probability P will be independent of acceptor concentration. At low concentrations where intrinsic losses occur with a larger rate than absorption [i.e., $(c/n)\rho_a\sigma_a \ll \gamma$] one should find that the probability of transfer is proportional to acceptor concentration. It is in this previously inaccesible experimental region[1] where the photon lifetime γ^{-1} of the longest lived modes may be evaluated. The characteristic concentration at which the energy transfer falls by a factor of 2 from its plateau is

$\rho_{a,1/2} = \gamma n/(c\sigma_a)$.

Experiments were carried out in a similar fashion to those described in Ref.1, but to smaller acceptor concentrations. A single glycerol particle ~20μ in diameter and containing the dyes of interest is injected into an electrodynamic levitator-trap[6]. The particle is illuminated by radiation from a mercury arc with an intensity of less than 50 mW/cm^2 at a wavelength 365 nm. The fluorescence within an F/3 aperture at a scattering angle of 90^0 is imaged onto the entrance slit of a monochromator and detected at the exit by an optical multichannel analyzer. The peak height ratio R of acceptor to donor luminescence is extracted from the data as a function of acceptor concentration. Two donor-acceptor systems were examined, Coumarin 1 (C1) and 9-Aminoacridine (9AA) as donors and Rhodamine 6G (R6G) as the acceptor. Concentration ratios, donor to acceptor, of 10:1 and 100:1 were used with the C1/R6G system and ratios of 50:1 and 500:1 were used for the 9AA/R6G system. In all cases the ratio of acceptor to donor fluorescence was found to be independent of donor concentration. The dependence of the ratio on acceptor concentration is shown in Fig.1 along with predictions based on Forster transfer. Each point at a given concentration represents an average of five experiments on different particles. The error bar at 10^{-6} M represents a typical mean deviation. It should be noted that the curves drawn through the data points in this figure are simply hand drawn lines to show the general trend. As one can see although the energy transfer is independent of concentration above 10^{-6} M, a fall off in energy transfer is recorded in the 10^{-7}M acceptor region. It is apparent from the data that neither system is described by Forster transfer although their concentration dependences are very similar.

In order to compare the data in Fig.1 with Eqn.2 the plateau in transfer for each of the systems was normalized to 1 by multiplying a given set of data by an appropriate constant. In practice the constant was chosen for a given set of data by averaging the ratio data for all points above 2x10^{-6} M, and dividing all points in the data by this average. Fig.2 shows the collective effect of this process. The curve through the data represents the best fit to Eqn.2. Fig.2 clearly shows that Eqn.2 provides a good description for the concentration dependence. The characteristic concentration is found to be 4x10^{-7}M or 2.4x10^{14}cm^{-3}.

One can extract the photon lifetime from the characteristic concentration arrived at in Fig.3 since the photon lifetime $\tau_p = \gamma^{-1} = n/(c\ \sigma_a\ \rho_{a,1/2})$. The average cross section for absorption within the overlap region σ_a is arrived at from molar extinction measurements (on the acceptor, R6G) in this region and from the overlap function(the normalized product of the fluorescence spectrum of the donor and the absorption spectrum of the acceptor). Because the acceptor is the same in both energy transfer systems, the average cross sections are found to have the same value, σ_a =1.5x10^{-16}cm^2 . With this value for σ_a , a value for n of glycerol of 1.47 and the experimental value for $\rho_{a,1/2}$ of 2.4x10^{14} cm^{-3} we find that τ = 1.3x10^{-9} sec. This lifetime may be represented in terms of a quality factor

$Q = \omega\tau = 4.4 \times 10^6$. This number is as good as the experimental determination of the product $\sigma_a \rho_{a,1/2}$ which we consider to have an uncertainty of less than $\pm 50\%$ in the present study.

Although a Q of 4.4×10^6 is very large it is not nearly as large as the quality factor which would be predicted from Mie theory for the narrowest mode. For gycerol particle taken to have a refractive index of 1.45 and a diameter of 20μ the largest quality factor estimated from linewidth calculations using Mie theory is $\sim 10^{24}$.[7] This disparity in part can be understood when one realizes that all materials have some absorption. In glycerol, in the region of overlap, 530nm, the material is very transparent, however, even in ultapurified material(referred to as "gold label") there is intrinsic residual absorption. This is evidenced by our measurement of the decadic attenuation as shown in Fig.3. A slight Urbach extrapolation[8] reveals the decadic attenuation in the center of the overlap region (530nm) to be $1.1 \times 10^{-4} cm^{-1}$. This translates into an absorption cross section times density for glycerol, $\sigma_g \rho_g$, of $2.5 \times 10^{-4} cm^{-1}$. This attenuation may be incorporated into Mie theory by introducing an imaginary part into the refractive index. However it is easy to estimate the effect which the attenuation has on the Q. Simply put such an attenuation represents an energy loss rate $\gamma_g = (c/n)\sigma_g\rho_g = 5.1 \times 10^6 sec^{-1}$. This rate is orders of magnitude larger than that estimated from linewidths calculated (excluding absorption) in Ref.7. Thus the intrinsic Q from Mie theory is "loaded" and approxiamtely $\omega/\gamma_g \sim 10^9$. Aside from this absorption loss there is Rayleigh scattering from density fluctuations as well as Raman scattering from glycerol. However each of these processes has a decadic attenuation which is considerably smaller than $10^{-4} cm^{-1}$. Thus no linear bulk process can account for a Q as small as our measured value of 4.4×10^6.

Zhang et al[2] have written that the Q values estimated from the buildup in Stimulated Raman Scattering(SRS) are limited by nonlinear loss. This may be expected at the relatively large intensities used in their experiments, however, at the intensities for which our experiments are performed there is only one excited molecule in the particle at a time, and consequently nonlinear losses are negligible.

We believe that photon lifetimes are so long in the aerosol particle that to properly account for the measured Q values one must include intrinsic surface roughness into the analysis. No appropriate theory is currently available, however, the importance of such a theory is highlighted when one considers recent x-ray scattering results which reveal a 3.2Å r.m.s. roughness on a vibrationally isolated water surface at room temperature [9].

In summary, we have shown that the Leung-Young model of energy transfer in an aerosol particle is in good agreement with our experiments and enables us to estimate the photon lifetime of the longest lived morphological resonances at extremely low intensities. The prefactor in Eqn.1, describing the rate at which energy is coupled into the particle, merits further study. Experiments to quantitatively measure this rate by using an integrating sphere levitator [10,11] are currently underway.

References

1. L.M. Folan, S. Arnold, and S.D. Druger, Chem. Phys. Lett.118, 322(1986).

2. Jian-Zhi Zhang, D.L. Leach, and R.K. Chang, Opt. Lett. 13, 270(1988).

3. R.G. Pinnick, A. Biswas, P. Chylek, R.G. Armstrong, H. Latifi, E. Creegan, V. Srivastava, M. Jarzembski, and G. Fernandez Opt.Lett13, 494(1988).

4. S.D. Druger, S. Arnold, and L.M. Folan, and, J. Chem. Phys. 87, 2649(1987).

5. P.T. Leung and K. Young, J. Chem. Phys. 89, 2894(1988).

6. S. Arnold and L.M. Folan, Rev. Sci. Inst. 57, 2250(1986).

7. R. Thurn and W. Kiefer, Appl. Opt. 24, 1515(1985).

8. F. Urbach, Phys. Rev. 92, 1324(1953).

9. A. Braslau, M. Deutsch, P.S. Pershan, A.H. Weiss, J. Als-Nielsen and J. Bohr, Phys. Rev. Lett.54, 114(1985).

10. L.M. Folan and S. Arnold, Opt. Lett. 13, 1 (1988).

11. S. Arnold and L.M. Folan, Rev.Sci.Inst.58, 1732(1987).

Figures

1. Measured peak ratios of acceptor to donor fluorescence for the 9AA/R6G(Δ) and C1/R6G($\cdot$) systems in individual aerosol particles. The straight line represents a Forster theory fit to bulk measurements in the C1/R6G system.[1]

2. A fit of all data in Fig.1 to the concentration dependendce predicted by the Leung - Young model of energy transfer in an aerosol particle. The only adjustable parameter γ was found to be 7.7×10^8 sec^{-1}.

3. Measured decadic attenuation in glycerol. The midband of the overlap region for both energy transfer systems is 530nm.

338

FÖRSTER

9AA ●
Cl △

[A] (mole / liter)

R (%)

100

10

1

0.1

10^{-8} 10^{-7} 10^{-6} 10^{-5}

339

$$[A](moles/liter)$$
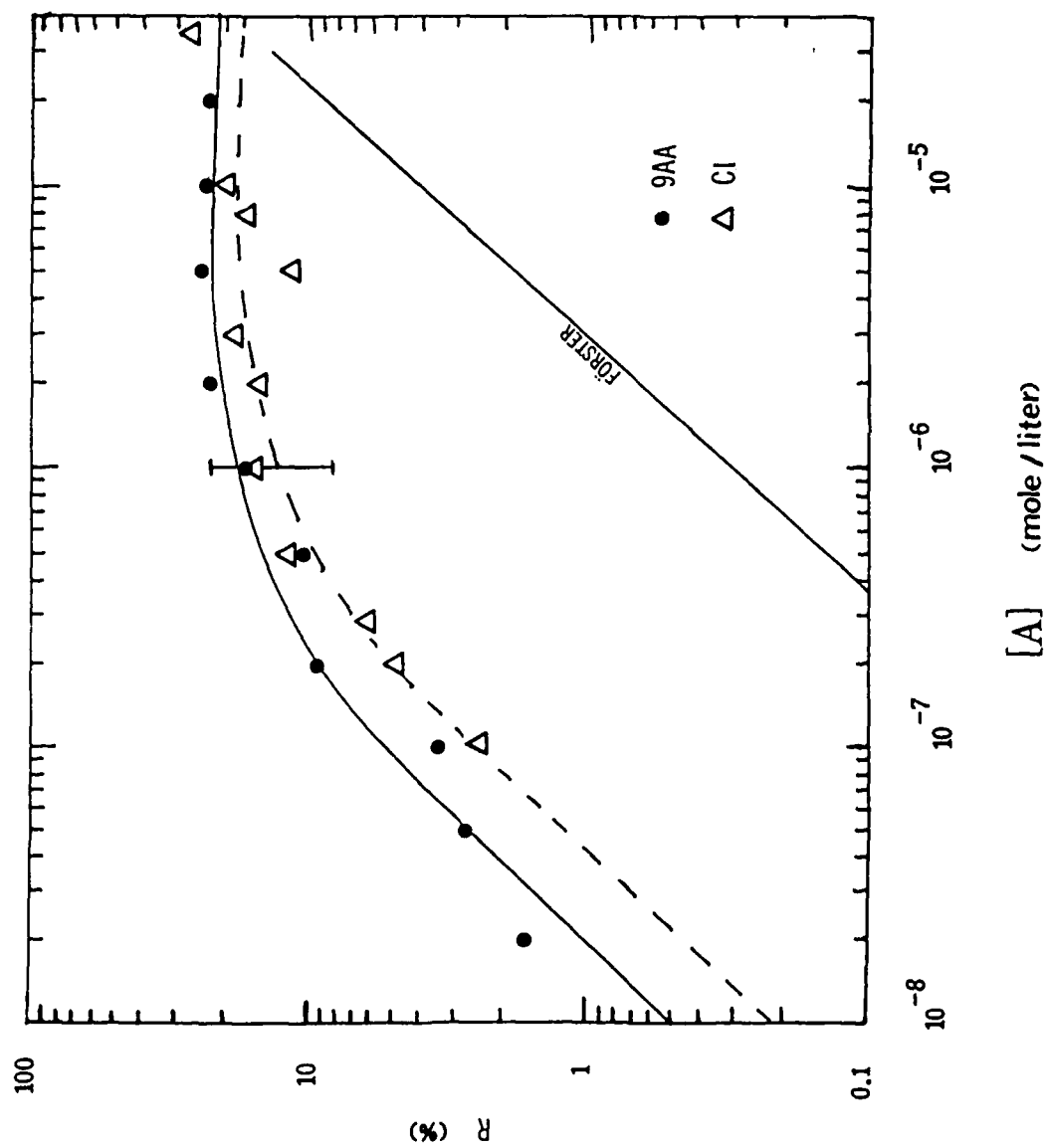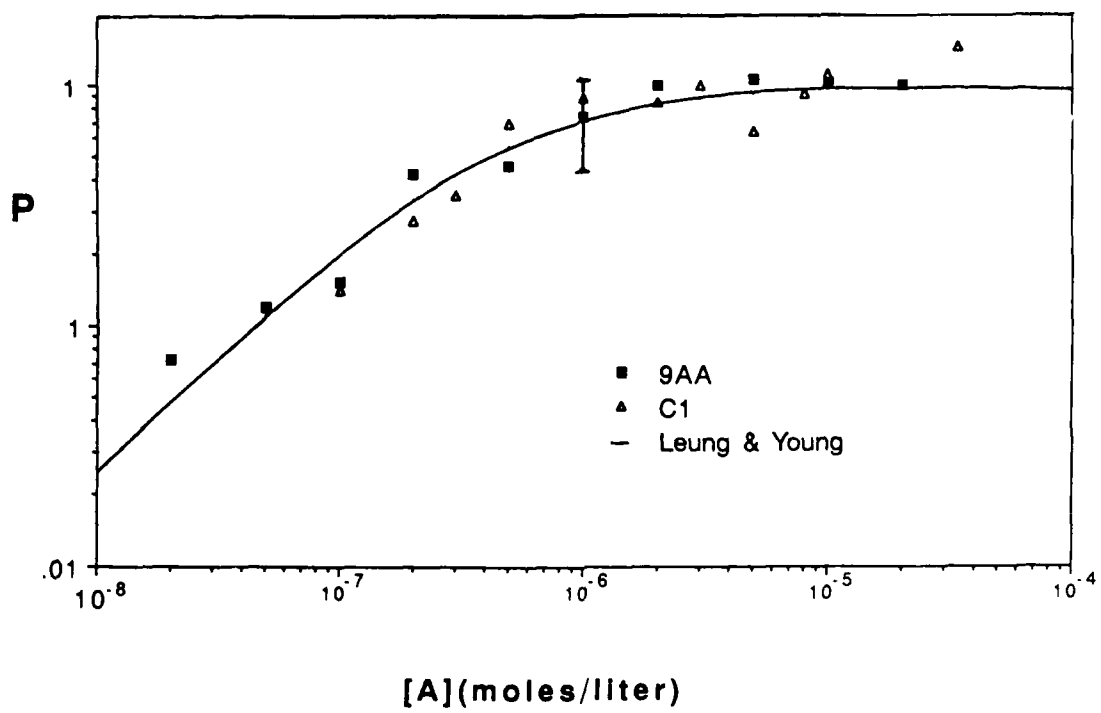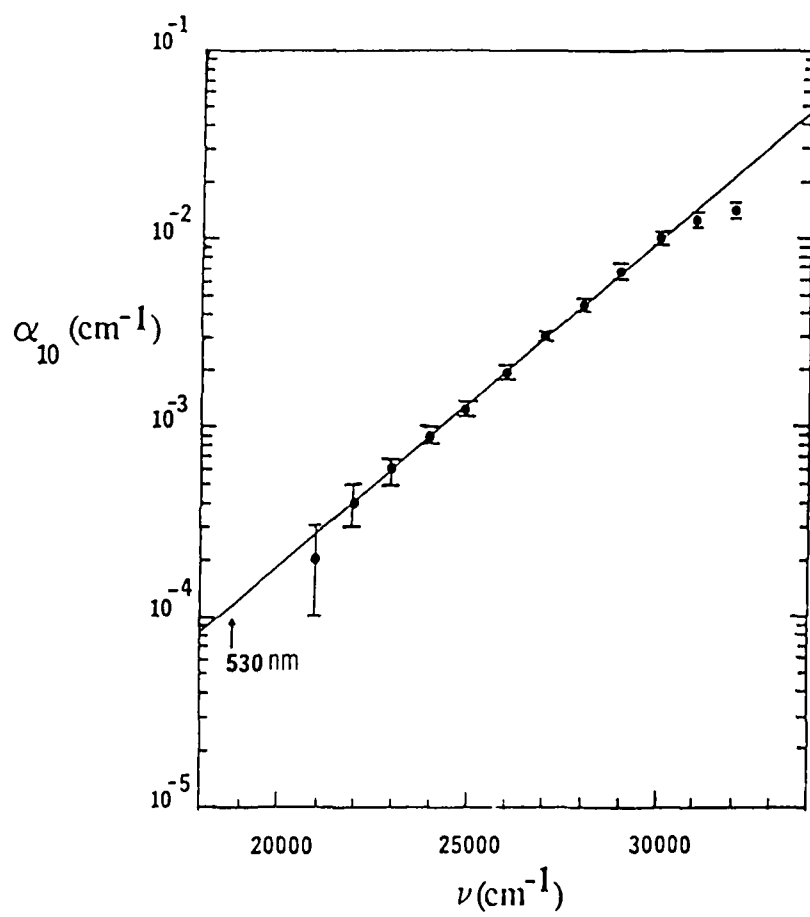
Blank

TIME RESOLVED RAMAN SPECTROSCOPY FROM OPTICALLY LEVITATED

REACTING PARTICLES

G. Moncivais, J. C. Carls and J. R. Brock

Department of Chemical Engineering

The University of Texas, Austin, Texas 78712

ABSTRACT

Time resolved Raman spectra of reacting suspended microdroplets have been acquired on a time scale of the order of one second. By considering the relative amplitude of various features, we have shown that the composition of a suspended droplet can be estimated as a function of time. In addition, for the D_2O - glycerol system studied it is possible to estimate the average temperature of an optically levitated droplet

INTRODUCTION

Recently there has been much interest in microprobe spectroscopy -- obtaining spectra from very small sample volumes. In this field, the development of single particle and aerosol spectroscopy has been at the forefront. There are many important problems in aerosol chemistry and aerosol technology in which single particle spectroscopic studies can make important contributions. Among these are the chemical mechanisms involved in oxidation of pollutant gases in aqueous atmospheric aerosols, the mechanisms of formation of particles in various combustion processes, the remote sensing of hazardous particles, and investigations of mechanisms of laser breakdown induced by particles, to name a few. In some of these problems, it is necessary to resolve processes with very small time scales; in these instances, the techniques using pulsed laser interactions with moving particles pioneered by Chang and coworkers[e.g.1,2] are invaluable. On the other hand, for slower processes, it may be desirable to capture and hold particles for extended periods of time; these instances have occasioned an increased interest in particle suspension techniques and single particle spectroscopy.

Two general techniques have been used for single particle suspension: electrodynamic suspension[3,4,5] and the more recent method of optical levitation[6]. Electrodynamic suspension involves suspension of a charged particle by electrical fields. In optical levitation, a small particle is suspended against gravity just above the focus of a laser beam by the radiation pressure of the light. Electrodynamic suspension has advantages over optical levitation, such as insensitivity to particle composition and morphology, and some limited stability against gas flows. However, for Raman spectroscopy, optical levitation provides a satisfactory suspension method because the droplet automatically resides close to the focus of the laser, where the light intensity is highest. In addition, the levitation laser can also be used as the pump laser for the spectroscopy. Thus, all except one of the Raman experiments on single suspended droplets have used this type of suspension. Thurn and Kiefer[7] seem to have been the first to acquire the Raman spectrum of single suspended particles, using glass spheres and quartz crystals. Later, they[8] investigated droplets composed of mixtures of glycerol and water. Lettieri and Preston[9] acquired the spectrum of an optically levitated dioctyl phthalate (DOP) droplet, and found that it agreed well with the bulk DOP spectrum. More recently, Kung and Tang[10] have used the electrodynamic suspension method for Raman spectroscopy of single drops.

Up to the present, a major limitation in studies in spectroscopy of single particles has been the poor time resolution. Most of the IR and Raman techniques that have been applied require about an hour to acquire a single spectrum. This is due to the use of scanning spectrometers with photomultipliers as the detector which can sample only one wavelength at a time. Therefore, Raman spectroscopy of single

344

suspended particles undergoing physicochemical processes with time scales as small as the order of a second, have until now not been explored. We have used optical levitation and a photodiode array to obtain time resolved Raman spectra at such scales. First, a brief description of the experimental system is given . Next, experiments are described, including a series in which time resolved Raman spectra are obtained for a glycerol droplet absorbing deuterium oxide. Finally, we present a brief analysis of the experimental results.

EXPERIMENTAL SYSTEM

The experimental arrangement for optical suspension is similar to that used by others[8]. The basic components of our system are a Spectra Physics 164 argon ion laser, 0.22 m SPEX monochromator, TN6500 Tracor Northern Rapid Scan Spectrometer, optical cell and collection and focussing optical elements. The light emitted from a particle captured in the optical focus in the suspension cell was collected at 90° using a 5X microscope objective. A Raman notch filter was placed between the microscope and the monochromator to eliminate the laser line and the signal was focussed into the spectrograph. At the exit of the spectrograph, the spectrum was detected by a Tracor model 6121 intensified diode array, with 512 diodes. Two diffraction gratings were used. One had 1200 grooves/mm, allowing about 0.12 nm/diode resolution. The second had 2400 gr/mm, giving a resolution of about 0.06 nm/diode. A Tracor 6500 computer operated the detector, processed and displayed the acquired spectrum.

In most of our experiments, an argon ion laser beam was used at around 250 mW operating at 488 nm in the TEM_{oo} mode; at this power, typically, particles in the range 10 - 30 μm could be suspended, depending on their densities.

With proper alignment of the optical system, it was possible to capture particles with an ease which was dependent on the particle material. In experiments using 30 μm glass spheres, the spheres were introduced through a tube above the focal point of the laser beam. Liquid droplets were produced by aspiration into a chamber above an opening to the cell. Liquid droplets studied included dioctyl phthalate (DOP), glycerol, and glycerol-deuterium oxide mixtures.

EXPERIMENTAL STUDIES

The first objective of this work was to see if reasonably high quality Raman spectra of single droplets could be acquired in times that would allow kinetic studies. Since a single spectrometer was used, it can be expected that the resolution and signal to noise ratio will be less than these quantities in previous single particle Raman studies. However, for our purposes, the higher light throughput with the single spectrometer coupled with parallel detection was considered desirable for time resolved studies.

Figure 1a shows the Raman spectrum of bulk liquid dioctyl phthalate (DOP). This spectrum was acquired through the collection optics system by placing a cuvette of DOP into the laser focus at the same location as would be occupied by a levitated droplet. Comparison of this spectrum with tabulated results in the literature and with the plots of Lettieri and Preston[9] shows good agreement both in the locations of the spectral features and in the relative magnitudes of the individual features. As expected however, the results here are not as well resolved and in some cases, close spectral features get smeared into a single peak. Figure 1b shows the corresponding Raman spectrum of an optically levitated DOP droplet. Comparison of this figure with the bulk spectrum shows very good agreement in the locations of the peaks. The relative amplitudes of the peaks agree with the bulk spectrum for the most part. However, the amplitudes of the peaks are generally sharper than in the bulk case. This sharpness can be attributed to optical resonances occurring within the bandwidth of the Raman peaks, and amplifying specific wavelengths within that region.

Fig. 2a shows the bulk spectrum of glycerol. There are two broad features, one centered on 2900 cm^{-1}, and the other at 3340 cm^{-1}. The first feature is actually three peaks, shown in the figure as a shoulder and two peaks. The positions of the three correspond quite well to literature values. The transition represented by these peaks is a C-H stretch for saturated hydrocarbons. The very broad second feature also corresponds well with tabulated values. This feature corresponds to an -OH stretch in the glycerol molecule. It is very broad because hydrogen bonding in glycerol allows this group to be found in a wide variety of energy states centered about the most probable one. Thus, the energy required to make this transition depends on the extent of hydrogen bonding of the -OH group undergoing the transition . Fig. 2b shows the corresponding spectrum for a suspended glycerol droplet. The two features are clearly visible is this figure although the -OH stretch shows the presence of noise and the resonances. Fig. 2b shows three peaks, one a resonance, where there are only two in the bulk spectrum. The strength of this line probably allows it to maintain its relative amplitude at such a high level, much like the strong lines in the DOP sample that were not so strongly affected by the resonances.

The average exposure time required to collect the droplet spectra presented here was about 5 seconds. For the best case with a very large droplet (~ 25 μm diameter), a spectrum having a highest peak at about 10000 counts (out of maximum possible of 16000) was acquired in 0.1 seconds. The average exposure time represents an almost three order of magnitude reduction in acquisition time in comparison with previous studies. The reduction in acquisition time brings kinetic studies with time scales as small as the order of a second well within grasp.

With the demonstration that Raman spectra of reasonable quality could be obtained with our system in times of the order of a second, we now describe our experiments in time resolved Raman spectroscopy.

An attractive dynamic process for our first study was the uptake of D_2O by glycerol droplets. H_2O was less suitable since the -OH stretch for it was at the same location as the -OH stretch for glycerol . Fig. 3a shows the bulk Raman spectrum of pure D_2O in the same Stokes shift range as in Figs. 2a and 2b. The -OD stretch is the only feature in this range and is centered about 2500 cm^{-1}. Like the -OH stretch in glycerol, it is quite broad as a result of hydrogen bonding. Fig. 3b is the bulk Raman spectrum of a 50-50 mixture by volume of glycerol and D_2O. All of the features present in the individual spectra remain in the mixture spectra, and the relative intensities are comparable.

For the time resolved experiments, the cell used for levitation (a parallelepiped, 3cmx3cmx7cm) was modified by inserting a small reservoir for the D_2O into the cell at the end opposite to the drop suspension position. A hole was drilled into the side of the cell and a small tube inserted through the hole, leading to the reservoir. A glycerol droplet was levitated and the vertical position of the droplet adjusted to maximize the signal received at the detectors. The computer was programmed to acquire a time series of Raman spectra and started so that the first few spectra represented the pure glycerol before the introduction of the D_2O. Then, a small amount of liquid D_2O (0.5 ml) was injected into the reservoir through the tube. D_2O vapor from the evaporating sample diffused to the glycerol droplet. Gas phase mass transfer from the reservoir controlled the kinetic process, since the relaxation time for the diffusion of D_2O vapor to a droplet (~ 200 sec.) was much larger than that for diffusion and reaction inside the glycerol droplet (~ 0.1 sec.).

Fig. 4 shows a time resolved sequence of Raman spectra for the absorption of D_2O vapor by an optically levitated glycerol droplet. The 1200 gr/mm grating was used. The foremost spectrum is that of pure glycerol. The large feature on the right is the C-H stretch centered on 2950 cm^{-1}. As time proceeds, the O-D stretch of the D_2O appears and becomes more and more prominent as its concentration within the droplet increases. The chemical evolution occurring with time is evident. The time series in Fig. 4 represents data acquired over the course of about four minutes. It was confirmed experimentally that vapor phase D_2O did not contribute measurably to the spectra. Fig. 5 shows a comparable time series from a different trial. In this run, the 2400 gr/mm grating was used. The range of Stokes shifts was from 2200 - 3500 cm^{-1}. As can be seen, the general features are the same as in the previous figure. This run was carried out for about 30 min.

DISCUSSION

Quantitative interpretation of the time resolved Raman spectra of Figs. 4 and 5 is complicated by presence of the structure resonances. These resonances themselves provide a great deal of information, and their analysis is a subject for continuing study.

However, as a simple way of studying droplet concentration as a function of time, the integral under the O-D stretch peak at 2500 cm^{-1} from D_2O was compared to the integral under the C-H stretch at 2900 cm^{-1} from glycerol. This comparison was made for each spectrum acquired as a function of time. Even though the spectra contain the resonances, the resonances occur at fairly regular intervals, and so there is reason to suspect that to some approximation the area under each curve could be affected equally. By taking the ratio of the two areas, the effects of resonance, as well as fluctuations in the amount of light collected should be cancelled.

Fig. 6 presents the results of this procedure applied to the experimental data of Fig. 5. The ordinate in Fig. 6 is the ratio of the integral under the OH peak to that for CH. As was supposed above, this procedure produces a relatively smooth curve compared to the time series of the individual OH and CH integrals.

The relation of the OD:CH area ratio to droplet composition can be made by calibration. This can be done approximately by carrying out measurements of the OD:CH area ratios for various bulk calibration samples of known OD:CH composition. Mixtures of varying composition were used for this calibration procedure. The bulk spectrum for a 50-50 volume percent D_2O - glycerol mixture was shown in Fig. 3b. Fig. 7 gives a plot of the bulk calibration data for the 1200 gr/mm grating.

A better understanding of the results displayed in Fig. 6 requires consideration of the physicochemical processes occurring in these experiments.

Upon introduction of liquid D_2O into the experimental cell, the liquid begins to evaporate and D_2O vapor begins to diffuse from the small reservoir located at the base of the 3cmx3cmx7cm cell approximately 6.5 cm from the location of the suspended droplet. Under the assumption that diffusive transport is the dominant transport mechanism (some convection cannot be ruled out) we have computed numerically the D_2O vapor concentration as a function of time at the droplet position.

As the D_2O vapor reaches the droplet, the glycerol begins to absorb the vapor. However, this is not simply physisorption. In the droplet deuterium exchange reactions occur according to the following overall schemes [e.g.11]:

$$C_3H_5(OH)_3 \text{ (l)} + 1.5D_2O \text{ (l)} \ \text{-----} \ C_3H_5(OD)_3 \text{ (l)} + 1.5H_2O \text{ (l)} \qquad (1)$$

$$0.5H_2O \text{ (l)} + 0.5D_2O \text{ (l)} \ \text{-----} \ HDO \text{ (l)} \qquad (2)$$

348
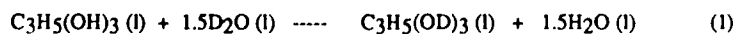
Reaction (2) is known to be very rapid, but no direct information was found on the rate of (1). The rate of proton exchange in water-ethanol mixtures has been found to be dependent on solution concentration[12]. However, since deuterium exchange reactions in associated solutions are usually found to be rapid, it is reasonable to expect that (1) and (2) occur on time scales commensurate with the internal diffusive time scales, 0.1 sec.

No special measures were taken to remove existing humidity from the cell at the beginning of an experiment. However, the amount of D_2O in the cell after its introduction is at least four orders of magnitude larger than any possible H_2O in the cell. Therefore H_2O and HDO produced by (1) and (2) continually diffuse from the suspended droplet. At the end of the process, there can be only a relatively small amount of HDO at a cell background level. This is confirmed by reference to Fig. 4 showing an OH background level.

There are two stages in the process of absorption of D_2O vapor by the suspended droplet. The first stage is the reaction of D_2O with the OH in the glycerol according to eq. (1). During this stage, D_2O is believed to have a short lifetime in the droplet. This stage continues until all the glycerol-OH is titrated. This is followed by a second stage involving absorption of D_2O driven by the D_2O chemical potential difference between the vapor and liquid states.

The droplet temperature may be estimated according to the following procedure. The data of Fig. 6 will be used in this example. The OD:CH area ratio can be related to the number ratio of OD:CH in the droplet through the calibration data. The quasistationary state shown in Fig. 6 corresponds to a number ratio OD:CH of around 0.84 . At complete titration, the OD:CH number ratio of $C_3H_5(OD)_3$ is 0.6. Therefore the difference, 0.24, is related to the amount of D_2O absorbed at this quasistationary condition; each D_2O molecule supplies two OD bonds. From this value and with a Duhring plot for the H_2O - glycerol system [13] (the Duhring plot for D_2O - glycerol-OD should be almost identical) , the droplet temperature is estimated to be approximately 45 °C. Therefore, weak absorption of the laser radiation in the droplet maintains the droplet temperature some 20°C above the ambient cell temperature. The droplet is so small (approximately 20 µm in diameter) that it produces no significant change in ambient cell temperature.

Clearly, the procedures outlined above for interpretation of our experiments are very approximate. The analysis did not distinguish the different states of the OD bonds between the bulk calibration samples and the suspended droplets. More generally, procedures must be developed for analyzing Raman spectra of

suspended droplets in the presence of the structure resonances. As a possible approach to this problem, it is suggested here that by collecting a broad band elastic scattering spectrum in the range of the Raman emissions, the location of the resonances can be found. With this extra bit of information, signal analysis techniques can be used to extract more reliable composition information.

CONCLUSIONS

Time resolved Raman spectra of reacting suspended microdroplets have been acquired on time scales of the order of one second. The time series of the spectra presented for a suspended droplet clearly shows the chemical evolution occurring in the droplet. Thus, time resolved Raman spectroscopy shows promise as a method by which reactions within single suspended droplets can be studied. Quantitative analysis of droplet composition is difficult because of the structure resonances that are almost always present in the spectra. Nonetheless, by considering the relative amplitude of various features, we have shown that the composition of a droplet can be estimated as a function of time. In addition, for the D_2O - glycerol system studied it was possible to estimate the temperature of the suspended droplets.

ACKNOWLEDGMENTS

REFERENCES

1. W. F. Hsieh, J. B. Zheng, C. F. Wood, B. T. Chu and R. K. Chang, Opt. Lett. 12, 576 (1987).

2. J. B. Snow, S. X. Qian and R. K. Chang, Opt. Lett. 10, 37 (1986).

3. S. Ataman and D. Hanson, I&EC Fundamentals 8, 833 (1969).

4. G. O. Rubel, J. Colloid Interface Sci.85, 549 (1982).

5. I. N. Tang and H. R. Munkelwitz, J. Colloid Interface Sci. 98, 430 (1984).

6. A. Ashkin and J. M. Dziedzic, Appl. Phys. Lett. 19, 283 (1971).

7. R. Thurn and W. Kiefer, Appl. Spectrosc.38 , 78 (1984).

8. R. Thurn and W. Kiefer, Appl. Opt. 24, 1515 (1985).

9. T. R. Lettieri and R. E. Preston, Opt. Commun. 54, 59 (1985).

10. K. H. Fung and I. N. Tang, Appl. Opt. 27, 206 (1988).

11. D. V. Fenby and G. L. Bertrand, Aust. J. Chem. 35,237 (1982).

12. I. Weinberg and J. R. Zimmerman, J. Chem. Phys. 23, 748 (1955).

13. A. R. Carr, R. E. Townsend and W. L. Badger, Ind. Eng. Chem.17, 643 (1925).
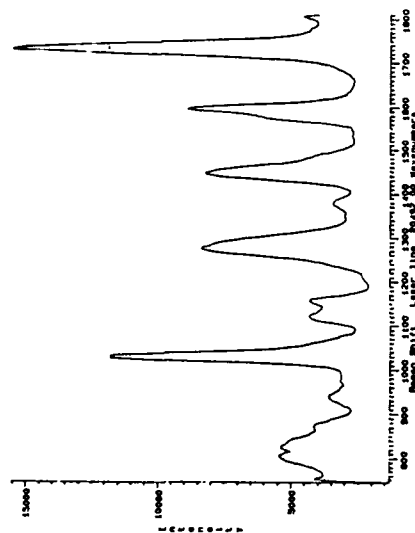
Figure 1a. Raman spectrum of bulk dioctyl phthalate (DOP).
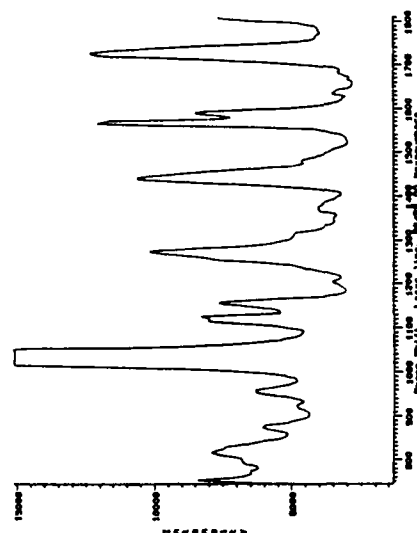

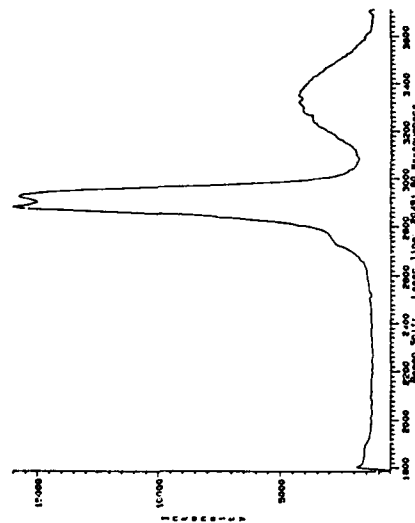Figure 1b. Raman spectrum of optically levitated dioctyl phthalate (DOP) droplet.

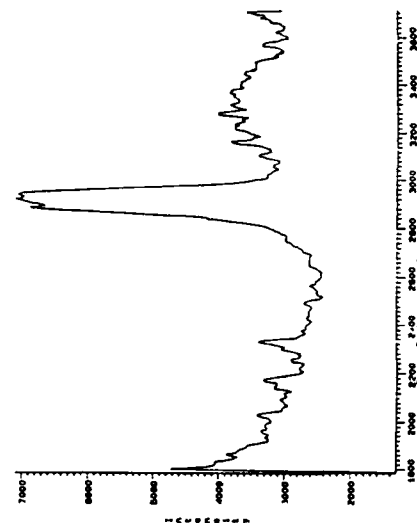Figure 2a. Raman spectrum of bulk glycerol.

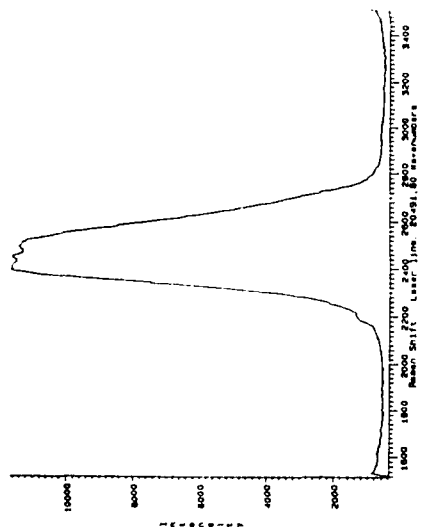Figure 2b. Raman spectrum of optically levitated glycerol droplet.

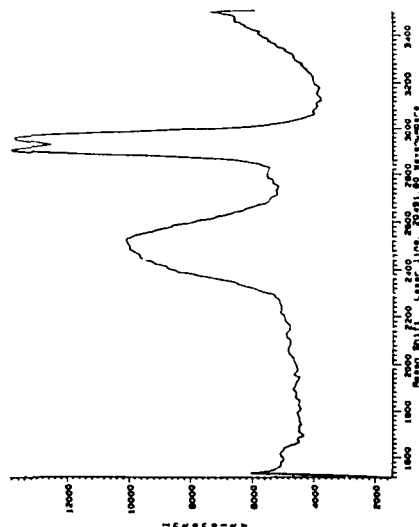Figure 3a. Raman spectrum of bulk deuterium oxide

Figure 3b. Raman spectrum of optically levitated droplet composed of a 50-50 volume % mixture of deuterium oxide and glycerol
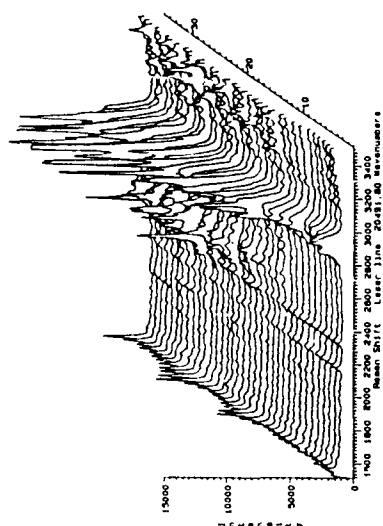

Figure 4. Time resolved sequence of Raman spectra for the absorption of deuterium oxide by an optically levitated glycerol droplet. 1200 gr/mm grating.
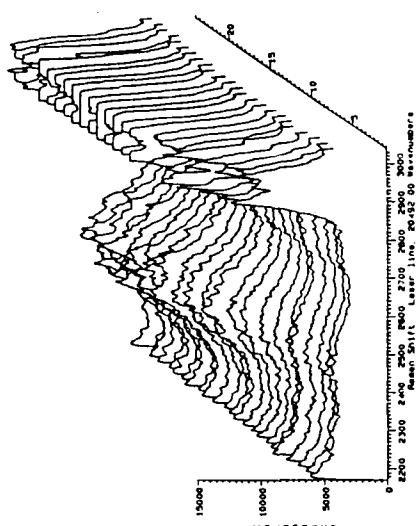
Figure 5. Time resolved sequence of Raman spectra for the absorption of deuterium oxide by an optically levitated glycerol droplet. 2400 g/mm grating.
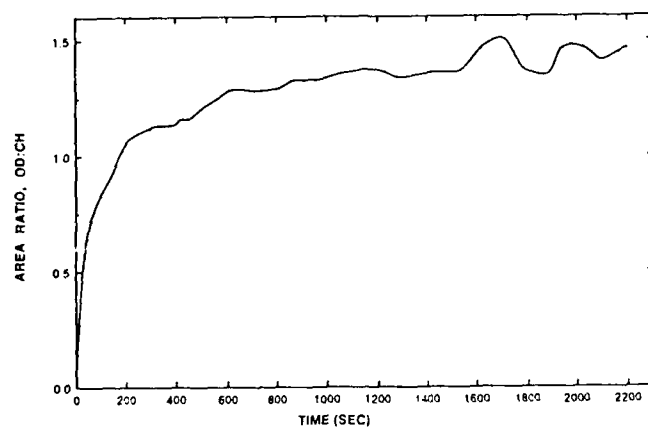
Figure 6. Area ratio of OD:CH Raman peaks as a function of time for the absorption of deuterium oxide by an optically levitated glycerol droplet.
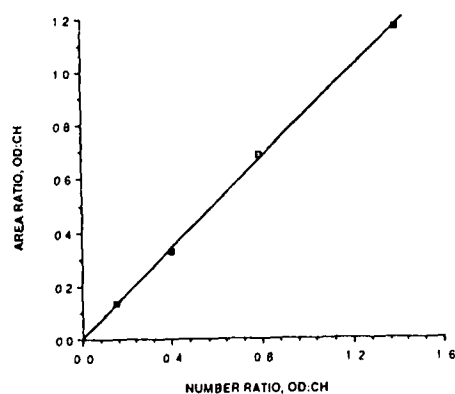
Figure 7. Calibration data for bulk samples of glycerol-D_2O giving relation of area ratios of OD:CH Raman peaks to number ratios of OD:CH bonds in samples.

353

Blank

SINGLE-PARTICLE RAMAN SPECTROSCOPY

I. N. Tang and K. H. Fung
Environmental Chemistry Division
Department of Applied Science
Brookhaven National Laboratory
Upton, NY 11973

RECENT PUBLICATIONS, SUBMITTALS FOR PUBLICATION AND PRESENTATIONS:

A) K. H. Fung and I. N. Tang, "Thermal-Accommodation Measurement of Helium on a Suspended Water Droplet", Phys. Rev. A 37, 2557, 1988.

B) K. H. Fung and I. N. Tang, "Raman Scattering from Single Solution Droplets", Appl. Opt. 27, 206, 1988.

C) K. H. Fung and I. N. Tang, "Raman Spectra of Single Suspended Supersaturated Ammonium Bisulfate Droplets", Chem. Phys. Lett. 147, 509, 1988.

D) K. H. Fung and I. N. Tang, "Composition Analysis of Suspended Aerosol Particles by Raman Spectroscopy: Sulfates and Nitrates", J. Coll. Interface Sci., in press, September 1988.

E) I. N. Tang and K. H. Fung, "Characterization of Inorganic Salt Particles by Raman Spectroscopy", submitted to J. Aerosol Sci., September 1988.

ABSTRACT

Raman spectra of suspended single aerosol particles were obtained for several environmentally important species, such as sulfates and nitrates. Quantitative measurements were also established for sulfate and nitrate mixtures in both crystalline and aqueous states under controlled laboratory conditions. The present work demonstrates the feasibility of a non-destructive and unique technique for aerosol composition analysis.

In recent years, experimental methods developed for trapping a single micron-sized particle in a stable optical or electrical potential cavity have made it possible to study many physical and chemical properties which are either unique to the small particle or otherwise inaccessible to measurement with bulk samples. Two types of scattering techniques have been applied to study these suspended particles, namely, Mie scattering and Raman scattering. The Mie scattering, which is an elastic process, can yield information leading to the physical and macroscopic properties of these particles such as particle size and index of refraction. In contrast Raman scattering is an inelastic process and consequently yields molecular and microscopic information. When combined, these two techniques can form a powerful tool for aerosol particle analysis. Recently, we have improved the sensitivity of the Raman spectroscopic technique and used it successfully to characterize aerosol particles composed of either pure or mixed inorganic salts. In this report, we further demonstrate the feasibility of Raman spectroscopy for in situ chemical composition analysis of a multicomponent aerosol particle. It will be shown that the concentrations of the component species in the particle can also be determined quantitatively from relative intensity measurements.

The particle levitation cell used in the present experiment consists of a central AC ring electrode and two DC endcap electrodes. This particle containment trap is fitted with port holes for gas inlet, excitation laser beam, alignment laser beam and scattering light collection optics. The 4880 Å line of a Coherent (Model CR-15) argon-ion laser serves as the excitation light source. The nominal laser power used is about 750 mW. The scattered light is collected with a 35 mm condenser lens and is imaged onto the entrance slit of a double monochromator (SPEX 1403) with a resolution of 4 cm^{-1} (1.0 Å). The light collecting optics are optimized at f/1 and set to project and match the f/7 of the monochromator. The photon detection system consists of a RCA 31034-A cooled photomultiplier tube and photon counting electronics. Optical scattering spectra are recorded on an IBM PC-XT computer and stored on disks for data analysis.

Raman spectra of mixed sulfate and nitrate particles are investigated. In the dissolved form, both the nitrate and the sulfate free ions in a solution droplet have quite straightforward Raman spectrum. This is due to the formation of a single type of free ions in the solution. This is shown in Figure 1(a), which is the spectrum of a solution droplet of mixed sodium nitrate and ammonium sulfate. The Raman frequencies for free nitrate and sulfate ions are 1050 cm^{-1} and 980 cm^{-1}, respectively. However, when this same solution droplet crystallizes, the resultant particle shows a rather complex Raman spectrum, Figure 1(b), in which Raman scattering peaks can be readily identified as ammonium sulfate (978 cm^{-1}), ammonium nitrate (1050 cm^{-1}), sodium sulfate (995 cm^{-1}) and sodium nitrate (1065 cm^{-1}). More work needs to be done to understand the partitioning of the various crystalline salts.

In order to illustrate the quantitative aspect of the Raman spectroscopy, one must establish an internal standard for such measurement. The reasons are the following. Since the Raman intensity from a single particle depends on the amount of the material and the intensity of the excitation laser focused on the particle, it may vary from particle to particle. Two particles containing equal amounts of Raman active material may show different Raman intensities simply because they are focused differently in the laser beam. Therefore, an internal standard is required for quantitative measurements. The concept was tested by preparing solutions of sodium sulfate and sodium nitrate of known composition, levitating the particles in the cell, and measuring the relative Raman intensity for each composition. The results of this study is summarized in Figure 2, where the relative intensity of the sulfate to nitrate Raman peaks is plotted as a function of the sulfate to nitrate molar ratio in the solid particles.

The linearity of the plot shown in Figure 2 demonstrates the promise of this technique for quantitative aerosol composition analysis. In addition, the slope of the line is a measure of the relative Raman cross-section of the two species in the crystalline states. A value of 0.56 is

obtained from the present study. The literature value of 0.79 as the relative cross-section of sulfate to nitrate ions in solutions is about 40% higher than that of our measurements for solid particles. Meanwhile, our measurements for droplets agree equally well with the literature data for bulk solution samples. Thus, the present study demonstrates the feasibility of applying Raman spectroscopic technique for aerosol composition analysis.

ACKNOWLEDGEMENT
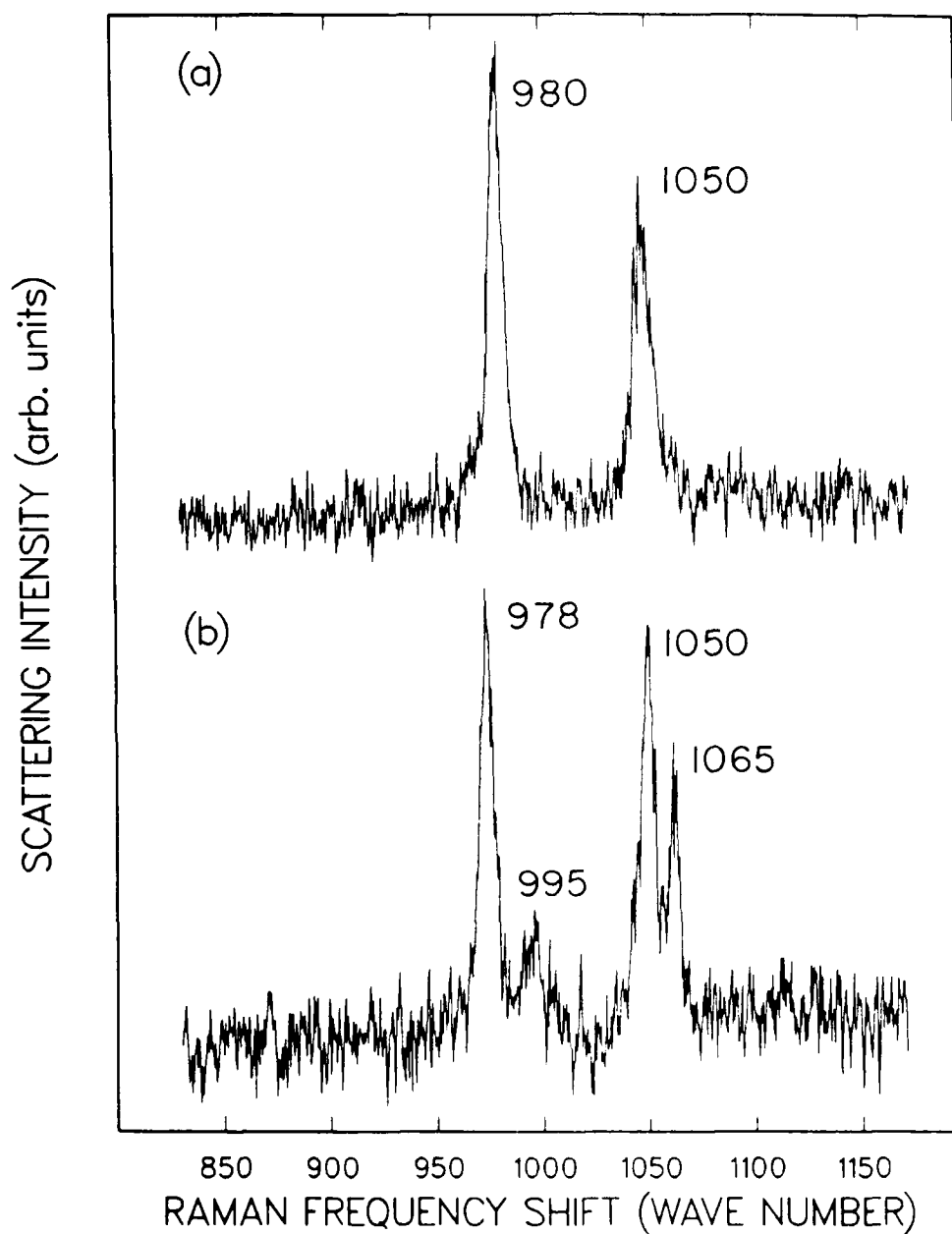
FIGURE 1. Raman spectra of (a) aqueous solution droplet of mixed ammonium sulfate and sodium nitrate, (b) dehydrated particle of the same droplet as in (a).
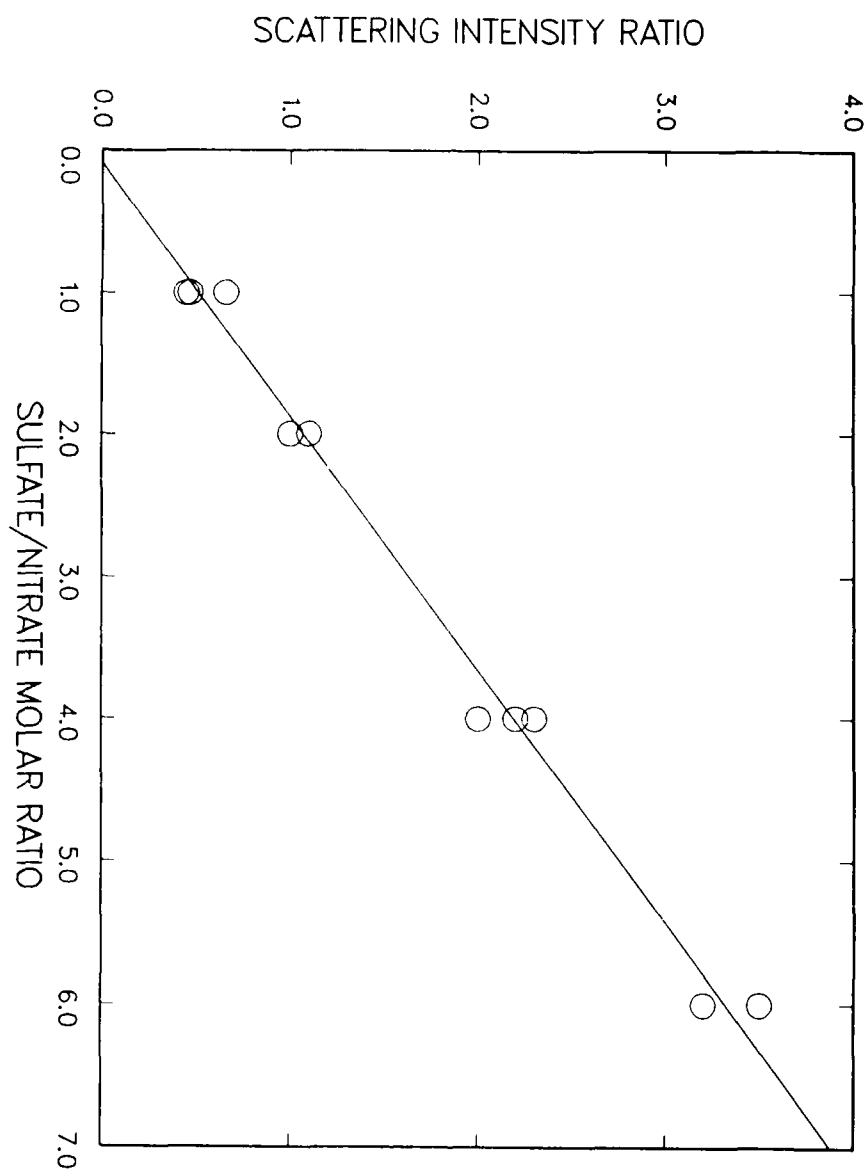
FIGURE 2. Plot of the scattering intensity ratios of several mixtures of sodium sulfate and sodium nitrate as a function of their molar ratios.

Blank

SPECTROSCOPY OF THE PHENYLACETYLENE-AMMONIA CLUSTER SYSTEM

J. J. Breen, W. B. Tzeng, R. G. Keesee, and A. W. Castleman, Jr.

Department of Chemistry
The Pennsylvania State University
University Park, PA 16802

RECENT PUBLICATIONS, SUBMITTALS FOR PUBLICATION AND PRESENTATIONS:

ABSTRACT

The results of a systematic study of the spectral shifts of the S_1-S_0 transition in phenylacetylene (PA) ($^1B_2(^1L_b) \leftarrow {}^1A_1(^1A)$) due to solvation by NH_3 are reported based on two-photon resonant enhanced multiphoton ionization (REMPI). A unique aspect of the present work is comparison of the red shifts for clusters produced by coexpansion techniques with those where phenylacetylene is attached to preformed ammonia clusters. Structural differences for clusters produced by the two different techniques are believed to be responsible for contrasting trends in spectral shift with cluster size. Work is continuing on examining the properties, including the spectroscopy and dissociation mechanisms, of aerosol precursors that are produced by both coexpansion and attachment techniques.

INTRODUCTION

The study of the formation and properties of small aggregates of molecules, or clusters, is an important approach to interrogating the changes in matter as it evolves form the gaseous to the condensed phase. It has been recognized that the frequency of a molecular absorption band is altered when a molecule is immersed in a solvent medium. The "solvent" can be a solid, liquid, gas or even a cluster of molecules. Recently a considerable amount of experimental and theoretical attention has been given to cluster systems in which a small number of solvent

molecules are bound to a solute molecule. The expectation is that these "microscopic solutions" will reveal molecular details of the collective effects responsible for solvation phenomena and improve the understanding of particle size effects in aerosols. Several review articles recounting the progress made in understanding these small clusters are available (1-5).

Typically the displacement of the frequency of an electronic absorption band of a molecule in solution is shifted towards longer wavelengths, although the opposite can also occur. These red shifts arise from the dispersion forces between the solute and solvent molecules. In order to account properly for the magnitude of the spectral shifts, consideration is required of the changes a molecule undergoes during an electronic transition. Upon absorption or emission of a photon, both the energy and charge distribution of the molecule change. For a molecule surrounded by solvent molecules, the interaction energy between the molecules is dependent upon the dipole moment of the molecule and the collective interactions of the solvent. Because of the difference in the molecular dipole moment in the two states, the interaction energy for a molecule undergoing an electronic transition is different for the ground and excited states. The spectral shift arises from the difference between the stabilization energy of the ground and excited states in the solvent. Studies of the spectral shifts which arise in various chromophores upon complexation with solvents comprised of atoms or molecules provide important information needed in quantifying the magnitudes and interactions responsible for the spectral properties of condensed matter.

The present paper presents new data on the spectroscopy of phenylacetylene (PA) attached to ammonia clusters with emphasis on larger clusters, namely those clusters of PA attached to more than one solvent molecule. The spectral region investigated, via mass resolved one-color two-photon REMPI, is in the vicinity of the S_1-S_0 transition ($^1B_2(^1L_b) \cdot {}^1A_1(^1A)$) in phenylacetylene (6). A unique aspect of the present work is a study of the spectroscopic shifts which arise upon the attachment of PA to a preformed ammonia cluster. Data on clusters produced by a conventional coexpansion method are given as a contrasting comparison to the attachment results.

EXPERIMENTAL

The experiments were performed by using a laser based time-of-flight (TOF) mass spectrometer. Resonance enhanced ionization is employed to probe some of the excited electronic states of these weakly bound systems. The laser system is comprised of a 10 Hz Q-switched Nd:YAG laser (Quanta Ray DCR-2A) which pumps a dye laser whose output can be doubled or mixed with the 1.06 micron fundamental of the Nd:YAG laser in the Wavelength Extension System (Quanta Ray WEX-1b) to get tunable ultraviolet light. The laser beam is perpendicular to both the cluster beam and TOF axes. The laser ionizes clusters in an electric field that accelerates the ions into the flight tube of the mass spectrometer.

Clusters are generated by either of two methods. In coexpansions, $PA(NH_3)_n$ clusters are made by expanding a mixture of PA (less than 1%), NH_3 (about 2%) and argon (98%) through a pulsed valve. In attachment experiments, clusters are created by crossing a beam of preformed ammonia clusters from the pulsed valve with a stream of PA and helium (Ratio = 1/4) from a stainless steel capillary tube. The end of the stainless steel capillary tube is about 2 cm downstream from the pulsed nozzle and 0.2 cm off the ammonia cluster beam axis.

RESULTS AND DISCUSSION

In the present study the investigation of $PA(NH_3)_n$ clusters has been extended from the $PA(NH_3)$ adduct previously reported (7), to clusters containing 2 to 7 ammonia molecules in the case of coexpansion experiments and to as many as 16 in the case of PA attachment. Reexamination in the present study of $PA(NH_3)$ yielded resonances around the O_0^o origin of the S_1-S_0 transition for uncomplexed PA which were consistent with those reported previously.

Typical spectra are shown in Figures 1 and 2. In each figure, the upper spectrum is from the coexpansion while the lower one is from attachment. The spectra from the attachment experiments are noticeably broader than those obtained by coexpansion. This behavior is indicative of phenylacetylene being spectroscopically warmer in the attachment study. In the

coexpansion phenylacetylene is adiabatically cooled, while in the attachment case phenylacetylene is introduced at room temperature to the ammonia clusters and the attachment process itself is somewhat exothermic. On the other hand, the spectral peak width for the clusters resulting from the attachment is less than that of the introduced phenylacetylene itself. The apparent cooling of PA can be attributed to heat transfer to the cold preformed ammonia cluster to which it attaches. The cooling which takes place in the 5 μsec transit time between the formation and ionization of the cluster should be a function of the energy match between vibrational modes of the PA molecule and the ammonia cluster.

The red shift of the spectral feature for each cluster size relative to the band origin of the S_1-S_0 transition for unclustered phenylacetylene is illustrated in Figure 3. The interesting finding is the rather different trend in the variation of the red shift with cluster size between the two methods of cluster preparation. Temperature effects noted for the attachment experiments alone should not be responsible for the very large red shifts in the spectra. Simple calculations of the rotational distribution at realistic temperatures could not account for such a shifted peak. Vibrational temperatures between adjacent cluster sizes should be relatively equal. Thus, since the broad spectra are observed to shift and not merely broaden, changing vibrational temperatures are not thought to be responsible for the nature of the trends reported.

The difference between these two experiments is apparently related to the different interactions present in nucleated $PA(NH_3)_n$ clusters versus those in complexes in which a PA is attached to a pre-existing cluster. These experiments clearly demonstrate the exciting prospects of cluster spectroscopy as a way of probing molecular interactions at cluster surfaces. Furthermore, they offer the possibility of observing energy flow from warm molecules attached to a cluster surface with the underlying colder temperature of a preformed cluster surface (8).

ACKNOWLEDGMENTS

REFERENCES

1. D. H. Levy, Ann. Rev. Phys. Chem. **31**, 197 (1980).
2. S. Leutwyler and J. Jortner, J. Phys. Chem. **91**, 5558 (1987).
3. A. W. Castleman and R. G. Keesee, Ann. Rev. Phys. Chem. **37**, 525 (1986).
4. A. W. Castleman, Jr. and R. G. Keesee, Accts. Chem. Res. **19**, 413 (1986).
5. R. G. Keesee and A. W. Castleman, Jr., "Photoabsorption and Photoionization of Clusters," in **Photophysics and Photochemistry of Cold van der Waals Clusters** (E. R. Bernstein, Ed.) Elsevier Science, in press.
6. L. Goodman and R. P. Rava, Acc. Chem. Res. **17**, 250 (1984).
7. P.D. Dao, S. Morgan and A. W. Castleman, Jr., Chem. Phys. Lett. **111**, 38 (1984).
8. R. N. Zare and R. D. Levine, Chem. Phys. Lett. **136**, 593 (1987).
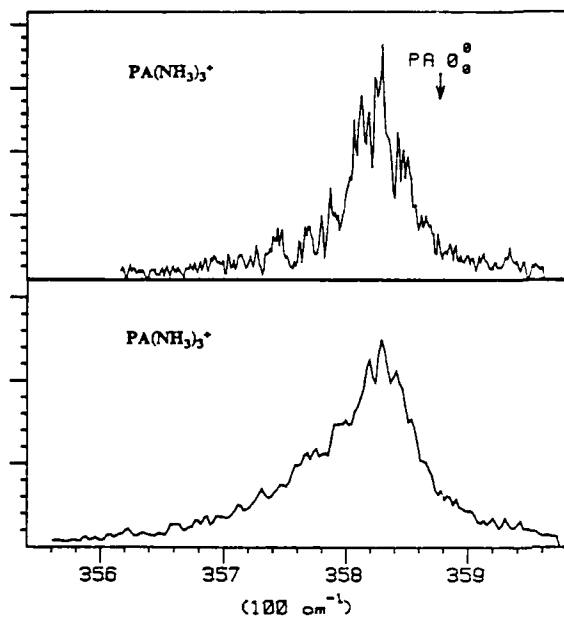
FIGURE 1. One-Color REMPI Spectrum for PA(NH$_3$)$_3$ in the region of the phenylacetylene S$_0$-S$_1$ band origin. Upper spectrum for clusters produced by coexpansion and lower spectrum for clusters as the result of attachment of PA to ammonia clusters.
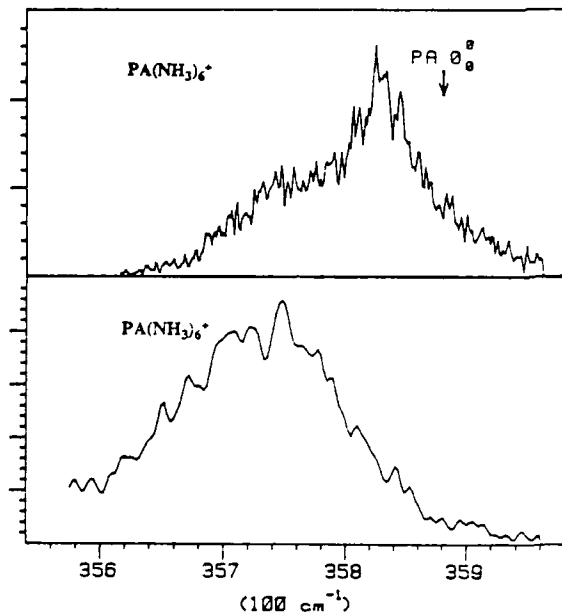

FIGURE 2. REMPI Spectrum for PA(NH$_3$)$_6$. Upper and lower spectra for respective cluster production methods given in Figure 1.

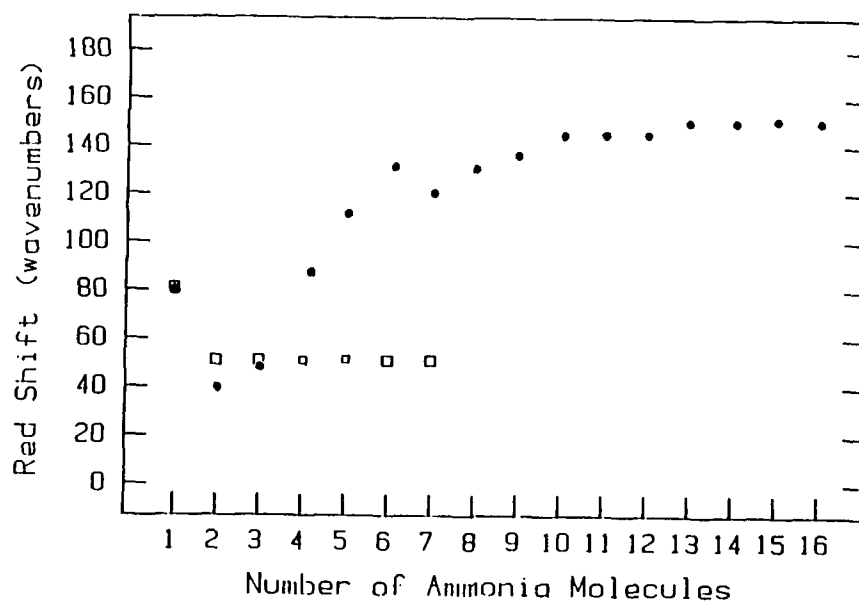FIGURE 3. Spectral shifts for PA(NH$_3$)$_n$ clusters made in the co-expansion are indicated by squares (□) and those in the attachment experiments by solid circles (●).

Blank

INDEX A

INDEX OF AUTHORS

Index A

INDEX B

Index of Authors' Organizations

Index B

APPENDIX A
PHOTOGRAPH OF 1988 CONFERENCE ATTENDEES
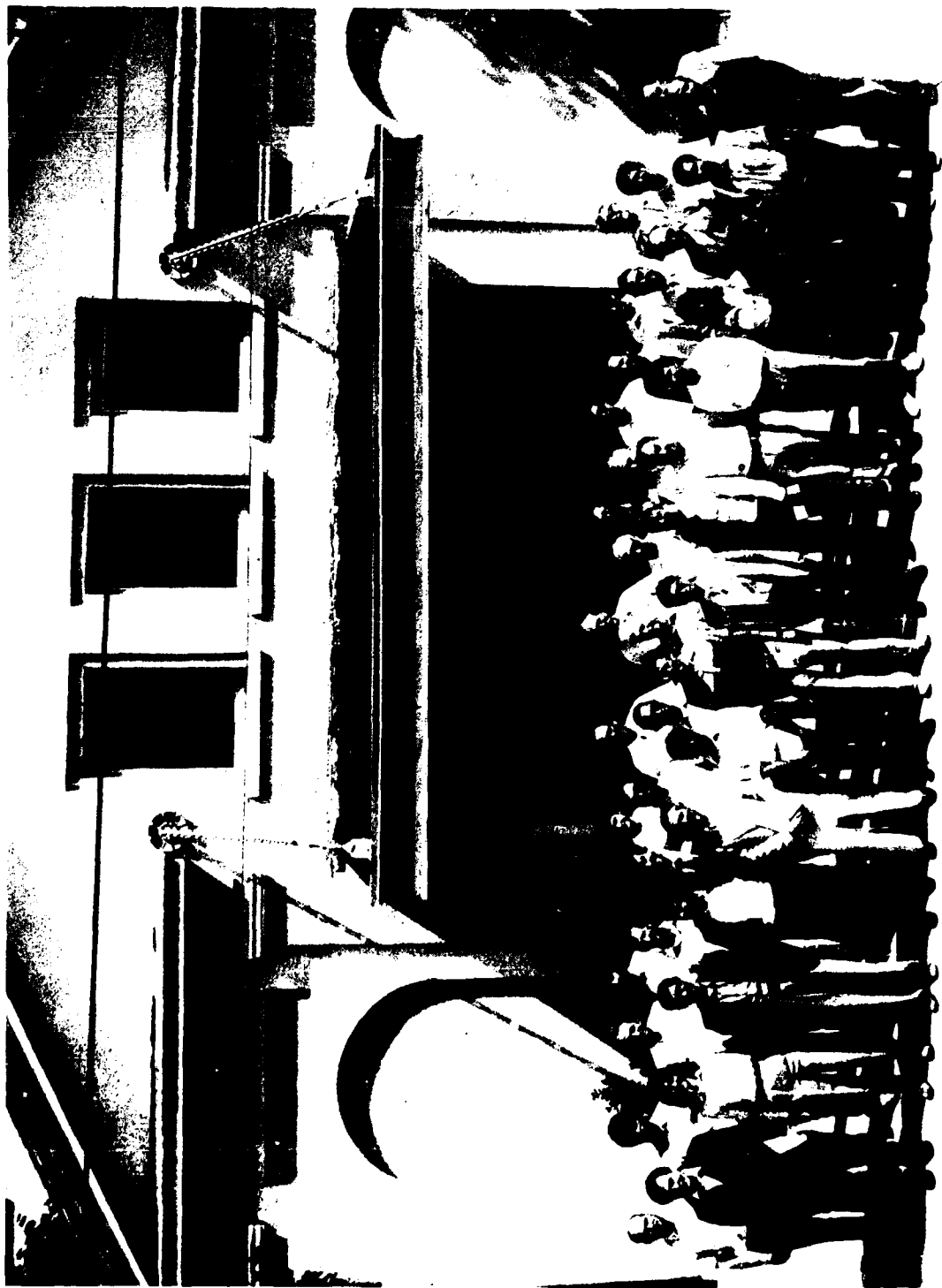
Blank

**1988 CRDEC Scientific Conference
on Obscuration and Aerosol Research**

Pictured left to right are:

.

First Row	Second Row	Third Row
Steve Arnold	Arlon Hunt	Lorcan Folan
Kelly Thieme	Bill White	Leland Pierce
Chia-Ren Hu	Ed Fry	Ira Goldberg
Tony Pluchino	Ron Pinnick	Janon Embury
Orazio Sindoni	Gerard Jennings	Bob Keese
Abhijit Biswas	Kirk Fuller	Jay Eversole
Roger Johnston	Ru Wang	Craig Herzinger
Ignatius Tang	Herschel Weil	Melvin Lax
William Bickel	Richard Frickel	
William Whitten	Burt Bronk	
Maurice Jarzembski	Ed Stuebing	
Vandana Srivastava	Ezekiel Bahar	
Dennis Flanigan	David Krueger	
George Kattawar	Elmer Engquist	
John Stephens		

Photograph taken Friday, June 24, 1988

Appendix A

Blank

LIST OF 1988 ATTENDEES

WILLIAM ACKER
(203) 432-4235
YALE UNIVERSITY
APPLIED PHYSIC LABORATORY
P.O. BOX 2157, YALE STATION
NEW HAVEN, CT 06520

DENNIS ALEXANDER
(402) 472-3091
UNIVERSITY OF NEBRASKA-LINCOLN
MECHANICAL ENGINEERING DEPT.
255 WSEC
LINCOLN, NE 68588-0525

MARK ALTHOUSE
671-3358
COMMANDER US ARMY
CRDEC
APG, MD 21010-5423

STEPHEN ARNOLD
POLYTECHNIC INSTITUTE OF NEW YORK
PHYSICS DEPT.
333 JAY ST.
BROOKLYN, NY 11201

EZEKIEL BAHAR
(402)472-1966
UNIVERSITY OF NEBRASKA-LINCOLN
ELECTRICAL ENGINEERING DEPT.
209N WSEC
LINCOLN,NE 68588-0511

JOHN BARTON
UNIVERSITY OF NEBRASKA-LINCOLN
MECHANICAL ENGINEERING DEPT.
255WSEC
LINCOLN, NE 68588-0525

WILLIAM BICKLE
(602) 621-2524
UNIVERSITY OF ARIZONA
PHYSIC PASCKEL
TUSCON, AZ 85721

A. BISWAS
NEW MEXICO UNIVERSITY
COLLEGE OF ARTS AND SCIENCES
BOX 3D
LAS CRUCES, NM 88003

MAX BLEIWESS
COMMANDER USA PGP
DUGWAY, UT P .2

JEROLD BOTTIGER
COMMANDER US ARMY
CRDEC
APG, MD 21010-5423

JAMES BROCK
(512) 471-3348
UNIVERSITY OF TEXAS
CHEMICAL ENGINEERING DEPT.
AUSTIN, TX 78712

BURT BRONK
(301)671-3741
COMMANDER US ARMY
CRDEC
APG, MD 21010-5423

JAMES BROWN
(303) 273-3835
COLORADO SCHOOL OF MINES
PHYSICS DEPT.
GOLDEN, CO 80401

HUGH CARLON
COMMANDER US ARMY
CRDEC
APG, MD 21010-5423

SHIRISH CHITANVIS
(505) 667-0956
LOS ALAMOS, NATIONAL LABORATORY
T-DOT MS-P371
LOS ALAMOS, NM 87545

T. CLEARY
UNIVERSITY OF MARYLAND
CHEMICAL ENGINEERING DEPT.
COLLEGE PARK, MD 20742

ARIEL COHEN
HEBREW UNIVERSITY
ATMOSPHERIC SCIENCES DEPT.
JERUSALEM
ISREAL   AIR MAIL

LEN COHEN
(215) 895-2710
DREXEL UNIVERSITY
PHYSICS & ATMOSPHERIC SCIENCES DEPT
PHILADELPHIA, PA 19104

EDWIN DAUBER
(301) 392-3300
W. L. GORE & ASSOCIATES
P.O. BOX 1100
ELKTON, MD 21921

ROBERT DOHERTY
COMMANDER US ARMY
CRDEC
APG, MD 21010-5423

KENNETH EVANS
COMMANDER US ARMY
CRDEC
APG, MD 21010-5423

JAY EVERSOL
COMMANDER NAVAL RESEARCH LAB
WASHINGTON, DC 20375

RICHARD FARRELL
(301) 953-6236
JOHN HOPKINS UNIVERSITY
APPLIED PHYSICS LAB
JOHN HOPKINS ROAD
LAUREL, MD 20707

DENNIS FLANNIGAN
COMMANDER US ARMY
CRDEC
APG, MD21010-5423

LORCAN FOLAN
POLYTECHNIC INSTITUTE OF NEW YORK
PHYSICS DEPT.
333 JAY ST.
BROOKLYN, NY 11201

DAVID FREUD
(301) 792-6260
JOHN HOPKINS UNIVERSITY
APPLIED PHYSICS LAB
LAUREL, MD 20707

ROBERT FRICKEL
COMMANDER US ARMY
CRDEC
APG, MD21010-5423

EDWARD FRY
(409) 845-7717
TEXAS A&M UNIVERSITYS
PHYSICS DEPT.
COLLEGE STATION, TX 77843

Appendix B

KIRK FULLER   E. GAUZE
(505) 678-5634   HEBREW UNIVERSITY
US ARMY ATMOSPHERIC SCIENCES LAB   ATMOSPHERIC SCIENCES DEPT.
WHITE SANDS, NM 88002   JERUSALEM 91904
                                         ISREAL   AIR MAIL

TOM GURBACH   GREG HALL
(805) 373-4276   UNIVERSITY OF KENTUCKY
ROCKWELL INTERNATIONAL   CHEMICAL ENGINEERING
T. GURBACH C/O I. GOLDBERGE   161 ANDERSON HALL
1049 CAMINO DOS RIOS   LEXINGTON,KY 40506-0046
THOUSANDS OAKS, CA 91360

DICK HARACZ   CECIL HESS
DREXEL UNIVERSITY   (714) 553-0688
PHYSICS & ATMOSPHERIC SCIENCES DEPT.   METROLASER
PHILADELPHIA, PA 19104   18004 SKYPARK BLVD, #254
                                         IRVINE, CA 92714-6428

CHIA-REN HU   PO HU
TEXAS A&M UNIVERSITY   CITY COLLEGE OF NEW YORK
PHYSICS DEPT   PHYSICS DEPT
COLLEGE STATION, TX 77843   CONVENT AVE & 137 STREET
                                         NEW YORK, NY 10031

DONALD HOFFMAN   ARLON HUNT
(602) 621-4804   (415) 486-5370
UNIVERSITY OF ARIZONA   LAWRENCE BERKELEY LAB
PHYSICS DEPT   90-2024
TUSCON, AZ 85721   BERKELEY, CA94720

MAURICE JARZEMBSKI   S. G. JENNINGS
(405) 321-0615   0113539124411
THE UNIVERSITY OF OKLAHOMA   UNIVERSITY COLLEGE GALWAY
SCHOOL OF METEROLOGY   PHYSICS DEPT.
200 FELGAR ST/ RM 219   GALWAY
NORMAN, OK 73019   IRELAND   AIR MAIL

ROGER JOHNSTON   GEORGE KATTAWAR
(505)667-2730   (409) 845-1180
MS M880   TEXAS A&M UNIVERSITY
LOS ALAMOS NATIONAL LAB   PHYSICS DEPT
LOS ALAMOS,NM 87545   COLLEGE STATION TX 77843

Appendix B

379

ROBERT KEESEE
(814) 863-3574
PENN STATE UNIVERSITY
CHEMICAL ENGINEERING DEPT
UNIVERSITY PARK, PA 16802

RALPH E. KLEINMAN
(302) 451-2266
UNIVERSITY OF DELAWARE
MATHEMATICS DEPT
NEWARK, DE 19716

JAMES KLETT
(505) 522-4381
PAR ASSOC.
1741 POMONA DR.
LAS CRUCES, NM 88001

WALTER KOSKI
(301) 338-7418
JOHN HOPKINS UNIVERSITY
CHEMISTRY DEPT
BALTIMORE, MD 21218

JOHN LATHAM
061-236-3311
U.M.I.S.T.
PURE & APPLIED PHYSICS DEPT
P.O. BOX 88
MANCHESTER, M60 IQD
ENGLAND   AIR MAIL

MELVIN LAX
(212) 690-6864
CITY COLLEGE OF NEW YORK
PHYSICS DEPT
NEW YORK, NY 10031

DAVID LEACH
(203)432-4234
YALE UNIVERSITY
APPLIED PHYSICS
P.O. BOX 2157, YALE STATION
NEW HAVEN, CT 06520

HOWARD LITTMAN
(518) 276-6039
RENSSELAER POLYTECHNICAL INSTITUTE
CHEMICAL ENGINEERING DEPT
123 RICKETTS BUILDING
TROY, NY 12180-3590

YUSHEIM MA
PENNSYLVANIA STATE UNIVERSITY
ENGINEERING SCIENCE & MECHANICS DEPT
227 HAMMOND BUILDING
UNIVERSITY PARK, PA 16802

ANDREW MACKENZIE
(301) 278-5221
COMMANDER
US ARMY TECOM
APG, MD 21005-5055

JOHN MAJESKI
PM/ SMOKE
USA TECOM
APG, MD 21005-5005

MORRIS H. MORGAN
(518) 276-6059
RENSSELAER POLYTENIC INISTITUTE
CHEMISTRY DEPT
TROY, NY 12180-3590

TUNG NGUYEN
PHILIP MORRIS USA
P.O. BOX 26583
RICHMOND, VA 23261-6583

ELWIN PENSKI
(301) 671-3953
COMMANDER US ARMY
CRDEC
APG, MD 21010-5423

Appendix B

380

LELAND PIERCE
UNIVERSITY OF MICHIGAN
EECS DEPT.
ANN ARBOR, MI 48109-2122

RONALD PINNICK
ATMOSPHERIC SCIENCES LAB
WHITE SANDS, NM 88002

ANTONIO (TONY) PLUCHINO
(213) 648-7060
AEROSPACE CORPORATION
P.O. BOX 92957, BLDG A 6-1647
LOS ANGELES, CA 90009

ASIT RAY
(606)257-7999
UNIVERSITY OF KENTUCKY
CHEMICAL ENGINEERING DEPT
161 ANDERSON HALL
LEXINGTON, KY 40506-0046

CHUN HSUN RIN
COMMANDER US ARMY
CRDEC
APG, MD 21010-5423

GLENN RUBEL
671-2395
COMMANDER US ARMY
CRDEC
APG, MD 21010-5423

MARK SEAVER
NAVAL RESEARCH LAB
CODE 6540
WASHINGTON, DC 20375

DAVID SHAW
(716(636-3112
STATE UNIVERSITY OF NEW YORK
ELECTRICAL ENGINEERING DEPT
330 BONNER HALL
BUFFALO, NY 14260

ORAZIO SINDONI
671-4256
COMMANDER US ARMY
CRDEC
APG, MD 21010-5423

MAREK SITARSKI
(304) 291-4834
US DEPARTMENT OF ENERGY
MORGANTOWN ENERGY TECHNOLOGY CTR.
PO BOX 880
COLLINS FERRY ROAD
MORGANTOWN, WV 26505

HOWARD SMALLEY
301 278-5355
PM SMOKE/OBSCURANTS
APG, MD 21005

ALAN SNELSON
312 567-4260
ILLINOIS INSTITUTE OF TECHNOLOGY
RESEARCH INSTITUTE
10 WEST 35TH STREET
CHICAGO, IL 60616

VANDANA SRVIVASTAVA
405 321-0615
THE UNIVERSITY OF OKLAHOMA
SCHOOL OF METEOROLOGY
200 FELGARR ST, RM 219
NORMAN, OKLAHOMA 73019

JOHN STEPHENS
505 667-7363
LOS ALAMOS NATIONAL LAB
CHM-2 M/S C-348
LOS ALAMOS, NM 87545

Appendix B

BASIL STOYANOV
301 953-6261
JOHN HOPKINS UNIVERSITY
JOHN HOPKINS APPLIED PHYSICS LAB
LAUREL, MD 20707

IGNATIUS TANG
BROOKHAVEN NATIONAL LAB
BLDG. 815
UPTON, NY 11973

K. THEIME
TEXAS A&M UNIVERSITY
PHYSICS DEPT
COLLEGE STATION,TX 77843

LEAH TRUITT
COMMANDER US ARMY
CRDEC
APG, MD 21010-5423

T.H. TSANG
606 257-2825
UNIVERSITY OF KENTUCKY
CHEMICAL ENGINEERING DEPT
LEXINGTON, KENTUCKY 40506

W.VAN DE MERWE
LASER BIO PHYSICS
UNIFORM SERVICES OF THE HEALTH SCI.
4301 JONES BRIDGE RD.
BETHESDA, MD 20814-4799

BOB VIMSON
BUREAU OF MINDS
COCHRANS RD.
PO BOX 18070
PITTSBURG, PA 15236

RU. T. WANG
904-392-5450
UNIVERSITY OF FLORIDA
SPACE ASTRONOMY LAB
1810N.W. 6TH ST.
GAINESVILLE, FL 23601

HERSCHEL WEIL
313-764-0500
UNIVERSITY OF MICHIGAN
ELECTRICAL ENG. & COMP SCI DEPT
EECS BUILDING
ANN ARBOR, MI 48109-2122

J. WHITE
COMMANDER US ARMY
CRDEC
APG, MD 21010-5423

W.E. WHITE
TEXAS A&M UNIV.
PHYSICS DEPT.
COLLEGE STATION, TX 77843-4242

BILL WHITTEN
615-574-4921
OAK RIDGE NATIONAL LAB
ANALYTICAL CHEMISTRY DIVISION
MS 6142
PO BOX 2008
OAK RIDGE, TN 37831

DAVID WIELICZKA
UNIV. OF MISSOURI-KANSAS CITY
PHYSICS DEPT
1110 E. 48TH ST.
KANSAS CITY MI.64110

DONALD WOODBURY
US ARMY LAB COM
2800 POWDER MILL RD
ADELPHI,MD 20783

Appendix B

ANDREW ZARDECKI
505-667-0954
LOA ALAMOS NATIONAL LAB
LOS ALAMOS, NM 87545

JIAN-ZHI ZHANG
203-432-4235
YALE UNIVERSITY
APPLIED PHYSICS
P.O. BOX 2157, YALE STATION
NEW HAVEN, CT 06520

Appendix B

Blank

APPENDIX C

CONFERENCE AGENDA

AGENDA

1988 CRDEC SCIENTIFIC CONFERENCE

ON

OBSCURATION AND AEROSOL RESEARCH

21-24 JUNE 1988

Bldg. E4810 (Conference Center/Post Theater) Edgewood Area

TUESDAY, 21 JUNE

8:00 Registration Opens

8:45 Opening of Conference

Dr. Edward W. Stuebing, *Aerosol Science Coordinator*

Welcome

William H. Collins, *Dep. Director of Research, CRDEC*

Administrative Announcements

Elmer Engquist, *Conference Administrator*

I. AEROSOL DYNAMICS

Moderator: *Glenn Rubel*

A. Fundamental Properties of Single Droplets

9:00 Glenn Rubel (CRDEC), Measurement of the Solubility of Methyl Salicylate in Aqueous Droplets [15]

9:20 Asit Ray and Annick Souyri (U.Ky), Dynamics of Evaporation and Growth of Glycerol Droplets in Humid Environments [20]

9:45 BREAK

10:15 Asit Ray and Jeff Lee (U.Ky), Ultrasensitive Method for the Measurement of the Evaporation Rate of DOP Droplets [20]

10:40 Elwin Penski, *Helen Walker* (CRDEC), Sessile Droplet, Humectants and Evaporation Methodology [15]

B. Fundamental Properties of Aerosols

11:00 Tate Tsang (U.Ky), Evaporation of Polydisperse Aerosols [20]

11:25 James Brock (U.Tx), Particle Formation During Explosions [20]

11:50 LUNCH

1:30 I. Gallily and E. Gauss (Hebrew U.), The Coagulation and Dispersion of Nonspherical Aerosol Particles in a Turbulent Field II [20]

1:55 John Latham (UMIST— England), Mixing Processes in Clouds [20]

II. AEROSOL CHARACTERIZATION METHODS

Moderator: *Jerold Bottiger*

2:15 Cecil Hess (Spectron Development Labs), Particle Sizing [15]

2:35 David Shaw (SUNY), Investigations of Fibrous Aerosols Using a Digital Image System [15]

2:55 BREAK

3:25 David Shaw (SUNY), Smoke Clearing Technology [15]

385

3:45 Tom Ceary, James Gentry (University of Maryland), Sizing of Soot Particles [15]

4:05 Marv'n Querry (University of Missouri – Kansas City), Optical Properties of Selected Materials [15]

4:25 Roger Johnston (LANL), Interferometry with a Two-frequency Laser [15]

WEDNESDAY, 22 JUNE

III. NONLINEAR EFFECTS AT HIGH ENERGY

Moderator: Orazio I. Sindoni

08:30 R. Lacy, S. Amimoto, R. Hofland (Aerospace Corporation), Pulsed Laser Interaction with Materials in Vacuum [15]

08:50 J. R. White, J. E. Rice, R. L. Kremens (ORDEO) High Energy Laser Interaction with Particulate Clouds [15]

09:10 D. R. Alexander, D. Poulain, J. P. Barton, S. A. Schaub, J. Zhang (University of Nebraska –Lincoln), Nonlinear Effects of Excimer Laser Radiation with Solid Particles in a Vacuum [15]

09:30 R. S. Dingus, E. K. Stover, L. Montierk (LANL) Modeling of the Response of Particles in Vacuum to High Energy Laser Exposure [15]

09:50 BREAK

10:20 M. Lax, Po Hu, B. Yudanin (City College of New York), Test of the Goudinov Hydro–algorithm with Heat Source. [20]

10:4. J. R. Brock, J. C. Carls (University of Texas), Comparison Between Experiments and Theory for High Energy Laser Beam—Particle Interactions [20]

11:10 S. M. Chitanvis (Los Alamos National Laboratory), High Energy Laser Interactions with Transparent Aerosols [15]

11:30 LUNCH

01:00 J. P. Barton, D. R. Alexander, and S. A. Schaub (University of Nebraska), Experimental and Theoretical Analysis of Liquid Droplets Falling Through a Focused Laser Beam [15]

01:20 C. F. Wood, L. A. Melton, and R. K. Chang (Yale University), Temperature Mapping within a CO_2 Laser Heated Droplet by Excimer—Monomer Fluorescence [15]

1:40 A. Zardeki, R. L. Armstrong (LANL, and NMSU), Plasma Dynamics in Metallic Vapors Produced by Pulsed Lasers [15]

2:00 M. Sitarski (Clarkson University, c/o DOE/METC), Vaporization Dynamics of a Small Multiphase Droplet Exposed to High Temperature Thermal Radiation Fields [20]

IV. POSTER PROGRAM

Posters are identified by proper session topic symbol (I, II, III, IV, V) and in sequence of preview presentations.

A. Poster Previews

III. D. H. Leach, J. Zheng, and R. Chang (Yale University), Lifetime Measurement of Photons Trapped within a Droplet

III. W. P. Acker, D. H. Leach, and R. Chang (Yale University), Nonlinear Optical Sum Frequency Generation in Single Droplets

V W. White, E. Fry and G. W. Kattawar, (Texas A & M), Scattering of Femtosecond Pulses from Dielectric Spheres

V Ru T. Wang, (U. of Florida) Experimental Microwave Scattering from Dumbbells and Spheroids

V D. Krueger, (Colorado State) Mechanical Surface Waves on Twenty Micron Droplets

OVERVIEW AND DISCUSSION

10:00 Dr. Edward W. Stuebing (CRDEC), Overview of Aerosol Research Program and Discussion of Directions for Future Research in the CRDEC Aerosol Science Program

11:40 LUNCH

V. OPTICAL PROPERTIES OF AEROSOLS

Moderators: *Burt V. Bronk and Robert H. Frickel*

A. Scattering by Single Particles and Small Aggregates

1:20 *D. Freund, R. Farrell* (The Johns Hopkins Applied Physics Lab), Near Field Variational Principal: Scattering from Spheres [15]

1:40 *G. H. Rose, Chia-Ren Hu, G. W. Kattawar* (Texas A&M), Calculations of Time-Resolved Scattering of Femtosecond Pulses from Dielectric Spheres [15]

2:00 *W. Van de Merwe* (USUHS), D. H. Huffman (University of Arizona), and B. V. Bronk (CRDEC), Can Reproducibility be Established for S_{34} Scattering in a Microbial System? [15]

2:20 *R. D. Haracz, L. D. Cohen, A. Cohen and A. Presley* (Drexel University), Scattering of Light from a Dielectric Target Including Target Self-interaction [15]

2:40 *Ariel Cohen, L. D. Cohen and R. D. Haracz* (Drexel University), Single and Double Scattering from a Spiral Composed of Long Cylinders [15]

3:00 BREAK

3:20 *Ru T. Wang*, (University of Florida), Application of a New Theory to Rainbows, Glory and Resonance [15]

▽   *J.P. Barton, D.R.Alexander and S.A.Schaub* (University of Nebraska—Lincoln) Internal and Near Surface Electromagnetic Fields for a Spherical Particle in a Focused Laser Beam

▽   M. Althouse, (CRDEC) "Spectral Degradation Due to Scattering in Particulate Samples".

▽   L. Pierce and H. Weil, (U. of Michigan) Resonances and Near and Internal Fields of Spheres with Cavities and Coagulated Spheres

▽   K. Fuller Orientation and Angular Dependent Scattering from Ensembles of Spheres

B. Poster Session

3:00 – 3:30 Posters Open (Seminar Center)

4:00 *Nonlinear effects working group meeting in auditorium*

THURSDAY, 23 JUNE

8:30 *R. G. Pinnick, A. Biswas, H. Latifi, R. L. Armstrong, E. Gregan, V. Srivastava* (ASL), Stimulated Raman Scattering From Micron Sized Drops; Angular Scattering Characteristics [15]

8:50 *Jian-Zhi Zhang and R. K. Chang* (Yale University), Droplet Shape Distortions by The electrostrictive Effect of High Energy Lasers [15]

9:10 *A. Biswas, H. Latifi, R. L. Armstrong, P. Chŭlek, E. Gregan, G. Fernandez, R. Pinnick* (ASL), Stimulated Raman Scattering from Micron Sized Droplets; Time Resolved Measurements [15]

9:30 BREAK

3:40 O. I. Sindoni (CRDEC), F. Borghese, P. Denti, R. Saija and G. Toscano (University of Messina), Computations of the Absorption Coefficient of a Dispersion of Clusters –– Comparison of Computed Data with Experimental for Small Clusters [15]

4:00 K. Fuller (U. S. Army Atmospheric Sciences Lab), The Effect of Cooperative Scattering on Morphology–Dependent Resonances of Spheres [15]

4:20 K. Thieme and E. S. Fry (Texas A&M), Mueller Matrix Measurements for Sphere Aggregates [15]

FRIDAY, 24 JUNE

V. OPTICAL PROPERTIES OF AEROSOLS (continued)

Moderators: Robert H. Frickel and Burt V. Bronk

C. Multiple Scattering and Radiative Transfer

08:30 V. K. Varadan and V. V. Varadan (Pennsylvania State University), Multiple Scattering of Waves in Chiral Composites [15]

08:50 Ezekiel Bahar, (University of Nebraska – Lincoln), Non–Specular Scattering by Irregular Layered Media –– Full Wave Approach [15]

09:10 W. S. Bickel, D. Abromson, Shu–Chang Chiao, P. Bandu, Sung–Yann Shu and T. Wentzel (University of Arizona (Tucson)), Polarized Light Scattering Mueller Matrix Elements for Some Interesting Scatterers [15]

09:30 Yushieh Ma (The Pennsylvania State University), Pulse Propagation in Discrete Random Media [15]

09:50 Yushieh Ma (The Pennsylvania State University), Wave Propagation in Inhomogeneous Media Containing Randomly Oriented Nonspherical Scatterers [15]

10:10 BREAK

B. Single Particle Spectroscopy

10:40 L. M. Folan and S. Arnold (Polytechnic University of New York), Aerosol Particle Ellipsometry [15]

11:00 S. Arnold, L. M. Folan, K. M. Leung and A. Pluchino (Polytechnic University of New York), Aerosol Bistability as a Tool for Spectroscopy [15]

11:20 J. R. Brock, J. C. Carls and G. Monciuais (University of Texas (Austin)), Time–Resolved Raman Spectroscopy of Reactions in Single Particles [15]

11:40 Ignatius Tang (Brookhaven National Lab), Single–Particle Raman Spectroscopy [16]

Appendix C